ASME
SETTING THE STANDARD

Journal of Fluids Engineering

Published Monthly by ASME

VOLUME 129 • NUMBER 4 • APRIL 2007

Transactions of the ASME, Journal of Fluids Engineering (ISSN 0098-2202) is published monthly by The American Society of Mechanical Engineers, Three Park Avenue, New York, NY 10016. Periodicals postage paid at New York, NY and additional mailing offices.
POSTMASTER: Send address changes to Transactions of the ASME, Journal of Fluids Engineering, c/o THE AMERICAN SOCIETY OF MECHANICAL ENGINEERS, 22 Law Drive, Box 2300, Fairfield, NJ 07007-2300.
CHANGES OF ADDRESS must be received at Society headquarters seven weeks before they are to be effective. Please send old label and new address.

EDITORIAL

TECHNICAL PAPERS

(Contents continued on inside back cover)

This journal is printed on acid-free paper, which exceeds the ANSI Z39.48-1992 specification for permanence of paper and library materials. ♾™
♻ 85% recycled content, including 10% post-consumer fibers.

Journal of Fluids Engineering Volume 129, Number 4 APRIL 2007

The ASME Journal of Fluids Engineering is abstracted and indexed in the following:

Applied Science & Technology Index, Chemical Abstracts, Chemical Engineering and Biotechnology Abstracts (Electronic equivalent of Process and Chemical Engineering), Civil Engineering Abstracts, Computer & Information Systems Abstracts, Corrosion Abstracts, Current Contents, Ei EncompassLit, Electronics & Communications Abstracts, Engineered Materials Abstracts, Engineering Index, Environmental Engineering Abstracts, Environmental Science and Pollution Management, Excerpta Medica, Fluidex, Index to Scientific Reviews, INSPEC, International Building Services Abstracts, Mechanical & Transportation Engineering Abstracts, Mechanical Engineering Abstracts, METADEX (The electronic equivalent of Metals Abstracts and Alloys Index), Petroleum Abstracts, Process and Chemical Engineering, Referativnyi Zhurnal, Science Citation Index, SciSearch (The electronic equivalent of Science Citation Index), Shock and Vibration Digest, Solid State and Superconductivity Abstracts, Theoretical Chemical Engineering

Journal of Fluids Engineering

Editorial

Special Issue on the Magnetic and Electric Field Effects at the Micro- and Nano-Scale Systems and Flows in Material Processing

This collection of selected papers is drawn from those presented at the IMECE 2005 in Orlando, Florida at the Symposia on "Rheology & Fluid Mechanics of Non-Linear Materials" and "Electric and Magnetic Phenomena in Micro- and Nano-Scale Systems" sponsored by the Fluids Engineering Division and the Materials Division as well as the Symposium on "Flows in Manufacturing Processes" held at the 2nd Joint US-European Fluids Engineering Summer Meeting in Miami, Florida in July 2006.

The first group of eight papers in this collection investigates electric and magnetic effects in flows at the micro and nano scales. The next group of seven papers on flows in manufacturing processes and complex industrial flows at the macro scale deals with issues relevant to paper making, coating, mixing, high-speed water jets, drag reduction, and heat transfer, respectively.

At very small scales, electric and magnetic field effects, such as dielectrophoresis and electro-osmosis are gaining greater focus as important tools in flow control, and magneto-electro-microfluidics is increasingly viewed as one of the most promising techniques for separating, controlling, and manipulating fine particles, cells, and micro-organisms in flowing suspensions. The issue is gaining in magnitude as sophisticated micro-fabrication technologies make miniaturization of a range of analytical devices possible, all requiring effective actuation mechanisms. Effective and rapid mixing of liquids in small scale devices is essential in many applications, such as hand-held pollution monitoring devices, drug delivery, DNA analysis and sequencing, pheromone synthesis in micro bio-reactors, and biological and chemical agent detection. However, mixing in micro-devices is a challenge as low Reynolds number flows encountered in these systems are in general not turbulent, and diffusion dominates mixing processes. Improving the efficiency of mixing through diffusion alone in the absence of turbulence is impractical. For instance, the diffusion coefficients of large molecules such as proteins and DNA are of the order of $\mathcal{O}(10^{-10})$ m^2/s and even smaller. Hence, the mixing time can be prohibitively long, not to speak of the mixing length. A highly efficient fast micro-level mixer will greatly benefit a number of critical applications, such as immunological studies, DNA hybridation, and cytometric analysis. In this context, flow manipulation through judicious use of magnetic and electric fields or with actuators and internal micro-pumps becomes a central issue in applications. It should be noted that the bulk motion of electrolyte solutions driven by electric fields, electro-osmotic flows, requires large electrostatic potentials. In contrast, magnetic field driven effects do not, and may be preferable in some applications.

Two novel ways to achieve effective flow manipulation are through the organized motion of particles in a controllable manner and through the phenomenon of electrowetting. In the former, the motion of suspended magnetic or paramagnetic particles are driven by the application of magnetic fields, leading to the formation of controllable self assembling aggregates. The latter takes advantage of the dominance of surface tension at the micro scale and utilizes the modulation of surface tension as an effective actuation mechanism in micro-devices. Electrowetting was first advanced by Berge in France in the early 1990s. It is based on the modification of the wetting property of a liquid droplet resting on a dielectric surface by an external electric field set up when a voltage is applied between the liquid droplet and a counter-electrode beneath the solid dielectric layer. Low voltage, large actuation amplitude, and high reversibility make electrowetting a promising actuation technique for MEMS devices. Micro-pumps driven by electro-hydrodynamic and electro-osmotic effects are also the focus of intensive research to achieve effective mixing and flow manipulation. They tend to have a simpler design and are easily controllable, as opposed to diaphragm micro-pumps, which are more complicated actuation mechanisms and are affected by fatigue. These issues are investigated in the first four papers. The dynamic self-assembly of neutrally buoyant particles rotating in a plane in a viscous fluid driven by a magnetic field is studied by Climent et al. The electrowetting actuation of droplets of mercury on dielectric insulation films is the focus of the investigation of Wan et al. The characteristics of a Y-form hybrid electro-kinetic-passive micro-mixer are presented in the work of Wang et al. The concept and operation of a novel electro-hydrodynamic menisci pump is introduced by Herescu and Allen.

Magnetic fluids are suspensions of fine stable single domain magnetic particles in non-conducting fluids. They are not found in nature and must be artificially synthesized. The particles are coated with a surfactant and Brownian motion keeps the fine particles from settling under gravity. They lead to innovative applications and have been used in seals, as dampers in steeper motors and shock absorbers, to cool loud-speaker coils, as a lubricant in various machines, and in non-invasive circulatory measurements as a tracer of blood flow. There are two distinct families of magnetic fluids: ferrofluids and magnetorheological (MR) fluids. Conventional MR fluids date back to their discovery in 1948 by Rabinow right after electrorheological fluids in 1947. Ferrofluids are colloidal suspensions in a non-conducting liquid carrier whose surfactant stabilized and permanently magnetized magnetite particle constituents are 10–20 nm in size. In some ways they behave like a paramagnetic gas of high permeability. The Cauchy body stress field is asymmetric and the medium is anisotropic through magnetization. A general theory for ferrofluids with internal rotation and vortex viscosity, particle-particle interaction, magnetization relaxation, and couple stresses has been only recently formulated by Rosensweig in 2004. In contrast, magnetorheological fluids are suspensions of micrometer-sized magnetic particles dispersed in a carrier fluid such as a mineral or silicon oil. Rheological and thermal transport properties of MR fluids can be changed reversibly through the application of an external magnetic field, which explains their appeal as fluid clutches for automotive and sports equipment applications. The formation of chainlike structures under a strong magnetic field increases the thermal conductivity of the MR fluid several-fold, thus dissipating the heat energy resulting from viscous work. Due to their constitutive structure, the response of a MR fluid to a magnetic field is quite different from that of a ferrofluid. A new generation of MR fluids that offer

potentially unparalleled performance is based on carbon nanotubes (CNTs) magnetized through hybridization with other magnetic materials either encapsulated or incorporated within the walls or deposited on the outer surface of the nano-tube. Successful magnetization makes CNT manipulation possible at very small scales by magnetic actuation, thus creating a new class of MR fluids that incorporates the highly desirable electrical, thermal, and mechanical properties of CNTs. The papers by Chaves et al. and Lloyd et al. investigate aspects of ferrofluids and MR fluids, respectively, and the work of Samouhos and McKinley explores the properties and feasibility of CNT based MR fluids. A potentially promising application of strong magnetic fields concerns oxygen separation from air. Evidence indicates that the efficiency of fuel cells is increased by pure oxygen or oxygen enriched air. In the last paper concerning magnetic effects, Asako and Suzuki study by Monte Carlo simulation the characteristics of oxygen separation and enrichment from atmospheric air.

The turbulent flow of the flexible fiber suspension in the paper-making production line determines the distribution, the orientation, and the aggregation of the fibers in the suspension, thus affecting the properties and the quality of the final product. The mechanical properties of the manufactured paper are strongly dependent on the fiber orientation and on the degree of the uniformity of the distribution of cellulose fibers suspended in water with mass concentration typically below 1% used in paper making. The word "floc" refers in industry terminology to groups of fibers clumped together, which may break and self-assemble again during the course of processing depending on whether they are hard or soft flocs. Flocculation of fibers is widely observed in paper-making industries, and floc strength and size as a function of added chemicals and of applied shear are pivotal factors in designing the process. Turbulence is the most important mechanism behind the formation and destruction of fiber flocs. Knowledge of the flexible fiber suspension behavior, including fluid-fiber and fiber-fiber interaction, and the physics of floc formation and destruction are very helpful in designing any unit operation in the paper-making process. In addition, the lamellas used in the head box to damp out turbulence create shear layers affecting the orientation and the concentration of the fibers, which, close to the solid boundary are likely to pole vault and perform Jeffrey orbits. The papers dedicated to paper-making issues in this collection present dynamic simulations of viscoelastic fibers, and introduce a multiscale numerical simulation of the turbulent suspension flow using a hybrid method between direct numerical simulations and large eddy simulations that takes into account fibrous structure interactions (Arezou et al.), and an experimental investigation of the orientation and concentration of fibers suspended in a shear flow over a solid wall (Carlsson et al.).

Industrial processes such as paper and photographic film manufacturing, wire coating, and the iron and steel industries use a coating technique based on the deposition of a very thin liquid film on a solid substrate. Hot-dip galvanization is widely used in steel industry to coat steel strips with a thin layer of zinc against oxidation. Coating thickness and uniformity is controlled by the jet wiping technique also referred to as air-knife coating. The technique based on two-dimensional high-speed gas jets impinging on the liquid layer on the moving substrate yields a thin and even coating of constant thickness. However, an instability called splashing, which occurs downstream of the gas jet nozzles, limits productivity increases by limiting the strip speed. Gosset and Buchlin present a new analysis of air-knife coating and derive the optimum conditions to improve the efficiency.

Positive displacement gear pumps consume relatively more energy and are not used on an industrial scale for mixing and blending of additives. However, they are widely used for viscous flow metering in both plastics and food manufacturing. Thus, although the installation of a new gear pump for mixing and blending may not be cost effective, if there is one already in use for metering purposes, to use it for mixing would be advantageous. Numerical investigation of the mixing process in gear pumps requires a boundary fitted mesh with automatically created and agglomerated cells to maintain grid quality and to accommodate changes in the shape of the base geometry. Strasser investigates numerically the performance of an existing in-service industrial-scale gear pump in blending additives.

High-speed water jets are proven to be feasible replacements for cutting tools, be it surgical scalpels or rock cutting. Among the myriad of applications in various industries, the capability of high-speed water jets and of water/ice slurries to perfectly clean contaminated surfaces in a relatively inexpensive and environmentally sound way is particularly noteworthy. For instance, paint can be neatly blasted off any surface, say a metallic can, without any damage to the surface. Surface finish describes the exterior features of the surface such as roughness, texture, and pits, while surface integrity defines the condition of a surface layer, properties such as micro-structural transformations, hardness alteration, residual stress distribution, and the depth of induced plastic deformation. Manufacturing processes on material surfaces are controlled by surface finish and integrity. Chillman et al. evaluate and discuss the surface characteristics induced by different jet conditions.

Drag reduction by polymeric additives helps to reduce the cost of pumping in pipelines, to stabilize and increase the range of jets in fire fighting, to prevent cavitation in turbo machines, to reduce noise, and to save energy in ship and submarine propulsion, to name but a few of the applications. The physics of drag reduction is not completely understood and the root cause remains controversial. Small concentrations of anisotropic additives drastically reduce the efficiency of the transversal transport of momentum by turbulent fluctuations. The stress anisotropy created translates into a substantial decrease of the friction factor. The merits of the competing theories behind the physics, the role of stress anisotropy due to polymer extension versus elasticity in governing drag reduction, is still debated. Lumley was the first to suggest that the phenomenon has less to do with the viscous sublayer, and that an effective viscosity increase of the turbulent flow caused by the extensional viscosity of additives is responsible for the phenomenon. On the other hand, De Gennes and Joseph, among others, argue that polymer elasticity governs drag reduction. Elastic energy is transported in the boundary layer thanks to the relaxation time. The article by Cunha and Andreotti contributes to the characterization of the mechanism of drag reduction with low volume fractions of anisotropic additives in turbulent channel flow.

Studies of the flow past a square heated cylinder with its longitudinal axis aligned normal to the direction of the flow are motivated, aside by the fundamental significance, by their importance in applications such as combustion chambers in chemical processes, flow dividers in polymer processing, cooling of electronic components, and compact heat exchangers. Many non-Newtonian fluids of industrial interest can be adequately characterized by their shear rate-dependent viscosity behavior. Mixed convection from hot square rods to inelastic generalized Newtonian fluids has not received the attention it deserves. Dhiman et al. investigate numerically mixed convection from a two-dimensional rod.

In closing, I would like to thank the numerous reviewers and the authors who made this issue possible.

Dennis Siginer
Associate Editor
e-mail: dennis.siginer@wichita.edu

Eric Climent
Laboratoire de Génie Chimique,
UMR 5503,
CNRS/INPT/UPS,
5 Rue Paulin Talabot,
31106 Toulouse, France
e-mail: eric.climent@ensiacet.fr

Kyongmin Yeo
e-mail: kyeo@dam.brown.edu

Martin R. Maxey
e-mail: maxey@dam.brown.edu

George E. Karniadakis
e-mail: gk@dam.brown.edu

Center for Fluid Mechanics,
Division of Applied Mathematics,
Brown University,
Box F,
Providence, RI 02912

Dynamic Self-Assembly of Spinning Particles

This paper presents a numerical study of the dynamic self-assembly of neutrally buoyant particles rotating in a plane in a viscous fluid. The particles experience simultaneously a magnetic torque that drives their individual spinning motion, a magnetic attraction toward the center of the domain, and flow-induced interactions. A hydrodynamic repulsion balances the centripetal attraction of the magnetized particles and leads to the formation of an aggregate of several particles that rotates with a precession velocity related to the inter-particle distance. This dynamic self-assembly is stable (but not stationary) and the morphology depends on the number of particles. The repulsion force between the particles is shown to be the result of the secondary flow generated by each particle at low but nonzero Reynolds number. Comparisons are made with analogous experiments of spinning disks at a liquid–air interface, where it is found that the variation in the characteristic scales of the aggregate with the rotation rate of individual particles are consistent with the numerical results. [DOI: 10.1115/1.2436587]

Keywords: magnetic particles, rotating aggregate, hydrodynamic interactions, direct simulation

1 Introduction

Flows in microsystems have received increasing attention over the past decade because of the broad range of potential applications, as described in the review paper of Stone et al. [1]. Microdevices can be used for multiple purposes ranging from biomedicine (drug delivery, molecular diagnostic using Lab-On-Chip equipment) to the transport of fluids in aerospace engineering [2]. Microfabrication techniques primarily developed for microelectronics provide a convenient way to achieve channels with complex geometries and also surface patterning. Both academic research and engineering applications [2] have revealed the particular behavior of flows in very confined geometries. It is now possible to control more efficiently the basic transport phenomena (heat and mass) that drive the overall performance of the system. Mixing in such small-scale devices [3] is a challenge as turbulence is generally absent at the low Reynolds numbers encountered in flows in these systems. Different strategies, ranging from passive to dynamically enhanced mixing [4,5], have been proposed to overcome these limitations. Manipulating the flow with actuators or internal micropumps is another important issue. One way to achieve this is through the organized motion of particles in a controllable manner. For example, experiments by Terray et al. [6] have demonstrated the peristaltic pumping action produced by a transverse wave traveling along a chain of micron scale beads. Numerical simulations [7] confirm the basic flow features and provide additional information including the effects of different channel sizes. The application of magnetic fields to magnetic or paramagnetic beads provides a valuable means to drive the particle motion. Magnetic fields, in general, are more benign for handling biological samples and do not require large electrostatic potentials encountered in flows driven by electro-osmosis.

Recently, there has been a focus on fabricating self-assembled structures using paramagnetic particles suspended by liquids in microchannels [8,9]. In an open suspension, at void fractions of a few percent or less, magnetic beads form linear chains under the action of a steady magnetic field. The beads acquire a magnetic dipole parallel to the applied field and then align themselves in response to the mutual interaction of the dipoles, forming long chains through aggregation. For micron-sized particles, there are competing effects of Brownian motion and magnetic forces and the average length of the chains has a power law growth in time [10,11]. In a confined microchannel, the length and position of the chains is controlled by the geometry. Experiments by Hayes et al. [8] show that paramagnetic particles suspended in a pipe will form a chain along a diameter of the pipe when a transverse magnetic field is applied. This represents the longest available dimension parallel to the applied field. The chain, once formed, will then rotate as the magnetic field is rotated, maintaining the alignment of the chain with the magnetic field. Corresponding numerical simulations by Liu et al. [12] confirm this behavior and show similar preferred alignments of paramagnetic chains in ducts with a triangular cross section. Self-assembled matrices of paramagnetic particles in a microchannel have been proposed for DNA separation chips [9].

Self-assembly is a specific form of particle manipulation. Autonomous organization can spontaneously lead to the formation of large-scale structures and through the balance of opposing forces or processes, particles can form stable patterns. This behavior is common to several systems ranging from molecular to planetary scales [13]. Studies of self-organization have been mainly focused on static structures, such as crystal formation, where a static equilibrium is achieved through an energy minimization. In contrast, a stable particle aggregate that is moving in a viscous fluid is continuously dissipating energy and a dynamic equilibrium between the external forcing and the viscous dissipation is needed to maintain the self-assembled pattern. This represents, in general, a dissipative dynamical system rather than a conservative system governed by Hamiltonian dynamics.

The present paper is motivated by the experiments reported by Grzybowski et al. [14–16] in which the self-assembling system is composed of millimeter-sized disks floating just beneath a liquid–air interface. These disks are doped with magnetite resulting in magnetized particles with a permanent dipole moment coplanar with the disk. A large permanent bar magnet rotates at a constant angular frequency above the interface in a plane parallel to the interface. The disks spin about their centers at the same rotation

Contributed by the Fluids Engineering Division of ASME for publication in the JOURNAL OF FLUIDS ENGINEERING. Manuscript received May 24, 2006; final manuscript received October 18, 2006. Assoc. Editor: Theodore Heindel.

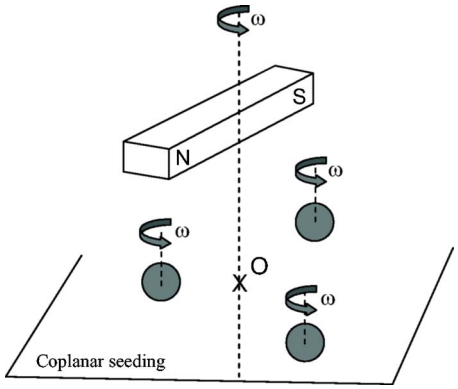

Fig. 1 Sketch of the experimental configuration [15]

rate as the rotating bar magnet in response to the magnetic torque on the disks. The particles experience also a gradient of the mean magnetic field resulting in a centripetal force toward the axis of rotation of the bar magnet. As the disks are rotating in a viscous fluid, they force the formation of a vortex like flow around their surfaces. Complex hydrodynamic interactions between the spinning disks then take place and drive the formation of supraparticle aggregates.

By comparison, the interactions of these vortical flows differ from the motion of two-dimensional point vortices in an inviscid fluid described by Aref [17]. In the latter case, the system is Hamiltonian and nondissipative. The dynamics can be complex and chaotic motions may occur depending on the number of vortices and the initial separation distance of the vortex centers. Similarly, Campbell and Ziff [18] have investigated theoretically the possible equilibrium patterns formed by point vortices in an inviscid superfluid using energy minimization principles. In the present study, viscous forces and viscous dissipation play a central role in damping fluctuations and sustaining the stable dynamic equilibrium.

The aim of this paper is to present results of numerical simulations for an analog of the physical situation described by Grzybowski et al. [15,16]. The floating disks are instead neutrally buoyant spheres, suspended in a viscous liquid and initially seeded in a coplanar configuration (see Fig. 1). A constant torque is applied to each particle to generate their spinning motion and the centripetal attraction force due to the radial gradient of the ambient magnetic field is prescribed. In the following sections, we describe the numerical approach used to simulate the flow and particle trajectories, giving details of the force coupling method. The flow around individual spinning particles is described and the hydrodynamic interactions of the particles evaluated. Then, we describe the results obtained from simulations of systems of particles and compare these carefully with the experimental data [15]. We emphasize the effect of the low but finite Reynolds number on the flow dynamics. This point is particularly important as the Reynolds number is of order unity in the experiments and no reliable analytical theory is available for such an intermediate regime.

2 Simulation methods

The physical problem under discussion involves magnetic attraction forces and torques as well as fluid forces induced by the rotation of small particles embedded in a viscous fluid. The crucial mechanism that needs to be represented is the repulsion force between spinning particles produced by their hydrodynamic interactions. We use the force coupling method (FCM) [19,20] to describe the coupled dynamics of the dispersed two-phase flow of the particles in suspension. The resulting equations are solved numerically, in a three-dimensional periodic domain using a standard Fourier pseudo-spectral method.

2.1 Overview of the Force Coupling Method. The basic concept of the FCM is to represent the presence of particles in a fluid flow by locally distributed body forces added to the Navier–Stokes equations for the fluid momentum. Fluid is assumed to fill the whole domain including the volume occupied by the particles. The body forces result in a low-order, finite multipole expansion for the disturbance flow of each particle and the forces effectively constrain the fluid to respond locally as a rigid body. Multibody interactions are achieved by solving the Navier–Stokes Eqs. (1) and (2) including simultaneously the forcing $\mathbf{f}(\mathbf{x},t)$ from all the particles

$$\rho\frac{D\mathbf{u}}{Dt} = -\nabla p + \mu\nabla^2\mathbf{u} + \mathbf{f}(\mathbf{x},t) \tag{1}$$

The velocity field is $\mathbf{u}(\mathbf{x},t)$; μ is the fluid viscosity; and p is the pressure. The fluid motion is incompressible, with uniform density ρ, and the velocity field satisfies the continuity equation

$$\nabla\cdot\mathbf{u} = 0 \tag{2}$$

The momentum source term $\mathbf{f}(\mathbf{x},t)$ on the right-hand side of Eq. (1) is expanded using a multipole decomposition

$$f_i(\mathbf{x},t) = \sum_{n=1}^{N_B} F_i^{(n)}\Delta[\mathbf{x}-\mathbf{Y}^{(n)}(t)] + G_{ij}^{(n)}\frac{\partial}{\partial x_j}\Delta'[\mathbf{x}-\mathbf{Y}^{(n)}(t)] \tag{3}$$

where $\mathbf{Y}^{(n)}$ is the position of the nth spherical particle and $\mathbf{F}^{(n)}$ is the force it exerts on the fluid. The first term on the right-hand side of Eq. (3) is a force monopole. The force dipole term, the second term on right-hand side of Eq. (3), is a combination of a symmetric stresslet term and an antisymmetric part related to the torque $\mathbf{T}^{(n)}$ exerted on the fluid by the nth particle. These terms are summed over the total number of particles, N_B. The density functions Δ and Δ' are spherical Gaussian envelopes that model the finite size of the particles

$$\Delta(\mathbf{x}) = (2\pi\sigma^2)^{-3/2}\exp(-\mathbf{x}^2/2\sigma^2) \tag{4}$$

with corresponding length scales σ for $\Delta(\mathbf{x})$ and σ' for $\Delta'(\mathbf{x})$. In terms of the particle radius a, these scales are set as $a/\sigma=\sqrt{\pi}$ and $a/\sigma'=(6\sqrt{\pi})^{1/3}$.

The strength of each force monopole $\mathbf{F}^{(n)}$ is related to the external force on the particle $\mathbf{F}_{\text{ext}}^{(n)}$ and the excess buoyancy force or inertia of the particle relative to that of the displaced fluid as

$$\mathbf{F}^{(n)} = (m_P - m_F)\left(\mathbf{g} - \frac{d\mathbf{V}^{(n)}}{dt}\right) + \mathbf{F}_{\text{ext}}^{(n)} \tag{5}$$

Similarly, the torque term $\mathbf{T}^{(n)}$ is specified by a combination of the external torque on the particle and excess inertia

$$\mathbf{T}^{(n)} = -(I_P - I_f)\left(\frac{d\boldsymbol{\omega}^{(n)}}{dt}\right) + \mathbf{T}_{\text{ext}}^{(n)} \tag{6}$$

Here, m_P and m_F are the mass of the particle and mass of displaced fluid, respectively; and I_P and I_F are appropriate coefficients for the moment of inertia. The contribution of the torque term to the force dipole coefficient is $G_{ij}^{(n)}=1/2\varepsilon_{ijk}T_k^{(n)}$. In general, the symmetric stresslet coefficient for each particle is set through an iteration process to ensure that the average rate of strain within the volume occupied by each particle

$$S_{ij}^{(n)} = \frac{1}{2}\int\left(\frac{\partial u_i}{\partial x_j} + \frac{\partial u_j}{\partial x_i}\right)\Delta'[\mathbf{x}-\mathbf{Y}^{(n)}(t)]d^3\mathbf{x} \tag{7}$$

is zero.

The particles move in a Lagrangian framework with their trajectories computed from the local fluid velocity. Particle velocities and rotation rates are obtained by a spatial average of the fluid velocity and vorticity over the volume of fluid occupied by the particle, based on the spherical Gaussian envelopes Eq. (4) as

$$\mathbf{V}^{(n)}(t) = \int \mathbf{u}(\mathbf{x},t)\Delta[\mathbf{x} - \mathbf{Y}^{(n)}(t)]d^3\mathbf{x} \tag{8}$$

$$\boldsymbol{\omega}^{(n)}(t) = \frac{1}{2}\int \nabla \times \mathbf{u}(\mathbf{x},t)\Delta'[\mathbf{x} - \mathbf{Y}^{(n)}(t)]d^3\mathbf{x} \tag{9}$$

From this the trajectory of each spherical particle is computed as

$$\frac{d\mathbf{Y}^{(n)}}{dt} = \mathbf{V}^{(n)}(t) \tag{10}$$

In a Stokes flow, FCM gives exact results for the drag force on an isolated particle as well as the torque on a rotating sphere or the stresslet for a spherical particle in a uniform straining flow [19,20]. The response to a single force monopole captures both the usual Stokeslet and the associated degenerate force quadrupole needed to represent the flow past an isolated sphere. Even though boundary conditions are not imposed on the particle surface and only the constraints Eqs. (7)–(9) are imposed, the flow field is generally a good approximation at distances greater than 25–50% of the particle radius from the particle surface. Similarly, the hydrodynamic interaction of a pair of particles is well represented when the gap between the particles is larger than 25% of the radius, or 50% for the specific case of particles moving toward each other their line of centers where lubrication forces are then an issue [21].

The effects of finite fluid and particle inertia are well represented by the FCM scheme under low, but finite Reynolds numbers. This has been tested by comparisons with experiments for sedimenting particles [22] and against full direct numerical simulations for a variety of flows including particles in wall-bounded shear flows [23–25]. For flow past a fixed sphere, it has been verified so far that the drag forces and flow structure agree well with full direct numerical simulations at particle Reynolds numbers up to 12 [25]. FCM also gives good estimates for the lift forces on particles near a wall in a parallel shear flow, including situations involving a pair of interacting particles [26]. The computational effort for FCM as compared to direct numerical simulations for particulate flows is discussed by [23,24].

The Navier–Stokes Eqs. (1) and (2) are solved for a periodic cubic domain, large compared to the size of the particles and the typical scale of the aggregate. A Fourier pseudo-spectral representation is used for the flow field and a standard Fourier collocation scheme. Second-order time accuracy is achieved by using an Adams–Bashforth scheme for both the fluid and the particle motions. Simulations are carried out on both 64^3 and 128^3 grids. Typically 5–6 grid points per particle diameter are needed to ensure that the Gaussian force envelope Eq. (4) is resolved and that the body force distributions Eq. (3) are accurately represented, without aliasing errors.

2.2 Magnetic Forces. We now consider the effect of the magnetic field on the particles and the conditions relevant to the experiments [15] used here to motivate the simulations. The magnetized disks are of uniform size with diameter in the range of 1–2 mm and the final aggregated clusters are 10 mm or less in diameter. At 2–4 cm above the free surface a large permanent bar magnet is suspended, with horizontal dimensions 5.6 cm by 4 cm, which is then rotated rapidly at rates variously between ~200 rpm and 1200 rpm. On the free surface, the magnitude of the magnetic field has a maximum at the axis of rotation and the magnetic field is aligned with the long axis of the bar magnet. Locally, the magnet exerts a torque on a magnetized disk equal to $\mathbf{m}\times\mathbf{B}$ where $\mathbf{B}$ is the local magnetic flux density of the bar magnet and $\mathbf{m}$ is the fixed dipole moment of the disk [27]. Provided the two are aligned the torque is zero but any misalignment will generate a significant torque tending to bring the two back into alignment. The torque is more than sufficient to overcome the viscous resistance to rotation and so the disks rotate in synchrony with the bar magnet.

The bar magnet also exerts a force on each disk $\mathbf{m}\cdot\nabla\mathbf{B}$ associated with the gradient of the magnetic field. As the dipole moment is aligned with the bar magnet and the magnetic flux density is diminishing away from the axis of rotation, the force is directed toward the axis at all times. The magnitude of the force fluctuates as the magnet is rotated but as the rotation rate is much larger than the precession rate of the cluster of disks, the force may be represented by a time-averaged, constant force. The magnetic force also varies with radial distance from the axis of rotation. If the dimensions of the magnet were very large, we would expect a linear variation in the gradient of the flux density $\nabla\mathbf{B}$ with radial distance and so too of the magnetic force. This is only partially true and an alternative is to assume a locally uniform value of the flux gradient density over a limited range of distances from the axis. Both representations were used by Grzybowski et al. [15]. In the present simulations, we consider both a constant and a linearly varying radial magnetic force directed towards the axis of rotation to set $\mathbf{F}_{\text{ext}}$. The magnetic forces between individual disks, due to their dipole moments, are negligible by comparison.

The present numerical analogy of the experiments is composed of neutrally buoyant particles instead of disks floating at a liquid/air interface. It has been argued in the physical analysis of the self-assembly dynamics that capillary effects related to particle-interface interactions have no role. The net effect is only to prevent disks from settling under gravity in the fluid layer. We agree with such an analysis and set the density ratio $m_P/m_F=1$ throughout all the simulations. The hydrodynamic interactions are obtained by the force coupling method and these drive the Lagrangian motion of the spherical particles. The magnetic torque $\mathbf{T}_{\text{ext}}$ acting on each particle is fixed so that the angular velocity for a single particle matches the rotation of the magnetic field and that the corresponding rotational Reynolds numbers match.

3 Flow Interactions of Isolated Particles

The dynamics of self-assembly for particles under rotation and magnetic attraction are closely related to the hydrodynamic interactions of spinning spheres. In this section, we consider the flow generated by a single spinning sphere and the fluid forces acting on a pair of particles. We first compute the fluid velocity induced by a single isolated particle rotating around the fixed z axis passing through the center of the sphere. The particle radius is a and the rotation rate about the axis is ω. All quantities are made dimensionless using these two characteristic scales. In Fig. 2, we compare the radial profile of the azimuthal velocity, u_ϕ in the equatorial plane $\theta=\pi/2$ specified in terms of spherical polar coordinates (r,θ,φ). Simulations using the Stokes equations, at zero Reynolds number, are in good agreement with the analytic profile $u_\phi=a^3\omega/r^2$, for $r\geqslant a$. Close to the sphere surface at $r/a=1$ the discrepancy is slightly greater but at distances larger than $r/a=1.5$, good agreement is achieved. The FCM profile is smoothly varying and peaks inside the sphere volume. As the particle Reynolds number $\text{Re}_\omega=\omega a^2/\nu$ for the rotation is increased, where ν is the kinematic viscosity μ/ρ, the FCM results (with both torque and stresslet terms) indicate that there is little change in the azimuthal velocity profile. At $\text{Re}_\omega=8$, the profile is essentially identical to that at zero Reynolds number. At higher Reynolds number it is known that a boundary layer structure eventually develops [28] and the variation in azimuthal velocity with θ also changes.

In using the force coupling method here, the particle rotation rate $\boldsymbol{\omega}$ is determined from the simulation, using Eq. (9), in response to the flow generated by a prescribed torque $\mathbf{T}_{\text{ext}}$. We initially imposed $T_{\text{ext}}=8\pi\mu a^3\omega$, based on the reference set of scales and the viscous torque in Stokes flow [29], and then varied the fluid viscosity μ to achieve the required particle rotation Reynolds number. The relation between the torque and the angular velocity has been thoroughly investigated in the literature. The nondimensional torque $M=2T_{\text{ext}}/(\rho a^5\omega^2)$ varies with the Reynolds number

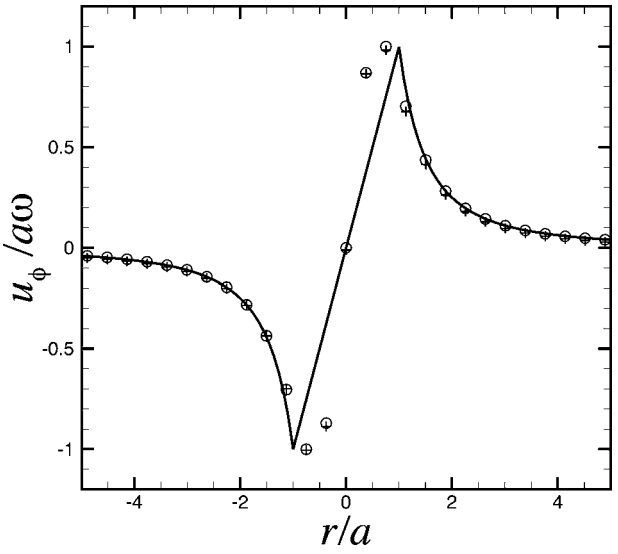

Fig. 2 Profile of the azimuthal velocity u_φ in the equatorial plane: Stokes flow (solid line); force coupling method–Stokes flow (open circles); force coupling method –Re_ω=8(+)

Re_ω. Experiments carried out by Sawatzki [30] are in good agreement with Lamb's result $M=16\pi/Re_\omega$ for Stokes flow [29] provided Re_ω is less than 3. This is confirmed by the numerical simulations of Dennis et al. [31]. When Re_ω becomes finite, the empirical relation $M=16\pi(1+f(Re_\omega))/Re_\omega$ is more appropriate. In the range $0 \leqslant Re_\omega \leqslant 10$, the correction term $f(Re_\omega)$ remains small, less than 0.075, and the results for M obtained by Dennis et al. [31] agree well with the asymptotic approximations due to Bickley [32] and Takagi [33]. Results for M as a function of Re_ω obtained from the FCM simulations are shown in Fig. 3, where we include results with both torque and stresslet terms (FCM-TS) or with just a torque term (FCM-T). The stresslet term has a significant effect in improving the estimate of M as a function of Re_ω and improves the representation of the flow. At Re_ω=8, the expected value of $[1+f(Re_\omega)]$ is 1.050 while the results for FCM-TS give 1.016. The results are closer at lower Reynolds numbers.

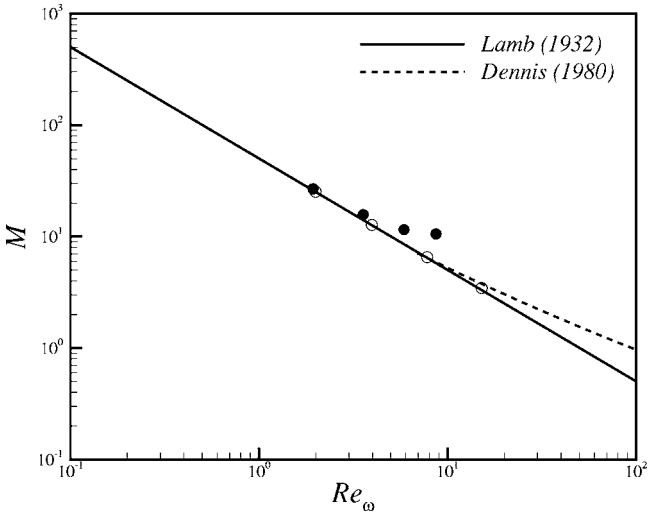

Fig. 3 Nondimensional torque coefficient M against Reynolds number Re_ω: solid line, Lamb's theory (Stokes flow); dashed line, correlation from the experiments of Sawatzki [30] and simulations of Dennis et al. [31]; filled circles, FCM-T results; open circles, FCM-TS results

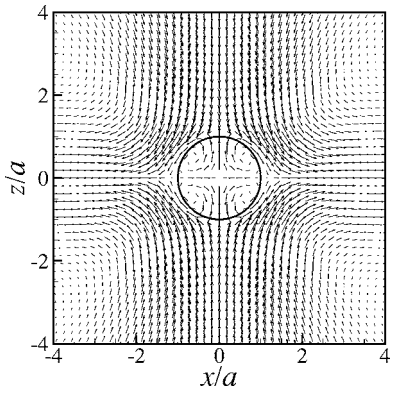

Fig. 4 Secondary flow in *x*, *z* plane for sphere spinning about the *z* axis at Re_ω=2

Overall, the estimate from Stokes flow provides a good approximation for the torque and the FCM results tend to underestimate the increase in torque. The working range for the experiments [15] is $0<Re_\omega<4$.

At finite Reynolds number a secondary, meridional circulation develops with an inflow at the poles and outflow near the equator. Figure 4 shows the simulation results for Re_ω=2 with rotation about the z axis. We have included the volume inside the particle to illustrate the internal circulation and the location of the stagnation points. The secondary flow can be approximately estimated by a regular perturbation expansion at low Reynolds number. Following Bickley [32], the three velocity components in terms of spherical polar coordinates are

$$u_r = -\frac{\omega a^3}{8r^2}(3\cos^2\theta - 1)\left(1 - \frac{a}{r}\right)^2 Re_\omega$$

$$u_\theta = \frac{\omega a^4}{4r^3}\left(1 - \frac{a}{r}\right)\sin\theta\cos\theta\, Re_\omega$$

$$u_\phi = \frac{\omega a^3}{r^2}\sin\theta + O(Re_\omega^2) \tag{11}$$

This result illustrates the low Reynolds number stresslet component of the radial velocity in the plane $\theta=\pi/2$, where u_r varies asymptotically as $(\omega a^3/8r^2)Re_\omega$.

If in addition to rotation, a sphere is moving with a translational velocity U through still fluid there will be both a drag force and a lift force. The lift is orthogonal to both the linear velocity and the angular velocity. Rubinow and Keller [34] have estimated these forces for small, but finite Reynolds number using an Oseen representation for the far field flow. The drag coefficient is equal to the usual Oseen prediction, $C_D=24(1+3Re/16)/Re$, where the Reynolds number $Re=2aU/\nu$ and the lift coefficient is $C_L=3/4$. A force balance can be derived for steady motion with velocity $\mathbf{V}$

$$\mathbf{F}_{ext} = 6\pi\mu a\mathbf{V}\left(1 + \frac{3}{16}Re\right) + \frac{3}{4}m_F\mathbf{V}\times\boldsymbol{\omega} \tag{12}$$

while the particle is driven by a constant external force and $Re \ll 1$. Similarly for a sphere translating relative to a flow with a uniform shear, there is also a lift force. This is again an effect of finite Reynolds number and has been estimated by Saffman [35,36] to first order in Re. Extensive comparisons with FCM and full direct numerical simulations [23,25] have shown that the present simulation methods accurately capture these lift forces for low to moderate Reynolds numbers.

We now consider the motion of a pair of co-planar particles, each subject to a constant torque and co-rotating with an angular velocity ω. In a Stokes flow, at zero Reynolds number, the particles will follow a circular path moving in response to the flow

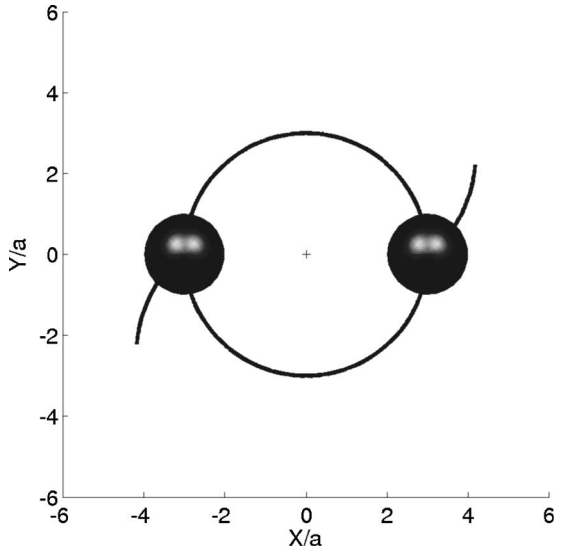

Fig. 5 Trajectories of two spinning particles without magnetic attraction: closed circular trajectories (Stokes flow); open trajectories (low, but finite Reynolds number)

generated by the other particle. There is no repulsion force between the particles and the radius of the circular path R does not change. This is shown by the closed path trajectories in Fig. 5 which are computed for zero Reynolds number. This agrees with the properties of linearity and reversibility for Stokes flows. When including low, but finite fluid inertia ($\mathrm{Re}_\omega=2$) in the simulation, we see that the particles repel each other. The particles follow open trajectories while the center to center distance increases steadily. The repelling behavior of spinning particles is clearly an effect of fluid inertia. If the particles are counter-rotating under the action of equal and opposite torques then in a Stokes flow the particles move in parallel with a constant velocity again in response to the flow induced by the other particle. Their separation distance $2R$ again remains constant.

This situation may be thought (as in the original discussions of the experiments) to give rise to a lift force at finite Reynolds number, either due to the shear flow (Saffman lift force) of the induced fluid motion or the rotation of the particles (Rubinow–Keller lift force). If this were the case then corotating particles would repel and counter-rotating particles would attract at finite Reynolds number. A simulation, similar to that shown in Fig. 5, with counter-rotating particles demonstrates that there is a repulsion not an attraction between the particles. Both the Rubinow–Keller lift force due to rotation and the Saffman lift force due to a local mean shear require a relative motion between the particle and the ambient fluid. Specifically, some wake region must develop behind each particle. The particles here are neutrally buoyant and their translational motion is due to the motion of the surrounding fluid, induced by the spinning particles. No such wake region will develop.

The flow structure for a pair of corotating particles is shown in Fig. 6. The particles are spinning about axes parallel to the z axis at $\mathrm{Re}_\omega=2$. They are subject to a fixed force of attraction that in the stationary state keeps them at a constant separation distance and the particles move in a circular path in the x,y plane. The distance between the particle centers, $2R$ is approximately $6a$. The secondary flow effect is clearly evident and the radial outflow in their common plane tends to push the particles apart. The flow structure is similar if the particles are counter-rotating, i.e., there is a common radial outflow for each particle.

We have computed the hydrodynamic repulsion force between a pair of particles, at fixed Reynolds numbers Re_ω, as a function of the particle separation distance $2R$. In the simulations, a constant force of attraction is set and then the equilibrium distance is determined. The results are show in Fig. 7 for $\mathrm{Re}_\omega=0.25$, 2, and 8. The force is scaled as $F/\rho a^4\omega^2$. The results for $\mathrm{Re}_\omega=0.25$ and 2 are very similar for $R/a>2$. There is no simple power law for the variation with separation distance but the trend is not far from an R^{-3} dependence. At the higher Reynolds number, the decrease with R is less.

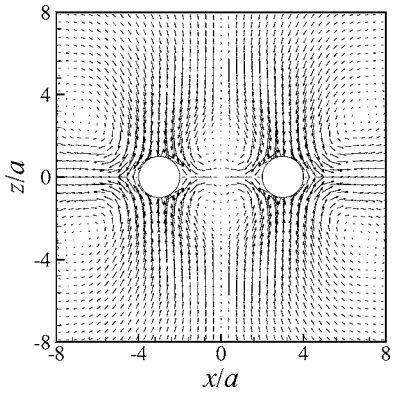

Fig. 6 Secondary flow for two spheres, spinning about axes parallel to the *z* axis, at $\mathrm{Re}_\omega=2$

The precession angular velocity Ω of the pair of particles can be theoretically predicted in Stokes flow by a linear summation of the velocity perturbations of each particle. Considering one particle of the aggregate, we can predict the azimuthal velocity induced by the rotation of the second particle as $u_\phi=\omega a^3/(2R)^2$. The angular frequency of the two particle system (precession velocity) is $\Omega=u_\phi/R$, and

$$\frac{\Omega}{\omega}=\frac{1}{4}\left[\frac{a}{R}\right]^3 \tag{13}$$

The relation strongly depends on the separation distance, varying as $1/R^3$. For an aggregate of three particles, following the same arguments we can derive

$$\frac{\Omega}{\omega}=\frac{1}{2\cos(\pi/6)}\left[\frac{a}{R}\right]^3 \tag{14}$$

Figure 8 summarizes the simulation results for a pair of particles. The results were obtained in the same way as in Fig. 7. It is important to note that the rotation rate of the aggregate Ω is typically one or two orders of magnitude lower than the reference angular frequency ω of the bar magnet. The above theoretical prediction based on Stokes flow is in good agreement with the

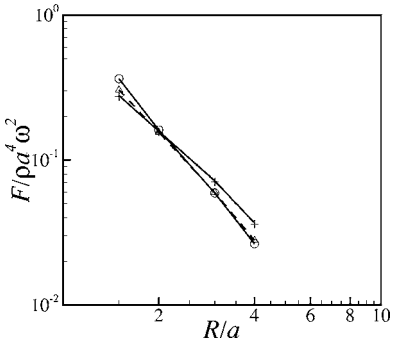

Fig. 7 Repulsion force *F* between two corotating particles against distance *R*, where 2*R* is the distance between particles. Results at $\mathrm{Re}_\omega=0.25$ (open circles), 2 (triangles), and 8 (cross)

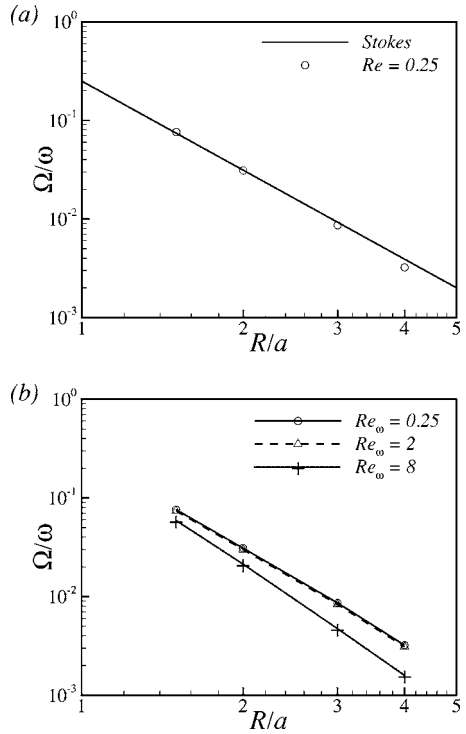

Fig. 8 Precession angular velocity Ω for a pair of corotating spheres against *R*: (*a*) comparison of results at $Re_\omega=0.25$ with estimate from Stokes flow; and (*b*) comparison of results at $Re_\omega=0.25$, 2, and 8

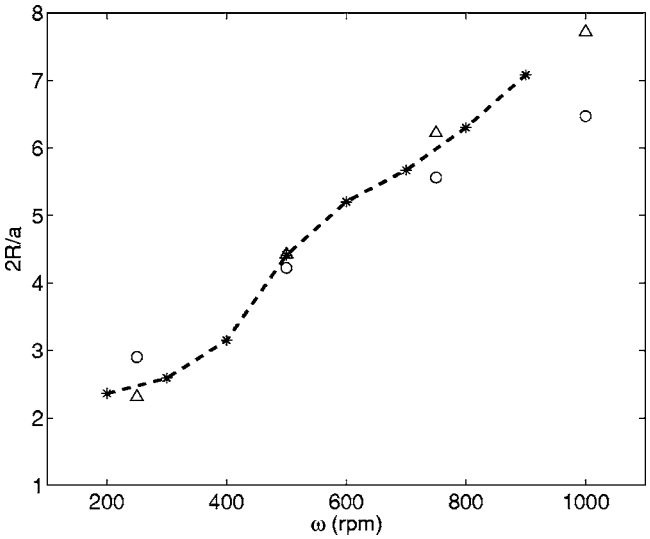

Fig. 9 Comparison of simulation results with experiments for the separation distance of the stable pattern (two particles) at different rotation rates ω: (stars) experiments of Grzybowski et al. [15] (dashed line is only a guide for the eye); (triangles) FCM results with a constant magnetic attraction force; (circles) FCM results with a linear magnetic attraction force

simulations at $Re_\omega=0.25$ and 2 for smaller separation distances. At the higher Reynolds number, $Re_\omega=8$, the decrease in Ω is more rapid with separation distance.

4 Self-Assembly of Rotating Particles

We now consider the motion of spinning particles that are also subject to a central attraction force due to the rotating magnetic field and make comparisons with the experiments [15]. Particles are initially seeded at random positions in the same plane (see Fig. 1) to correspond to the coplanar experimental conditions where disks were floating beneath a liquid–air interface. We do not force the particles to stay in the initial plane and the particles may move freely within the three-dimensional periodic domain. Throughout, a stable coplanar configuration of the aggregate is reached as self-assembly occurs. It is important to note that the typical size of the cluster of particles is small compared to the domain width (24 or 48 particle radii) and the periodic boundary conditions have been verified to have only a small effect on the overall dynamics.

4.1 Two Particle System. The simplest stable aggregate is composed of two particles, where the repelling hydrodynamic force is balanced by a centripetal force given by the magnetic attraction toward the rotation axis of the bar magnet. Note that stable does not mean fixed since the particles are spinning around their own axes, and they induce a disturbance flow leading to the precession of the aggregate itself. We consider both a constant value for the magnetic attracting force and a linearly varying force to compare with the experimental data [15]. In Fig. 9, the increasing separation distance between the two particles of the rotating aggregate depends on the angular frequency. With increasing rotation rate of the bar magnet, the magnitude of the flow associated with the spinning particles increases and so too the inertial repulsion force. The particles then move apart from each other giving larger separation distance $2R/a$. In order to set an appropriate magnitude for the magnetic attraction force the result at $\omega=500$ rpm, which corresponds to $Re_\omega=2$, was used as reference point. The separation distance $2R/a$ is equal to 4.42 in this case.

There is good general agreement between the experimental data and the results of the simulations over the entire range of angular frequency. The results with the constant value of the magnetic force, shown by the triangular symbols in the figure, are in better agreement to the experiments than those for the linearly varying magnetic force, shown by the open circles. Note that with a linearly varying force, the attraction is stronger for larger values of R while the hydrodynamic repulsion becomes weaker. As a result, the separation distance $2R$ is smaller for a high rotation rate and conversely larger at a low rotation rate. The largest distance between the particles is less than 8 particle radius which is much lower that the width of the simulation domain (24 particle radius).

4.2 Multiple Particle System. As the number N_B of particles involved in an aggregate is increased, the topology of the self-assembling cluster changes. From two to five particles, the aggregate is composed of one single shell without particle in its center. The particles are distributed evenly on the circular orbit described by each particle trajectory. When N_B equals six, seven, or eight particles, one particle is located in the center of the circular orbit of the rotating aggregate. If nine particles are initially seeded at random positions, the aggregate achieves a stable configuration composed of two shells: two inner particles rotating around the rotation axis of the bar magnet and an outer shell composed of seven particles following circular paths (see Fig. 10 for stable

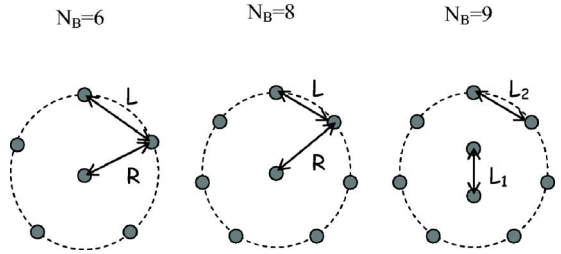

Fig. 10 Definition of length scales for a rotating aggregate

Table 1 Typical scales of a rotating aggregate (experiments, simulations)

$N_B=6$	$N_B=8$	$N_B=9$
$R/a=4.33$	$R/a=4.54$	$L_1/a=3.38$
$L/a=5.08$	$L/a=4.17$	$L_2/a=4.33$
$L/R=1.17$ (simulation)	$L/R=0.91$ (simulation)	$L_1/L_2=0.78$ (simulation)
$L/R=1.13$ (experiments)	$L/R=0.80$ (experiments)	$L_1/L_2=0.80$ (experiments)

configurations for $N=6$, 8, or 9). We checked the stability of these aggregate organizations by simulating the self-assembling transient from different initial random seeding. The particles always reach the same configuration as observed experimentally. At this point, we do not have a complete understanding of the selection mechanism for the aggregate patterns but the simulations show clearly that the FCM simulations are able to reproduce such complex dynamics.

In Table 1, the geometric parameters that define the aggregate pattern for $N=6$, 8, and 9 particles are given. These are compared with the experimental data and it can be seen that the agreement is more than qualitative for the cases $N=6$ and $N=9$. Our simulations overestimate slightly (13% error) the separation distance for a cluster composed of eight particles, as compared to the experiments. Full agreement is not to be expected because of the differences in the configuration of the experiments (disks) and the simulations (spheres). The values of R/a are all in a similar range and the results are similar whether a linearly varying or constant magnetic force is used. Figure 11 shows the flow field for a stable aggregate of seven particles, plotted for their common plane of motion.

For the particular values of $N=10$ and $N=12$, a polymorphism was observed in the experiments [16], whereby two different stable configurations of the particles can occur. Figure 12 shows the corresponding simulation results for ten particles at $\mathrm{Re}_\omega=2$. The two stable patterns have either seven or eight particles in the outer shell and correspondingly three or two particles nearer the center. For $N=12$, Fig. 13 shows that the stable patterns have either eight or nine particles in the outer shell. Both observations agree with the experiments. Starting from different, random initial positions of the particles it was seen in the experiments that the eight particles in the outer shell were more common for $N=10$ and the nine particles in the outer shell for $N=12$. The statistics varied somewhat with the rotation rate. We do not have sufficient data to estimate the relative frequency of each pattern but the results show a similar trend.

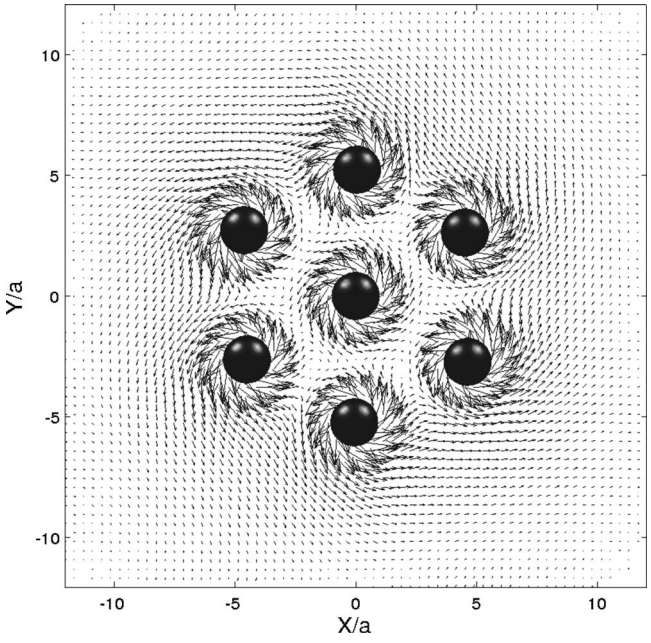

Fig. 11 Fluid velocity vectors for a stable aggregate of rotating spheres, $N=7$, at $\mathrm{Re}_\omega=2$. The aggregate precesses about the center particle in this common plane.

5 Discussion

In this paper, we give results from the numerical simulation of dynamic self-assembly of spinning particles. The key mechanism is the hydrodynamic repulsion between the particles that balances the magnetic attraction toward the center of the domain. Multibody hydrodynamic interactions are determined by numerical solutions of the Navier–Stokes equations combined with the force

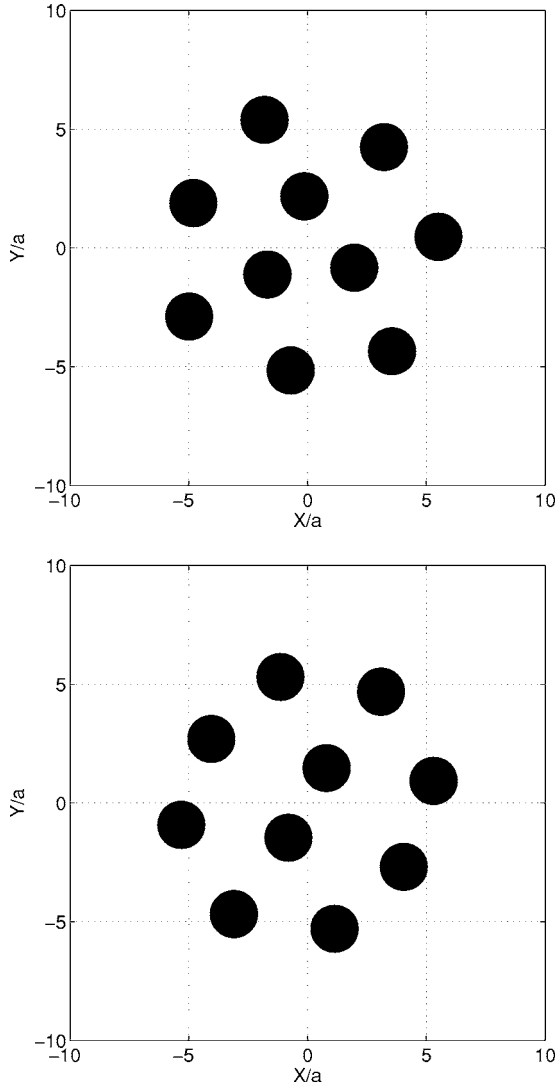

Fig. 12 Stable aggregation patterns for $N=10$ at $\mathrm{Re}_\omega=2$

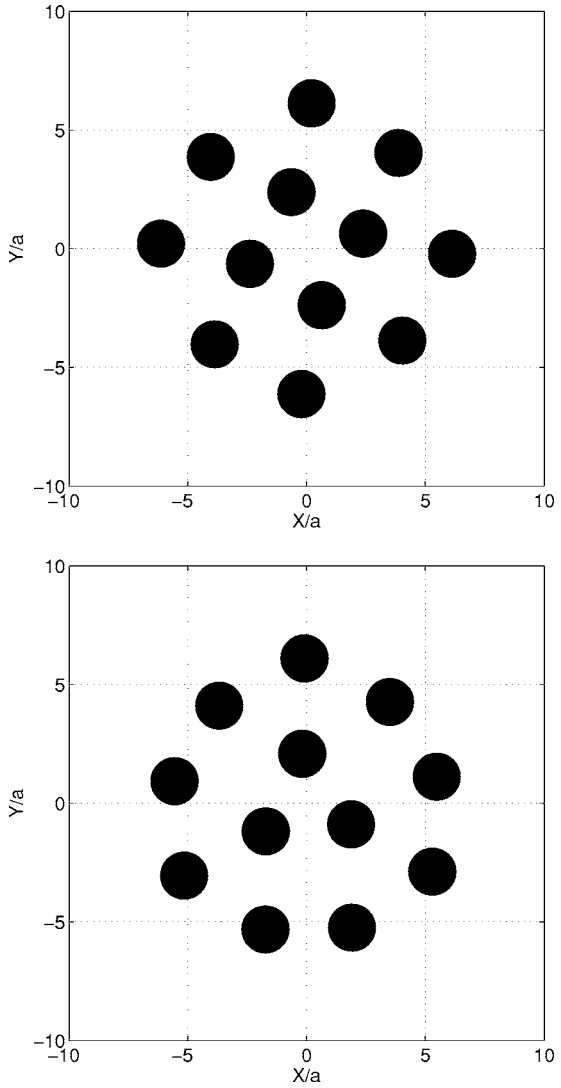

Fig. 13 Stable aggregation patterns for $N=12$ at $\mathrm{Re}_\omega=2$

coupling method as a representation for the interphase coupling between the fluid flow and the particles. The model is fully coupled in that particle rotations induce velocity perturbations in the flow that in turn drive the overall dynamics of the aggregate formation and govern the stability.

We simulate the formation of self-assembling aggregates composed of different numbers of particle. The configuration of two particles was compared to the reference experiments of Grzybowski et al. [15,16]. Our simulations on the evolution of the interparticle distance with the rotation rate of the bar magnet are in good agreement with the experiments carried out with spinning disks at a liquid–air interface. This demonstrates that the dynamics are purely related to hydrodynamic interactions and are not driven by interfacial phenomena. An important conclusion of our simulations is that the basic features are prescribed by low but finite Reynolds number dynamics and would not develop in the absence of fluid inertia. The repulsion force is Reynolds number dependent and the precession velocity is a function of the Reynolds number of the flow and the interparticle distance. When the number of particles is further increased, the arrangement of the particles displays symmetric patterns with one or more particles in the center surrounded by a rotating shell of equidistant particles. Polymorphism is observed too for groups of 10 or 12 particles.

Such tunable properties are highly desirable at microscales where the precise control of particle organization can drive the macroscopic properties of the equivalent medium. We may expect a high efficiency of mixing in a flow using such active microsystems, as indicated by Campbell and Grzybowski [37]. Although the effects depend on fluid inertia at finite Reynolds number, a low value of $\mathrm{Re}_\omega \sim 0.1$ would be sufficient to produce self-assembly. Such values are quite feasible in microflow systems at high rotation rates.

We have demonstrated that the source of the hydrodynamic repulsion force observed in the simulations and the experiments is the secondary flow generated by the spinning particles as opposed to lift forces. The variation of the force with separation distance, shown in Fig. 7, is consistent with the observations from the experiments. Grzybowski et al. [15] postulate scaling relations for the repulsion force assuming some form of lift force but conclude that straightforward estimates do not agree with the observed variations of the force with separation distance. By assuming a radial repulsion force that scales as r^{-3} [16] and suitable scaling coefficients, they were able to obtain a good correspondence between analytical model estimates and the experiments. In the present simulations, no such assumptions are required. Qualitatively, the secondary flow around each spinning particle will further produce a pressure force that will tend to support the particle at the free surface between the liquid and the air and the spinning particles could be viewed as roughly analogous to spinning hemispheres.

Finally, we note that there are several unresolved issues. The most important is that the FCM simulations tend to underpredict the strength of the secondary flow, although the spatial variation is approximately correct. Preliminary investigations have shown this to be the result of limited resolution of the flow near the surface of the sphere. The secondary flow is forced by pressure variations on the surface of the particle and is sensitive to the profile of u_ϕ. The differences between the exact solution and the FCM results shown in Fig. 2, while small, are significant for $1<r/a<1.5$. We are continuing to investigate this issue and improve the accuracy of the simulations.

Acknowledgment

The research was supported by the National Science Foundation under Grant No. CTS-0326702 and by CNRS under a PICS CNRS–USA collaborative program. Simulations were performed with the support of regional and national supercomputing centers Calmip, CINES/IDRIS. Findings and conclusions expressed here are those of the authors do not necessarily reflect the views of the funding agency. We are grateful to Professor Grzybowski of Northwestern University for discussion of the experiments.

References

[1] Stone, H. A., Stroock, A. D., and Ajdari, A., 2004, "Engineering Flows in Small Devices: Microfluidics toward a Lab-on-a-Chip," Annu. Rev. Fluid Mech., **36**, pp. 381–411.
[2] Stone, H. A., and Kim, S., 2001, "Microfluidics: Basic Issues, Applications, and Challenges," AIChE J., **47**(6), pp. 1250–1254.
[3] Nguyen, N.-T., and Wu, Z., 2005, "Micromixers-A Review," J. Micromech. Microeng., **15**, pp. R1–R15.
[4] Ottino, J. M., and Wiggins, S., 2004, "Introduction: Mixing in Microfluidics," Philos. Trans. R. Soc. London, Ser. A, **362**, pp. 923–935.
[5] Biswal, S. L., and Gast, A. P., 2004, "Micromixing with Linked Chains of Paramagnetic Particles," Anal. Chem., **76**, pp. 6448–6455.
[6] Terray, A., Oakley, J., and Marr, D. W., 2002, "Microfluidic Control Using Colliodal Devices," Science, **296**, pp. 1841–1843.
[7] Liu, D., Maxey, M. R., and Karniadakis, G. E., 2004, "Modeling and Optimization of Colloidal Micro-Pumps," J. Micromech. Microeng., **14**(4), pp. 567–575.
[8] Hayes, M. A., Polson, N. A., and Garcia, A. A., 2001, "Active Control of Dynamic Supraparticle Structures in Microchannels," Langmuir, **14**, pp. 2866–2871.
[9] Doyle, P. S., Bibette, J., Bancaud, A., and Viory, J.-L., 2002, "Self-Assembled Magnetic Matrices for DNA Separation Chips," Science, **295**, p. 2237.
[10] Promislow, J. H., Gast, A. P., and Fermigier, M., 1995, "Aggregation Kinetics of Paramagnetic Colloidal Particles," J. Chem. Phys., **102**, pp. 5492–5498.
[11] Climent, E., Maxey, M. R., and Karniadakis, G. E., 2004, "Dynamics of Self-Assembled Chaining in Magneto-Rheological Fluids," Langmuir, **20**, pp.

507–513.
[12] Liu, D., Maxey, M. R., and Karniadakis, G. E., 2005, "Simulations of Dynamic Self-Assembly of Paramagnetic Microspheres in Confined Microgeometries," J. Micromech. Microeng., **15**(12), pp. 2298–2308.
[13] Whitesides, G. M., and Grzybowski, B., 2002, "Self-Assembly at All Scales," Science, **295**, pp. 2418–2421.
[14] Grzybowski, B. A., Stone, H. A., and Whitesides, G. M., 2000, "Dynamic Self-Assembly of Magnetized, Millimeter-Sized Objects Rotating at a Liquid-Air Interface," Nature (London), **405**, pp. 1033–1036.
[15] Grzybowski, B. A., Jiang, X., Stone, H. A., and Whitesides, G. M., 2001, "Dynamic, Self-Assembled Aggregates of Magnetized, Millimeter-Sized Objects Rotating at the Liquid-Air Interface: Macroscopic, Two-Dimensional Classical Atoms and Molecules," Phys. Rev. E, **64**, 011603.
[16] Grzybowski, B. A., Stone, H. A., and Whitesides, G. M., 2002, "Dynamics of Self-Assembly of Magnetized Disks Rotating at the Liquid-Air Interface," Proc. Natl. Acad. Sci. U.S.A., **99**(7), pp. 4147–4151.
[17] Aref, H., 1983, "Integrable, Chaotic and Turbulent Vortex Motion in Two-Dimensional Flows," Annu. Rev. Fluid Mech., **15**, pp. 345–389.
[18] Campbell, L. J., and Ziff, M., 1979, "Vortex Patterns and Energies in a Rotating Superfluid," Phys. Rev. B, **20**(5), pp. 1886–1902.
[19] Maxey, M. R., and Patel, B. K., 2001, "Localized Force Representations for Particles Sedimenting in Stokes Flows," Int. J. Multiphase Flow, **27**, pp. 1603–1626.
[20] Lomholt, S., and Maxey, M. R., 2003, "Force-Coupling Method for Particulate Two-Phase Flow. Stokes Flow," J. Comput. Phys., **184**, pp. 381–405.
[21] Dance, S. L., and Maxey, M. R., 2003, "Incorporation of Lubrication Effects into the Force-Coupling Method for Particulate Two-phase Flow," J. Comput. Phys., **189**, pp. 212–238.
[22] Lomholt, S., Stenum, B., and Maxey, M. R., 2002, "Experimental Verification of the Force Coupling Method for Particulate Flows," Int. J. Multiphase Flow, **28**, pp. 225–246.
[23] Liu, D., Maxey, M. R., and Karniadakis, G. E., 2002, "A Fast Method for Particulate Microflows," J. Microelectromech. Syst., **11**, 691–702.
[24] Dong, S., Liu, D., Maxey, M. R., and Karniadakis, G. E., 2004, "Spectral Distributed Lagrange Multiplier Method: Algorithm and Benchmark Tests," J. Comput. Phys., **195**, pp. 695–717.
[25] Liu, D., 2004, "Spectral Element/Force Coupling Method: Application to Colloidal Micro-Devices and Self-Assembled Particle Structures in Three-Dimensional Domains," Ph.D. thesis, Brown University, Providence, RI.
[26] Maxey, M. R., Liu, D., Dong, S., and Karniadakis, G. E., 2006, "New Advances in Force-Coupling Method: From Micro to Macro," *Proceedings of the IUTAM Symposium on Computational Multiphase Flow*, S. Balachandar and A. Prosperetti, eds, Springer, New York, pp. 237–246.
[27] Jackson, J. D., 1999, *Classical Electrodynamics*, 3rd ed., Wiley, New York.
[28] Howarth, L., 1951, "Note on the Boundary Layer on a Rotating Sphere," Philos. Mag., **42**, pp. 1308–1315.
[29] Lamb, H., 1932, *Hydrodynamics*, Cambridge University Press, Cambridge, UK, pp. 558–559.
[30] Sawatzki, O., 1970, "Flow Field around a Rotating Sphere," Acta Mech., **9**, pp. 159–214.
[31] Dennis, S. C. R., Singh, S. N., and Ingham, D. B., 1980, "The Steady Flow due to a Rotating Sphere at Low and Moderate Reynolds Number," J. Fluid Mech., **101**, pp. 257–279.
[32] Bickley, W. G., 1938, "The Secondary Flow due to a Sphere Rotating in a Viscous Liquid," Philos. Mag., **25**, pp. 746–752.
[33] Takagi, H., 1977, "Viscous Flow Induced by Slow Rotation of a Sphere," J. Phys. Soc. Jpn., **42**(1), pp. 319–325.
[34] Rubinow, S. I., and Keller, J. B., 1961, "The Transverse Force on a Spinning Sphere Moving in a Viscous Fluid," J. Fluid Mech., **11**, pp. 447–459.
[35] Saffman, P. G., 1965, "The Lift on a Small Sphere in a Slow Shear Flow," J. Fluid Mech., **22**, pp. 385–400.
[36] Saffman, P. G., 1968, "Corrigendum: The Lift on a Small Sphere in a Slow Shear Flow," J. Fluid Mech., **31**, pp. 624.
[37] Campbell, C. J., and Grzybowski, B. A., 2004, "Microfluidic Mixers: From Microfabricated to Self-Assembled Devices," Philos. Trans. R. Soc. London, Ser. A, **362**, pp. 1069–1086.

Reversible Electrowetting of Liquid-Metal Droplet

Zhiliang Wan[1]
e-mail: zlwan@ece.uic.edu

Hongjun Zeng
e-mail: hzeng@ece.uic.edu

Alan Feinerman
e-mail: feinerman@uic.edu

Department of Electrical and Computer Engineering,
University of Illinois at Chicago,
851 South Morgan St.,
Chicago, IL 60607

This paper reports experimental investigations on the electrowetting effect of liquid metals, e.g., mercury, on dielectric films. Largest contact angle change of 74 deg (*from* 141 deg to 67 deg*) is achieved on top of a Parylene film. Highly reversible electrowetting with very low hysteresis* (2–4 deg) *is demonstrated on the Teflon®-coated surfaces. The actuation voltage for* 30 deg *contact angle change* (*from* 148 deg to 118 deg*) is largely reduced to* 25 V *by using a high-dielectric-constant tantalum oxide film as the dielectric layer. The effect of trapped charges in the dielectric film on the electrowetting is observed and measured. The rise and fall times of the electrowetting actuation are inversely proportional to the droplet diameter and as short as* 0.1–0.2 ms *for a* 50 μm dia *droplet. The actuation reliability is tested, and a long-time operation is achieved in an oil environment.* [DOI: 10.1115/1.2436582]

Keywords: contact angle, electrowetting, hysteresis, liquid metal, surface tension

1 Introduction

When a voltage is applied between a liquid droplet and a counterelectrode beneath a dielectric layer, the wetting property of the liquid on this solid surface is modified by the external electric field. The phenomenon is so-called electrowetting and was first demonstrated by Berge in 1993 [1]. As the surface tension is inherently a dominant force in microscale, modulation of the surface tension can be utilized as an effective actuation mechanism for microdevices. Recently, an increasing research interest has been focused on this subject. As the surface of very low hysteresis can be achieved by applying a Teflon® AF or Teflon-like coating [2,3], the electrowetting actuation becomes highly reversible. In addition, the driving voltage of electrowetting is reduced by decreasing the insulation layer thickness [4]. Reversible low-voltage electrowetting actuation opens up a broad application area. Many promising applications have been proposed for micro-electromechanical systems (MEMS) [5–9] and for microfluidics [10–13]. Our group has demonstrated that electrocapillarity is able to actuate a micromirror with a large piston displacement at a low voltage ($\leqslant$2 V) [6]. Berge and Peseux applied the electrowetting effect to change the focal length of a transparent drop [7]. Hayes and Feenstra reported a reflective display based on electrowetting [8]. A micromotor was achieved by Lee and Kim based on the continuous electrowetting [9]. Prins et al. reported their control of fluid motion by the electrocapillary pressure in three-dimensional structures of microchannels [10]. A review of the electrowetting and its applications was given recently by Mugele and Baret [14]. Compared to some other modulation strategies of surface tension, such as thermocapillarity and electrochemical effects, electrowetting has advantages of easy implemetation, fast response, and large tunability [14]. Most of the past electrowetting work is on the liquids, such as deionized water, aqueous salt solutions, and ionic liquids. As the electrowetting becomes a promising technique to drive droplet microfluidic systems, people have begun to explore the actuation of biological fluids for biorelated applications [13]. Our investigations of electrowetting focus on the liquid metals, e.g., mercury droplet. Compared to the above liquids, liquid metals offer a higher electrical conductivity, optical reflectivity, surface tension, and lower vapor pressure, which make them suitable for some MEMS applications, such as microrelay [15], microswitch [16], and integrated circuits (IC) cooling [17]. We first investigated the electrowetting of liquid metals on a dielectric film, such as Parylene [5]. Here we extend our previous work and perform a more systematic study on this phenomenon. At the same time, the dielectric film and the surface are greatly optimized for achieving a highly reliable actuation with a low driving voltage.

2 Electrowetting Equation

The electrowetting effect can be quantitatively characterized by measuring the contact angle of liquid droplet. When a liquid droplet is placed on a solid surface, the wettability is indicated by the angle between the interface of the droplet and the horizontal surface, which is termed contact angle. On a real surface with physical roughness and chemical heterogeneity, the equilibrium contact angle may not be a unique value. The contact-angle hysteresis (CAH) is defined by the difference between the advancing and receding contact angles and can be measured by the classic tilting-plate method. The electrowetting equation, which is first obtained by Berge through energy minimization method [1], describes the relationship between the contact angle and the applied voltage. Considering a mercury droplet on top of a dielectric film, the charges accumulate at the liquid-solid and liquid-vapor interfaces as a voltage is applied. Since mercury is a good conductor, there is no net charge inside the droplet. We also assume the dielectric film is an ideal insulation layer with no current leakage. If we neglect the fringe field and take the parallel-plate capacitor approximation, the electrowetting equation is

$$\cos\theta_v = \cos\theta_0 + \frac{1}{2}\frac{\varepsilon_0\varepsilon}{\gamma_{lv}d}V^2 \tag{1}$$

where ε_0 is the dielectric constant of vacuum, ε is the relative constant of the insulation layer, d is the dielectric film thickness, γ_{lv} is the mercury-vapor surface tension, θ_0 is the contact angle in the absence of an electric field, and θ_v is the contact angle at a voltage V. The electrowetting equation indicates that the contact angle decreases monotonically with the increasing voltage. The initial contact angle of a droplet is very important for device operation as a higher initial angle offers a wider angle tuning range. The electrowetting efficiency (contact-angle change per unit voltage) is proportional to $\varepsilon_0\varepsilon/2d$, which also is the unit-area capacitance between the droplet and buried electrode. Choosing a high dielectric constant material and decreasing the film thickness are two practical ways to lower the electrowetting actuation voltage.

[1]Corresponding author.

Contributed by the Fluids Engineering Divison of ASME for publication in the JOURNAL OF FLUIDS ENGINEERING. Manuscript received April 6, 2006; final manuscript received June 2, 2006. Assoc. Editor: Dennis Siginer.

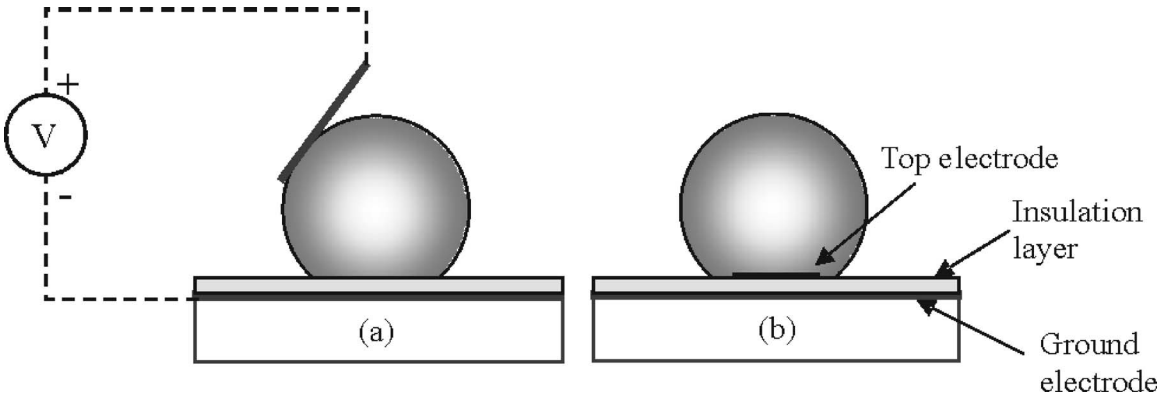

Fig. 1 Schematic sketches of electrowetting experimental setups: (*a*) with a fine metal probe and (*b*) with an on-plane electrode

Both approaches are investigated in our experiments and are described in detail in this paper. Another critical aspect of the electrowetting is surface hysteresis, which is ignored in the electrowetting equation, but needs to be seriously considered, in reality. Low-hysteresis surface is a necessity for large and reversible electrowetting actuation. The electrowetting equation is verified experimentally for aqueous conductive liquids, and the smallest contact angle of 30 deg was reported [12]. The surface tension of liquid metals, such as mercury and gallium-indium-tin alloy (which is liquid at room temperature), is much larger than that of aqueous liquids, which implies that a higher voltage is needed to achieve the same contact angle change.

3 Experimental Setup

Two setups are used in our electrowetting experiments. Figure 1(*a*) is a configuration similar to the conventional setup used for studying the electrowetting phenomenon of aqueous liquids [18]. In this setup, the liquid-metal droplet is electrically connected to an external voltage source through a fine metal probe. Since the aqueous droplets are usually several millimeters in diameter, the effect of the probe on the experimental results can be ignored. In our case, however, due to the smaller dimension of the mercury droplet ($\leqslant$400 μm dia) and higher surface tension (435 mN/m), the mercury droplet acts more like a solid ball. In the experiment, a 37.5 μm dia tungsten probe is gently manipulated to touch the side surface of the droplet for an electrical contact instead of immersion in the case of an aqueous droplet. To minimize the probe effect on the electrowetting, the contact area is kept as small as possible and the probe is kept clean. The other electrical contact is through a metal film buried under the dielectric insulation film. The dielectric films used in the electrowetting experiment include Parylene C, Parylene N, silicon nitride, silicon dioxide, Teflon AF, anodized tantalum oxide, etc.

The second electrowetting setup is illustrated in Fig. 1(*b*). The probe is replaced by an electrode fabricated on top of the dielectric film. The circular electrode is designed to be smaller than the droplet base area to avoid blocking of the electric field. From experiments, we found no significant difference between the results from these two configurations for big droplets (e.g., diameter $>$400 μm). The second configuration offers some advantages which were discussed in our previous publication [5]. For smaller droplets ($\leqslant$ 100 μm), the diameter of circular contact and the width of the conducting line are decreased accordingly. We define a positive potential when the mercury droplet is connected to the anode of the voltage source, as shown in the Fig. 1(*a*). The droplet is illuminated with a light source, and its projection image is captured by using a charge-coupled device (CCD) camera. The stills and videos are taken for studying of the static and dynamic responses of the electrowetting, respectively. In the case of the dynamic study, a high-speed camera (up to 10 k frames per second (fps)) is used to record the details of electrowetting actuation. The contact angle is calculated based on the projection images.

A precise control of the droplet dimension is critical for fabricating MEMS devices. A few techniques, such as electroplating [19] and vapor deposition [20], have been developed for mercury droplet formation. In the vapor deposition, the droplet size is controlled by the deposition time. This technique is promising because it is suitable for batch droplet formation. However, it is only suitable for the formation of small droplets ($<$40 μm) since, if the exposure time is too long, mercury condenses randomly on the sample, decreasing the desired selectivity [21]. Our method for forming mercury droplets is jetting. The droplets are jetted either by using a Hamilton 7000 series microliter syringe or by using a Jetlab microdispensing system (from MicroFab Technologies, Inc.). The diameter of the droplet jetted from Hamilton syringe is 229$\pm$17 μm. A much higher precise control of droplets can be achieved by using the Jetlab system. The droplet from a single dispense is 50$\pm$2 μm. The positioning of the droplet to the circular electrical contact is accomplished with the help of a microscope and an *x*-*y*-*z* translation stage. The surface property also has a very important effect on the droplet dispensing. As an example, it is much easier to form a droplet on a high-adhesion-force surface (such as Parylene, glass, and gold) than on a low-adhesion-force surface (such as Teflon, rough Parylene). The jetted droplets often bounce back by those low-adhesion-force solid surfaces. A small circular gold spot is used to anchor the droplets in those situations. Figure 2 is a plot of the diameter of the droplets on a Parylene surface as a function of the number of dispenses. The squares are the measured diameters of the droplets, and the solid line is a calculation curve based on the average volume of a single dispense and the average contact angle of mercury droplet on the Parylene surface. This curve demonstrates a precise control of the formation of mercury droplets. For a 400 μm dia droplet, a single dispense will make a difference of $\sim$0.13 μm dia, theoretically.

4 Static Measurements

4.1 Electrowetting on a Parylene Film. The dielectric layer for the electrowetting experiment is a 0.6 μm Parylene C film deposited in a Labcoater PDS 2010 system. The diameter of the droplet is $\sim$390 μm. Two micrographs in the inset of Fig. 3 show the profiles of the droplet at 0 V and 180 V. The contact angle is initially 141 deg and decreases to 67 deg when the voltage increases to 180 V. The contact angle change due to the electrowetting effect is 74 deg, which is the largest value that has ever been achieved for a mercury droplet. The droplet starts to move laterally when the voltage is larger than 180 V. The squares in Fig. 3 are the measurements of the contact angle versus the applied voltage. The solid line is a theoretical curve based on Eq. (1). The

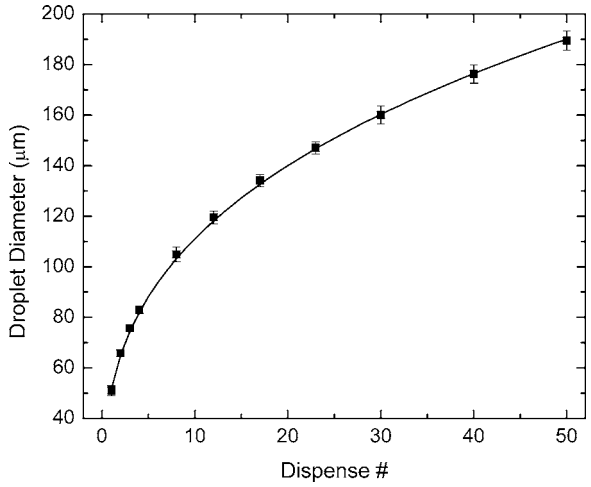

Fig. 2 Diameter of the droplet jetted by Jetlab system as a function of the number of dispenses

relative dielectric constant of the Parylene C film is 3.15, and the initial contact angle θ_0 is set to be 141 deg for matching the experimental results. The standard deviation of the contact angle measurement is <5 deg, which is resulted from the hysteresis of the Parylene surface. At low voltages, the experimental results agree well with the theoretical values; at high voltages ($\geqslant$140 V), a large deviation between the experimental and theoretical results occurs, implying a saturation phenomenon of the electrowetting. Because Eq. (1) is a linear equation with the parallel-plate approximation, it does not apply well at high electric field, where the decrease of contact angle slows down and saturation occurs according to the experimental results. The saturation phenomenon was observed in many aqueous liquids [22] as well as in liquid metals [5]. The saturation mechanism is not fully understood and believed to be related to air ionization around the contact line, trapped charges in the film, and polarization of the film [22,23].

4.2 Electrowetting Hysteresis. The surface chemical inhomogeneity and physical roughness cause the CAH, which is a very important effect on the electrowetting experiment. As the voltage increases, the droplet expands and the corresponding

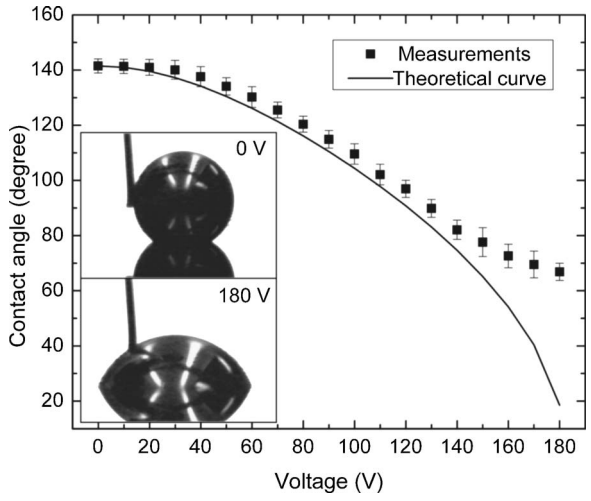

Fig. 3 Electrowetting of a mercury droplet on a parylene film: the squares are measured contact angles and the solid line is a calculation based on Eq. (1). The inset shows the stills of the droplet at 0 V and 180 V.

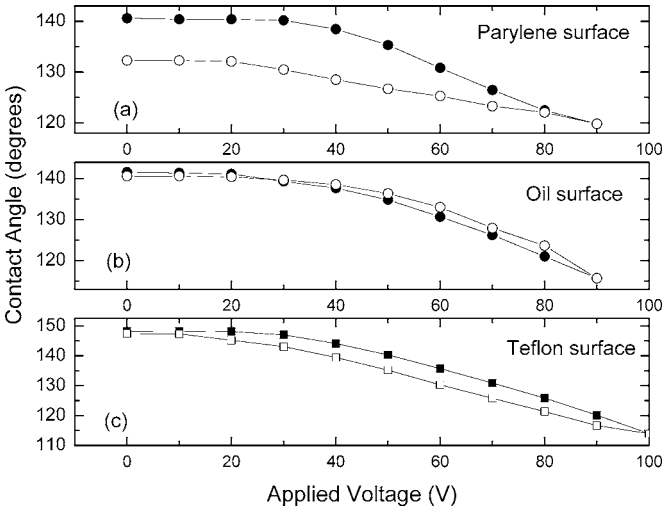

Fig. 4 Trajectory electrowetting measurements: (*a*) on a parylene surface, (*b*) on a vacuum-oil impregnated surface, and (*c*) on a Teflon AF-coated surface

angles are considered as advancing contact angles. The angles are receding contact angles as the voltage decreases. In Fig. 4(*a*), the curve shows a typical trajectory electrowetting measurement on a Parylene surface (the film is 0.6 μm thick). The droplet has an initial contact angle of around 141 deg. The angle decreases to 120 deg as the voltage increases to 90 V (which is much smaller than the saturation voltage according to the result of Fig. 3). As the voltage decreases from 90 V back to 0 V, the restored contact angle $\sim$132 deg, which is 9 deg smaller than the initial contact angle. From Fig. 4, we can see that the CAH opposes the electrowetting actuation, decreases the angle tuning range, and reduces the actuation reversibility. If we take the CAH effect into account, Eq. (1) can be rewritten as

$$\theta_v = \cos^{-1}\left(\cos\,\theta_0 + \frac{1}{2}\frac{\varepsilon_0\varepsilon}{\gamma_{lv}d}V^2\right) \pm \Delta\theta(\mathrm{CAH}) \qquad (2)$$

where the plus and minus signs apply to the situations of increasing voltage and decreasing voltage, respectively. $\Delta\theta$(CAH) represents the effect of the CAH on the contact angle in the electrowetting actuation. The magnitude of $\Delta\theta$(CAH) is implied by the difference between the trajectory curves in Fig. 4. We define the difference between the advancing angles (solid symbols) and the receding angles (open symbols) as electrowetting hysteresis (EWH). To decrease the CAH effect and thus to increase the actuation reversibility, we first tried to impregnate the dielectric film in a vacuum pumping oil (Maxima C Plus from Fisher Scientific), which is expected to produce a low CAH surface [2]. The samples are immersed in the oil for a couple of hours and then blown with a nitrogen gun. The curve (b) shows the trajectory measurements of the electrowetting on an oil-impregnated Parylene surface (the oil film is very thin and does not contribute to the insulation layer thickness). The $\Delta\theta$(CAH) of the oil-impregnated surface is much less than that of the pure Parylene surface. The oil-impregnation is a promising technique to produce a low contact-angle hysteresis surface. However, it is not compatible with the microfabrication process. Another way of achieving a low-hysteresis surface is coating the surface with a layer of Teflon AF or Teflon AF-like film. A very thin layer of Teflon AF 2400 ($\leqslant$1000 Å) is spin coated on top of a Parylene film. In Fig. 4(*c*), the curve shows the electrowetting measurements (0–100 V) on top of a Teflon AF-coated parylene film. The Teflon AF coating is 500 Å thick. The initial contact angle of the mercury droplet on Teflon AF surface is 150 deg.

In Table 1 are measurements of the CAH from the tilting-plate

Table 1 Measurements of CAH and EWH

Surfaces	CAH (deg)	EWH (deg)
Silicon nitride (LPCVD)	18	—
Silicon dioxide (LPCVD)	10	—
Parylene C	25	5–10
Parylene N	21	5–10
Oil-soaked parylene	2	1–2
Teflon AF-coated surfaces	4	2–4

measurements and of the EWH from the trajectory electrowetting experiments on several kinds of surfaces. The CAH of mercury droplet on most of the surfaces is larger than 10 deg. Very low hysteresis is observed on the oil-soaked surfaces and on the Teflon AF-coated surfaces. During the experiments, the mercury droplets are kept very clean to achieve reliable data. On the high hysteresis surfaces, such as silicon nitride, silicon dioxide, and Parylene N, the EWH is very large and the electrowetting actuation is very small or almost irreversible. On the other hand, at the very low hysteresis surface, such as oil-soaked surfaces, the electrowetting measurement is very difficult as the droplet starts to move around when a voltage is applied. The coating of Teflon AF film is a very simple process. The film is very reliable and can be micromachined [24]. These make Teflon AF coating a good choice for the electrowetting experiment.

4.3 Actuation Voltage Reduction. As implied by the electrowetting equation, there are two ways to reduce the actuation voltage: decreasing film thickness and increasing film dielectric constant. For comparison, we measure the driving voltage for achieving the same amount of contact angle change. A 200 Å thick Teflon AF film is coated on top of the dielectric films to lower the surface hysteresis with an initial contact angle of ~148 deg. The experimental data in Fig. 5 show the applied voltages for achieving 30 deg of contact angle change on the films of different thickness. The squares are the data of the Parylene films. As the thickness of the Parylene C film decreases from 2.4 μm to 0.14 μm, the driving voltage is lowered down from 245 V to 46 V. The theoretical calculation is also shown by the solid curve in Fig. 5. From these results, we can see that the decreasing of actuation voltage is approximately inversely proportional to the square root of the film thickness. However, further reducing the thickness becomes impractical as the film quality degrades due to occurring of pinholes. The breakdown voltage

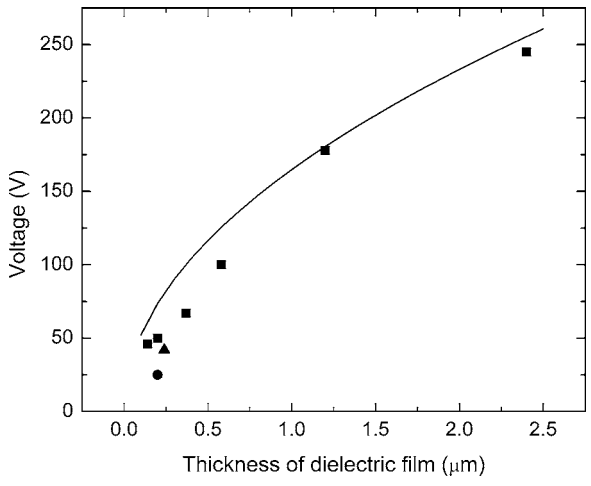

Fig. 5 Electrowetting actuation voltage for achieving 30 deg contact-angle change on dielectric films with different thickness and different dielectric constant (squares, parylene; triangle, silicon nitride; circle, tantalum oxide).

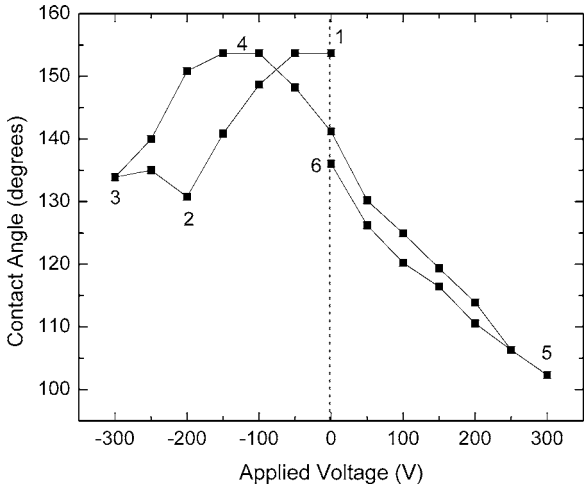

Fig. 6 Shifting of electrowetting curve due to the charges trapped in the insulating film in the electrowetting experiment.

will also limit the thinnest film for electrowetting actuation [25]. The driving voltage can be further decreased by choosing high dielectric constant materials. On a 0.24 μm thick nitride film (ε ~7), the driving voltage is 42 V (triangle). On a 0.2 μm thick tantalum oxide film (ε~25), the driving voltage is only 25 V (circle). The dielectric constant of tantalum oxide film is about eight times larger than that of Parylene film, which will cause a 2.8 times reduction in actuation voltage. The experimental results show that the actuation voltage of tantalum oxide film is about half of that of Parylene film with same thickness. The discrepancy is mainly due to the Teflon AF film coating. The tantalum oxide film is grown through an anodization process in a 40% phosphorous acid at 100°C and shows very high quality as a dielectric material. The film of barium strontium titanate (BST) is reported to have a dielectric constant as high as 180 [4], which seems to be a good candidate for the dielectric material. However, the reliability issues, such as leakage current and time-dependent dielectric breakdown, limit the usage of BST film for electrowetting actuation. In addition, further reduction of the driving voltage is limited by the 200 Å thick Teflon coating, which is equivalent to a ~2500 Å thick tantalum oxide film or a ~1.9 μm BST film in the electrowetting experiment.

4.4 Effect of Trapped Charges. As indicated in Eq. (1), the electrowetting effect should be symmetric between the positive and negative voltages. Verheijen and Prins [2] observed the influence of trapped charges on the electrowetting phenomenon of aqueous liquid and introduced a quantity V_T for the trapped charges in the electrowetting equation

$$\cos\theta_V = \cos\theta_0 + \frac{1}{2}\frac{\varepsilon_0\varepsilon}{\gamma_{lv}d}(V - V_T)^2 \tag{3}$$

where V_T is the voltage that needs to compensate the influence of the trapped charges. In Fig. 6, the measurements from 1 to 6 sequentially demonstrate the formation of trapped charges and its influence on the electrowetting results. From 1 (0 V) to 2 (−200 V), the contact angle decreases normally. The angle does not decrease any more from 2 (−200 V) to 3 (−300 V), which indicates an electrowetting saturation and some electrostatic charges are injected into the insulator. As the voltage changes back from −300 V to −150 V, the angle restores to 152 deg. From 4 (−150 V) to 5 (+300 V), the angle decreases from 152 deg to 105 deg. As the voltage changes back to 0 V, the angle restores to ~135 deg, which is 17 deg smaller than the initial value. The electrowetting curve is shifted from 0 V to ~−150 V due to the trapped charges. The trapped charges do not

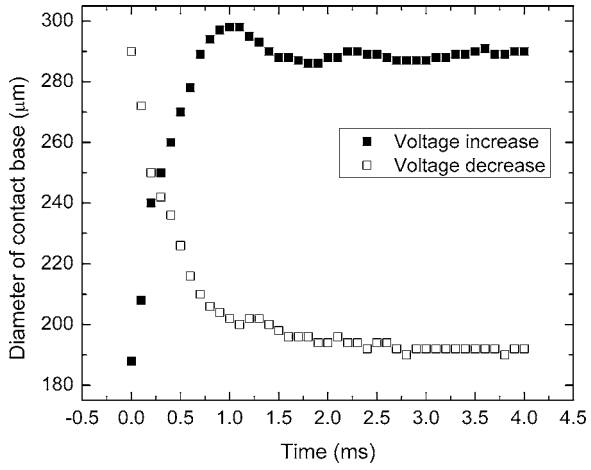

Fig. 7 Voltage step-response of electrowetting actuation on a Teflon AF-coated parylene film: evolution of the contact line length with time

disappear when an opposite voltage is applied. From this curve, we can see that $V_T \sim 150$ V and the trapped charge density is $\sim 1.4 \times 10^{-7}$ C/cm^2 (3 μm thick Parylene film). The trapped charges decrease the electrowetting force on the negative side and increase the force on the positive side, as indicated by Eq. (3).

5 Dynamic Response

The dynamic response of the electrowetting actuation is measured by using the high-speed camera. The dielectric film for the experiment is a 0.2 μm thick Parylene with a 200 Å thick Teflon AF coating. The camera starts video recording triggered by the rising/falling edge of a voltage step (from 0 V to 50 V or from 50 to 0 V). The rise/fall time of the voltage step is <20 μs. When the video recording speed is 10 k fps, the resolution of the camera is limited to 256×48 pixels. As a result, only the region close to the liquid-solid interface is recorded. In this situation, it is more convenient and accurate to examine the contact line change than the contact angle change. Figure 7 is the evolution of the contact line length (or the diameter of the contact base) with time for a 350 μm dia droplet. The up-triangles are the measurements of the rising voltage step (from 0 V to 50 V), and the down-triangles are the data of the falling voltage step (from 50 V to 0 V). The rise time of the electrowetting actuation is ~ 0.5 ms, and the fall time is ~ 1 ms. For the rising voltage step, the contact line expands from 190 μm to 290 μm. The expanding velocity of the droplet base is 250 μm/ms at $t=0$ and decreases with time. Conversely, the contact line recedes from 290 μm to 190 μm at the falling voltage step and the expanding velocity is 200 μm/ms at $t=0$.

Since the capacitance formed between the droplet base and the buried electrode is very small ($\leqslant 5$ pF), the electron charging time in the electrical circuit is as fast as 0.5 ns (the serial resistance is around 100 Ω). The rise/fall time of the electrowetting actuation is mainly determined by the droplet hydrodynamic properties [14]. The results of dynamic response could be explained by a molecular kinetic model [26]. During the electrowetting actuation, the droplet is spreading or receding on a solid surface. According to this model, the main energy dissipation of a liquid droplet spreading on a solid surface is resulted from the molecular displacements within the immediate vicinity of the three-phase contact line. We can also think that the dissipation is due to the friction between the liquid molecules and the solid surface when there is relative movement. As discussed in Ref. [27], the spreading rate of the droplet base radius is

Table 2 Measured rise and fall time of droplets with different diameters

Droplet diameter (μm)	Rise time (ms)	Fall time (ms)
820	1.4	2.6
475	0.9	2.4
350	0.5	1.0
50	0.1	0.2

$$\frac{dr}{dt} = \frac{1}{\xi}\gamma_{lv}(\cos\theta_v - \cos\theta) \tag{4}$$

where r is the radius of the drop base, ξ is the coefficient of friction between the solid and the liquid per unit length of the wetting line, and θ is the contact angle at time t. Equation (4) states that the spreading rate is proportional to the electrowetting force $\gamma_{lv}(\cos\theta_v - \cos\theta)$. From Fig. 7, the friction coefficient ξ is calculated to be ~ 0.35 Ns/cm^2 for the case of rising voltage step and ~ 0.5 Ns/cm^2 for the case of falling voltage step. Equation (4) also indicates that the radius spreading rate does not scale with the droplet dimension as long as the friction coefficient is a constant. Hence, we expect that the decay time of the electrowetting actuation decreases linearly with the droplet size if the contact angle change is the same. Table 2 shows the rise and fall times of the electrowetting actuation for the droplets with different diameters. The contact angle change is ~ 30 deg. As the diameter of the droplet decreases from 820 μm to 50 μm, the rise and fall times decrease from 1.4 ms and 2.6 ms to 0.1 ms and 0.2 ms, respectively. Both of the rise and fall times are inversely proportional to the droplet diameter, which agrees with our conclusion based on Eq. (4). The data also show that the fall time is usually larger than the rise time, which is due to a larger friction coefficient at a falling voltage step. All of the measurements are done on the Teflon AF-coated surfaces. The second electrowetting setup of Fig. 1(*b*) is used to avoid the probe effect, especially for the small droplets.

Figure 8 shows the response to a 100 Hz, 100 V square voltage pulse. The experiment is performed on a 1 μm thick Teflon AF-coated Parylene film. The amplitude of the contact angle change is ~ 20 deg, and the height changing amplitude is ~ 20 μm. The evolutions of the contact angle and of the droplet height are very similar, indicating that the height change is directly resulted from the contact angle change. From Figs. 7 and 8 we see that the droplet also oscillates during the electrowetting deformation, which is illustrated by the evolutions of the contact base, contact

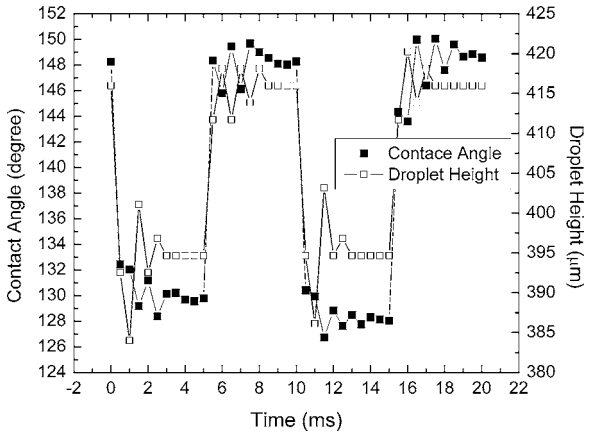

Fig. 8 Electrowetting actuation of droplet driven by a 100 Hz, 100 V square voltage pulse: The evolutions of the contact angle (solid squares) and droplet height (open squares)

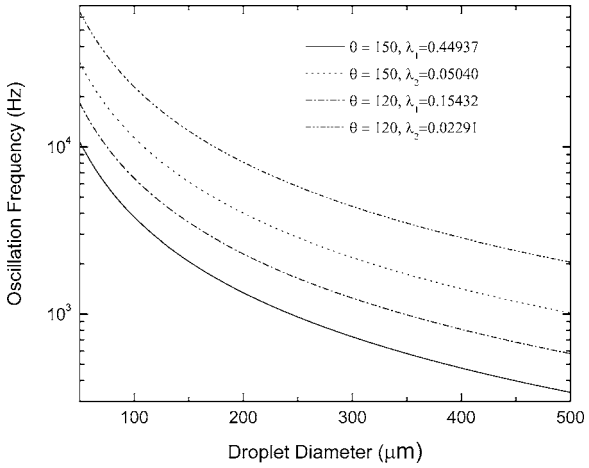

Fig. 9 Oscillation frequency of a bound liquid droplet as a function of the diameter

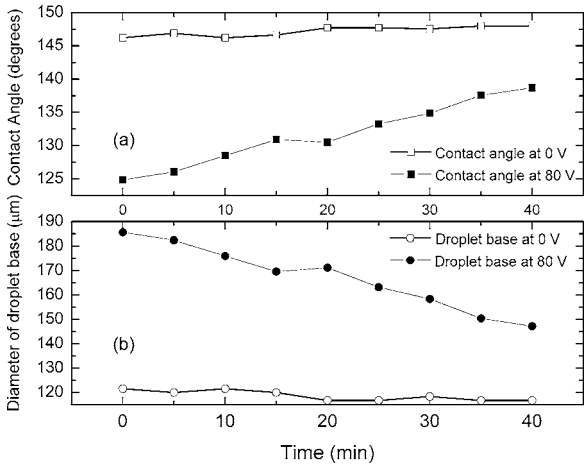

Fig. 10 Decaying of electrowetting actuation amplitude with time: (*a*) contact angle and (*b*) droplet base diameter

angle, and droplet height. We have reported the observed mercury droplet oscillation in our previous electrowetting experiments [5]. The oscillation is underdamped, which is different from the results of critically damped or overdamped oscillations shown in [27]. The oscillation frequency in Fig. 8 is ~667 Hz, which will be compared to the theoretical value in the following paragraph. We also observe in Fig. 8 that the evolution of the contact angle is little different from the height evolution, which implies that higher mode droplet oscillation is excited during the electrowetting actuation. To achieve a pure and stable electrowetting actuation, these resonant frequencies should be avoided for the driving voltage signal. Equation (1) is only a static description of droplet electrowetting behavior under an electrical field. The dynamic response is closely related to the droplet natural oscillation modes.

As reported in Ref. [28], the oscillation of a sessile liquid droplet is also excited in the electrowetting actuation. The oscillation frequency of a bound liquid droplet on a flat solid surface, derived by Strani and Sabetta [29], is

$$f_i = \frac{1}{2\pi}\left[\frac{\gamma}{\rho R^3 \lambda_i}\right]^{1/2} \tag{5}$$

where γ is surface tension of liquid droplet, R is droplet radius, ρ is mass density, and λ_i is the eigenvalue corresponding to mode i. The relationship of the oscillation frequency versus droplet diameter is plotted in Fig. 9, where we used the eigenvalues λ_1 and λ_2 from Ref. [30] for the first two modes with contact angles of 150 deg and 120 deg. As the diameter droplet decreases, the oscillation frequency increases dramatically. Figure 9 also shows that the oscillation changes with the contact angle. The diameter of this droplet is 440 μm for the experiment of Fig. 8, and the oscillation frequency of the first mode is 410 Hz and of the second mode is 1200 Hz (θ=150 deg). The oscillation frequency from Fig. 8 is closer to the first mode. We need to note that the frequency varies with contact angle, as shown in Fig. 9. In the case of electrowetting actuation, the droplet is not bound on the surface. The contact angle decreases and the diameter increases as the droplet expands. The droplet oscillation excited during the electrowetting actuation, which cannot be described by Eq. (5), is much more complicated and new mathematical model needs to be established to address this motion.

6 Reliability Test

To apply the electrowetting for MEMS devices, the actuation needs to be highly reliable. Although reversible electrowetting actuation has been reported by many research groups [2–5], the long-term reliability, to our knowledge, has not yet been addressed. The reliability is investigated by applying a continuous voltage actuation signal to the droplet. The evolutions of the contact angle and of the diameter of the droplet base are recorded. Figure 10 shows the results of a reliability test performed in a normal air environment with a square voltage waveform (from −80 V to 80 V) of 10 Hz. As we can see from the curve in Fig. 10(*a*), the actuation amplitude (i.e., contact angle change) decays with time. Initially, the contact angle change is 21 deg and decreases to 10 deg after 40 min. We also note that the contact angle at 0 V does not change, obviously, while the contact angle at 80 V increases with time. The curve in Fig. 10(*b*) shows the corresponding evolution of the droplet base diameter. The base diameter does not change too much at 0 V, and at 80 V, it decreases from 187 μm to 150 μm. The droplet motion ceases after ~2 hr. We believe that there are two main reasons for the electrowetting actuation decay and failure: charge trapping and surface degradation. The dielectric film may trap charges under a high electric field, especially the vicinity of contact line. The air ionization also induces the trapped charges on the surface, which may migrate into the film. The charges can be accumulated during a continuous pulse driving and form a trapped charge layer. As we see from Eq. (2), this charge layer will cancel out part of or all of the applied electric field, which thus results in the actuation decay or case. The effect of the charge trapping on the reliability can be verified by comparing the results between unipolar and bipolar pulse drivings. The bipolar pulse is expected to reduce the charge accumulation by changing the polar of the electrical field periodically. We found the actuation driven by a bipolar pulse lasts about two times longer than the case of a unipolar pulse. This indicates that charge trapping does affect the reliability. However, we think there are some other reasons for the decay as the bipolar pulse driving cannot dramatically improve the reliability. Since the testing is performed in the air, the charged surfaces of the droplet and of dielectric film will trap the dust from the air and, thus, the droplet surface and the film surface are contaminated. We observed in the microscope that the surface degradation first occurs at the vicinity of the contact line. As the surface area degrades, the contact angle hysteresis increases. Thus, the actuation amplitude decreases and the contact line recedes. We further proved our thought by performing a test in Fomblin vacuum oil. Fomblin oil has very good insulating properties and low vapor pressure. It can prevent dust accumulation from air and thus avoid surface degradation. More than a million cycles of actuation have been recorded without any measurable degradation. We expect there may be some other issues beyond the charge trapping and surface degradation causing actuation decay. A more dedicated experiment needs to be done to explore this area and improve the electrowetting reliability.

7 Conclusion

We present the results of our investigations on the electrowetting actuation of mercury droplets on dielectric insulation films. Static measurements show good agreement with electrowetting equation at low voltages while electrowetting saturates at high voltages. Very large contact angle change and very low actuation voltage have been achieved. Because of the successfully developed low-hysteresis surfaces, the electrowetting actuation is highly reversible with a long-time operation. Dynamic testing results show that a rise and fall times are inversely proportional to the droplet diameter and can be less than 1 ms. The fast response implies that the electrowetting can be used for high-frequency actuation. Low voltage, large actuation amplitude, and high reversibility make this electrowetting a promising actuation technique for MEMS devices. A piston-motion micromirror actuated by this mechanism was successfully demonstrated by our group. Other MEMS devices, including a capacitive RF switch and a reflective display device, have been investigated and demonstrated, which are going to be reported in future publications. The electrowetting of other liquid metals, such as gallium-indium-tin alloy, is also under investigation. Compared to mercury, the alloy has advantages of lower vapor pressure and nontoxicity. However, the electrowetting experiment on liquid-metal alloy is much more difficult since it will be oxidized in air very quickly and sticks to most of surfaces.

References

[1] Berge, B., 1993, "Electrocapillarity and Wetting of Insulator Films by Water," CR Acad. Sci. Ser. II, **317**, pp. 157–163.

[2] Verheijen, H. J. J., and Prins, M. W. J., 1999, "Reversible Electrowetting and Trapping of Charge Model and Experiments," Langmuir, **15**, pp. 6616–6620.

[3] Seyrat, E., and Hayes, R. A., 2001, "Amorphous Fluoropolymers as Insulators for Reversible Low Voltage Electrowetting," J. Appl. Phys., **90**, pp. 1383–1386.

[4] Moon, H., Cho, S. K., Garrell, R. L., and Kim, C. J., 2002, "Low Voltage Electrowetting-on-Dielectric," J. Appl. Phys., **92**, pp. 4080–4087.

[5] Zeng, H., Feinerman, A. D., Wan, Z., and Pancham, R. P., 2005, "Piston-Motion Micromirror Based on Electrowetting of Liquid Metals," J. Microelectromech. Syst., **14**, pp. 285–294.

[6] Wan, Z., Feinerman, A. D., and Zeng, H., 2004, "Electrocapillary Piston Motion and a Prototype of Phase-Manipulating Micromirror," J. Microelectromech. Syst., **13**, pp. 620–627.

[7] Berge, B., and Peseux, J., 2000, "Variable Focal Lens Controlled by an External Voltage: An Application of Electrowetting," Eur. Phys. J. E, **3**, pp. 159–163.

[8] Hayes, R. A., and Feenstra, B. J., 2003, "Video Speed Electronic Paper Based on Electrowetting," Nature (London), **425**, pp. 383–385.

[9] Lee, J., and Kim, C. J., 1999, "Liquid Micromotor Driven by Continuous Electrowetting," *Proc. IEEE MEMS*, IEEE, New York, pp. 538–543.

[10] Prins, M. W. J., Welters, W. J. J., and Weekamp, J. W., 2001, "Fluid Control in Multichannel Structures by Electrocapillary Pressure," Science, **291**, pp. 277–280.

[11] Darhuber, A. A., Valentino, J. P., Davis, J. M., Troian, S. M., and Wagner, S., 2003, "Microfluidic Actuation by Modulation of Surface Stresses," Appl. Phys. Lett., **82**, pp. 657–659.

[12] Pollack, M. G., Fair, R. B., and Shenderov, A. D., 2000, "Electrowetting-Based Actuation of Liquid Droplets for Microfluidic Applications," Appl. Phys. Lett., **77**, pp. 1725–1726.

[13] Srinivasan, V., Pamula, V. K., and Fair, R. B., 2004, "An Integrated Digital Microfluidic Lab-on-a-Chip for Clinical Diagnostics on Human Physiological Fluids," Lab Chip, **4**, pp. 310–315.

[14] Mugele, F., and Baret, J. C., 2005, "Electrowetting: From Basics to Applications," J. Phys.: Condens. Matter, **17**, pp. 705–774.

[15] Simon, J., Saffer, S., and Kim, C. J., 1997, "A Liquid-Filled Microrelay With a Moving Mercury Microdrop," J. Microelectromech. Syst., **6**, pp. 208–216.

[16] Kondoh, Y., Takenaka, T., Hidaka, T., Tejima, G., Kaneko, Y., and Saitoh, M., 2005, "High-Reliability, High Performance RF Micromachined Switch Using Liquid Metal," J. Microelectromech. Syst., **14**, pp. 214–220.

[17] Mohseni, K., 2005, "Effective Cooling of Integrated Circuits Using Liquid Alloy Electrowetting," 21st IEEE SEMI-THERM Symposium.

[18] Vallet, M., Berge, B., and Vovelle, L., 1996, "Electrowetting of Water and Aqueous Solutions on Poly(ethylene Terephthalate) Insulating Films," Polymer, **37**, pp. 2465–2470.

[19] Kounaves, S. P., and Buffle, J., 1987, "An Iridium-Based Mercury-Film Electrode, Part I Selection of Substrate and Preparation," J. Electroanal. Chem., **216**, pp. 53–69.

[20] Simon, J., Saffer, S., and Kim, C. J., 1997, "A Liquid-Filled Microrelay With a Moving Mercury Microdrop," J. Microelectromech. Syst., **6**, pp. 208–216.

[21] Latorre, L., Kim, J., Lee, J., Guzman, P. P. D., Lee, H. J., Nouet, P., and Kim, C. J., 2002, "Electrostatic Actuation of Microscale Liquid-Metal Droplets," J. Microelectromech. Syst., **11**, pp. 302–307.

[22] Vallet, M., Vallade, M., and Berge, B., 1999, "Limiting Phenomena for the Spreading of Water on Polymer Films by Electrowetting," Eur. Phys. J. B, **11**, pp. 583–591.

[23] Peykov, V., Quinm, A., and Ralston, J., 2000, "Electrowetting: A Model for Contact-Angle Saturation," Colloid Polym. Sci., **278**, pp. 789–793.

[24] Hsieh, W. H., Hsu, T. Y., and Tai, Y. C., 1997, "A Micromachined Thin-Film Teflon Electret Microphone," *Solid State Sensors and Actuators*, Transducers '97 International Conference, IEEE, Chicago, Vol. 1, pp. 425–428.

[25] Lee, J., Moon, H., Fowler, J., Schoellhammer, T., and Kim, C. J., 2002, "Electrowetting and Electrowetting-On-Dielectric for Microscale Liquid Handling," Sens. Actuators, A, **95**, pp. 259–268.

[26] Blake, T. D., and Haynes, J. M. J., 1969, "Kinetics of Liquid/Liquid Displacement," J. Colloid Interface Sci., **30**, pp. 421–423.

[27] Decamps, C., and De Coninck, J., 2000, "Dynamics of Spontaneous Spreading Under Electrowetting Conditions," Langmuir, **16**, pp. 10150–10153.

[28] Klingner, A., Herminghaus, S., and Mugele, F., 2003, "Self-Excited Oscillatory Dynamics of Capillary Bridges in Electric Fields," Appl. Phys. Lett., **82**, pp. 4187–4189.

[29] Strani, M., and Sabetta, F., 1984, "Free Vibrations of a Drop in Partial Contact With a Solid Support," J. Fluid Mech., **141**, pp. 233–247.

[30] Smithwick III, R. W., and Boulet, J. A. M., 1989, "Vibrations of Microscopic Mercury Droplets on Glass," J. Colloid Interface Sci., **130**, pp. 588–596.

A Microfluidic Mixer Utilizing Electrokinetic Relay Switching and Asymmetric Flow Geometries

Yiou Wang

Jiang Zhe

Department of Mechanical Engineering,
The University of Akron,
Akron, OH 44325

Prashanta Dutta
School of Mechanical and Materials Engineering,
Washington State University,
Pullman, WA 99164-2920
e-mail: dutta@mail.wsu.edu

Benjamin T. Chung
Department of Mechanical Engineering,
The University of Akron,
Akron, OH 44325

Performances of a hybrid electrokinetic-passive micromixer are predicted numerically. An h/p-type spectral element method is used to simulate the mixing behavior in microdevices. The numerical algorithm employs modal spectral expansion in quadrilateral and unstructured triangular meshes and provides high-order numerical accuracy. A second-order accurate, stiffly stable integration scheme is used for temporal integration. In the numerical technique, the electric double layer is not resolved to avoid expensive computation, rather a slip velocity is assigned at the channel surface based on the electric field and the electroosmotic mobility. The presented hybrid mixing scheme takes advantages of mixing enhancements induced by asymmetric flow geometries and electrokinetic relay actuation. Effects of relay frequency, applied electric potential, channel width, and channel geometry on micromixing have been conducted. Numerical results show that electrokinetic relay at an appropriate frequency causes effective mixing. Moreover, asymmetric flow geometries and narrow channel width are critical for ultraeffective mixing. The proposed hybrid mixing scheme not only provides excellent mixing within very short time, but also can easily be integrated with microdevices for "lab-on-a-chip" applications because there is no need of any external mechanical pumps. [DOI: 10.1115/1.2436578]

Keywords: electrokinetic flow, hybrid mixing, microfluidic, zeta potential

1 Introduction

Mixing of liquid samples is an important task in microfluidic-based biological and chemical systems, such as "lab-on-a-chip" or micro-total-analysis-systems (μTAS) applications. Rapid mixing permits quick processing and analysis of samples and, hence, allows a high throughput system. However, fast mixing in microchannels has been a challenging problem. Because of the nature of laminar flow in the microscale, mixing is mainly dominated by diffusion. In the absence of any turbulence, it is difficult to improve the mixing simply through diffusion. In particular, for large molecules, such as DNA and proteins, the diffusion coefficients are on the order of 10^{-10} m^2/S or less. Hence, the resulting mixing time and the mixing length can both be prohibitively long and impractical. A highly efficient micromixer that permits fast mixing is greatly expected to benefit a number of critical applications, such as DNA hybridation, cytometric analysis, and immunoassays.

Existing micromixers fall into two categories: active mixers and passive mixers. Passive mixers have been studied extensively because of the advantages of low cost, ease of fabrication, and no need for additional power input. Passive mixers have no moving parts and achieve mixing by virtue of their structure or topology alone. Using passive structures, the fluids are forced to change directions, split, or reunify to increase the contact areas of substreams [1–4]. As the microchannel dimensions are scaled down to smaller values, larger flow impedance will be generated that requires higher pump power. Thus, most passive mixers reported thus far only show relatively high mixing efficiency at a low flow rate. Recently, a rotation mechanism has been introduced to increase the contact area by utilizing three-dimensional (3D) serpentine microchannel and bias-relief structures [5,6]. In spite of high mixing efficiency at high flow rates, the complex 3D structures are hard to fabricate and create large flow impedances.

Active mixers can produce excellent mixing by using external energy. A variety of active chaotic mixing schemes has been applied to microfluidic devices to enhance the micromixing efficiency. These schemes include electrokinetic mixing [7–9], ultrasonic excitation [10], magnetic stirring [11], thermal bubble mixing [12], magnetic beads excitation [13,14], dielectrophoretic mixing [15], bubble acoustic agitation [16], shear superposition micromixer [17], etc. Among them, electrokinetic mixing is a favorable mixing scheme for ease of manufacturability and simplicity. Another advantage is that electrokinetic mixing scheme can be easily integrated into the microfluidic chips. Furthermore, there is no penalty of dramatic pressure drop with electrokinetic driven flow. Recently, He et al. [18] reported a micromixer based on flow splitting and a lateral transport mechanism under electroosmotic flow at a low flow rate. Johnson et al. [19] presented a T-microchannel with ablated walls for improving mixing efficiency over a broad range of electroosmotic flow rates.

Although passive mixing and electrokinetic relay mixing are efficient mixing schemes, if one mixing mechanism is used individually, it cannot meet the requirements in some biochemical analysis for μTAS applications because the mixing times are in the order of seconds, especially at large flow rates. In this paper, a numerical study is presented for a hybrid rapid micromixer. The proposed hybrid micromixer takes advantages of both mixing enhancements induced by asymmetric serpentine structures and the electrokinetic relay actuation. In order to obtain the high mixing performance, the effects of microchannel geometry, electrokinetic relay frequency, and electric field strength on mixing performance are investigated systematically.

The rest of the paper is organized as follows. In Sec. 2, the micromixer design is introduced. In Sec. 3, the mathematical model for the electrokinetic relay mixing is presented along with underlying assumptions and approximations. Next, the numerical algorithm used to compute the electric field, velocity field, and concentration in the microfluidic mixer is discussed. In Sec. 5,

Contributed by the Fluids Engineering Division of ASME for publication in the JOURNAL OF FLUIDS ENGINEERING. Manuscript received February 3, 2006; final manuscript received June 29, 2006. Review conducted by Ali Beskok. Paper presented at the 2005 ASME International Mechanical Engineering Congress (IMECE2005), Orlando, Florida, November 5–11, 2005.

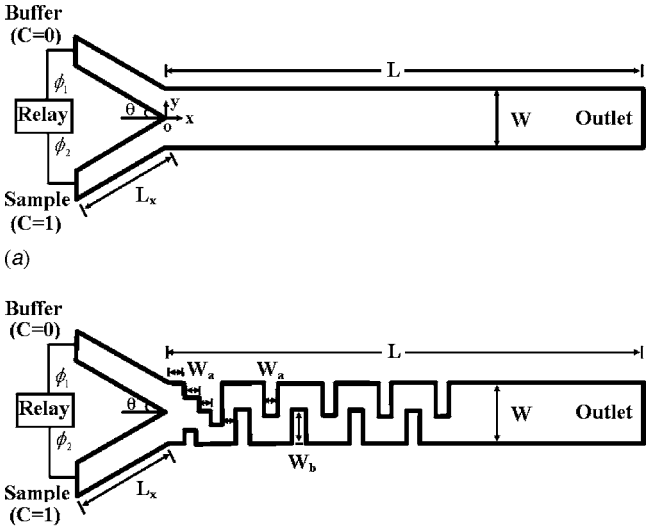

Fig. 1 Schematic diagram of (*a*) electrokinetic relay micromixer and (*b*) hybrid (electrokinetic asymmetric structure) micromixer

simulation results are provided for electrokinetic relay mixer and hybrid mixer. Finally, a summary and conclusions of this numerical work are presented.

2 Micromixer Design

Figure 1(*a*) shows the schematic view of a Y-form electrokinetic micromixer considered in this study. Two different fluids are periodically pumped into the mixing chamber through two branches of Y-channel. Inlet 1 brings buffer solution of scalar concentration $C=0$, and inlet 2 feeds sample solution of scalar concentration $C=1$. In this study, an electrokinetic pumping mechanism is used to drive the fluid from inlet reservoirs to outlet through the mixing chamber. In order to obtain electrokinetic relay effects, the externally applied electric potentials at inlets 1 and 2 are set as

$$\phi_1 = \phi_s + m(t)\phi_a \tag{1}$$

$$\phi_2 = \phi_s + [1 - m(t)]\phi_a \tag{2}$$

where ϕ_s and ϕ_a are the steady and alternating parts of the externally applied electric potential, respectively. The time-dependent parameter $m(t)$ is given as

$$m(t) = 0, \quad \text{if} \quad \sin(\pi f t) > 0 \tag{3}$$

$$m(t) = 1, \quad \text{if} \quad \sin(\pi f t) \leq 0 \tag{4}$$

In this paper, we set $L_x=200$ μm, $L=1000$ μm, and $\theta=30$ deg. The channel width (W), applied electric potentials (ϕ_s and ϕ_a), and relay frequency (f) are varied from case to case. The width of each inlet channel is one-half of the width of mixing channel. To further intensify the mixing, asymmetric serpentine structures are placed into the mixing channel, as shown in Fig. 1(*b*).

3 Mathematical Model

Electroosmotic flow is the bulk motion of an electrolyte solution under the action of an electric field. When an electrolyte comes in contact with a channel (dielectric) surface, the surface generally acquires net surface charges due to ionization, ion adsorption, or ion absorption. These surface charges influence the distribution of counterions close to the surface, and form an electric double layer (EDL) adjoining to the surface. The extent of EDL depends on the ion concentration in the electrolytes and is normally characterized by the Debye layer thickness (λ). For example, ion concentration of 1 mM and 100 mM corresponds to Debye length thickness of 10 nm and 1 nm, respectively. If an external electric field, $\vec{E}=-\nabla\phi$, is applied along the channel surface by setting electric potential (ϕ) at end reservoirs, there will be net movement of electrolyte due to the formation of an electrokinetic body force. The governing equations for ionized incompressible flow with electrokinetic body forces are given by the continuity and Navier-Stokes equations [20]

$$\frac{\partial u}{\partial x} + \frac{\partial v}{\partial y} = 0 \tag{5}$$

$$\rho_f\left(\frac{\partial \mathrm{u}}{\partial \mathrm{t}} + u\frac{\partial u}{\partial x} + v\frac{\partial u}{\partial y}\right) = -\frac{\partial P}{\partial x} + \mu\left(\frac{\partial^2 u}{\partial x^2} + \frac{\partial^2 u}{\partial y^2}\right) + \rho_e E_x \tag{6}$$

$$\rho_f\left(\frac{\partial v}{\partial t} + u\frac{\partial v}{\partial x} + v\frac{\partial v}{\partial y}\right) = -\frac{\partial P}{\partial y} + \mu\left(\frac{\partial^2 v}{\partial x^2} + \frac{\partial^2 v}{\partial y^2}\right) + \rho_e E_y \tag{7}$$

where u is the streamwise velocity, v is the cross-stream velocity, ρ_f and ρ_e are the fluid density and electric charge density, respectively, t is the time, P is the pressure, and μ is the viscosity. The externally applied electric potential (ϕ) is governed by the charge conservation equation

$$\frac{\partial}{\partial x}\left(\sigma\frac{\partial \phi}{\partial x}\right) + \frac{\partial}{\partial y}\left(\sigma\frac{\partial \phi}{\partial y}\right) = 0 \tag{8}$$

where σ is the electrical conductivity of fluid. The electrokinetic potential distribution (ψ) due to the presence of EDL is related to electric charge density (ρ_e) by the Poisson equation [20]

$$\frac{\partial^2 \psi}{\partial x^2} + \frac{\partial^2 \psi}{\partial y^2} = -\frac{\rho_e}{\varepsilon} = -\frac{e(n^+ z^+ + n^- z^-)}{\varepsilon} \tag{9}$$

where e is the electron charge, z is the valence, n is the ion density (concentration). For a symmetric, dilute, and univalent electrolyte ($z^+=-z^-=z$), the charge density can be expressed as [21]

$$\rho_e = -2ezn_0 \sinh\left(\frac{ez\psi}{k_B T}\right) \tag{10}$$

where k_B is the Boltzmann constant, T is the absolute temperature, and n_0 is the ion concentration at the bulk region.

The scalar transport (concentration) equation for the mixing fluids can be given as

$$\frac{\partial C}{\partial t} + u\frac{\partial C}{\partial x} + v\frac{\partial C}{\partial y} = D\left(\frac{\partial^2 C}{\partial x^2} + \frac{\partial^2 C}{\partial y^2}\right) \tag{11}$$

where C is the concentration of species (sample or buffer) and D is the mass diffusion coefficient of the species.

The aforementioned mathematical model is based on a number of assumptions and approximations. First, fluids (both sample and buffer) are incompressible and Newtonian. Fluid properties, such as viscosity, permittivity, and electric conductivity, are independent of local and overall electric field strength. Moreover, ion convection effects are negligible; thus, the Poisson-Boltzmann equation is valid. Second, there is no gravitational effect, and no chemical reaction between species is considered. Third, temperature variation due to Joule heating is negligible. This can be justified for low electric field (<500 V/cm) cases investigated here. Fourth, species concentrations remain unaffected by the electromigration.

In this study, we have considered a two-dimensional (2D) (spatial) model to quantify the mixing efficiency in the microchannel. It is assumed that the variation of dependent variables in channel height direction is negligible. Note that the 2D assumption is commonly adopted in modeling of electroosmotic flow [22,23]. Patankar and Hu [24] verified the validity of this assumption in electroosmotic flow by comparing two- and three-dimensional

models. Moreover, Lin et al. [25] have shown that 2D numerical model can effectively predict the electrokinetic mixing phenomena observed (experimentally) in microchannels. However, the 3D effect might be present in the hybrid micromixer due to the presence of serpentine structures.

4 Numerical Model

The electrokinetic velocity field and concentration distribution in the micromixer can be obtained by solving Eqs. (5)–(11) with appropriate boundary conditions. However, the direct solution of the coupled system will be extremely expensive (computationally) due to different length scales associated with microfluidic devices. Generally, microfluidic channels are $1-10$ μm thick, $10-500$ μm wide, and $1-5$ cm long. In addition to the diverse spatial length scales, the EDL thickness ranges between 0.1 nm and 10 nm. The complete numerical solution of electrokinetic flows were presented in [24] based on the Debye-Huckel approximation. Later, Dutta et al. presented the steady electroosmotic flow in 2D planar geometries using spectral element method [26]. In that study, they have resolved the EDL for dilute electrolytes where the channel height was two orders of magnitude higher than Debye length (λ). However, in most microfluidic devices, the ratio of channel height to Debye length ranges between 10^3 and 10^5. Therefore, device level simulation will be computationally expensive, if one would like to resolve all length scales appropriately. The computational effort of electrokinetic flow can be minimized considerably by introducing an effective slip velocity at the channel wall [21]. This slip velocity captures the thin EDL effects on the fluid flow. This concept has been reported recently in a number of numerical works to study electrokinetic flow injection [22], electrokinetic flow control [27], etc. Thus, in this study the flow field is obtained from the continuity and Navier-Stokes equations under effective slip velocity conditions without considering the body force terms ($\rho_e\vec{E}$).

4.1 Boundary Conditions. The external electric potential distribution (ϕ) is obtained from Eq. (8), which is subjected to insulating boundary conditions ($\nabla\phi.\vec{n}=0$) on the channel surfaces. The insulating boundary condition at the channel wall is justified for the microfluidic chip because silicon, glass, poly-di-methyl siloxane (PDMS), or other insulating material is used as channel wall. The electric potentials at the inlet reservoirs are obtained from Eqs. (1)–(4), while the exit reservoir is connected to a ground ($\phi=0$). In our numerical formulation, the time-dependent boundary conditions provide unsteady electric field at every time step.

For electrokinetic relay actuation, the velocity at the slip plane is specified as

$$\vec{V}=\left(-\frac{\varepsilon\zeta}{\mu}\frac{\partial\phi}{\partial l},0\right) \tag{12}$$

where l is the direction tangent to the channel wall and ζ is the zeta potential. For simplicity, ζ is assumed constant along the channel wall. The velocities at the exit reservoir are set as fully developed ($\partial u/\partial x=0$ and $\partial v/\partial x=0$). In solving velocity field, pressure is maintained atmospheric at both inlet and exit reservoirs. That means fluid flow is entirely driven by the electrokinetic effects. Hence, the mixing performances presented in this study are for different electric potentials. Finally, to solve Eq. (11), the dimensionless species concentration is set at 0 and 1 for inlets 1 and 2, respectively, while the outlet condition is $\partial C/\partial x=0$.

4.2 Numerical Scheme and Accuracy. An h/p-type spectral element method is used to calculate electric potential (ϕ), velocity fields ($\vec{V}$), and species concentration (C) in the micromixer. The numerical algorithm employs modal spectral expansion of Jacobi polynomials in quadrilateral and unstructured triangular meshes [28]. Thus, we can discretize the complex engineering geometry with great flexibility due to the unstructured grid and can still maintain the high-order numerical accuracy. Time integration is performed by a second-order accurate, stiffly stable integration scheme. Details of the numerical scheme and convergence results were presented in [26,29,30], and hence, those will not be repeated here.

In the numerical simulation of 50 μm wide micromixer, 250 elements (50 elements in the streamwise direction and 5 elements in the cross-stream direction) are used in the active part of the mixer. This corresponds to $\Delta x=20$ μm and $\Delta y=10$ μm for h-type discretization. For 100 μm and 300 μm wide channel, the number of h-type elements in the cross-stream direction is increased to 10 and 30, respectively. By keeping the elemental discretization (h-type) of the domain fixed, the p-type refinement is employed by increasing the expansion order of polynomial within each element. One of the main features of this algorithm is the exponential decay of discretization errors on p-type refinement for a sufficiently smooth problem. Since we do not have analytical expressions for velocity and concentration fields presented in this study, p-type refinement is used to obtain grid-independent results. For electrokinetic relay mixing, the time accuracy is also very important for the simulation results. The h/p-type spectral algorithm also reduces the dispersion errors for long-time integration of transient problems [28]. In a previous study, it has been reported that this algorithm is second-order accurate in time for reciprocating flow forced convection [29]. For our numerical work, the grid-independent results are obtained at modal expansion order $N=9$ for $\Delta t=10^{-4}$ s.

5 Results and Discussion

In this section, we present the mixing performances of an electrokinetic relay micromixer without and with serpentine channel structures. Parameters considered in this numerical work are channel width, applied electric field, and relay frequency. Numerical results are obtained based on a 2D model where the variation in the height direction is neglected. The ionic concentration considered in this study is in the range between 10 mM and 100 mM, which corresponds to Debye length of 3 nm and 1 nm, respectively. Therefore, the slip (velocity) boundary condition is justified for high ionic concentration solution. Properties of water ($\rho=1000$ kg/m^3 and $\mu=0.001$ Kg/m s) are used for momentum equations as the thermodynamic properties of sample and buffer used in various bioanalytical processes are very similar to water. The simulation results presented here are performed for $\zeta=-60$ mV. This value was chosen based on experimental results in poly-di-methyl siloxane (PDMS) microchannel. Experimental results show that the zeta potential of PDMS microchannel varies between -25 mV and -80 mV, depending on the charge state and ionic concentration of buffer solution [31]. In this numerical study, species are considered to be electrically neutral. Hence, they do not alter the electrokinetic effects within the micromixer. For the concentration equation, $D=10^{-10}$ m^2/s ($\varepsilon_r=80$ and $S_c=10^4$) is used in order to obtain appropriate molecular diffusion effects in the species transport equation. In the numerical simulation, it is assumed that at $t=0$, the inlet channels 1 and 2 are filled with the buffer solution and the sample solution, respectively, while the rest of the mixing channel is filled with buffer solution.

To evaluate the mixing rate at a particular cross section, a parameter called mixing efficiency (η) is defined as the following:

$$\eta=\left(1-\frac{\int_{-W/2}^{W/2}|C-C_\infty|dy}{\int_{-W/2}^{W/2}|C_0-C_\infty|dy}\right)\times 100\% \tag{13}$$

where C is the concentration distribution in the lateral direction, C_∞ is the concentration at the ideal (complete) mixing at outlet

(which is 0.5 for our case), and C_0 is the concentration at the inlets for completely unmixed buffer or sample (0 or 1).

5.1 Effects of Channel Width. In this section, numerical simulations are performed to study whether the channel width has an effect on the mixing efficiency. Three micromixers of various channel widths (50 μm, 100 μm, and 300 μm) are considered. The applied potentials are fixed as $\phi_s=20$ V and $\phi_a=20$ V. To study the channel width effect, three relay frequencies, $f=0$ Hz, $f=5$ Hz, and $f=10$ Hz, are used. Figures 2(*a*), 2(*b*), and 2(*c*) show the numerical solution of the mixing efficiencies at the outlet ($x=1000$ μm) when channel width is 50 μm, 100 μm, and 300 μm, respectively. For no actuation case ($f=0$ Hz), the electrical potential at both inlets is 40 V. In this case, the mixing efficiency at the channel outlet is 39.2% when the channel width is 50 μm, while this value reduces to 19.6% and 6.6%, respectively, for channel widths of 100 μm and 300 μm. Although the application of an electroosmotic relay loading ($f=5$ Hz) helps improve mixing efficiency for all three micromixers, the mixing efficiency of the 50 μm wide channel is still higher than those of $W=100$ μm and 300 μm. Similar mixing tendency is observed for the 10 Hz relay frequency. Note that the mixing efficiency curves at $f=5$ Hz are oscillatory because the alternative loading of two fluids formed banded structures. However, for 10 Hz relay frequency, the mixing becomes stable at the outlet for all three channel widths considered here. The data show that a micromixer with a smaller channel width has a higher mixing efficiency than that of a larger channel width. This is because one fluid can be impinged into and mixed with the other fluid more efficiently when the channel width becomes smaller. This can be seen from the concentration contour of three micromixers shown in Fig. 3, when the mixing reached stable state at the outlet. Figures 3(*b*) and 3(*c*) show the contour plots of the three micromixers at $f=5$ Hz and 10 Hz, respectively. The blue color (dark gray) represents the concentration of buffer solution, and the pink color (light gray) represents the concentration of the sample solution. For comparison, the concentration contour of no-relay case ($f=0$ Hz) is also presented in Fig. 3(*a*). In this case, the micromixing is completely dependent on diffusion. The mixing efficiency in the 300 μm wide micromixer is the lowest among three because the diffusion length is longer than the other two micromixers.

The above numerical results imply that the maximum efficiency will be obtained if we design a micromixer with a smaller channel width. However, a decrease in channel width will impact the mixing capacity of the micromixer (flow rate of the micromixer). For the three micromixers studied here, assuming the electric field is kept the same, numerical results show that the outlet velocity (and, hence, the volume flow rate) of the micromixer is reduced 84% as the channel width is decreased from 300 μm to 50 μm. The channel width will also cause the shift of the optimal relay frequency, a frequency at which the maximum mixing efficiency occurs. As shown in Fig. 2, the maximum mixing efficiencies occurs at $f=10$ Hz for $W=50$ μm, and 100 μm, while for $W=300$ μm, the maximum mixing efficiency takes place at around $f=5$ Hz. Therefore, the numerical results suggest that a large channel width shifts the optimum relay frequency to a lower value at which fluids can be mixed more effectively. This effect will be discussed in more detail in Sec. 5.2.

5.2 Effects of Relay Frequency. In electrokinetic mixing, alternating electrokinetic sample loading facilitates larger interfacial surface areas between two fluids by stretching/folding streamlines and forming cellular structures of alternating fluids. Hence, the relay frequency is one critical factor affecting the mixing. Seven different relay frequencies are considered to optimize the mixing performance in a 50 μm wide electrokinetic micromixer. The applied potentials are fixed as $\phi_s=20$ V and $\phi_a=20$ V for $f>0$ Hz, while electric potential is 40 V at both inlets for $f=0$ Hz. The mixing efficiencies at channel outlet ($x=1000$ μm) predicted by the numerical scheme are presented in Fig. 4(*a*). For no actuation case ($f=0$ Hz), where both fluids are loaded simultaneously, the mixing efficiency is only 39.2%. Numerical results

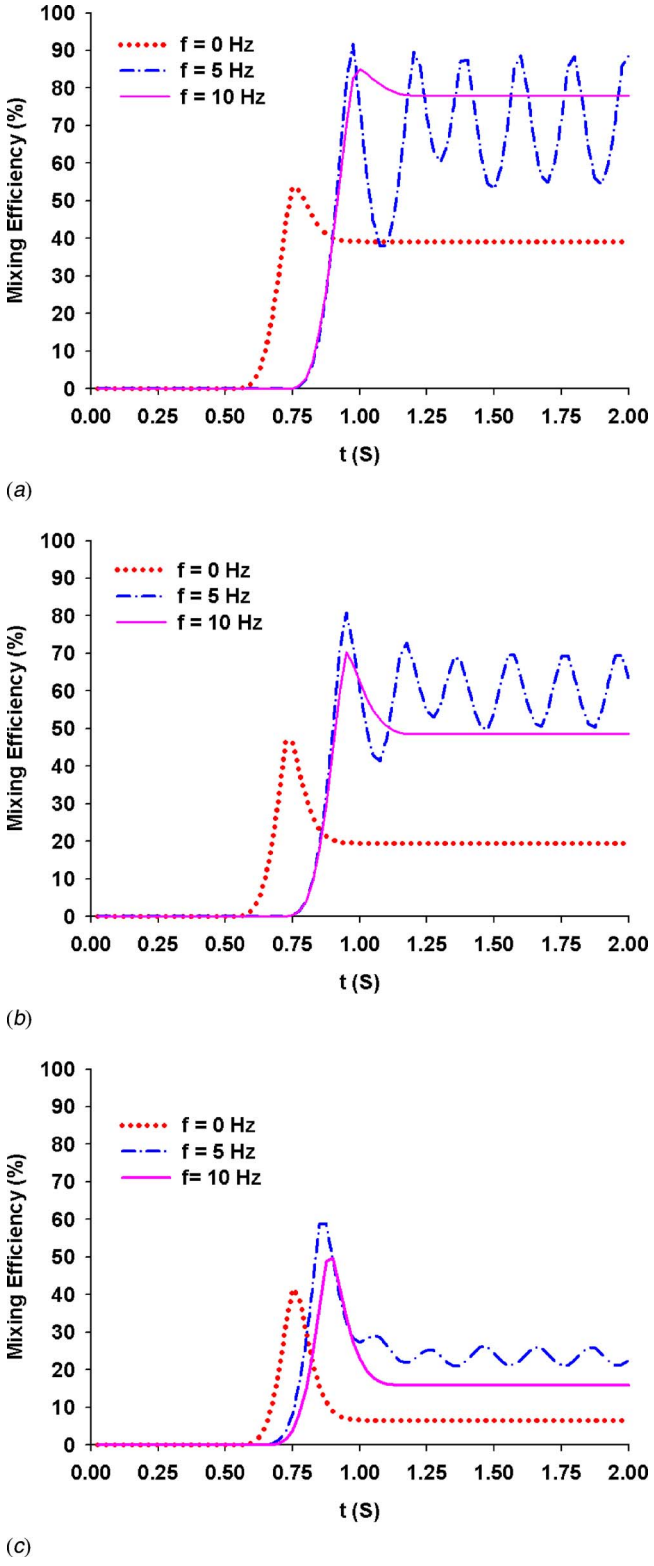

Fig. 2 Effects of microchannel width on mixing efficiency at the micromixer outlet ($x=1000$ μm) under different relay frequencies for $\phi_a=20$ V and $\phi_s=20$ V: Case (*a*) Pe=510, $W=50$ μm; (*b*) Pe=1028, $W=100$ μm; and (*c*) Pe=3208, $W=300$ μm

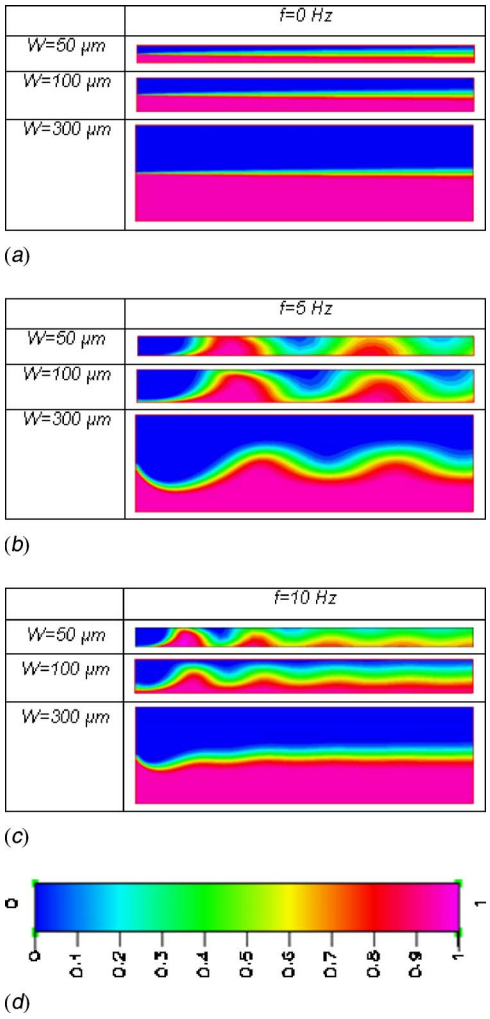

Fig. 3 Concentration contour for three electrokinetic micromixers presented in Fig. 2, under three relay frequencies (*a*) *f* =0 Hz (*b*) *f*=5 Hz, and (*c*) *f*=10 Hz. Mixing performances are presented 2 s after the initiation of electric field.

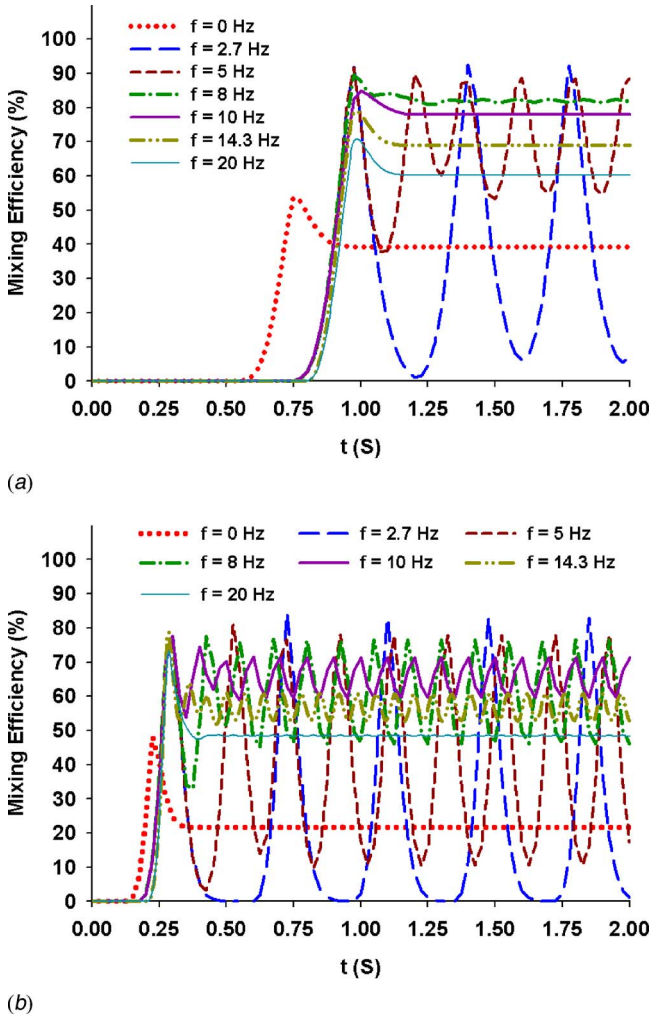

Fig. 4 Mixing efficiency for electrokinetic relay micromixer (*a*) at the micromixer outlet (x=1000 μm); (*b*) at an intermediate location (x=300 μm) under different relay frequencies. Here, ϕ_s=20 V, ϕ_a=20 V, and Pe=510.

also show that at low relay frequencies (f=2.7 Hz), the mixing efficiency is quite oscillatory, ranging from 6.1% to 92.3%. This is because at a low relay frequency, the channel width is primarily flooded by one fluid before the electrical signal is switched to the other fluid. Thus, a wide-banded composition structure is created and the mixing frequency curve has a zigzag shape, implying a uniform mixing cannot be achieved within limited time and length. These findings are consistent with results of Tang et al. [27], which predicted similar banded structures at low relay frequencies.

Thus to reach efficient mixing, the electrical potential has to be switched at a higher frequency to avoid formation of banded structure. At f=5 Hz, the mixing efficiency oscillates between 53.1% and 88.7% indicating the mixing is not yet stable. Figure 4(*a*) shows that at a relay frequency of f=8 Hz and 10 Hz, the mixing efficiency reaches 82.0% and 78.1%, respectively, and the mixing becomes stable. However, if the relay frequency is too high, one fluid cannot be impinged into the other fluid within a very short time period before the potential (voltage) signal is switched. This explains why a very high frequency ($f \geq 14.3$ Hz) is not as efficient as f=8 Hz. Figure 4(*b*) illustrates the above phenomenon at location x=300 μm. The oscillation of mixing efficiency is obvious at low frequencies, i.e., f=2.7 Hz and f =5 Hz since the banded structures have been formed. It is worth mentioning that in the absence of an electrokinetic relay mechanism (f=0 Hz), the mixing efficiency at x=300 μm is only 21.7%.

Assuming the goal of the device is to obtain maximum mixing of sample and buffer solutions, an appropriate relay frequency (the optimum relay frequency) would be necessary to increase the interfacial areas of two fluids without forming cellular structures. There are two factors that affect the maximum frequency: the impingement velocity and the channel width. The former is determined by the applied electrical field. Since the impingement velocity cannot be obtained directly, the average channel outlet velocity (U) is normally used to get an approximate optimum relay frequency f_m as [27]

$$f_m = \frac{U}{W/\sin\theta} = \frac{U\sin\theta}{W} \tag{14}$$

where θ is the Y-channel angle, and ($W/\sin\theta$) represents the travel length of impingement flow across the channel. Tang et al. pointed out that when actual relay frequency is much less than f_m ($f < 0.1 f_m$ for a case of θ=90 deg), the cellular structures are formed in the microchannel [27]. In order to remove the cellular structures, the relay frequency should be increased close to f_m.

The average mixing efficiency at the outlet of micromixers for

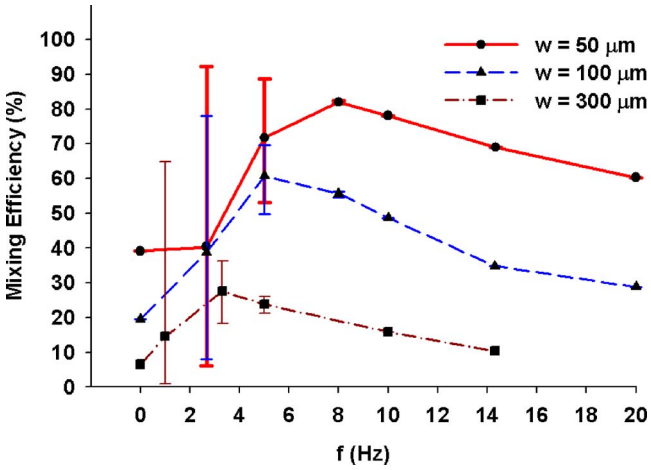

Fig. 5 Average mixing efficiency at the micromixer outlet for different electroosmotic relay frequency. Here ϕ_s=20 V and ϕ_a=20 V. The error bars indicate the oscillation range of the mixing efficiency. The data points on the curves are the average values calculated by integrating mixing efficiency over a relay cycle. The optimum frequency for 50 μm, 100 μm, and 300 μm wide micromixers are 8 Hz, 5 Hz, and 3.3 Hz, respectively.

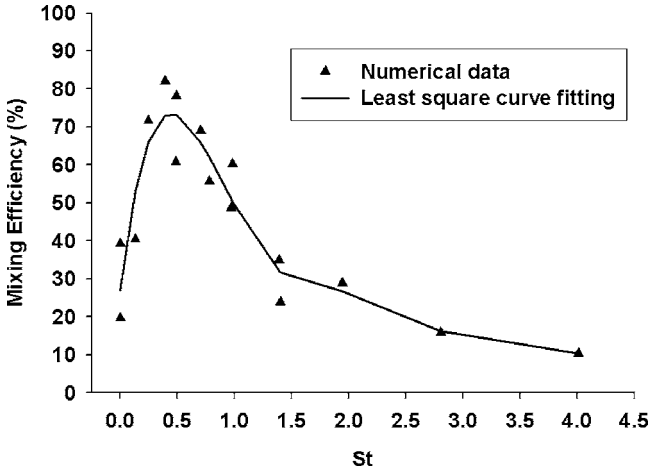

Fig. 6 Mixing efficiency variation with Strouhal number (St). For the current micromixer (θ=30 deg), the optimum efficiency takes place at St≈0.5.

different electroosmotic relay frequency is presented in Fig. 5. Numerical results of optimal relay frequency appear consistent with Eq. (14). Note that the optimum relay frequency is defined as the frequency for which the average mixing efficiency is the maximum. The average mixing efficiency is calculated by integrating mixing efficiency over a relay cycle, i.e., $\bar{\eta}=\int_{t_1}^{t_1+T}\eta(t)dt/T$, where $T=1/f$, t_1 is an arbitrary moment after a repeatable fluid pattern is reached. The error bars in Fig. 5 indicate the oscillation range of the mixing efficiency. The optimum relay frequency provided by the numerical scheme for the cases of W=50 μm and W=100 μm, as shown in Fig. 5, is 8 Hz and 5 Hz, while Eq. (14) suggests 10.2 Hz and 5.2 Hz. For W=300 μm, the numerically predicted optimum relay frequencies (~3.3 Hz) appears to have a slightly larger derivation from the prediction by Eq. (14). It is obvious that the increase of channel width reduces the mixing efficiency and shifts the optimal relay frequency to low level. It can be also predicted from Eq. (14) that the application of a lower electrical field will shift the optimal frequency to low level because it reduces the impingement velocity. Figure 6 shows the mixing efficiency dependence on Strouhal number ($\mathrm{St}=Wf/U=(f/f_m)\sin\theta$) in electrokinetic relay mixing without any serpentine structure. The solid line is based on a fifth-order polynomial curve fit of the numerical data points. It is obvious that the maximum mixing efficiency occurs at $\mathrm{St}=\sin\theta\approx0.5$. We should note here that Eq. (14) only provides a rough prediction of optimum frequency for electrokinetic relay micromixers without passive structures. It cannot be applied to a micromixer with complicated geometries because of the complex flow patterns inside the channel, which prevents the formation of cellular structures. The channel geometry might affect the electric field, the impingement flow velocity, and travel length, and hence, the optimum frequency. Further study needs to be done to provide a more accurate formula of the optimal frequency by considering the above issues.

5.3 Effects of External Electrical Potential. Here, both fluids are driven by the electrokinetic body forces, and no external pressure head is applied in this micromixer. In the electrokinetic micromixer, the effect of externally applied electric potentials is very significant because external electric fields determine the amount of liquid pumped through particular flow geometry. To investigate the effects of externally applied electric potential, we have varied the value of both steady (ϕ_s) and fluctuating (ϕ_a) parts for a 50 μm wide electrokinetic micromixer. Figures 7(*a*) and 7(*b*) show the mixing performance at different electric field strengths at x=1000 μm and x=300 μm, respectively. In order to obtain the optimum mixing performance, effects of electrokinetic relay frequencies are also presented in Fig. 7. For a particular electrokinetic relay frequency, electric field cases with no steady component (ϕ_s=0) generates a slightly higher mixing efficiency. This is because part of the flow from one inlet channel (Y-branch) enters into the other inlet channel (Y-branch) due to potential difference, and this facilitates mixing even in the branch channels. In other words, in the absence of a steady potential component, two fluids started interacting with each other in the branch channels. However, the early mixing created in the branch channels slows down the fluid entering the mixing channel. As a result, it requires more mixing time to reach a stable mix than that of the other case presented here. In both figures, mixing efficiency curve at f=0 Hz (ϕ_1=40 V and ϕ_2=40 V) is included. It is obvious that electroosmotic relay driving with appropriate relay frequency (f≈10 Hz, St=0.49) enhances micromixing. Note that the electrical potential will also affect the optimum rely frequency in terms of affecting the fluid velocity in the microchannel.

5.4 Hybrid Micromixing Schemes. Although electrokinetic micromixer has demonstrated mixing ability with self-sustained pumping, the overall mixing efficiency is relatively low (<80%) for the case presented in this study. There are several factors contributing to this low mixing performance. First, while the electrokinetic relay mechanism stretches the fluid streams to increase the interfacial surface area, its influence is limited in the contact regions of two fluids near the entrance. Second, at the downstream of the micromixer, because the velocity in the y direction is negligible, chaotic advection that distorts and elongates fluid interface is missing. Third, without chaotic advection, mass diffusion is restrained due to limited interfacial area between two fluids. One way to induce advection is to introduce "complicated" structures in the mixing channel.

In order to reach a high mixing efficiency (>95%), asymmetric serpentine structures are introduced in the mixing chamber as shown in Fig. 1(*b*). Like the electrokinetic micromixer, the main driving mechanism is alternating electrokinetic forces. This particular design is introduced to bring in chaotic advection and force the fluid to change its directions dramatically to induce efficient mixing. Note that the entry region of the micromixer is adopted to keep the flow rate of two inlets approximately the same. The numerical results of concentration distributions in hybrid micromixer are presented in Fig. 8(*a*) for an electrokinetic relay fre-

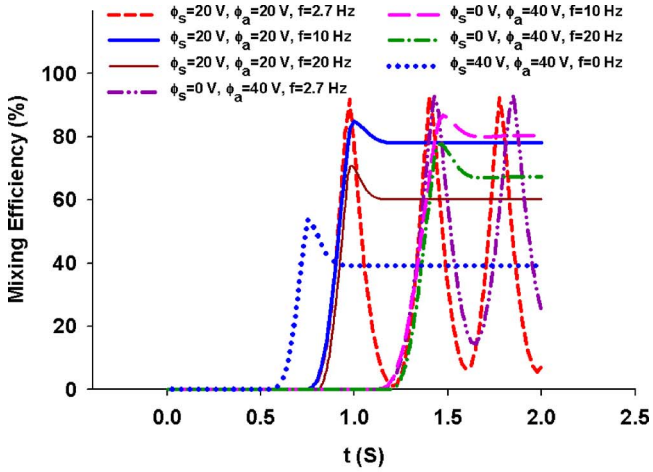

(*a*)

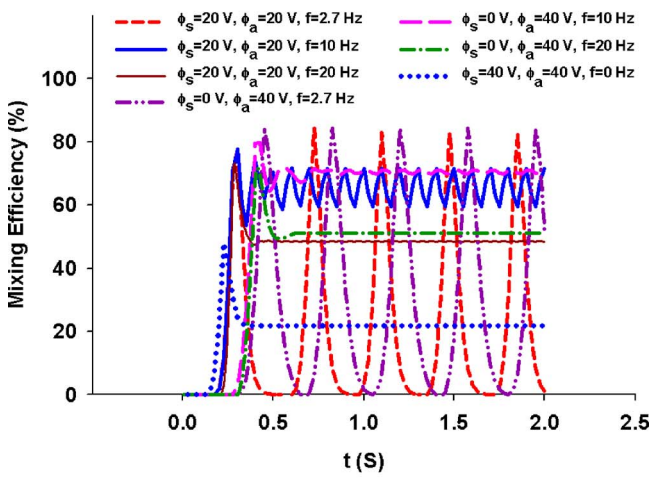

(*b*)

Fig. 7 Effects of applied electric potential on mixing efficiency (*a*) at the micromixer outlet (x=1000 μm) and (*b*) at an intermediate location (x=300 μm) under different relay frequencies. Here, Pe=510.

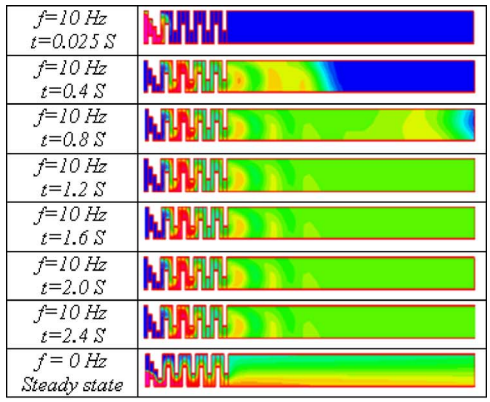

(*a*)

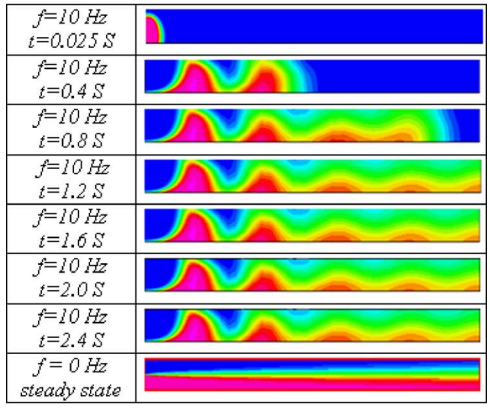

(*b*)

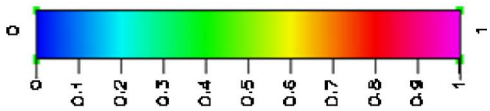

(*c*)

Fig. 8 Concentration contour for (*a*) the hybrid micromixer and (*b*) the electrokinetic micromixer at different times. The corresponding micromixer design is presented in Figs. 1(*b*) and 1(*a*), respectively. Here, ϕ_s=20 V, ϕ_a=20 V, and Pe=262 and 510 for the electrokinetic and hybrid micromixers, respectively.

quency of 10 Hz. Here the dimensions of the channels are W =50 μm, L_x=200 μm, L=1000 μm, θ=30 deg, and W_a =12.5 μm. The alternating component of electric potential is set at 20 V and the steady component of electric potential is fixed at 20 V. The blue color (dark gray) represents the concentration of buffer solution and the pink color (light gray) represents the concentration of the sample solution. Like previous cases, at time t =0, inlet channels 1 and 2 are filled with the buffer (blue) and the sample (pink) fluids, respectively (not shown in Fig. 8), while the rest of the mixing chamber contains buffer. To compare the mixing process, the concentration contour for electrokinetic relay micromixer without asymmetric serpentine structures is also presented (Fig. 8(*b*)) for the same frequency (f=10 Hz).

In the electrokinetic relay micromixer, mixing starts happening at $t>0$ due to selective pumping of sample and buffer. As shown in Fig. 8(*b*), starting at t=0.4 s, stable mixing is achieved in the middle of the channel, and the mixed fluid starts to fill in the downstream section. The mixing condition in the absence of relay frequency is also presented in the last row in Fig. 8(*b*). It is obvious that in the absence of electrokinetic relay loading, the mixing is dominated by the diffusion and the mixing performance is low. On the other hand, in the hybrid micromixer (see Fig. 8(*a*)), a complete mixing can be achieved rapidly due to the presence of asymmetric serpentine structures. In the hybrid micromixer, the flow begins to mix at t=0.025 s. At t=0.4 s, the mixing front enters the straight part of the micromixer and efficient mixing is developed (Fig. 8(*a*)). At t=0.8 s, the microflow is already highly mixed at x=300 μm. The average mixing efficiency reaches 84.9% at this position. At x=500 μm, this number becomes 95.6%. Starting from t=0.8 s, the highly mixed flow begins to fill in the rest of the channel. Eventually, a completely mixed flow is developed in the downstream and the mixing efficiency reaches 98.6% at the channel outlet. However, in the absence of electroosmotic relay driving, a relatively low mixing efficiency of 82.0% is obtained. The mixing performances at x=1000 μm and at x =300 μm are presented in Figs. 9(*a*) and 9(*b*), respectively. These results indicate that the hybrid micromixing scheme, which utilizes electroosmotic relay driving and asymmetric serpentine structures, offers a highly efficient and stable mixing within a very short time.

6 Summary and Conclusions

Effective mixing of liquids is essential in many applications, such as drug delivery, DNA analysis/sequencing, pheromone syn-

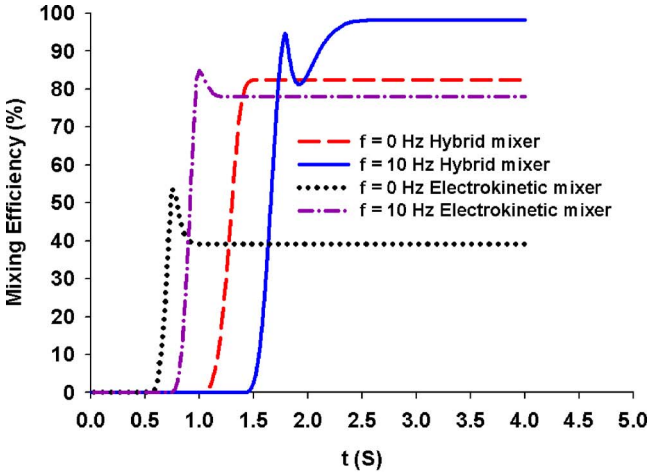

(*a*)

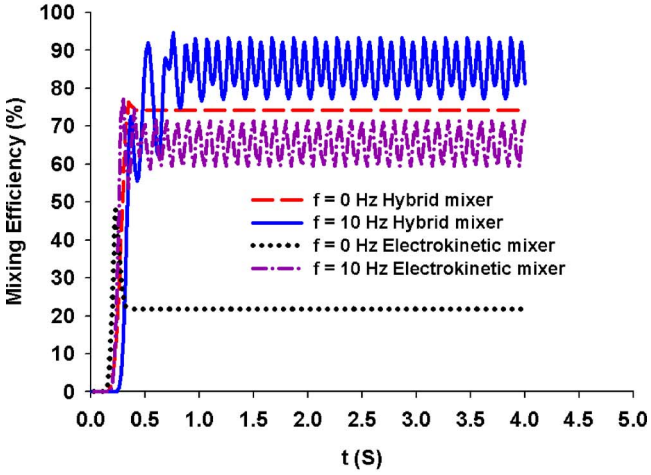

(*b*)

Fig. 9 Comparison of mixing efficiency (*a*) at the micromixer outlet (x=1000 μm) and (*b*) at an intermediate location (x =300 μm) with and without asymmetric serpentine structures. Here, ϕ_s=20 V and ϕ_a=20 V. The Peclet numbers for the electrokinetic and hybrid micromixers are 510 and 262, respectively.

thesis in microbioreactors, and biological/chemical agent detections. Rapid mixing can reduce the analysis time and permit high throughput in lab-on-a-chip devices. For rapid mixing of liquids, a Y-form hybrid electrokinetic-passive micromixer is presented.

The effects of various design parameters, such as channel width, relay frequency, external electric potential, and asymmetric serpentine structures, have been studied. In an electrokinetic micromixer, the critical (optimum) relay frequency depends on the channel width and the applied electric potential. For a wider microchannel, the maximum efficiency is obtained at relatively low actuation frequency, while the optimum relay frequency obtained from numerical prediction is relatively high for a narrower channel. Moreover, for a particular relay frequency, the mixing performance is better if the channel width becomes smaller. Simulation results also show that the mixing performance is slightly better if the steady component of electric potential is zero. In this case, the mixing originates at the branch channel. However, this case takes longer to reach a stable mixing state.

Numerical results also illustrate that pure electrokinetic relay actuation is not enough for a complete micromixing within a short distance and time. In a hybrid micromixer, the asymmetric serpentine structure plays an active role in ultrafast mixing within a short distance. With this hybrid micromixer, a very high mixing efficiency (95.6%) can be reached within 1.0 s at x=500 μm for a 50 μm wide channel. However, passive serpentine structures induce flow impedance and reduces the flow velocity in the micromixer. For the same applied potentials, the flow velocity in the hybrid micromixer is only 51% of that of an electrokinetic micromixer.

Acknowledgment

This work was supported by the Washington Technology Center and University of Akron Firestone Research Initiative Fellowship.

Nomenclature

C = dimensionless concentration
D = mass diffusivity, m^2/s
e = electron charge, C
$\vec{E}$ = electric field, V/m
f = relay frequency, Hz
k_B = Boltzmann constant, J/K
l = direction tangent to the channel wall
L = length of the mixing chamber, μm
L_x = length of the inlet channel, μm
m = alternating parameter
n^+/n^- = ion density of positive or negative charges
P = pressure, N/m^2
Pe = Peclet number, UW/D
Re = Reynolds number, UW/v
Sc = Schmidt number, v/D
St = Strouhal number, fW/U
t = time, s
T = temperature, K
u = streamwise velocity, μm/s
U = streamwise velocity at channel outlet, μm/s
v = cross-stream velocity, μm/s
W = width of the microchannel, μm
W_a = width of asymmetric structures, μm
x = x position of the coordinate system, μm
y = y position of the coordinate system, μm
z^+/z^- = valence of positive or negative charges

Greek Letters

ε = permittivity, F/m
ε_r = relative permittivity
ϕ = external electric potential, V
ϕ_1 = electric potential at inlet 1, V
ϕ_2 = electric potential at inlet 2, V
η = mixing efficiency
μ = dynamic viscosity, kg/m s
λ = Debye length, nm
θ = angle of Y-channel, degree
ρ_e = electric charge density, C/m^3
ρ_f = density of the fluid, kg/m^3
σ = electrical conductivity, $1/\Omega$ m
ψ = electrokinetic potential, V
ζ = zeta potential, mV

Subscripts

a = alternating component
e = electric
f = fluid
o = bulk region or inlets
s = steady component
∞ = complete mixing state

References

[1] Bessoth, F. G., DeMello, A. J., and Manz, A., 1999, "Microstructure for Efficient Continuous Flow Mixing," Anal. Commun., **36**, pp. 213–215.

[2] Losey, M. W., Jackman, R. J., Firebaugh, S. L., Schmidt, M. A., and Jensen, K. F., 2002, "Design and Fabrication of Microfluidic Devices for Multiphase Mixing and Reaction," J. Microelectromech. Syst., **11**, pp. 709–717.
[3] Hong, C. C., Choi, J. W., and Ahn, C. H., 2004, "A Novel In-Plane Passive Microfluidic Mixer With Modified Tesla Structures," Lab Chip, **4**, pp. 109–113.
[4] Mengeaud, V., Josserand, J., and Girault, H. H., 2002, "Mixing Processes in a Zigzag Microchannel: Finite Element Simulations and Optical Study," Anal. Chem., **74**, pp. 4279–4286.
[5] Liu, R. H., Stremler, M. A., Sharp, K. V., Olsen, M. G., Santiago, J. G., Adrian, R. J., Aref, H., and Beebe, D. J., 2000, "Passive Mixing in a Three-Dimensional Serpentine Microchannel," J. Microelectromech. Syst., **9**, pp. 190–197.
[6] Park, S. J., Kim, J. K., Park, J., Chung, S., Chung, C., and Chang, J. K., 2004, "Rapid Three-Dimensional Passive Rotation Micromixer Using the Breakup Process," J. Micromech. Microeng., **14**, pp. 6–14.
[7] Stroock, A. D., Dertinger, S. K. W., Ajdari, A., Mezic, I., Stone, H. A., and Whitesides, G. M., 2002, "Chaotic Mixer for Microchannels," Science, **295**, pp. 647–651.
[8] Jacobson, S. C., McKnight, T. E., and Ramsey, J. M., 1999, "Microfluidic Devices for Electrokinetically Driven Parallel and Serial Mixing," Anal. Chem., **71**, pp. 4455–4459.
[9] Oddy, M. H., Santiago, J. G., and Mikkelsen, J. C., 2001, "Electrokinetic Instability Micromixing," Anal. Chem., **73**, pp. 5822–5832.
[10] Yang, Z., Matsumoto, S., Goto, H., Matsumoto, M., and Maeda, R., 2001, "Ultrasonic Micromixer for Microfluidic Systems," Sens. Actuators, A, **93**, pp. 266–272.
[11] Lu, L. H., Ryu, K. S., and Liu, C., 2002, "A Magnetic Microstirrer and Array for Microfluidic Mixing," J. Microelectromech. Syst., **11**, pp. 462–469.
[12] Tsai, J. H., and Lin, L., 2002, "Active Microfluidic Mixer and Gas Bubble Filter Driven by Thermal Bubble Micropump," Sens. Actuators, A, **97–98**, pp. 665–671.
[13] Rong, R., Choi, J. W., and Ahn, C. H., 2003, "A Functional Magnetic Bead/Biocell Sorter Using Fully Integrated Magnetic Micro/Nano Tips," *Proc. IEEE MEMS*, IEEE, New York, pp. 530–533.
[14] Suzuki, H., and Ho, C. M., 2002, "A Magnetic Force Driven Chaotic Micro-Mixer," *Proc. of 15th IEEE International Conference on MEMS*, IEEE, New York, pp. 40–43.
[15] Deval, J., Tabeling, P., and Ho, C. M., 2002, "A Dielectro-phoretic Chaotic Mixer," *Proc. of 15th IEEE International Conference on MEMS*, IEEE, New York, pp. 36–39.
[16] Liu, R. H., Yang, J., Pindera, M. Z., Athavale, M., and Grodzinski, P., 2002, "Bubble-Induced Acoustic Micromixing," Lab Chip, **2**, pp. 151–157.
[17] Bottausci, F., Mezic, I., Meinhart, C. D., and Cardonne, C., 2004, "Mixing in the Shear Superposition Micromixer: Three-Dimensional Analysis," Philos. Trans. R. Soc. London, Ser. A, **362**, pp. 1001–1018.
[18] He, B., Burke, B. J., Zhang, X., Zhang, R., and Regnier, F. E., 2001, "A Picoliter-Volume Mixer for Microfluidic Analytical Systems," Anal. Chem., **73**, pp. 1942–1947.
[19] Johnson, T. J., Ross, D., and Locascio, L. E., 2002, "Rapid Microfluidic Mixing," Anal. Chem., **74**, pp. 45–51.
[20] Probstein, R. F., 1994, *Physicochemical Hydrodynamics*, Wiley, New York.
[21] Dutta, P., and Beskok, A., 2001, "Analytical Solution of Combined Electroosmotic/Pressure Driven Flows in Two-Dimensional Straight Channels: Finite Debye Layer Effects," Anal. Chem., **73**, pp. 1979–1986.
[22] Ren, L., Sinton, D., and Li, D., 2003, "Numerical Simulation of Microfluidic Injection Processes in Crossing Microchannels," J. Micromech. Microeng., **13**, pp. 739–747.
[23] Ermakov, S. V., Jacobson, S. C., and Ramsey, J. M., 2000, "Computer Simulation of Electrokinetic Injection Techniques in Microfluidic Devices," Anal. Chem., **72**, pp. 3512–3517.
[24] Patankar, N. A., and Hu, H. H., 1998, "Numerical Simulation of Electroosmotic Flow," Anal. Chem., **70**, pp. 1870–1881.
[25] Lin, C. H., Fu, L. M., and Chien, Y. S., 2004, "Microfluidic T-Form Mixer Utilizing Switching Electroosmotic Flow," Anal. Chem., **76**, pp. 5265–5272.
[26] Dutta, P., Beskok, A., and Warburton, T. C., 2002, "Numerical Simulation of Mixed Electroosmotic/Pressure Driven Flows," Numer. Heat Transfer, Part A, **41** pp. 131–148.
[27] Tang, Z., Hong, S., Djukic, D., Modi, V., West, A. C., Yardley, J., and Osgood, R. M., 2002, "Electrokinetic Flow Control For Composition Modulation in a Microchannel," J. Micromech. Microeng., **12**, pp. 870–877.
[28] Karniadakis, G. E., and Sherwin, S. J., 1999, *Spectral HP Element Methods for CFD*, Oxford University Press, London.
[29] Sert, C., and Beskok, A., 2003, "Numerical Simulation of Reciprocating Flow Forced Convection in Two-Dimensional Channels," ASME J. Heat Transfer, **125**, pp. 403–412.
[30] Dutta, P., Beskok, A., and Warburton, T. C., 2002, "Electroosmotic Flow Control in Complex Microgeometries," J. Microelectromech. Syst., **11** pp. 36–44.
[31] Keisuke, H., and Dutta, P., 2005, "Flow Diagnosis in a Trapezoidal Microchannel," *Proc. of JSME conference on Fluid Mechanics*, JSME, Paper No. AM05-07-002.

A Theoretical Discussion of a Menisci Micropump Driven by an Electric Field

Alexandru Herescu

Jeffrey S. Allen[1]
e-mail: jstallen@mtu.edu

Michigan Technological University,
Houghton, MI 49931

The potential for miniaturization of analytical devices made possible by advances in micro-fabrication technology is driving demand for reliable micropumps. A wide variety of micropumps exist with many types of actuating mechanisms. One such mechanism is electrohydrodynamic (EHD) forces which rely upon Coulomb forces on free charges and/or polarization forces on induced dipoles within the liquid to induce fluid motion. EHD has been used to pump liquid phases and to displace gas–liquid interfaces for enhanced boiling heat transfer as well as to displace gas/vapor bubbles. A novel concept for using EHD polarization forces to deflect a stationary meniscus in order to compress and pump a gaseous phase is described. The pumping mechanism consists in alternative compression of two gas volumes by continuous deflection of the two pinned menisci of an entrapped liquid slug in an electric field. Using the Maxwell stress relations, the electric field strength necessary to operate the pump is determined. The operational limits are determined by analyzing the stability limits of the two menisci from inertial and viscous standpoints, corroborated with the natural frequencies of the gas–liquid interfaces.
[DOI: 10.1115/1.2710241]

Keywords: microfluidics, micropump, electrohydrodynamic (EHD), meniscus

1 Introduction

The need to develop reliable micropumps is continuously growing as microfabrication technology has made the miniaturization of analytical devices possible. Applications such as the autonomous chemical/biological detection system Micro-Chem-Lab developed at Sandia National Laboratories [1], in vivo organ process monitoring and diagnostics, and hand-held pollution monitoring systems are only a few examples from a large variety of mini-instruments that require micropumps.

There are a variety of micropump technologies which can be grouped into two distinct categories, displacement, and dynamic pumps. In the first category, and perhaps the most extensively researched, lie reciprocating displacement (diaphragm) micropumps, using various displacement mechanisms such as piezoelectric [2–4] and thermo-pneumatic with phase change [5,6] or without [7,8]. The electrohydrodynamic [9–12] and electroosmotic [13–15] pumps lie in the second (dynamic) category [9–12].

In terms of output flow rates and pressure generation, displacement (diaphragm) micropump models perform well, making the manufacturing process and their operational nature decisive factors when selecting a pump for a certain application. The electrohydrodynamic/electroosmotic micropumps tend to have a simpler design and are easily controllable while the diaphragm micropumps have more complicated actuation mechanisms and are exposed to fatigue stresses. On the other hand, the magnitude of the electric field necessary to operate an electrohydrodynamic/electro-osmotic micropump is an important factor when choosing a dynamic model and also the occurrence of electrolytic gas at the electrodes and significant Joule heating in some cases must be taken into account. An exhaustive review of micropumps is provided by [16].

2 EHD Menisci Pump

Research on electrohydrodynamic (EHD) enhanced heat and mass transfer has traditionally been focused on industrial applications, such as evaporators and condensers [17–21]. The application of EHD to heat and mass transfer problems continues to show promise in industrial applications where special requirements and restrictions are imposed but enhanced transport is required. One example is in a microgravity environment where single-phase liquid or two-phase liquid–vapor transport is required with high reliability and little or no vibrations [22]. EHD offers advantages over more traditional pumping mechanisms by virtue of the ability for rapid control, a simple, nonmechanical design with high reliability, suitability for harsh environments, and applicability to both single-phase and multiphase flows [23].

EHD pumping is divided into two principle mechanisms; Coulomb forces acting on free charges and polarization forces due to induced dipoles. EHD Coulomb-type micropumps have used induction [24] and charge injection [25] to induce fluid motion. This style of EHD pump has been investigated for use in enhancing the heat transfer capability of a space-based monogroove heat pipes [26]. The polarization-type EHD mechanism (dielectrophoretic force) has also been used for heat transport in heat pipes [27,28]. The proposed EHD mechanism discussed herein uses polarization forces to deflect a meniscus between two fluids of different electric permittivity.

The pumping mechanism described herein consists of cyclic adiabatic, reversible compression of two gas volumes by the cyclic deflection of the surfaces of an entrapped liquid plug as shown in Fig. 1. The liquid plug is circular in cross section and the Bond number[2] is assumed to be very small which implies that the

[1]Corresponding author.

Contributed by the Fluids Engineering Division of ASME for publication in the JOURNAL OF FLUIDS ENGINEERING. Manuscript received July 31, 2006; final manuscript received December 8, 2006. Assoc. Editor: Dennis Siginer.

[2]The Bond number, Bo, is the ratio of gravitational forces to capillary forces on a static gas–liquid interface. It is defined as $\mathrm{Bo} \equiv \Delta\rho g L^2/\sigma$, where $\Delta\rho$ is the density difference across the interface, g is the gravitational acceleration, L is the characteristic length scale, and σ is surface tension. If the Bond number is greater than one, then gravitational forces dominate the interface shape resulting in a flat interface which is perpendicular to the direction of the gravitational acceleration. If the Bond number is much less than one, the capillary forces dominate the static interface shape resulting in a meniscus.

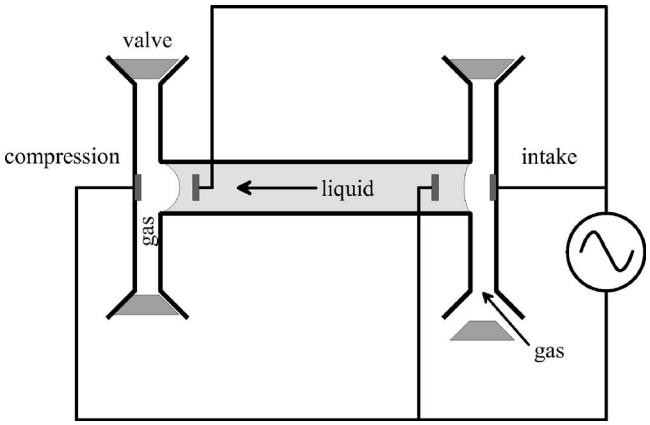

Fig. 1 Schematic of EHD Menisci micropump

menisci of the liquid plug may be considered as spherical caps. The gas phase is compressed by deflection of the two pinned menisci (A and B) characterized by the contact angles θ_A and θ_B which can vary from 0 deg to 90 deg. At 0 deg the meniscus forms a hemispherical cap while at 90 deg the meniscus is a flat interface perpendicular to the cylinder wall. The contact lines are assumed to remain pinned as the menisci are deflected.

The valves open and close to allow for intake, compression and exhaust during the cycle. As the gas volume corresponding to Meniscus A is compressed, gas will be drawn into the volume corresponding to Meniscus B and vice versa such that for a half-cycle one of the gas chambers is at ambient pressure while compression takes place in the other volume. The electric field is applied alternatively to each meniscus; for the first half-cycle to Meniscus A and for the second half-cycle to Meniscus B. To the authors' knowledge, this particular pump configuration has not previously been investigated.

2.1 Force Balance. A static force balance applied to the liquid plug provides a quasi-equilibrium expression for the electric field stress required to overcome capillary pressures and the gas pressures. Figure 2 illustrates the various stresses and line forces acting on the liquid plug. The electric field stress, τ_E, is only applied to the compression side of the plug (Meniscus A as shown in Fig. 2). Because the Bond number is small, the gravitational body force is neglected and the line force generated by the curvature of the liquid–vapor interface may be described as $\sigma\cos(\theta)$. The normal stress on the menisci created by the gas pressure is P_A and P_B. The static force balance subject to the described restraints is

$$(P_A - \tau_E - P_B)\pi a^2 - (\sigma_A \cos\theta_A - \sigma_B \cos\theta_B)2\pi a = 0 \qquad (1)$$

Viscous dissipation due to liquid motion is neglected in this quasi-equilibrium analysis.

Rearrangement of Eq. (1) to isolate the electric field stress with the assumption that the surface tension at Meniscus A and Meniscus B is the same ($\sigma_A = \sigma_B = \sigma$) results in the following expression

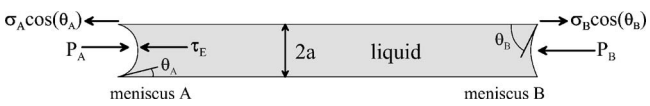

Fig. 2 Parameters and designations of the liquid plug used for the gas compression

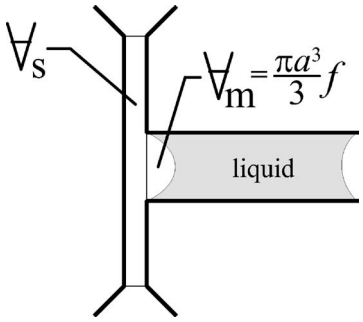

Fig. 3 Volume displaced by meniscus, $\forall_A = \pi a^3 f(\theta_A)/3$, and static volume, $\forall_s$, of Meniscus A side of the pump

$$\tau_E = P_A - P_B - \frac{2\sigma}{a}(\cos\theta_A - \cos\theta_B) \qquad (2)$$

The electric field stress is dependent upon the gas pressure over the two menisci and the menisci curvature as expressed through the contact angles.

2.2 Gas Pressures and Displaced Volumes. The gas pressures, P_A and P_B, can be determined using the ideal gas law assuming adiabatic, reversible compression with constant specific heats

$$P_{A,B} = P_0\left[\frac{\forall_0}{\forall(\theta_{A,B})}\right]^k \qquad (3)$$

where P_0 is the uncompressed or ambient gas pressure; $\forall_0$ is the uncompressed gas volume; $\forall(\theta)$ is the compressed gas volume corresponding to a contact angle θ; and k is the ratio of specific heats. The minimum gas pressure, P_0, occurs at the maximum volume which corresponds to $\theta=0$ while the maximum pressure occurs at the minimum volume ($\theta=\pi/2$). The compression ratio, C_R, is defined as $\forall_0/\forall(\pi/2)$ and can be used to determine the maximum gas pressure expected in the cycle.

The gas volume at each meniscus is divided into a static volume, $\forall_s$, which remains constant throughout the cycle and a meniscus volume, $\forall_m$, which varies with contact angle, θ (see Fig. 3). The meniscus volume is dependent upon the contact angle, θ, and can be found from the expression for the volume of a spherical cap [29]

$$\forall_m = \frac{\pi}{3}a^3\left(\frac{\sin^3\theta - 3\sin\theta + 2}{\cos^3\theta}\right) \qquad (4)$$

with $0 \leqslant \theta \leqslant \pi/2$. For convenience, the θ dependency of the gas volume is defined as

$$f(\theta) = \frac{\sin^3\theta - 3\sin\theta + 2}{\cos^3\theta} \qquad (5)$$

where $f(0)=2$ and $f(\pi/2)=0$. Thus, the maximum meniscus volume, occurring at $\theta=0$, is $2\pi a^3/3$ which is equal to the volume of a hemisphere of radius a. The total gas volume at any meniscus deflection for either side of the liquid plug can be written as

$$\forall(\theta) = \forall_s + \frac{\pi}{3}a^3 f(\theta) \qquad (6)$$

with the uncompressed gas volume as

$$\forall_0 = \forall_s + \frac{2\pi}{3}a^3 \qquad (7)$$

A relationship between the two variable contact angles that define the menisci curvature, θ_A and θ_B, can be obtained through applying conservation of mass to the liquid plug. The volumes of the two menisci must sum to a hemispherical volume

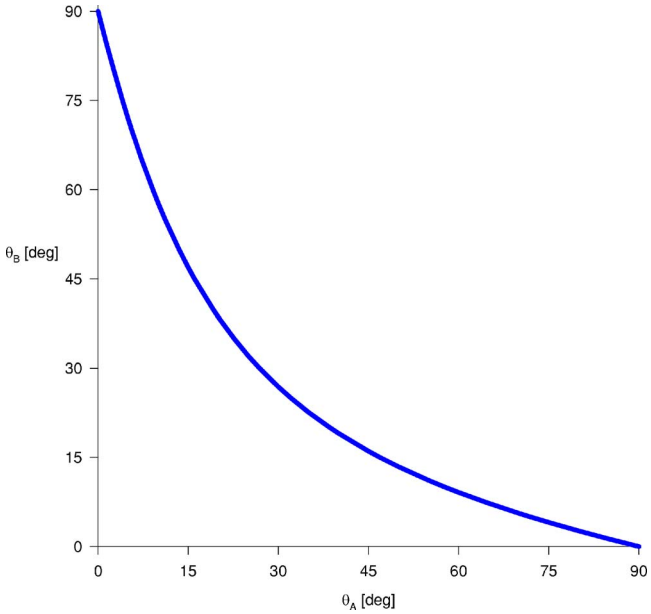

Fig. 4 Relation between θ_A and θ_B per Eq. (10)

$$\frac{\pi}{3}a^3\left(\frac{\sin^3\theta_A - 3\sin\theta_A + 2}{\cos^3\theta_A}\right) + \frac{\pi}{3}a^3\left(\frac{\sin^3\theta_B - 3\sin\theta_B + 2}{\cos^3\theta_B}\right) = \frac{2\pi}{3}a^3 \tag{8}$$

which is equivalent to

$$f(\theta_A) + f(\theta_B) = 2 \tag{9}$$

An expression for θ_B as a function of θ_A can be found by implicitly solving Eq. (8) for θ_B and using a sixth-order regression. The resulting expression has an r^2 greater than 0.9999

$$\theta_B = 0.10691\theta_A^6 - 0.92850\theta_A^5 + 3.20152\theta_A^4 - 5.82472\theta_A^3 + 6.20685\theta_A^2 - 4.15750\theta_A + 1.57312 \tag{10}$$

where θ_A varies from 0 to $\pi/2$ rad. The relationship between θ_A and θ_B which satisfies conservation of mass on the liquid plug is shown in Fig. 4.

The volumes are normalized using the maximum meniscus volume, $2\pi a^3/3$, resulting in a dimensionless static volume of $\forall_s^* = 3\forall_s/2\pi a^3$ and an uncompressed volume of $\forall_0^* = \forall_s^* + 1$. The gas volumes at Meniscus A and Meniscus B can be expressed using only $f(\theta_A)$ via Eq. (9)

$$\forall_A^* = \forall_s^* + \tfrac{1}{2}f(\theta_A) \tag{11}$$

$$\forall_B^* = \forall_s^* + 1 - \tfrac{1}{2}f(\theta_A) \tag{12}$$

The gas pressures at each meniscus can now be written as

$$P_A = P_0\left[\frac{\forall_s^* + 1}{\forall_s^* + f(\theta_A)/2}\right]^k \tag{13}$$

and

$$P_B = P_0\left[\frac{\forall_s^* + 1}{\forall_s^* + 1 - f(\theta_A)/2}\right]^k \tag{14}$$

with the compression ratio now expressed as

$$C_R = 1 + \frac{1}{\forall_s^*} \tag{15}$$

2.3 Electric Field Stress. The electric body force density acting on the molecules of a fluid in the presence of an electric field was derived by [30] through a thermodynamic approach with the assumption that the polarization is a linear function of the applied electric field and is dependent on the fluid density only. It accounts for the force acting on the free charges (Coulomb) and for the polarization force induced in the fluid. At a fluid–fluid interface in a nonuniform electric field, a polarization force is created that draws the fluid of higher permittivity (liquid) toward the region of higher electric field strength. This attraction force will occur for either a dc or ac nonuniform field. For a liquid–vapor interface, the liquid is drawn towards the higher electric field. Generally, the higher electric field exists at the positive electrode due to the electrode design; the ground electrode generally being planar while the positive electrode being a pin or ring configuration.

Use of the Maxwell stress tensor [23,30] avoids the singularity of the electric permittivity that would arise from a direct use of the polarization force equation at the interface of liquid–vapor media

$$\tau_{ij} = \epsilon E_i E_j - \frac{\epsilon}{2}\delta_{ij}E_k E_k\left[1 - \frac{\rho}{\epsilon}\left(\frac{\partial\epsilon}{\partial\rho}\right)_T\right] \tag{16}$$

where $\epsilon = \epsilon_r\epsilon_0$ and ϵ_r is the dielectric constant which is equal to 82 and 1 for air and water, respectively. For a planar gas–liquid interface, the normal stress can be simplified to

$$\tau_E \approx \tfrac{1}{2}\epsilon E^2 \tag{17}$$

where ϵ is the electric permittivity of the liquid phase. This simplification was done considering a nonuniform electric field $(E,0,0)$ and neglecting the contribution from the lateral surfaces of the integration volume. The value of the electric field is taken as that at the gas–liquid interface. Only the planar interface is considered; that is, the meniscus with a 90 deg contact angle.

The electric field stress expressed in Eq. (2) can now be written in terms of the ambient gas pressure, the static gas volume, and the contact angle of Meniscus A. Using the nondimensional quantities $\tau_E^* = a\epsilon E^2/4\sigma$ and $P_0^* = aP_0/2\sigma$, the following expression for the nondimensional electric field stress is derived

$$\tau_E^* = P_0^*\left[\left(\frac{\forall_s^* + 1}{\forall_s^* + 0.5f_A}\right)^k - \left(\frac{\forall_s^* + 1}{\forall_s^* + 1 - 0.5f_A}\right)^k\right] - (\cos\theta_A - \cos\theta_B) \tag{18}$$

where $f_A = f(\theta_A)$ and $\cos\theta_B$ in the right-most term can be evaluated using Eq. (10).

An interesting feature of Eq. (18) is that the imbalance in menisci curvature ($\cos\theta_A - \cos\theta_B$) is sufficient to compress the gas during the beginning of a compression stroke. In other words, the unequal curvatures created during a compression stroke result in an energy recovery at the beginning of the next compression stroke. The energy recovery can be seen in Fig. 5 where the dimensionless electric field stress appears to be negative for values of θ less than 28 deg. This indicates that as the contact angle varies from zero to approximately 28 deg the electric field is not required in order for a menisci to compress the gas. This behavior is the same for the entire range of capillary radii considered (from 1 to 1000 μm) and all specific heat ratios considered (from 1 to 1.667). The electric field is required to compress the gas once the contact angle exceeds 28 deg and the electric field must be at the maximum when the contact angle reaches 90 deg.

The maximum nondimensional electric field stress occurs at $\theta_A = \pi/2$. This corresponds to a flat interface with $f(\theta_A) = 0$ and $\cos\theta_B = 1$. Thus, the maximum dimensionless electric field stress is

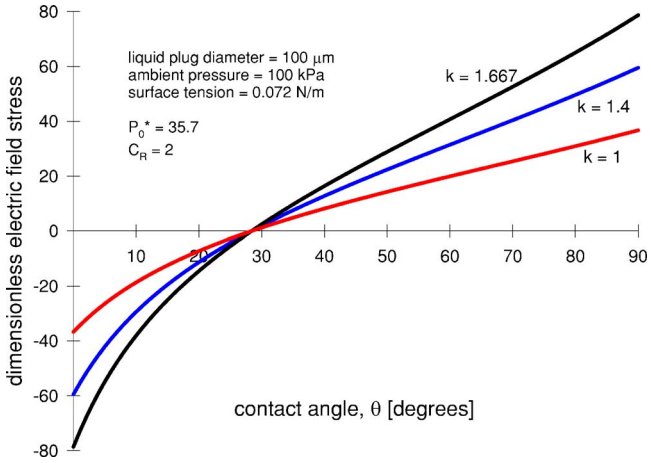

Fig. 5 Dimensionless electric field stress, τ_E^*, versus contact angle using water for the liquid plug with $P_0^*=35.7$ and $C_R=2$ for various specific heat ratios, k

$$\tau_{E_{\max}}^* = P_0^*(C_R{}^k - 1) + 1 \tag{19}$$

which, after returning to dimensional variables, yields the following expression for the maximum electric field strength necessary to operate the pump

$$E_{\max} = \sqrt{\frac{4\sigma}{a\epsilon}[P_0^*(C_R{}^k - 1) + 1]} \tag{20}$$

Equations (19) and (20) represent the maximum electric field stress and maximum electric field required to isentropically compress an ideal gas through the deformation of a pinned meniscus.

Equation (20) provides the upper value of the electric field required for gas compression which occurs only at $\theta=\pi/2$. The actual electric field can vary with meniscus deflection. For example, using water and air as working fluids with a cylindrical liquid plug 100 μm in diameter, the electric field variation with contact angle varies from 0 at $\theta\approx 28$ deg to approximately 21 kV/mm for a compression ratio of 2 and $k=1.4$ as shown in Fig. 6. The value for the dimensionless pressure, P_0^*, is 35.7 which indicates that the uncompressed pressure, $P_0=100$ kPa, is significantly greater than the maximum capillary pressure which for this case is approximately 2800 Pa. Thus, electric field is primarily required for gas compression and very little is required for meniscus deflection for contact angles greater than 28 deg. Again, below contact angles of 28 deg the imbalance in capillary pressure can compress the gas without the electric field. The values for additional dimensional and nondimensional parameters for this particular pump configuration are given in Table 1.

2.4 Power Requirements. The work per cycle is primarily dependent upon the compression ratio. The pump power required to compress the gas will also depend on the oscillation frequency. The power required to compress the gas is not equivalent to the power required to generate the electric field due to the energy recovery of the menisci between compression and expansion.

For an adiabatic, reversible process, the work required for compression of an ideal gas over a full cycle is

$$W_m = \frac{2P_1\forall_1}{1-k}\left(\frac{P_2\forall_2}{P_1\forall_1} - 1\right). \tag{21}$$

State 1 is the uncompressed gas which results in $P_1=P_0$ and $\forall_1=\forall_s+2\pi a^3/3$. State 2 is the compressed gas which implies

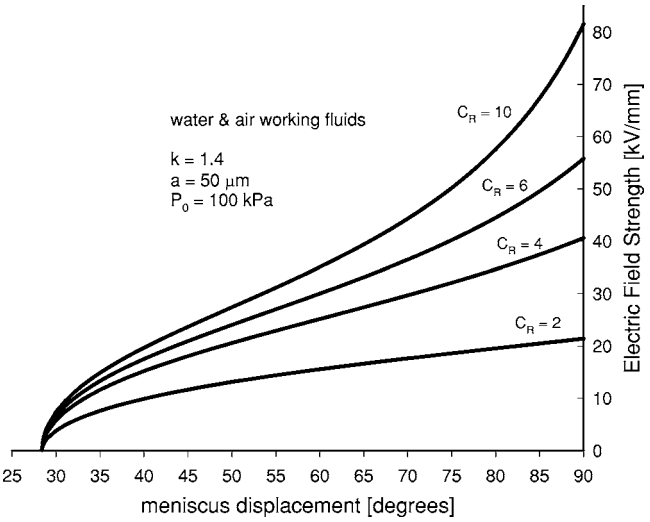

Fig. 6 Electric field strength vs meniscus displacement for room temperature water and air as the working fluids. The uncompressed pressure is 100,000 Pa, the pump radius is 50 μm, and a specific heat ratio of 1.4. Table 1 lists additional parameters, dimensional, and nondimensional, associated with this pressure, radius, and fluid selection.

$$P_2 = P_0\left(\frac{\forall_s^* + 1}{\forall_s^*}\right)^k = P_0 C_R^k \tag{22}$$

and $\forall_2=\forall_s$. Combining the expressions for pressures and volumes into Eq. (21) results in the work per cycle as

$$W_m = 2P_0\forall_s\left(\frac{C_R{}^k - C_R}{k-1}\right) \tag{23}$$

Equation (23) represents the ideal work per cycle required for gas compression and does not include viscous dissipation in the liquid.

The power required for gas compression is equal to the work per cycle multiplied by the frequency in Hz, power$=W_m\cdot f_m$, or

$$\text{power} = 2f_m P_0\forall_s\left(\frac{C_R{}^k - C_R}{k-1}\right) \tag{24}$$

The actual input power needed to operate the device may be lower than the gas compression power as determined by Eq. (24) since for each half-cycle energy is recovered through surface tension work from $\theta=0$ to about 28 deg as seen in Fig. 5. Equation (24) can be rewritten in terms of the volumetric flow rate which is found by multiplying the displaced volume for one cycle by the frequency of menisci oscillation, $\dot{\forall}=4\pi a^3 f_m/3$, where f_m is the meniscus oscillation frequency in Hz

$$\text{power} = \dot{\forall} P_0(\forall_s^* C_R{}^k)\left(\frac{C_R{}^{k-1} - 1}{k-1}\right) \tag{25}$$

Defining a dimensionless power as $\Gamma=\text{power}/\dot{\forall}P_0$ and using the relationship between $\forall_s^*$ and C_R (Eq (15)), the relationship between required power and compression ratio becomes

$$\Gamma = \left(\frac{C_R}{C_R - 1}\right)\left(\frac{C_R{}^{k-1} - 1}{k-1}\right) \tag{26}$$

Figure 7 illustrates the relationship between Γ, k, and C_R.

Using a menisci oscillation frequency of 1000 Hz and the same pump parameters given above (see Table 1) with a compression ratio of 2 and $k=1.4$, the volumetric flow rate is 0.524 μL/s. The work per cycle in order to compress the gas is $8.36\cdot 10^{-8}$ J/cycle. This is only the work for compression of an ideal gas and does not include viscous dissipation. The power associated with this work

Table 1 Values for a case study on the electric field strength required to operate the EHD Menisci pump using water and nitrogen as working fluids in a 100-μm-diameter capillary with a 2:1 compression ratio. The operating requirements are for operation at 1000 Hz.

Physical parameters	Dimensionless numbers	Frequency limits (Hz)	Operating requirements
$a=50\ \mu$m	$C_R=2$	$f_\mu=7000$	$E_{\max}=21$ kV/mm
$g=9.81$ m/s^2	$P_0^*=35.7$	$f_\rho=11{,}800$	$\dot{\forall}=0.524\ \mu$L/s
$P_a=100{,}000$ Pa	$\tau_{E_{\max}}^*=36.7$	$f_0=6074$	$W_m=8.36\cdot10^{-8}$ J/cycle
$\rho_l=1000$ kg/m^3	$\forall_0^*=2$	$f_{90}=9400$	$P_m=83.6\ \mu$W
$\mu_l=0.001$ kg/ms	$\mathrm{Bo}=3.5\cdot10^{-4}$		
$\sigma_l=0.07$ N/m	$\mathrm{We}_c=1$		
$\epsilon_{r_l}=82$	$\mathrm{Ca}_c=10^{-2}$		
$\epsilon_{r_g}=1$	Oh=0.017		
$\epsilon_0=8.854$ pF/m	$f_{\rho\mu}^*=1.7$		
$k=1.4$	$\Gamma=1.6$		

at a 1000 Hz is 83.6 μW.

The EHD menisci micropump can theoretically achieve a pressure head of 264 kPa operating at 1000 Hz (see Table 1). This is comparable to the maximum pressure achieved by existing reciprocating displacement pumps (diaphragm pumps) such Kamper 1998 (200 kPa) or Li 2000 (304 kPa, operating at 3500 Hz and 1200 V), as reported in [16]. The flow rate of the EHD menisci pump (31.44 μL/min), however, is one or two orders of magnitude lower than that produced by the aforementioned micropumps. Higher flow rates can be achieved by increasing the operating frequency. At a frequency of 6000 Hz a flow rate of 188.64 μL/min is possible.

The available EHD pumps (injection, induction, or polarization) such as Wong 1996, Ahn 1998, and Darabi 2001 and 2002 ([16]) report pressure heads under 1 kPa and comparable or lower flow rates to the EHD menisci pump. A theoretical model of an EHD-actuated diaphragm micropump (piezoelectric)[4] predicted flow rates of 33 μL/min for a 1-mm-diameter diaphragm operating at 1 kHz. Electro-osmotic pumps can operate at similar maximum pressure as the EHD menisci pump (Gan 2000, Yao 2001 and 2003, Zeng 2002, as reported in [16]), but with higher flow rates due to bundling of multiple, parallel pumps. As such the volume of these devices range from 1200 mm^3 to 9500 mm^3 while the EHD menisci pump is on the order of 1 mm^3.

3 Operational Limits

There are a number of physical limits associated with gas compression at the microscale. Most of these limits involve temperature and pressure constraints of the pump materials and manifolds which are common to many micropumps. However, an operational limit, or constraint, unique to the menisci pump, is the rate at which the menisci can be stably oscillated. A meniscus is considered to be oscillating stably as long as an undistorted spherical interface can exist for the contact angle range considered ($0 \leqslant \theta \leqslant \pi/2$).

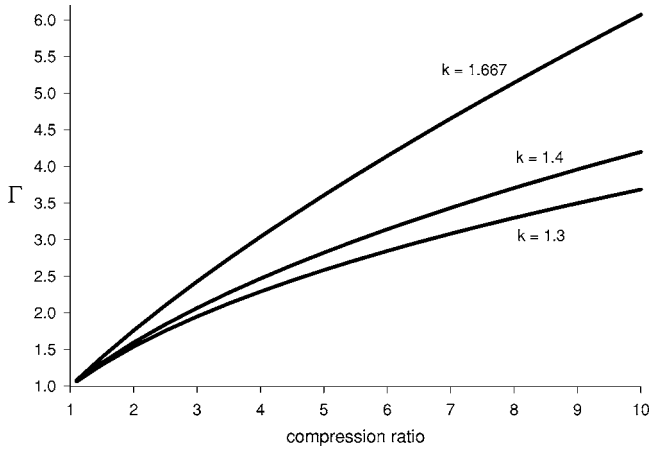

Fig. 7 Relationship between dimensionless power, Γ, and the compression ratio, C_R, for various specific heat ratios, k

The operational limits in which the menisci can stably oscillate can be analyzed from inertial and viscous standpoints. In addition, the menisci will have a variation in natural frequency based on the curvature as defined by θ and these natural frequencies also represent an operational limit. These various oscillation limits will bound the operational domain of the menisci pump.

3.1 Inertial and Viscous Limits. The inertial limit of an oscillating meniscus may be examined via the Weber number. The Weber number is a measure of inertial effects to capillary effects on a dynamic gas–liquid interface and is defined as

$$\mathrm{We} \equiv \frac{\rho U^2 a}{\sigma} \tag{27}$$

If a critical Weber number is exceeded, a gas–liquid interface may break up. For small Bond number systems, the critical Weber number, We_c, is on the order of one [31]. Substituting in for the critical Weber number, the maximum meniscus velocity may be obtained

$$U_\rho = \sqrt{\frac{\sigma}{\rho a}\mathrm{We}_c} \tag{28}$$

The maximum meniscus displacement is a where $2a$ represents one complete cycle. Thus, the frequency in Hz follows as

$$f_\rho = \frac{U_\rho}{2a} = \frac{1}{2}\sqrt{\frac{\sigma}{\rho a^3}\mathrm{We}_c} \tag{29}$$

The characteristic frequency, ω, is defined as

$$\omega \equiv \sqrt{\frac{\sigma}{\rho a^3}} \tag{30}$$

which gives an inertial frequency limit of

$$f_\rho = \frac{\omega}{2}\sqrt{\mathrm{We}_c} \tag{31}$$

The viscous limit of an oscillating meniscus may be examined via the Capillary number which, for a small Bo system, is a measure of the relative influence between capillarity and viscous effects. The Capillary number is defined as

$$\mathrm{Ca} \equiv \frac{\mu U}{\sigma} \tag{32}$$

When a critical capillary number is exceeded significant distortion of the gas–liquid interface may occur due to viscous stresses. The critical Capillary number, Ca_c, for low Bo systems is on the order of 10^{-2} [31]. The critical viscous velocity scale is

$$U_\mu = \frac{\sigma}{\mu}\mathrm{Ca}_c \tag{33}$$

which yields a viscous frequency limit of

$$f_\mu = \frac{U_\mu}{2a} = \frac{\sigma}{2\mu a}\mathrm{Ca}_c \tag{34}$$

expressed in Hz.

In order to compare the viscous and inertial stability limits a nondimensional parameter $f^*_{\rho\mu}$ is defined as the ratio of the two frequency limits

$$f^*_{\rho\mu} = \frac{f_\rho}{f_\mu} = \frac{\mu a\omega}{\sigma}\left(\frac{\mathrm{We}_c}{\mathrm{Ca}_c^2}\right)^{1/2} \tag{35}$$

The physical property ratio in Eq. (35) is another frequently used dimensionless parameter; the Ohnesorge number, Oh

$$\frac{\mu a\omega}{\sigma} = \left(\frac{\mu^2}{\rho a\sigma}\right)^{1/2} \equiv \mathrm{Oh} \tag{36}$$

which is a measure of the damping in a capillary-dominated interface. For small Oh, the surface may be underdamped resulting in the growth of inertial disturbances. If the Oh is large then inertial disturbances may be damped before significant distortion of the interface occurs. For the critical Capillary and Weber numbers specified above, the ratio of inertial to viscous frequency limits is

$$f^*_{\rho\mu} \approx 100\ \mathrm{Oh} \tag{37}$$

If $f^*_{\rho\mu} < 1$ then the inertial frequency, f_ρ, is the upper limit for the meniscus oscillation and if $f^*_{\rho\mu} > 1$ then the viscous frequency, f_μ, is the upper limit.

3.2 Natural Frequency Limits. The natural frequencies of the meniscus also represent an oscillation limit for the menisci pump. If the pump cycle approaches the natural frequency of the menisci then significant distortion of the gas–liquid interface is probable. The natural frequency of the menisci will be examined for the limiting cases of $\theta = \pi/2$ and $\theta = 0$. For a hemispherical meniscus, $\theta = 0$, the natural frequency of a perfectly wetting meniscus is [32]

$$f_0 = \frac{1}{2\pi}\left[(2.6 + 1.84\ \mathrm{Bo})\frac{\sigma}{\rho a^3}\right]^{1/2} \tag{38}$$

For a flat interface, $\theta = \pi/2$, and a relatively long liquid plug (length $> 2a$) the natural frequency is [33]

$$f_{90} = \frac{1}{2\pi}\left[(\lambda^3 + \lambda\mathrm{Bo})\frac{\sigma}{\rho a^3}\right]^{1/2} \tag{39}$$

where $\lambda \equiv$ eigenvalues corresponding to oscillation modes. For the first subharmonic, $\lambda = 1.84$. The expressions for frequencies can be simplified using the expression for the characteristic frequency (Eq. (30)) to

$$f_0 = \frac{\omega}{2\pi}\sqrt{2.6 + 1.84\mathrm{Bo}} \tag{40}$$

$$f_{90} = \frac{\omega}{2\pi}\sqrt{1.84^3 + 1.84\mathrm{Bo}} \tag{41}$$

The theories and correlations for the natural frequencies [32,33] are based on an inviscid interface and, as such, also represent a form of inertial limit. By inspection, f_{90} is always larger than f_0 for small Bond numbers. Therefore, the oscillation limit based on the meniscus natural frequency will be Eq. (40).

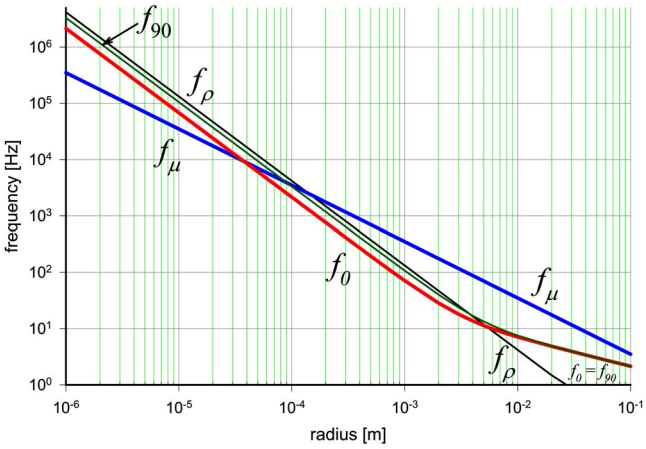

Fig. 8 Comparison of operational limits as a function of liquid column radius. The properties used are for water (ρ = 1000 kg/m^3, μ = 0.001 kg/ms, σ = 0.07 N/m) and for normal gravitational acceleration (g = 9.81 m/s^2). Stable menisci oscillation occurs at frequencies below the limits shown.

A comparison of the frequency limits is shown in Fig. 8 which illustrates the menisci oscillation limits for the case of room temperature water in a cylindrical tube. The menisci can stably oscillate at frequencies which lie below the limits shown. The stability limit for the oscillating meniscus is viscous (Eq. (34)) up to approximately a 40 μm tube radius while between 40 μm and 6 mm the stability limit should remain the inertial limit given by the lower natural frequency (Eq. (40)).

As the radius becomes larger than about 6 mm, the stability limit, while still inertial, appears to be given by f_ρ. However, for a radii greater than 6 mm with room temperature water, the Bond number will be greater than one. The liquid–gas interface becomes increasingly flat with increasing Bond number, assuming the gravitational acceleration is normal to the interface. Thus, the upper and lower natural frequencies, f_0 and f_{90}, converge since the contact angle plays a small role in determining the interface shape at large Bond numbers. The critical Weber number used in f_ρ is predicated on a small Bond number system and therefore the stability limit in this range is still the natural frequency of the menisci (Eq. (40)).

For the pump parameters studied above (see Table 1), the dimensionless frequency limit, $f^*_{\rho\mu}$, is greater than 1; therefore, it is anticipated that the oscillation limit of the meniscus for this particular case will be an inertial limit (f_ρ, f_0, or f_{90}). From Table 1, the lowest frequency limit is $f_0 = 6074$ Hz. This frequency represents the upper value for which the meniscus will stably oscillate. Therefore, oscillating the pump at 1000 Hz as described earlier is feasible.

4 Conclusion

In this discussion, the concept and operation of an EHD menisci pump have been introduced. The theoretical electric field strength required for operation appears reasonable given the very small length scales of the system. And the cyclic operation can be in the kHz range based on hydrodynamic limitations which implies that a small system could provide relatively large flow rates.

There are several advantages of using a meniscus as a naturally occurring diaphragm pump over more traditional style micropumps. The naturally existing diaphragm defined by the gas–liquid meniscus is not constrained to a limited deflection as in the case of a classical diaphragm and it is not exposed to fatigue

failure, although the pinning of the interface will pose challenges. Another advantage of the EHD menisci pump is a low power input resulting from the operating principle and from the energy recovery associated with the curvature imbalance of the gas–liquid interfaces at the beginning of each compression cycle; the compression on the first one-third of each cycle is done by the surface tension forces at no cost. It should be noted here that the electrode design is a critical issue because of the possibility of charge accumulation at the gas–liquid interface which could destabilize the meniscus. Reliable operation will also be influenced by issues such as the ability to keep the contact line pinned, dissipation of thermal energy, and viscous stresses at the menisci. Resolution of these issues will require experimental investigations. The compactness of the menisci micropump and the simple design together with pressure head and flow rate capabilities comparable to much larger pumps makes this an attractive candidate for commercial applications.

Nomenclature

a = capillary radius (m)
Bo = Bond number
Ca = capillary number
C_R = compression ratio
E = electric field strength (V/m)
$f(\theta)$ = dimensionless meniscus volume θ
f_A = abbreviation for $f(\theta_A)$
f_0 = lower natural frequency limit (Hz)
f_{90} = upper natural frequency limit (Hz)
f_ρ = inertial frequency limit (Hz)
f_μ = viscous frequency limit (Hz)
$f^*_{\rho\mu}$ = dimensionless frequency limit
g = gravitational acceleration (m/s^2)
k = specific heat ratio
P = pressure (N/m^2)
P_0 = uncompressed gas pressure (N/m^2)
P_m = menisci power (W)
U = characteristic meniscus velocity (m/s)
$\forall$ = volume (m^3)
$\dot{\forall}$ = volumetric flow rate (m^3/s)
$\forall_s$ = static gas volume (m^3)
$\forall_0$ = total uncompressed volume (m^3)
We = Weber number
W_m = menisci work (J)
Γ = dimensionless power
δ_{ij} = Kronecker delta
ϵ = electric permittivity (pF/m)
ϵ_0 = vacuum permittivity=8.854 (pF/m)
ϵ_r = dielectric constant
θ = contact angle of meniscus (rad)
λ = eigenvalues corresponding to oscillation modes
μ = viscosity (kg/ms)
ρ = mass density (kg/m^3)
σ = surface tension (N/m)
τ = stress (N/m)
ω = characteristic frequency (rad/s)

Subscripts

A = meniscus A
B = meniscus B
g = gas phase
l = liquid phase
c = critical parameter
ρ = inertial parameter
μ = viscous parameter
E = electric field parameter

Superscript

$*$ = nondimensional parameter

References

[1] Frye-Mason, G. C. et al., 2000, "Hand-Held Miniature Chemical Analysis System for Detection of Trace Concentrations of Gas Phase Analytes," *Micro Total Analysis Systems 2000*, Kluwer Academic, Enschede, The Netherlands.
[2] Kamper, K.-P., Dopper, J., Ehrfeld, W., and Oberbeck, S., 1998, "A Self-Filling Low-Cost Membrane Micropump," *Proceedings 11th Annual International Workshop on MicroElectroMechanical Systems*, Heidelberg, Germany, January 25–29.
[3] Li, H. Q. et al., 2000, "A High Frequency High Flow Rate Piezoelectrically Driven MEMS Micropump," *Proceedings 2000 Solid-State Sensor and Actuator Workshop*, Hilton Head, SC, June 4–8.
[4] Garimella, S., Killion, J. D., and Coleman, J. W., 2005, "An Experimentally Validated Model for Two-Phase Pressure Drop in the Intermittant Flow Regime for Circular Microchannels," J. Fluid Mech., **124**, pp. 205–214.
[5] Yoon, H. J., Sim, W. Y., and Yang, S. S., 2001, "The Fabrication and Test of a Phase-Change Micropump," *Proceedings ASME International Mechanical Engineering Congress and Exposition*, New York, November 11–16.
[6] Zimmermann, S., Frank, J. A., Liepmann, D., and Pisano, A. P., 2004, "A Planar Micropump Utilizing Thermopneumatic Actuation and In-Plane Flap Valves," *Proceedings 17th IEEE International Conference on Micro Electro Mechanical Systems*, Maastricht, The Netherlands, January 25–29.
[7] Grosjean, C., and Tai, Y. C., 1999, "A Thermopneumatic Peristaltic Micropump," *Proceedings Transducers 99*, Sendai, Japan, January 17–21.
[8] Wego, A., and Pagel, L., 2001, "A Self-Filling Micropump Based on PCB Technology," Sens. Actuators, A, **88**, pp. 220–226.
[9] Wong, C. C., Adkins, D. R., and Chu, D., 1996, "Development of a Micropump for Microelectronic Cooling," *Micro-Electro-Mechanical Systems, Proceedings of the 1996 ASME International Mechanical Engineering Congress and Exposition*, Atlanta, GA, Nov. 17–22, pp. 239–244.
[10] Ahn, S. H., and Kim, Y. K., 1998, "Fabrication and Experiment of a Planar Micro Ion Drag Pump," Sens. Actuators, A, **70**, pp. 1–5.
[11] Darabi, J., Ohadi, M. M., and DeVoe, D., 2001, "An Electrohydrodynamic Polarization Micropump for Electronic Cooling," J. Microelectromech. Syst., **10**, pp. 98–106.
[12] Darabi, J., Rada, M., Ohadi, M. M., and Lawler, J., 2002, "Design, Fabrication and Testing of an Electrohydrodynamic Ion-Drag Micropump," J. Microelectromech. Syst., **11**, pp. 684–690.
[13] Yao, S. H., Huber, D. E., Mikkelsen, J. C., and Santiago, J. G., 2001, "A Large Flow Rate Electroosmotic Pump with Micron Pores," *Proceedings 2001 ASME International Mechanical Engineering Congress and Exposition*, New York, November 11–16.
[14] Yao, S. H., Hertzog, D. E., Zeng, S. L., Mikkelsen, J. C., and Santiago, J. G., 2003, "Porous Glass Electroosmotic Pumps: Design and Experiments," J. Colloid Interface Sci., **268**, pp. 143–153.
[15] Zeng, S. L. et al., 2002, "Electroosmotic Flow Pumps with Polymer Frits," Sens. Actuators B, **82**, pp. 209–212.
[16] Laser, D. J., and Santiago, J. G., 2004, "A Review of Micropumps," J. Micromech. Microeng., **14**, pp. R35–R64.
[17] Damianidis, C. et al., 1992, "EHD Boiling Enhancement in Shell-and-Tube Evaporators and Its Application in Refrigeration Plants," ASHRAE Trans., **98**(2), pp. 462–472.
[18] Ogata, J. et al., 1992, "Boiling Heat Transfer Enhancement in Tube-Bundle Evaporators Utilizing Electric Field Effects," ASHRAE Trans., **98**(2), pp. 435–444.
[19] Yabe, A. et al., 1992, "Experimental Study of Electrohydrodynamically Enhanced Evaporator for Nonazeotropic Mixtures," ASHRAE Trans., **98**(2), pp. 455–461.
[20] Yabe, A. et al., 1982, "Augmentation of Condensation Heat Transfer by Applying Non-Uniform Electric Fields," *Proceedings 7th International Heat Transfer Conference*, Munich, Germany, September 6–10, Vol. 5, pp. 189–194.
[21] Yamashita, K. et al., 1991, "Heat Transfer Characteristics on an EHD Condenser," *Proceedings 3rd ASME/JSME Thermal Engineering Joint Conference*, Reno, NV, pp. 61–67.
[22] Sankaran, S., Allen, J. S., and Gumennik, L., 2003, "Electric Field Effects on the Stability of Vapor Microlayers—Enhancement of Heat Transfer," *Proceedings of 2003 ASME International Mechanical Engineering Congress and RD&D Exposition*, Washington, D.C., November 15–21, Paper No. IMECE2003–42974.
[23] Seyed-Yagoobi, J., and Bryan, J. E., 1999, "Enhancement of Heat Transfer and Mass Transport in Single-Phase and Two-Phase Flows with Electrohydrodynamics," Adv. Heat Transfer, **33**, pp. 95–186.
[24] Bart, S. F. et al., 1990, "Microfabricated Electrohydrodynamic Pumps," J. Am. Ceram. Soc., **21**, pp. 193–197.
[25] Richter, A. et al., 1991, "The Electrohydrodynamic Micro Flow Meter," *Proceedings IEEE International Conference on Solid State Sensors*, San Francisco, CA, June 24–28, pp. 935–938.
[26] Bryan, J. E., and Seyed-Yagoobi, J., 1997, "Heat Transport Enhancement of Monogroove Heat Pipe with Electrohydrodynamic Pumping," J. Thermophys. Heat Transfer, **11**(3), pp. 454–460.
[27] Jones, T. B., 1974, "An Electrohydrodynamic Heat Pipe," Mech. Eng. (Am. Soc. Mech. Eng.), **96**(1), pp. 27–32.
[28] Bologa, M. K., and Savin, I. K., 1990, "Electrohydrodynamic Heat Pipes,"

Proceedings 7th International Heat Pipe Conference, Minsk, USSR, May 21–25.
[29] Allen, J. S., 2003, "An Analytical Solution for Determination of Small Contact Angles from Sessile Drops of Arbitrary Size," J. Colloid Interface Sci., **261**(2), pp. 481–489.
[30] Melcher, J. R., 1981, *Continuum Electromechanics*, MIT Press, Cambridge, MA.
[31] Weislogel, M. M., 1998, "Fluid Interface Phenomena in a Low-Gravity Environment: Recent Results from Drop Tower Experimentation," Space Forum, **3**, pp. 59–86.
[32] Salzman, J. A., and Masica, W. J., 1969, "Lateral Sloshing in Cylinders Under Low Gravity Conditions," NASA TN D-5058, NASA Lewis Research Center, February.
[33] Benjamin, T. B., and Ursell, F., 1954, "The Stability of a Plane Free Surface of a Liquid in Vertical Periodic Motion," Proc. R. Soc. London, Ser. A, **225**, pp. 505–515.

Torque and Bulk Flow of Ferrofluid in an Annular Gap Subjected to a Rotating Magnetic Field

Arlex Chaves

Fernando Gutman

Carlos Rinaldi[1]
e-mail: crinaldi@uprm.edu

Department of Chemical Engineering,
University of Puerto Rico,
Mayagüez,
P.O. Box 9046,
Mayagüez, PR 00681

We report analysis and measurements of the torque and flow of a ferrofluid in a cylindrical annulus subjected to a rotating magnetic field perpendicular to the cylinder axis. The presence of the inner cylinder results in a nonuniform magnetic field in the annulus. An asymptotic analysis of the ferrohydrodynamic torque and flow assuming linear magnetization and neglecting the effect of couple stresses indicated that the torque should have a linear dependence on field frequency and quadratic dependence on field amplitude. To the order of approximation of the analysis, no bulk flow is expected in the annular gap between stationary cylinders. Experiments measured the torque required to restrain a polycarbonate spindle surrounded by ferrofluid in a cylindrical container and subjected to the rotating magnetic field generated by a two-pole magnetic induction motor stator, as a function of the applied field amplitude and frequency, and for various values of the geometric aspect ratios of the problem. The ultrasound velocity profile method was used to measure the azimuthal and axial velocity profiles in the ferrofluid contained in the annular gap of the apparatus. Flow measurements show the existence of a bulk azimuthal ferrofluid flow between stationary coaxial cylinders with a negligible axial velocity component. The fluid was found to corotate with the applied magnetic field. Both the torque and flow measurements showed power-of-one dependence on frequency and amplitude of the applied magnetic field. This analysis and these experiments indicate that the action of antisymmetric stresses is responsible for the torque measured on the inner cylinder, whereas the effect of body couples is likely responsible for bulk motion of the ferrofluid. [DOI: 10.1115/1.2567918]

Keywords: ferrofluid, ultrasound velocity profile, rotating magnetic field, antisymmetric stress

1 Introduction

The flow of a ferrofluid contained in the annular gap between two concentric cylinders and subjected to a rotating magnetic field has been investigated by several authors [1–5]. The problem is closely related to the observation of ferrofluid motion in a cylindrical container under an applied uniform rotating magnetic field [3,6–9], except that the field in the case of the ferrofluid in the annular gap is not uniform owing to the presence of the inner cylinder. The initial work is due to Tsebers [1], who obtained an expression for azimuthal flow, arguing that tangential stresses are zero at the boundary of a freely suspended cylinder. That analysis predicted no bulk flow when both cylinders are held fixed. Rosensweig et al. [3] obtained experimental top free-surface velocity profiles for the case in which both cylinders are stationary. The velocity profile at the free surface was observed to reverse direction along the annulus, with the ferrofluid corotating with the field near the surface of the inner cylinder and counterrotating with the field near the surface of the outer cylinder. Rosensweig et al. [3] compared these observations to their analysis in which the transport of internal angular momentum included the effects of spin viscosity, neglected by Tsebers [1]. Based on their experimental observations and the lack of qualitative agreement with the available analysis, Rosensweig et al. [3] concluded that the observed flow was solely due to magnetic surface stresses on the ferrofluid-air interface. Unfortunately, both Tsebers [1] and Rosensweig et al. [3] assumed in their models that the magnetic field in the annular gap was homogeneous, an error that was later corrected by Lebedev and Pshenichnikov [2], who obtained expressions for flow and torque in the absence of free-surface effects and when the fluid temperature and concentration are homogeneous. Their analysis predicted flow only when the inner cylinder is free to rotate, whereas when both cylinders are stationary flow was considered possible only if the fluid had a concentration or temperature gradient, as discussed by Shliomis et al. [10]. Predictions for the torque were compared to experimental data obtaining poor agreement. Another expression was later obtained by Pshenichnikov and Lebedev [4] in which flow was attributed to tangential stresses at the free cylinder, which, on rotating, induces flow in the bulk due to the action of viscous stresses, especially at low magnetic field frequency and amplitude, in which case thermal effects are not important. The analysis of Pshenichnikov and Lebedev [4] predicted no bulk flow when both cylinders were stationary. They obtained expressions for the torque on the inner cylinder and the angular rotation of a freely rotating cylinder immersed in the fluid. Torque predictions were in good agreement with their experimental measurements, but predictions of the amplitude of free cylinder rotation were found in poor agreement. Still, the analysis of Pshenichnikov and Lebedev [4], though it illustrated the role of interfacial stresses in inducing flow in ferrofluids, is internally inconsistent, as the integration constants obtained for the magnetic field are incorrect [11].

An asymptotic expression for the torque on the inner cylinder, valid for $\Omega_f \tau \ll 1$, where Ω_f is the applied field frequency and τ is

[1]Author to whom correspondence should be addressed.

Contributed by the Fluids Engineering Division of ASME for publication in the JOURNAL OF FLUIDS ENGINEERING. Manuscript received July 31, 2006; final manuscript received November 29, 2006. Assoc. Editor: Dennis Siginer.

the effective magnetic relaxation time of the suspension, was given by Rinaldi et al. [5]. Therein, measurements were reported for the viscous torque when ferrofluid is either entirely inside (torque on the inner surface of the cylindrical container in so-called spin-up flow) or entirely outside (annular flow) of a stationary infinitely long cylinder, subjected to a rotating magnetic field. The predictions of their torque expression were found in good agreement with a limited set of torque measurements.

In the assessment of the theories summarized above, experimental data, such as torques and surface velocity profile measurements, have been used [3,12,13], because of the inherent difficulty in obtaining experimental bulk velocity profiles by conventional methods owing to the opacity of the ferrofluid. Unfortunately, surface measurements are affected by the surface stresses demonstrated and qualitatively explained by Rosensweig et al. [3]; therefore, the corresponding observations cannot be compared to analyses of bulk flow. The focus of this work is to provide measurements of the bulk velocity profile, in addition to torque measurements, for ferrofluid in an annular gap, and results that may then be compared to the available analyses.

In this contribution, we derive the expression reported by Rinaldi et al. [5] for the torque on the inner cylinder through a regular perturbation expansion using the small parameter $\varepsilon=\Omega_f\tau$. Then we present torque and flow measurements for various aspect ratios γ of inner-to-outer cylinder radii of the annular gap using water-based ferrofluids with two different particle volume fractions in a rotating magnetic field. We have used the ultrasound velocity profile (UVP) technique to visualize the flow in our experiments. This technique was initially developed in the study of liquid-metal flow [14] and more recently has been used to study the flow of ferrofluids confined in various geometries, such as the rotating Couette system [15–17] and in the study of ferrofluid flow in a cylindrical container driven by a rotating uniform magnetic field [9]. Finally, we compare the experimental results to the analysis.

2 Analysis of Torque and Flow

In this section, we obtain an asymptotic solution of the coupled ferrohydrodynamic equations for the ferrofluid in the annular gap. To make the solution mathematically tractable, we focus on the linear magnetization limit. Furthermore, because the spin viscosity is commonly regarded to be negligibly small, we neglect the effect of couple stresses in the internal angular momentum equation.

Conceptually, we consider the experimental situation to consist of an infinite column of ferrofluid contained in a nonmagnetic cylinder of radius R_O with an internal concentric stationary spindle of radius R_I and magnetic permeability μ_0. Hence, the column of ferrofluid is assumed to be long enough in the z direction, such that end effects may be considered negligible. The magnetic field is generated in the gap by a two-pole three-phase stator winding, which (i) is modeled as a surface current distribution in the $-z$ direction with real amplitude K

$$\mathbf{K}(\theta,t)=\mathrm{Re}\{-K\mathbf{i}_z e^{j(\Omega_f t-\theta)}\}, \tag{1}$$

located at radius $r=R_O$, and (ii) varies sinusoidally with time at radian frequency Ω_f. In Eq. (1), we use the notation $j=\sqrt{-1}$ and have chosen the direction of the surface current for convenience in the derivations that follow. We assume the winding is backed with a material, such as cast iron, of infinite magnetic permeability, $\mu\to\infty$. This geometry is a simplification of the general three-region problem found in the experiments described below, where a nonmagnetic annulus separates the ferrofluid from the stator current winding. Considering the more general situation merely results in more complicated expressions with the same key features and does not provide a better fit to the experiments. We present the solution to the two-region problem for simplicity.

2.1 Governing Equations. The basic equations for describing the flow of dilute-limit suspensions of magnetic nanoparticles in a Newtonian fluid under applied magnetic fields are summarized in [18]. A phenomenological derivation, based on Dahler and Scriven's seminal work [19,20] is provided in [21]. At a macroscale for which the magnetic nanoparticles represent subcontinuum units, a homogeneous isothermal suspension of magnetic nanoparticles in an incompressible medium obeys the continuity equation $\nabla\cdot\mathbf{v}=0$, where $\mathbf{v}$ is the mass-averaged velocity [22]. The corresponding linear momentum equation is

$$\rho\frac{D\mathbf{v}}{Dt}=\rho\mathbf{g}+\mu_0\mathbf{M}\cdot\nabla\mathbf{H}-\nabla p-2\zeta\nabla\times\left(\frac{1}{2}\nabla\times\mathbf{v}-\boldsymbol{\omega}\right)+\eta\nabla^2\mathbf{v}, \tag{2}$$

where ρ is the density, $\mathbf{g}$ is the gravitational acceleration, p is the pressure, $\mathbf{M}$ is the magnetization vector of the suspension, $\mathbf{H}$ is the applied magnetic field vector, ζ is the vortex viscosity (a dynamical parameter analogous to the shear viscosity and that characterizes the asymmetric component of the Cauchy stress), $\boldsymbol{\omega}$ is the spin velocity vector (representing the subcontinuum rotation of the suspended particles [20,23]), and η is the suspension-scale shear viscosity. The second term on the right-hand side represents the magnetic body forces due to field inhomogeneities, whereas the fourth term represents the antisymmetric component of the Cauchy stress, occurring when the particles rotate at a rate different than half the local vorticity of the flow. When solving Eq. (2) in problems with solid boundaries, the no-slip and no-penetration boundary conditions are employed. A dilute limit expression for monodisperse nanoparticle suspensions in Newtonian fluids for the vortex viscosity was obtained by Brenner [22], $\zeta=3\phi_h\eta_0/2$, where ϕ_h is the hydrodynamic volume fraction of suspended particles and η_0 is the shear viscosity of the suspending fluid.

The reason for the appearance of antisymmetric stresses in these systems is the action of body couples on the subcontinuum units; hence, the Cauchy moment-of-momentum principle no longer applies and a balance of internal angular momentum must be considered. In the corresponding balance equation, the rate of change of angular momentum and the couple stress term are commonly neglected, resulting in

$$\mathbf{0}=\mu_0\mathbf{M}\times\mathbf{H}+2\zeta(\nabla\times\mathbf{v}-2\boldsymbol{\omega}). \tag{3}$$

The first term on the right-hand side represents the body couple acting on the structured continuum whenever the local magnetization is not aligned with the applied magnetic field. The second term is the antisymmetric vector of the Cauchy stress and represents the interchange of momentum from internal angular and macroscopic linear forms.

The suspension magnetization $\mathbf{M}$ represents the local alignment of subcontinuum units and, as such, also obeys a balance equation. The original equation [24] has been the subject of recent debate [25–29], but is regarded as correct for low applied field amplitude and frequency when the local magnetization is not far from its equilibrium value. The magnetization relaxation equation, as it is usually called, is then

$$\frac{D\mathbf{M}}{Dt}=\boldsymbol{\omega}\times\mathbf{M}-\frac{1}{\tau}(\mathbf{M}-\mathbf{M}_{\mathrm{eq}}), \tag{4}$$

where $\mathbf{M}_{\mathrm{eq}}$ represents the magnetization in equilibrium with the local magnetic field, given by the Langevin relation [18]

$$\frac{\mathbf{M}_{\mathrm{eq}}}{\phi M_d}=\left[\coth\alpha-\frac{1}{\alpha}\right]\hat{\mathbf{H}}, \tag{5}$$

in which $\alpha=(\mu_0 M_d H V_c)/(k_B T)$ is the Langevin parameter, a measure of the relative magnitudes of magnetic and thermal energy. In these expressions, ϕ is the volume fraction of magnetic cores, M_d is the domain magnetization for the magnetic nanoparticles, k_B is Boltzmann's constant, T is the absolute temperature, and V_c is the volume of the magnetic cores. In the limit of small α, the Lange-

vin equation may be linearized to obtain $\mathbf{M}_{eq}=\chi_i\mathbf{H}$, where χ_i is the initial susceptibility. All that remains to complete our description are Maxwell's equations in the magnetoquasistatic limit [30,31]

$$\boldsymbol{\nabla}\cdot(\mathbf{M}+\mathbf{H})=0; \quad \boldsymbol{\nabla}\times\mathbf{H}=\mathbf{0}, \tag{6}$$

and the corresponding interfacial boundary conditions for the magnetic field, namely, continuity of the normal component of magnetic induction and the jump in the tangential magnetic field due to surface currents

$$\mathbf{n}\cdot[\ (\mathbf{H}+\mathbf{M})|_a-\ (\mathbf{H}+\mathbf{M})|_b]=0, \tag{7}$$

$$\mathbf{n}\times[\mathbf{H}_a-\mathbf{H}_b]=\mathbf{K}, \tag{8}$$

in which $\mathbf{n}$ is a unit vector locally normal to the interface, pointing from phase b to phase a.

2.2 Scaling of the Governing Equations. Scaling of the governing equations is necessary in order to formulate a regular perturbation problem that permits an analytical solution by decoupling the ferrohydrodynamic equations (2)–(6). As particle rotation is induced by the rotating magnetic field of angular frequency Ω_f, we have chosen this quantity as the scale for the spin velocity $\boldsymbol{\omega}$. If any flow is to occur, then it must be driven by the spin velocity due to the action of the antisymmetric stresses; hence, we choose $\Omega_f R_o$ as the scale for the mass-average velocity $\mathbf{v}$. The magnetic field quantities have been scaled with respect to the surface current K. The resulting scaled variables are denoted with a $(\sim)$ and are assumed to be of order unity

$$\tilde{\mathbf{M}}\equiv\frac{\mathbf{M}}{K}; \quad \tilde{\mathbf{H}}\equiv\frac{\mathbf{H}}{K}; \quad \tilde{\boldsymbol{\omega}}\equiv\frac{\boldsymbol{\omega}}{\Omega_f}; \quad \tilde{\mathbf{v}}\equiv\frac{\mathbf{v}}{\Omega_f R_O}; \quad \tilde{t}\equiv t\Omega_f;$$
$$\tilde{p}\equiv\frac{p}{\eta\Omega_f}; \quad \tilde{\boldsymbol{\nabla}}\equiv R_O\nabla. \tag{9}$$

By substituting these definitions into Eqs. (2)–(6), the scaled governing equations are obtained. The small perturbation parameter $\varepsilon\equiv\boldsymbol{\Omega}_f\boldsymbol{\tau}$ arises in the magnetization equation and the magnetic Mason number $\mathrm{Ma}\equiv\mu_0K^2/\eta\Omega_f$ appears in both the linear and internal angular momentum equations. We may also combine the linear and internal angular momentum equations to obtain the following set of differential equations to be solved:

$$\tilde{\boldsymbol{\nabla}}\cdot(\tilde{\mathbf{M}}+\tilde{\mathbf{H}})=0, \tag{10}$$

$$\tilde{\boldsymbol{\nabla}}\times\tilde{\mathbf{H}}=0, \tag{11}$$

$$\varepsilon\left[\frac{\partial\tilde{\mathbf{M}}}{\partial\tilde{t}}+\tilde{\mathbf{v}}\cdot\tilde{\boldsymbol{\nabla}}\tilde{\mathbf{M}}-\tilde{\boldsymbol{\omega}}\times\tilde{\mathbf{M}}\right]=-(\tilde{\mathbf{M}}-\chi_i\tilde{\mathbf{H}}), \tag{12}$$

$$\mathbf{0}=-\tilde{\boldsymbol{\nabla}}\tilde{p}+\mathrm{Ma}\left[\tilde{\mathbf{M}}\cdot\tilde{\boldsymbol{\nabla}}\tilde{\mathbf{H}}+\frac{1}{2}\tilde{\boldsymbol{\nabla}}\times(\tilde{\mathbf{M}}\times\tilde{\mathbf{H}})\right]+\tilde{\boldsymbol{\nabla}}^2\tilde{\mathbf{v}}, \tag{13}$$

$$\tilde{\boldsymbol{\omega}}=\frac{1}{2}\tilde{\boldsymbol{\nabla}}\times\tilde{\mathbf{v}}+\frac{1}{4}\frac{\eta}{\zeta}\mathrm{Ma}\tilde{\mathbf{M}}\times\tilde{\mathbf{H}}. \tag{14}$$

2.3 Zeroth-Order Problem. To obtain the governing equations for the zeroth-order problem, a regular perturbation scheme in the small parameter ε is applied to all magnetic and dynamical field quantities using a series expansion of the form

$$f(x,t)=\sum_{n=0}^{\infty}\varepsilon^n f_n(x,t). \tag{15}$$

Introducing these expansions into the governing equations (10)–(14) and keeping only those terms that are zeroth order in ε yields the equations for the zeroth-order problem

$$\tilde{\boldsymbol{\nabla}}\cdot(\tilde{\mathbf{M}}_0+\tilde{\mathbf{H}}_0)=0, \tag{16}$$

$$\tilde{\boldsymbol{\nabla}}\times\tilde{\mathbf{H}}_0=\mathbf{0}, \tag{17}$$

$$\tilde{\mathbf{M}}_0=\chi_i\tilde{\mathbf{H}}_0, \tag{18}$$

$$\mathbf{0}=-\tilde{\boldsymbol{\nabla}}\tilde{p}_0+\mathrm{Ma}[\tilde{\mathbf{M}}_0\cdot\tilde{\boldsymbol{\nabla}}\tilde{\mathbf{H}}_0]+\tilde{\boldsymbol{\nabla}}^2\tilde{\mathbf{v}}_0, \tag{19}$$

$$\tilde{\boldsymbol{\omega}}_0=\frac{1}{2}\tilde{\boldsymbol{\nabla}}\times\tilde{\mathbf{v}}_0. \tag{20}$$

It is clear from Eqs. (16)–(20) that the zeroth-order magnetic-field and fluid-mechanical problems have become decoupled. It is possible then to solve for the magnetic quantities independently of the fluid-mechanical state of the system. Once the magnetic quantities $\mathbf{H}_0$ and $\mathbf{M}_0$ are known, we may obtain the magnetic forces and couples needed to solve the fluid mechanical problem.

2.3.1 Zeroth-Order Magnetic Field and Magnetization. We assume the magnetic field $\tilde{\mathbf{H}}_0$ and magnetization $\tilde{\mathbf{M}}_0$ are of a form similar to equation (1)

$$\tilde{\mathbf{H}}_0=\mathbf{Re}\{(\hat{H}_{0,r}(\tilde{r})\mathbf{i}_r+\hat{H}_{0,\theta}(\tilde{r})\mathbf{i}_\theta)e^{j(\tilde{t}-\theta)}\}, \tag{21}$$

$$\tilde{\mathbf{M}}_0=\mathbf{Re}\{(\hat{M}_{0,r}(\tilde{r})\mathbf{i}_r+\hat{M}_{0,\theta}(\tilde{r})\mathbf{i}_\theta)e^{j(\tilde{t}-\theta)}\}, \tag{22}$$

where a hat indicates a complex quantity (in this case complex amplitude vectors), scaled with respect to K and dependent only on $\tilde{r}=r/R_o$. Using this expression for $\tilde{\mathbf{H}}_0$ and substituting the relation $\tilde{\mathbf{M}}_0=\chi_i\tilde{\mathbf{H}}_0$ into Eq. (16), we obtain

$$\frac{d}{d\tilde{r}}(\tilde{r}\hat{H}_{0,r})-j\hat{H}_{0,\theta}=0. \tag{23}$$

Similarly, Eq. (17) becomes

$$\frac{d}{d\tilde{r}}(\tilde{r}\hat{H}_{0,\theta})+j\hat{H}_{0,r}=0. \tag{24}$$

Solving (23) for $\hat{H}_{0,\theta}$ and substituting into (24), we obtain the equidimensional equation

$$\frac{d}{d\tilde{r}}\left[\tilde{r}\frac{d}{d\tilde{r}}(\tilde{r}\hat{H}_{0,r})\right]-\hat{H}_{0,r}=0, \tag{25}$$

which we solve to obtain

$$\hat{H}_{0,r}(\tilde{r})=\hat{C}_1+\hat{C}_2\tilde{r}^{-2}, \tag{26}$$

$$\hat{H}_{0,\theta}(\tilde{r})=-j(\hat{C}_1-\hat{C}_2\tilde{r}^{-2}). \tag{27}$$

Because the magnetic field must remain finite everywhere in the region for which $r<R_I$, we necessarily have $\hat{C}_2=0$ in that region, then the corresponding complex amplitude magnetic-field components are given by

$$\hat{H}^I_{0,r}(\tilde{r})=\hat{C}^I_1 \quad \hat{H}^I_{0,\theta}(\tilde{r})=-j\hat{C}^I_1. \tag{28}$$

Next, we apply the interfacial conditions for the magnetic field and magnetization given by (7) and (8), expressed for the complex amplitude components of the magnetic field and magnetization and evaluated at $\tilde{r}=R_I/R_O\equiv\gamma$ and at $\tilde{r}=1$ to obtain the relations

$$\mu_0\hat{H}^I_{0,r}(\gamma)=\mu_0(1+\chi_i)\hat{H}_{0,r}(\gamma), \tag{29}$$

$$\hat{H}^I_{0,\theta}(\gamma)=\hat{H}_{0,\theta}(\gamma), \tag{30}$$

$$\hat{H}_{0,\theta}(1)=1. \tag{31}$$

Solving Eqs. (29)–(31) for the integration constants and defining the parameter $\beta\equiv\gamma^2\chi_i/(2+\chi_i)$, we obtain the zeroth-order

complex-amplitude magnetic-field components for the annular region

$$\hat{H}_{0,r}(\tilde{r}) = \frac{j(1-\beta\tilde{r}^{-2})}{1+\beta}, \tag{32}$$

$$\hat{H}_{0,\theta}(\tilde{r}) = \frac{(1+\beta\tilde{r}^{-2})}{1+\beta}. \tag{33}$$

The complex-amplitude magnetization components are found simply by multiplying the corresponding complex-amplitude magnetic-field components by the initial magnetic susceptibility χ_i.

2.3.2 Zeroth-Order Body Force and Body Couple. To obtain the zeroth-order body force density, we evaluate $\tilde{\mathbf{M}}_0 \cdot \tilde{\boldsymbol{\nabla}}\tilde{\mathbf{H}}_0 = (1/2)\chi_i \tilde{\boldsymbol{\nabla}}(\tilde{\mathbf{H}}_0 \cdot \tilde{\mathbf{H}}_0)$. Clearly, a force which is a gradient of a potential is absorbed into the definition of the dynamic pressure and hence results in no bulk flow. Regardless, we evaluate the expression in order to illustrate the procedure to follow for higher order terms. The relevant force component for the flow problem under consideration is the θ-directed magnetic force

$$\tilde{f}_{0,\theta} = (\tilde{\mathbf{M}}_0 \cdot \boldsymbol{\nabla}\tilde{\mathbf{H}}_0)_\theta = \chi_i \left[\tilde{H}_{0,r} \frac{d\tilde{H}_{0,\theta}}{d\tilde{r}} + \tilde{H}_{0,\theta}\left(\frac{1}{\tilde{r}} \frac{d\tilde{H}_{0,\theta}}{d\theta} + \frac{\tilde{H}_{0,r}}{\tilde{r}} \right) \right]. \tag{34}$$

Substituting the corresponding magnetic-field quantities, the time-averaged azimuthal zeroth-order body force is obtained from

$$\langle \tilde{f}_{0,\theta} \rangle_t = \frac{\chi_i}{4} \left\{ \hat{H}_{0,r} \frac{d\hat{H}^*_{0,\theta}}{d\tilde{r}} + \hat{H}^*_{0,r} \frac{d\hat{H}_{0,\theta}}{d\tilde{r}} + \frac{\hat{H}_{0,\theta}\hat{H}^*_{0,r} + \hat{H}^*_{0,\theta}\hat{H}_{0,r}}{\tilde{r}} \right\}, \tag{35}$$

where a superscript asterisk denotes the complex conjugate of a complex quantity. Using the solution for the zeroth-order magnetic-field problem, we obtain

$$\langle \tilde{f}_{0,\theta} \rangle_t = 0. \tag{36}$$

The zeroth-order body couple $\tilde{\mathbf{M}} \times \tilde{\mathbf{H}}$ is clearly zero owing to Eq. (18).

2.3.3 Zeroth-Order Linear and Spin Velocity Fields. The zeroth-order body force and body couple have been found to be zero; hence, in the absence of outer or inner cylinder rotation, the translational velocity in the gap must be zero

$$\tilde{v}_{0,\theta}(\tilde{r}) = 0, \tag{37}$$

and therefore owing to Eq. (20), the corresponding spin velocity must also be zero

$$\tilde{\omega}_{0,z}(\tilde{r}) = 0. \tag{38}$$

2.4 First-Order Problem. The equations governing the first-order problem are obtained in similar fashion as the zeroth-order problem, resulting in

$$\tilde{\boldsymbol{\nabla}} \cdot (\tilde{\mathbf{M}}_1 + \tilde{\mathbf{H}}_1) = 0, \tag{39}$$

$$\tilde{\boldsymbol{\nabla}} \times \tilde{\mathbf{H}}_1 = \mathbf{0}, \tag{40}$$

$$\frac{\partial \tilde{\mathbf{M}}_0}{\partial \tilde{t}} = -(\tilde{\mathbf{M}}_1 - \chi_i \tilde{\mathbf{H}}_1), \tag{41}$$

$$0 = -\tilde{\boldsymbol{\nabla}}\tilde{p}_1 + \mathrm{Ma}\left[\tilde{\mathbf{M}}_0 \cdot \tilde{\boldsymbol{\nabla}}\tilde{\mathbf{H}}_1 + \tilde{\mathbf{M}}_1 \cdot \tilde{\boldsymbol{\nabla}}\tilde{\mathbf{H}}_0 + \frac{1}{2}\tilde{\boldsymbol{\nabla}} \times (\tilde{\mathbf{M}}_0 \times \tilde{\mathbf{H}}_1 + \tilde{\mathbf{M}}_1 \times \tilde{\mathbf{H}}_0) \right] + \tilde{\boldsymbol{\nabla}}^2 \tilde{\mathbf{v}}_1, \tag{42}$$

$$\tilde{\boldsymbol{\omega}}_1 = \frac{1}{2}\tilde{\boldsymbol{\nabla}} \times \tilde{\mathbf{v}}_1 + \frac{\eta}{4\zeta}\mathrm{Ma}(\tilde{\mathbf{M}}_0 \times \tilde{\mathbf{H}}_1 + \tilde{\mathbf{M}}_1 \times \tilde{\mathbf{H}}_0). \tag{43}$$

As in the zeroth-order problem, the first-order magnetic-field and fluid-mechanical problems have become decoupled. Hence, we solve for the magnetic-field quantities independently using the results of the zeroth-order problem. Once the first-order magnetic field quantities are known, we obtain the first-order body force and body couple terms needed to solve for the fluid mechanical fields.

2.4.1 First-Order Magnetic Field and Magnetization. We proceed as in the corresponding zeroth-order problem by assuming the magnetic field and magnetization have functional forms similar to Eq. (1). Substituting these into the first-order Maxwell's equations (39) and (40), one finds that the first-order magnetic field obeys the same equidimensional equation as the zeroth-order magnetic field. Hence, the solution for the first-order magnetic field is of the same form as in the zeroth-order problem. The first-order interfacial conditions at the ferrofluid-inner cylinder interface ($\tilde{r}=\gamma$) and at the outer radius ($\tilde{r}=1$) become

$$\hat{H}^I_{1,r}(\gamma) = \hat{H}_{1,r}(\gamma) + \hat{M}_{1,r}(\gamma), \tag{44}$$

$$\hat{H}^I_{1,\theta}(\gamma) = \hat{H}_{1,\theta}(\gamma), \tag{45}$$

$$\hat{H}_{1,\theta}(1) = 0. \tag{46}$$

Evaluating the integration constants, the complex-amplitude magnetic-field components are

$$\hat{H}_{1,\theta} = \frac{j2\chi_i\gamma^2(1-\tilde{r}^{-2})}{[2+\chi_i(1+\gamma^2)]^2}, \tag{47}$$

$$\hat{H}_{1,r} = \frac{-2\chi_i\gamma^2(1+\tilde{r}^{-2})}{[2+\chi_i(1+\gamma^2)]^2}. \tag{48}$$

The corresponding first-order complex amplitude magnetization components are obtained from Eq. (41) and are

$$\hat{M}_{1,\theta} = j\left\{ \frac{2\chi_i^2\gamma^2}{[2+\chi_i(1+\gamma^2)]^2}(1-\tilde{r}^{-2}) - \frac{\chi_i(1+\beta r^{-2})}{1+\beta} \right\}, \tag{49}$$

$$\hat{M}_{1,r} = \frac{-2\chi_i^2\gamma^2}{[2+\chi_i(1+\gamma^2)]^2}(1+\tilde{r}^{-2}) + \frac{\chi_i(1-\beta\tilde{r}^{-2})}{1+\beta}. \tag{50}$$

2.4.2 First-Order Magnetic Body Force and Body Couple. The scaled magnetic body force term, to first order in ε, is given by

$$\tilde{\mathbf{f}}_1 = \tilde{\mathbf{M}}_0 \cdot \boldsymbol{\nabla}\tilde{\mathbf{H}}_1 + \tilde{\mathbf{M}}_1 \cdot \boldsymbol{\nabla}\tilde{\mathbf{H}}_0. \tag{51}$$

As it was pointed out in the zeroth-order problem, only the body force's θ component

$$\tilde{f}_{1,\theta} = \tilde{M}_{0,r}\frac{\partial \tilde{H}_{1,\theta}}{\partial \tilde{r}} + \tilde{M}_{0,\theta}\left(\frac{1}{\tilde{r}}\frac{\partial \tilde{H}_{1,\theta}}{\partial \theta} + \frac{\tilde{H}_{1,r}}{\tilde{r}} \right) + \tilde{M}_{1,r}\frac{\partial \tilde{H}_{0,\theta}}{\partial \tilde{r}} + \tilde{M}_{1,\theta}\left(\frac{1}{\tilde{r}}\frac{\partial \tilde{H}_{0,\theta}}{\partial \theta} + \frac{\tilde{H}_{0,r}}{\tilde{r}} \right), \tag{52}$$

is relevant in the analysis. By substituting the zeroth- and first-order magnetic field and magnetization components, it can be shown that $\tilde{f}_{1,\theta}$ is given by a time-invariant component and an oscillatory contribution that may be expressed as the gradient of a scalar potential. Only the time-invariant component, corresponding to the time-averaged θ-directed magnetic body force

$$\langle \tilde{f}_{1,\theta} \rangle_t = \frac{2\chi_i \beta^2 \tilde{r}^{-5}}{(1+\beta)^2}, \tag{53}$$

is relevant in the analysis that follows, as the scalar potential term would be absorbed into the dynamic pressure in the momentum equation.

Next, we evaluate the first-order magnetic body couple

$$\tilde{\mathbf{l}}_1 = [\tilde{\mathbf{M}}_0 \times \tilde{\mathbf{H}}_1 + \tilde{\mathbf{M}}_1 \times \tilde{\mathbf{H}}_0], \tag{54}$$

which, on substitution of the respective magnetic quantities, yields

$$\tilde{\mathbf{l}}_{1,z} = \chi_i \frac{(1+\beta\tilde{r}^{-2})(1-\beta\tilde{r}^{-2})}{(1+\beta)^2}. \tag{55}$$

2.4.3 First-Order Linear and Spin Velocity Fields. In the zeroth-order problem, both the magnetic body force and body couple were zero individually; hence, the zeroth-order translational and spin velocities were zero. In the first-order problem, we find a similar situation because the magnetic "momentum source" term in the θ component of the linear momentum equation (42) can be shown to be zero by taking the curl of the first-order body couple (55) and combining with (53) to show that

$$\left[\tilde{\mathbf{M}} \cdot \tilde{\nabla}\tilde{\mathbf{H}} + \frac{1}{2}\tilde{\nabla} \times (\tilde{\mathbf{M}} \times \tilde{\mathbf{H}}) \right]_\theta = 0. \tag{56}$$

With both cylinders stationary, the resulting first-order translational velocity is zero

$$\tilde{v}_{1,\theta} = 0. \tag{57}$$

Here, however, the first-order spin velocity is not zero, as can be verified through equation (43). The resulting first-order spin velocity is

$$\tilde{\omega}_{1,z} = \frac{1}{4}\frac{\eta}{\zeta}\mathrm{Ma}\chi_i \frac{1-\beta^2\tilde{r}^{-4}}{(1+\beta)^2}. \tag{58}$$

2.4.4 First-Order Torque. As seen above, the zeroth- and first-order solutions predict zero translational flow; hence, the rate of strain tensor in the symmetric part of the ferrofluid's Cauchy stress is zero. However, a nonzero first-order body couple results in a nonzero first-order spin velocity, which in turn indicates that the corresponding antisymmetric stress component must result in a torque contribution. The antisymmetric component of the stress is given by

$$\mathbf{T}^a = \tfrac{1}{2}\boldsymbol{\varepsilon} \cdot \mathbf{T}_x, \tag{59}$$

where $\mathbf{T}_x = 2\zeta(\nabla \times \mathbf{v} - 2\boldsymbol{\omega})$ is the antisymmetric vector of the stress. The relevant component resulting in a z-directed torque with respect to the inner cylinder axis is $\mathbf{T}^a_{r\theta}$, given by

$$\mathbf{T}^a_{r\theta} = \frac{1}{2}\varepsilon_{r\theta z} T_z = \zeta[(\nabla \times \mathbf{v})_z - 2\omega_z]. \tag{60}$$

To first order, the curl of the velocity is zero, whereas the spin velocity is given by (58) multiplied by the perturbation parameter $\varepsilon = \Omega_f \tau$. Substituting these into Eq. (60), integrating the z-directed torque over the internal cylinder surface, and using the definitions for β, the Mason number, and the perturbation ε parameter yields

$$L_z = \int_0^{2\pi}\int_0^l T^a_{r\theta} R^2 d\theta dz = -\frac{4\mu_0\chi_i(1+\chi_i)K^2(\pi R_I^2 l)}{[2+\chi_i(1+\gamma^2)]^2}\Omega_f\tau + O(\Omega_f^2\tau^2), \tag{61}$$

where l is the inner cylinder height. Substituting K by the rms magnetic-field amplitude $H_{\mathrm{rms}} = K/\sqrt{2}$ results in

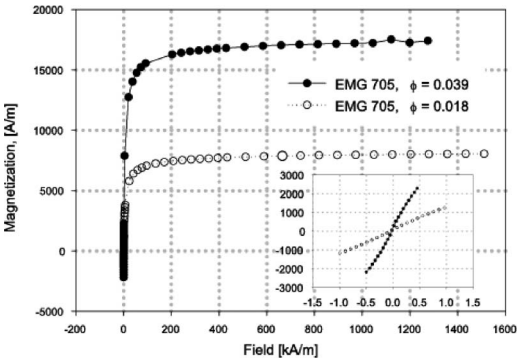

Fig. 1 Magnetization curve for the water-based ferrofluid (Ferrotec EMG 705). The inset shows the low field response of the ferrofluid.

$$L_{th} = -\frac{8\mu_0\chi_i(1+\chi_i)H^2_{\mathrm{rms}}(\pi R_I^2 l)}{[2+\chi_i(1+\gamma^2)]^2}\Omega_f\tau + O(\Omega_f^2\tau^2), \tag{62}$$

which is the expression given by Rinaldi et al. [5]. Note that H_{rms} corresponds to the rms magnetic field in the stator gap in the absence of ferrofluid.

3 Ferrofluid Characterization

Water-based ferrofluid (EMG 705) was obtained from Ferrotec Corporation (Nashua, NH, USA). Fluid characterization and all experiments described below were carried out while the ferrofluid was colloidally stable. Ferrofluid with a lower particle volume fraction was obtained by diluting EMG 705 using deionized water. Mass density was determined gravimetrically. The shear viscosity was measured using a STRESSTECH HR rheometer (ATS Rheosystems, Bordentown, NJ, USA) with double-gap geometry in a shear rate range of 10–110 s^{-1}. The ferrofluid showed Newtonian behavior under these conditions. The magnetic properties of the ferrofluid were measured using a MPMS-XL7 SQUID (superconducting quantum interference device) magnetometer (Quantum Design, San Diego, CA, USA) at 300 K. The results are presented in Fig. 1, where abscissa corresponds to internal magnetic field which can be obtained from external magnetic field using the relation, $\mathrm{H}_i = \mathrm{H}_e - D\mathrm{M}$ with a demagnetization factor D of 0.5 [32]. In Fig. 1, the inset shows the linear relation between magnetization and applied field at low magnetic-field amplitude. From the high-field asymptote of the magnetization curve, using the Langevin equation [18], we obtained values for the saturation magnetization M_S of the ferrofluids. The magnetic volume fractions were estimated using the relation $M_S = \phi M_d$, and a value of 446 kA/m for the domain magnetization of magnetite. The initial susceptibility of each fluid was obtained from the low field slope of the magnetization curve. These results are summarized in Table 1.

Assuming a log-normal particle size distribution, the median particle diameter and geometric deviation were determined using two methods: (i) using the low- and high-field asymptotes of fluid magnetization as described by Chantrell et al. [33], and whose expression are given, respectively, by

Table 1 Physical and magnetic properties at room temperature for EMG 705 and its dilution

Ferrofluid	ρ (kg/m^3)	η (N sm^{-2})	$\mu_o M_s$ (mT)	ϕ	χ_i
EMG-705	1220	2.49×10^{-3}	21.9	0.039	4.99
EMG-705 (diluted)	1120	1.67×10^{-3}	10.1	0.018	1.28

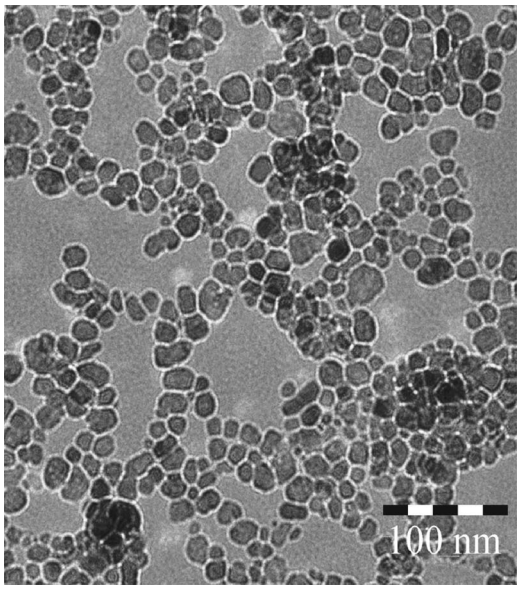

Fig. 2 TEM image of magnetite nanoparticles in the water-based ferrofluid (Ferrotec EMG 705)

$$D_{pgv} = \left[\frac{18 k_B T}{\pi \mu_0 M_d} \sqrt{\frac{\chi_i}{3 \phi M_d H_0}} \right]^{1/3}, \tag{63}$$

$$\ln \sigma_g = \frac{1}{3} \left[\ln \left(\frac{3 \chi_i H_0}{\phi M_d} \right) \right]^{1/2}, \tag{64}$$

where H_0 corresponds to the extrapolated intercept with the abscissa of a plot of M versus $1/H$ at high fields, and (ii) from direct measurements of particle diameter by TEM (Fig. 2). The method of Chantrell et al. [33] yields the volume median diameter D_{pgv}, whereas TEM measurements yield the number median diameter D_{pg}. The two are ideally related by the expression

$$\ln D_{pgv} = \ln D_{pg} + 3 \ln^2 \sigma_g, \tag{65}$$

where σ_g is the geometric deviation. Because of the existence of a "magnetically dead" layer on the nanoparticle surface, the volume median diameters and geometric deviations determined from magnetic measurements and TEM cannot be expected to agree exactly, but should be in the same order of magnitude. The estimated values for median particle diameter D_{pgv} are summarized in Table 2.

It is of interest to estimate the effective Brownian and Neel relaxation time, taking into account the effect of particle polydispersity. In a system of noninteracting particles, the magnetic relaxation of particles of different diameters is expected to occur in parallel. This motivates us to define an effective Brownian relaxation time through the expression

Table 2 Estimated magnetic particle diameters and relaxation times at room temperature for EMG 705 and its dilution

Ferrofluid	D_{pgv}[a] (nm)	$\ln \sigma_g$[a]	D_{pgv}[b] (nm)	$\ln \sigma_g^2$[b]	$\bar{\tau}_B$[c] (s)	$\bar{\tau}_N$[d] (s)
EMG-705	14.9	0.535	20.1	0.288	2.1×10^{-6}	4.4×10^{-5}
EMG-705 (Diluted)	12.4	0.525				

[a]Determined using Eqs. (63) and (64), respectively.
[b]Obtained from TEM image analysis.
[c]Determined using Eq. (66) and D_{pgv} determined from TEM.
[d]Determined using Eq. (67) and D_{pgv} determined from TEM.

$$\bar{\tau}_B \equiv \left[\int_0^\infty \frac{n_v(D_p)}{\tau_B(D_p)} dD_p \right]^{-1} = \frac{\pi \eta_0}{2 k_B T} D_{pgv}^3 \exp\left(-\frac{9}{2} \ln^2 \sigma_g \right), \tag{66}$$

and an effective Neel relaxation time

$$\bar{\tau}_N \equiv \left[\int_0^\infty \frac{n_v(D_p)}{\tau_N(D_p)} dD_p \right]^{-1}, \tag{67}$$

where $n_v(D_p)$ is the lognormal particle volume distribution function and

$$\tau_B = \frac{3 \eta_0 V_h}{k_B T} \quad \text{and} \quad \tau_N = \frac{1}{f_0} \exp\left(\frac{K V_c}{k_B T} \right), \tag{68}$$

are the Brownian rotational relaxation time of a single particle of hydrodynamic volume $V_h = \pi (D_p + 2\delta)^3 / 6$ and the Neel relaxation time, respectively. In (68), f_0 is a characteristic frequency of the magnetic material [18], K is the magnetocrystalline anisotropy constant of the magnetite nanoparticles for which the value used was 78 kJ/m^3 [34], and V_c is the magnetic volume. In deriving Eq. (66), we have assumed the particle hydrodynamic diameter to be the same as the particle core diameter D_p (i.e., $\delta = 0$). The effective Neel relaxation time $\bar{\tau}_N$ was estimated through numerical integration in Eq. (67). The effect of an adsorbed surfactant layer δ on the effective relaxation time can be accounted for in (66) by performing a numerical integration, with similar qualitative and quantitative results. The physical relevance of Eqs. (66) and (67) is that they illustrate the effect of particle polydispersity (characterized by the geometric deviation σ_g) in decreasing the effective Brownian and Neel relaxation times of the collection of magnetic nanoparticles. Table 2 shows values of both effective relaxation time for our ferrofluid, calculated using Eqs. (66) and (67), and the size distribution parameters obtained from TEM. In what follows, the diameters determined from TEM, rather than the magnetic diameter, are used in calculations of particle size as the former represent the actual physical particle size, whereas the latter are subject to error due to the assumed value of the domain magnetization (the bulk value of magnetite is used) and the existence of the so-called magnetically dead layer on the surface of the particles.

The speed of sound in the ferrofluid was determined to be 1450 m/s by measuring the time required for a pulse to traverse a known distance. In ferrofluids, Sawada et al. [35] and Motozawa et al. [36], demonstrated that an applied magnetic field has a slight effect on the speed of sound, so small as to be negligible in our experiments.

4 Apparatus and Experimental Method

4.1 Torque Measurements. Torque measurements were made using a rotational viscometer (Brookfield Engineering Laboratories, model LV-III+, Brookfield, MA, USA) as a torque meter, with a full-scale range of −6.73 μNm to 67.3 μNm. The viscometer measures the torque necessary to keep a spindle, submerged in a fluid, rotating at a constant angular velocity (including zero rotation). Standard spindles are made of stainless steel, which would be subject to induced eddy currents and torques in the presence of a rotating magnetic field; hence, we replaced them with custom polycarbonate spindles.

The relevant dimensions of the apparatus are the inner (spindle) and outer (container) radii, R_I and R_O, respectively, and the submerged spindle length l. Four values of the radial aspect ratio $\gamma = R_I / R_O$ were studied: $\gamma_1 = 0.32$ ($R_I = 9.36$ mm and $R_O = 29.62$ mm), $\gamma_2 = 0.52$ ($R_I = 12.70$ mm and $R_O = 24.64$ mm), $\gamma_3 = 0.64$ ($R_I = 19.05$ mm and $R_O = 29.62$ mm), and $\gamma_4 = 0.77$ ($R_I = 19.05$ mm and $R_O = 24.64$ mm). The submerged spindle length was $l = 58.42$ mm for all experiments. The polycarbonate container was centered in the gap of a two-pole, three-phase induction

motor stator winding, and subsequently, the spindle was centered inside the container. In all experiments, the angular velocity of the inner spindle was set to zero.

A rotating magnetic field was obtained by exciting the two-pole three-phase winding using balanced three phase currents each with 120 deg phase difference from each other. We do this by grounding one phase, exciting the remaining two phases with equal amplitude sinusoidal voltages at ±60 deg phase difference, and letting the neutral point float. This results in balanced three phase currents in the windings to create clockwise or counterclockwise rotating magnetic fields. The amplitude, frequency, and direction of the field can be controlled using the signal generator or linear amplifier gain. The length and diameter of the stator winding were 68.58 mm and 78.74 mm, respectively.

Measurements of the magnetic fields produced by the stator, with and without ferrofluid in the cylindrical container, were made using a gaussmeter (Sypris Test & Measurement, Orlando, FL, USA) with a three-axis probe (model ZOA73). From these measurements, it was determined that the stator produces a magnetic field of 4.54 mT rms per ampere rms of input current in the absence of the ferrofluid. The radial field in-homogeneity of the magnetic field amplitude was determined to be 2.2% from axis to outer container radius at midheight, with a maximum of 6% at the top of the container, while axial field in-homogeneity was ~4% from middle to 3/4 height and 21% to top, along the gap axis.

In all experiments, the direction of the rotating field was set counterclockwise in order to obtain positive torque measurements and thereby utilize the full instrument range. Reversing the field rotation direction merely reversed the direction of torque and flow.

The torque required to restrain the spindle from rotating was measured for field frequencies from 25 Hz to 500 Hz and field amplitudes from 0 mT to 17.0 mT rms, for the four different values of the aspect ratio γ. This series of measurements was made for the EMG 705 ferrofluid and its dilution. Figure 3 presents typical measurements of torque as a function of applied magnetic field amplitude and frequency for the EMG-705 ferrofluid using two geometric aspect ratios.

4.2 Velocity Profile Measurements. Bulk velocity profiles were obtained by the UVP technique [14,37] using a DOP2000 ultrasound velocimeter (Signal Processing, Lausanne, Switzerland). This technique allows measurement of velocity profiles in opaque liquids, such as ferrofluids. An ultrasonic pulse is emitted periodically from a transducer and sent through the fluid. Echoes due to tracer particles are recorded by either a separate or the same transducer. The equipment measures the component of the velocity vector parallel to the direction of beam propagation $v_{\parallel}$, with the spatial location being determined from the time delay between emitted burst and recorded echo, and the magnitude of velocity being determined from the correlation of the random echo signals from a pulsed emission train [37]. The velocity signal is positive when tracers are moving away from the probe. Assuming that flow is purely in the azimuthal direction the relation between parallel and azimuthal component is given by

$$v_{\parallel} = v_{\theta} \cos \varphi. \tag{69}$$

From the geometry of the problem, illustrated in Fig. 4, $\cos \varphi$ can be expressed as a function of the radius of the external cylinder R_O and the angle β between the propagation direction of the ultrasonic beam and the diagonal of the cylinder resulting in $\cos \varphi = R_O \sin \beta / r$. Replacing this expression in Eq. (69), the azimuthal component v_{θ} of the velocity can be related to the measured velocity $v_{\parallel}$ by

$$v_{\theta} = v_{\parallel} \frac{\sqrt{R_O^2 + x^2 - 2R_O x \cos \beta}}{R_O \sin \beta}. \tag{70}$$

Because the magnetite particles suspended in a ferrofluid are too small to produce a UVP signal, we used polyamide powder as a tracer. These microparticles had mean diameter of 15–20 μm and

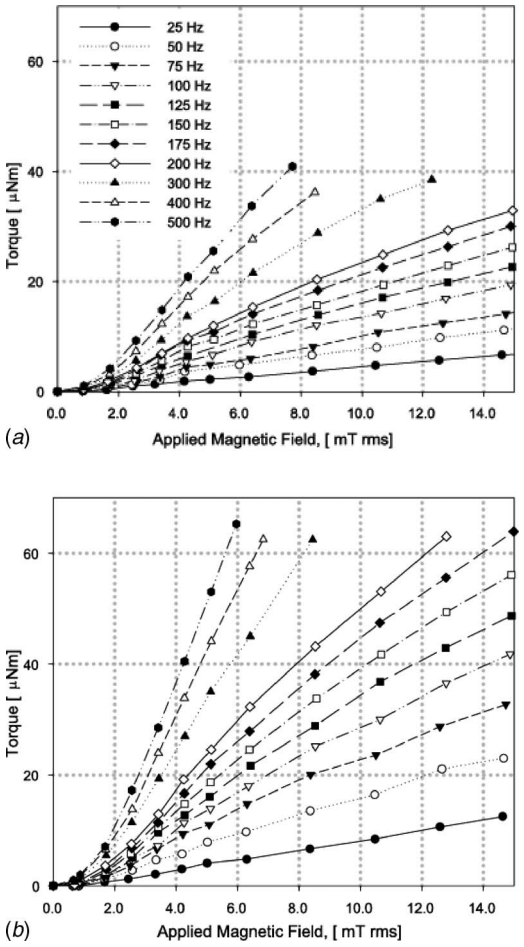

Fig. 3 Torque required to restrain the spindle from rotating when surrounded by ferrofluid filling the annular space between the spindle and outer container, as a function of magnetic-field amplitude and frequency, and for radial aspect ratios of (*a*) $\gamma_1 = 0.32$ and (*b*) $\gamma_2 = 0.52$

density of 1.13 g cm^{-3}. Minute amounts were used, such that the estimated weight fraction of tracer particles was <0.00015. Using such low tracer fractions ensures that the measured profiles are representative of the ferrofluid flow, avoiding other phenomena, such as is found in so-called inverse ferrofluids [38–41]. Our transducers had an emission frequency of 4 MHz, a diameter of 8 mm, and a length of 10 mm. We used a pulse repetition frequency of 200 Hz, taking 100 emissions per profile and averaging over 70 profiles to obtain our reported results. These conditions ensured a spatial resolution of 0.36 mm along the beam propagation direction and a maximum measurable velocity of

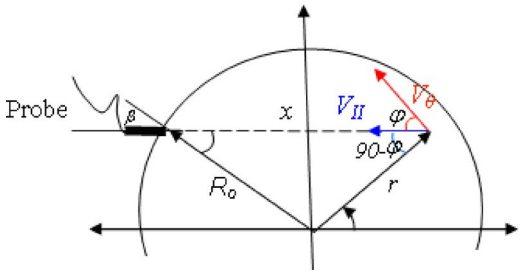

Fig. 4 Sketch of experimental geometry used to obtain the relation between parallel and azimuthal velocity components in a cylindrical container, assuming there is no radial flow

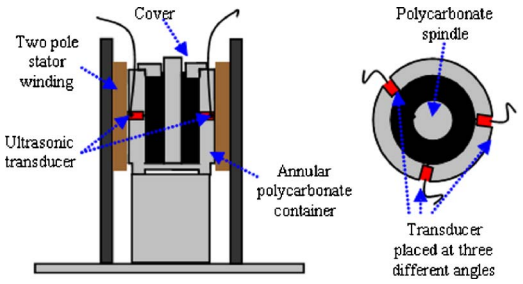

Fig. 5 Illustration of the experimental setup for measuring torques and velocity profiles of ferrofluids filling an annular space and subjected to a rotating magnetic field. Left: Annular container with ultrasonic transducers located inside a two-pole induction motor stator. Right: Top view showing transducers at different incident angles. The transducers are separated from the ferrofluid by a thin polycarbonate wall.

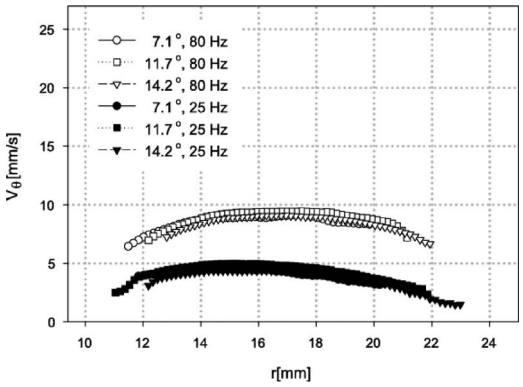

Fig. 6 Velocity profile for ferrofluid filling the annular gap between stationary coaxial cylinders obtained with three transducers at different angles with respect to the diagonal and magnetic field amplitude of 8.3 mT rms. The external radius is 24.64 mm, and the internal radius is 9.4 mm.

18.12 mm/s. The spatial resolution transverse to beam propagation is set by the diameter of the emitter element and was ~3 mm in our experiments.

Velocity profiles were measured for the ferrofluid contained in the annular space between a cylindrical container of 49.4 mm i.d. and solid cylinders of 18.7 mm diameter (wall-to-wall distance of 15.35 mm) and 10 mm diameter (wall-to-wall distance of 19.7 mm). Our apparatus design, illustrated in Fig. 5, permitted simultaneous measurement of velocity profiles relative to ultrasonic beams propagating at three distinct angles (using three transducers) relative to the diagonal. The container and spindle were made of polycarbonate, in this case to avoid internal reflections inside the wall, which would produce atypical saturation of the transducer. A cover was used to eliminate the free surface and thereby avoid interfacial effects which could confound our measurements.

The rotating magnetic field was generated using the three-phase, two-pole magnetic induction motor stator winding described above. Experiments were carried out for field frequencies between 20 Hz and 120 Hz and amplitudes between 8.3 mT and 14.3 mT. The experiments were carried out at time intervals to avoid temperature increases of $>2°C$.

The limitations of the UVP method are the inability of obtaining measurements within 5 mm to 8 mm of the ultrasonic transducer and inaccuracy in the velocity measurements at the far wall (in the boundary of the container). The first limitation is due to saturation of the transducer receiver because the same probe acts as emitter of the acoustic signal. The second limitation arises because the ultrasonic beam is reflected by the far wall, introducing errors in the measured velocity.

In the first series of experiments, transducers were placed at half the height of the container and a cover was used to suppress surface driven flow. Three transducers, at angles of 7.1 deg, 11.7 deg, and 14.2 deg, were used and a counterclockwise rotating field was applied such that a positive velocity measurement implied corotation of field and fluid. Figure 6 shows the velocity profiles for frequencies of 25 Hz and 80 Hz and applied magnetic field amplitude of 8.3 mT rms for EMG 705. Clearly, bulk flow is observed with both cylinders stationary, contrary to the predictions of [2,4] and the analysis given above. We measured the radial temperature gradient during the experiment and found variations of $<0.2°C$. In order to do this, one thermometer was placed in the middle of the annular space and two thermometers were placed adjacent to the inner and outer cylinder walls. Measurements were taken for time intervals equal to that required to obtain a velocity profile, for the range of frequencies and amplitudes of the applied magnetic field. As can be observed in Fig. 6, the annular bulk flow is unidirectional in the same direction of field rotation. This observation is in contrast with the surface velocity profile measured by Rosensweig et al. [3], where the flow changes direction in the annular space. In addition, velocity profiles taken with different probe angles superimpose one another, confirming that the flow is predominantly azimuthal. Finally, as can be seen in Fig. 6 and in all measured velocity profiles, the velocity is fairly uniform in the gap, which is indicative of the fact that azimuthal field inhomogeneities due to the use of an imperfect two-pole stator winding are not responsible for the observed flow. If they were, one would expect the fluid to be accelerated close to the outer cylinder (where the effects of azimuthal inhomogeneities in the winding would be relevant) and monotonically decelerate to zero velocity at the inner cylinder. The velocity profiles show that this is clearly not the case.

Another series of experiments studied the variation of velocity profile with axial position by using probes at h, $(3/4)h$, $(1/2)h$, and $(1/4)h$ ($h \approx 63.5$ mm being the container height). Simultaneously, the axial velocity profiles were measured using a probe placed in the middle of the annular space. Figure 7(a) shows that the velocities measured at the middle of the container are slightly higher than those measured at $(1/4)h$, $(3/4)h$, and h. This slight variation is not due to misalignment of the inner spindle axis with the outer container and stator axis as we have used three probes placed at 120 deg from each other to verify that the flow does not have an azimuthal variation as would be expected with an eccentric inner cylinder. We therefore attribute the slightly higher velocity in the middle to the effect of viscous drag exerted by the top and bottom surfaces of the container. Figure 7(b) shows that the axial velocity is negligibly small compared to the azimuthal velocity. The observation of negligible axial velocity is indicative that though the magnetic field generated in the stator varies by as much as 21% along the vertical axis (4% throughout most the fluid), this variation does not induce appreciable flow in the axial direction.

Figure 8 shows the effect of frequency on velocity profiles measured at a magnetic field amplitude of 12.5 mT, and the effect of magnetic field amplitude and inner cylinder radius on velocity profiles for a magnetic field frequency of 80 Hz. As can be noted from Fig. 8(b), under similar conditions the ferrofluid contained in the narrower annular gap was observed to rotate at a faster rate. This is counterintuitive, as one would expect the flow to be retarded as the surface-to-volume ratio in the gap increases. Similar observations were made for the free surface driven flow by Rosensweig et al. [3]. Their observations can be explained by considering that the surface flow is induced by a narrow region close to the container wall, corresponding to the meniscus region, in which the interfacial balance of asymmetric stresses induces fluid motion. In our experiments, however, no such free surface

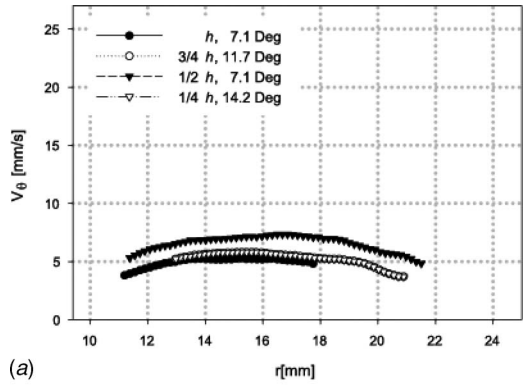

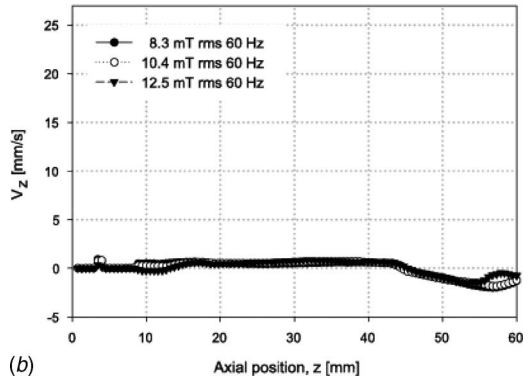

Fig. 7 Velocity profiles in the (*a*) azimuthal direction using fixed transducers placed at four different heights (h =63.5 mm) of the container for 60 Hz frequency and 8.3 mT rms amplitude of the applied magnetic field, and (*b*) in the axial direction obtained using a transducer placed in the cover of the container in the middle of the annular gap (r=17.2 mm). The external radius is 24.64 mm, and the internal radius is 9.4 mm.

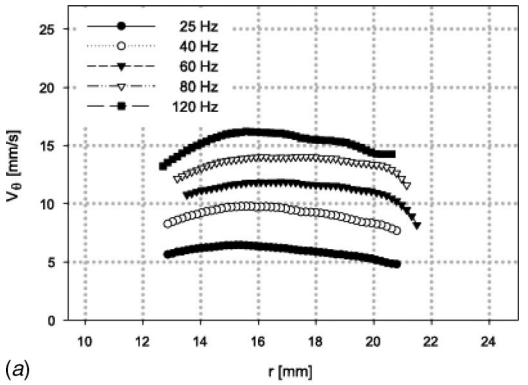

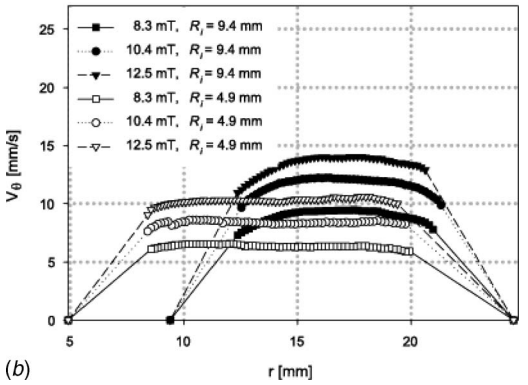

Fig. 8 Velocity profile dependence on (*a*) magnetic field frequency with constant amplitude of 12.5 mT rms and on (*b*) magnetic field amplitude with constant frequency of 80 Hz. In (*b*), profiles are shown for two distinct inner cylinder radii, with dashed lines added to aid in distinguishing between the two inner and outer radii. In (*a*) and (*b*), the external radius is 24.64 mm. In (*a*), the internal radius is 9.4 mm.

exists. One possible explanation for our observations is that whatever causes the flow is limited to a fluid layer close to the container walls. This is the case in the spin-diffusion analysis used by Zaitsev and Shliomis [8] to explain the phenomenon of spin-up flow of a ferrofluid in a cylindrical container with a rotating uniform magnetic field. Our recent measurements of bulk flow in that situation [9] are in qualitative agreement with the analysis of Zaitsev and Shliomis [8]. However, the spin viscosity term, which is an essential element of the analysis, is commonly regarded to be negligibly small.

5 Scaling Analysis of Torque and Flow Measurements

Since the angular velocity of the spindle was set to zero in our experiments, the torque measured by the viscometer should correspond to the result given by Eq. (62). This torque is due to the viscous shear stress on the spindle resulting from the magnetic-field induced flow of the ferrofluid around the spindle. Because the viscous stress tensor in ferrofluids is asymmetric in the presence of rotating fields, this shear stress has two contributions, illustrated in Fig. 9. As the particles rotate counterclockwise, a clockwise torque is induced on the spindle, corresponding to the antisymmetric component of the stress (Fig. 9(*a*)). As the fluid corotates with the field a counterclockwise torque is induced on the spindle, corresponding to the symmetric component of the stress (Fig. 9(*b*)).

In our experiments, the antisymmetric stresses dominate. This can be verified by estimating the contribution of the symmetric stresses to the torque by assuming that the velocity goes from a measured value U to zero in a boundary layer of thickness δ_t close to the inner cylinder. The corresponding torque is $2\pi R_I 2l\ \tau^S|_{R_I}$, where we assume a linear velocity profile to estimate the symmetric stress $\tau^S = \eta U/\delta_t$. As an example, for a measured velocity of 15 mm/s and R_I=4.9 mm, corresponding to the conditions of Fig. 8(*b*), assuming the velocity goes to zero linearly in a layer of thickness δ_t=1 mm, the contribution of the symmetric stress is estimated to be 0.32μNm, which is negligibly small in comparison to the measured torques ($\approx$30 μNm).

Figure 10 shows torque measurements L_{exp} normalized using the theoretical torque L_{th} according to Eq. (62) as a function of the dimensionless field frequency $\Omega_f\tau$, and as a function of magnetic field amplitude, made dimensionless using the Langevin parameter α. Comparison of the results for the various aspect ratios and

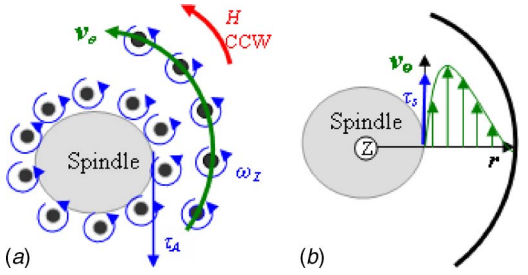

Fig. 9 Phenomenological model of ferrofluid torque on cylindrical walls in a rotating magnetic field H: (*a*) Axially directed torque induced by rotation of magnetic nanoparticles and (*b*) torque produced by viscous shear stress at the spindle due to magnetic field induced flow

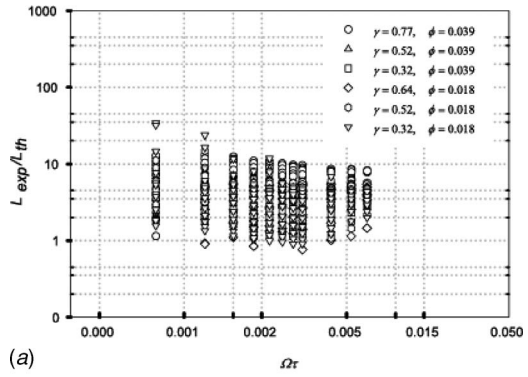

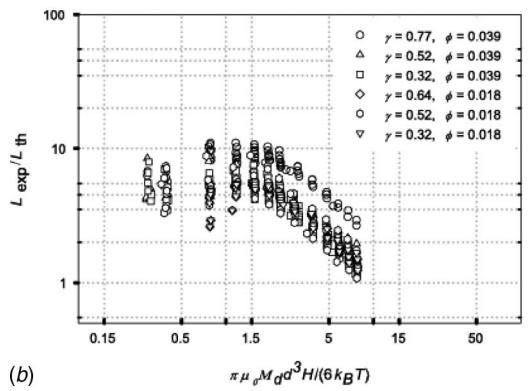

Fig. 10 Log-log plot of the complete dimensionless torque data set versus (*a*) dimensionless frequency from 25 Hz to 500 Hz and (*b*) dimensionless amplitude of the magnetic field from 0.61 mT rms to 17 mT rms. A value of $\tau_B = 2.1 \times 10^{-6}$ s has been used to calculate the theoretical torque.

for two volumetric fractions shows that the dimensionless torque collapses the data set well. The dispersion seen at low fields corresponds to the lowest torques, which are most susceptible to measurement error. As can be seen in Fig. 10, the normalized data are close to order unity (1–10), indicating that Eq. (62) predicts the right order of magnitude for the torque. Because the only estimated parameter in using Eq. (62) is the Brownian relaxation time, this is an indication that our estimated values, shown in Table 2 are of the right order of magnitude. The torque measurements show a power-of-one dependence on magnetic field frequency and amplitude. Equation (62) predicts a power-of-one dependence with field frequency, but a power-of-two dependence with field amplitude. However, Eq. (62) is strictly applicable in the linear magnetization limit, for which the field is small and the Langevin parameter much smaller than unity. As can be seen in Fig. 10(*b*), our experiments were carried out at moderate field amplitudes, for which the Langevin parameter is of order unity; hence, saturation effects will have begun to affect the field amplitude dependence of the torque. It is expected that as the fluid magnetically saturates the torque dependence with field amplitude should decrease to power unity.

A similar scaling analysis was made for the velocity using the value at $r = 17.2$ mm for all profiles obtained. The characteristic velocity $v_\theta \sim \Omega_f R_O$ was used to plot the scaled velocity ($\tilde{v}_\theta = v_\theta / \Omega_f R_O$) as a function of the Langevin parameter in Fig. 11. The scaled velocity was found to have roughly power-of-one dependence on the applied field amplitude and frequency, in agreement with the torque data. This is an interesting result in light of the fact that all available analyses, including the asymptotic analysis shown above, predict a negligible azimuthal velocity in the annular gap when both cylinders are held fixed.

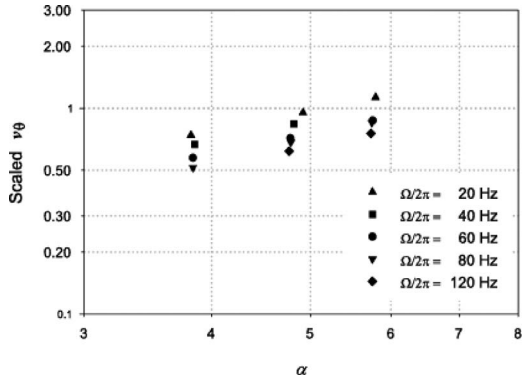

Fig. 11 Log-log plot of the scaled azimuthal velocity at $r = 17.2$ mm versus dimensionless amplitude of the magnetic field for experiments made with the water-based ferrofluid (with $\phi = 0.039$) and an internal cylinder radius of $R_i = 9.4$ mm. A value of $\tau_B = 2.1 \times 10^{-6}$ s has been used to calculate the dimensionless velocity.

6 Conclusions

Torque and flow measurements demonstrate the existence of bulk flow of ferrofluid contained in an annular gap and subjected to a rotating magnetic field, for the case when both cylinders are held stationary. The experiments were carried out under conditions such that energy dissipation and radial temperature gradients are negligible. The observation of bulk azimuthal flow with negligible axial velocity is in stark disagreement with the analysis of Pshenichnikov and Lebedev [4] and with the asymptotic analysis presented herein. Both analyses were done in the linear magnetization, zero-spin viscosity limits, and predict zero bulk flow with both cylinders stationary. Arguably, the asymptotic analysis presented here could be extended to second order in the perturbation parameter ε however the resulting velocity would be expected to have a power-of-four dependence with field amplitude. The measurements presented above clearly show that both the torque and azimuthal velocity have a power-of-one dependence with field frequency and amplitude. Similar observations were made by Chaves et al. [9] for the situation of ferrofluid in a cylindrical container subjected to a uniform rotating magnetic field. In that case, the only explanation available in the literature which agreed with the experimental observations was the spin diffusion theory of Zaitsev and Shliomis [8]. It is likely that the mechanism that drives the flow in the annular gap experiments reported herein is the same as that which drives the flow in the experiments reported by Chaves et al. [9]. Unfortunately, the analysis of Zaitsev and Shliomis [8] hinges on the existence of couple stresses and the spin viscosity, which is commonly regarded to be negligibly small based on dimensional arguments of the hydrodynamic interactions occurring at the particle scale [42]. Further work is needed to elucidate if other mechanisms are responsible for the observed flow, such as spin-magnetization coupling in the magnetization relaxation (neglected in all analyses discussed above). Alternatively, other forms of the magnetization relaxation equation [25–29], valid far from equilibrium, could be tested.

Acknowledgment

The authors are indebted to Prof. Markus Zahn for valuable discussions and advice. This work was supported by the US National Science Foundation (CTS-0320534, CTS-0331379, and CTS-0457359). Acknowledgement is made to the Donors of the American Chemical Society Petroleum Research Fund (ACS-PRF 40867-G 9) for partial support of this research.

References

[1] Tsebers, A. O., 1975, "Interfacial Stresses in the Hydrodynamics of Liquids

With Internal Rotation," Magn. Gidrodin., **11**, pp. 79–82.
[2] Lebedev, A. V., and Pshenichnikov, A. F., 1991, "Motion of a Magnetic Fluid in a Rotating Magnetic Fluid," Magn. Gidrodin., **1**, pp. 7–12.
[3] Rosensweig, R. E., Popplewell, J., and Johnston, R. J., 1990, "Magnetic Fluid Motion in Rotating Field," J. Magn. Magn. Mater., **85**, pp. 171–180.
[4] Pshenichnikov, A. F., and Lebedev, A. V., 2000, "Tangential Stresses on the Magnetic Fluid Boundary and the Rotational Effect," Magnetohydrodynamics (N.Y.), **36**, pp. 254–263.
[5] Rinaldi, C., Gutman, F., He, X., Rosenthal, A. D., and Zahn, M., 2005, "Torque Measurements on Ferrofluid Cylinders in Rotating Magnetic Fields," J. Magn. Magn. Mater., **289**, pp. 307–310.
[6] Moskowitz, R., and Rosensweig, R. E., 1967, "Nonmechanical Torque-Driven Flow of a Ferromagnetic Fluid by an Electromagnetic Field," Appl. Phys. Lett., **11**, pp. 301–303.
[7] Brown, R., and Horsnell, T. S., 1969, "The Wrong Way Round," Elec. Rev., **183**, pp. 235–236.
[8] Zaitsev, V. M., and Shliomis, M. I., 1969, "Entrainment of Ferromagnetic Suspension by a Rotating Field," J. Appl. Mech. Tech. Phys., **10**, pp. 696–700.
[9] Chaves, A., Rinaldi, C., Elborai, S., He, X., and Zahn, M., 2006, "Bulk Flow in Ferrofluids in a Uniform Rotating Magnetic Field," Phys. Rev. Lett., **96**, pp. 194501–194504.
[10] Shliomis, M. I., Lyubimova, T. P., and Lyubimov, D. V., 1988, "Ferrohydrodynamics—An Essay on the Progress of Ideas," Chem. Eng. Commun., **67**, pp. 275–290.
[11] Rinaldi, C., and Chaves, A., "Comment on Tangential Stresses on the Magnetic Fluid Boundary and Rotational Effect," Magnetohydrodynamics, to be published.
[12] Kagan, I. Y., Rykov, V. G., and Yantovskii, E. I., 1973, "Flow of a Dielectric Ferromagnetic Suspension in a Rotating Magnetic Field," Magn. Gidrodin., **9**, pp. 135–137.
[13] Kikura, H., Sawada, T., and Tanahashi, T., 1991, "Transportation of a Magnetic Fluid by Rotating Magnetic Field," *Electromagnetic Forces and Application: Proceedings of the International ISEM Symposium on Electromagnetic Force*, Sendai, Japan, January, pp. 103–104.
[14] Takeda, Y., 1995, "Velocity Profile Measurement by Ultrasonic Doppler Method," Exp. Therm. Fluid Sci., **10**, pp. 444–453.
[15] Kikura, H., Aritomi, M., and Takeda, Y., 2005, "Velocity Measurement on Taylor-Couette Flow of a Magnetic Fluid With Small Aspect Ratio," J. Magn. Magn. Mater., **289**, pp. 342–345.
[16] Kikura, H., Takeda, Y., and Durst, F., 1999, "Velocity Profile Measurements of the Taylor Vortex Flow of a Magnetic Fluid Using the Ultrasonic Doppler Method," Exp. Fluids, **26**, pp. 208–214.
[17] Kikura, H., Takeda, Y., and Sawada, T., 1999, "Velocity Profile Measurements of Magnetic Fluid Flow Using Ultrasonic Doppler Method," J. Magn. Magn. Mater., **201**, pp. 276–280.
[18] Rosensweig, R. E., 1997, *Ferrohydrodynamics*, Dover, New York.
[19] Dahler, J. S., and Scriven, L. E., 1961, "Angular Momentum of Continua," Nature (London), **192**, pp. 36–37.
[20] Dahler, J. S., and Scriven, L. E., 1963, "Theory of Structured Continua I. General Consideration of Angular Momentum and Polarization," Proc. R. Soc. London, Ser. A, **276**, pp. 504–527.
[21] Rinaldi, C., 2002, "Continuum Modeling of Polarizable Systems," Ph.D. thesis, Massachusetts Institute of Technology, Cambridge, MA.
[22] Brenner, H., 1970, "Rheology of Two-Phase Systems," Annu. Rev. Fluid Mech., **2**, pp. 137–176.
[23] Dahler, J. S., 1959, "Transport Phenomena in a Fluid Composed of Diatomic Molecules," J. Chem. Phys., **30**, pp. 1447–1475.
[24] Shliomis, M. I., 1974, "Concerning One Gyromagnetic Effect in a Liquid Paramagnet," Sov. Phys. JETP, **39**, pp. 701–704.
[25] Shliomis, M. I., 2001, "Ferrohydrodynamics: Testing a Third Magnetization Equation," Phys. Rev. E, **6406**, p. 060501.
[26] Shliomis, M. I., 2001, "Comment on 'Magnetoviscosity and Relaxation in Ferrofluids'," Phys. Rev. E, **6406**, pp. 063502.
[27] Felderhof, B. U., 2000, "Steady-State Magnetoviscosity of a Dilute Ferrofluid," Magn. Gidrodin., **36**, pp. 329–334.
[28] Felderhof, B. U., 2000, "Magnetoviscosity and Relaxation in Ferrofluids," Phys. Rev. E, **62**, pp. 3848–3854.
[29] Felderhof, B. U., 2001, "Reply to Comment on 'Magnetoviscosity and Relaxation in Ferrofluids'," Phys. Rev. E, **6406**, pp. 063502.
[30] Stratton, J. A., 1941, *Electromagnetic Theory*, McGraw-Hill, New York.
[31] Melcher, J. R., 1981, *Continuum Electromechanics*, MIT Press, Cambridge, MA.
[32] Rosenthal, A. D., Rinaldi, C., Franklin, T., and Zahn, M., 2004, "Torque Measurements in Spin-Up Flow of Ferrofluids," ASME J. Fluids Eng., **126**, pp. 198–205.
[33] Chantrell, R. W., Popplewell, J., and Charles, S. W., 1978, "Measurements of Particle Size Distribution Parameters in Ferrofluids," IEEE Trans. Magn., **14**, pp. 975–977.
[34] Lehlooh, A. F., Mahmood, S. H., and Willians, J. M., 2002, "On the Particle Size Dependence of the Magnetic Anisotropy Energy Constant," Physica B, **321**, pp. 159–162.
[35] Sawada, T., Nishiyama, H., and Tabata, T., 2002, "Influence of a Magnetic Field on Ultrasound Propagation in a Magnetic Fluid," J. Magn. Magn. Mater., **252**, pp. 186–188.
[36] Motozawa, M., and Sawada, T., 2005, "Influence of Magnetic Field on Ultrasonic Propagation Velocity in Magnetic Fluids," J. Magn. Magn. Mater., **289**, pp. 66–69.
[37] Takeda, Y., 1999, "Ultrasonic Doppler Method for Velocity Profile Measurement in Fluid Dynamics and Fluid Engineering," Exp. Fluids, **26**, pp. 177–178.
[38] de Gans, B. J., Blom, C., Mellema, J., and Philipse, A. P., 1999, "Preparation and Magnetisation of a Silica-Magnetite Inverse Ferrofluid," J. Magn. Magn. Mater., **201**, pp. 11–13.
[39] de Gans, B. J., Blom, C., Philipse, A. P., and Mellema, J., 1999, "Linear Viscoelasticity of an Inverse Ferrofluid," Phys. Rev. E, **60**, pp. 4518–4527.
[40] de Gans, B. J., Duin, N. J., Den Ende, D. V., and Mellema, J., 2000, "The Influence of Particle Size on the Magnerheological Properties of an Inverse Ferrofluid," J. Chem. Phys., **113**, pp. 2032–2042.
[41] de Gans, B. J., Hoekstra, H., and Mellema, J., 1999, "Non-linear Magnetorheological Behaviour of an Inverse Ferrofluid," Faraday Discuss., **112**, pp. 209–224.
[42] Feng, S., Graham, A. L., Abbott, J. R., and Brenner, H., 2006, "Antisymmetric Stresses in Suspensions: Vortex Viscosity and Energy Dissipation," J. Fluid Mech., **563**, pp. 97–122.

Internal Organizational Measurement for Control of Magnetorheological Fluid Properties

John R. Lloyd
University Distinguished Professor
e-mail: lloyd@egr.msu.edu

Miquel O. Hayesmichel
Former Graduate Student

Clark J. Radcliffe
Professor

Department of Mechanical Engineering,
Michigan State University,
East Lansing, MI 48824

Magnetorheological (MR) fluids change their physical properties when subjected to a magnetic field. As this change occurs, the specific values of the physical properties are a function of the fluid's time-varying organization state. This results in a nonlinear, hysteretic, time-varying fluid property response to direct magnetic field excitation. Permeability, resistivity and permittivity changes of MR fluid were investigated and their suitability to indicate the organizational state of the fluid, and thus other transport properties, was determined. High sensitivity of permittivity and resistivity to particle organization and applied field was studied experimentally. The measurable effect of these material properties can be used to implement an MR fluid state sensor. [DOI: 10.1115/1.2436588]

Introduction

Magnetorheological (MR) fluids, are part of a class of controllable fluids. MR fluids are suspensions of micron-sized magnetic particles dispersed in a fluid carrier such as a mineral or silicon oil. In these fluids physical properties of the fluid such as rheological and thermal transport properties can be changed reversibly, through the application of an externally applied magnetic field [1–3].

The property changes of MR fluids result from alignment of micron sized iron/magnetic particles into long columns within the fluid along the lines of the magnetic field in response to an application of a magnetic field. The stronger the field the greater the effect on the properties of the MR fluid such as viscosity. Current commercial applications of MR fluids include controllable damping elements using the variable rheology of these fluids [4], jet finishing of ultra smooth surfaces [5], and in torque transfer devices [6].

The physical properties of an MR fluid change as a nonlinear time-varying function of applied field driven particle alignment with the typical hysteresis of magnetic materials. The external magnetic field applied to the MR fluid causes changes in all physical properties of the fluid, e.g. electrical conductivity, thermal conductivity [2,3], permeability [7], as well as viscosity [1]. If the MR fluid response can be sensed electrically, then changes in physical properties can be precisely controlled. This strategy has been followed by the authors for Electrorheological fluids in 1996 [8,9],

Winslow [10] is generally credited as the first person to recognize the potential of controllable fluids in the 1940s. The first electrorheological (ER) fluids patent paper describing the ER effect. MR fluid discovery can be credited to Jacob Rabinow [11,12] at the US National Bureau of Standards. Interestingly, this work was almost concurrent with Winslow's ER fluid work. The late 1940s and early 1950s actually saw more patents and publications relating to MR fluids than to ER fluids. While Rabinow's work is largely overlooked today, Winslow discussed the work on MR fluids going on at the National Bureau of Standards in his seminal paper on ER fluids [10].

The transient and steady-state behavior of MR fluids has been investigated extensively. Fluid viscosity is very sensitive to changes on external magnetic fields [13–15]. Viscosity dependence on particle concentration, particle shape, size, and material in combination with several carrier fluids have been evaluated. Because MR fluid viscosity changes are large, most applications exploit these changes to produce various designs of controllable damping or torque conversion devices [4,6].

Control of the viscosity in current MR devices is performed by direct excitation of the external magnetic field. The nonlinear, hysteretic, time-varying response of the fluid is an obstacle to precision viscosity control despite the fast response time. Controlling the external magnetic field yields a fast but imprecise response of the fluid. To design for high-speed precise control, a more sophisticated strategy for the control of the fluid response is required.

The MR fluid organizational state is the level of geometrical organization of particles in the fluid. The magnetorheological effect was demonstrated in the view of an optical microscope with a low concentration (3% estimated). MR fluid suspension under a magnetic field applied from 0 kA/m to 40 kA/m was observed. The nonenergized state of the fluid (Fig. 1(*a*)), shows a random orientation and positioning of particles. When energized with a magnetic field, H, the MR fluid shows particle organization patterns parallel to the flux lines of the magnetic field (Figs. 1(*b*)–1(*f*)). The particle organizational state of the fluid is indicative of the induced interparticle magnetic forces generated by the applied magnetic field. An important fact is that for MR fluids, the ability to physically observe the chaining process is reserved only for low concentrations of particles, which we do. To date, no experiments have been devised to directly observe chaining of MR fluids when high particle concentrations are present. We will therefore relate our work directly to low concentration applications, but direct observation towards what is expected at high concentrations based on our experiences with ER controllable fluids.

The physical properties of the fluid are functions of the particle organizational state of the fluid, physical properties of the particles, and the magnetically induced forces between them. Conceptually, the particle organizational state, x, of the MR fluid combined with the applied field input, B, governs the time rate of change of organizational state, dx/dt, of the particles in the fluid. The resulting combination of organizational state and applied field then governs all of physical property values, y

Contributed by the Fluids Engineering Division of ASME for publication in the JOURNAL OF FLUIDS ENGINEERING. Manuscript received June 19, 2006; final manuscript received November 21, 2006. Assoc. Editor: Dennis Siginer.

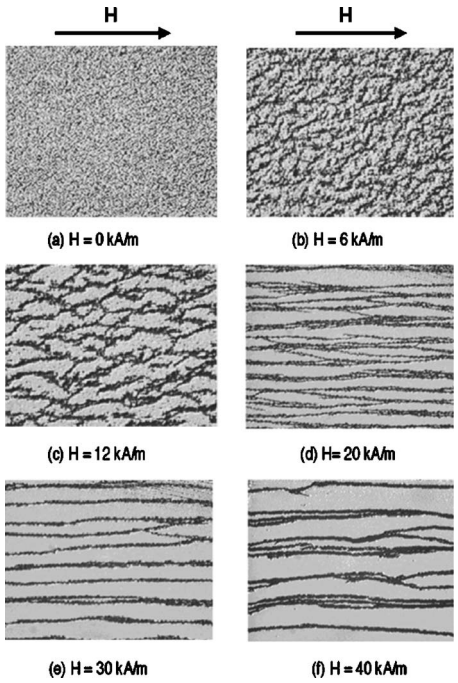

Fig. 1 Visualization of particle organization of a magnetorheological fluid as a function of applied magnetic field strength, *H*

$$\dot{x} = f(x,B)$$
$$y = g(x,B) \tag{1}$$

A measurable effect representative of the state of the fluid must be identified to implement a sensor of particle organizational state. The state descriptor property should be sensitive to changes in internal particle organizational state and easy to implement in real devices. Sensitivity of three magnetoelectric properties: resistance, inductance, and capacitance will be tested and their suitability for use in describing other properties will be evaluated.

Experimental Apparatus

Three properties that react to the external field were considered for evaluation in the present study: inductance, capacitance, and resistance. The first property studied was the inductance because it would give the possibility of using the same electric circuit that generates the field, thus avoiding the need for an additional secondary circuit. Capacitance and resistance of a secondary circuit connecting the MR fluid in series was used to test their response to changes in applied field.

The device used to generate the magnetic field for all experiments was a magnetic core with a MR fluid gap (Fig. 2). The magnetic core was made of laminated ferromagnetic material and had a reduced cross section at the MR fluid gap to concentrate the field. The fluid was located in thin wall plastic reservoirs to perform static fluid measurements. A plastic duct was located through the gap to carry out measurements with MR fluid flow. A dc powered positive displacement pump was used to pump the MR fluid. A dc voltage was applied to the winding to generate the external magnetic field. The MR fluid used on all the experiments was the VersaFlow MRX-135CD manufactured by Lord Corporation. The MR fluid was mechanically mixed before every experiment to ensure homogeneity.

Inductance Testing

To measure magnetic permeability, μ, the inductance change in the drive circuit was evaluated as a function of magnetic field strength. The inductance of a magnetic circuit is a function of the

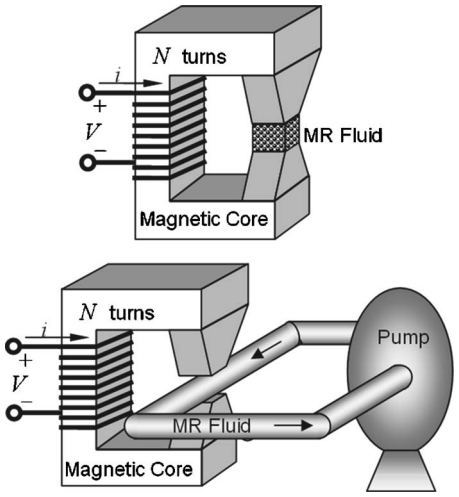

Fig. 2 MR fluid experimental facilities for measurements of properties in static and moving fluids

permeability of the materials that make up the magnetic circuit, the number of turns of the winding and of the geometric characteristics of each part of the core. The magnetic circuit includes the ferromagnetic core and the MR fluid gap. Ohm's law for magnetic circuit provides a formula for the total magnetic circuit inductance

$$L = \frac{N^2}{\frac{l_1}{\mu_c \cdot A_1} + \frac{l_2}{\mu_c \cdot A_2} + \cdots + \frac{l_{n-1}}{\mu_c \cdot A_{n-1}} + \frac{l_{\mathrm{MR}}}{\mu_{\mathrm{MR}} \cdot A_{\mathrm{MR}}}} \tag{2}$$

For constant geometric parameters and number of turns, the inductance is a function of the permeability only. If the permeability of the MR fluid, μ_{MR}, is sensitive to changes in particle organization state, a measurable change in inductance would indicate a change in the state of the fluid, and a measure of the organizational state of the fluid.

The electromagnetic circuit works as both an actuator and as a sensor in the above system. The complete circuit includes the winding (inductance and resistance) and a known resistance resistor (Fig. 3). A small ac voltage is superimposed on the dc voltage.

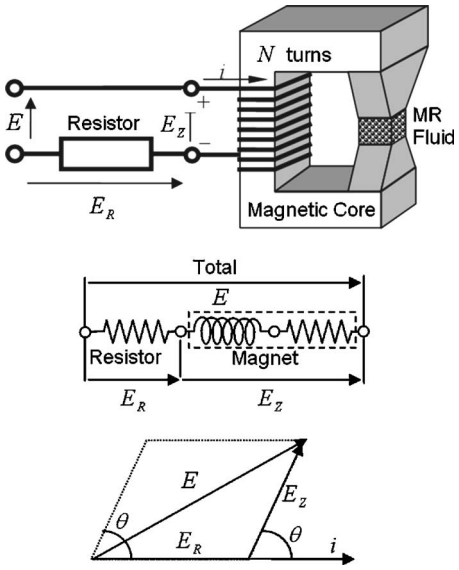

Fig. 3 Schematic diagram of the three voltmeter method to compute inductance: experimental system, equivalent circuit diagram, and vector diagram

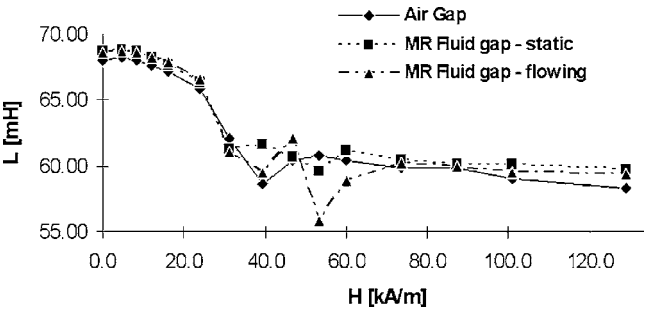

Fig. 4 Initial measured inductance versus applied field results showing an external, indirect, sensor yields small measured changes in inductance

This small ac voltage was used only to sense the impedance of the electrical signal, and it was kept small enough to have discernible effect on the fluid state. The measurement method used to measure inductance was the three voltmeter method applied to the ac component amplitudes [16]. A typical result is the relationship for inductance

$$L = \frac{R_1 \cdot E_Z \cdot \cos\theta}{E_R \cdot 2 \cdot \pi \cdot f} \tag{3}$$

where

$$\cos\theta = \frac{E^2 - E_R^2 - E_Z^2}{2E_R E_Z}$$

This method (Fig. 3) uses three ac amplitudes to compute inductance L, capacitance C, and/or resistance R accurately because it does not require a difficult direct measurement of phase angle θ.

A LabVIEW program was written to acquire the ac measurements required to compute inductance. A Wavetek 12 MHz synthesized function generator and an HP bipolar power supply–amplifier were used to generate the input voltage. Two Hewlett Packard 3478As and one Keithey 175 Multimeter were used to acquire the voltage measurements. All instruments were connected to the computer by general purpose interface bus (GPIB) connections.

Steady-state inductance measurements were taken with the gap filled with MR fluid. The dc voltage was increased from 0 to 20 V to generate magnetic dc fields that ranged from 0 to 128 kA/m. A 100 Hz ac voltage frequency was applied and the amplitude of the source was kept constant at 0.25 V. This ac amplitude represented only 1.25% of the full scale dc applied field. This measurement methodology used small ac field only to monitor changes in inductance as large variations in the dc field resulted in changes in magnetorheological state.

Inductance measurements were performed with the gap occupied by the static MR fluid, the flowing MR fluid, and air only (Fig. 4). The total measured value of inductance is dominated by the inductance of the ferromagnetic core itself, which showed a typical saturation curve. The data revealed a 16.7%, 15.0%, and 15.6% decrease in inductance for the air gap, static MR fluid gap, and flowing MR fluid, respectively, over the entire change of magnetic field. The measurements for low field regions (0–30 kA/m) were stable and repeatable. The higher field region (>30 kA/m) produced unstable results. The difference associated with the fluid state in the core's gap represented only $16.7\% - 15.6\% = 1.9\%$ change in measured inductance due to MR fluid particle chain formation. This small change in inductance indicates that magnetic permeability is not a strong candidate for organizational state sensing. The results below were obtained with a more direct method that demonstrated higher sensitivity to applied field.

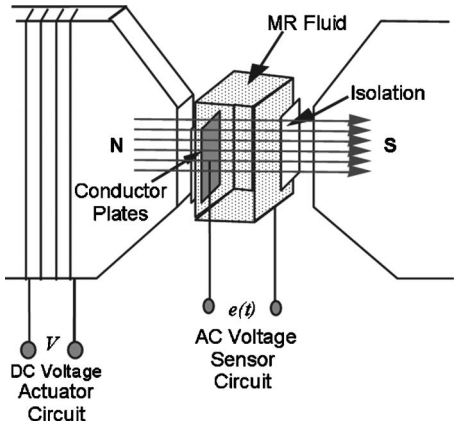

Fig. 5 Schematic diagram of experimental facility for capacitance and resistance measurements

Capacitance and Resistance Testing

The MR fluid properties of permittivity, ε, and resistivity, ρ, were evaluated simultaneously as candidates for state sensor effectiveness using the same laboratory test system (Fig. 5). Permitivity and resistivity change of the MR fluid as a function of a magnetic field was evaluated between two parallel conductor plates applied directly to the fluid in the MR fluid gap. The plates and MR fluid formed a parallel plate resistor/capacitor.

Steady state permittivity, ε, change affects capacitance of a secondary circuit as a function of the magnetic field strength. The capacitance values for a parallel plates capacitor is a function of the area of the conductors, the distance between them, and the permittivity of the material filling that space. Capacitance changes for constant geometry are functions of the permittivity, ε, of the material only

$$C = \frac{\varepsilon * A}{d} \tag{4}$$

The resistance value between the plates is a function of the area of the plates, the distance between plates, and the resistivity of the MR fluid between the plates

$$R = \rho \cdot \frac{d}{A} \tag{5}$$

Two electrical circuits (Fig. 6) were used to perform these measurements: the actuator circuit and the sensor circuit. The actuator circuit was an HP power supply that produced a dc actuation field. A Wavetek function generator and another HP power supply/amplifier generated the ac actuation fields. The sensor circuit connected the two parallel plates located in the MR fluid with a constant separation between them. The sensor circuit was connected to a Fluke RCL meter used to measure series and parallel equivalent capacitance and resistance. The Fluke RCL meter applied a

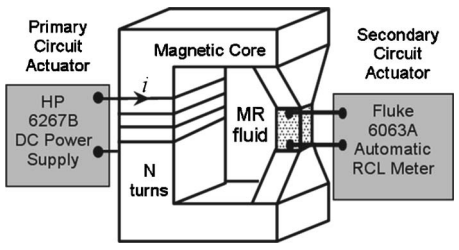

Fig. 6 Schematic diagram of equipment setup for MR fluid capacitance and resistance measurements

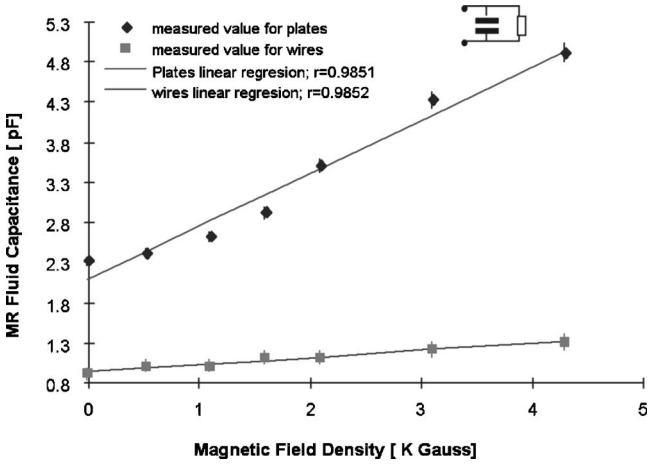

Fig. 7 Measurements of parallel equivalent capacitance of the MR fluid as a function of applied field

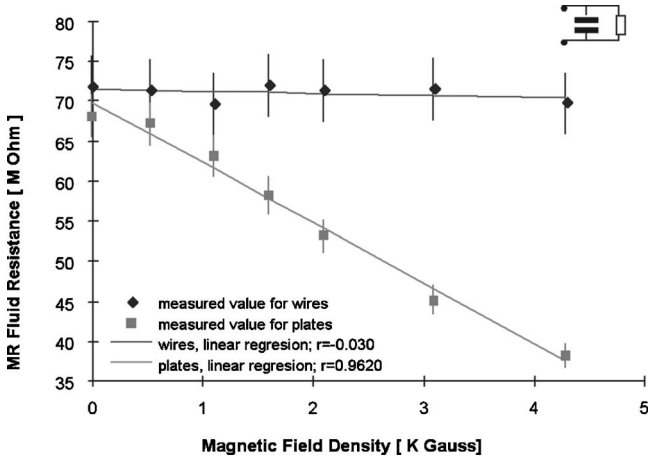

Fig. 9 Measurements of parallel equivalent resistance of the MR fluid as a function of applied magnetic field

small ac field to the secondary circuit and used this ac circuit to measure changes in capacitance and resistance across the plates.

Capacitance Measurements

As stated previously measurements were taken with the plates inside the MR fluid. The plates were carefully positioned parallel to each other and perpendicular to the field lines. 20 mm plates and 28 gage wires were tested. Using a parallel equivalent capacitance model, measurements (Fig. 7), showed an increase of 44.4% and 113% for a total increase of 340 kA/m of the applied field for the wires and plates, respectively. A correlation factor of 0.9852 and 0.9851 for a linear regression analysis belong to the two corresponding sets of data although the plate data show a saturation curve trend. Using a series equivalent capacitance model, measurements (Fig. 8) showed no change in capacitance for the wire capacitor and a 28.2% increment for the plate capacitor. Linear regression on these showed 0.030 and 0.9620 correlation factors, respectively. It should be noted that in this work correlation factors are employed to provide information on both repeatability and reproducibility. As expected, the larger cross sectional area made plate capacitance measurements more sensitive to changes in magnetorheological fluid response.

Resistance Measurements

Measurements using a parallel equivalent resistance model for the MR fluid with the plates placed along the magnetic field (Fig. 9), showed a 1.4% resistance decline between 28 AWG wires and a 44.1% resistance decrease between 20 mm plates over the 340 kA/m variation on the applied magnetic field. Correlation factors of 0.381 and 0.993 were computed for the linear regression of both sets of data, respectively. Measurements using a series equivalent resistance model (Fig. 10) showed a 17.2% decrease between 28 AWG wires and a 40.5% decrease between the 20 mm plates over the 340 kA/m increase of the applied field. Correlation factors of 0.995 and 0.992 were computed for the linear regression of both sets of data, respectively.

Resistance measurements with the plates placed across the field showed no change over the a 340 kA/m increase in the applied field in either parallel or series equivalent circuits. Capacitance with the plates across the field showed no change for a parallel equivalent measurement and showed a 2.8% increase over the 340 kA/m change on the applied field for a series equivalent measurement. These measurements demonstrate the ability to measure the directional orientation of field induced internal structure and hence the directionality of the internal organization state of MR fluids.

Sensitivity of Inductance, Resistance, and Capacitance

Sensitivity of the three measured electric properties as a function of the applied field was investigated. Sensitivity was com-

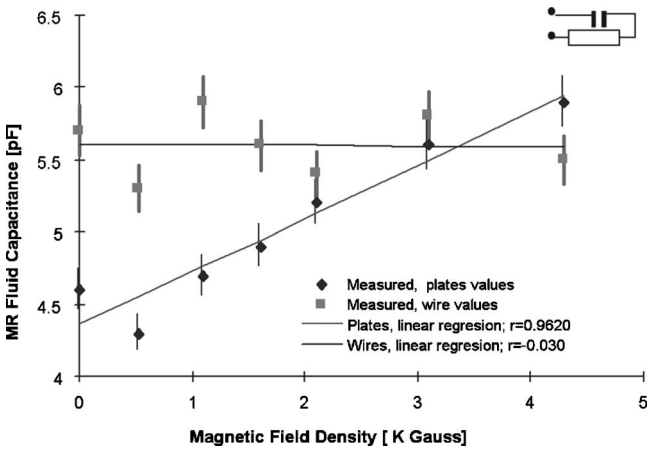

Fig. 8 Measurements of series equivalent capacitance of the MR fluid as a function of applied field

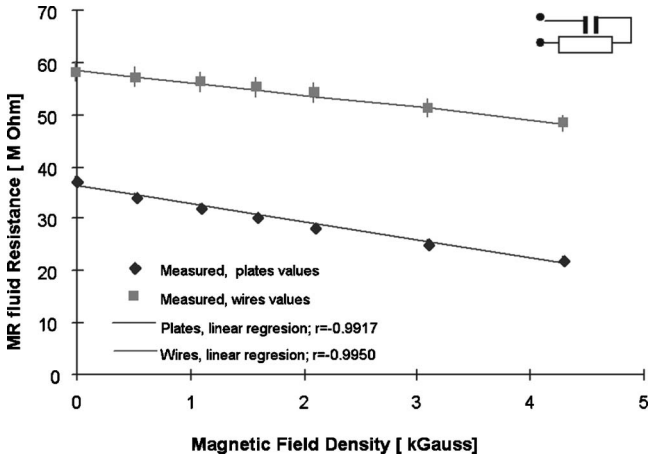

Fig. 10 Measurements of series equivalent resistance of the MR fluid as a function of applied magnetic field

Table 1 Sensitivity of magnetic and electric properties of the MR fluids to strength of applied magnetic fields

Property	Range	Applied field H (kA/m)	Sensitivity S_H^*	Correlation
Inductance (mH)	4.84–4.88	0–30	0.004	0.953
Relative permeability	31.5–31.8			
Resistance (M Ω)	37–22	0–340	−0.254	0.992
Resistivity (kΩ m)	148–88			
Capacitance (pF)	2.3–4.9	0–340	0.361	0.985
Relative permittivity	65–139			

puted as the ratio of the total increment of every one of these properties over its average value to the total variation in applied field over its average value

$$S_H^Q = \frac{(Q_2 - Q_1) \cdot (H_2 + H_1)}{(H_2 - H_1) \cdot (Q_2 + Q_1)} \tag{6}$$

The measured sensitivity for inductance measurements showed the lowest sensitivity to applied field, $S_H^L = 0.004$ (Table 1). The MR fluid resistance connected in series showed sensitivity to applied field, $S_H^R = -0.2542$. The sensitivity of the capacitance to applied field, $S_H^C = 0.361$, was the highest. Although the highest correlation factor for a linear regression analysis of all sets of data belongs to the resistance, the repeatability of the measurements is demonstrated by the correlation factors above 0.95 for all measurements in the table.

Permeability, permittivity, and resistivity are the material properties sensed by the inductance, resistance, and capacitance changes, respectively. These changing properties reflect changes in the particle state organization. Using inductance measurements, the computed relative permeability increased from 31.5 to 31.76. Using resistance measurements, the resistivity was larger and decreased from 148 kΩ m to 88 kΩ m. Using capacitance measurements, the relative permittivity was the largest and increased from 65 to 138.

Conclusions and Recommendations

Sensitivity of inductance, resistance, and capacitance of a VersaFlow MRX–153CD MR fluid to changes in magnetic field was investigated in order to determine their suitability for use as an MR fluid state sensor. Changes in inductance, resistance, and capacitance reflect associated changes in the material properties: permeability, resistivity, and permittivity. Sensitivities to field variation for these properties were demonstrated for fields up to 340 kA/m. Large dc magnetic fields were applied to excite changes in magnetorheological fluid properties while small ac magnetic fields were used to sense the changes in the electrical properties of the fluid. The Inductance of the MR fluid core under magnetic fields in the range of 0–30 kA/m showed a very low sensitivity of $S_H^I = 0.004$ Unstable and unpredictable inductance values were obtained for higher fields. These results indicated that inductance is a poor candidate for a magnetorheological state sensor.

Resistance and capacitance measurements showed a stronger sensitivity to applied field. Resistance sensitivity was of $S_H^R = -0.254$. Capacitance showed highest sensitivity of $S_H^C = 0.361$. The applied field ranged from 0 to 340 kA/m for capacitance and resistance measurements. The relative magnitudes of these measured changes (Fig. 11) demonstrate that permittivity is most strongly affected by particle organization and is the most likely candidate for a state sensor, followed closely by resistivity.

Inductive sensing is not attractive because inductance change has a small sensitivity to both internal particle organization and low applied fields. Under higher fields unstable measurements were obtained. Real MR fluid devices will always have an electromagnetic circuit with a very small MR fluid gap. Because of this geometry, the total inductance measured will be dominated by the inductance of the non-MR fluid portion of the electromagnetic circuit, i.e., the ferromagnetic core, making changes in MR fluid permeability even more difficult to detect.

Resistance and capacitance sensor circuits are highly sensitive to both applied magnetic field and particle organization, and provide an accurate measure of MR fluid internal state. Parallel conductor plates placed normal to field lines gave the most predictable signal and had the highest sensitivity. Resistance and capacitance sensors have a big advantage over traditional shear rate sensing used to compute viscosity where fluid movement is required because they provide accurate measures of particle organization state for both static and moving fluid. The correlation factors found over a large number of independent measurements (Table 1) varied between 0.953 and 0.992 indicating the reproducibility and repeatability of the measurements.

As has been demonstrated in many studies of controllable fluids, most notably ER fluids (e.g., Refs. [14,17]), the organizational state of the controllable fluid is directly related to physical transport properties. While viscosity is the most observed transport property, thermal conductivity is also significantly controlled by the organizational state. It is not unreasonable to expect the same general behavior of non-Newtonian behavior in viscosity and a strong increase in thermal conductivity resulting from an increase in particle chaining or organizational state. The yield stress in the viscosity measured by many does not reveal any significant change in the properties directly measured in this study. This suggests that the transport properties such as thermal conductivity exhibit a similar smoothness or change in property as a result of flow. Thus, the present study suggests the need for confirming experiments to confirm this, no matter how difficult the experiment may be.

In concluding, it is important to discuss application of the

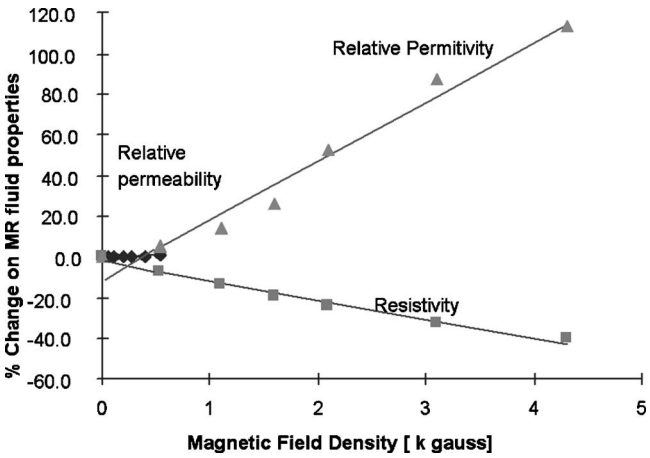

Fig. 11 Relative property changes in permeability, permittivity, and resistivity of the MR fluid as a function of applied magnetic field

knowledge presented in this paper. MR fluids have found an important market in fluid clutches for automotive and sports equipment applications. In automotive applications especially, where the clutches operate at 4000 rpm or more, the application of a strong magnetic field across the plates of the clutch creates the chain structures, and the apparent "viscosity" of the MR fluid increases until it effectively becomes a solid link with no slippage. There is a very high yield stress for the non-Newtonian fluid at this state. As a result of the "viscous" work done on the fluid in the clutch, the temperature of the fluid reaches very high values. This energy must be transferred from the clutch if it is to continue effective operation. The fact that the chains have formed also increases the effective thermal conductivity of the clutch fluid several times its nonstructured value, and the energy is transported away from the clutch gap more effectively. Without the increase in effective thermal conductivity resulting from the chaining of the magnetic particles, the magnetic fluid clutch would not be successful. The knowledge provided in this paper provides effective, direct methods for measurement of MR fluid chaining state allowing accurate electrical measurement of the fluid properties resulting from the formation of those particle chains.

Nomenclature

x = particle state
S_H^Q = sensitivity of Q with respect to H
μ = magnetic permeability (H/m)
θ = phase angle (deg)
ε = permitivity (F/m)
ρ = resistivity (MΩ m)
A = cross section (m^2)
B = magnetic field density (G)
C = capacitance (F)
d = distance (m)
E = system potential amplitude (V)
E_r = potential amplitude across the resistor (V)
E_z = potential amplitude across the magnet (V)
f = frequency (Hz)
H = magnetic field strength (kA/m)
L = inductance (mH)
l = length (m)
N = number of turns on the winding
R = resistance (Ω)

References

[1] Ciocanel, C., Lipscom, G., and Naganathan, N. G., 2005, "Evaluation of a Constituitive Equation for Magnetorheological Fluids in Shear and Elongational Flows," *Proceedings of IMECE2005-79974*, Orlando, FL.
[2] Ganguly, R., Gaind, A. P., and Puri, I. K., 2004, "Ferrofluid Transport Analysis for Micro- and Mesosclae Applications," Proceedings of IMECE2004-60045, Anaheim, CA.
[3] Massoudi, M., and Phuoc, T. X., 2002, "A Simple Model for the Effective Thermal Conductivity of a Particulate Mixture," Proceedings of IMECE2002-32493, New Orleans, LA, November 17–22.
[4] Carlson, J. D., Catanzarite, D. M., and St. Clair, K. A., 1996, "Commercial Magneto-Rheological Fluid Devices," Int. J. Mod. Phys. B, **10**, pp. 2857–2865.
[5] Kordonski, W. I., Shorey, A. B., and Tricard, M., 2004, "Magnetorheological (MR) Jet Finishing Technology," Proceedings of IMECE2004-61214, Anaheim, CA, November 13–19.
[6] Molyet, K., Ciocanel, C., Yamamoto, H., and Naganathan, N., 2005, "Design and Performance of a MR Torque Transfer Device," Proceedings of IMECE 2005-81428 Orlando, CA, November 6–11.
[7] Hayes, M., Miguel, O., 1997, "Internal Organizational State Sensing For Magnetorheological Fluids," M.S. thesis, Mechanical Engineering, Michigan State University, East Lansing, MI.
[8] Winslow, W. M., 1947, "Translating Electrical Impulses into Mechanical Force," U.S. Patent No. 2,417,850, March 25.
[9] Radcliffe, C. J., Lloyd, J. R., Andersland, R. M., and Hargrove, J. B., 1996, "State Feedback of Electrorheological Fluids," Proceedings of the Dynamic Systems and Control Division, Proceedings ASME IMECE, Atlanta, GA, Nov. 17–22.
[10] Lloyd, J. R., and Radcliffe, C. J., 1996, "Feedback Control of Electrorheological Fluid Response," U.S. Patent No. 5,493,127.
[11] Rabinow, J., 1948, "The Magnetic Fluid Clutch," AIEE Trans., **67**, pp. 1308–1315.
[12] Rabinow, J., 1951, "Magnetic Fluid Torque and Force Transmitting Device," U.S. Patent No. 2,575,360.
[13] Shulman, Z. P., and Kordonsky, V. I., 1982, *Magnetorheological Effect*, Nauka Press, Moscow, Russia, p. 184.
[14] Shulman, Z. P., Kordonsky, V. I., Zaltsgendler, E. A., Prokhorov, I. V., Khushid, B. M., and Demchuk, S. A., 1986, "Structure, Physical properties and Dynamics of Magnetorheological Suspensions," Int. J. Multiphase Flow, **12**(6), pp. 935–955.
[15] Kordonsky, W., 1993, "Elements and Devices Based on Magnetorheological Effect," J. Intell. Mater. Syst. Struct., **4**, pp. 65–69.
[16] Siskind, C. H., 1956, *Electrical Circuits Direct and Alternating Currents*, McGraw–Hill, New York.
[17] Lloyd, J. R., and Radcliffe, C. J., 2001, *Transient Control of Thermophysical Properties of Controllable Fluids Through the Application of Externally Applied Electric Fields*, Electrostatics Society of America.

Carbon Nanotube–Magnetite Composites, With Applications to Developing Unique Magnetorheological Fluids

Stephen Samouhos[1]
e-mail: stratos@mit.edu

Gareth McKinley

Hatsopoulos Microfluids Laboratory,
MIT,
Department of Mechanical Engineering,
77 Massachusetts Avenue,
Cambridge, MA 02139

The development of carbon nanotube (CNT) based technology is limited in part by the lack of effective bulk methods for precisely manipulating and aligning nanotubes at the very fine scale. Moreover, the innate hydrophobic and inert nature of the CNT surface limits their compatibility with aqueous systems and flexibility for surface chemistry functionalization. This paper assesses the variety of methods developed to couple magnetically susceptible components such as ferromagnetic material with CNTs in order to overcome these limitations. In addition to reviewing the past 16 years of relevant literature, our own methods for noncovalent surface coating of CNT's with magnetite nanoparticles are described. The application of such composites is then explored within the framework of a magnetorheological (MR) fluid. It is found that the addition of magnetite nanoparticles to a MR fluid enriches the available MR response, resulting, in some cases, in an increased sedimentation stability, larger saturation critical stresses, and faster response to time varying magnetic fields. Finally, our own composite based MR fluid is discussed, and shown to possess a field dependent response that is a hybrid between that observed in ferrofluids and conventional MR fluids. [DOI: 10.1115/1.2436581]

Keywords: carbon nanotube, magnetite nanoparticles, magnetorheological, nanocomposite

Introduction

Carbon nanotubes (CNT) have received a tremendous amount of attention due to their unique and highly desirable electrical, thermal, and mechanical properties [1]. A variety of potential CNT applications exist, however, technology development is in part hampered by the lack of effective means for manipulating these materials at very fine scales [1]. Magnetic actuation of CNTs offers a potentially simple means for exerting this necessary control; however success is dependent on the ability to magnetize the CNT. Due to the absence of any natural CNT paramagnetism [1], their magnetization is only accomplished through hybridization with other magnetic materials, in particular cobalt, iron, nickel, and gadolinium. In this paper, we review the variety of methods demonstrated to couple magnetic materials with CNTs, as well as the performance of the composite as a magnetorheological fluid.

There are three general approaches to creating a magnetic CNT composite; magnetic material can be encapsulated [2–7], incorporated within the walls [8–15], or deposited on the outer surface of the nanotube [16–18]. All three methods have been shown to impart some magnetic character to the nanotube. Each approach, however also modifies the nanotube in ways that may ultimately restrict the applications of the composite. Beyond these three material addition categories, methods can be further subdivided into chemical and physical techniques that result in magnetic CNT composites. Physical additions include most of the processes in which material is encapsulated or imbibed by the nanotube, and as such, the majority of the molecular structure is kept intact. Wall embedding and outer surface decoration generally require, or induce some change in the wall or outer surface chemistry.

[1]Corresponding author.

Contributed by Fluids Engineering Division of ASME for publication in the JOURNAL OF FLUIDS ENGINEERING. Manuscript received June 28, 2006; final manuscript received December 5, 2006. Assoc. Editor: Dennis Siginer.

Filling Techniques for Composite Formation

The earliest methods to create magnetic CNTs followed from the work of Ajayan and Iijima in 1993 [3], who successfully demonstrated the oxidative cleavage of CNT end caps and subsequent filling with nonmagnetic liquid metals. Approaches derived from the work of Ajayan and Iijima relied upon filling a tube with magnetically susceptible liquids. Initially this was accomplished by selectively oxidizing the ends of a fully formed nanotube, and then using capillary suction to imbibe a volume of liquid metal into the freshly opened tube [2,3]. This two step process was executed by first depositing metallic nanoparticles onto a pristine nanotube outer surface, and then heating the composite material in air to beyond the melting temperature of the metal. The heating process both oxidized the tube end caps, as well as liquefied the metal. With the advent of techniques for creating vertically aligned, open ended CNTs [19], several other filling methods were also established.

In 2002, Bao et al. [4] showed that electrodeposition could be used to directly create continuous wires of cobalt within vertical nanotubes on an alumina template. Leonhardt et al. [5] provides a review of analogous chemical vapor deposition techniques for creating metal nanowires of iron, nickel, and cobalt within nanotubes. In a slightly different approach, Wu et al. [7] demonstrated that an aqueous solution of Fe and Ni ions could be drawn into a CNT and, through wet chemistry, form Fe–Ni alloy nanoparticles within the CNT. Finally, Korneva et al. [6] in 2005, also showed that an aqueous suspension of magnetic nanoparticles could be drawn by capillary suction, directly into an open ended nanotube. Subsequent evaporation of the solvent resulted in nanotubes loaded with magnetic nanoparticles. Most of these processes involve physical deposition, with minimal molecular modification of the CNT. In contrast, wall embedding and surface decoration generally involve significant chemical alterations of the CNT surface.

Wall Embedding and Surface Decoration Pathways

One of the earliest chemical additions of magnetic material to CNTs, performed by Lafdi et al. in 1996, was accomplished through cobalt doping of the graphite electrode used in arc-discharge CNT synthesis [10]. The CNTs subsequently produced from the doped electrode possessed walls that were infused with cobalt nanoparticles. Alternatively, Rao et al. [11] used pyrolitic synthesis, catalyzed by ferrocene, to form CNTs that had a magnetic nanoparticle embedded within the tube, at the catalyst anchoring point. Whereas Lafdi [10] was able to distribute the cobalt along the entire length of the tube, this latter approach could inherently only place a nanoparticle at one point. The methods employed by Rao were expanded in 2000 and 2001, by Liu et al. [12,13], and Zhang [15], respectively. Barnhart [14] provides a more complete review of the chemical and physical effects of metal atom inclusions within CNT walls, as well as the synthesis pathways leading to such composites.

In 2005, Bottini et al. [20] showed that multiwalled CNTs could be covalently decorated with silica nanoparticles. The protocol required a long oxidation step to carboxylate the surface, after which various nanoparticle precursor groups could be attached to the induced surface defects. Extended oxidation in concentrated nitric acid was necessary in order to stud the largely inert pristine CNT surface with reactive carboxylic groups. The protocol stems from an established method of using moderate etching periods in strong oxidizers to create nanotubes of uniform and predictable length, with minimal aberrations of the outer surface [21]. By dramatically extending the etch time, Bottini et al. increased the surface concentration of carboxyl group defects. As evidenced by transmission electron microscope (TEM) imaging of the composite material, the defect concentration was not sufficient to support total outer surface coverage by silica nanoparticles.

Georgakilas et al. [16] used a slight variation of this method in that same year, to stud the outer wall surface with magnetite. Utilizing π bond stacking, carboxylic defect groups on the CNT surface were bonded to a pyrene-bearing magnetite nanoparticle, with an average diameter of 25 nm. As with other approaches that utilize surface defects, the coating process resulted in only partial coverage of the tube. Similar work was also presented in 2005 by Stoffelbach et al. [18] for decorating the outer surface with magnetite, and also in 2006 by Cao et al. [22]. Finally in 2005, Wu et al. [23] showed that by a similar process, nickel–iron alloy nanoparticles could be grown on the outer surface of the nanotube. In their protocol, the nanotube is again subjected to a prolonged oxidative bath in boiling nitric acid, which results in the formation of carboxylic surface defects. These imperfections provide the point of attachment for subsequent nanoparticle precursors. In all cases, the density of surface defects is insufficient for complete coverage of the nanotubes by magnetic materials.

Selection Considerations for CNT–Nanoparticle Hybridization Techniques

External magnetic coatings offer the capability of magnetic actuation as well as continued CNT surface functionalization [22]. As the pristine CNT surface is chemically inert, localized magnetic surface groups, attached to the CNT, can provide points of attachment for materials that would otherwise not adhere to the CNT. Along those lines, the utility of such coatings, either in magnetic control or surface functionalization, is limited by the extent of surface coverage. One of the goals of our work is to develop magnetite surface coating techniques that result in complete coverage of the CNT.

The scientific interest in developing and reviewing the current techniques for nanotube-to-nanoparticle hybridization is ultimately driven by the needs of the design engineer who wishes to create precise multiscale systems. Our particular work is devoted to hybridization techniques that do not destroy the innate surface chemistry of either particle.

Choosing amongst the existing art is dictated mostly by chemistry and application criteria of the hybrid materials. For a generic magnetic application, it may be sufficient to rely solely upon the incorporation of the magnetic catalyst used during tube synthesis. This simple approach may prevail for long tubes that eventually only need one magnetic anchoring point. On the other hand, many synthetic processes are followed by a cleavage etch that would create tube segments with no magnetic character. Such situations can be resolved either by post-etch addition steps of either physical or chemical nature, or impregnation of the tube wall with magnetic particles during growth. Tube filling is another option that offers certain advantages to surface engineering, and can also be performed in situ with tube growth or post-cleavage etch. Applications that demand preservation of the outer tube surface chemistry should look to tube filling techniques. These same methods have generally also resulted in superior addition of magnetic character to the nanotubes.

Other than chemical and design criteria, production cost is certainly important for choosing a hybridization technique. Surface additions stem from the acid etch induced carboxylation of the CNT, which is a relatively low-cost process step. The oxidation of the surface provides reaction sites that can be harnessed by numerous chemical means to deposit materials on the CNT surface. In general, these post-synthesis steps are easy to apply, and can be performed by any laboratory. In contrast, the deposition techniques for in situ tube filling during synthesis require a reaction chamber set up for the particular chemical vapor deposition (CVD) process. Most CNT synthesis laboratories already have such utilities, but groups who purchase CNT might have to consider the added cost of that process in comparison to surface chemistry methods. The development of simple capillary suction methods for filling CNT represents a significant departure to this classical CVD paradigm, creating a low-cost, highly effective tube filling procedure. Our efforts to develop simple, analogous low-cost surface encapsulation techniques that preserve the CNT outer surface chemistry would also provide additional options for the design engineer.

Method for Total Encapsulation of Carbon Nanotubes by Magnetite

A surface-preserving encapsulation procedure seemed feasible through noncovalent bonding between nanoparticles and tubes. In the absence of a chemical reaction or electrostatic bonding with surface defects, such a process could most likely proceed from the minimization of the van der Waals potential between the spherical nanoparticles and cylindrical nanotubes [24,25]. Kirsch [25] has shown that for certain geometric and material parameter values, the van der Waals attraction is greatest between a sphere and cylinder than for either species to a neighbor of its own kind. In reality, minimal surface defects always arise from the brief oxidative bath, as prescribed by Liu et al. [21], used to cut CNTs to a desired length. In the case of defects, electrostatic interactions introduce random points of attachment that do not usually support full tube encapsulation. Not having to depend on defect anchor points, the desired noncovalent bonding mechanism may result in full surface coverage.

The CNTs used to explore this technique were acquired from NanoLabs (Newton, MA), who carried out the ferrocene pyrolitic synthesis of 30 nm outer diameter stock multiwalled CNTs. The synthesis was followed by a 3 h concentrated nitric acid reflux etch, performed by NanoLabs, that cleaved the stock material into 5 μm long, open-ended segments. TEM inspection coupled with the low aqueous miscibility confirmed that the outer tube surface acquired minimal carboxylation defects during the etch. No further oxidation steps or chemical treatments were employed after the etching bath.

To explore the noncovalent bonding mechanism, 10 ml of an organic ferrofluid (EFH-1, Ferrotec, Nashua, NH), and a water-based ferrofluid (MSG-W11, Ferrotec, Nashua, NH) were added

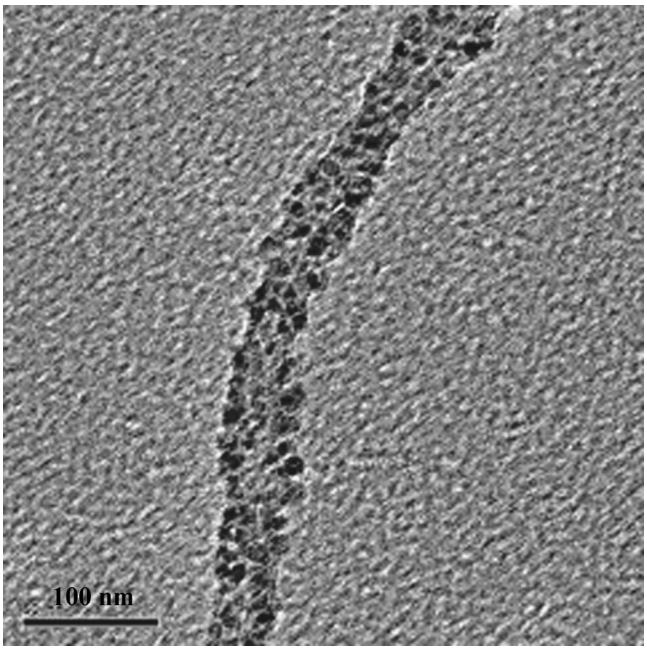

Fig. 1 TEM of organic ferrofluid nanoparticles bound to a CNT

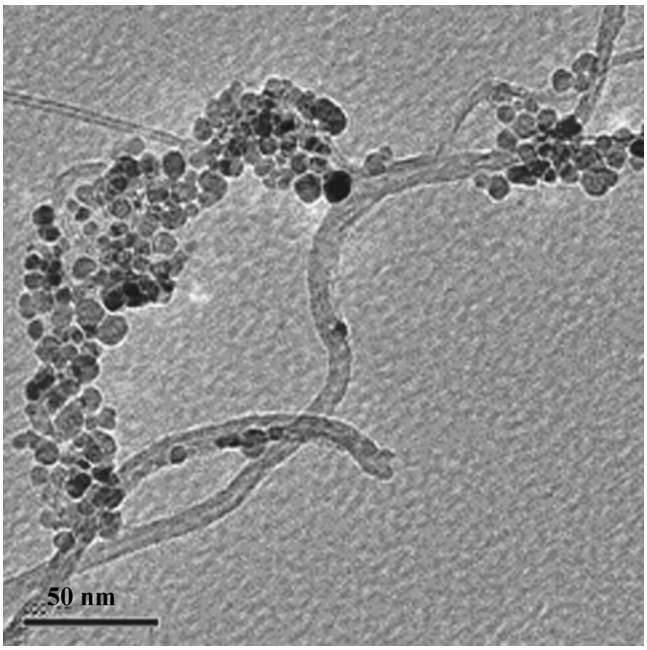

Fig. 2 TEM of aqueous ferrofluid nanoparticles excluding CNTs

drop wise to separate Petri dishes each containing 1.0 g dry CNT samples. Both ferrofluids were constituted of 10 nm magnetite nanoparticles, coated with an appropriate surfactant, and loaded to 6% volume fraction in their respective carrier liquid. As expected from prior miscibility experiments, the CNTs exhibited strong hydrophobicity, and the aqueous ferrofluid did not spontaneously wet the nanotubes. Conversely, the CNTs were immediately wet by the organic ferrofluid. The contents of each dish were mixed with a glass rod, and then washed with excess ethanol into 45 ml plastic tubes, without any sonication. The tubes were shaken vigorously to further mix the materials. The tube contents were separately washed with excess ethanol, and then excess kerosene, through a vacuum filtration system. In both cases, a reddish brown filtrate ensued, with a dark pink colored solid remaining on the filter paper.

The filtrate was discarded, and the filter paper contents were washed with ethanol back into glass vials for storage. Figures 1 and 2 show TEM micrographs (100 kV acceleration potential) of both the oil and water based ferrofluid reaction products in ethanol, following 3 h of sonication.

The magnetite particle and CNT diameters can be estimated from the TEM images as approximately 10 nm and 30 nm, respectively. These values match the quoted sizes given by the manufacturers. The initial hydrophobic interaction and poor miscibility between aqueous ferrofluid and CNT may have foretold the results shown in Fig. 2. The aqueous ferrofluid particles generally agglomerate with themselves, and occasionally attach to the surface of the CNT. The sporadic surface deposition may be attributed to the presence of a low concentration of carboxyl surface defects initiated by the oxidation etch. These defects facilitate electrostatic bonding with the charged surfactant group of the aqueous ferrofluid magnetite particle. In stark contrast, the organic ferrofluid appears to have fully coated the entire CNT. This image is reproduced in several other TEM micrographs, and indicates that our process results in complete CNT coating by magnetite nanoparticles. Based on the conditions of the experiments, noncovalent bonding due to van der Waals attraction or surfactant–CNT surface affinity has produced hybrids with high surface coverage. Moreover, the composite products of the organic reaction can be stabilized by a surfactant such as CTAB, or SDS and show satisfactory sedimentation stability in water, up to 0.1% volume fraction. The composite material alone shows higher stability against sedimentation in organic media without the aid of any surfactants.

The scanning electron microscope (SEM) image in Fig. 3 shows a larger object, comprised of several of these magnetite/CNT composites. Considering the dimensions of an individual strand, as shown in the TEM above, this SEM suggests that several composite strands can braid or envelope each other to form a bamboo structured micron-sized cylinder.

Figures 4 and 5 present static snapshots of the alignment of these braided composite strands to a lateral and normal induction field of 20 mT. The composite is clearly manipulated by the field to remain parallel with the field lines. There is likely a critical size, or number of strands per cylindrical agglomerate, that is indicative of steric and perhaps magnetic interactions between individual composite tubes. This saturation size is supported by the observation that Figs. 3–5 show a large number of these agglomerate braids all with roughly 2.5 μm diameter and 20–30 μm in length. The manufacturer's quoted dimensions for the nanotubes are 30 nm diameter, by 5–20 μm long; considering that a mag-

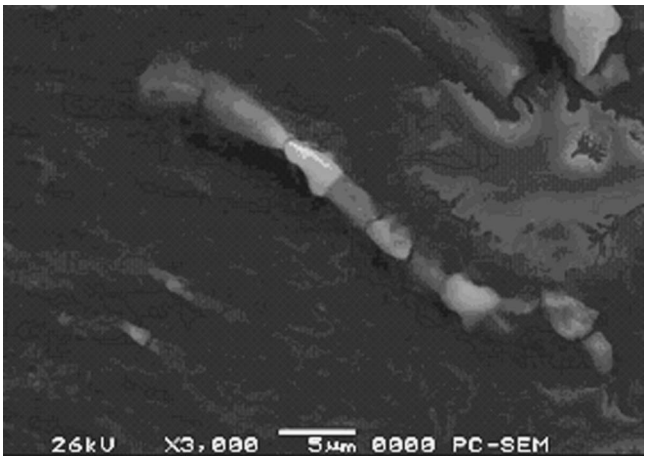

Fig. 3 SEM of bamboo structured ferrofluid nanoparticle–CNT composite

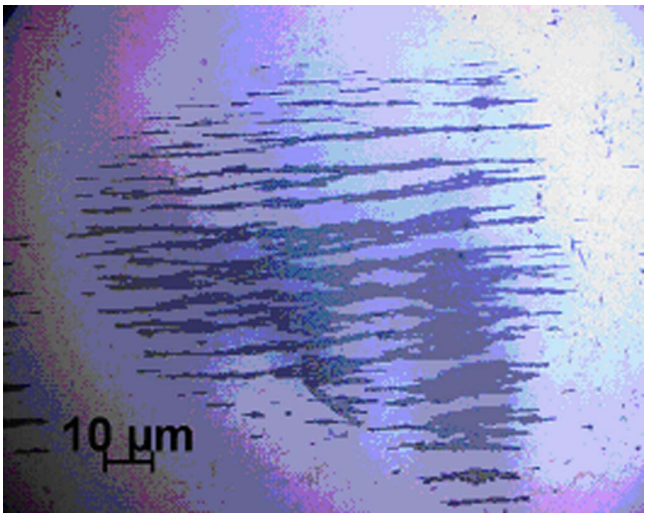

Fig. 4 Micrograph of composite filaments aligned by 20 mT field applied parallel to the page

netic coat increases the outer diameter to 60 nm, these braided agglomerates are comprised of roughly 40–50 individual strands.

Correa-Duarte et al. [26] also achieved complete coverage with magnetite through a noncovalent bonding mechanism based on polymer wrapping and layer-by-layer (LbL) electrostatic self-assembly. Poly(sodium 4-styrene sulfonate) chains were driven to wrap around the CNT via hydrophobic interactions, thereby encapsulating the CNT in a negatively charged polymer coat. The polymer surface charges then acted as anchors for the subsequent deposition of magnetic nanoparticles via LbL, and total surface coverage ensued. Pu and Jiang [27] also attempted surface coating via extended oxidation to create carboxyl defects on the CNT surface. These defects served as nucleation sites in the subsequent chemical synthesis of magnetite from ferrous and ferric salts. This approach resulted in the formation of a 10-nm-thick shell of magnetite surrounding the CNT. TEM analysis, however, shows a shell that only covers certain portions of the CNT, as opposed to the total surface coverage wrought by our noncovalent bonding. In contrast to other carboxylation-based methods, however, which result in only particle decoration of the CNT surface, Pu and Jiang were successful in producing continuous magnetite shells on the CNT surface, albeit without total surface coverage.

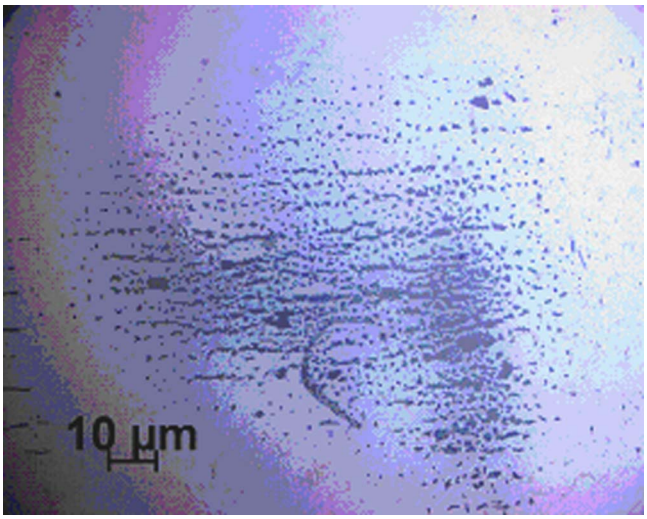

Fig. 5 Micrograph of composite filaments aligned by 20 mT field applied normal to the page

Sedimentation Stability of CNT/Magnetite Composite Based MR Fluids

Part of the motivation for creating a CNT/magnetite composite stems from the goal of creating a magneto-rheological (MR) fluid with increased sedimentation stability. The density of the magnetite/CNT composite formed by our protocol was approximately 1.8 g/cm^3, which is less than a quarter of that of carbonyl iron, $Fe(CO)_5$, a material commonly used to form particles for MR fluids. By comparing the buoyancy of a particle against the viscous drag experienced as it falls within a fluid, the sedimentation velocity may be expressed by [28]

$$V_0 = 2(\rho_s - \rho_f)ga^2/9\eta \tag{1}$$

where V_0 is the sedimentation velocity; ρ_s and ρ_f are the particle and fluid densities respectively; a is the particle radius; η is the viscosity of the fluid; and g is the gravitational acceleration. The difference in density between a 1-μm-diameter CNT/Fe_3O_4 composite particle and 1-μm-diameter iron oxide particle should result in a 17-fold reduction in the sedimentation velocity of the composite as compared to iron oxide particles, dispersed in water. Moreover, at high enough volume fractions (above 10%), the elongated cylindrical shape of the braided composite particles should also provide sedimentation stability via the formation of a percolated network. Pu and Jiang created a composite with similar density and cylindrical geometry, and found that the sedimentation stability of their CNT/magnetite composites dispersed in water increased with increasing volume fraction. Their result was attributed to the formation of a percolated support structure that prevented sedimentation.

The sedimentation stability of MR fluids has been a continual problem in the development of MR fluid technology [29,30]. The combination of hollow, lighter weight CNTs with superparamagnetic [31] magnetite nanoparticles can lead to a unique MR fluid that does not suffer from sedimentation limitations. The improved stability may be realized through both the use of composite materials with lower mass densities as well as particle geometries such as elongated cylinders that form percolated networks. The success of these novel MR fluids, however is contingent upon the preservation of the field-dependent critical stress and modulus seen in conventional iron oxide and carbonyl iron based MR fluids [32–35].

Magnetorheological Fluids and Ferrofluids

Conventional MR fluids date back to their discovery in 1948 by Rabinow [36]. They followed as a natural magnetic analog to the electro-rheological fluid patented by Winslow [37] in 1947. Depending on the desired effect, the fluids are surfactant-stabilized suspensions of either dielectric, or paramagnetic micron sized particles, dispersed in a carrier liquid. Ferrofluids [31] are another family of magnetically active liquids, whose surfactant stabilized particle constituents are 10–20 nm in size, and consist of single domain, permanently magnetized magnetite. Consequently, the response of a ferrofluid to a magnetic field is markedly different from that of an MR fluid [31].

MR fluids consisting of 1 μm carbonyl iron particles, at 30% volume fraction, have a maximum critical stress in the range of 10–100 kPa for applied induction fields near 0.2 T [32,34]. The zero-shear-rate viscosity, which persists until the critical stress is surpassed, may exceed 1 MPa s. In contrast, the electro-rheological (ER) effect provides critical stresses typically no greater than 1 kPa, at fields near 1 kV/mm. This performance limitation is imposed by impurities within the carrier liquid, oxide layers on the dispersed particles, and the dielectric breakdown voltage of the ER suspension carrier fluid. Analogously, the MR effect is limited by the saturation magnetization of the constituent

magnetic material. Coating techniques similar to the surface decoration methods we have discussed above have also been used to overcome these ER limitations by creating a high dielectric constant suspension of urea-coated barium titanate oxalate nanoparticles, suspended in silicone oil. The resulting ER fluid exhibits an unprecedented 130 kPa yield stress without dielectric breakdown [38].

MR fluids show an apparent viscosity that is dependent on the applied magnetic field, shear stress, particle volume fraction, and carrier viscosity [35]. With the application of a magnetic field at values below the saturation value for the paramagnetic material, a magnetic dipole results according to

$$\vec{m} = \tfrac{4}{3}\pi a^3 \mu_0 \chi \vec{H} \tag{2}$$

where $\vec{m}$ is the particle polarization; a and χ are the particle diameter and dimensionless susceptibility, respectively; and μ_0 and H are the free space permeability and applied field, respectively [35]. The induced dipoles interact with one another to form particulate aggregates whose size grow with the square root of elapsed time (measured from the onset of the magnetic field) [39]. The particle aggregates grow into longer bundles, and eventually into threads extending along the magnetic field lines. Eventually, these threads coarsen due to lateral attraction and form crystalline pillars of magnetized particles [34,40]. The formation of aggregates is opposed by Brownian dispersion, and as such the potential for field induced aggregation versus Brownian dispersion can be expressed in terms of a governing dimensionless parameter, often referred to as a coupling coefficient

$$\lambda = \frac{\pi(\mu_0 \chi H)^2 a^3}{18 k_B T} \tag{3}$$

where the parameters T and k_B are the temperature and Boltzmann constants, respectively [35]. For the case $\lambda \gg 1$, aggregation is highly favored, and at $\lambda \ll 1$, dispersion is favored. The case of small λ is used as a design parameter for the creation of ferrofluids, or stable dispersions of superparamagnetic nanoparticles in organic and aqueous carriers [31], whereas $\lambda \gg 1$ commonly results in MR fluids [35]. Due to the presence of permanent magnetic material within ferrofluids, as opposed to the paramagnetic material typically found in MR fluids, the aggregation parameter for ferrofluids is calculated according to

$$\lambda = \frac{\mu_0 M_s H \pi a^3}{6 k_B T} \tag{4}$$

where $\mu_0 M_s$ is the remnant magnetization of the particle [31].

The reorganization of the MR fluid microstructure due to shearing comes via the interplay of hydrodynamic and magnetic forces. The ratio of these interactions within an MR fluid forms a second dimensionless parameter known as the Mason number [32,35,41] that governs the breakup of magnetic microstructure due to shear

$$\mathrm{Ma} = \frac{9\sigma}{2(\mu_0 \chi H)^2} \tag{5}$$

where the parameter σ is the applied shear stress. Alternate governing dimensionless parameters include a Péclet number (dimensionless time) formed by the ratio of shear rate to the Brownian diffusion time as well as the particle volume fraction. The Mason number (Eq. (5)), Péclet number, and coupling coefficient (Eqs. (3) and (4)) are interrelated via $\mathrm{Pe} \sim \mathrm{Ma} \times \lambda$. An analogous ferrofluidic Mason number can be constructed by the ratio of the applicable Peclet and aggregation parameters. In contrast to MR fluids, the field-independent rheological properties of ferrofluids reduce the utility of a ferrofluidic Mason number.

At low applied fields, where saturation effects are completely absent, the Maxwell magnetostatic stress accurately predicts that the yield stress σ_c within MR fluids is proportional to the square of the applied magnetic field [33]. As the field intensity is increased such that saturation begins to occur at the surface of the dipolar particles, the critical stress (σ_c) transitions to a weaker dependence on the applied field, and the elastic modulus (G) grows linearly with the applied field. Ginder et al. [33] were able to model this saturation effect and found analytical models for the critical stress and elastic modulus that accurately predicted the data for carbonyl iron MR fluids [33,42]

$$\sigma_c = \sqrt{6}\phi \mu_0 M_s^{1/2} H^{3/2} \tag{6}$$

$$G = 3\phi \mu_0 M_s H \tag{7}$$

where ϕ is the volume fraction. This saturation effect is amplified by the increased field density within the small gap between particles undergoing aggregation. At still higher fields that exceed the physical saturation magnetization of the magnetic material, the response becomes field independent and limited only by the saturation of the material and particle volume fraction

$$\sigma_c^{\mathrm{sat}} = 0.086 \phi \mu_0 M_s^2 \tag{8}$$

$$G^{\mathrm{sat}} = 0.3 \phi \mu_0 M_s^2 \tag{9}$$

In stark contrast to the performance of MR fluids, ferrofluids do not display a dramatic change in viscosity as a function of applied field [43]. There is a marginal change in fluid viscosity at very small shear rates with an applied field, but at high shear rates or strong applied fields, the apparent viscosity does not change. Moreover, an exceedingly small (if any) critical stress exists for the ferrofluid, irrespective of the applied field [31]. This difference in response between these two magnetically-active fluids results from the typical magnitudes of the λ parameter previously defined in Eqs. (3) and (4) for MR and ferrofluids, respectively; for $\lambda \ll 1$, as is the case with ferrofluids, persistent filamentous or tertiary aggregates cannot form even in strong magnetic fields. In the absence of such a microstructure, the ferrofluid does not exhibit a critical stress induced by a magnetic field [31]. A field dependent viscosity is observed in ferrofluids, but is attributed to the torque of a rotating magnetic field on the nanoparticles themselves [44]. Represented as an unsymmetric stress tensor within the continuum description of the ferrofluid, so called negative or zero fluid viscosities can be observed, and are a result of the rotating magnetic field [45,46]. In the absence of a magnetic field, the viscosity shows some shear thinning at high shear rates. The apparent viscosity is generally considered to be volume fraction dependent according to the Einstein relation in the dilute suspension limit [31]

$$\frac{\eta}{\eta_0} = 1 + \frac{5}{2}\phi \tag{10}$$

where η_0 is the nominal carrier viscosity, and η is the apparent viscosity of the suspension. Higher order terms can be included to account for volume fractions beyond the dilute limit [31]. Whereas MR fluids typically have volume fractions exceeding 30%, commercial ferrofluids do not extend beyond 10%.

Combined MR and Ferrofluids

Several approaches have been taken to improve the magnitude and speed of MR fluid response [29,47]. Of note are methods for increasing the field-on viscosity to attain a more solid-like response below the critical stress [48], as well as methods for decreasing the response time, or lag between fluctuating field and particle tracking [49], and finally increasing the critical stress via reducing the limitations imposed by magnetic saturation [50]. These methods tend to employ mixtures of both nano- and micro-sized magnetic material, which often has the additional benefit of increasing sedimentation stability [49–51].

Popplewell et al. [48] explored inverse MR fluids in 1995 to achieve some of these improvements. A commercial ferrofluid was used as the carrier liquid, with a suspension of 1 μm glass beads. It was found that application of a magnetic field induced

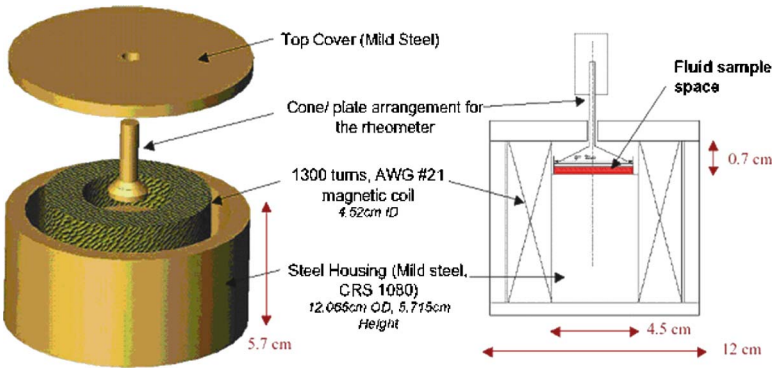

Fig. 6 Custom designed MR fixture for AR2000 rheometer

the formation of rudimentary glass bead columnar structures, and a typical MR response ensued, albeit with reduced critical stress. For bead volume fractions at 60%, and 36 mT induction field, the critical stress was about $\sigma_c \sim 20$ Pa, with an ensuing viscosity of 0.4 Pa s. Experiments were repeated with aluminum and iron parallel plates, and the iron geometry was found to produce a greater divergence in the zero shear rate viscosity. It was proposed that the lack of magnetic attraction between the aluminum geometry and ferrofluid provided a mechanism for slip and hence a reduction in the zero-shear rate viscosity. Owing to the paramagnetic nature of both the ferrofluid and iron, and the diamagnetic nature of aluminum, the ferrofluid magnetically adheres to the iron plate, and provides a more accurate measurement of the viscoplastic solid-like creep response below yield.

The limitations due to saturation and sedimentation were both explored by Chin et al. [50] in 2001. Building on prior work by Phule and Ginder [52] and Chen et al. [53], MR fluids comprised of micron sized carbonyl particles, interspersed with cylindrical nanoparticles of Co–γ–Fe_2O_3 and CrO_2, were created and shown to have a dramatically increased sedimentation stability and saturation critical stress. The critical stress enhancement was found to be a strong function of applied magnetic field, with an increase of 30% in a 64 mT field, versus less than 5% for a 16 mT field. This enhancement phenomenon was attributed to a shielding effect owing to the greater saturation magnetization found within cobalt materials as compared to carbonyl iron.

As was shown by Ginder et al. [33], saturation begins to limit the MR effect once the MR particles begin to experience localized saturation due to the increased field density within the thin gap between magnetic particles. By interspersing the gap with nanoparticles of higher magnetic saturation (cobalt materials can have nearly double the saturation of purely ferromagnetic species), the increasing field density can be distributed between MR particles and cobalt particles, where the greater saturation of the cobalt can shield the MR particles from reaching saturation. This shielding effect proposed by Ginder is less pronounced at lower fields, where neither the nanoparticles nor MR particles are near saturation. However, as the field strength increases, the saturation mitigated by the nanoparticles results in a greater interaction between MR particles, and hence stronger columnar structures and increased critical stress.

Based purely on nanoparticle MR fluids have also been explored independently by Kormann et al. [49]. Ferrite nanoparticle suspensions of roughly 30 nm diameter, and 60% mass fraction, were shown to behave as MR fluids. This is in stark contrast to ferrofluids with particle sizes only half the diameter, and volume fractions less than a sixth that value. At zero applied field there was only a small critical stress resulting from a percolated network, but as the field was increased to 0.4 T, the critical stress rose almost to $\sigma_c \sim 4000$ Pa. The direction of the applied magnetic field in 100 Hz AC experiments was not observed to affect the critical stress, which suggests that the switching speed of the nano-MR fluid is less than 5 ms, and there was no lag between the AC induction field and particle tracking of that field.

Poddar et al. [51] provide a complete comparison of conventional (micron sized), nanoparticle, and hybrid particle MR fluids. The essential results are that MR fluids with micron sized particles exhibit superior critical stress, but poor sedimentation stability. Conversely, nano-MR fluids are found to have a much smaller critical stress, but much improved sedimentation stability. Hybrid systems offer a mix of both desirable qualities, where the actual performance may be tuned via the use of appropriate materials and sizes for the micro- and nanoparticles. The performance of an MR fluid formed by dispersion of our own magnetite/CNT composite in silicon oil differs from both the traditional MR and ferrofluid responses.

Magnetorheology of Novel Ferrofluids–CNT (FFCNT) Particle Suspensions

The ferrofluid–CNT (FFCNT) composite was dispersed in silicon oil (100 cSt PDMS oil, siloxane terminated, Gelest Inc., PA) at 5%, 10%, and 20% w/w fractions. Creep tests were performed in a parallel plate geometry, with a 40 mm anodized steel rotating plate, on an AR2000N rheometer (TA Instruments) (see Fig. 6). A custom designed MR fixture was employed to produce a uniform magnetic field normal to the sample [54].

Several creep experiments at constant shear stress were performed for each of three different stresses and volume fractions, and four different induction field strengths.

After each experiment, the sample was examined to ensure that the particles had not settled out of the suspension. The experiments were all conducted at 25°C, and maintained by a Peltier element below the MR fixture and a small fan that was used to intermittently cool the induction field coils after prolonged use. Figure 7 shows a consistent viscosity between samples within the field off regions. As expected, the rate of strain changes for each sample as a function of applied induction field, with the highest field strength resulting in the most diminished strain rate. Once the field is removed, the strain rate returns to its prefield value, regardless of the applied field intensity. These experiments were also repeated with other volume fractions of FFCNT composite. Figure 8 shows the viscosity shift as a function of increasing volume fractions. The greatest strain rate is observed at the lowest volume fraction, as is expected. The shift in zero field strain rate also appears to vary linearly with increasing volume fraction.

The shear rates for these creep experiments can be determined and used to evaluate the steady-state shear viscosity $\eta(\varphi, B, \sigma)$ as shown in Figs. 9–11. Apparently irrespective of applied field or particle mass fraction, these figures show that the FFCNT composite exhibits a critical stress between 20 Pa and 30 Pa. As the stress is progressively decreased the viscosity diverges and the fluids become increasingly solid-like. Continued shear thinning, albeit at a lesser rate, is expected as the shear stress increases,

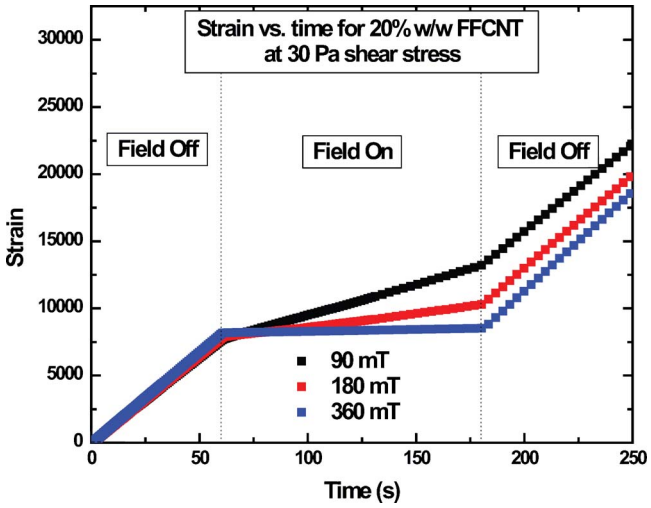

Fig. 7 Strain versus time for 20% w/w FFCNT, at 30 Pa shear stress, and three different induction fields

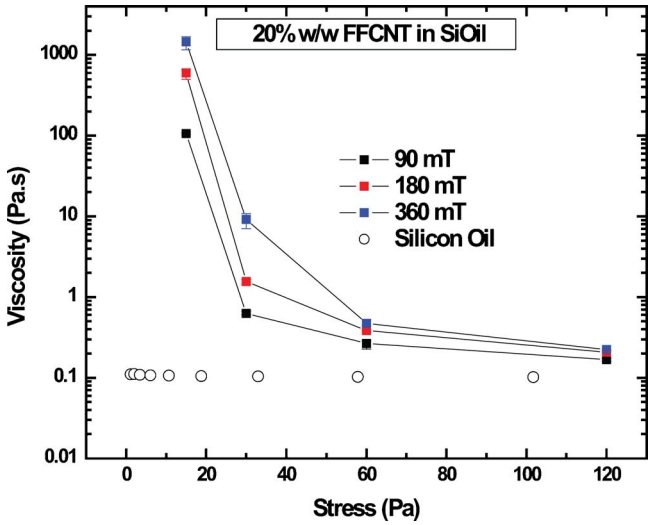

Fig. 9 Viscosity versus stress for 20% FFCNT at three induction fields

until the carrier viscosity is ultimately attained. As evidenced by the data, the rate of approach to this minimum is a function of both applied field and mass fraction. The 5% fraction reached the carrier viscosity (0.1 Pa s) by 60 Pa for all field strengths. The 20% and 10% samples exhibit a more gradual asymptotic approach at stresses $\sigma > 60$ Pa. Beyond 60 Pa, for all mass fractions, and applied induction fields, the test samples approached an infinite shear viscosity nearly equivalent to the carrier viscosity.

To model our CNT/Fe_3O_4 composite, it is assumed that the magnetic material lies within an external cylindrical coating of thickness ε, and is composed of randomly oriented superparamagnetic particles. This formation is a unique departure from the conventional carbonyl iron MR fluid particle, because the material composition allows for self-interaction in the absence of an applied external magnetic field. As such, the FFCNT may be considered to possess a combination of ferrofluid and MR particle properties. Due to the magnetic character of the hybrid, the aggregation parameter for our composite is likely to follow the ferrofluids model, as developed by Rosensweig [31], with an adjustment for the cylindrical shell geometry [35]. The greatest possible self-interaction field between two FFCNT cylinders would be 0.56 T, in the limit of favorable alignment of the superparamagnetic particles whose remnance magnetization is 0.56 T. Equation (4), which gives the aggregate parameter for ferrofluids can be modified for a cylindrical superparamagnetic shell of thickness ε, tube radius a, and composite length L and becomes

$$\lambda_m = \frac{\mu_0 MH[(\varepsilon + a)^2 - a^2]L\pi}{12k_B T\left(\ln\left(\frac{L}{2\varepsilon + 2a}\right) - 0.8\right)} \tag{11}$$

Calculating the value of this parameter for our magnetite–CNT composite gives $\lambda \cong 630$ and the self-interaction potential in the absence of external fields is therefore much closer to that seen in conventional MR fluids during actuation by an applied field. Based on this calculation, magnetic aggregation in the absence of an external field could be a partial explanation for the existence of micron-sized cylinders composed of multiple FFCNT threads. In MR fluids, $\lambda \gg 1$ leads to spontaneous agglomeration and sample-spanning structures upon application of an external field, and this leads to solidification of the entire fluid volume. In contrast,

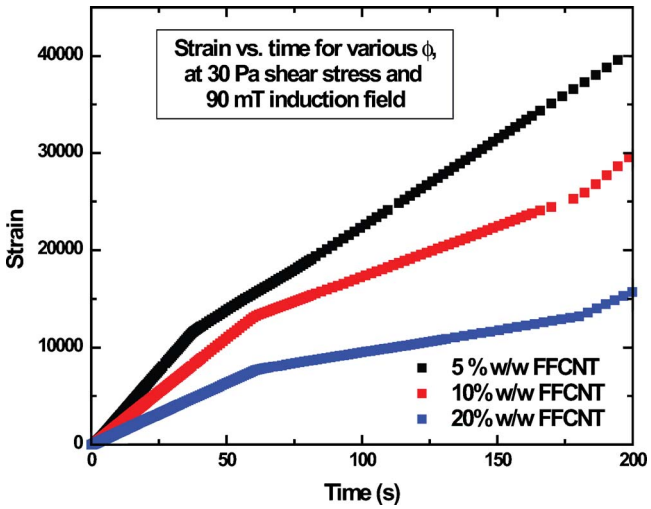

Fig. 8 Strain versus time for a 30 Pa shear stress and 90 mT induction field, at thee different mass fractions

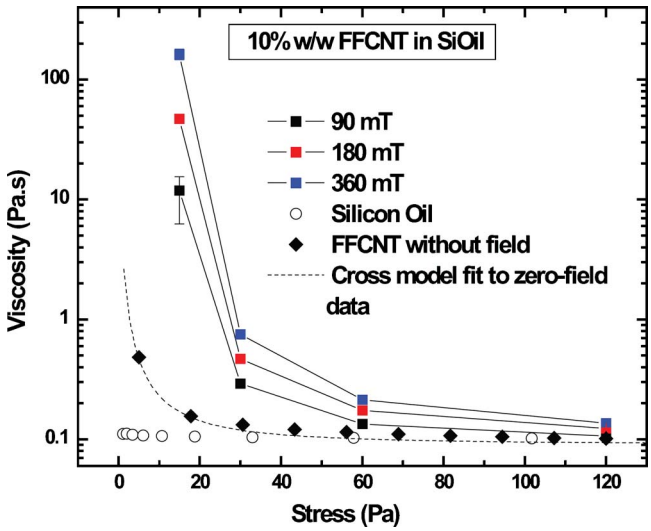

Fig. 10 Viscosity versus stress for 10% FFCNT at four different field strengths, with a Cross model fitting to the zero field data

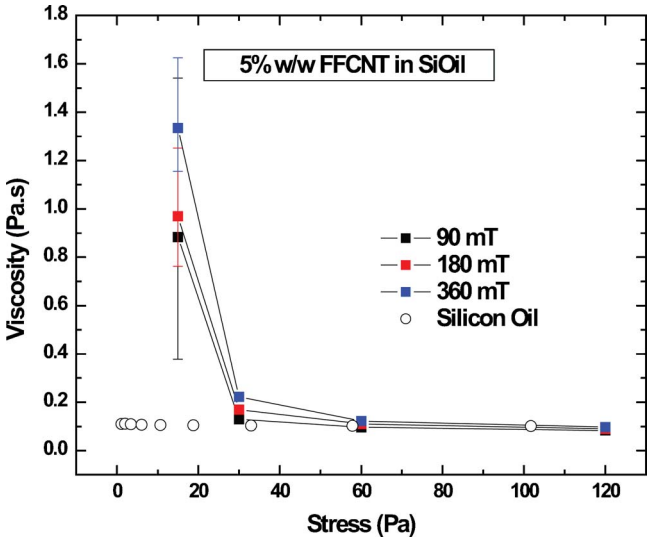

Fig. 11 Viscosity versus stress for 5% FFCNT at three induction fields

FFCNT aggregation induced by self-interaction appears to terminate after the combination of a sufficient number of individual threads.

The response to the imposed fields and shear stresses can also be quantified by considering an appropriate Mason number for each experimental data point. The Mason number as defined in Eq. (6) is not correctly formulated for a field responsive fluid composed of cylindrical, superparamagnetic components such as these FFCNT composites. Relying upon the relationship between Péclet and Mason numbers, and the coupling coefficient as defined in Eq. (11), a modified Mason number better suited for the FFCNT can be calculated in the form

$$\mathrm{Ma} = \frac{3\sigma(2\varepsilon + 2a)^2 \ln\left[\left(\frac{L}{2\varepsilon + 2a}\right) - 0.8\right]}{\mu_0 MH[(\varepsilon + a)^2 - a^2]} \tag{12}$$

Equation (12) demonstrates the appropriate interplay of hydrodynamic forces and those arising from the applied magnetic field, modified for the cylindrical geometry and superparamagnetic material. The calculated Mason number for these flows varies from 0.29 for a shear stress of 120 Pa and an induction field of 90 mT, to 0.009 for $\sigma = 15$ Pa and $\mu_0 H = 360$ mT. These values represent the two extremes in the range of Mason numbers for the experiments shown in Figs. 9–11. As expected, the highest values coincide with a Newtonian fluid-like response as observed when the fluid approaches an infinite shear-rate viscosity, and the lowest values coincide with the viscoplastic response observed at low shear stresses.

The fluid viscosities both below and above the critical stress, show a significant dependency on the magnitude of applied field and particle mass fraction. Likewise, the rate of shear thinning in the critical stress zone varies by orders of magnitude between different mass fractions.

The shear thinning behavior of CNT dispersions was also studied by Yang et al. [55]. Critical stresses for CNT volume fraction samples ranging from 0.04% to 0.42%, dispersed in low viscosity (4–6 cSt) poly-olefins, ranged from 0.04 Pa to 0.13 Pa, respectively. Flow experiments were performed, and the shear thinning behavior was fitted to the Cross model

$$\frac{\eta - \eta_\infty}{\eta_0 - \eta_\infty} = \frac{1}{1 + b\dot{\gamma}^P} \tag{13}$$

with values for P ranging from 0.560 to 0.772 in CNT suspensions. This expression also accurately describes the present zero-field rheological data as shown in Fig. 10. The range of data available preclude accurate determination of η_0, however the values of $b = 205$ and $P = 0.725$ are consistent with Ref. [55]. Further rheological characterization with our FFCNT suspensions demonstrated that a critical stress range still persists between 6 Pa and 12 Pa, even in the absence of a magnetic field.

Given the magnitude of the critical stress, and its persistence from 5% to 20% w/w, the critical stress appears to arise due to percolation of the cylindrical FFCNT composite. The range is amplified from the previously mentioned critical stress based on particle percolation due to the addition of superparamagnetic material that provides an additional strengthening interaction among the network elements. The lack of a stronger field dependence in the critical stress is expected for ferrofluids but not for a MR fluid in which the response is dominated by field-induced particle chaining. Conversely, the dependence of the zero shear-rate and infinite shear-rate viscosities on the induction field are expected for an MR fluid, but not found in a ferrofluid. It seems that this unique FFCNT composite exhibits attributes from both constituents, displaying a critical stress derived from a magnetically strengthened percolation network as well as field- and mass-fraction-dependent zero and infinite shear viscosities.

Final Remarks

We have reviewed the extensive literature on formulation techniques that exist to create magnetically-modified carbon nanotubes and their suitability for a wide variety of applications. Chemical and physical techniques have been utilized to introduce a diverse range of magnetic materials within CNTs, thus dramatically enhancing our ability to manipulate individual nanotubes, functionalize their surface, and induce self-assembly of complex nanostructures. Several of these techniques have been utilized to create novel MR fluids, and their viscometric properties have been demonstrated to enrich the range of rheological behavior that can be achieved with this class of non-Newtonian fluids. With the successful coupling of magnetic character to CNTs, it is possible to explore other interesting combinations of magnetism with unique CNT properties such as high electrical and thermal conductivity. Ongoing work includes combined magnetoelectric rheology, which capitalizes on the strong dielectrophoretic forces generated within the highly electrically conducting CNT, and the magnetic coating surrounding the CNT.

Acknowledgment

We would like to thank the Fannie and John Hertz Foundation for their support of this research, as well as the entire Non-Newtonian Fluids group within the Hatsopoulos Microfluids Laboratory at MIT.

Nomenclature

V_0 = sedimentation velocity (m/s)
ε = magnetic shell thickness (m)
L = aggregate length (m)
ρ_s = particle density (kg/m^3)
ρ_f = fluid density (kg/m^3)
g = gravitational acceleration (9.81 m/s^2)
a = particle, tube radius (m)
η = fluid viscosity (Pa s)
μ_0 = permeability of free space ($4\pi \times 10^{-7}$ N/A^2)
H = magnetic field (A/m)
χ = magnetic susceptibility
λ = ratio of magnetic aggregation force versus Brownian dispersion force

k_B = Boltzmann constant (1.38×10^{-23} J/K)
T = temperature (K)
Ma = Mason number, dimensionless ratio of hydrodynamic to magnetic forces
σ_c = critical yield stress (Pa)
σ = applied shear stress (Pa)
ϕ = particle volume fraction (v/v)
G = elastic modulus (Pa)

References

[1] Dresselhaus, M. S., Dresselhaus, G., and Jorio, A., 2004, "Unusual Properties and Structure of Carbon-Nanotubes," Annu. Rev. Mater. Res., **34**, pp. 247–278.
[2] Ajayan, P. M., Ebbesen, T. W., Ichihashi, T., Iijima, S., Tanigaki, K., and Hiura, H., 1993, "Opening Carbon Nanotubes With Oxygen and Implications for Filling," Nature (London), **362**(6420), pp. 522–525.
[3] Ajayan, P. M., and Iijima, S., 1993, "Capillarity-Induced Filling of Carbon Nanotubes," Nature (London), **361**(6410), pp. 333–334.
[4] Bao, J. C., Tie, C., Xu, Z., Suo, Z. Y., Zhou, Q. F., and Hong, J. M., 2002, "A Facile Method for Creating an Array of Metal-Filled Carbon Nanotubes," Adv. Mater., **14**(20), p. 1483.
[5] Leonhardt, A., Ritschel, A., Kozhuharova, R., Graff, A., Muhl, T., Huhle, R., Monch, I., Elefant, D., and Schneider, C. M., 2003, "Synthesis and Properties of Filled Carbon Nanotubes," Diamond Relat. Mater., **12**(3–7), pp. 790–793.
[6] Korneva, G., Ye, H. H., Gogotsi, Y., Halverson, D., Friedman, G., Bradley, J. C., and Kornev, K. G., 2005, "Carbon Nanotubes Loaded With Magnetic Particles," Nano Lett., **5**(5), pp. 879–884.
[7] Wu, H. Q., Wei, X. W., Shao, M. W., Gu, J. S., and Qu, M. Z., 2002, "Preparation of Fe–Ni Alloy Nanoparticles Inside Carbon Nanotubes via Wet Chemistry," J. Mater. Chem., **12**(6), pp. 1919–1921.
[8] Muhl, T., Elefant, D., Graff, A., Kozhuharova, R., Leonhardt, A., Monch, I., Ritschel, M., Simon, P., Groudeva-Zotova, S., and Schneider, C. M., 2003, "Magnetic Properties of Aligned Fe-Filled Carbon Nanotubes," J. Appl. Phys., **93**(10), pp. 7894–7896.
[9] Zhenyu Sun, Z. L., Wang, Y., Bursik, J., and Kadlecikov, M., 2005, "Fabrication and Characterization of Magnetic Carbon Nanotube Composites," J. Mater. Chem., **15**(42), pp. 4497–4501.
[10] Lafdi, K., Chin, A., Ali, N., and Despres, J. F., 1996, "Cobalt-Doped Carbon Nanotubes: Preparation, Texture, and Magnetic Properties," J. Appl. Phys., **79**(8), pp. 6007–6009.
[11] Rao, C. N. R., Sen, R., Satishkumar, B. C., and Govindaraj, A., 1998, "Large Aligned-Nanotube Bundles from Ferrocene Pyrolysis," Chem. Commun., **15**, pp. 1525–1526.
[12] Liu, S. W., Tang, X. H., Mastai, Y., Felner, I., and Gedanken, A., 2000, "Preparation and Characterization of Iron-Encapsulating Carbon Nanotubes and Nanoparticles," J. Mater. Chem., **10**(11), pp. 2502–2506.
[13] Liu, S. W., Zhu, J. J., Mastai, Y., Felner, I., and Gedanken, A., 2000, "Preparation and Characteristics of Carbon Nanotubes Filled With Cobalt," Chem. Mater., **12**(8), pp. 2205–2211.
[14] Banhart, F., Grobert, N., Terrones, M., Charlier, J. C., and Ajayan, P. M., 2001, "Metal Atoms in Carbon Nanotubes and Related Nanoparticles," Int. J. Mod. Phys. B, **15**(31), pp. 4037–4069.
[15] Zhang, X. X., Wen, G. H., Huang, S. M., Dai, L. M., Gao, R. P., and Wang, Z. L., 2001, "Magnetic Properties of Fe Nanoparticles Trapped at the Tips of the Aligned Carbon Nanotubes," J. Magn. Magn. Mater., **231**(1), pp. L9–L12.
[16] Georgakilas, V., Tzitzios, V., Gournis, D., and Petridis, D., 2005, "Attachment of Magnetic Nanoparticles on Carbon Nanotubes and Their Soluble Derivatives," Chem. Mater., **17**(7), pp. 1613–1617.
[17] Peng, D. L., Zhao, X., Inoue, S., Ando, Y., and Sumiyama, K., 2005, "Magnetic Properties of Fe Clusters Adhering to Single-Wall Carbon Nanotubes," J. Magn. Magn. Mater., **292**, pp. 143–149.
[18] Stoffelbach, F., Aqil, A., Jerome, C., Jerome, R., and Detrembleur, C., 2005, "An Easy and Economically Viable Route for the Decoration of Carbon Nanotubes by Magnetite Nanoparticles, and Their Orientation in a Magnetic Field," Chem. Commun., **36**, pp. 4532–4533.
[19] Choi, Y. C., Shin, Y. M., Lee, Y. H., Lee, B. S., Park, G. S., Choi, W. B., Lee, N. S., and Kim, J. M., 2000, "Controlling the Diameter, Growth Rate, and Density of Vertically Aligned Carbon Nanotubes Synthesized by Microwave Plasma-Enhanced Chemical Vapor Deposition," Appl. Phys. Lett., **76**(17), pp. 2367–2369.
[20] Bottini, M., Tautz, L., Huynh, H., Monosov, E., Bottini, N., Dawson, M. I., Bellucci, S., and Mustelin, T., 2005, "Covalent Decoration of Multi-Walled Carbon Nanotubes with Silica Nanoparticles," Chem. Commun. (Cambridge), **6**, pp. 758–760.
[21] Liu, J., Rinzler, A. G., Dai, H. J., Hafner, J. H., Bradley, R. K., Boul, P. J., Lu, A., Iverson, T., Shelimov, K., Huffman, C. B., Rodriguez-Macias, F., Shon, Y. S., Lee, T. R., Colbert, D. T., and Smalley, R. E., 1998, "Fullerene Pipes," Science, **280**(5367), pp. 1253–1256.
[22] Cao, H. Q., Zhu, M. F., and Li, Y. G., 2006, "Decoration of Carbon Nanotubes With Iron Oxide," J. Solid State Chem., **179**(4), pp. 1208–1213.
[23] Wu, H. Q., Cao, Y. J., Yuan, P. S., Xu, H. Y., and Wei, X. W., 2005, "Controlled Synthesis, Structure and Magnetic Properties of Alloy Nanoparticles Attached on Carbon Nanotubes," Chem. Phys. Lett., **406**(1–3), pp. 148–153.
[24] Gu, Y. and Li, D., 1999, "The Van Der Waals Interaction Between a Spherical Particle and Cylinder," J. Colloid Interface Sci., **217**(1), pp. 60–69.
[25] Kirsch, V. A., 2003, "Calculation of the Van Der Waals Force Between a Spherical Particle and an Infinite Cyinder," Adv. Colloid Interface Sci., **104**, pp. 311–324.
[26] Correa-Duarte, M. A., Grzelczak, M., Salgueirino-Maceira, V., Giersig, M., Liz-Marzan, L. M., Farle, M., Sierazdki, K., and Diaz, R., 2005, "Alignment of Carbon Nanotubes Under Low Magnetic Fields Through Attachment of Magnetic Nanoparticles," J. Phys. Chem. B, **109**(41), pp. 19060–19063.
[27] Pu, H. T., and Jiang, F. J., 2005, "Towards High Sedimentation Stability: Magnetorheological Fluids Based on CNT/Fe_3O_4 Nanocomposites," Nanotechnology, **16**(9), pp. 1486–1489.
[28] Razavian, S. M., Wenby, R. B., Fisher, T. C., and Meiselman, H. J., 1997, Biorheology, **34**, pp. 349–362.
[29] Klingenberg, D. J., 2001, "Magnetorheology, Applications and Challenges," AIChE J., **47**(2), pp. 246–249.
[30] Stanway, R., 2004, "Smart Fluids: Current and Future Developments," Mater. Sci. Technol., **20**(8), p. 931–939.
[31] Rosensweig, R. E., 1985, *Ferrohydrodynamics*, 2nd ed., Dover, Mineola, NY.
[32] Bossis, G., Lacis, S., Meunier, A., and Volkova, O., 2002, "Magnetorheological Fluids," J. Magn. Magn. Mater., **252**(1–3), pp. 224–228.
[33] Ginder, J. M., Davis, L. C., and Elie, L. D., 1996, "Rheology of Magnetorheological Fluids: Models and Measurements," Int. J. Mod. Phys. B, **10**(23–24), pp. 3293–3303.
[34] Tao, R., 2001, "Super-Strong Magnetorheological Fluids," J. Phys.: Condens. Matter, **13**(50), pp. R979–R999.
[35] Larson, R. G., 1999, *The Structure and Rheology of Complex Fluids*, Oxford University Press, New York.
[36] Rabinow, J., 1948, AIEE Trans., 67, p. 1308.
[37] Winslow, 1947, U.S. Patent No. 2,417,850.
[38] Wen, W. J., Huang, X. X., Yang, S. H., Lu, K. Q., and Sheng, P., 2003, "The Giant Electrorheological Effect in Suspensions of Nanoparticles," Nat. Mater., **2**(11), pp. 727–730.
[39] Promislow, J. H. E., Gast, A. P., and Fermigier, M., 1995, "Aggregation Kinetics of Paramagnetic Colloidal Particles," J. Chem. Phys., **102**(13), pp. 5492–5498.
[40] Fermigier, M., and Gast, A. P., 1992, "Structure Evolution in a Paramagnetic Latex Suspension," J. Colloid Interface Sci., **154**(2), pp. 522–539.
[41] Claracq, J., Sarrazin, J., and Montfort, J. P., 2004, "Viscoelastic Properties of Magnetorheological Fluids," Rheol. Acta, **43**(1), pp. 38–49.
[42] Ginder, J. M., 1998, "Behavior of Magnetorheological Fluids," MRS Bull., **23**(8), pp. 26–29.
[43] Rosensweig, R. E., Kaiser, R., and Miskolczy, G., 1969, "Viscosity of Magnetic Fluid in a Magnetic Field," J. Colloid Interface Sci., **29**(4), pp. 680–686.
[44] Rosensweig, R. E., 1996, "Negative Viscosity in a Magnetic Fluid," Science, **271**(5249), pp. 614–615.
[45] Rinaldi, C., and Zahn, M., 2002, "Effects of Spin Viscosity on Ferrofluid Duct Flow Profiles in Alternating and Rotating Magnetic Fields," J. Magn. Magn. Mater., **252**(1–3), pp. 172–175.
[46] Zahn, M., and Pioch, L. L., 1999, "Ferrofluid Flows in AC and Traveling Wave Magnetic Fields With Effective Positive, Zero or Negative Dynamic Viscosity," J. Magn. Magn. Mater., **201**, pp. 144–148.
[47] Kordonsky, W. I., Demchuk, S. A., 1996, "Additional Magnetic Dispersed Phase Improves the MR-Fluid Properties," J. Intell. Mater. Syst. Struct., **7**(5), pp. 522–525.
[48] Popplewell, J., Rosensweig, R. E., and Siller, J. K., 1995, "Magnetorheology of Ferrofluid Composites," J. Magn. Magn. Mater., **149**(1–2), pp. 53–56.
[49] Kormann, C., Laun, H. M., and Richter, H. J., 1996, "MR Fluids With Nano-Sized Magnetic Particles," Int. J. Mod. Phys. B, **10**(23–24), pp. 3167–3172.
[50] Chin, B. D., Park, J. H., Kwon, M. H., and Park, O. O., 2001, "Rheological Properties and Dispersion Stability of Magnetorheological (MR) Suspensions," Rheol. Acta, **40**(3), pp. 211–219.
[51] Poddar, P., Wilson, J. L., Srikanth, H., Yoo, J. H., Wereley, N. M., Kotha, S., Barghouty, L., and Radhakrishnan, R., 2004, "Nanocomposite Magneto-Rheological Fluids With Uniformly Dispersed Fe Nanoparticles," J. Nanosci. Nanotechnol., **4**(1–2), pp. 192–196.
[52] Phule, P. P., and Ginder, J., 1999, "Synthesis and Properties of Novel Magnetorheological Fluids Having Improved Stability and Redispersibility," Int. J. Mod. Phys. B, **12**, pp. 2019–2027.
[53] Chen, Z. Y., Tang, X., Zhang, G. C., Lin, Y., Ni, W., Zhu, Y. R., 1998, "A Novel Approach of Preparing Ultra Fine Magnetic Metallic Particles and Magnetorheology Measurements for Suspensions Containing These Particles," *Electro-rheological Fluids, Magneto-Rheological Suspensions and Their Applications*, M. Nakano and K. Koyama, eds., World Scientific, Singapore.
[54] Deshmoukh, S., 2006, Ph.D. thesis.
[55] Yang, Y., Grulke, E. A., Zhang, Z. G., and Wu, G. F., 2005, "Rheological Behavior of Carbon Nanotube and Graphite Nanoparticle Dispersions," J. Nanosci. Nanotechnol., **5**(4), pp. 571–579.

Oxygen Separation/Enrichment From Atmospheric Air Using Magnetizing Force

Yutaka Asako
e-mail: asako@ecomp.metro-u.ac.jp

Yohei Suzuki

Department of Mechanical Engineering,
Tokyo Metropolitan University,
1-1 Minami-Osawa, Hachioji,
Tokyo 192-0397, Japan

Oxygen is a paramagnetic gas and it has relatively high magnetic susceptibility. On the contrary, nitrogen is a diamagnetic gas and it has relatively low and negative magnetic susceptibility. This results in countermagnetizing forces acting on these gases. The characteristics of oxygen separation/enrichment from atmospheric air in a capsule and air flow in a parallel-plate duct using a magnetizing force were investigated numerically. The direct simulation Monte Carlo (DSMC) method was utilized to obtain distribution of oxygen concentration of air under a strong magnetic field gradient. The molecular movement was calculated by taking into account the magnetizing forces on the molecules. The computations were performed for a wide range of pressure and magnetic flux density gradient. Quantitative characteristics of oxygen separation/enrichment from atmospheric air under a strong magnetic field gradient and a parameter which governs this phenomenon are obtained from the simulation results. [DOI: 10.1115/1.2436584]

Keywords: oxygen separation, enrichment, magnetizing force, paramagnetic gas

Introduction

A fuel-pure oxygen fired system is expected to reduce the generation of the nitric oxide. Pure oxygen or oxygen enriched air is also expected to increase an efficiency of a fuel cell system. The needs of pure oxygen or oxygen enriched air will increase in many engineering fields.

The magnetizing force acts on both paramagnetic and diamagnetic materials under a strong magnetic field gradient. Paramagnetic materials are attracted to a direction of high magnetic flux density like iron sands [1]. Oxygen is a paramagnetic gas and it has relatively high magnetic susceptibility. On the other hand, nitrogen is diamagnetic and it has relatively low and negative magnetic susceptibility. This results in a countermagnetizing force that acts on these gases. Pauling et al. [2] employed this force to develop an oxygen analyzer. Recently, superconducting magnets have been developed and strong magnetic fields can be easily deployed.

Many interesting phenomena for gas convection under a strong magnetic field have been reported. For example, Kaneda et al. [3] reported numerical and experimental results for magnetic induced air convection in a cubical enclosure under a strong magnetic field gradient.

Recently, many patents concerned with oxygen separation/enrichment from atmospheric air using a strong magnet had been applied (e.g., Refs. [4,5]). However, quantitative data of this technique are not in the open. Therefore, it was impossible to assess the feasibility of this technique. This is the motivation of the present study. The oxygen separation/enrichment from atmospheric air in a small capsule and air flow in a parallel-plate duct under a strong magnetic field gradient were investigated numerically. The direct simulation Monte Carlo (DSMC) method was utilized to obtain distribution of oxygen concentration of air in a capsule and air flow in a duct under a strong magnetic field gradient. The molecular movement was calculated by taking into consideration the magnetizing force on the molecules. The computations were performed for a wide range of pressure, magnetic flux density gradient, and the capsule height or the duct height. Quantitative characteristics of oxygen separation/enrichment from atmospheric air under a strong magnetic field gradient and a parameter which governs this phenomenon are obtained from the simulation results.

Magnetizing Force

The magnetizing force acting on a paramagnetic gas of unit volume can be expressed as [6]

$$\vec{f}_m = \frac{1}{2\mu_0}\rho\chi\vec{\nabla}B^2 \tag{1}$$

Dividing Eq. (1) by the number density, the magnetizing force which acts on a molecule, $\vec{f}_p$, is obtained as

$$\vec{f}_p = \frac{\vec{f}_m}{n} = \frac{M}{N_A}\frac{1}{2\mu_0}\chi\vec{\nabla}B^2 = m\frac{1}{2\mu_0}\chi\vec{\nabla}B^2 \tag{2}$$

A schematic diagram of the magnetizing force under a magnetic field that is generated by a permanent magnet is presented in Fig. 1. Note that the magnetizing force acts in the direction of gradient of B^2 and it does not coincide with the direction of the line of magnetic force.

The volumetric magnetic susceptibilities ($\rho\chi$) of representative gases at 1 atm and 0 °C are tabulated in Table 1. Nitrogen and hydrogen are diamagnetic gases and they have relatively low and negative magnetic susceptibility. Therefore, a molecule of nitrogen or hydrogen moves in counter direction to oxygen.

An acceleration of a molecule by the magnetizing force, $\vec{\alpha}$, is expressed as

$$\vec{\alpha} = \frac{\vec{f}_p}{m} = \frac{1}{2\mu_0}\chi\vec{\nabla}B^2 \tag{3}$$

Therefore, the location of a molecule of a paramagnetic gas under the magnetizing force deviates from the location of a molecule of a conventional gas, after a time interval of Δt. The deviation is expressed as

Contributed by the Fluids Engineering Division of ASME for publication in the JOURNAL OF FLUIDS ENGINEERING. Manuscript received April 13, 2006; final manuscript received October 3, 2006. Assoc. Editor: Dennis Siginer. Paper presented at the 2005 ASME International Mechanical Engineering Congress (IMECE2005), Orlando, FL, USA, November 5–11, 2005.

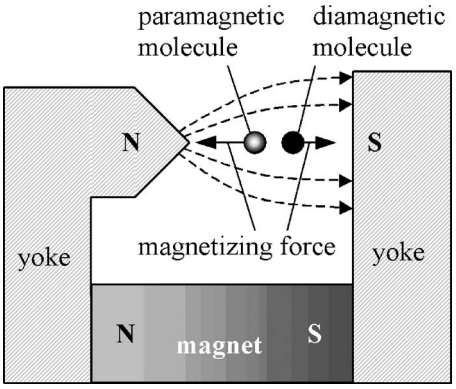

Fig. 1 Magnetizing force under magnetic field

$$\Delta\vec{x}' = \int_0^{\Delta t} \vec{\alpha} t \, dt = \tfrac{1}{2}\vec{\alpha}\Delta t^2 \tag{4}$$

The concentration of a paramagnetic gas can be obtained by the DSMC method [8,9], which simulates the molecular movement by taking into consideration, the deviation $\Delta\vec{x}'$.

Computation Methodology

Bird [8] introduced the DSMC method to simulate rarefied gases in the 1960s. A real gas is modeled through thousands or millions of simulated "molecules" in DSMC. DSMC simulations describe the time-dependent evolution of the molecules. The DSMC algorithm consists of four primary processes:

1. Index molecules into cells;
2. Molecular movements;
3. Simulate the collisions; and
4. Sample the flow field.

Prior to simulation, the domain of the field is divided into a number of cells that are utilized to sample the macroscopic properties. The mean free path is chosen for the cell size. The cell size effect will be discussed later. The number of real molecules of the gas are approximated by a lesser number of molecules called simulated molecules because of the current memory constraints as well as CPU processing time consideration. Simulated molecules are distributed in each cell randomly at the beginning. During the simulation, the four processes are uncoupled using a time step that is one-tenth of the mean collision time.

The molecular movement process is modeled deterministically and the simulation follows on a fixed spatial grid that defines the spatial cells. Molecules are allowed to move along their trajectory over a time interval Δt for a distance depending on their calculated speed at t. The distance traveled is calculated from the following

$$\Delta x = u_t \times \Delta t + \tfrac{1}{2}\alpha_x \Delta t^2$$

$$\Delta y = v_t \times \Delta t + \tfrac{1}{2}\alpha_y \Delta t^2 \tag{5}$$

Table 1 Volumetric magnetic susceptibility for gas at 1 atm and 0°C[a]

$H_2 = -2.23 \times 10^{-9}$
$N_2 = 6.8 \times 10^{-9}$
$O_2 = 1.91 \times 10^{-6}$

[a]See Ref. [7].

$$\Delta z = w_t \times \Delta t + \tfrac{1}{2}\alpha_z \Delta t^2$$

The velocity components for each molecule at $t = t + \Delta t$ are given as

$$u_{t+\Delta t} = u_t + \alpha_x \Delta t$$

$$v_{t+\Delta t} = v_t + \alpha_y \Delta t \tag{6}$$

$$w_{t+\Delta t} = w_t + \alpha_z \Delta t$$

When a molecule is moved, it either stays in the same cell, passes on to an adjacent cell, is reflected from the wall boundary, or collides with another molecule. The molecular movement is uncoupled from its collision phase through the use of some fraction of its mean time between collisions. However, the collision of molecules with the boundaries is still performed in the molecular movement phase. In this study, the diffuse reflection model was used for the calculation of wall reflection.

Modeling molecule–surface interactions requires applying the conservation laws to individual molecules. Although nitrogen and oxygen are diatomic molecules, the rotational energy is assumed to be negligible and the variable hard sphere (VHS) model was used to determine the collision. Diameters of 0.407 nm and 0.417 nm for oxygen and nitrogen molecules, respectively, were used for computations. The index parameters of $\omega = 0.77$ and 0.74 for oxygen and nitrogen molecules, respectively, were used. The difference of masses of oxygen and nitrogen molecules which affects velocities after the collision, was considered in the computation. The molecular weights of 32 and 28 for oxygen and nitrogen, respectively, were used for the calculation of velocities after collision. The indexing and tracking process is the prerequisite for modeling collisions and sampling the flow field. Molecular collision is a probabilistic process that sets DSMC apart from deterministic simulation methods such as molecular dynamics. The "time counter method" was used for the calculation of molecular collision.

The final process is sampling the macroscopic properties. The spatial coordinates and velocity components of molecules in a particular cell are used to calculate macroscopic pressure and temperature at the geometric center of the cell. Figure 2 illustrates the DSMC processes for steady-state flow simulation. More details of DSMC methodology are documented by Bird [9].

The self-diffusion coefficient of nitrogen gas was calculated to verify the code. The computational model to obtain the self-diffusion coefficient described in Bird [9] was used. The obtained self-diffusion coefficient at 273.15 K and 101.3 kPa is 1.57×10^{-5} m^2/s and this value is 1.5% higher than the measured value of 1.55×10^{-5} m^2/s [10]. A supplementary run was performed for oxygen enrichment in a capsule (No. 13 in Table 2) with cells of 1/2 mean free path to investigate the cell size effect. The mole fraction of oxygen in a capsule is plotted in Fig. 3 as a function of y/h. Both results coincide well and the cell size effect on the mole fraction of oxygen is relatively small.

Description of Problem

The oxygen separation/enrichment from atmospheric air in a capsule and air flow in a parallel-plate duct under a strong magnetic field gradient are investigated. Schematic diagrams of the problems under consideration are illustrated in Figs. 4(*a*) and 4(*b*), respectively. A capsule of height h in which air of p and T is filled, is placed in a magnetic field gradient (Fig. 4(*a*)). The behavior of air in the capsule is assumed to be one dimensional. A parallel plate duct whose height and length are h and ℓ, is placed in a magnetic field gradient. Air of p_{in}, T_{in}, and C_{in} inflows into the duct. The exit of the duct is connected to a vacuum chamber (Fig. 4(*b*)). For both cases, at time $t = 0$, the oxygen molecules are uniformly assigned in a whole region of the capsule or the duct with the mole fraction of C. It is also assumed that the magnetic flux density square is a linear function of y such that grad(B^2)

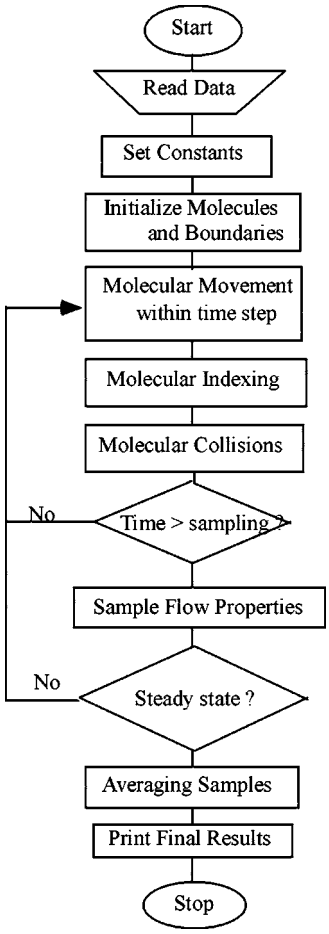

Fig. 2 Flow chart of direct simulation Monte Carlo

=constant. This assumption is valid when an area is small. Note the magnetizing force acts in only the y direction under the situation considered. The dashed arrows in the figure indicate the direction of grad(B^2) and they are not lines of the magnetic force.

The mole fraction of oxygen in a cell is defined by

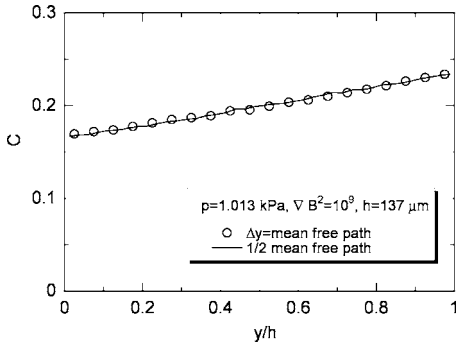

Fig. 3 Cell size effect on mole fraction of O_2

$$C = \frac{\text{number of oxygen molecules in a cell}}{\text{number of molecules in a cell}} \tag{7}$$

The DSMC simulation is applied to the gas separation inside the capsule and the duct. In this study, the magnetic susceptibility of nitrogen gas is neglected because it is 1/1000th of that of oxygen and only the magnetizing force of the oxygen is considered.

Results and Discussions

The computations for the capsule were conducted for the case of $T=300$ K and $C=0.2$. The computational parameters are tabulated in Table 2. Corresponding values of Kn(=λ/h), $\vec{\nabla}B^2/\mathrm{Kn}$, $\vec{\nabla}B^2/p$, and $\vec{\nabla}B^2/(p\,\mathrm{Kn})$ calculated from the computational parameters, are also tabulated in the table. The computations for the duct were conducted for the case of $\ell/h=4$, $T_{in}=300$ K, and $C_{in}=0.2$. In the actual computations, the mass flux at the inlet was adjusted in such a way that the inlet pressure p_{in} meets the specified pressure. The computational parameters are tabulated in Table 3. Corresponding values of Kn_{in}, $\vec{\nabla}B^2/\mathrm{Kn}_{in}$, $\vec{\nabla}B^2/p_{in}$, and $\vec{\nabla}B^2/(p_{in}\,\mathrm{Kn}_{in})$ calculated from the computational parameters, are also tabulated in the table. Note that Kn_{in} is the Knudsen number at the inlet.

Mole Fraction, Temperature, and Pressure Distribution. Contour plots of the mole fraction of oxygen, temperature, pressure, and velocity vectors for the flow in the duct of h

Table 2 Computational parameters for a capsule

Run No.	p (kPa)	T (K)	h (μm)	$\vec{\nabla}B^2$ (T^2/m)	Number of cells	Kn	$\frac{\vec{\nabla}B^2}{\mathrm{Kn}}$ (T^2/m)	$\frac{\vec{\nabla}B^2}{p}$ (T^2/Pa m)	$\frac{\vec{\nabla}B^2}{p\,\mathrm{Kn}}$ (T^2/Pa m)
1	101.3		1.37	10^{10}	20	0.05	2×10^{11}	9.87×10^{4}	1.97×10^{6}
2	101.3		1.37	10^{11}	20	0.05	2×10^{12}	9.87×10^{5}	1.97×10^{7}
3	101.3		1.37	10^{12}	20	0.05	2×10^{13}	9.87×10^{6}	1.97×10^{8}
4	0.1013		1370	10^{8}	20	0.05	2×10^{9}	9.87×10^{5}	1.97×10^{7}
5	1.013		137	10^{8}	20	0.05	2×10^{9}	9.87×10^{4}	1.97×10^{6}
6	10.13		13.7	10^{8}	20	0.05	2×10^{9}	9.87×10^{3}	1.97×10^{5}
7	101.3		1.37	10^{8}	20	0.05	2×10^{9}	9.87×10^{2}	1.97×10^{4}
8	0.1013	300	340	10^{8}	5	0.2	5×10^{8}	9.87×10^{5}	4.94×10^{6}
9	0.1013		680	10^{8}	10	0.1	10^{9}	9.87×10^{5}	9.87×10^{6}
10	0.1013		1370	10^{8}	20	0.05	2×10^{9}	9.87×10^{5}	1.97×10^{7}
11	0.1013		2730	10^{8}	40	0.025	4×10^{9}	9.87×10^{5}	3.95×10^{7}
12	0.1013		1370	10^{8}	20	0.05	2×10^{9}	9.87×10^{5}	1.97×10^{7}
13	1.013		137	10^{9}	20	0.05	2×10^{10}	9.87×10^{5}	1.97×10^{7}
14	10.13		13.7	10^{10}	20	0.05	2×10^{11}	9.87×10^{5}	1.97×10^{7}
15	101.3		1.37	10^{11}	20	0.05	2×10^{12}	9.87×10^{5}	1.97×10^{7}

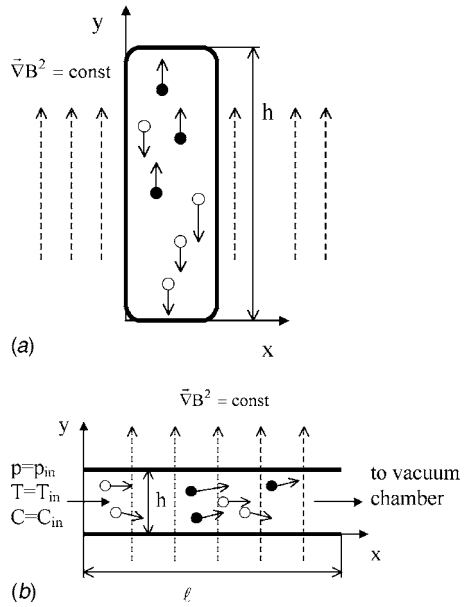

Fig. 4 Schematic diagrams of problems: (*a*) capsule; and (*b*) parallel-plate duct

$=1.37$ μm and $\ell=5.47$ μm are presented in Fig. 5. These are the results for the case of No. 2. The oxygen enrichment can be seen in the region of $x>h$.

Since the outlet of the duct is connected to the vacuum chamber, the air flow is accelerated along the duct. The air temperature drops near the outlet of the duct (Fig. 5(*b*)). This is due to the energy conversion from the thermal energy into the kinetic energy.

The pressure decreases along the duct. However, the inclination of the iso-pressure lines can be seen in Fig. 5(*c*). To find the physical reason for the inclination of the iso-pressure lines, the computation for the case of low magnetic flux density gradient, $\vec{\nabla}B^2=10^8$ T^2/m. The results are presented in Fig. 6. In this case, all the iso-pressure lines are almost vertical so the inclination of the iso-pressure lines in Fig. 5(*c*), which is the effect of the magnetizing force. Also, the pressure rise at the inlet of the duct can be seen in Fig. 5(*c*). The magnetizing force abruptly acts on molecules at the inlet in the analytical model. It seems that this is one of the reasons for this pressure rise.

Effect of $\vec{\nabla}B^2$. Three runs (Nos. 1–3) were performed to obtain the effect of $\vec{\nabla}B^2$ on the oxygen separation under the atmospheric pressure. The heights for three cases are identical. Contour plots of the mole fraction of oxygen in the duct (Nos. 1–3) are presented in Fig. 7. Note that the gray scale of each figure is not identical. The mole fractions of oxygen in the capsule and at the outlet of the duct are plotted in Figs. 8(*a*) and 8(*b*), respectively, where $\vec{\nabla}B^2$ is the curve parameter. From these figures, it can be concluded that higher oxygen enrichment is achieved when the magnetic flux density gradient $\vec{\nabla}B^2$ is high and the mole fractions of oxygen at the outlet of the duct almost coincide with that in the capsule.

Effect of Pressure. Four runs (Nos. 4–7) were performed to obtain the effect of pressure on the oxygen enrichment under the identical magnetic flux density gradient of $\vec{\nabla}B^2=10^8$. The capsule height and the duct height were chosen in such a way that the Knudsen number became identical. The number of cells was fixed at 20 for the capsule and 80×20 for the duct.

The mole fractions of oxygen in the capsule and at the outlet of the duct are plotted in Figs. 9(*a*) and 9(*b*), respectively. The mole fraction of oxygen at the outlet of the duct almost coincides with that in the capsule. The mole fractions of oxygen are almost uniform under $p=101.3$ kPa in the case of the capsule and $p_{in}=99.7$ kPa in the case of the duct. However, a slight gradient of the mole fraction of oxygen is observed in the capsule of $p=0.1013$ kPa and in the duct of $p_{in}=0.1003$ kPa. From these results, it can be concluded that there is a possibility of oxygen separation/enrichment from decompressed air under the low magnetic flux density gradient.

Although each of $\vec{\nabla}B^2$, Kn (or Kn_{in}), and $\vec{\nabla}B^2/\mathrm{Kn}$ (or $\vec{\nabla}B^2/\mathrm{Kn}_{in}$) are identical in these four runs (Nos. 4–7), different plots for these four runs are obtained. Therefore, $\vec{\nabla}B^2$, Kn (or Kn_{in}) and $\vec{\nabla}B^2/\mathrm{Kn}$ (or $\vec{\nabla}B^2/\mathrm{Kn}_{in}$), itself, are not the governing parameters of this phenomenon. Among these four runs, the values of $\vec{\nabla}B^2/p$ (or $\vec{\nabla}B^2/p_{in}$) are not identical. The oxygen enrich-

Table 3 Computational parameters for air flow in a duct

Run No.	p_{in} (kPa)	T_{in} (K)	h (μm)	ℓ/h	$\vec{\nabla}B^2$ (T^2/m)	Number of cells	Kn_{in}	$\frac{\vec{\nabla}B^2}{\mathrm{Kn}_{in}}$ (T^2/m)	$\frac{\vec{\nabla}B^2}{p_{in}}$ (T^2/Pa m)	$\frac{\vec{\nabla}B^2}{p_{in}\,\mathrm{Kn}_{in}}$ (T^2/Pa m)
1	99.6		1.37	4	10^{10}	80×20	0.05	2×10^{11}	10^5	2×10^6
2	100		1.37	4	10^{11}	80×20	0.05	2×10^{12}	10^6	2×10^7
3	110		1.37	4	10^{12}	80×20	0.05	2×10^{13}	9.12×10^6	1.82×10^8
4	0.100		1370	4	10^8	80×20	0.05	2×10^9	9.97×10^5	1.99×10^7
5	0.997		137	4	10^8	80×20	0.05	2×10^9	10^5	2×10^6
6	9.98		13.7	4	10^8	80×20	0.05	2×10^9	10^4	2×10^5
7	99.7		1.37	4	10^8	80×20	0.05	2×10^9	10^3	2×10^4
8	0.103		340	4	10^8	20×5	0.2	5×10^8	9.70×10^5	4.85×10^6
9	0.102		680	4	10^8	40×10	0.1	10^9	9.78×10^5	9.78×10^6
10	0.100	300	1370	4	10^8	80×20	0.05	2×10^9	9.97×10^5	1.99×10^7
11	0.107		2730	4	10^8	160×40	0.025	4×10^9	9.36×10^5	3.74×10^7
12	0.100		1370	4	10^8	80×20	0.05	2×10^9	9.97×10^5	1.99×10^7
13	1.00		137	4	10^9	80×20	0.05	2×10^{10}	9.98×10^5	2×10^7
14	10.0		13.7	4	10^{10}	80×20	0.05	2×10^{11}	9.97×10^5	1.99×10^7
15	100		1.37	4	10^{11}	80×20	0.05	2×10^{12}	9.97×10^5	1.99×10^7
16	0.100		1370	4	10^8	80×20	0.05	2×10^9	9.97×10^5	1.99×10^7
17	0.104		1370	10	10^8	200×20	0.05	2×10^9	9.66×10^5	1.93×10^7
18	0.107		2730	4	10^8	160×40	0.025	4×10^9	9.36×10^5	3.74×10^7
19	0.0988		2730	4	10^7	160×40	0.025	4×10^8	1.01×10^5	4.05×10^6

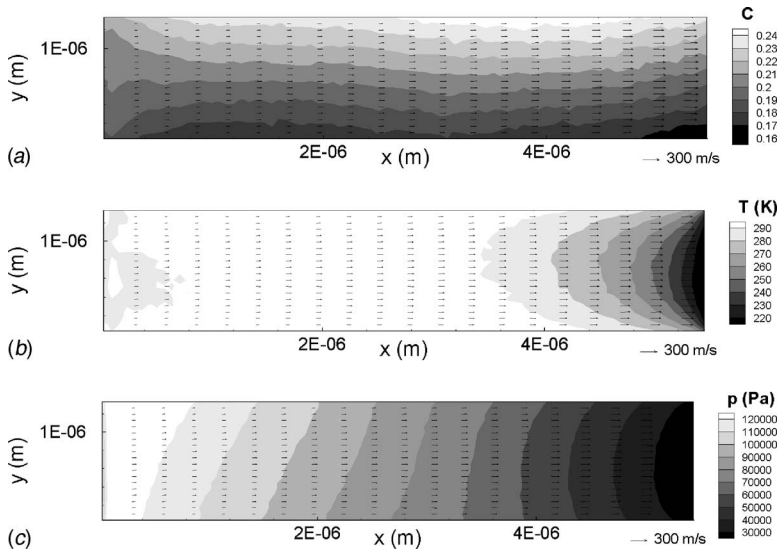

Fig. 5 Contour plots for No. 2: (*a*) mole fraction; (*b*) temperature; and (*c*) pressure

ment is observed with increasing $\vec{\nabla}B^2/p$ in the case of the capsule and with increasing $\vec{\nabla}B^2/p_{\text{in}}$ in the case of the duct.

Effect of Duct Height *h*. Four runs for $h=0.34$ mm, 0.68 mm, 1.37 mm, and 2.73 mm (Nos. 8–11) were performed to obtain the effect of the height on the mole fraction of oxygen. The duct length and height ratio is fixed at 4. The pressure in a capsule is fixed at 0.1013 kPa and the inlet pressure p_{in} of a duct is fixed at nearly 0.1 kPa. The gradient of the magnetic flux density $\vec{\nabla}B^2$ is fixed at 10^8 T^2/m for both cases. Computational parameters of these runs are identical with the exception of the height. The mole fractions of oxygen in the capsule and at the outlet of the duct are plotted in Figs. 10(*a*) and 10(*b*), respectively. A slight oxygen enrichment is observed when $h=0.34$ mm. However, the obvious oxygen enrichment is observed as increasing the height under the identical pressure and identical $\vec{\nabla}B^2$.

Although the values of $\vec{\nabla}B^2/p$ (or $\vec{\nabla}B^2/p_{\text{in}}$) are almost identical in these four runs, different plots for these four runs are observed. Therefore, $\vec{\nabla}B^2/p$ (or $\vec{\nabla}B^2/p_{\text{in}}$) itself is not the governing parameter of this phenomenon. Among these four runs, the values of $\vec{\nabla}B^2/\text{Kn}$ (or $\vec{\nabla}B^2/\text{Kn}_{\text{in}}$) are not identical. The oxygen enrichment is observed with increasing $\vec{\nabla}B^2/\text{Kn}$ (or $\vec{\nabla}B^2/\text{Kn}_{\text{in}}$).

Effect of $\vec{\nabla}B^2/(p\,\text{Kn})$. An additional four runs (Nos. 12–15) were also performed to obtain the effect of $\vec{\nabla}B^2/(p\,\text{Kn})$ (or $\vec{\nabla}B^2/(p_{\text{in}}\,\text{Kn}_{\text{in}})$) on the oxygen enrichment. The height was chosen in such a way that the Knudsen number became identical and also $\vec{\nabla}B^2$ was changed to maintain $\vec{\nabla}B^2/p$ (or $\vec{\nabla}B^2/p_{\text{in}}$) constant. The number of cells in the height direction was fixed at 20. Therefore, the values of $\vec{\nabla}B^2/(p\,\text{Kn})$ (or $\vec{\nabla}B^2/(p_{\text{in}}\,\text{Kn}_{\text{in}})$) for these four runs are almost identical. The mole fractions of oxygen in the capsule and at the outlet of the duct are plotted in Figs. 11(*a*) and 11(*b*), respectively. All the plots coincide with each other in each figure. This result indicates that $\vec{\nabla}B^2/(p\,\text{Kn})$ or $\vec{\nabla}B^2/(p_{\text{in}}\,\text{Kn}_{\text{in}})$ is one of the governing parameters of this phenomenon. A slight oxygen enrichment is observed in No. 8 of Fig. 10; therefore, the oxygen enrichment occurs when $\vec{\nabla}B^2/(p\,\text{Kn})>5\times10^6$ or $\vec{\nabla}B^2/(p_{\text{in}}\,\text{Kn}_{\text{in}})>5\times10^6$ $\text{T}^2/(\text{Pa m})$.

Here, the attention will turn to the order of $\vec{\nabla}B^2$. It is obvious that $\vec{\nabla}B^2$ is 0 under the uniform magnetic field. On the contrary, $\vec{\nabla}B^2$ takes a high value under a strong magnetic field gradient. It is well known that magnetic lines of force concentrate on a sharp edge. A strong magnetic field gradient can be obtained under a combination of a sharp edge and a flat surface, and those are pictured schematically in Fig. 1. A preliminary static magnetic field analysis was conducted to find the order of $\vec{\nabla}B^2$ by using the

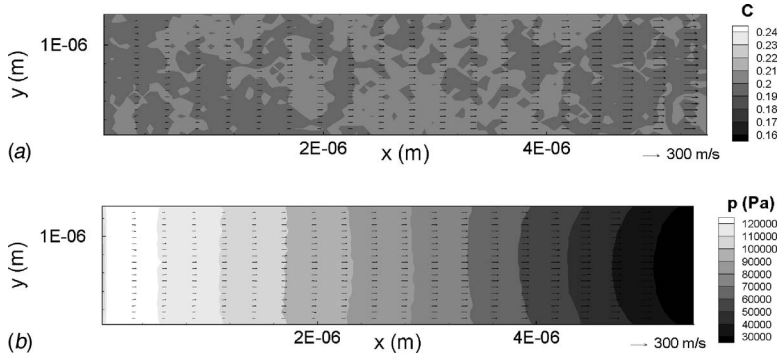

Fig. 6 Contour plots for $\vec{\nabla}B^2=10^8$ T^2/m: (*a*) mole fraction; and (*b*) pressure

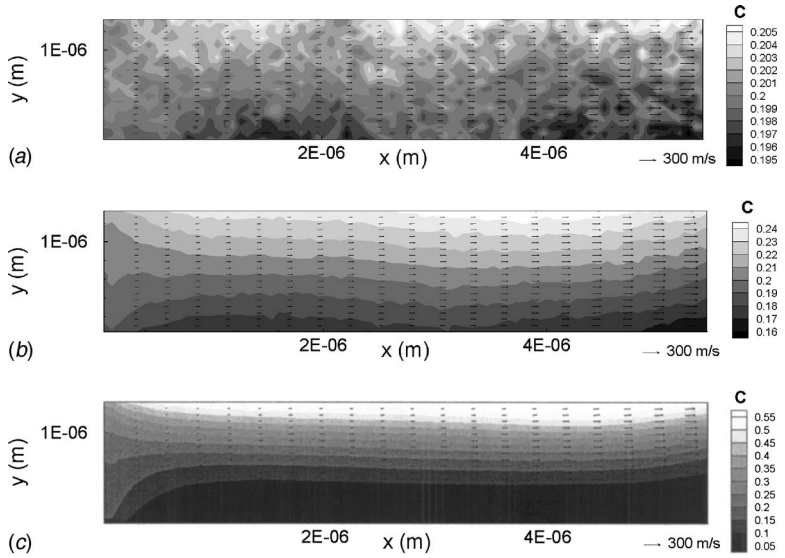

Fig. 7 Contour plots of mole fraction of O_2: (*a*) No. 1 ($\vec{\nabla}B^2=10^{10}$ T^2/m); (*b*) No. 2 ($\vec{\nabla}B^2=10^{11}$ T^2/m); and (*c*) No. 3 ($\vec{\nabla}B^2=10^{12}$ T^2/m)

magnetic moment scheme. $\vec{\nabla}B^2$ is about 10^5 T^2/m at the point which is 5 μm apart from the sharp edge when a permanent magnet of 1.5 T is used. $\vec{\nabla}B^2$ of 5×10^5 T^2/m is obtained under the same geometrical configuration, using a superconducting magnet of 20 T which is the highest level of the superconducting magnet at present. If a superconducting magnet of 100 T is developed or a geometrical configuration to obtain a strong magnetic field gradient is found, this technique becomes feasible.

Effect of Duct Length ℓ. An additional two runs for $\ell/h=4$ and 10 (Nos. 16 and 17) were performed to obtain the effect of the duct length on the oxygen enrichment. The height of both ducts is identical but only the duct length is different. Contour plots of the mole fraction of oxygen in the duct are plotted in Figs. 12(*a*) and 12(*b*). The mole fraction of oxygen at the duct outlet of both results coincide with each other. This concludes that the duct length of $\ell/h=4$ is enough to enrich the oxygen.

Under Low Gradient of Magnetic Density Flux $\vec{\nabla}B^2$. It is very useful if the oxygen separation/enrichment occurs under a low gradient of the magnetic flux density $\vec{\nabla}B^2$. To ensure this, the

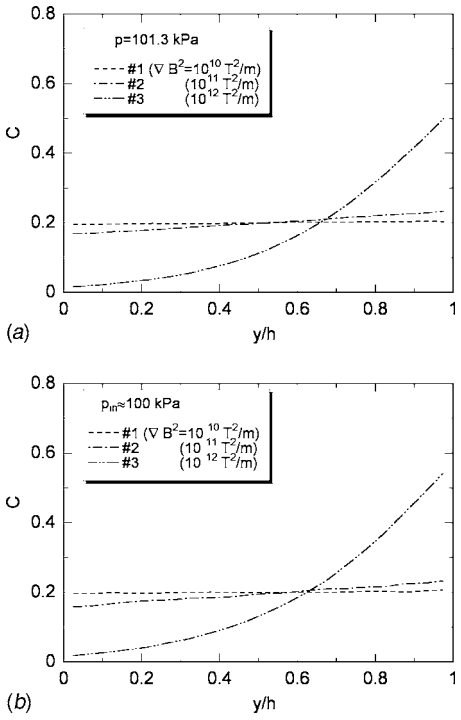

Fig. 8 Effect of $\vec{\nabla}B^2$ on mole fraction of O_2: (*a*) capsule; and (*b*) parallel-plate duct

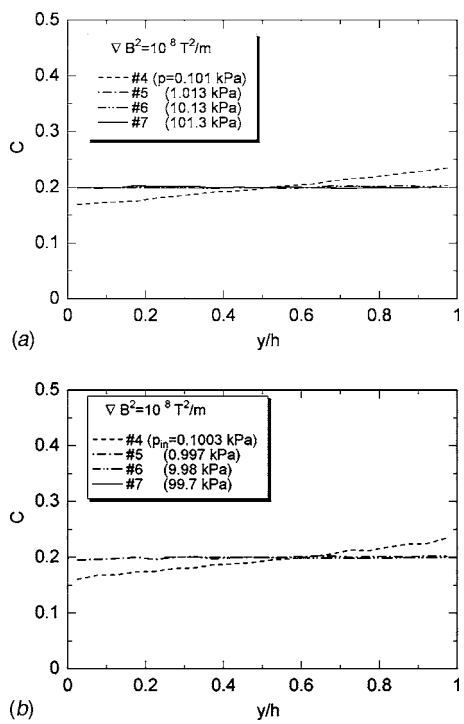

Fig. 9 Effect of pressure on mole fraction of O_2: (*a*) capsule; and (*b*) parallel-plate duct

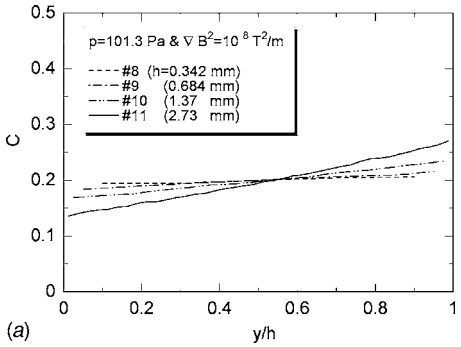

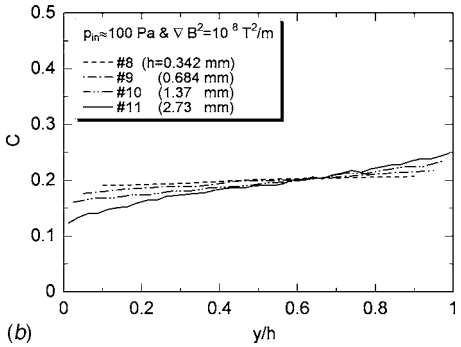

Fig. 10 Effect of h on mole fraction of O_2: (*a*) capsule; and (*b*) parallel-plate duct

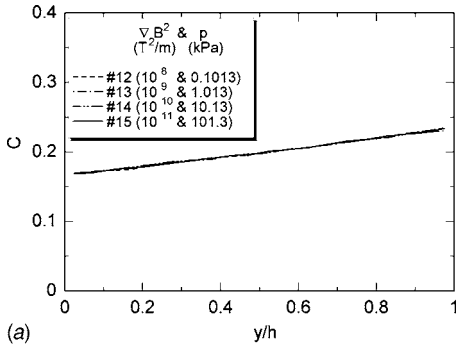

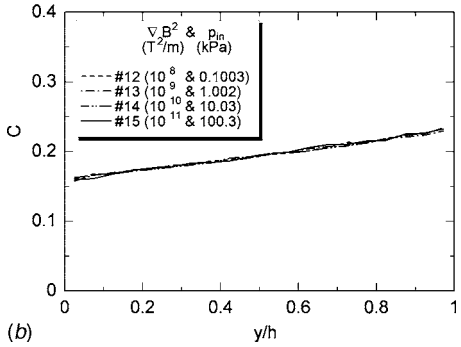

Fig. 11 Effect of $\vec{\nabla}B^2/(p\,\mathrm{Kn})$ on mole fraction of O_2: (*a*) capsule; and (*b*) parallel-plate duct

case of $\vec{\nabla}B^2=10^7\ \mathrm{T}^2/\mathrm{m}$ was examined. As mentioned above, the oxygen separation/enrichment occurs by increasing the parameter $\vec{\nabla}B^2/(p_{\mathrm{in}}\,\mathrm{Kn}_{\mathrm{in}})$. That is, the oxygen separation/enrichment occurs easier when the pressure is low and the duct height is large. The computations were conducted for, $p_{\mathrm{in}}\approx 0.1$ kPa and $h=2.73$ mm (Nos. 18 and 19). The contour plots of the mole fraction of oxygen are presented in Fig. 13. As shown in the figures, the slight oxygen separation/enrichment occurs under $\vec{\nabla}B^2=10^7\ \mathrm{T}^2/\mathrm{m}$. The

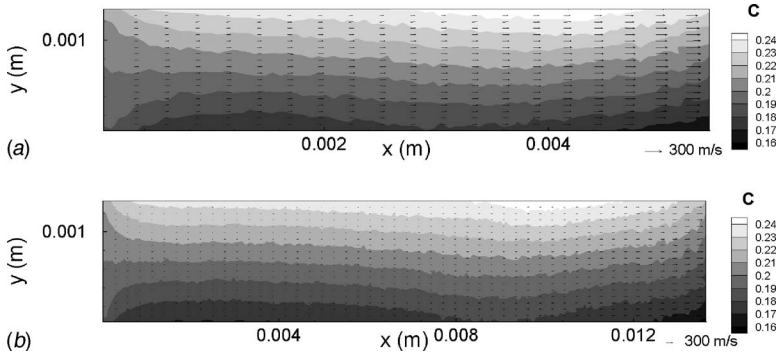

Fig. 12 Contour plots of mole fraction of O_2: (*a*) No. 16 ($\ell/h=4$); and (*b*) No. 17 ($\ell/h=10$)

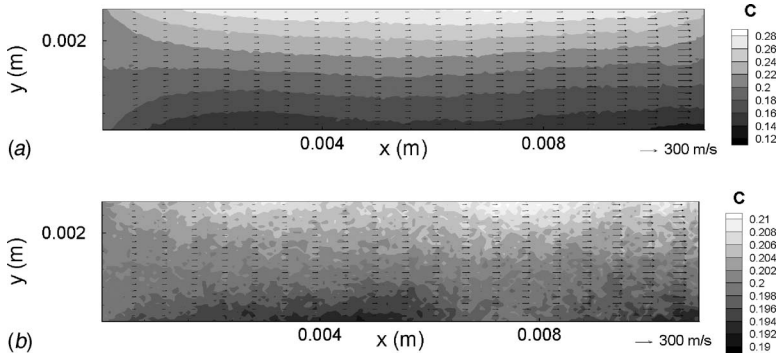

Fig. 13 Contour plot of mole fraction of O_2: (*a*) No. 18 ($\vec{\nabla}B^2=10^8\ \mathrm{T}^2/\mathrm{m}$); and (*b*) No. 19 ($\vec{\nabla}B^2=10^7\ \mathrm{T}^2/\mathrm{m}$)

vale of $\vec{\nabla}B^2/(p_{\text{in}}\,\text{Kn}_{\text{in}})$ for the case of No. 19 is 4×10^6 T^2/(Pa m). Therefore, the oxygen enrichment occurs when $\vec{\nabla}B^2/(p_{\text{in}}\,\text{Kn}_{\text{in}})>4\times10^6$ T^2/(Pa m).

Concluding Remarks

The DSMC method was utilized to obtain distribution of mole fraction of oxygen in a capsule and in a duct under a strong magnetic field gradient. The molecular movement was calculated by taking into consideration the magnetizing forces on the molecules. The computations were performed for a wide range of the pressure and magnetic flux density gradient. The simulation results showed that $\vec{\nabla}B^2/(p\,\text{Kn})$ is one of the governing parameters of this phenomenon and the oxygen enrichment occurs when $\vec{\nabla}B^2/(p\,\text{Kn})>4\times10^6$ or $\vec{\nabla}B^2/(p_{\text{in}}\,\text{Kn}_{\text{in}})>4\times10^6$ T^2/(Pa m) and there is a possibility of oxygen separation/enrichment from decompressed air under a strong magnetic field gradient if a superconducting magnet of 100 T is developed.

Nomenclature

$\vec{B}$ = magnetic flux density (T)
C = mole fraction of oxygen (−)
D = diffusion coefficient (m^2/s)
$\vec{f}_m$ = magnetizing force per unit volume (N/m^3)
$\vec{f}_p$ = magnetizing force on a molecule (N)
Kn = Knudsen number, $=\lambda/h$ (−)
h = capsule height or duct height (m)
ℓ = duct length (m)
M = molecular weight (kg/kmol)
m = mass of a molecule (kg)
N_A = Avogadro number 6.02×10^{26} (1/kmol)
n = number density (1/m^3)
Δt = time interval (s)
α = acceleration (m/s^2)
χ = magnetic susceptibility per unit mass (m^3/kg)
λ = mean free path (m)
μ_0 = magnetic permeability of vacuum $4\pi\times10^{-7}$ (H/m)
ρ = density (kg/m^3)
ω = VHS model index parameter (−)

Subscript

in = value at inlet

References

[1] Feynman, R. P., 1965, *Lectures of Physics III*, Addison–Wesly, Reading, MA.
[2] Pauling, L., Wood, R. E., and Sturdivant, J. H., 1946, "An Instrument for Determining of Partial Pressure of Oxygen in a Gas," J. Am. Chem. Soc., **68**, p. 795.
[3] Kaneda, M., Tagawa, T., and Ozoe, H., 2002, "Convection Induced by a Cusp-Shaped Magnetic Field for Air in a Cube Heated from Above and Cooled from Below," J. Heat Transfer, **124**, pp. 17–25.
[4] Toshiba Co., "Separation of Materials Having Different Magnetisms, Device Therefor and Thermal Power Generating System," JP Published patent 2000-15136,2001.
[5] Toyota Motor Co., "Gaseous Oxygen Supplying Device," JP Published patent, 2001-221111,2001.
[6] Kittel, C., 1966, *Introduction to Solid Physics*, 3rd ed., Wiley, New York.
[7] Dean, J. A., 1992, *Lange's Handbook of Chemistry*, 14th ed., McGraw-Hill, New York.
[8] Bird, G. A., 1976, *Molecular Gas Dynamics*, Oxford University Press, Oxford, UK.
[9] Bird, G. A., 1994, *Molecular Gas Dynamics and the Direct Simulation of Gas Flows*, Oxford University Press, Oxford, UK.
[10] Hewitt, G. F. et al., *International Encyclopedia of Heat & Mass Transfer*, CRC, New York.

Simulation of Fiber Suspensions—A Multiscale Approach

Krista Mäkipere
Laboratory of Computational Fluid & BioFluid Dynamics,
Lappeenranta University of Technology,
Lappeenranta, Finland

Piroz Zamankhan
School of Energy Engineering,
Power and Water University of Technology,
P.O. Box 16765-1719,
Tehran, Iran

The present effort is the development of a multiscale modeling, simulation methodology for investigating complex phenomena arising from flowing fiber suspensions. The present approach is capable of coupling behaviors from the Kolmogorov turbulence scale through the full-scale system in which a fiber suspension is flowing. Here the key aspect is adaptive hierarchical modeling. Numerical results are presented for which focus is on fiber floc formation and destruction by hydrodynamic forces in turbulent flows. Specific consideration was given to dynamic simulations of viscoelastic fibers in which the fluid flow is predicted by a method that is a hybrid between direct numerical simulations and large eddy simulation techniques and fluid fibrous structure interactions will be taken into account. Dynamics of simple fiber networks in a shearing flow of water in a channel flow illustrate that the shear-induced bending of the fiber network is enhanced near the walls. Fiber-fiber interaction in straight ducts is also investigated and results show that deformations would be expected during the collision when the surfaces of flocs will be at contact. Smaller velocity magnitudes of the separated fibers compare to the velocity before collision implies the occurrence of an inelastic collision. In addition because of separation of vortices, interference flows around two flocs become very complicated. The results obtained may elucidate the physics behind the breakup of a fiber floc, opening the possibility for developing a meaningful numerical model of the fiber flow at the continuum level where an Eulerian multiphase flow model can be developed for industrial use. [DOI: 10.1115/1.2567952]

Keywords: fiber suspension, multiscale modeling, direct numerical simulations, large eddy simulation, fluid fibrous structure interactions, floc strength

1 Introduction

Flocculation or aggregation of fibers is widely observed in the paper making industries [1]. In fact, strategies are required to achieve retention, drainage, and good formation uniformity while making papers. In papermaking, the word "flocs" usually refers to groups of fibers clumped together as illustrated schematically in Fig. 1.

Strong hydrodynamic forces, such as those of pressure screens, can be very effective in redispersal of flocs where shear forces may cause fibers to bend as depicted in Fig. 2. As the fibers straighten out, they may lock together again mechanically. Papermakers sometimes make the distinction between hard flocs and soft flocs [2]. Hard flocs, which are quite strong, are those formed by very-high-mass retention aid polymers. When broken, they are not able to form as strong flocs the next time. By contrast, moderate levels of shear readily break soft flocs and are completely reversible [2].

Factors causing soft flocs to form in a shearing flow include colloidal forces of attraction [3]. The specialists in papermaking investigate floc strength and floc size as a function of addition of chemicals and application of hydrodynamic shear. Their studies involve probing the mechanisms, such as charge effects, polymer bridging, and microparticle effects by which chemical additives work.

Many different forces contribute to the floc strength including those arise from the interlocking of elastically bent fibers [4]. Chaouche and Koch [5] suggested that the interlocking process might be characterized by $S^{\text{eff}}=E_Y I/\eta_0\dot{\gamma}l^4$, where no elastically interlocking can occur when $S^{\text{eff}}\gg 1$.

The factors affecting the magnitude of network-type floc strength are the fiber concentration and the aspect ratio, which is the ratio of fiber length to its diameter. Apparently, other effects of importance are the stiffness of the fibers and the coefficient of friction between the fibers [6]. Another parameter that effects on the flocculation process is viscosity of fluid [7,8], where the suspending liquid viscosity seems to enhance tendency of the fiber suspension towards uniformity. Attractive forces cause a significant increase in the specific viscosity. Somewhat perfect uniformity may be reached at consistencies where water alone would yield gross flocculation. Also it should be noted that variations of viscosity due to temperature of suspending liquid seem to have no significant influence on the floc size [9].

The fiber suspensions in the production line from wood to paper are subjected to many types of chemical and mechanical processes, in which the flow of the suspension is of vital importance. The flow of the suspension determines the degree of uniformity of the fibers through the processing, which in return affects the properties of the fiber suspension. In order to optimize the process, thorough knowledge of the suspension flow is necessary, both on the level of suspension, fiber networks and individual fibers. Knowledge of the fiber suspension behavior combined with numerical simulations provide an efficient design method for any unit operation in the papermaking process.

Flow modeling of fiber suspensions started as early as 1959 when Baines [10] presented the Navier-Stokes–based solution for the height of the water annulus, the existence of which had been determined by Head and Durst [11]. Myréen introduced the rheological modeling in [12]. In that paper, the rheology model is shown to work for both the Couette flow and the pipe flow on the

Contributed by the Fluids Engineering Division of ASME for publication in the JOURNAL OF FLUIDS ENGINEERING. Manuscript received August 17, 2006; final manuscript received August 18, 2006. Assoc. Editor: Dennis Siginer.

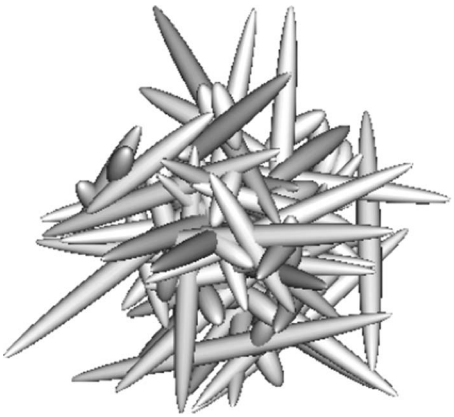

Fig. 1 A schematic of a group of fibers clumped together.

Durst [13] measurements. This was an important step, because he introduced a flow model that was not restricted to pipe flow, but could be applied in any other geometry. Huhtanen [14] applies the generalized Newtonian models to the flow of paper pulp suspensions, his data is the same as used by Hämäläinen [15]. He showed that the commercial flow simulation programs, in this case POLYFLOW, are able to model the plug flow region, and also the wall slip phenomenon. A vast literature exists focusing on viscoelastic nature of fiber-water suspensions. The viscoelastic properties of fiber suspensions were investigated by Damani et al. [16] for 2–13 % suspensions, and Swerin et al. [17] evaluated 3–8 % pulp suspensions. They investigated the loss and storage modulus for different straining frequencies and amplitudes. The maximum straining amplitude corresponded quite well with the yield stresses, as measured by Bennington et al. [4], but this is hardly surprising. For modeling purposes, viscoelastic properties have to be accounted for flowing fiber suspensions under high shear.

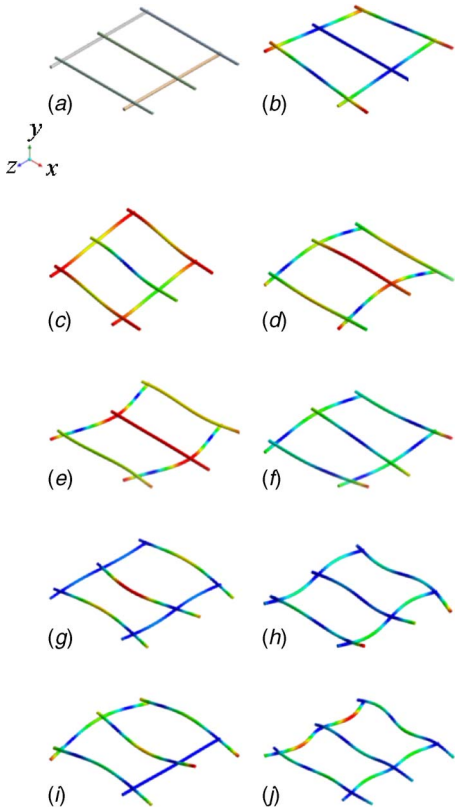

Fig. 2 (*a*) The original shape of the fiber network whose fibers are bonded together due to colloidal forces of attraction, (*b–j*) Deformed shape of the fibrous network under different shearing motion. In (*f*), the contact of middle fiber with its right-hand side neighbor is frictional. The material properties and the dimensions of the fibers are given in Sec. 3.

Turbulence is present in most applications involving flow of fiber suspensions. Turbulence is assumed to be one of the most important mechanisms behind formation and destructions of fiber flocs. As the material properties are very different from any single-phase fluids, the parameters of any of the existing turbulence models are probably not suited for the fiber suspensions. In fact, each fiber suspension probably needs its own addition to the turbulence models, for instance, in the form of additional damping, depending on the fiber length, concentration, and degree of fibrillation of the fiber. Among the earlier efforts for describing turbulent flow of fibers suspensions, the work of Wikström [18] is the study of different methods for simulating both the laminar and turbulent state of fiber suspensions. Hämäläinen [15] introduced mathematical modeling of dilute fiber suspensions in application-based flows with a simulation program for head box flows. Lindroos et al. [19] studied the effect of the fibers on turbulence created in a backward-facing step, based on an additional dissipation term in the Reynolds stress model. Kuhn and Sullivan [20] made a similar set of measurements and simulations of a flowing fiber suspension after a grid in a thin two-dimensional (2D) channel. The simulations were transient large-eddy simulations (LES), the turbulent intensity was equal to the measured values.

As has been shown, a lot of simulation and measurement data is available either to be used as reference for fitting material models or as validation for the simulations. There are only a few attempts at describing the flow phenomena through mathematical modeling. None of the published measurement results contradict using multiscale flow models. Hence, the objective of this paper is the development of a multiscale modeling and simulation for investigating complex phenomena arising from flowing fiber suspensions mainly of interest to paper makers. The present efforts include the development of (i) a mathematically rigorous multiscale modeling methodology capable of coupling behaviors from the Kolmogorov turbulence scale through the full-scale system in which a fiber suspension is flowing, (ii) a computational simulation framework built around this methodology into which techniques for investigating behaviors at the various scales can be effectively integrated, and (iii) a proof of concept of the developed core technologies using synergetic interactions with experimental studies. Efforts are mainly focused on fiber floc formation and destruction by hydrodynamic forces in turbulent flows, the key aspect of which is adaptive hierarchical modeling. Specific consideration will be given to simulations of viscoelastic fibers in which the fluid flow will be predicted by a method that is a hybrid between direct numerical simulations (DNS), and large eddy simulation techniques [21]. In addition, fluid fibrous structure interactions (FSI) [22] will be taken into account. Fiber-orientation distribution and floc formation breakup are to be studied in shear flows. The results can elucidate the physics behind the break up of a fiber floc, opening the possibility for developing a meaningful numerical model of the fiber flow at the continuum level where an Eulerian multiphase flow model will be developed for industrial use.

2 Mathematical Formulation

2.1 Fluid Phase. Calculating turbulent flows in fiber suspension whose results can be validated against the data from particle image velocimetry (PIV) [23] requires solution of the Navier-Stokes equations, which is referred to as direct numerical simulation. However, it is currently not feasible to perform DNS for fiber suspension flows due to prohibitive computational requirements. Considering the current rates of increase of computational power, it is quite unlikely that DNS will become a popular engineering tool in the near future. Engineering interest is mainly focused on

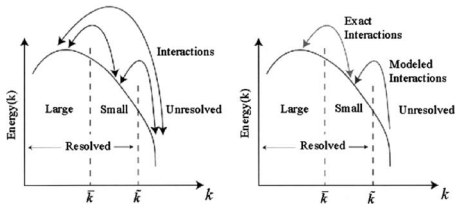

Fig. 3 Interaction regions between resolved and subgrid scales

the behavior of larger scales. However, the dynamics of larger scales is influenced by the presence of small scales because of nonlinear interactions.

It is important to distinguish between turbulence in the fibrous assembly and turbulence on the global scales in that of the channel. In some sections of the fibrous assembly, a smaller fraction of the mechanical energy is converted to turbulence, resulting in relaminarization. For such flows, a simulation method, such as large eddy simulation would be required. In fact, the LES has proven to be a valuable technique for the calculation of turbulent flows in complex geometries [23]. LES is a technique in which only larger scales are resolved numerically while effects of smaller scales are modeled. In this case, large-scale unsteadiness can be captured.

In brief, LES consists of resolving large-scale flow features and modeling subgrid-scale stresses, which represent the effect of unresolved scales on resolved scales within the filtered Navier-Stokes equations with the Smagorinsky eddy viscosity model, which has been widely used. The Smagorinsky model requires definition of a constant, a length scale, and a time scale. There are difficulties near boundaries and with stretched meshes. Currently, dynamic Smagorinsky models are preferred for wall bounded and free shear flows. However, the model should be improved for pressure-driven separation.

Recently, Hughes et al. [24] argued that many shortcomings of Smagorinsky-based approaches were associated with their inability to successfully differentiate between large and small scales. More recently, Collis [25] suggested that by assuming sufficient scale separation between unresolved scales and larger scales, direct influence on the evolution of the larger scales by unresolved scales could be neglected. However, the unresolved scales are expected to significantly influence the small scales; therefore, they must be modeled.

In brief, incompressible Navier-Stokes equations may be given as [25]

$$N(U_i) = \begin{Bmatrix} \dfrac{\partial u_k^f}{\partial t} + (u_j^f u_k^f)_{,j} + \dfrac{p_{,k}}{\rho_f} - \nu u_{k,jj}^f \\ u_{j,j}^f \end{Bmatrix} = \begin{Bmatrix} f_k \\ \psi \end{Bmatrix} = S_i, \quad \text{in } \Omega_f \tag{1}$$

where $u_k^f (k=1,2,3)$ represents the velocity vector of the fluid phase and p is the pressure, ν is the kinematic viscosity, f_k is a body force, ψ is a volumetric mass source, and Ω_f is the spatial domain for the fluid phase with boundary $\Gamma_f = \partial\Omega_f$. The state vector, $U_i \equiv \{u_k, p\}$, is defined on the space-time domain of the fluid phase, Q, whose boundary is denoted by P.

Equation (1) may be solved subject to appropriate boundary and initial conditions. To derive the variational form of Eq. (1), the entire equations are dotted with a vector of the test functions, W_i^f, and integrated over the spatial domain. The variational multiscale form of the equations, $B(W_i^f, U_i) \equiv (W_i^f N(U_i))_Q$, may be obtained using a three level partition, as illustrated in Fig. 3. Here, $(f_i g_i)_Q = \int_Q f_i g_i dQ$.

For three-level partition, the solution is partitioned as $U_i = \bar{U}_i + \tilde{U}_i + \hat{U}_i$, and the test function $W_i^f \equiv \{w_k^f, r\}$ is given as $W_i = \bar{W}_i + \tilde{W}_i + \hat{W}_i$, where the first and second terms on the right-hand side represent resolved quantities. Following Collis [25], the exact equations of motion for each scale, namely, large-scale, small-scale and unresolved scales, may be given as, respectively,

$$\begin{aligned} &B(\bar{W}_i^f, \bar{U}_i) + B'(\bar{W}_i^f, \bar{U}_i, \tilde{U}_i) - R(\bar{w}_k^f, \tilde{u}_k^f) \\ &\quad = (\bar{W}_i^f F_i)_Q - B'(\bar{W}_i^f, \bar{U}_i, \hat{U}_i) + R(\bar{w}_k^f, \hat{u}_k^f) + C(\bar{w}_k^f, \tilde{u}_k^f, \hat{u}_k^f) \\ &B'(\bar{W}_i^f, \bar{U}_i, \tilde{U}_i) - R(\tilde{w}_k^f, \tilde{u}_k^f) \\ &\quad = -[B(\tilde{W}_i^f, \bar{U}_i) - (\tilde{W}_i^f F_i)_Q] - B'(\tilde{W}_i^f, \bar{U}_i, \hat{U}_i) + R(\tilde{w}_k^f, \hat{u}_k^f) \\ &\quad + C(\tilde{w}_k^f, \tilde{u}_k^f, \hat{u}_k^f) \\ &B'(\hat{W}_i^f, \bar{U}_i + \tilde{U}_i, \hat{U}_i) - R(\hat{w}_k^f, \hat{u}_k^f) = -[B(\hat{W}_i^f, \bar{U}_i + \tilde{U}_i) - (\hat{W}_i^f F_i)_Q] \end{aligned} \tag{2}$$

where the Reynolds stress projection (of the unresolved Reynolds stress onto the large scales), namely, $R(\bar{w}_k^f, \tilde{u}_k^f)$, and the cross-stress projection of the large-unresolved cross-stress onto the large scales) are defined as, respectively,

$$\begin{aligned} R(\bar{w}_k^f, \tilde{u}_k^f) &= (\bar{w}_{k,p}^f \tilde{u}_k^f \hat{u}_p^f)_Q - (\bar{w}_k^f n_p \tilde{u}_k^f \hat{u}_p^f)_P \\ C(\bar{w}_k^f, \tilde{u}_k^f, \hat{u}_k^f) &= [\bar{w}_{k,p} : (\tilde{u}_k^f \hat{u}_p^f + \tilde{u}_p^f \hat{u}_k^f)]_Q - [\bar{w}_k^f n_p (\tilde{u}_k^f \hat{u}_p^f + \tilde{u}_p^f \hat{u}_k^f)]_P \end{aligned} \tag{3}$$

Here, n_p is the unit outward pointing normal on the boundary Γ_f.

A useful feature of variational multiscale method is the projection operator by which scales can be separated utilizing a set of basis functions. As illustrated in Fig. 3, by choosing sufficient scale separation, the small scales insulate the larger scales from unresolved scales; therefore, unresolved scales have a negligible direct influence on the dynamics of large scales. With this assumption, the modeled large and small scale may be simplified as, respectively,

$$\begin{aligned} &B(\bar{W}_i^f, \bar{U}_i^h) + B'(\bar{W}_i^f, \bar{U}_i^h, \tilde{U}_i^h) = R(\bar{w}_k^f, \tilde{u}_k^h) + (\bar{W}_i^f F_i)_Q \\ &B'(\tilde{W}_i^f, \bar{U}_i^h, \tilde{U}_i^h) - R(\tilde{w}_k^f, \tilde{u}_k^h) = M - [B(\tilde{W}_i^f, \bar{U}_i^h) - (\tilde{W}_i^f F_i)_Q] \end{aligned} \tag{4}$$

where M represents the model term and the superscript h denotes the approximate solution due to modeling error.

The model term M can be given in terms of eddy viscosity as

$$M \approx -\left[\frac{\tilde{\nu}_T}{2(\tilde{w}_{k,p}^f + \tilde{w}_{p,k}^f)(\tilde{u}_{k,p}^f + \tilde{u}_{p,k}^f)} \right]_Q \tag{5}$$

with $\tilde{\nu}_T = 1/2(C_s\tilde{\Delta})^2[(\tilde{u}_{k,p}^f + \tilde{u}_{p,k}^f)(\tilde{u}_{k,p}^f + \tilde{u}_{p,k}^f)]^{1/2}$. Here, C_s is the Smagorinsky constant and $\tilde{\Delta}$ represents the length of the small scales.

The large-scale equation, namely, the first equation in (4), also has a modeling approximation as clarified by Collis [25]. However, the large scales do not include any direct model terms, such as M. In this light, the aforementioned model can be thought of as a hybrid between DNS and LES. The advantage of this approach is that even coarse-grid results obtained using the aforementioned model would be superior to those obtained with other discretizations.

2.2 Fibers. In the following, the mathematically rigorous multiscale model for the fluid phase is generalized in order to couple the fluid and solid fields. The model can be applied to complex flows, such as fiber suspension, with use of finite element method. In fiber suspension flows, fluid-structure analysis plays a key role. On one hand, the analysis presented in the preceding section predicts how the fluid presses around and against the fibrous structure, along with the distribution of pressure. On the other hand, structural analysis is required to determine the behavior of fibrous structure under fluid loading conditions as well as

complicated contact stresses. The two disciplines meet at the surfaces of the solid structure, and each may provide loads and boundaries for the other.

In light of the above, the procedure for a coupled-field analysis, such as fiber suspension, requires a sequential method, which involves fluid and fiber sequential analyses. In the present study, the two fields of fluid and solid are coupled by applying results from fluid analysis as loads in the structural analysis presented below.

The general equations of motion in referential coordinates for an elastic continuum such as neutrally buoyant fibers as illustrated in Fig. 2 (in absence of body forces) may be given as [26]

$$\rho_s \ddot{\boldsymbol{D}}_i^s = \sigma_{ij,j}^{(el)}, \quad \text{in } \Omega_s \tag{6}$$

The displacements in a fixed rectangular Cartesian coordinate system X_j $(j=1,2,3)$ are denoted by $\boldsymbol{D}_i^s = x_i - X_i = \boldsymbol{D}_i(X_j,t)$ with kinematical relations $\ddot{\boldsymbol{D}}_i^s = \partial/\partial t^2 x_i(X_j,t)$. Equation (6) with constitutive equation $\sigma_{ij}^{(el)} = \lambda(E_{kk})\delta_{ij} + 2GE_{ij}$ and geometric equations $E_{ij} = 1/2(S_{ij} + S_{ji})$, where S_{ij} represents the displacement gradient provide 15 equations for the 15 unknowns comprising six stresses $\sigma_{ij}^{(el)}$, six strains E_{ij}, and three displacements $\boldsymbol{D}_i^s$.

The set of equations given above has to be solved for appropriate boundary and initial conditions listed below:

$$\sigma_{ij} n_j = T_i(t), \quad \text{on } \partial b_1$$

$$(\sigma_{ij}|_{x_i^+} - \sigma_{ij}|_{x_i^-}) n_j = 0, \quad \text{on } \partial b_2$$

$$x_i(X_j,0) = X_i^0$$

$$\dot{x}_i(X_j,0) = V_i(X_j) \tag{7}$$

The first condition in (7) is related to interaction between fluid-solid particles, and the second one explains the solid-solid particles interactions. In other words, the second condition in (7) represents the contact discontinuity given along an interior boundary ∂b_2 when $x_i^+ = x_i^-$. Hence, the present modeling methodology is capable of prediction of contact behavior of solid particles via the second condition in (7). In addition, the fluid-solid interaction may be accurately modeled utilizing the first condition in (7).

The variational formulation may be obtained from (6) and (7) by using the Gauss theorem. That is,

$$\int_{V_b} \rho \ddot{\boldsymbol{D}}_i^s \delta \boldsymbol{D}_i^s dV_b + \int_{V_b} \sigma_{ij} \delta \boldsymbol{D}_{i,j}^s dV_b - \int_{\partial b_1} T_i \delta \boldsymbol{D}_i^s dS_b = 0 \tag{8}$$

Equation (8) is the weak form of the equilibrium equation.

The analysis is based on a single spatial discretization across the $\Omega = \Omega_f \cup \Omega_s$. The load transfer occurs via boundary conditions (7), and no slip boundary condition is assumed for the fluid phase at the solid boundaries. Modeling of fiber-fiber interaction requires a single method such Lagrange, Euler, or a mixture of Lagrange and Euler (arbitrary Lagrange Euler). Lagrange method is mainly used in structural dynamics, while the Euler method is more common for fluid dynamics. The first approach allows one to describe small displacements and material interfaces more exactly than Euler method. Load histories of material fixed to a Lagrange cell provide the usage of special material laws, which are not as easily applicable in Euler method [27]. For the numerical simulation of the collision of fibers, each of the different methods mentioned above has unique advantages and there is no single ideal numerical method that would be appropriate to the various regimes of a collision. In the present study, the Lagrange method of space discretization is used for which the numerical grid moves and deforms with the material.

The advantages of Lagrange method are computational efficiency and ease of incorporating complex material models. The disadvantage of the method used is that the numerical grids may become severely distorted in an extremely deformed region. This can cause adverse effects on the integration time step and accuracy. However, these problems can be somewhat overcome by applying numerical techniques such as rezoning.

One of the central problems in devising descriptions of viscoelastic materials in fiber suspension flows is the question of how to describe the manifestation of both elastic and viscous effects. Mase [28] suggested that in developing the three-dimensional theory for viscoelasticity, distortional and volumetric effects must be treated independently. To this end, the stress tensor may be resolved into deviatoric and spherical parts, given as

$$\sigma_{ij} = S_{ij} + \frac{1}{3}\delta_{ij}\sigma_{kk} \tag{9}$$

where $S_{ij} = \int_0^t \phi_s(t-t') de_{ij}/dt' dt'$, and the relaxation function used in the model is given by $\phi_s(t) = G_\infty + (G_0 - G_\infty)e^{-t/\tau}$. Note that in the present study the so-called summation convention is used. Moreover, it is assumed that the stress and strain vanish for times $-\infty < t' < 0$.

The volumetric part of stress tensor would have a similar form, but with different relaxation functions. Therefore, the governing field equations for an isotropic viscoelastic continuum body such as fibers illustrated in Figs. 1 and 2 take the following form:

$$\rho \ddot{\boldsymbol{D}}_i^s = (\sigma_{ij})_{,j}$$

$$\varepsilon_{ij} = \frac{(\boldsymbol{D}_{i,j}^s + \boldsymbol{D}_{j,i}^s)}{2}$$

$$\frac{\dot{S}_{ij} + S_{ij}}{\tau} = \frac{(G_0 + G_\infty)\dot{e}_{ij} + G_\infty e_{ij}}{\tau} \tag{10}$$

The first equation in (10) is equation of motion, the second equation is strain-displacement expressions, and the third equation is stress-strain relation.

Because of prohibitive computational requirements, it is unlikely that any nonlinear viscoelastic model can be implemented for the above-mentioned fluid fiber interaction system in a foreseeable future. In this light, in the present study fibers are assumed to be made of a linear viscoelastic material. The advantage of the proposed model is that the complex fiber-fiber interactions, including contact due to colloidal forces of attraction and even collision can be modeled with computational efficiency.

2.3 Stabilization Methods. The stabilization methods, such as streamline-upwind/Petrov-Galerkin (SUPG) and pressure-stabilizing/Petrov-Galerkin (PSPG) methods [29] are indispensable in the analysis of fiber suspension. The family of the Petrov-Galerkin methods has been known to be free from artificial diffusion, theoretically. However, the stabilization methods and their performances depend on the finite elements that are used in the analysis. In the present attempt, SUPG stabilization method is used in conjunction with appropriate finite elements in order to obtain both the stability and accuracy.

In some cases, the bending stiffness of fibers could be small and, therefore, their motion may be sensitively affected by a pressure oscillation, which is created by numerical instability of the employed method. In addition, the presence of sharp boundary layers near the fibers could lead to unrealistic response of fibers using an inappropriate combination of stabilization method and finite element interpolation.

The finite element analysis employed in the present study is briefly described below. The arbitrary Lagrangian-Eulerian (ALE) finite element formulation is used for the fluid, and total Lagrangian formulation for the fibers. Because the velocity-pressure mixed interpolation plays a key role for the fluid element, tetrahedral elements are utilized in conjunction with SUPG stabilization method. The combination of SUPG stabilization method and

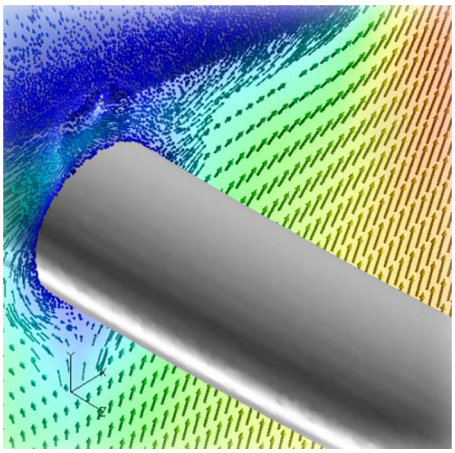

Fig. 4 Instantaneous vector plot of the velocity field in the vicinity of a point of contact between two fibers in an accelerating fiber network whose schematic is illustrated in Fig. 5. An observer moving with the fibrous system makes the realization.

tetrahedral elements appears to be the most suitable approach.

The formulations specified in this section with the stabilization method mentioned above provide the numerical results presented in Sec. 3.

3 Results and Discussions

As mentioned earlier, a sequentially coupled analysis is required from fluid and solid disciplines, which interact to solve the fiber suspension problem that is a transient problem. Here, the calculation of the flow field over the spatial domain Ω_f at a time step provides stress loads, which must be used in the structural analysis of the fiber system a sample of which is illustrated in Fig. 4. The stress loadings result in a deflection of the fiber as illustrated in Fig. 5. The fiber deflection changes the geometry of the flow field around the fiber network. However, if the time step δt is small enough, then the change is small and there is no need to iterate. Since the analysis is fully coupled, results of the structural analysis will change the input to the fluid analysis in the next time step.

In order to obtain an overall converged coupled fluid-structure solution, it would be necessary to update the finite element mesh in the fluid region to coincide with the structural deflection. The major challenge faced in simulating the system such as fiber network in a channel flow discussed below is resolving the interfacial motion. The remedy for this problem is to employ dynamic interfaces treatment for modeling the flow passing the accelerating fiber network. Generally speaking, the natural framework for dynamic interface problems is the Lagrangian method, in which the interface representation is embedded in the material description of flow and the mesh, convects and deforms with the flow, and therefore, interfaces that are well resolved initially remain sharp during simulations. The disadvantage of the aforementioned method is that unless the interface motion is small, the mesh quickly distorts and becomes inappropriately coarse or fine which is not desirable for flow-field calculations. It may be useful to treat the large interfacial motion by employing fixed spatial resolution. This approach is called Eulerian approach in which the meshes are static and need not to evolve in time. However, the major drawback of using a fixed-grid method is that a fine mesh is required everywhere to achieve high resolution, which could be far too costly. As an alternative, a moving body-fitted mesh can be used, which follows closely the moving interfaces. This approach is called the arbitrary Lagrangian-Eulerian method. The appeal of this method is that when interfacial motion is small, mesh topology can kept fixed over time. However, for problems with large relative interfacial motion the mesh regenerated frequently to follow the evolving and deforming boundaries. In the simulations described in the following section a Lagrangian framework is adopted that evolves the grid points at each time step. In the following example, only a portion of the model requires remeshing, which is the region in the immediate vicinity of the fiber network region.

3.1 Single-Fiber Network in a Channel Flow. The dynamics of a fiber network consists of five straight and cylindrical fibers, as illustrated in Fig. 5(*b*), is investigated in a duct flow. The diameter of a single fiber is 0.1 mm and whose length is 3 mm. The duct is

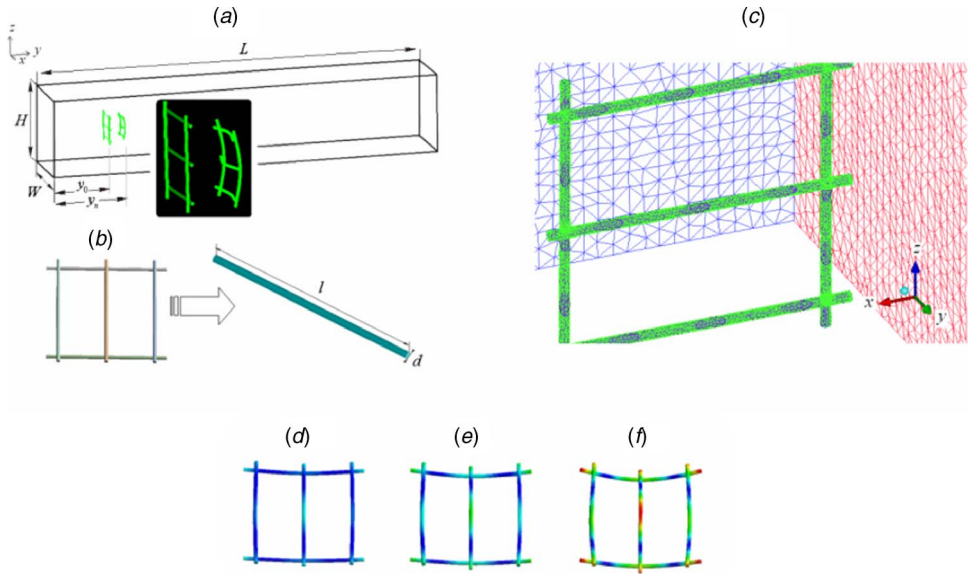

Fig. 5 (*a*) Schematic of a fiber-water suspension flow in a channel. The dimensions of the channel are *L*=5 cm and *H*=*w*=1 cm, (*b*) the original shape of the fiber network. The dimensions of a single fiber are *l*= 3mm and *d*=0.1 *mm*. (c) Á sample of the mesh used in the fiber-water system. (*d*–*f*) Temporal evolution of the fiber network. Note that fluid-fiber interaction caused the fibers to bend and the network to deform. The pressure at the outlet of the channel is assumed to be atmospheric.

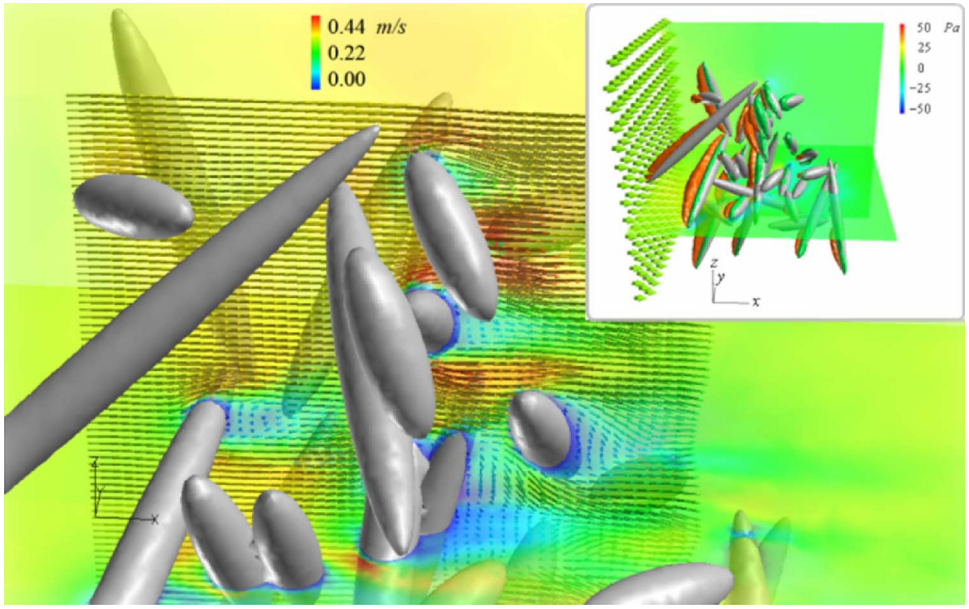

Fig. 6 Vector plot of a velocity field in a moderately dense fiber suspension of thirty multisized fiber assembly. To improve the visualization of the vector field, a low-resolution grid is used. The dimensions and the material properties of the fibers are given in the text. Water flows from the left to the right in a parallelepiped duct with rectangular cross section cubic duct with dimensions of 4×3.5 cm^2, and the length of channel is only 4 cm. (Inset) Fluid pressure distribution around the fibrous assembly. Also shown is the fluid pressure distribution on two perpendicular plane, *xy* plane and *xz* plane located at $Z=-5.4$ mm and $Y=-8.5$ mm, respectively, with respect to the origin located at the center of the inlet.

a parallelepiped with rectangular cross section whose dimensions are $H=1$ cm, $W=1$ cm, and $L=5$ cm, as illustrated in Fig. 5(*a*). To obtain a better understanding of fluid-fiber interaction, the fiber network is initially placed at $y_0=1$ cm from the inlet of the duct from which water is flowing at the rate of $\dot{m}=0.05$ kg/s. The velocity profile in the duct can change from 0.1 m/s to 0.6 m/s so the maximum Reynolds number can reach ~6000. The fluid velocity profile at the inlet of the channel is perturbed to obtain a profile that closely resembles a turbulent channel flow. The fiber network is assumed to be initially at rest.

The fibers are elastic material with the material properties of $\rho\approx\rho_w$, $E=10^6$ Pa, and Poisson's ratio of $\nu_s\approx0.01$. The physical properties of water are $\rho_w=998.2$ kg/m^3 and $\nu_w\approx1\times10^{-6}$ m^2/s. The fibers are assumed to be bonded together due to colloidal forces of attraction. The domain is discretized using 4×10^5, 3D tetrahedral elements, and 8×10^4 nodes a sample of which is depicted in Fig. 5(*c*). Using appropriate values for the underrelaxation factors for the pressure and velocities, a reasonable rate of convergence was achieved. The convergence was considered to be achieved when the conservation equations of mass and momentum were satisfied, which was considered to have occurred when the normalized residuals became smaller than 5×10^{-5}. The normalization factors used for the mass and momentum were the maximum residual values after the first few iterations. It is worth noting that refinement of the grids did not produce any significant differences in the results. Using a time step of 1×10^{-3} s, the unsteady calculations were performed until the fiber network had reached to $y_n=1.5$ cm, as illustrated in Fig. 5(*a*). Temporal evolution of the fiber network shape is illustrated in Figs. 5(*d*)–5(*f*). To obtain better visualization, the network deflection is scaled in the aforementioned figures. The unscaled deflections are of order of fiber diameter. The result of this section provides insight into the dynamics of simple fiber networks in a shearing flow of water in a channel flow. It would be expected that the shear-induced bending of the fiber network is enhanced near the walls. The forces acting on the fibers are the normal force and adhesive force that is independent on the normal force. The normal forces increase with crowding factor, which means that the yield stress of a fiber suspension would be different for suspensions characterized by a large adhesive force than for suspensions with a larger friction coefficient. The adhesive force and friction forces relate to the state of the fiber, the degree of fibrillation and swelling.

Flexible fibers in a flow with nonzero velocity gradients will be exposed to viscous and dynamic forces, as well as interfiber contact forces which elastically deform the fibers. Thus, fibers bending are high near the wall. An example of deformed network in the wall region is illustrated in Fig. 2(*i*), which clearly represents that shear forces may cause fibers to bend. Figure 2(*f*) represents the deformed shape of the fiber network in a channel flow when the contact between the middle fiber and its right-hand side neighbor is set as frictional, with the coefficient of friction of 0.8. The experimentations using particle image velocimetry (PIV) techniques are required to guide modifying the present model for predicting the dynamics of fiber suspension more accurately.

The results presented in this section may be useful to predict breakage and to improve fiber network stability. The present model may be further generalized to investigate mechanisms, such as charge effects, polymer bridging, and microparticle effects by which chemical additives work. This would be the approach to pursue the present research in the future.

3.2 Random Fibrous System in a Duct Flow. The cylindrical model may be not the only geometrical system for the description of the fibers. There are a number of open questions regarding the convection of fibers near walls, including flow-induced alignment and dispersion rate.

In the present section, the velocity and pressure fields are illustrated around a randomly oriented fibrous system in a duct flow. Figure 6 represents an instantaneous distribution of the aforementioned fields taken after 5×10^{-3} s. To divide the geometry into discrete control volumes, more than 5×10^5, 3D tetrahedral computational cells and 10^5 nodes were used. In addition, roughly 10^6

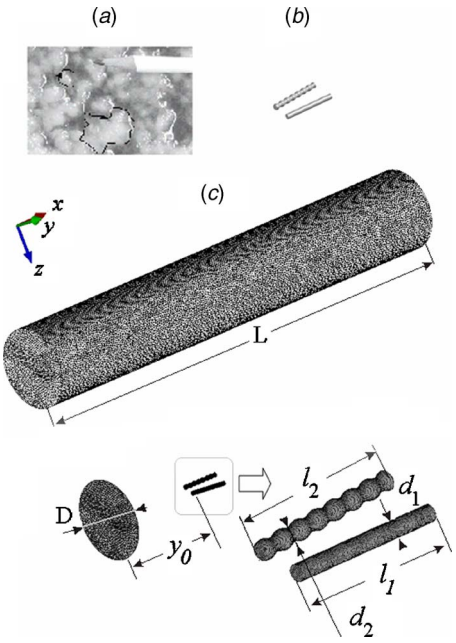

Fig. 7 (*a*) **Flocculated suspension observed in the extrusion of an ultra-high consistency fiber suspension.** (*b*) **Schematics of fiber aggregates.** (*c*) **Schematic of the pipe whose dimensions are** $D=2$ **cm and** $L=35$ **cm. In addition, samples of triangular meshes used to discretize the inlet, outlet, and wall faces of the pipe are shown. The number of elements used for the aforementioned faces are 12,994, 12,933, and 168,285, respectively. The boundary condition at the outlet is pressure constant and is set to the atmospheric pressure. The dimensions of aggregates initially located at** $y_0 \approx 20$ **mm, are as follows:** $l_1=l_2=8$ **mm, and** $d_1=d_2=0.75$ **mm, and the triangular finite element meshes used are 22,772, and 20,054. The total tetrahedral elements used to discretize the grid is 3,311,197.**

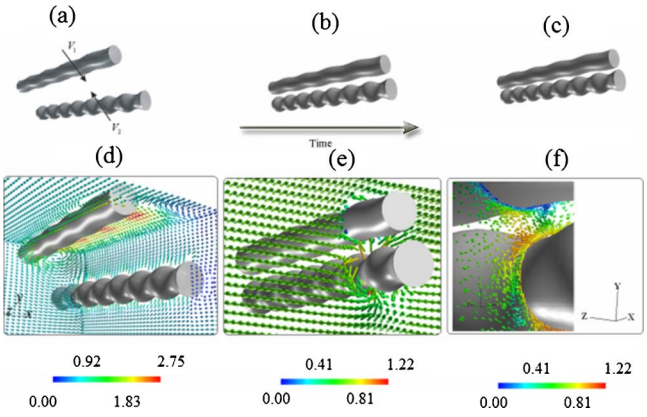

Fig. 8 (*a*) **Initial configuration of the two aggregates. The arrows represent their initial velocity vectors.** (*b*) **Configuration of aggregates after** 3×10^{-3} **s.** (*c*) **Configuration of aggregates after** 5×10^{-4} **s from that shown in** (*b*)**.** (*d*) **and** (*e*) **are vector plots of the velocity field around the aggregates whose arrangements are illustrated in** (*a*) **and** (*b*)**, respectively. The simulations are unsteady and the time step for the liquid phase equals** 5×10^{-6}**.** (*f*) **The magnified velocity vector field for the configuration as illustrated in** (*c*) **when the aggregates are very close to each other. The velocity magnitudes are dimensionless defines as** $V_s^*=V_s/V_{\text{inlet}}$**, where the average velocity of water at the inlet,** V_{inlet}**, is set to 0.5 m/s.**

wall triangular elements were generated for fibers. The results appear to be grid independent because different meshes applied for the investigation.

The shape of the fiber is assumed to be prolate spheroid, as illustrated in Fig. 6. The analysis is made for a multisized assembly of 30 fibers to investigate the conditions for which an orientated fibrous system can be achieved. There are four groups of spheroids. The groups consist of six very long spheroids with a polar radius of 12.5 mm and the ellipticity of 0.998, four long spheroids with a polar radius of 10 mm and the ellipticity of 0.997, six medium-sized spheroids with a polar radius of 7 mm and the ellipticity of 0.994, and 14 small spheroids with a polar radius of 3 mm and the ellipticity of 0.94. The surface area of a prolate spheroid may be given as

$$S_{\text{fiber}} = 2\pi a^2 + 2\pi \frac{ac}{e} \sin^{-1} e \tag{11}$$

where a is the equatorial radius, c is the polar radius and $e = \sqrt{c^2-a^2}/c$ is the ellipticity.

As can be seen from Fig. 6, the fluid velocity field in a duct flow of a random fibrous assembly is quite complex. Two types of vortices may be observed (namely, the void and pseudo vortices), which play an important role in the transport mechanism of the turbulence and redispersal of fiber, in fiber in the fibrous system. Dispersing of fibers results in a dramatic reduction in the apparent viscosity of the fiber suspensions, which allows the suspension to flow up to very high fiber concentrations.

The results presented in Fig. 6 may be used for accurately evaluating the hydrodynamic forces and torques in a system for which the occurrence of relaminarization from turbulent to laminar regime is quite likely leading to the conditions at which combination of different flow types exists. In the gaps between contacting fibers, velocity can be higher than the velocity in the duct; therefore, the Reynolds number will reach more than 6000.

The model described in this section and in Sec. 3.1 is a particle-level, dynamic simulation technique to investigate the structural behavior of fiber suspensions flowing in straight ducts. The model incorporates a variety of features, including fluid-fiber interaction, multisized assembly, fiber flexibility, fiber-fiber interaction, and irregular fiber shapes. Investigating flocculation processes in a complex geometry such as that shown in Fig. 6 deserves further study.

3.3 Interaction of Two Aggregates of Fibers. It is known from experimental data [30] that flexible fibers tend to aggregate as illustrated in Fig. 7(*a*). The aggregates are undesirable in fiber processing because they lead to problems in resulting products. Indeed, dispersing the fibers is thought to result in a dramatic reduction in the apparent viscosity of the fiber suspension. In this section, the mathematical approach detailed in Sec. 3.2 is used to investigate further the aggregate-aggregate interaction in a turbulent pipe flow whose Reynolds number is ~10,000. To this end, numerical results are presented, obtained by three-dimensional computation, for fluid field around two moving circular cylinders with irregular surface shape, whose initial arrangement is illustrated in Fig. 7(*b*). The cylinders with irregular surface shapes, as shown in Fig. 7(*b*), are used to reproduce approximate shapes for the aggregates of fibers. The schematics of the tube as well as the fiber aggregates are illustrated in Fig. 7(*c*), which presents detailed information, including the dimensions as well as the samples of triangular meshes used in order to discretize the surfaces.

As shown in Fig. 8(*a*), initial velocities in the y and z directions are given to the cylinders to investigate the hydrodynamics as well as the solid mechanics interactions between the two approaching cylinders in a pipe flow. As illustrated in Figs. 8(*b*) and 8(*c*), the cylinders in the flowing stream of water (mainly in the x direction) are gradually aligned due to drag in a side-by-side arrangement and a collision would be expected to occur when the surfaces will be at contact. Figures 8(*d*)–8(*f*) represent sample results of flow fields around two moving cylinders. As it can be seen from the

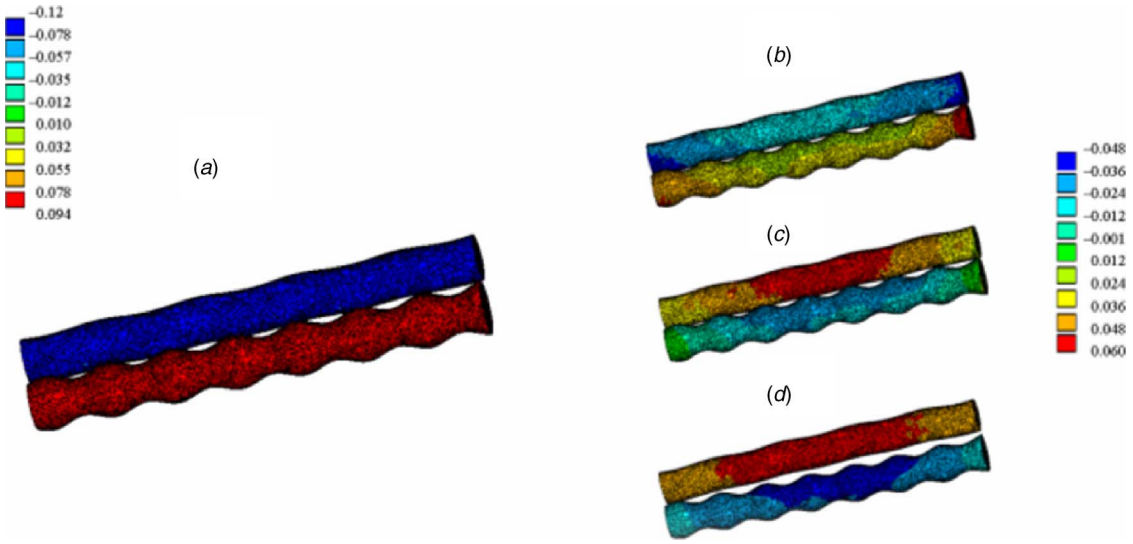

Fig. 9 Solid-body collision of aggregates: (*a*) the instant of contact and (*b–d*) three instantaneous configurations of the aggregates in contact each separated by 3×10^{-7} s. The configurations in (*b–c*) represent the approach and the restitution periods, respectively. The configuration in (*d*) represents the instant of separation. The simulations are unsteady and the time step for the aggregate-aggregate contact equals 4×10^{-10}. The surface elements are color coded using the magnitude of the dimensionless velocity of the aggregates. Here, the velocities are normalized using the magnitude of the inlet velocity of water. Physical properties used in solid body collision of the aggregates are listed in Table 1.

aforementioned figures, flows around two circular cylinders become very complicated due to interference of vortices separated from the cylinders. The results presented in Fig. 8 are based on an approach that is performed on the basis of the Petrov-Galerkin formulation of the Navier-Stokes equations for the fluid phase. The present approach appears to extend the range of accuracy and reliability of predictions important to applications, such as fiber suspension, where technological progress requires confronting turbulence.

Figure 9 represents the solid body interactions where the instant of contact between two aggregates is illustrated in Fig. 9(*a*). Currently, no reliable information for physical properties of viscoelastic fibers can be found in the literature. For example, Bennington et al. [4] reported a value for the elastic modulus of fibers, which appears to be quite high. In addition, a very low value is reported by Swerin [31]. In the present mesostructure approach, reasonable values for the physical properties are assumed and the consequences are then explored at the macrostructural level. The advantage of this is that, if a particular phenomenon is not well modeled, the physical properties can be revised and even the relevant physics put in place. Note that the physics of turbulent fiber suspension is so complex that one must guess which variables to put in the model hoping to produce features of use for the design process. Indeed, simple models with the right physics should be favored.

In light of the above, the physical properties are listed in Table 1 is used to predict the collision behavior of the aggregates whose geometry at contact is illustrated in Fig. 8(*a*). Geometrically nonlinear analysis is used throughout the simulation due to large deformations expected during the collision. At first, a suitable level of mesh refinement is established on the basis of the Hertz elastic contact problem. The surface elements are colorcoded using the dimensionless solid velocity defined as $V_s^*=V_s/V_{\text{inlet}}$. Next, a viscoelastic model is utilized consists of auxiliary spring in series with the Kelvin model [32]. However, this model is not sufficient for analyzing the cases at which the adhesive effects are relatively large. Figures 9(*b*)–9(*d*) represent three instantaneous configurations of the aggregates each separated by 3×10^{-7} s. As can be seen from Fig. 9(*d*), the velocity magnitudes of the separated fibers are smaller than those before the collision implying the occurrence of an inelastic collision. The coefficient of restitution defined as the ratio of the relative velocity of the aggregates after the collision to that before the collision may be controlled by the value of relaxation time as introduced in Table. 1.

The fibers as depicted in Fig. 9(*d*) appear to slightly bend due to contact forces. Here, the deformation history is very similar to that presented by Goldsmith [33], as an assumed scenario for deformation history in stereomechanical impacts. At this stage, it is instructive to consider an adhesion force as a parameter to investigate cohesive characteristics of the aggregates. As illustrated in Fig. 10, in the absence of any adhesive forces, the inelastic solid body interaction between two aggregates whose configuration is shown in Fig. 10(*a*) leads to separation of cylinders after a short contact time of order of 10^{-6} s as illustrated in Fig. 10(*b*). However, as depicted in Fig. 10(*c*), by adding an adhesive force the collision becomes completely plastic and two aggregates form a lager floc of fibers. Figure 10(*d*) represents the zone model geometry as well as the force-separation relationship used in the present attempt. Therefore, the aforementioned viscoelastic model is generalized by including a Lenard-Jones–type adhesive interaction [34] when two surfaces approach or are separated. Any kind of functional can be used for the force-separation interaction in order

Table 1 Physical properties of fiber and water

Material	Properties	Symbol	Value
Fiber	Elastic modulus	E	6×10^6 Pa
	Density	ρ	$\approx\rho_w$
	Poisson's ratio	ν_s	0.05
	Instantaneous shear modulus	G_0	2.86×10^6 Pa
	Long-time shear modulus	G_∞	0
	Relaxation time	τ	10^{-5} s
	Material type		Pulp fiber suspension
	Surface friction coefficient	μ	0.8
Water	Density	ρ_w	998.2 kg/m^3
	Temperature	T_w	293 K
	Kinematics viscosity	ν_w	10^{-6} m^2/s

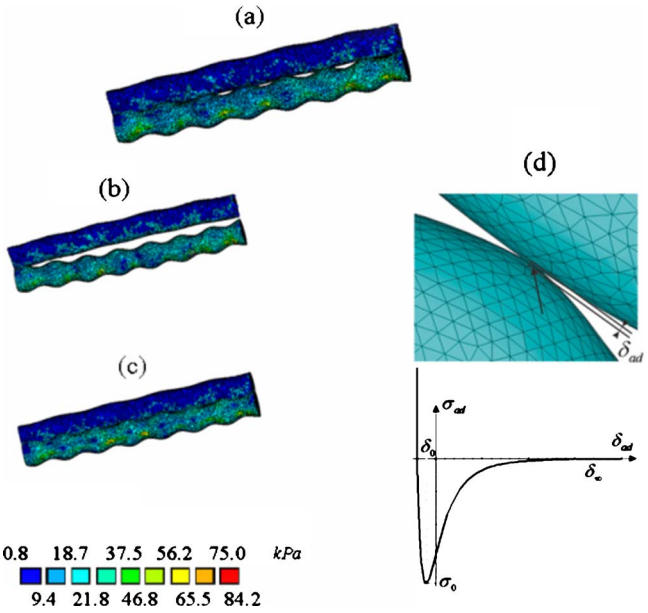

Fig. 10 (*a*) **Initial configuration of two aggregates at the instant of contact. The simulations are unsteady and the time step for the aggregate-aggregate contact equals 4×10^{-10}. (*b*) The separation of configuration of the aggregates at the instant of separation (at the end of restitution period). Here, no adhesive force is taken into account. (*c*) Final configuration of aggregates for which a Lenard-Jones–type potential for attraction is considered. (*d*) The force separation relationship for contact surfaces. In the present attempt a suitable value for s_0 is set to in order to finalize the collision at the end of approaching period. Here, d_{ad} represents the separation of the aggregates in cohesive zone. The surface elements are color coded using the effective stress defined as $s_{\text{eff}}=s_{xx}^2+s_{yy}^2+s_{zz}^2-(s_{xx}s_{yy}+s_{xx}s_{zz}+s_{yy}s_{zz})+3(t_{xy}^2+t_{xz}^2+t_{yz}^2)$.**

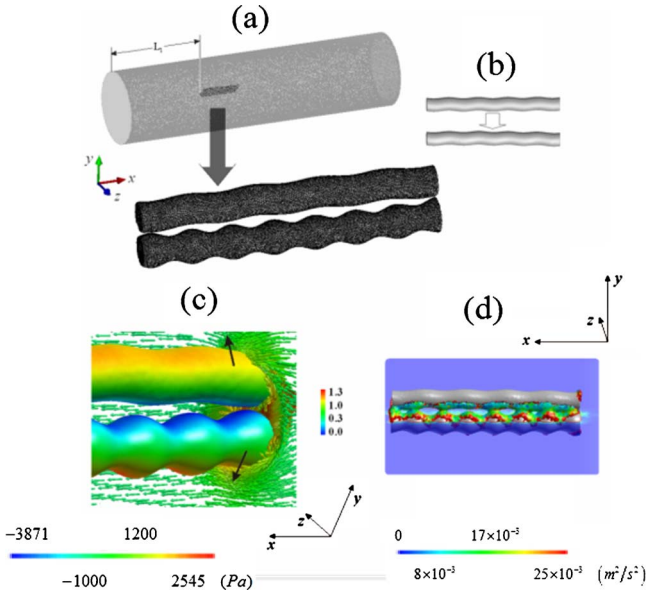

Fig. 11 (*a*) **Grid for the deformed aggregates whose configuration is shown in Fig. 9(*d*) whose location from the inlet is $L_1 \gg 25$ mm. The number of cells used are nearly the same as those reported in Fig. 7(*b*). The geometries of one of the aggregates before and after the collision. Here, slide bending occurred during the collision in the aggregate. (*c*) Velocity vector field around the aggregates 5×10^{-5} s, after the separation. The simulations are unsteady and the time step for the liquid phase equals 5×10^{-6}. The arrows represent their initial velocity vectors. The surface of the aggregates is color coded using the magnitude of their normal stresses. (*d*) Iso surface of the liquid velocity magnitude of 0.6 m/s color coded using subgrid kinetic energy of turbulence. The boundary condition at the outlet is pressure constant and it is set to the atmospheric pressure.**

to find the right physics. The results presented in Fig. 10 highlight the key role plays by adhesive forces in formation of fiber flocs. The present efforts may be completed by conducting experiments to determine the extrudability of concentrated fiber suspension. The obtained results support the notion that wet-end chemical additive, such as water-soluble polymers might disperse fibers due to adjustments they may provide in the cohesiveness of the aggregates. In this light, the present approach appears of use to develop a meaningful picture of fiber-fiber interactions for which even no detailed information of physical or surface properties exists in the literature. However, the final goal would be simplicity in the correct theoretical framework such as that mentioned above, with enough empirical inputs to ensure a quantitative prediction.

Figure 11(*a*) illustrates the elements in the grid for deformed aggregates after the inelastic collision detailed in Fig. 9. The fibers can bend and their geometry become distorted after the collision as shown in Fig. 11(*b*). Figure 11(*c*) reveals that the slip velocity between aggregates and water could be large after separation because the relaxation time for water velocity to conform to that of the aggregates could not be short compared with the collision time during which the velocity of aggregates varies significantly. In this light, the interaction between the solid and the liquid phase may generate a high pressure on the surface of aggregates as shown in Fig. 11(*c*), where the evolution of the pressure field can play a role in the rearrangement of aggregates and their translational movements as well as their orientations. The manner in which the fluid particles are agitated and the role of turbulence produced by rapid movements of aggregates, as illustrated in Fig. 11(*d*), in the dynamics of a fiber suspension are interesting issues for further investigations. Consider that the grid resolution has been decreased to improve the clarity of the figures presented in this section

4 Concluding Remarks

Examining floc strength as a function of a range of wet-end chemical additive, orders of addition, and effects of hydrodynamic shear is of interest to papermakers. In the present study, a particle-level dynamic-type model was employed for flexible fiber to investigate the fluid-fiber interaction, as well as the fiber-fiber interaction in straight ducts. By utilizing a variational multiscale method the complex flow of liquid was predicted through a fibrous assembly. The aforementioned multiscale method can be thought of as a hybrid between DNS and LES. By employing dynamic interfaces treatment, both the solid-body movement and deflection of fibers have been predicted. However, the results of simulations should be validated using data obtained with PIV techniques. A significant benefit of the method is that the flow of liquid may be predicted more accurately in situations in which the occurrence of relaminarization from turbulent to laminar regime is quite likely.

Our comparisons to other experimental and numerical results are thus far more qualitative, and therefore, a great deal of work is still required in order to validate the model and numerical results. To pursue the present research in the future, the goal is to reproduce measurements of the strength of fiber flocs at consistencies similar to those found in a headbox. The validated numerical results at particle-level may be used to develop the set of macroscopic model equations for which exhaustive numerical simulations are required at the particle-level as detailed in the present work.

Acknowledgment

Krista Mäkipere and Arezou Jafari wish to acknowledge the support of the Finnish Academy (Award No. 104840).

Nomenclature

a = equatorial radius

$B(W_i^f, U_i)$ = variational multiscale form defined as $(w_k \dot{u}_k)_Q - (w_{k,p} u_{kp})_Q - (w_{k,k} p)_Q + [1/2\nu(w_{k,p} + w_{p,k})(u_{k,p} + u_{p,k})]_Q + (r u_{k,k})_Q + (w_k n_p u_{pk})_P + (p w_k n_k)_P - [\nu w_k (u_{p,k} + u_{k,p}) n_p]_P$

$B'(W_i^f, U_i, U_i')$ = variational operator linearized about the field U_i defined as $(w_k \dot{u}_k')_Q - [w_{k,p}(u_k' u_p + u_p' u_k)]_Q - (p' w_{k,k})_Q + [1/2\nu(w_{k,p} + w_{p,k})(u_{k,p}' + u_{p,k}')]_Q + (r u_{k,k}')_Q + [w_k n_p (u_k' u_p + u_p' u_k)]_P + (p' w_k n_k)_P - [\nu w_k (u_{k,p}' + u_{p,k}') n_p]_p$

$C(\bar{w}_k^f, \bar{u}_k^f, \tilde{u}_k^f)$ = cross-stress projection

C_s = Smagorinsky constant

c = polar radius

d = diameter of fiber

D = diameter of pipe

$\boldsymbol{D}$ = displacement

E_{ij} = strain tensor

$E_Y I$ = intrinsic fiber stiffness

e = ellipticity

f_k = body force

G = modulus of rigidity

H = height of duct

L = length of duct

$\mathbf{L}$ = length of pipe

l = length of fiber

$\dot{m}$ = mass flow rate

n = fiber number density

n_p = unit outward normal on the boundary

P = lateral boundary of Q

p = pressure

Q = space-time domain of the fluid phase defined as $\Omega_f \times]0,T]$

$\mathrm{Re}(\bar{w}_k^f, \bar{u}_k^f)$ = Reynolds stress

S_{ij} = deviatoric stress

S^{eff} = effective stiffness

T_i = stress loads

$]0,T]$ = time interval of interest

t = time

$U_i \equiv \{u_k, p\}$ = state vector

$u_k (k=1,2,3)$ = velocity vector

W_i^f = test function

w_k = test function vector

W = width of duct

$X_j (j=1,2,3)$ = displacement in a fixed rectangular cartesian coordinate system

y = position of fiber from the inlet of channel

Greek

ε_{ij} = strain rate tensor

g = shear rate

ν = kinematic viscosity

ψ = volumetric mass source

Ω = spatial domain

$\sigma_{ij}^{(el)}$ = elastic stress

$\tilde{\Delta}$ = filter size for the small scales

Γ_f = boundary of Ω_f

η_0 = suspending fluid viscosity

ρ = density

λ = Lamé constant

δ_{ij} = Kronecker δ

$\tilde{\nu}_T$ = eddy viscosity

ϕ = relaxation function

d_{ad} = separation between fibers (used in force separation relation for contact surfaces)

s_{ad} = cohesive stress

Superscripts

- = large-scale resolved quantities

$\sim$ = small-scale resolved quantities

$\wedge$ = unresolved quantities

dot = derivative with respect to time

Subscripts

0 = initial condition

¥ = infinity

f = fluid phase

h = approximate solution due to modeling error

k,p = cross product

s = solid phase

w = water

comma = derivative with respect to spatial coordinates

References

[1] Scott, W. E., 1996, *Principles of Wet End Chemistry*, Tappi Press, Atlanta, Chaps. 6 and 16.

[2] Britt, K. W., and Unbehend, J. E., 1976, "New Methods for Monitoring Retention," Tappi J., **59**(2), pp. 67–70.

[3] Wu, J., Bratko, D., Blanch, H. W., and Prausnitz, J. M, 2000, "Effect of Three-Body Forces on the Phase Behavior of Charged Colloids," J. Chem. Phys., **113**, pp. 3360–3365.

[4] Bennington, C. P. J., Kerekes, R. J., and Grace, J. R., 1990, "The Yield Stress of Fiber Suspensions," Can. J. Chem. Eng., **68**, pp. 748–757.

[5] Chaouche, M., and Koch, D. L., 2001, "Rheology of Non-Brownian Rigid Fiber Suspensions With Adhesive Contacts," J. Rheol., **45**, pp. 369–382.

[6] Meyer, R., and Wahren, D., 1964, "On the Elastic Properties of Three-Dimensional Fiber Networks," Sven. Papperstidn., **67**, pp. 432–436.

[7] Soszynski, R. M., and Kerekes, R. J., 1988, "Elastic Interlocking of Nylon Fibers Suspended in Liquid, Part 1. Nature of Cohesion Among Fibers," Nord. Pulp Pap. Res. J., **3**, pp. 172–179.

[8] Zhao, R. H., and Kerekes, R. J., 1993, "The Effects of Suspending Liquid Viscosity on Fiber Flocculation," Tappi J., **76**(2), pp. 183–188.

[9] Beghello, L., 1998, "The Tendency of Fibers to Build Flocs," Doctoral thesis, Faculty of Chemical Engineering, Åbo Akademi University, Finland.

[10] Baines, W. D., 1959, "Laminar Flow of Dilute Fiber Suspension," Sven. Papperstidn., **62**, pp. 823–830.

[11] Head, V., and Durst, R., 1957, "Stock Slurry Hydraulics," Tappi J., **40**(12), pp. 958–966.

[12] Myréen, B., 1989, "Modeling the Flow of Pulp Suspensions in Pipes, Part I," Pap. Puu, **71**(5), pp. 497–504.

[13] Durst, R., and Jenness, L., 1954, "The Flow Properties of Paper Pulp Stocks. I. Relationship of Sheer Value to Pipe Friction for Bleached Sulphite Pulp Slurries," Tappi J., **37**(10), pp. 420–427.

[14] Huhtanen, J. P., 1998, "Non-Newtonian Flows in Paper Making," Licentiate thesis, Tampere University of Technology, Finland.

[15] Hämäläinen, J. P., 1993, "Mathematical Modeling and Simulation of Fluid Flows in the Headbox of Paper Machines," Doctoral thesis, University of Jyväskylä, Finland.

[16] Damani, R., Powel, R., and Hagen, N., 1993, "Viscoelastic Characterization of Medium Consistency Pulp Suspensions," Can. J. Chem. Eng., **71**, pp. 676–685.

[17] Swerin, A., Powell, R., and Ödberg, L., 1992, "Linear and Nonlinear Dynamic Viscoelasticity of Pulp Fiber Suspensions," Nord. Pulp Pap. Res. J., **3**, pp. 126–132.

[18] Wikström, T., 2002, "Flow and Rheology of Pulp Suspensions at Medium Consistency," Doctoral thesis, Chalmer's University of Technology, Sweden.

[19] Lindroos, K., Piirto, M., and Huhtanen, J. P., 2003, "The Effect of Fibers on Turbulent Quantities in Backward Facing Step Channel Flow: Measurements and Numerical Simulations," *Third International Symposium on Turbulence and Shear Flow Phenomena*, Sendai, Japan, pp. 233–238.

[20] Kuhn, D. C. S., and Sullivan, P., 2001, "Analysis and Measurement of the Flocculation Intensity of Flowing Pulp Suspensions," *TAPPI Papermakers Conference*, Cincinnati, OH, March 11–14, Session 14, TAPPI Press, Atlanta.

[21] Pope, S. B., 2000, *Turbulent Flows*, Cambridge Univ. Press, Cambridge.

[22] Peake, N., and Langre, E. de, 2005, "Special Issue on Fluid-Plate Interactions," J. Fluids Struct., **20**(7), p. 891.

[23] Honkanen, M., Koohestany, A., Hatunen, T., Saarenrinne, P., and Zamankhan, P., 2005, "Large Eddy Simulation and PIV Experiments of a Two Phase Air-Water Mixer," *Proceedings of ASME Fluids Engineering Summer Conference*, Houston, ASME, New York, Paper No. FEDSM2005-77185.

[24] Hughes, T. J. R., Mazzei, L., and Jansen, K. E., 2000, "Large Eddy Simulation and the Variational Multiscale Method," Comput. Visual. Sci., **3**(1-2), pp.

47–59.
[25] Collis, S. C., 2001, "Monitoring Unresolved Scales in Multiscale Turbulence Modeling," Phys. Fluids, **13**, pp. 1800–1806.
[26] Billington, E. W., and Tate, A., 1981, *The Physics of Deformation and Flow*, McGraw-Hill, New York.
[27] Libersky, L. D., Petschek, A. G., Carney, T. C., Hipp, J. R., and Allahdadi, F. A., 1995, "High Strain Lagrangian Hydrodynamics," J. Comp. Physiol., **109**, pp. 67–75.
[28] Mase, G. E., 1970, *Continuum Mechanics*, McGraw-Hill, New York.
[29] Hughes, T. J. R., and Brooks, N. A., 1979, "A Multi-Dimensional Upwind Scheme With no Crosswind Diffusion," In Hughes, T. J. R., ed. *Finite Element Methods for Convection Dominated Flows*, ASME, New York, AMD, 34, pp. 19–35.
[30] Zauscher, S., and Klingenberg, D. J., 2001, "Friction Between Cellulose Surfaces Measured with Colloidal Probe Microscopy," Colloids Surf., A, **178**, pp. 213–229.
[31] Swerin, A., 1998, "Rheological Properties of Cellulosic Fibre Suspensions Flocculated by Cationic Polyacrylamides," Colloids Surf., A, **133**, pp. 279–294.
[32] Zamankhan, P., and Bordbar, M. H., 2006, "Complex Flow Dynamics in Dense Granular Flows—Part 1: Experimentation," ASME J. Appl. Mech., **73**, pp. 648–657.
[33] Goldsmith, W., 2001, *Impact, the Technology and Physics Behavior of Colliding Solids*, Dover, New York.
[34] Allen, M. P., 1992, *Computer Simulation of Liquids*, Oxford University Press, London.

Fiber Orientation Control Related to Papermaking

Allan Carlsson
e-mail: allan@mech.kth.se

Fredrik Lundell

Department of Mechanics,
School of Engineering Sciences,
Royal Institute of Technology,
SE-100 44 Stockholm, Sweden

L. Daniel Söderberg
STFI-Packforsk AB,
SE-114 86 Stockholm, Sweden

The orientation of fibers suspended in a shear flow flowing over a solid wall has been studied experimentally. The possibility to control this orientation with physical surface modifications, ridges, has also been studied. The fiber suspension was driven by gravity down a slightly inclined glass plate and a charge-coupled device camera was used to capture images of the fibers in the flow. Image analysis based on the concept of steerable filters extracted the position and orientation of the fibers in the plane of the image. From these data, the velocity of the fibers was determined. When viewing the flow from the side, the velocity of the fibers at different heights was measured and found to agree with the theoretical solution for Newtonian flow down an inclined plate. Moving the camera so that the flow was filmed from below, the orientation, and velocity of fibers in the plane parallel to the solid surface was determined. The known relationship between the velocity and the wall normal position of the fibers made it possible to determine the height above the plate for each identified fiber. Far away from the wall, the fibers were aligned with the flow direction in both cases. In a region close to the smooth plate surface the fibers oriented themselves perpendicular to the flow direction. This change in orientation did not occur when the surface structure was modified with ridges.
[DOI: 10.1115/1.2436583]

1 Introduction

The present work is part of a larger undertaking aimed at understanding and controlling the flow physics involved in papermaking. When paper is produced, a fiber suspension consisting of cellulose fibers suspended in water is used. The suspension, with a mass concentration typically below 1%, enters a nozzle, usually called a headbox, through a pipe with a diameter of approximately 800 mm [1]. The main purpose of the headbox is to distribute the suspension evenly across one or between two permeable bands called wires. To do this the pipe flow entering the headbox is transformed to a jet with an approximate height of 10 mm and a width of about 10 m. The mechanical properties of the produced paper sheet are strongly coupled to the fiber orientation. Due to the contraction of the headbox, fibers tend to align in the flow direction. This orientation anisotropy is also reflected in the final product.

In order to damp out large-scale velocity fluctuations in the headbox, which can result in a bad formation of the paper, i.e., a variation in local mass distribution or basis weight, flexible flow dividers are often implemented in the headbox. These are fixed at the entrance to the nozzle contraction and allowed to adjust according to the flow field. The width of these flow dividers are the same as the width of the nozzle. The flow dividers will henceforth be called lamellas. At the surfaces of the lamellas the no-slip condition is valid, i.e., the velocity of the fluid relative to the surfaces is zero. As a result thin shear layers of fluid, i.e., boundary layers, will form along the lamella surfaces, where the velocity goes from zero at the surfaces to the velocity of the main stream further out. The aim of the present study is to investigate the physics controlling fiber orientation in a boundary layer close to a solid wall, aiming at understanding how the lamellas influence the fiber orientation and ultimately the properties of the final paper product. It is also of interest to investigate the possibility to use the lamellas as means of controlling the fiber orientation by modifying the structure of the lamella surfaces.

In order to interpret the results of the present study, the concept of Jeffery orbits [2] will be used, i.e., the motion of a solitary ellipsoid suspended in a laminar simple shear flow. The equations of motion for the ellipsoid has been solved theoretically [2] and the resulting expressions, frequently referred to as Jeffery's equations, are

$$\dot{\phi} = -\frac{\dot{\gamma}}{r_e^2+1}(r_e^2 \sin^2\phi + \cos^2\phi) \tag{1}$$

$$\dot{\theta} = \left(\frac{r_e^2-1}{r_e^2+1}\right)\frac{\dot{\gamma}}{4}\sin 2\phi \sin 2\theta \tag{2}$$

where ϕ is the angle of the particle projection in the flow-gradient plane with respect to the streamwise direction, (Fig. 1). The angle of the particle with respect to the vorticity axis is defined as θ. The aspect ratio, i.e., the length to diameter ratio of the ellipsoid, is denoted r_e and $\dot{\gamma}$ is the shear rate. The dots over the two angles ϕ and θ, represent differentiation with respect to time. The ellipsoid will remain in its initial orbit, which is defined by the initial conditions. The motion is periodic with a period

$$T = \frac{2\pi}{\dot{\gamma}}\left(\frac{r_e^2+1}{r_e}\right) \tag{3}$$

Integration of Eqs. (1) and (2) with respect to time yields

$$\tan\phi = \frac{1}{r_e}\tan\left[-\dot{\gamma}t\frac{r_e}{r_e^2+1} + \tan^{-1}(r_e \tan\phi_0)\right] \tag{4}$$

$$\tan\theta = \frac{Cr_e}{(r_e^2\sin^2\phi + \cos^2\phi)^{1/2}} \tag{5}$$

where C is the so called orbit constant and ϕ_0 is the initial value of ϕ.

Even though the original derivation of Jeffery's equations relied on the assumption of ellipsoidal particles, it has been shown that it is possible to extend Jeffery's equations to be valid for most bodies with a fore-aft symmetry, provided that an equivalent aspect ratio is used [3]. In particular, the equivalent aspect ratio for a cylindrical fiber is [4]

Contributed by the Fluids Engineering Division of ASME for publication in the JOURNAL OF FLUIDS ENGINEERING. Manuscript received April 20, 2006; final manuscript received August 9, 2006. Assoc. Editor: Dennis Siginer.

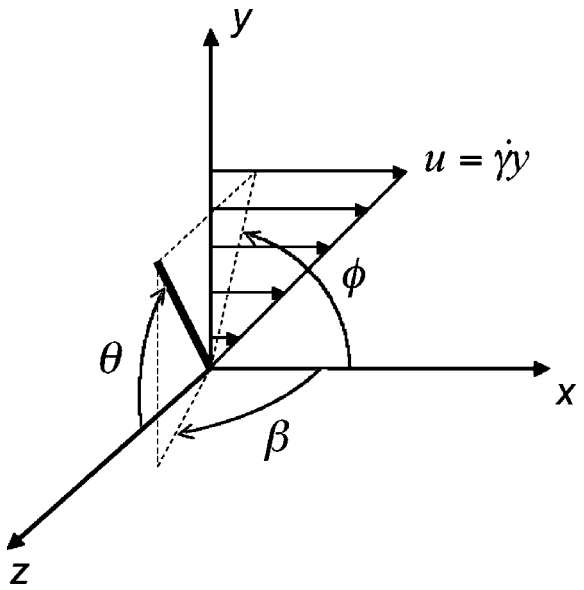

Fig. 1 Coordinate system

$$r_e = 1.24 r_p (\ln r_p)^{-1/2} \tag{6}$$

where r_p is the aspect ratio of the cylindrical fiber and r_e is the equivalent aspect ratio to be used in Jeffery's equations.

Some examples of Jeffery orbits are shown in Fig. 2. The orbits are calculated for an equivalent aspect ratio $r_e = 8.17$, which corresponds to a cylindrical fiber with aspect ratio 10 as used in the present study. The flow is in the x direction and the shear is in the y direction. Four different orbits are shown in Fig. 2. The orbits are shown as the path of a fiber end point. For high values of C the fiber spend most of its time oriented close to the flow direction. Periodically, with a period of $T/2$, it flips over 180 deg around the vorticity axis. As the value of C is lowered the amplitude of the motion in the y direction decreases. For very low values of C the fiber is almost parallel to the xz plane, oriented perpendicular to the flow direction.

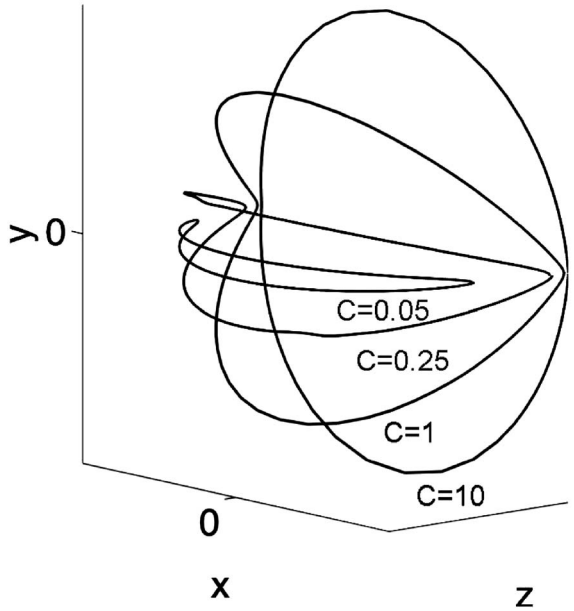

Fig. 2 Jeffery orbits for different values of the orbit constant C and $r_e = 8.17$

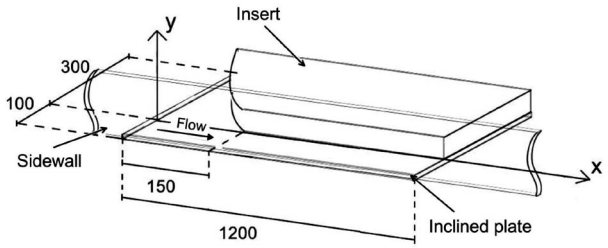

Fig. 3 Schematic figure of the test section. All lengths are given in mm.

Jeffery's equations have been verified by several researchers [5–7], but do not account for fiber–fiber interactions or wall effects. The wall effect has been investigated both experimentally [5] and theoretically [8]. For elongated particles, a good agreement of Jeffery's equations was found [5] for distances from the wall larger than one fiber length, whereas an increased rate of rotation was found closer to the wall. The spatial orbit was not considerably changed.

At higher concentrations, it has been shown [9] that the correction to the $O(\dot{\gamma})$ rotation rate is $O[\dot{\gamma}/\ln(1/\Phi)]$ where Φ is the volume fraction of the fibers. For a concentration of 1% this correction is $O(20\%)$.

Initially in this paper, the experimental setup and evaluation methods are described followed by a discussion regarding why the present experiments, performed at low velocities in a highly viscous fluid, are relevant for paper making. Thereafter the results are presented and discussed followed by conclusions. In the paper we present measurements of the previously discarded fiber orientation in the xz plane, and in particular the effect of a wall including the possibility to manipulate the orientation by modifying the surface structure of the wall.

2 Experimental Setup and Analyzing Techniques

To create a well-defined shear flow a fiber suspension was allowed to flow down a slightly inclined glass plate. To visualize the flow a charge-coupled device (CCD)-camera has been used, and by analyzing the captured images the velocity and orientation of the fibers in the shear flow can be obtained. Below, the flow loop, liquid, and fibers are described. Thereafter the image analysis methodology is introduced, which is performed in two steps: (i) detection of the position and orientation of fibers in an image; and (ii) determination of the velocity from a triplet of consecutive images. The flow in the apparatus is verified by comparing measured velocity profiles of the fibers with the theoretical profile.

2.1 Experimental Setup. The experimental setup, illustrated in Fig. 3, consists of a 1200×400 mm^2 glass plate with a thickness of 6 mm. A pivoting acrylic frame with for–aft reservoirs, not shown in the figure, supports the plate. A membrane pump (Dominator P30-ANN) is used to transfer the fluid between the reservoirs. By placing an insert on the glass plate the flow is given an inlet contraction followed by a parallel section of length 1050 mm and width 100 mm. The contraction stretches over a length of 150 mm and has a contraction ratio of four. Due to the acceleration in the contraction the fibers align themselves with the flow direction.

Experiments have been performed using two different surfaces. The first is a smooth surface and the second is a structured surface with ridges oriented 30 deg counter clockwise to the flow direction. The ridges were machined in four 100×100 mm^2 acrylic plates of height 6 mm. These plates covered the region from $x = 400$ mm to $x = 800$ mm. The position and structure of the ridges is illustrated in Fig. 4, where $H = 0.5$ mm. In the case of the smooth surface a 1200×100 mm^2 acrylic plate of height 6 mm is

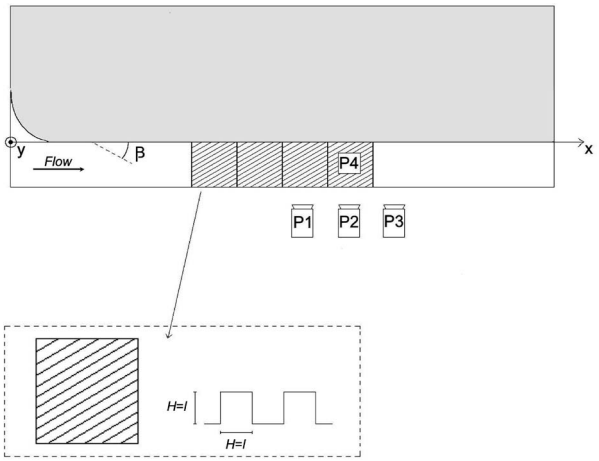

Fig. 4 Schematic figure illustrating the camera positions for the velocity profile measurements (P1, P2, and P3) and for the fiber orientation studies P4

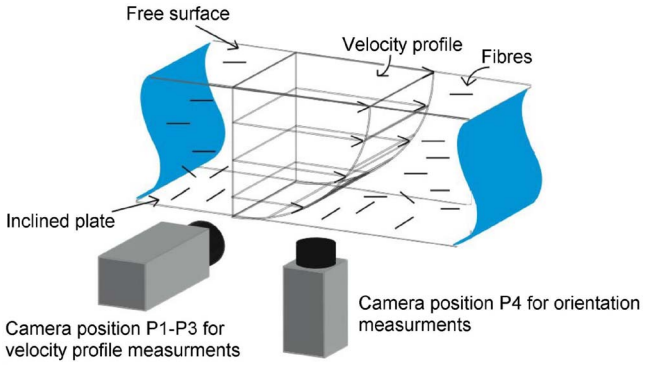

Fig. 5 Schematic figure illustrating the flow situation with the camera positions P1–P3 and P4

placed in the flow section on top of the glass plate in order to ensure that the flow situation was similar to the case with ridges.

2.2 Flow Situation. The theoretical velocity profile for a Newtonian fluid flowing down an inclined plate is given by

$$u = \frac{g}{2\nu} y(2h - y)\sin\alpha \tag{7}$$

where g is the gravitational constant; ν is the kinematic viscosity of the fluid; h is the fluid film thickness; and α is the inclination of the plate with respect to the horizontal [10]. The distance from the wall, y in Eq. (7), stretches from $y=0$ at the wall to the surface of the liquid film $y=h$. Equation (7) is thus a parabolic expression where the velocity is zero at the wall to gradually increase with the distance to the wall. The highest velocity is found at $y=h$, where $u=U_s$.

In the experiments a tilt angle of $\alpha=2.60$ deg ± 0.1 deg caused the suspension to form a liquid film along the plate with a thickness of 17.0 mm ± 0.2 mm. The film thickness was measured to be constant throughout the section between $x=650$ mm and $x=850$ mm. It can thus be established that there was no global acceleration in the flow. The Reynolds number, based on the film thickness and the velocity at the surface of the film, is defined as

$$\mathrm{Re} = \frac{U_s h}{\nu} \tag{8}$$

For the highly viscous flow in the experiments $\mathrm{Re} \approx 8$.

2.3 Fiber Suspension. The liquid containing the fibers was a mixture of glycerine and polyethyleneglycol (PEG-400). The temperature of the suspension was 295.5 K $\pm$ 0.5 K throughout the measurements. For this temperature the kinematic viscosity of the liquid was measured to $\nu=(383\pm10)\cdot10^{-6}$ m^2/s and the density to $\rho_f=1210$ kg/m$^3\pm15$ kg/m^3.

Cellulose acetate fibers were suspended in the liquid. The length of the fibers was $l=0.5$ mm and the diameter was approximately $d=50$ μm. The density of the fibers was approximately $\rho_p=1300$ kg/m^3. Since the density of the fibers is higher than the density of the liquid, the fibers will sediment slowly when suspended in the liquid. The suspension was dilute with a volume fraction of fibers $c_v=0.004$. This concentration can be expressed as $nl^3=0.48$, which is the number of fibers within a volume l^3 (n is the number density of fibers).

The index of refraction (IR) of the liquid was approximately matched to that of the fibers and the IR of the liquid was measured to $n=1.466\pm0.002$. IR matching is a frequently used tool in multiphase flows and has been used in several previous studies of fiber suspensions [11–14]. In order to visualize the fibers 4% were dyed black.

2.4 Measuring and Analyzing Method. In order to investigate the behavior of the suspended fibers, the fibers are visualized with a CCD camera, which captures images from underneath the flow. Image analysis is used to find the orientation and the velocity of the fibers. Furthermore the velocity profile of the fibers is measured and found to coincide well with the theoretical velocity profile defined in Eq. (7), which makes it possible to determine the distance from the wall of individual fibers based on their velocity.

2.4.1 Visualization. The CCD-camera (SONY DFW-X700, 1024×768 pixels) visualizing the fibers was mounted underneath the flow at $x=750$ mm (camera position P4 in Fig. 5) in order to capture images for orientation studies. To find the velocity profile of the fibers the camera was also mounted at the side of the flow (camera position P1–P3 in Fig. 5). A stroboscope (Drelloscop 200) was synchronized to the CCD camera in order to illuminate the field of view. A typical image captured by the camera is shown in Fig. 6.

2.4.2 Image Analysis. To find the position and orientation of the individual fibers in the captured images a second-order ridge detector is used [15]. The correlation between a captured image and the filter in Fig. 7, is calculated. A high value of the correlation at a certain position in an image indicates that there is a local similarity of the fiber and the filter at that position. The filter is

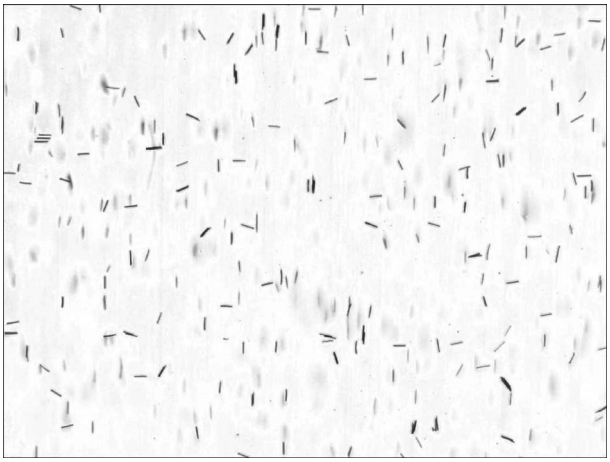

Fig. 6 Image captured underneath of the flow for orientation studies (camera position P4)

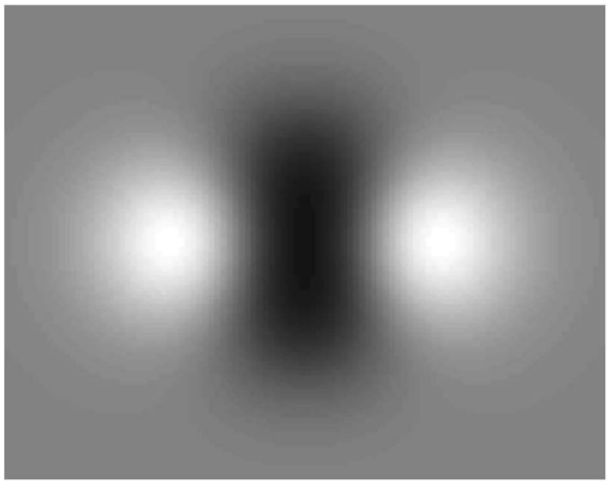

Fig. 7 Filter used to find the orientation of the fibers

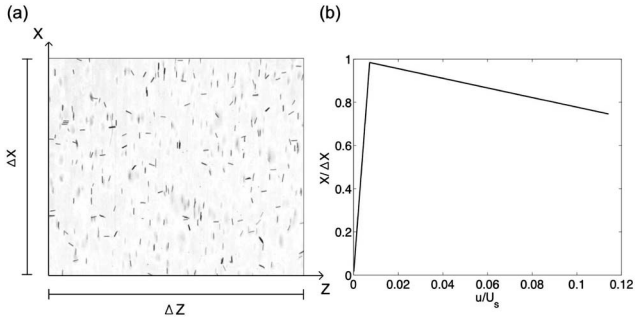

Fig. 8 Region in image where fibers can be detected

within the class of steerable filters, which means that the correlation of the filter, rotated to a certain angle, with the image can be found through a linear combination of a limited amount of correlations of filters with the image. Thus, it is not necessary to perform correlations for a large number of rotated versions of the filter with the image. For the particular filter used, only three correlations are performed in order to find the angle of the filter that will result in the highest correlation of the filter for each position in the image.

2.4.3 Particle Tracking Velocimetry. To find the velocity of the fibers at a certain time, three consecutive images were captured with a frequency of $f=10.27$ Hz$\pm$0.05 Hz. Between every set of three images a delay of $T_s=12$ s was implemented. This will give the majority of the fibers an opportunity to pass the field of view, which determines that the following triplet of images will be statistically independent. This aspect will be returned to below. Each measuring series lasted for approximately 1 h, resulting in 900 images to analyze.

Based on the position of the fibers in the images the velocity can be found through a particle tracking velocimetry (PTV) algorithm that locates the individual fibers in subsequent images. The principal idea of the algorithm is to start from the position of a fiber in an image and search for fibers in the flow direction in a narrow region downstream of this position in the following (second) image. The velocity is calculated for all the candidate fibers found in the prescribed region of the second image.

Based on the calculated velocities, the positions in the narrow region in the third image, where the fibers would be located if they continued with the same velocity, are calculated. If a fiber is located at any of the proposed positions in the third image it is considered to be the same fiber as the original fiber in the first image. This method is not flawless since it is possible for three different fibers, all traveling with different velocities, to result in a match in the algorithm. Analyzing longer image sequences could reduce this problem. This would however decrease the maximum velocity that can be detected. Decreasing the width of the region where the fibers have to be found in the second image, as well as decreasing the area where the fiber has to be found in the third image, can also reduce the error. In the studies performed here, only three images have been used to track the fibers and incorrect matches do appear occasionally, as will be seen in the velocity profile measurements.

2.4.4 Permissible Regions for PTV. In order to ensure statistically independent samples of the orientation and velocity of fibers, it is necessary that each fiber be sampled only once. This is achieved by limiting the region where the fibers have to be found in the first image. The permissible region is shown in Fig. 8 where a typical image is shown in (*a*) and the region where fibers have to be found for different velocities is shown in (*b*). This region is defined so that: (i) detection in two subsequent sets of three images is avoided (for low velocities) and (ii) the fiber is still located in the field of view when the third image is captured. In order for a fiber to be detected it has to be located below the solid line. For fibers traveling at velocities lower than $\Delta X/T_s$, where ΔX is the physical length of the image in the flow direction, the slope of the solid line is defined by the period T_s. Fibers located in this region travel too slow to pass the field of view in the period T_s. Thus, if a fiber is located above the solid line, it should have been found in the preceding set of three images. Hence, fibers with velocities smaller than $\Delta X/T_s$, located above the solid line, are not considered.

The second effect that has to be taken into account is that the region where a fiber can be detected decreases with an increased velocity of the fibers. The largest detectable velocity of a fiber is $\Delta Xf/2$. For a fiber traveling with this velocity to be detected it has to be located sufficiently far upstream in the first image, so that it can be found in the two subsequent images. For fibers traveling at velocities larger than $\Delta X/T_s$, the slope of the solid line in Fig. 8(*b*) is thus defined by the period $2/f$. Fibers located above the solid line in the first image will leave the field of view, before the third image is captured. This effect is also present at velocities smaller than $\Delta X/T_s$, although since $2/f \ll T_s$, the slope of the solid line does not change substantially.

2.5 Velocity Profile of Fibers. To verify that there was no acceleration in the flow and that the velocity profile was fully developed, the camera was mounted at the side of the flow, camera positions P1–P3 ($x=650$ mm, 750 mm, and 850 mm) (see Figs. 4 and 5). The measurements in this configuration were performed on the smooth surface at an early stage of this work in order to validate the setup, and therefore the fiber suspension was not identical to the suspension used for the orientation studies. The length and diameter of the fibers was $l=2$ mm and $d=50$ μm respectively, and the concentration of fibers was $nl^3=0.31$. The liquid mixture was essentially the same as mentioned earlier. The results from these measurements are shown in Fig. 9, where the velocities of individual fibers are marked with dots. The solid line in the figure is the theoretical velocity profile, defined by Eq. (7). The velocity has been normalized with the surface velocity of the liquid film U_s and the distance from the wall is normalized with the film thickness h. The velocities of most of the fibers found coincide very well with the theoretical profile. However, a few of the dots deviate substantially from the theoretical profile, although the amount of these dots is very small compared to the amount of fibers coinciding with the profile. It is believed that the deviating dots are a result of incorrect matches in the particle-tracking algorithm. If the deviating dots are disregarded it can be concluded that there is a strong correlation between the velocity

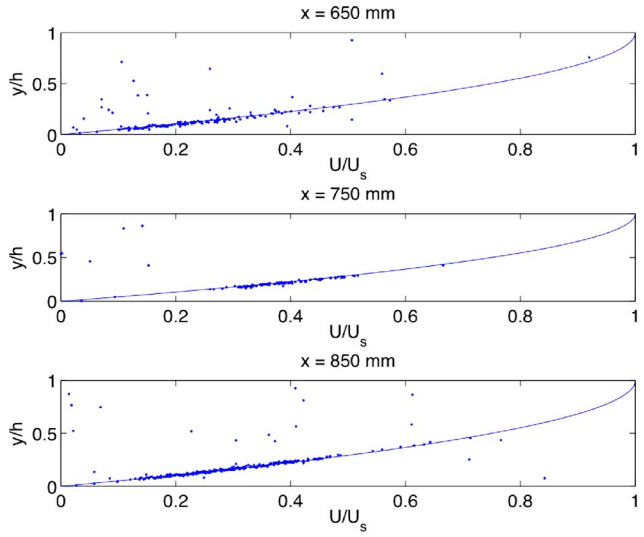

Fig. 9 Velocity profiles measured at three different position along the *x* axis (camera position P1–P3)

and the distance from the wall of the fibers. This makes it possible to convert the determined velocity of the fibers to a distance from the wall.

3 Relevance for Paper Manufacturing

In a paper machine, the jet leaving the headbox can reach velocities of more than 30 m/s. A natural question that arises is whether the fiber dynamics in the present experiments has any relevance for the fibers flowing over the lamellas in a headbox. The experiments are performed at a 400 times higher viscosity and 1/200 of the velocity as compared to the situation in the headbox. This issue will be discussed in terms of boundary layers and the forces exerted on a fiber in the headbox flow and turbulent/laminar retransition.

3.1 Fibers in the Headbox Boundary Layers. Below, a rough estimation of the force exerted on a fiber in the headbox boundary layer will be compared with the torque in the present experiments. An estimation of the velocity profiles along the lamellas in the headbox is given by the similarity solution for flow in a two-dimensional convergent channel [16]. The velocity u is given by

$$\frac{u}{U_e} = 3\tanh^2\left(\frac{\eta}{\sqrt{2}} + 1.146\right) - 2 \tag{9}$$

where U_e is the velocity of the fluid outside the boundary layer and η is defined as

$$\eta = y'\sqrt{\frac{U_e}{-(x'-x_0')\nu}} \tag{10}$$

The definitions of the coordinates x' and y' are shown in Fig. 10.

U_e will grow as the fluid travels downstream due to the contraction. The acceleration will also force the boundary layer thickness to decrease in the downstream direction. Lamellas implemented in a headbox typically end about 100 mm upstream from the outlet of the headbox. At this position the boundary layer thickness will be of the order of 1 mm. At a distance from the solid surface of 0.5 mm, i.e., one fiber length, the shear rate is about 1000 s^{-1}. For comparison, the shear rate at the same distance from the surface in the experiments is about 20 s^{-1}.

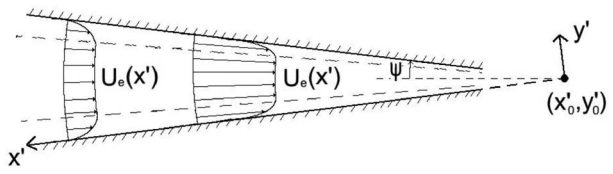

Fig. 10 Two-dimensional convergent channel

The torque on the fibers is estimated under the assumption that they are standing still, straight up from the wall. This assumption is very rough and the following analysis should only be seen as an order of magnitude analysis. If one wants to compare the motions of free fibers, careful analysis at the correct particle Reynolds numbers has to be performed. Attempts in this direction are reported in the literature [17] and show that fairly small Reynolds number can have a substantial effect on the fiber motion, but the complete description is yet to be established.

The force on a fiber standing straight up is estimated as follows. The velocity of the fluid surrounding the fiber is assumed to be linear with a shear rate $\dot{\gamma}$ and thus forms a linear velocity field $U=(a+0.5)\dot{\gamma}$ along the fiber. The coordinate a has its origin in the center of mass of the fiber and is directed along the fiber with value −0.5 and 0.5 at the fiber center points, respectively.

This velocity field gives rise to a force distribution on the fiber which can be estimated by integrating the local force per unit length on the fiber from one end to the other. In the experimental configuration the maximum $\mathrm{Re}_d = Ud/\nu$ is 0.001. For Re_d up to approximately 1, the force is given by [18]

$$F' = \frac{\rho U^2}{2}\frac{8\pi d}{\mathrm{Re}_d[0.5 - \Gamma + \ln(8/\mathrm{Re}_d)]} \tag{11}$$

where F' is the force per unit length, and $\Gamma = 0.57722\ldots$ is the Euler–Mascheroni constant. In the headbox the largest Re_d is about 25 and the force distribution is estimated by

$$F' = \frac{\rho U^2}{2} d C_d \tag{12}$$

where C_d is given by [18] $C_d = 1 + 10.0/(\mathrm{Re}_d^{2/3})$, a correlation value up to $\mathrm{Re}_d \approx 250000$.

The particle Reynolds numbers, $\dot{\gamma} l^2/\nu$, are typically 0.01 and 250 in the present experiments and a paper machine, respectively. Thus, inertial effects are considerable in the industrial application and the fibers cannot be expected to perform Jeffery orbits. Nevertheless, it will be shown below that the forces acting on a fiber during rotation can be expected to be of the same order.

By using Eqs. (11) and (12) and letting Re_d and U vary along the fiber, the force per unit length along the fiber can be calculated. The resulting force distribution for the present setup and in a paper machine is presented in Fig. 11. The lines are based on a velocity of the outgoing jet of 15 m/s, jet height of 10 mm, and a half contraction angle $\psi = 7$ deg (see Fig. 10). In spite of the large differences in the shear rate and the viscosity between the performed experiments and the situation in the headbox, the torque that the fibers will be subjected to, based on the assumption that the fiber is held fixed in the gradient direction, will only differ by a factor of 2.

3.2 Turbulence in Headbox. The flow in a headbox is normally considered to be turbulent. However, a turbulent boundary layer can return to laminar-like conditions if it is subjected to a strong acceleration. The acceleration is usually measured by the non-dimensional acceleration parameter

$$K = \frac{2\nu \tan\psi}{q} \tag{13}$$

where q is the total flow rate per unit width in the convergent channel. Experiments performed on a turbulent boundary layer for various rates of the free-stream acceleration show that an apparent retransition to a laminar boundary layer was found [19] for K

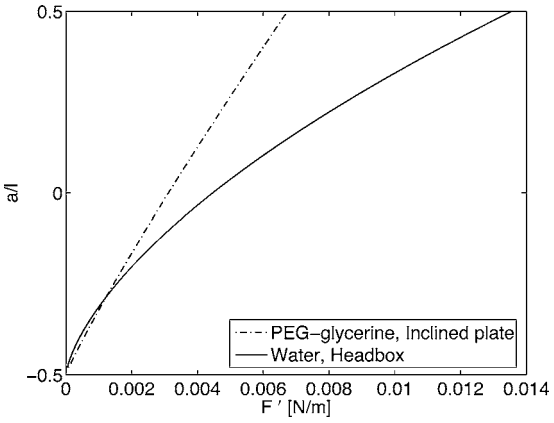

Fig. 11 Force distribution along fiber during rotation

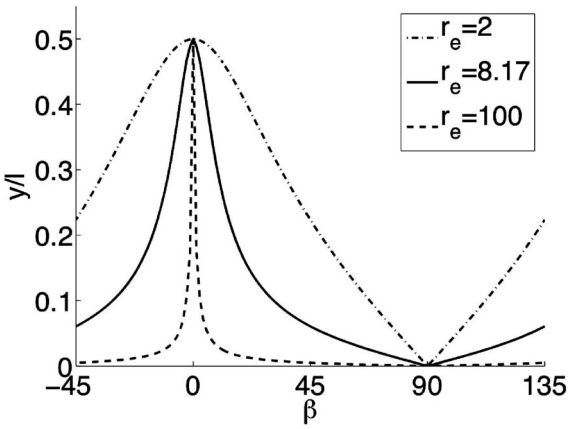

Fig. 12 Minimum distance from the wall where fibers performing Jeffery orbits can occur for different orientations and aspect ratios of the fibers

$>3.5\cdot10^{-6}$. Another experimental study of a flat-plate fully turbulent boundary layer subjected to an acceleration in a two-dimensional contraction showed that at $K\approx3.1\cdot10^{-6}$, the velocity profile approached a self-similar laminar state at the end of the contraction [20]. As seen in Eq. (13) K will depend on the flow rate in the headbox as well as the contraction ratio, defined by the angle ψ. In a papermachine, K is typically between $5\cdot10^{-7}$ and $6\cdot10^{-6}$. It is thus possible that the boundary layers will be relaminarized toward the end of the nozzle for some configurations. To the authors knowledge, all studies performed concerning the relaminarization of boundary layers are performed on one-phase flows, i.e., no particles have been suspended in the fluid.

4 Results and Discussion

Close to a solid surface it is not possible for fibers to perform all the Jeffery orbits illustrated in Fig. 2, since they would hit the wall when doing so if they are too close to the solid surface. For the case of $\beta=0$ ($C\rightarrow\infty$), i.e., fibers aligned with the flow, it has been shown that fibers can interact irreversibly with the wall and "pole vault" up to a position where the Jeffery orbit is possible to perform [21].

In the following, the restraint given by the Jeffery orbit will be examined further. This will be followed up with experimental data of the orientation of fibers in the xz plane. In addition to the orientation of the fibers, their velocities are determined. The velocity of the fibers, together with the known velocity profile, can then be used to determine the distance from the wall to the fiber. A strong effect on the orientation is found for the smooth surface but not for the one with ridges. The coordinate system used in the presentation of the results is defined in Figs. 3 and 4.

4.1 Jeffery Orbits Close to the Wall. For distances more than one fiber length away from the wall small effects of the presence of the wall have been seen. In this region most of the fibers keep their initial orientation, i.e., aligned with the flow. It was observed that fibers spend most of their time aligned with the flow and occasionally flip 180 deg around the vorticity axis. Although no measurements have been carried out in order to determine the periodicity of the motion, it appears as the fibers perform a motion similar to Jeffery orbits with a high value of C, as shown in Fig. 2. When $C\rightarrow\infty$ the amplitude of the orbit, in the y direction, is $l/2$. For distances from the wall closer than $l/2$ it is not possible for the fibers to perform this orbit without hitting the wall. As the distance to the wall decreases, the set of possible Jeffery orbits a fiber could perform is reduced. The only orbit that would be possible at the wall is the orbit given by $C=0$. The possible values of β for fibers performing Jeffery orbits in the near wall region are shown in Fig. 12. It is not possible for a fiber to perform a Jeffery orbit without hitting the wall if its combination of orientation and distance from the wall lies within the region below the solid line. It should be emphasized that this is only the case if the fibers are actually performing Jeffery orbits. As mentioned before, this assumption is reasonable for fibers close to the wall [8] and also at semi-dilute concentrations [9].

If a fiber would be located in the region below the line, the motion of the fiber could not possibly be described by Eqs. (1)–(5).

4.2 Fiber Orientation

4.2.1 Angular Distribution Prior to Particle-Tracking Analysis. In Fig. 13, the normalized distributions of orientations found in the images are shown. Data are shown for fibers flowing over the smooth (solid) and structured (dash–dot) surface. The distributions are determined based on 99,760 fibers detected over the smooth surface and 100,483 over the ridges. Since these values differ by less than 1%, it is reasonable to conclude that the fiber orientation detection algorithm described above also works as it should in the case with the structured surface. The two distributions in Fig. 13 are fairly similar where the main part of the fibers appear, at $\beta=0$, i.e., aligned with the flow. There is however one major difference, over the smooth surface, there is a considerable amount of fibers aligned *across* the flow direction, at $\beta=90$ deg, which can be seen as a bump in the distribution function.

The data presented in Fig. 13 are based on images captured with the focus of the camera set at $y=0$, i.e., at the wall. The depth of focus, measured as the region where almost all fibers are de-

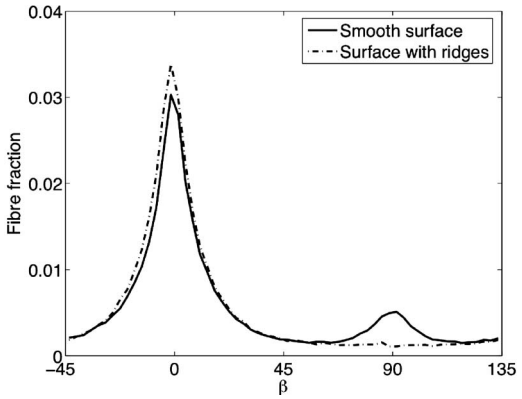

Fig. 13 Angular distribution of fibers before particle-tracking analysis (camera position P4)

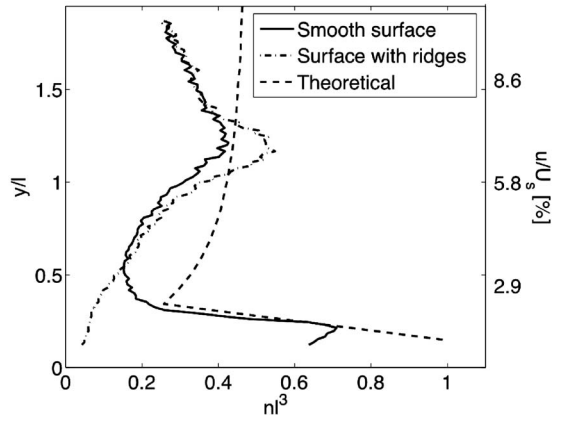

Fig. 14 Variations in concentration as a function of the distance from the wall (camera position P4)

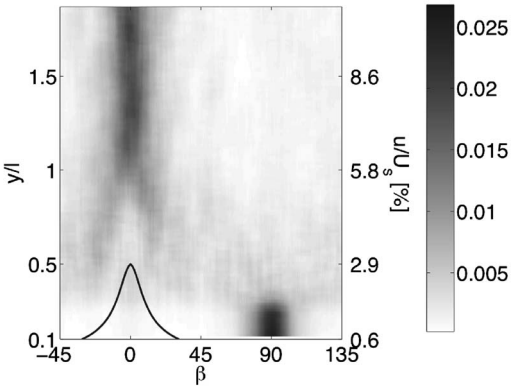

Fig. 15 Fiber fraction as a function of β for different distances from the wall. Measurements performed on smooth surface (camera position P4)

tected by the algorithm, was approximately 1 mm. Thus, the distribution functions in Fig. 13 are integrated over this region.

4.2.2 Wall-Normal Concentration Distribution. In order to obtain a more detailed knowledge of how the wall influences the fiber orientation, the velocity of individual fibers, given by the particle tracking algorithm, will be used. For the smooth surface, the known velocity profile gives a one-to-one relation between the velocity and distance to the wall of a fiber (assuming that the fibers follow the flow). Over the structured surface, this relation is less straightforward due to the complex and three-dimensional flow field that will appear close to the surface. This is reflected in the number of fibers that fulfils the conditions for having the velocity determined, as described previously. Over the smooth surface, the velocity of 12,164 fibers is determined, whereas only 10,530 remain after the particle tracking algorithm for the case over the structured surface. When comparing these numbers with the 100,000 fibers found in total, it has to be remembered that three consecutive images are used to determine one velocity value and that some parts of the images are not used in order to ensure statistically independent samples. Nevertheless, a considerable amount of fibers seem to be lost over the structured surface. Therefore, the results below have to be interpreted with care for this case.

Based on the velocities and the known velocity profile (Eq. (7)), concentration profiles can be determined. Such profiles are shown in Fig. 14 for the two cases (solid and dash–dot as in previous graph) together with a profile calculated based on the (very low but still significant) sedimentation velocities of the fibers (dash). The data will be discussed below, but first the origin of the theoretical curve has to be explained.

The theoretical line is calculated based on three assumptions:

1. That the fibers are evenly distributed at the inlet of the test section ($x=0$);
2. That the streamwise velocity of the fibers is given by the local flow velocity given by Eq. (7) and the wall-normal velocity by the sedimentation speed of a fiber oriented normal to gravity (this assumption is valid since the inclination of the plate is quite small and the fibers spend most of the time with this orientation to gravity); and
3. That fibers stay very close to the wall once they have fallen down to this region.

This simplified analysis, which neither includes the wall effect on the sedimentation speed nor other aspects of the situation, is only used in order to get a qualitative understanding of the phenomena.

The sedimentation velocity is calculated based on the sedimentation velocity of the fibers, which is given as

$$v_s = \frac{(\rho_p - \rho_f)d^2}{16\nu\rho_f}\{\ln 2r + 0.193 + O[(\ln 2r)^{-1}]\}g \qquad (14)$$

where r is the aspect ratio of the fibers; and g is the acceleration due to gravity [14,22]. The assumptions above make it possible to calculate an expected concentration variation at $x=750$ mm, where the measurements are taken. It is seen that the assumptions above give a concentration (measured by nl^3) that decays from 0.48 to around 0.25 closer to the wall. In the region closest to the wall, there is a sharp peak due to the fact that the fibers are assembled at the wall. The reason why the concentration decays toward the wall at first is that the streamwise velocity decreases toward the wall, and thus the angle at which the fibers are transported becomes steeper and steeper.

The experimental data from the flow over the smooth surface in Fig. 14 (solid) show a somewhat different behavior even though the qualitative profile is similar to the theoretical up to $y/l \approx 1.25$, a high concentration close to the wall (i.e., a lot of slow fibers), followed by a decrease and then an increase up to $nl^3 \approx 0.4$ at $y/l=1.25$. Above $y/l=1.25$, the number of fibers found in the images decreases due to the limited depth of focus of the camera.

For the flow over the structured surface, the concentration profile in Fig. 14 looks completely different and does not have the sharp peak close to the wall and the overshoot at $y/l \approx 1.25$ is considerably stronger. These differences have to be interpreted in the light of the complex flow field over the structured surface. For a complete understanding, the flow over the ridges would have to be studied in detail, but it can be assumed that the ridges induce wall normal movements and (at least locally over the ditches) higher velocities close to the wall. These features of the liquid flow could explain the smaller amount of slow fibers.

As will be seen below, the sharp peak in the concentration profile close to the wall (or at small velocities) over the smooth surface in Fig. 14 is related to the bump in the orientation distribution at $\beta=90$ deg in Fig. 13.

The fact that a large number of fibers are present very close to the wall is in conflict with the mechanism of "pole vaulting" previously proposed [21]. This discrepancy will be elaborated further on.

4.2.3 Orientation at Various Distances From the Wall. Finally, it is possible to look at the distribution at various distances (i.e., for fibers of different velocities) from the wall. These results are shown in Figs. 15 (smooth surface) and 16 (surface with ridges). In these figures, the orientation distributions for each distance from the wall are normalized in order to compensate for the varying concentration. The line defining the region in which Jeffery

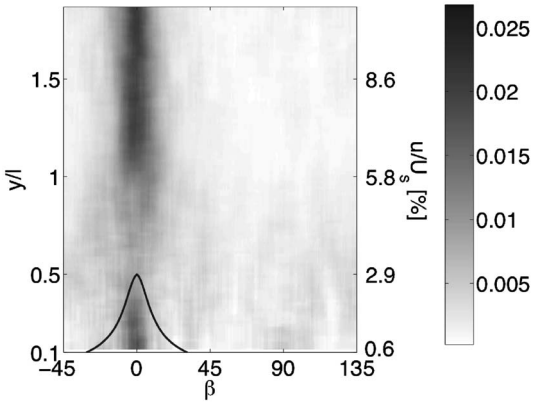

Fig. 16 Fiber fraction as a function of β for different distances from the wall. Measurements performed on surface with ridges (camera position P4).

orbits can be performed (see Fig. 12) is shown as a solid line.

Starting with the smooth surface, it is seen that almost all of the fibers that have collected at the wall are oriented normal to the flow direction. Thus, the bump in the orientation distribution in Fig. 13 originates from fibers positioned close to the wall.

This is somewhat surprising, since there are a lot of orientations which are allowed according to the Jeffery orbit. A possible explanation for this could be that close to the surface, where the velocity is very low, the fibers have performed a large number of orbits. Since the period is 2–3 s, the distance 750 mm, and the velocity <3 mm/s, the number of orbits performed are on the order of 100. It is thus possible that instead of performing the pole vault previously observed [21], the fibers are interacting with the wall through lubrication or direct contact and transfer to orbits with lower and lower C values (see Fig. 2) for each period. Finally, C would be close to 0 and the orientation is consequently close to $\beta=90$ deg. The fact that this, or any other mechanism that leads to $\beta=90$ deg occurs, implies that the previously observed mechanism for wall interaction [21] is not the only possible one.

Further out from the wall, the fibers illustrated in Fig. 15 seem to be more evenly distributed over the orientations from $y/l=0.2-1$ and concentrated around $\beta=0$ further out.

It is now time to take a closer look at the data from the flow over the structured surface. Before doing so, it is appropriate to remind the reader that the correlation between fiber velocity and distance from the wall is not valid in this case. It is therefore more appropriate to talk about fast and slow fibers. The orientation distribution for different fiber velocities is shown in Fig. 16 (the corresponding distance from the wall over the smooth surface is also shown). For fibers with a velocity down to that corresponding to $y>0.2l$, the data are very similar to the smooth surface case. For $y>l$, most fibers are oriented in the flow direction, in the region $0.2l<y<l$ the distribution of fiber orientations is more homogeneous. The (very few, compare Fig. 14) slow fibers are oriented in the streamwise direction.

There are two possible reasons why there is only a small amount of fibers with low velocities detected over the structured surface. The first is that the detection algorithm (which relies on the fibers moving straight downstream) fails. The second is that there are fewer slow fibers. These two effects are probably combined. During the experiments it was observed that fibers were trapped in the ridges and followed the ridges for a while before continuing downstream. As mentioned above, the complex flowfield over the surfaces with ridges, with transversal, wall-normal, and streamwise velocity fluctuations might also allow the fibers to travel faster, even though they are closer to the surface. Nevertheless, Fig. 13 clearly shows that there is no large portion of fibers with $\beta\approx90$ deg over the structured surface even before the particle tracking algorithm. It has thus been shown that the smooth surface gives the fibers collecting at the wall an orientation $\beta=90$ deg and that this effect is not present over the surface with ridges.

5 Conclusions

An experimental study has been performed on the subject of how fibers orient themselves in a shear flow close to a solid wall. A fiber suspension was allowed to flow down an inclined plate, thus forming a well-defined shear layer. As a visualization tool a CCD camera was mounted underneath the flow in order to find the orientation of the fibers in the plane parallel to the wall. Experiments were performed with two different surface structures of the plate to explore the possibility of influencing the orientation of the fibers by modifying the structure of the wall. The first structure used was a plain smooth surface, while the other surface used was a surface with ridges oriented −30 deg to the direction of the flow. For distances from the wall larger than one fiber length basically all fibers stayed aligned with the flow, for both surfaces. The fibers located in this region seemed to perform orbits similar to those described by Jeffery's mathematical analysis [2]. For distances from the wall closer than one fiber length a difference could be seen between the experiments performed on different surfaces.

For the smooth surface the majority of the fibers no longer oriented themselves in the flow direction. Very close to the wall, less than about a quarter of a fiber length, nearly all of the fibers were oriented close to perpendicular to the flow direction.

Concerning the experiments performed on the surface with ridges, it is concluded that the particle-tracking algorithm used to follow the fibers, fails to do this in a satisfactorily manner. The reason for this is probably the disordered motion occurring close to the structured surface, where some of the fibers change direction as they flow down the plate. It is thus not perfectly clear what happens close to the surface with ridges. Nevertheless, it has been possible to show that the effect found close to the smooth surface, where many fibers orient themselves perpendicular to the flow, is not present for the structured surface with ridges.

The insights of the present study gives two main directions for future work: The first is to study the selection between the "pole-vault" mechanism of fibers close to the wall identified earlier [21] and other mechanisms, leading to $\beta=90$ deg. The second direction, which is critical for industrial applicability, is to study the orientation at higher velocities/lower viscosities in order to study the effects of inertia and turbulence.

Acknowledgment

Thanks go to Dr. Richard Holm for performing initial experiments and providing valuable input in the startup of the project. Dr. Söderberg has been funded through the Biofibre Materials Centre (BiMaC) at KTH, Mr. Carlsson and Dr. Lundell has been funded by the European Commision under Contract No. 500345 (NMP2-CT-2004-500345). Dr. Lundell has also been funded by the Swedish Research Council (VR).

References

[1] Fellers, C., and Norman, B., 1998, *Pappersteknik*, KTH, Stockholm, Sweden.
[2] Jeffery, G. B., 1922, "The Motion of Ellipsoidal Particles Immersed in a Viscous Fluid," Proc. R. Soc. London, Ser. A **102**(715), pp. 161–179.
[3] Bretherton, F. P., 1962, "The Motion of Rigid Particles in a Shear Flow at Low Reynolds Number," J. Fluid Mech. **14**, pp. 284–304.
[4] Cox, R. G., 1971, "The Motion of a Long Slender Body in a Viscous Fluid. Part 2. Shear Flow," J. Fluid Mech. **45**, pp. 625–657.
[5] Moses, K. B., Advani, S. G., and Reinhardt, A., 2001, "Investigation of Fiber Motion Near Solid Boundaries in Simple Shear Flow," Rheol. Acta **40**, pp. 296–306.
[6] Taylor, G. I., 1923, "The Motion of Ellipsoidal Particles in a Viscous Fluid," Proc. R. Soc. London, Ser. A **103**, pp. 58–61.
[7] Binder, R. C., 1939, "The Motion of Cylindrical Particles in Viscous Flow," J. Appl. Phys. **10**, pp. 711–713.
[8] Pozrikidis, C., 2005, "Orbiting Motion of a Freely Suspended Spheroid Near a Plane Wall," J. Fluid Mech. **541**, pp. 105–114.

[9] Koch, D. L., and Shaqfeh, E. S. G., 1990, "The Average Rotation Rate of a Fiber in the Linear Flow of a Semidilute Suspension," Phys. Fluids A **2**, pp. 2093–2102.
[10] Acheson, D. J., 1990, *Elementary Fluid Dynamics*, Oxford University Press, Oxford, UK.
[11] Iso, Y., and Cohen, D. L., 1995, "Orientation in Simple Shear Flow of Semi-dilute Fiber Suspensions. 1. Weakly Elastic Fluids," J. Non-Newtonian Fluid Mech. **62**, pp. 115–134.
[12] Petrich, M. P., Koch, D. L., and Cohen, C., 2000, "An Experimental Determination of the Stress–Microstructure Relationship in Semi-concentrated Fiber Suspensions," J. Non-Newtonian Fluid Mech. **95**, pp. 101–133.
[13] Holm, R., 2005, "Fluid Mechanics of Fiber Suspensions Related to Papermaking," Ph.D. thesis, Royal Institute of Technology, Stockholm, Sweden.
[14] Herzhaft, B., and Guazzelli, E., 1999, "Experimental Study of the Sedimentation of Dilute and Semi-dilute Suspensions of Fibers," J. Fluid Mech. **384**, pp. 133–158.
[15] Jacob, M., and Unser, M., 2004, "Design of Steerable Filters for Feature Detection Using Canny-Like Criteria," IEEE Trans. Pattern Anal. Mach. Intell., **26**(8), pp 1007–1019.
[16] Schlichting, H., 1979, *Boundary Layer Theory*, 7th ed., McGraw–Hill, New York.
[17] Subramanian, G., and Koch, D. L., 2005, "Inertial Effects on Fiber Motion in Simple Shear Flow," J. Fluid Mech. **535**, pp. 383–414.
[18] White, F. M., 1991, *Viscous Fluid Flow*, 2nd ed., McGraw-Hill, New York.
[19] Moretti, P. M., and Kays, W. M., 1965, "Heat Transfer to a Turbulent Boundary Layer with Varying Free-Stream Velocity and Varying Surface Temperature—An Experimental Study," Int. J. Heat Mass Transfer **8**, pp. 1187–1202.
[20] Parsheh, M., 2001, "Flow in Contractions with Application to Headboxes," Ph.D. thesis, Royal Institute of Technology, Stockholm, Sweden.
[21] Stover, C. A., and Cohen, C., 1999, "The Motion of Rodlike Particles in the Pressure-Driven Flow Between Flat Plates," J. Non-Newtonian Fluid Mech. **87**, pp. 369–402.
[22] Batchelor, G., 1970, "Slender-Body Theory for Particles of Arbitrary Cross-Section in Stokes Flow," J. Fluid Mech., **44**, pp. 419–440.

Jet Wiping in Hot-Dip Galvanization

Anne Gosset[1]
e-mail: gosset@vki.ac.be

Jean-Marie Buchlin
e-mail: buchlin@vki.ac.be

von Karman Institute for Fluid Dynamics (VKI),
Chaussée de Waterloo 72,
1640 Rhode-St-Genèse, Belgium

This paper presents an analysis of the gas-jet wiping process in hot-dip galvanization. This technique consists of reducing the liquid film thickness on a moving substrate by applying gas slot jets. A theoretical development allows the computation of the film thickness evolution in the wiping zone. It is further simplified to an engineering model which predicts directly the final coating thickness, in good agreement with wiping experiments. The limit of applicability of jet wiping is due to the occurence of a violent film instability, called splashing, which takes the form of a liquid droplet emission just upstream the nozzle. An experimental investigation of this phenomenon is conducted on a water-model facility. Two nozzle designs are tested. The effect of process parameters such as the strip speed, the nozzle pressure, the standoff distance, and the tilt angle of the nozzle on splashing is emphasized. A dimensionless correlation is established to predict the operating conditions leading to splashing occurence. It is successfully confronted to observations made on galvanization lines. [DOI: 10.1115/1.2436585]

Keywords: coating flows, thin films, gas-jet wiping, droplet formation, spray

1 Introduction

The deposition of a very thin liquid film on a solid surface is the basis of numerous coating techniques used in industrial processes such as paper and photographic film manufacturing, wire coating, and in the iron and steel industries. In the case of hot-dip galvanization, moving steel strips are coated with a thin layer of zinc in order to resist to oxidization. The protective metal is applied in its liquid state, by dipping the substrate into a bath of coating. However, at common strip speeds, the liquid layer dragged by the moving web is far too thick and uneven for the applications considered. The final coating thickness is therefore controlled by the application of two-dimensional high-speed gas jets impinging on the liquid layer. They lead to the formation of a runback flow down to the bath, leaving a uniform and constant coating thickness dowsntream on the substrate. This process is referred to as the jet wiping technique, or air-knife coating, the principle of which is illustrated by the schematic shown in Fig. 1. The film thickness after wiping, h_f, depends on the substrate velocity U, the nozzle pressure P_n, the nozzle to substrate standoff distance Z, the nozzle slot width d, and the nozzle tilt angle α, as well as the liquid properties.

As the strip speed increases, the wiping technique is however limited by the occurence of a rather violent film instability called splashing, which occurs upstream the jet nozzle. Typical visualization of incipient splashing on a galvanization line is shown in Fig. 2(a), while Figs. 2(b) and 2(c) demonstrate that the splashing phenomenon is qualitatively well reproduced on a water model facility. This mechanism is characterized by the ejection of liquid droplets from the runback film flow, followed by its complete explosion in fully developed state. Splashing affects the final coating quality because the runback flow separates from the substrate when it develops. Such a behavior degrades significantly the wiping conditions (pressure gradient and shear stress at jet impingement), and leads to unstable conditions and to the formation of zinc droplets. The result is a very poor wiping efficiency, i.e., the film thickness is less efficiently reduced for given operating conditions, and a poor coating quality downstream. Moreover, the ejected droplets may reach the nozzle slit, and after solidification, block it. In the case of galvanization, there is also a safety concern because the molten zinc droplets at 460 °C may reach the workers in charge of removing regularly the layer of oxidized zinc at the free surface of the bath.

It is therefore of interest to have at disposal a predictive model for splashing occurrence on galvanization lines. Meanwhile, a major practical concern is the maintenance of high production rates of constant coating thickness products. Therefore, the prediction of the wiping efficiency is necessary to define completely an optimum process window.

This paper describes a simple engineering model for the final coating thickness after wiping. It is validated with experimental data in a process window in which surface tension can be neglected. A phenomenological approach for the prediction of splashing occurrence is then proposed. A database gathering splashing conditions for a wide range of parameters on a water test facility is used for the derivation of a dimensionless empirical model for splashing. The analysis emphasizes the effect of nozzle tilting. Optimum process windows can thus be defined from the combination of the wiping and splashing models. Finally, the engineering tools are applied to typical galvanization conditions.

2 Jet Wiping

An analytical model is developed for the prediction of the final film thickness. The effect of nozzle tilting is included in this model. It is validated with experimental data.

2.1 Analytical Model. The film interface shape in jet wiping is due to the pressure gradient and shear stress distributions produced by the impinging jet [1–3]. Typical profiles of the wiping actuators together with the interface shape are shown in Fig. 3. Various models for the film thickness profile in the wiping region are proposed in literature. The pioneer study in this field is the one by Thornton and Graff [1], who assume that the interface deformation is due only to the pressure gradient created by the impinging jet on the film. It is considered as a body force supplementing gravity. Tuck [2] adopts a similar approach, and checks the stability of the solutions for long wavelength perturbations. Ellen and Tu [3] propose a model which for the first time takes the shear stress into account. They show that it participates for 20–40% to the wiping action. Tuck et al. [4] quantify the inhibiting effect of surface tension on jet wiping, whereas it is neglected in previous studies. Following this, Yoneda [5,6] presents a complete numeri-

[1]Corresponding author.

Contributed by the Fluids Engineering Division of ASME for publication in the JOURNAL OF FLUIDS ENGINEERING. Manuscript received April 24, 2006; final manuscript received December 27, 2006. Assoc. Editor Theodore Heindel.

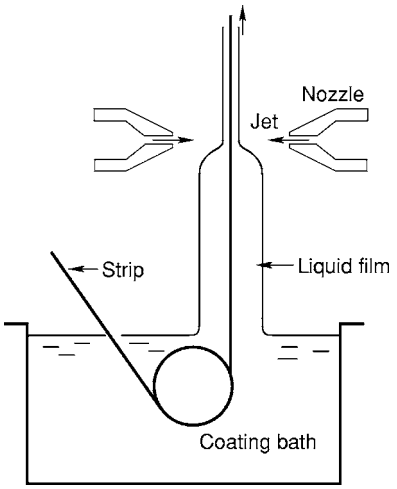

Fig. 1 Schematic of the jet wiping operation applied to the galvanization process

cal solution for the film interface, including both surface tension effects and shear stress. Moreover, he predicts the transition from "weak" air-knife action (no runback flow) to "strong" action (effective jet wiping). Finally, the originality of the development by Buchlin [7] lies in the fact that he proposes different levels of solution of the model, according to the assumptions made. For

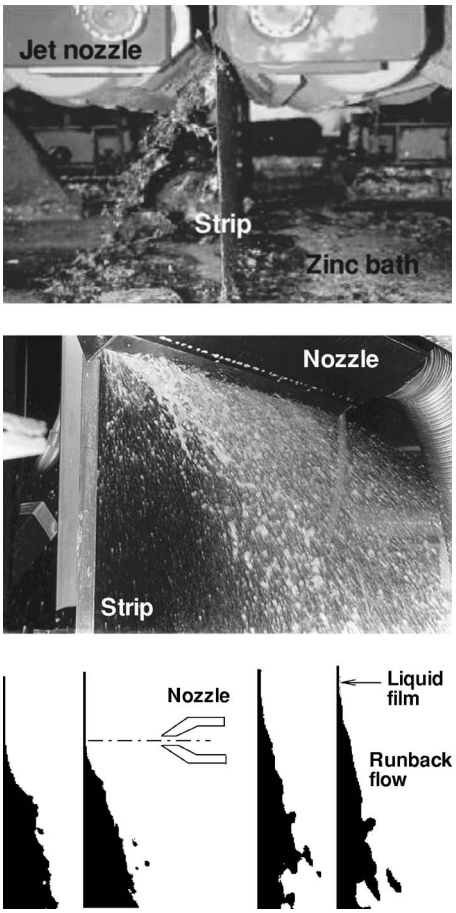

Fig. 2 (a) Splashing phenomenon on a galvanization line; (b) fully developed splashing with water; the runback flow is completely separated along the strip width; and (c) sideview visualization of splashing with water

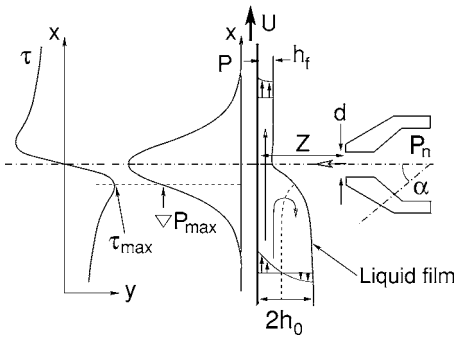

Fig. 3 Typical film shape in jet wiping with pressure gradient and shear stress profiles due to the jet

instance, when surface tension is taken into account, he presents a numerical solution for the thickness distribution in the wiping region. When surface tension is relaxed, he shows that a one-dimensional analytical solution exists. Assuming finally that the main wiping actuators (first maximum pressure gradient and shear stress met by the dragged film) act at the same location, he proposes the idea of a zero-dimensional model predicting directly the final film thickness.

The theoretical description of gas-jet wiping is usually based on the lubrication approach, which assumes negligible inertia with respect to viscous, gravity and pressure terms. If (Ox) is the axis along the substrate, and (Oy) the one across the substrate, it turns out that in jet wiping, variations along the x direction are very slow compared to variations along y and to the film thickness. The scaling factor $\epsilon = 2\pi h/\lambda \ll 1$ can thus be introduced, where h is the mean film thickness, and λ is the characteristic wavelength of a x fluctuation. Making the change of variables $x^* = \varepsilon x$ and $y^* = y$, the inertia terms in the Navier–Stokes equations are found to be of order $\epsilon \mathrm{Re}_f \ll \varepsilon$. Since the film Reynolds number Re_f based on the film velocity in the substrate referential and on the mean thickness is very small, inertia can be neglected, and the flow can be assumed parallel. The resulting (Ox) momentum equation of the film states that the shear stress balances the weight and pressure

$$\mu_l \frac{\partial^2 u}{\partial y^2} = \rho_l g + \frac{dP_l}{dx} \tag{1}$$

$$q = \int_0^{h(x)} u(x,y)dy \tag{2}$$

where $u(x,y)$ is the local film velocity; $h(x)$ is the local film thickness; μ_l and ρ_l are, respectively, the liquid dynamic viscosity and density; g is the acceleration of gravity; P_l is the pressure in the liquid; and q is the film volumetric flow rate. The film is thin enough to assume that the liquid pressure P_l is equal to the gas-jet pressure at impingement P_g corrected by a surface tension term due to the meniscus formation

$$\frac{dP_l}{dx} = \frac{dP_g}{dx} - \sigma_l \frac{d}{dx}\left[\frac{h_{xx}}{(1+h_x^2)^{3/2}}\right] \tag{3}$$

where σ_l is the liquid surface tension; and subscript x refers to derivation with respect to x. Subscript l refers to the liquid phase, and subscript g to the gas phase. The term containing σ_l represents the contribution of surface tension to the pressure gradient jump through the gas–liquid interface. The mean film curvature $h_{xx}/(1+h_x^2)^{3/2}$ can be linearized to get h_{xxx} on the grounds that the free surface slope is small. The boundary conditions to be associated with Eq. (1) express the no-slip condition of the film on the substrate, and the continuity of shear stress at the interface

$$u = U \quad \text{at} \quad y = 0 \tag{4}$$

$$\mu_l \frac{\partial u}{\partial y} = \tau(x) \quad \text{at} \quad y = h(x) \tag{5}$$

where τ is the shear stress due to the impinging jet on the film free surface. Equation (1) together with Eqs. (4) and (5) can be readily integrated to give the film velocity profile $u(x,y)$ from which the flow rate q is determined through Eq. (2). The resulting flow rate equation has the following nondimensional form

$$\Gamma \frac{d^3\hat{h}(X)}{dX^3} = 1 + \nabla \hat{P}_g(X) + \frac{2Q - 3\hat{h} - 1.5\hat{T}\hat{h}^2}{\hat{h}^3} \tag{6}$$

The normalized variables are defined as follows: $X=x/d$, $\hat{h}=h/h_0$ with $h_0=\sqrt{\mu_l U/\rho_l g}$; $\Gamma=\sigma_l h_0/\rho_l g d^3$; $Q=q/q_0$ with $q_0=2/3Uh_0$; $\nabla\hat{P}_g=\nabla P_g/\rho_l g$; and $\hat{T}=\tau/\tau_0$ with $\tau_0=\sqrt{\mu_l U \rho_l g}$. Subscript 0 refers to the dragged film flow without wiping. Γ is the dimensionless parameter which measures the influence of surface tension [4]. Though the pressure P is the only function of x, we choose deliberately to use $\nabla P_g(x)$ instead of dP_g/dx for convenience in writing.

Since the pressure gradient and shear stress distributions due to the jet are usually assumed to be known, Eq. (6) has basically two unknowns: the dimensionless film thickness $\hat{h}$ and flow rate Q. Because it was shown that the presence of the liquid film almost does not affect the jet profiles [8], the pressure gradient and shear stress profiles are given by experimental or numerical simulation of an impinging jet on a flat plate [9,10]. Assuming a negligible effect of surface tension, which will be justified later, Eq. (6) can be further simplified to

$$(1 + \nabla\hat{P})\hat{h}^3 - 1.5\hat{T}\hat{h}^2 - 3\hat{h} + 2Q = 0 \tag{7}$$

where P is now the liquid pressure, which is equal to the gas pressure. The solution of Eq. (7) is obtained by solving locally the cubic equation, using the pressure gradient and shear stress distributions $\nabla\hat{P}(X)$ and $\hat{T}(X)$ of an impinging jet on a flat surface. It is generally agreed that the pressure distribution at the wall is well described by a Gaussian law [9,10]

$$P(\xi) = P_s e^{-0.693\xi^2} \tag{8}$$

where P_s is the maximum pressure at the stagnation point; and $\xi=x/b_P$, where b_P is the distance between the jet axis and the location of $P_s/2$. The pressure gradient profile is therefore given by the following expression

$$\nabla P(\xi) = -1.386\frac{P_s}{b_P}\xi e^{-0.693\xi^2} = \frac{-1.386}{b_P}\xi P(\xi) \tag{9}$$

P_s and b_P are both functions of Z and d. When the potential core impinges onto the plate ($Z/d \leqslant 5$), the stagnation pressure remains constant and equal to the jet pressure P_n. For $Z/d > 5$, P_s decreases when Z/d increases

$$\frac{P_s}{P_n} = C_p \frac{d}{Z} \tag{10}$$

with $C_p \simeq 6.5$.

In the impingement region, the shear stress profile fits closely the distribution given by [9]

$$\tau(\xi) = \tau_{\max}[\mathrm{erf}(0.833\xi) - 0.2\xi e^{-0.693\xi^2}] \tag{11}$$

where erf is the error function. For a developed impinging jet ($Z/d > 8$), the maximum shear stress is given by [9,10]

$$\tau_{\max} = C_\tau(\mathrm{Re}_j)\frac{P_n}{Z/d} \tag{12}$$

where C_τ is a value depending on the jet Reynolds number Re_j based on the nozzle slot width d and the jet exit velocity V_{0j}, when it is lower than about 6000

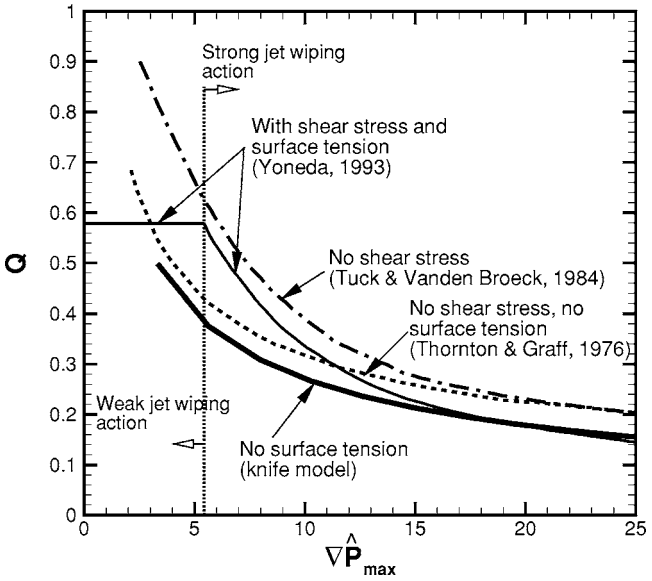

Fig. 4 Comparison of the dimensionless volumetric film flow rate predicted by the knife model and various models from literature as a function of the dimensionless jet pressure gradient for Ca=0.01

$$C_\tau = -10^{-5}\,\mathrm{Re}_j + 0.129 \tag{13}$$

Otherwise, $C_\tau=0.067$.

In the wall-jet region, the shear stress distribution is better approximated by [9]

$$\tau(\xi) = 0.26\frac{dP_n}{\mathrm{Re}_j^{0.2}}\left(\frac{1}{|\xi|+4}\right)\left(\frac{1}{b_P}\right) \tag{14}$$

In steady conditions, continuity implies that the liquid flow rate Q is constant throughout the wiping region. On the other hand, the film thickness h varies along x with the $\nabla P(x)$ and $\tau(x)$ distributions. The cubic Eq. (7), which has to be solved for all x values, has two, or no positive roots. There exists only one value of Q for which the film thickness evolution is physically acceptable. It corresponds to the condition when the derivative of the film flow rate with respect to the film thickness is null ($dQ/d\hat{h}=0$), that is to say when the flow rate is optimum. A zero-dimensional model (hereafter referred to as the knife model) can be derived from Eq. (7), relying on the observation that the position of the upstream maximum pressure gradient and shear stress corresponds approximately to the location where the film surface velocity is equal to zero (called location of film surface bifurcation) [10]. Therefore, we consider only this position where the net flow rate is "optimum" and name it X_{opt}. Equation (7) is written at that position to give Eq. (15), and the local film thickness is named $\hat{h}_{\mathrm{opt}}$

$$(1 + \nabla\hat{P}_{\max})\hat{h}_{\mathrm{opt}}^3 - 1.5\hat{T}_{\max}\hat{h}_{\mathrm{opt}}^2 - 3\hat{h}_{\mathrm{opt}} + 2Q = 0 \tag{15}$$

Then, in order to solve Eq. (15), a second equation is found by using the fact that the net flow rate is optimum, i.e., $dQ/d\hat{h}=0$. The value of $\hat{h}_{\mathrm{opt}}$ can thus be found through Eq. (16)

$$\hat{h}_{\mathrm{opt}} = \frac{\hat{T}_{\max} + \sqrt{\hat{T}_{\max}^2 + 4(1 + \nabla\hat{P}_{\max})}}{2(1 + \nabla\hat{P}_{\max})} \tag{16}$$

This value is replaced in Eq. (15), and Q is found. Far downstream the wiping region, the film thickness becomes constant and equal to its final value h_f. Using the value of Q and Eq. (2), h_f is computed (the velocity profile across the film is almost uniform and equal to the substrate velocity U at that positions).

The different aforementioned models are compared in Fig. 4,

where the evolution of the dimensionless film flow rate Q is plotted as a function of the dimensionless pressure gradient $\nabla \hat{P}_{\max}$ for a capillary number $\mathrm{Ca}=\mu_l U/\sigma_l$ equal to 0.01. If pure water is considered as the working fluid, it corresponds to a substrate velocity $U=0.67$ m/s. The values of $\nabla \hat{P}_{\max}$ and $\hat{T}_{\max}$ used for the computations in Fig. 4 are based on the experimental correlations Eqs. (9)–(14) from Beltaos et al. [9]. The comparison of the models of Thornton et al. [1] and Tuck [2] reveals that the surface tension effect becomes negligible beyond a certain value of the pressure gradient; the jet action then overcomes the capillary force in the wiping meniscus. The same conclusion is reached when comparing the results of Yoneda [5,6] with the ones of the knife model, which both take shear stress into account, in contrast to the previously cited models. As noted previously, the model proposed by Yoneda [5,6] predicts the jet threshold beyond which the film thickness is reduced. It appears as the straight line portion in Fig. 4.

It can be thus inferred that the knife model is perfectly reliable for a given Ca when the jet action is "strong" (compared to capillarity in the meniscus). It should be noted that the final film thickness h_f which is obtained very quickly with the zero-dimensional knife model differs by generally less than 1% from the value found when computing the whole thickness distribution with the one-dimensional (1D) model Eq. (7). A complete thickness profile thus obtained was validated with numerical data from volume of fluid-large Eddy simulation (VOF-LES) numerical simulations by Lacanette et al. [8] for $Z/d=8$ and a jet pressure $P_n=1450$ Pa. The pressure gradient and shear stress distributions used for the 1D model predictions have been measured experimentally [8], and they fit closely the empirical correlations Eqs. (9)–(10) and (11)–(14) from the literature [9]. The film interface shapes obtained analytically and with two-phase simulations are in good agreement both in the meniscus region and downstream the jet, proving that surface tension can be neglected in such conditions. The film thickness after wiping h_f is underestimated of about 15% by the wiping model with respect to the interface obtained numerically. Upstream the impinging zone, the runback flow from the 1D model is significantly thicker than the simulated interface. The reason for that may be the high aspect ratio of the mesh cells in that region, inducing a poor spatial resolution for the interface detection in VOF-LES simulations, or the fact that the lubrication assumption made in the analytical model is not be valid in the runback flow region.

2.2 Effect of Nozzle Tilting. When the nozzle is tilted, the impingement angle of the jet involves an asymmetry of the pressure and shear stress profiles, and thus a modification of the wiping actuators. For the purpose of splashing delay study, we will consider only downward nozzle tilting. In that case, it is expected that the usptream maximum pressure gradient is reduced due to the flattening of the pressure distribution. Expressions for $\nabla P_{\max}$ and $\tau_{\max}$ can be derived from the empirical relations provided by Beltaos for oblique impinging jets [11]. It follows that

$$\nabla P_{\max} = \frac{5.712}{b_P} P_n \frac{d}{Z'} \cos\alpha \tag{17}$$

Z' is the nozzle to wall distance along the jet axis, such that $Z(\alpha=0 \text{ deg})=Z'\cos\alpha$. The quantity b_P/Z is given by an empirical relation [11], and is almost insensitive to α for angles smaller than 30 deg. The maximum pressure gradient has therefore an evolution in $\cos^2\alpha$.

The shear stress $\tau_{\max}$ can be approximated by the following expression [11]

$$\tau_{\max} = C^*(\alpha)\frac{P_n d}{Z'} \tag{18}$$

where C^* is a coefficient which depends on the nozzle geometry, and is shown to be almost insensitive to the jet angle α when it remains lower than 30 deg [11]. Beltaos [11] proposes a value of 0.06 for developed impinging jets ($Z/d>8$). The maximum shear stress for a tilted jet therefore varies in $\cos\alpha$.

The pressure gradient being the main actuator for the Z/d values considered in the present study, it may be expected that the overall wiping efficiency is lower when the jet is tilted downward.

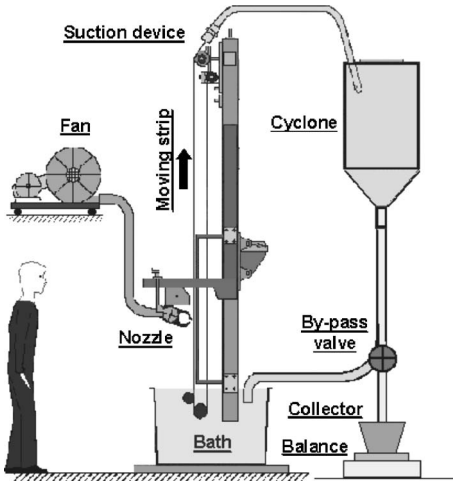

Fig. 5 Schematic of the water jet wiping facility

2.3 Validation With Experimental Data. The knife model has the advantage of being very simple and fast to implement. Its use for the present investigation and in industrial conditions requires its validation with experimental data, in very well controlled conditions.

2.3.1 Experimental Setup and Techniques. Therefore, wiping experiments are performed on a dedicated water model facility, which simulates a galvanization line. Figure 5 shows a schematic of the setup, which includes a vertical rubber strip 5 m long and 0.5 m wide, stretched between two rolls. The strip is set into motion by the upper roll, which is entrained by an electric motor. The strip velocity can be adjusted in the range 0.5–4.5 m/s, and it is measured using a tachometer. The substrate dips in a bath of water, to which a surfactant was added to ensure a good wettability. The water surface tension thus drops to 0.03 N/m±0.001 N/m. Normally, surfactant materials tend to remain at the free surface of a liquid, and surface tension gradients may occur. However, the capillary numbers remain sufficiently low here so that such an effect is not felt. Moreover, the wiping process ensures a continuous mixing of the working fluid and surfactant. The slot nozzle is positioned at 0.8 m above the free surface of the bath. Its tilt angle is adjustable, and the standoff distance Z between the nozzle and the strip is tuned thanks to shims within ±0.1 mm. Two nozzle geometries are tested. They are sketched in Fig. 6, together with their main geometrical characteristics. Nozzle T1 is fully symmetric, while T2 exhibits a bottom clearing and a more confined geometry. They are both 0.6 m wide to avoid edge effects. The

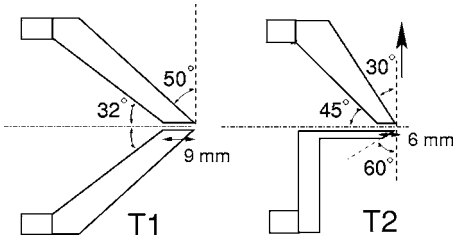

Fig. 6 Nozzle designs

nozzle is fed with compressed air up to 10 kPa. The slot width d can be adjusted between 0.7 mm and 2.1 mm within ±0.005 mm. In all the experiments presented here, $d=1.4$ mm. For sake of simplicity, the wiping mechanism is studied only on one side. To ensure a good stability of the strip in the impact zone, the rear face is sliding on an aluminum plate lubricated by the entrained water. The mean liquid film thickness in space and time is determined from the measured mass flow rate after wiping q

$$h_f = \frac{q}{\rho_l L U} \tag{19}$$

where L is the strip width. The assumption of a uniform velocity profile across the liquid film introduces an error of less than 0.1% on h_f, with respect to the value computed with the real film velocity profile computed from Eq. (1). The liquid film is withdrawn at the top of the band by the action of a rubber scraper combined to a sucking apparatus based on air ejectors. Two lateral small jets draw the liquid film towards suction ports, which are connected to a cyclone separator. A balance measures the amount of collected water, and a stopwatch the weighting time. Depending on the flow rate, the measuring time ranges between 1 and 6 min. Each experiment is repeated five times. The uncertainty on the mean value of a measurand X is given by $U=\sqrt{B^2+(tS_{\bar{X}})^2}$, where B is the bias error, $S_{\bar{X}}$ is the precision index of the mean $\bar{X}$, and t is the Student value which is a function of the degrees of freedom used in calculating $S_{\bar{X}}$. For the present measurements, t is equal to 2.776 for a confidence interval of 95%. The flow rate standard deviation over repeated measurements is an increasing function of q_f (higher flow rates are more difficult to measure) and it is of the order of ±0.5%, which gives a precision index of ±1.4% with 95% confidence. The bias error on the film flow rate is estimated to $\pm 5.10^{-5}$ kg/s, from which we finally get q_f±5.2% for the overall uncertainty. As for the strip velocity, its uncertainty is ±0.6% at 95% confidence level, in nominal wiping conditions. The precision index on h_f is therefore ±0.5% and the bias error about ±5%, which gives a final uncertainty of ±5.2% at 95% confidence. The uncertainty on the normalized film thickness h_f/h_0 and film Reynolds number Re is also about ±5.2%. The uncertainty on the jet pressure is about ±6 Pa, while the one on Z/d is estimated to ±4%.

2.3.2 Validation. The importance of capillary effects in the prediction of the final film thickness is illustrated in Fig. 7, for a water film flow. The standoff distance between the nozzle and the substrate is $Z/d=10$, and the strip velocity is 1.5 m/s, which gives a capillary number of 0.055. At the lowest values of $\nabla\hat{P}_{\max}$, the knife model underestimates the film thickness (normalized by the film thickness without wiping h_0) of almost 35% with respect to the experimental values, while the complete model of Yoneda [5,6] succeeds in providing reasonable values (overestimation of 9% at most). So it can be asserted with some confidence that the discrepancy between the knife model and the measurements is mainly due to the omission of surface tension. As the jet pressure gradient increases, the knife model prediction becomes more accurate, until it almost matches the measurements starting from $\nabla\hat{P}_{\max}=40$ approximately. It should be pointed out that we are interested primarily in the wiping efficiency in the neighborhood of splashing conditions, where the capillary number ranges from 0.07 to 0.14, thus where surface tension has a lower effect. Moreover, close to splashing, the jet pressure gradient action overcomes largely the capillary effects, and the knife model is expected to give accurate predictions for h_f.

Typical results for nozzle T1 in conditions where surface tension has little effect are shown in Fig. 8, where the nozzle dynamic pressure P_n is kept constant ($P_n=1450$ Pa, which corresponds to a jet Reynolds number Re_j of 4500), while the standoff distance Z/d varies between 2 and 14. The knife model predictions and the measurements are in good agreement (within 5–9%),

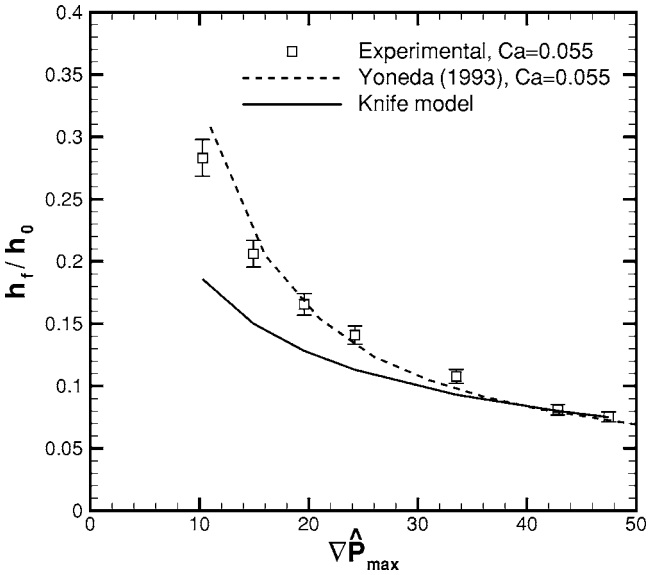

Fig. 7 Effect of surface tension in the prediction of final film thickness at $Z/d=10$ and Ca=0.055

except for large Z/d where it can be anticipated that the pressure gradient starts to be too weak to neglect capillarity (16% underestimation of h_f/h_0). The wiping plateau until $Z/d \simeq 8$ is well recovered by the analytical model. It is due to the specific behavior of the wiping actuators $\nabla P_{\max}$ and $\tau_{\max}$ in the region of the potential core [10,12]. The more important underestimation of h_f at $Z/d=12$ illustrates the rising effect of surface tension which becomes non-negligible due to the large standoff distance. The uncertainty of the thickness prediction here lies mainly in the uncertainty of the experimental or numerical estimation of $\nabla P_{\max}$ and $\tau_{\max}$. In the present study, we use the results of a prior characterization of nozzle T1 on a flat surface, performed during a parallel experimental study [12]. The facility used for this investigation consists of an instrumented plate on which the jet impinges normally. By displacing this plate equipped with a static pressure hole and Stanton probes, the pressure and shear stress distributions at impingement are measured. The uncertainty on the

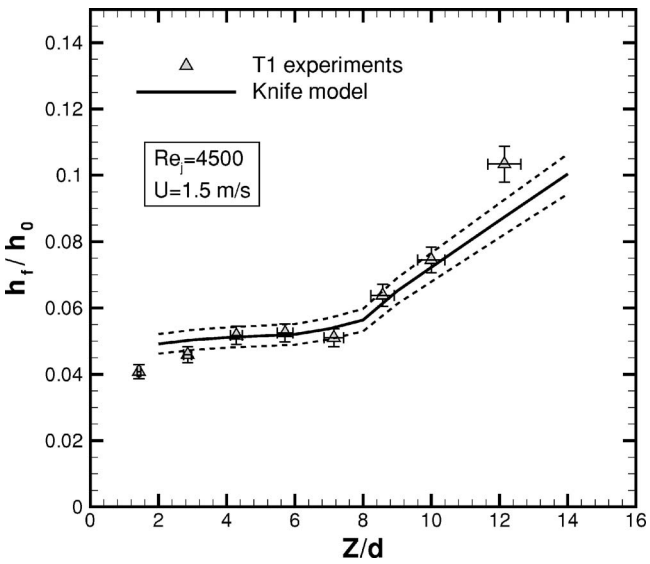

Fig. 8 Comparison of film thickness after wiping obtained experimentally, and predicted by the knife model for $\mathrm{Re}_j=4500$ and $U=1.5$ m/s

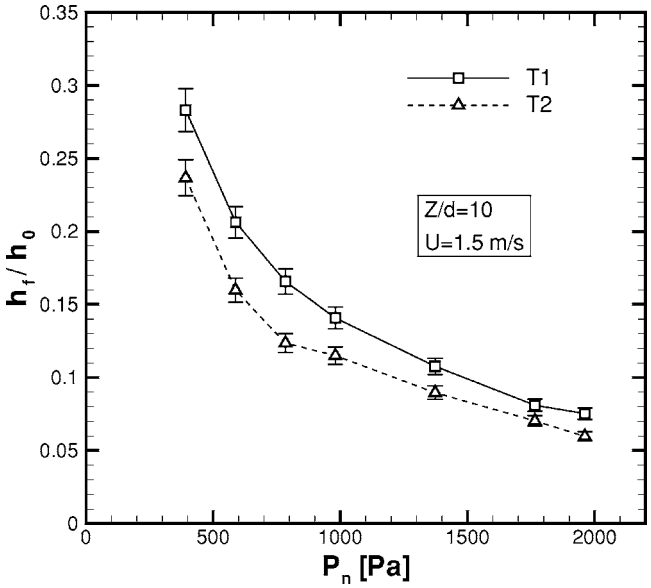

Fig. 9 Experimental wiping curves for the two nozzle geometries T1 and T2 at $Z/d=10$ and $U=1.5$ m/s

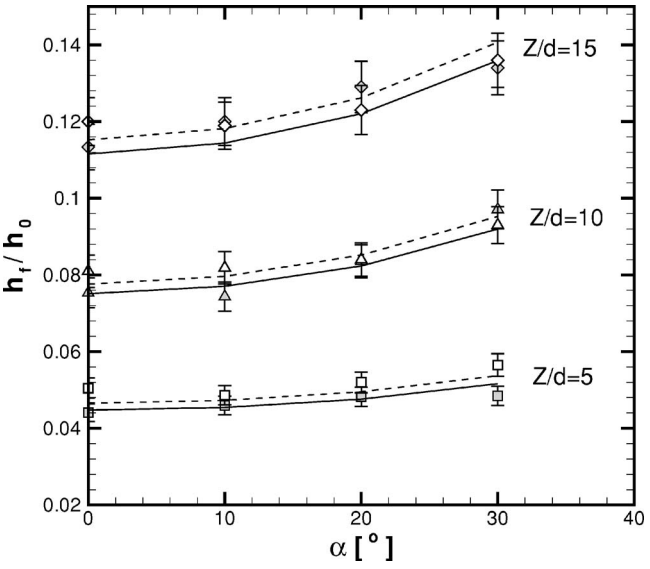

Fig. 10 Evolution of normalized final film thickness with the nozzle tilting angle at constant $Re_j=5100$ for different Z/d values

wiping actuators is estimated to ±4% for the pressure gradient, and presumably more than ±10% for the shear stress, due to the favorable pressure gradient which strongly affects the Stanton probe measurements [8]. A sensitivity study of the knife model shows that these values lead to a final ±6% uncertainty on the thickness h_f. It was also shown by Lacanette et al. [8] that the results of VOF-LES numerical simulations taking fully into account the surface tension effects are in reasonable agreement with the measurements and model predictions, except for small Z/d distances ($Z/d \leqslant 4$), where the important underestimation of h_f is probably due to an overestimation of $\nabla P_{\max}$ and $\tau_{\max}$. The latter is typical of an artificial confinement produced by the domain boundaries in impinging jets numerical simulations [13].

Typical experimental wiping curves obtained by varying the nozzle dynamic pressure P_n at constant $Z/d=10$ are shown in Fig. 9. It appears that nozzle T2 is about 15% more efficient in wiping than T1, that is to say for a constant nozzle pressure P_n, the final film thickness is 15% lower with T2 than with T1. The nozzle external and internal geometries seem therefore to have a nonnegligible influence on the wiping actuators $\nabla P_{\max}$ and $\tau_{\max}$. This could be quantified by characterizing the impinging jet produced by various nozzle geometries on a flat plate. Since wiping efficiency is controlled by the upstream maximum pressure gradient and shear stress, we can speculate that these wiping actuators are modified by the square corner shape of T2, which is favorable to flow recirculations.

Finally, the effect of nozzle tilting which is included in the knife model in Sec. 2.2 is validated by experiments in Fig. 10, for a jet Reynolds number of 5100, at two different substrate speeds $U=1.5$ m/s and 2 m/s. As it could be expected, the wiping efficiency drops more importantly with the tilt angle when the standoff distance Z/d is large. Because the jet is more developed at impingement when Z/d is larger, the pressure gradient and shear stress (and thus the wiping efficiency) are more sensitive to the tilt angle. The predictions of the knife model are in agreement within ±7% with the measurements, which is considered acceptable for the model validation. It will thus be used for the future wiping predictions at constant coating thickness.

3 Splashing

The splashing phenomenon occurring upstream the wiping jet is now investigated. Typical dimensionless parameters are derived through a phenomenological approach of the problem. An experimental database is used for the finding of an empirical model to predict splashing.

3.1 Phenomenological Approach. The ejection of droplets from liquid free surfaces exposed to gas flows has been extensively studied in basic configurations: sheared liquid films on pipe walls [14], still liquid free surfaces impinged by round jets [15]. However, there exist very few studies about splashing in the context of jet wiping. This film spraying mechanism may be seen as the ultimate development of a film instability [16], whose amplification factor may be high enough so that atomization occurs. Yoneda [5,17] uses Hinze's drop breakup model in turbulent gas flow [18] to derive a criterion for splashing in jet wiping. In fact, Yoneda [5,17] sees the liquid "bump" formed by the wiping meniscus as a droplet of diameter $(2h_0-h_f)$, which is subjected to a parallel incoming gas flow. To this extent, the problem can be related to the breakup of a single droplet in a turbulent flow, and Yoneda [5,17] postulates that the critical conditions for droplet disintegration into smaller droplets are those of splashing occurrence. As a typical length for the capillary contribution, he chooses the quantity $(2h_0-h_f)$, for which he gets a correlation depending on the film capillary number Ca and jet pressure P_n. He ends up with a splashing criterion in terms of Ca and critical jet pressure P_n^*. A more empirical approach is attempted here to identify the wiping conditions that may allow retarding splashing.

The present modeling postulates that the onset of splashing occurs when the shear effect produced by the downward gas wall jet overcomes the stabilizing effect of surface tension modeled here by σ_l/R, where R is the meniscus radius of curvature. The latter can be approximated by $(2h_0-h_f)$, as depicted in Fig. 3, but since $h_f \ll 2h_0$, we choose $R \simeq 2h_0$. Expressing the wall shear stress in terms of dynamic pressure of the wall jet $(0.5\rho V_{\mathrm{wj}}^2$, where ρ is the gas density, and V_{wj} is a typical wall-jet velocity), and evaluating the ratio of the dominating forces controlling the splashing mechanism leads to the effective jet Weber number $\mathrm{We}=\rho_g V_{\mathrm{wj}}^2 h_0/\sigma_l$. The critical Weber number We^* above which splashing develops is correlated with the film Reynolds number based on the strip velocity, U, and the final coating thickness $\mathrm{Re}=Uh_f/\nu_l$. The wall jet velocity, V_{wj}, is modeled by the following relation, which includes the effect of nozzle tilting [11]

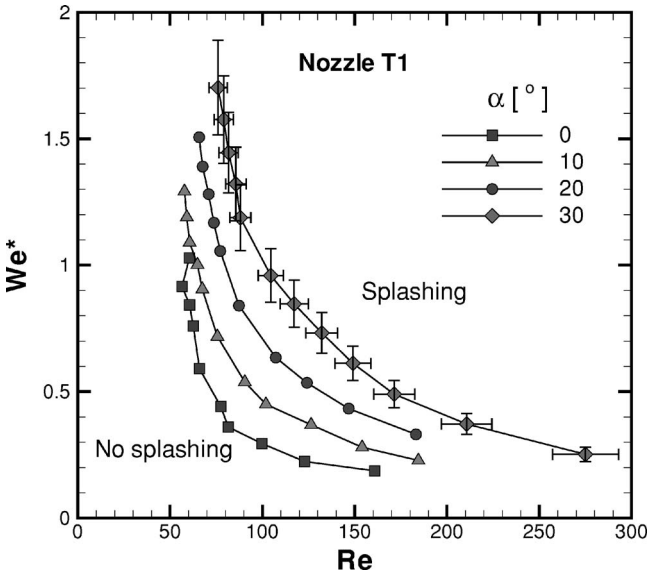

Fig. 11 Dimensionless splashing curves for $Z/d=10$, nozzle T1

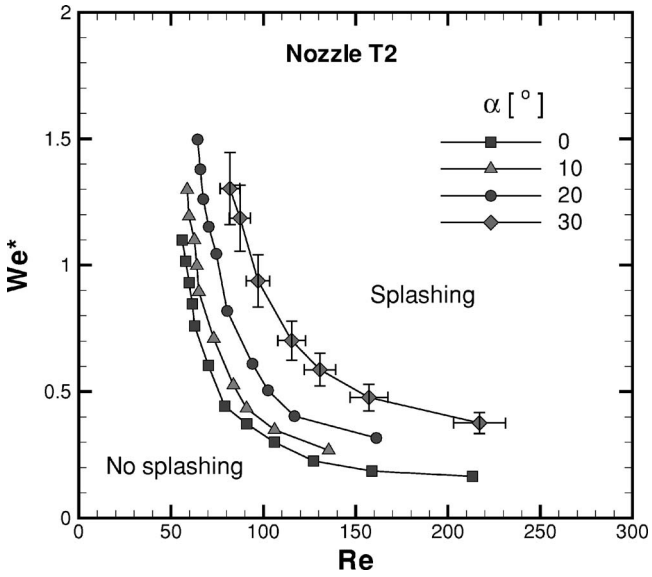

Fig. 12 Dimensionless splashing curves for $Z/d=10$, nozzle T2

$$V_{\mathrm{wj}} = \frac{V_{0j}}{Z/d}\sqrt{1+\sin\alpha} \tag{20}$$

It can be anticipated that downward tilting of the nozzle delays the occurrence of splashing. Indeed, the tendency of the jet streamlines to impact normally on the film in spite of its oblique position might force the film to stick to the substrate just below the stagnation point. This intuition was confirmed by preliminary tests.

It has to be seen now whether the loss of wiping efficiency induced by jet downward tilting compensates for the splashing delay at constant film thickness.

3.2 Empirical Model. The splashing experiments are performed on the facility described in Sec. 2.3.1. They consist of the visual detection of splashing for different wiping conditions. At constant jet pressure, the substrate velocity is increased until splashing occurs in its fully developed state along the strip. An hysteresis phenomenon is observed: the substrate speed at which splashing disappears is on average 7% lower than the one at which it appears. We will only consider splashing appearance here. The splashing tests are systematically repeated five times. At first, two observers reproduced independently the same experiments, and the difference in the results was found not to exceed $(U^*_{\max}-U^*_{\min})$ over a set of five tests performed by a single experimenter. The standard deviation of the detected critical velocity U^* is ±2%. The bias error on U being of 0.006 m/s, the final uncertainty on U^* is of the order of 3% at 95% confidence. The propagation of aforementioned errors lead to a final ±6.5% uncertainty on Re and ±11% on We^* in splashing conditions.

Figure 11 shows the evolution of critical conditions in terms of $\mathrm{Re}-\mathrm{We}^*$ stability curves for the symmetric nozzle T1. Splashing occurs above the curve, while jet wiping is stable below the curve. As expected, downward nozzle tilting allows delaying splashing. Splashing delay means that splashing occurs at higher strip speeds for a constant nozzle pressure. The comparison with Fig. 12 for T2 reveals that in terms of splashing, the nozzle geometry does not modify much the critical conditions, at least for lower tilting angles. For $\alpha=30$ deg, it seems that T1 is slightly more efficient (the same trend is observed for splashing disappearance). The worse performance of T2 is very likely due to the square shape of the nozzle upstream wiping, which makes it more sentitive to the tilt angle.

Figure 13 points out that the normalized standoff distance Z/d does not affect substantially the splashing correlation, which in turn can be formulated as follows

$$\mathrm{We}^* = e^{(a\alpha+b)}\mathrm{Re}^{-n} \tag{21}$$

The value of coefficients a and b as well as the exponent n depends on the nozzle design. For T1, $a=0.043$, $b=5.5$, and $n=1.44$, while for T2, $a=0.018$, $b=7.9$, and $n=1.91$. The different coefficients for T1 and T2 in correlation (21) result from a combination of the different performances of T1 and T2 in wiping and splashing. The improvement of the coating window reached by tilting the nozzle downward can be quantified by the net increase of the strip speed U, which is obtained for a given h_f value. To evaluate this enhancement, an optimum operating point is defined as the highest productivity condition below splashing. It corresponds to the intersection between the splashing critical curve given by Eq. (21) and the wiping curve at constant thickness. The

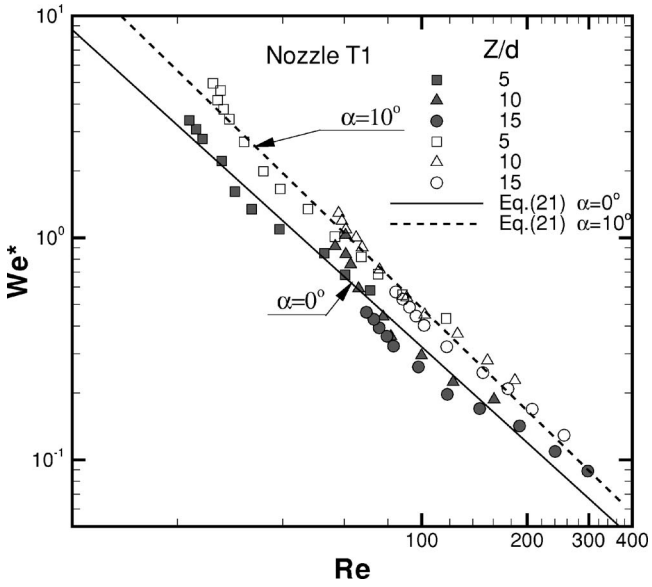

Fig. 13 Dimensionless splashing curves for Z/d values, for tilt angles $\alpha=0$ deg and 10 deg

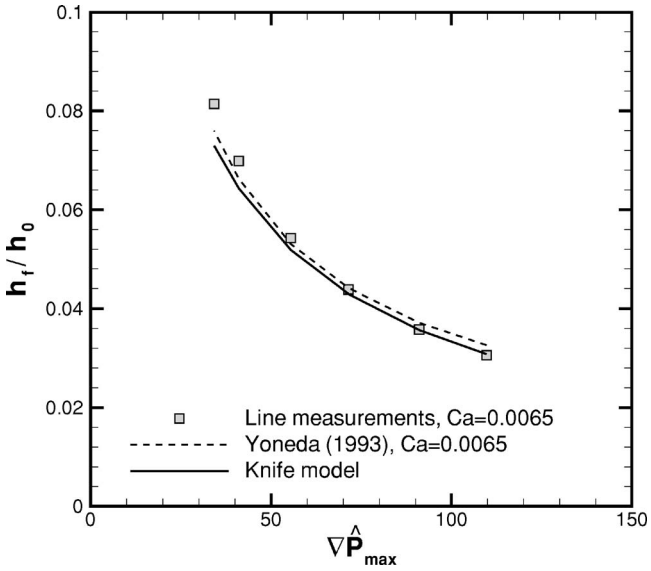

Fig. 14 Effect of surface tension in the prediction of final zinc coating thickness on galvanization lines at $Z/d=8$ and Ca =0.0065 ($U=1.5$ m/s)

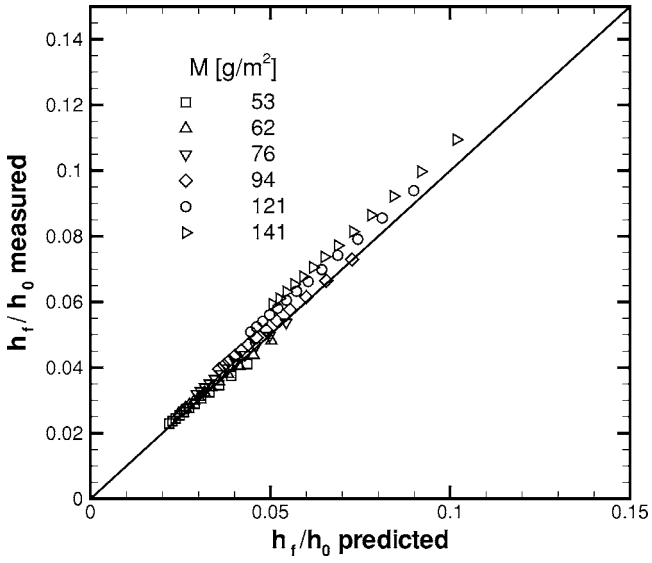

Fig. 15 Measured and predicted coating thickness on galvanization lines

latter is predicted by the knife model, in which correlations (17) and (18) for an oblique jet are used. This exercise will be done for industrial conditions in the following section.

The range covered by the dimensionless parameters allows a validation of the empirical correlations with galvanization line data. Indeed, it is found that $0.1 \leqslant \mathrm{We} \leqslant 1.8$ and $50 \leqslant \mathrm{Re} \leqslant 250$ for the water model, while $\mathrm{We} \geqslant 0.19$–$0.23$ and $\mathrm{Re} \geqslant 120$–$150$ correspond to line conditions. The capillary number range is generally lower in the industrial process window: $0.004 \leqslant \mathrm{Ca} \leqslant 0.0125$ while it is equal to $0.07 \leqslant \mathrm{Ca} \leqslant 0.14$ on the laboratory facility.

4 Application to Industrial Conditions

Depending on the desired final product, typical wiping conditions in galvanization include a strip velocity between 50 and 170 m/min, a nozzle pressure between 3 and 45 kPa, to reach coating weights M between 50 and 140 g/m^2 ($M=1000\rho_{\mathrm{Zn}}h_f$), that is to say zinc film thicknesses between 5 and 20 μm. The standoff distance Z is large enough to avoid contact between the strip and the nozzle: $8 \leqslant Z \leqslant 14$ mm. The nozzle slot is tuned between 0.8 and 1.2 mm. The liquid zinc properties are $\rho_{\mathrm{Zn}}=6540$ kg/m^3, $\mu_{\mathrm{Zn}}=0.0035$ Pa s, and $\sigma_{\mathrm{Zn}}=0.7$ N/m. Typically, very thin coatings are reserved to the automotive industry, while heavy coated products serve for furnitures and domestic appliances.

The importance of surface tension in typical wiping conditions on galvanization lines is comparatively lower than on the water model facility. Although the capillary numbers are lower ($0.004 \leqslant \mathrm{Ca} \leqslant 0.012$), the jet pressure gradient in nominal working conditions overcomes largely the surface tension effect, as it can be seen in Fig. 14 for $\mathrm{Ca}=0.0065$. The knife model is therefore sufficient to provide reliable predictions of the coating thickness.

The coating weights measured on galvanization lines are as presented versus knife model predictions in Fig. 15. The in-line data are based on the statistic treatment of a large number of measurements on dry samples (solidified zinc) with a thickness gauge. The standard deviation is lower than 0.5 g/m^2. The interpolation of this data for constant coating weights constitutes a simplified model which is used in practice on the line remote control systems. The empirical coefficients for the computation of the wiping actuators $\nabla P_{\max}$ and $\tau_{\max}$ are adjusted in the knife model to fit the measurements in the higher capillary and Weber number ranges, that is to say when surface tension has the lowest effect. Indeed, there is no possibility to characterize the industrial nozzles like it was done for laboratory tests. Following this adjustment, the agreement between the knife model and the measured thicknesses remains good ($\pm 4\%$) over the process windows for the different coating weights. A slight departure (underestimation of up to 15%) from the predictions can be depicted in Fig. 15 for higher h_f/h_0 values, for which surface tension starts to be non-negligible. Indeed, wiping conditions for large coating masses generally include low nozzle pressures, and therefore low-pressure gradient and shear stress. In such a situation, it can be anticipated that capillary effects come up gradually.

On galvanization lines, splashing is typically observed for high substrate velocities (above 150 m/min) and high coating weights (130–140 g/m^2) at Z/d about 10. All the operating points of Fig. 15 are plotted in Fig. 16 together with the dimensionless splashing correlation Eq. (21) for the symmetric nozzle T1. Most of the process points which are in the nonsplashing regime are found to be below the critical curve, while the ones for which splashing is

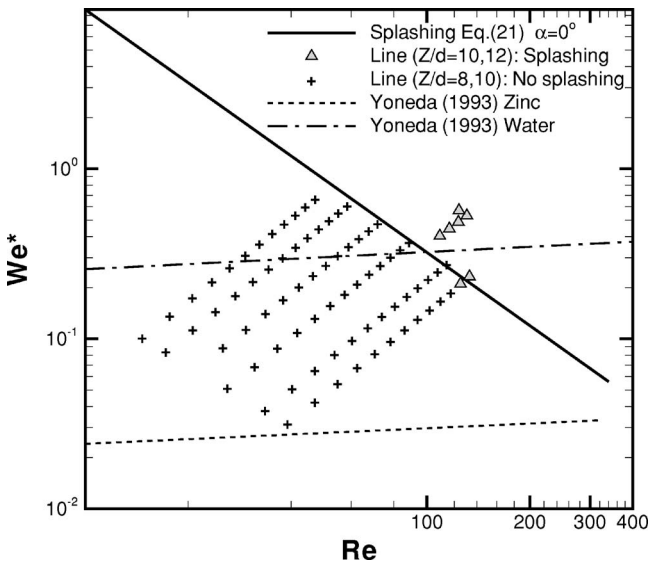

Fig. 16 Typical galvanization process points (stable and with splashing) with empirical correlation for splashing occurrence

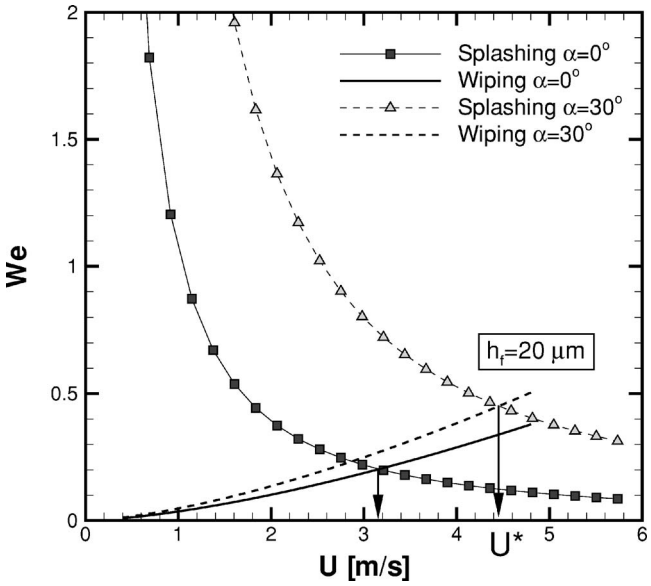

Fig. 17 Parallel evolution of splashing and wiping at α =0 deg and 30 deg for a constant coating thickness of 20 μm, in galvanization with liquid zinc

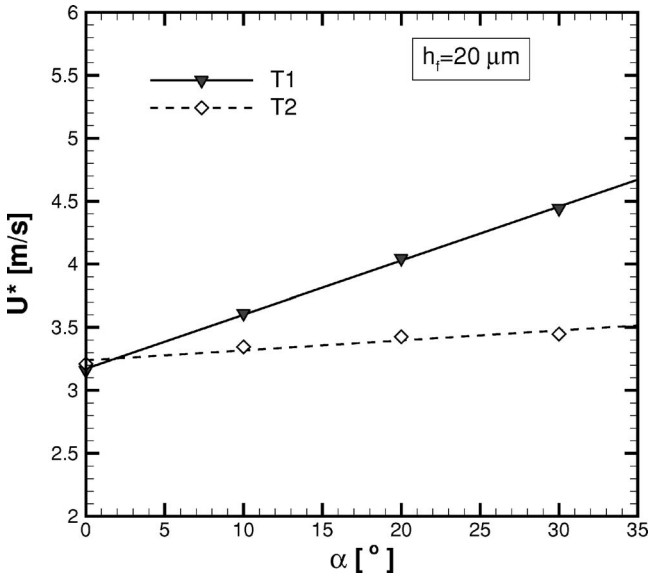

Fig. 18 Evolution of the estimated maximum substrate speed below splashing for the two nozzle geometries (Z/d=10, h_f =20 μm) in galvanization with liquid zinc

observed are correctly positioned above the curve. The agreement is therefore good, except for a few points which are very close to critical conditions. This is not surprising considering that the line process parameters are very difficult to assess. The curve corresponding to the criterion proposed by Yoneda [5,17] appears also on the plot. He finds that the critical jet pressure P_n^* is a fast decreasing function of the capillary number, which is consistent with experimental observations when U rises for a given liquid. In that conditions indeed, Ca increases, and one gets closer to splashing. However, when plotted in terms of Re–We^* with water and zinc as working fluids and using the knife model for h_f, it is found that the critical We^* increases slightly with Re (Fig. 16), in strong disagreement with the present experimental data. It is not very surprising actually that the drop breakup model does not compare well with splashing data, since the assumptions of Yoneda [5,17] are rather distant from the real wiping configuration.

Finally, the parallel evolution of splashing and wiping at constant film thickness is monitored, in order to compute the optimum working point in terms of substrate speed U. This exercise is done in Fig. 17 for galvanization conditions when α varies from 0 deg to 30 deg, and for a coating thickness of 20 μm. It appears that the maximum likely line speed U^* before film spraying can be substantially increased by tilting downwards the nozzle. This trend is detailed in Fig. 18, where the evolution of U^* is plotted versus the jet angle. Velocity gains of up to about 40% can be reached with nozzle T1, while only 8% is obtained with T2, probably as a result of its different performances both in wiping and splashing. In industrial conditions however, the nozzle can hardly be tilted of more than 10 deg, which limits the velocity gain to about 12%.

5 Conclusions

An overall analysis of the jet wiping technique for the galvanization process is presented. A theoretical development for the mean flow computation is first discussed. It is extended to a zero-dimensional model for the direct prediction of the film thickness after wiping. The importance of surface tension is emphasized, and it is shown that it can be neglected in the typical wiping process window which is under study. In such conditions, the knife model provides thickness predictions which compare well with the results of wiping experiments. Typical industrial working points are also well predicted, provided that an adjustment of the empirical coefficients depending on the nozzle geometry is made. The knife model is therefore an efficient tool to be used in the remote control system of industrial lines.

An experimental investigation of splashing in jet wiping is then undertaken. This phenomenon is featured by a strong instability of the runback flow leading to the ejection of droplets that may impinge on the slot nozzle. Such an event constitutes a severe limitation to the wiping technique.

An empirical splashing correlation expressed in terms of the critical jet Weber number and film Reynolds number is proposed. Very good agreement is found between the splashing criterion and the observations on industrial lines.

Comparing the splashing and wiping models at constant coating thickness leads to the definition of an optimum process window. Tilting the nozzle downward delays the occurrence of splashing, and allows higher line speed. A net increase of 40% of the productivity can be expected with a tilt angle of 30 deg. The nozzle design, on which both wiping and splashing performances depend, is shown to influence strongly the sensitivity of the jet to the tilt angle.

Acknowledgment

The authors gratefully acknowledge the financial support of Arcelor.

Nomenclature

Roman Letters

a = splashing correlation coefficient
b = splashing correlation coefficient
b_P = distance between the jet axis and the location of $P_s/2$ (m)
C = empirical coefficient for impinging jet shear stress estimation
Ca = film capillary number, $\mu_l U/\sigma_l$
C_p = empirical coefficient
C_τ = empirical coefficient
d = nozzle slot width (m)
g = acceleration of gravity (m s^{-2})
h = local film thickness (m)

h_f = film thickness after wiping (m)
L = strip width (m)
M = coating weight, $\rho_l h_f$ (kg/m^2)
n = splashing correlation coefficient
P = static pressure at jet impingement (Pa)
P_l = pressure in the liquid (Pa)
P_g = pressure in the gas (Pa)
P_n = nozzle exit dynamic pressure (Pa)
P_s = maximum pressure at the stagnation point for an impinging jet (Pa)
Q = dimensionless volumetric flow rate
q = film volumetric flow rate (m^3/s)
R = local film radius of curvature (m)
Re = film Reynolds number, Uh_f/ν_l
Re$_f$ = film Reynolds number based on the film velocity in the referential of the substrate and the local thickness
Re$_j$ = jet Reynolds number, $V_{0j}d/\nu_l g$
$\hat{T}$ = dimensionless shear stress
U = substrate velocity (m/s)
u = liquid film local velocity (m/s)
V_{0j} = jet exit velocity (m/s)
V_{wj} = characteristic wall jet velocity (m/s)
We = jet Weber number, $\rho_g V_{wj}^2 h_0/\sigma_l$
X = dimensionless spatial coordinate in the moving substrate direction
x = spatial coordinate in the moving substrate direction (m)
y = spatial coordinate in the direction normal to the substrate (m)
Z = nozzle to substrate distance (m)
Z' = nozzle to substrate distance along the jet axis for oblique jets (m)

Greek Letters

α = nozzle tilt angle [deg]
Γ = surface tension term, $\sigma h_0/\rho_l g d^3$
ε = scaling factor, $2\pi h/\lambda$
λ = characteristic wavelength of x fluctuations (m)
μ = dynamic viscosity (Pa s)
ν = kinematic viscosity (m^2/s)
ξ = normalized absissa for jet impingement, x/b_P
ρ = density (kg/m^3)
σ = surface tension (N/m)
τ = shear stress due to impinging jet (Pa)

Subscripts/Superscripts

g = gas
j = jet
l = liquid
max = maximum
opt = values at the location of the wiping point
0 = without wiping
$*$ = critical for splashing
$\hat{}$ = dimensionless quantities
Zn = liquid zinc

References

[1] Thornton, J. A., and Graff, M. F., 1976, "An Analytical Description of the Jet Finishing Process for Hot-Dip Metallic Coating on Strip," Metall. Trans. B, **7B**, pp. 607–618.
[2] Tuck, E. O., 1983, "Continuous Coating with Gravity and Jet Stripping," Phys. Fluids, **26**, pp. 2352–2358.
[3] Ellen, C. H., and Tu, C. V., 1984, "An analysis of Jet Stripping of Liquid Coatings," J. Fluids Eng., **106**, pp. 399–404.
[4] Tuck, E. O., and vanden Broeck, J.-M., 1984, "Influence of Surface Tension on Jet Stripped Continuous Coating of Sheet Materials," AIChE J., **30**(5), pp. 808–811.
[5] Yoneda, H., 1993, "Analysis of Air-Knife Coating," Master of Science dissertation, University of Minnesota, Minneapolis, MN.
[6] Yoneda, H., and Scriven, L. E., 1994, "Air-Knife Coating: Analysis of the Basic Mechanism," *Proceedings 7th Symposium on Coating Process Science and Technology at the AIChe Spring National Meeting*, Atlanta, GA, April 17–21.
[7] Buchlin, J.-M., 1997, "*Modeling of Gas-Jet Wiping*," Thin Liquid Films and Coating Processes, VKI Lecture Series, von Karman Institute for Fluid Dynamics, Brussels, Belgium.
[8] Lacanette, D., Gosset, A., Vincent, S., Buchlin, J.-M., Arquis, E., and Gardin, P., 2006, "Macroscopic Analysis of Gas-Jet Wiping: Numerical Simulation and Experimental Approach," Phys. Fluids, **18**, 042103.
[9] Beltaos, S., and Rajaratnam, N., 1976, "Plane Turbulent Impinging Jets," J. Hydraul. Res., **11**, pp. 29–59.
[10] Tu, C. V., and Wood, D. H., 1996, "Measurements Beneath an Impinging Plane Jet," Exp. Therm. Fluid Sci., **13**, pp. 364–373.
[11] Beltaos, S., 1976, "Oblique Impingement of Plane Turbulent Jets," J. Hydr. Div., **102**, pp. 1177–1192.
[12] Gosset, A., Rambaud, P., Castellano, L., Buchlin, J.-M., and Dubois, M., 2005, "Modeling of Gas Jet Wiping at Small Standoff Distances," *Proc. of European Coating Symposium*, University of Bradford, UK, Sept. 6–9.
[13] Babu, P. C., and Mahesh, K., 2004, "Upstream Entrainment in Numerical Simulations of Spatially Evolving Round Jets," Phys. Fluids, **16**(10), pp. 3699–3705.
[14] Paras, S. V., Vlachos, N. A., and Karabelas, A. J., 1994, "Liquid Layer Characteristics in Stratified-Atomization Flow," Int. J. Multiphase Flow, **20**, pp. 939–956.
[15] Trabold, T. A., and Obot, N. T., 1997, "The Onset of Splashing from Free Liquid Surfaces Exposed to Impinging Gas Jets," *Proc. ASME Fluids Eng. Div. Summer Meeting*, Vancouver, Canada, June 22–28, paper 3561.
[16] Tu, C. V., and Ellen, C. H., 1986, "Stability of Liquid Coating in the Jet Stripping Process," *Proceedings* 9th *Australasian Fluid Mechanics Conference*, Auckland, New Zealand, Dec. 8–12, pp. 316–319.
[17] Yoneda, H., and Scriven, L. E., 1994, "Analysis of Spray Generation in Air-Knife Coating," *Proceedings* 7th *Symposium on Coating Process Science and Technology at the AICHe Spring National Meeting*, Atlanta, GA, April 17–21.
[18] Hinze, J. O., 1955, "Fundamentals of the Hydrodynamics Mechanism of Splitting in Dispersion Processes," AIChE J., **1**, pp. 289–295.

CFD Investigation of Gear Pump Mixing Using Deforming/ Agglomerating Mesh

Wayne Strasser
Eastman Chemical Company,
Kingsport, TN 37660
e-mail: strasser@eastman.com

A moving-deforming grid study was carried out using a commercial computational fluid dynamics (CFD) solver, FLUENT® 6.2.16. The goal was to quantify the level of mixing of a lower-viscosity additive (at a mass concentration below 10%) into a higher-viscosity process fluid for a large-scale metering gear pump configuration typical in plastics manufacturing. Second-order upwinding and bounded central differencing schemes were used to reduce numerical diffusion. A maximum solver progression rate of 0.0003 revolutions per time step was required for an accurate solution. Fluid properties, additive feed arrangement, pump scale, and pump speed were systematically studied for their effects on mixing. For each additive feed arrangement studied, the additive was fed in individual stream(s) into the pump-intake. Pump intake additive variability, in terms of coefficient of spatial variation (COV), was >300% for all cases. The model indicated that the pump discharge additive COV ranged from 45% for a single centerline additive feed stream to 5.5% for multiple additive feed streams. It was found that viscous heating and thermal/shear-thinning characteristics in the process fluid slightly improved mixing, reducing the outlet COV to 3.2% for the multiple feed-stream case. The outlet COV fell to 2.0% for a half-scale arrangement with similar physics. Lastly, it was found that if the smaller unit's speed were halved, the outlet COV was reduced to 1.5%.
[DOI: 10.1115/1.2436577]

Introduction

Positive displacement gear pumps are commonly used for precise viscous fluid metering on an industrial scale in both plastics and food manufacturing. One would likely not propose installing a new gear pump simply for any potential mixing capabilities because of its high level of energy consumption. If a metering gear pump is already in use, however, the ability to also utilize this gear pump for additive blending offers certain advantages. The user could not only avoid both the purchase and installation costs of new mixing equipment, but could also alleviate the need to purchase and install more gear pump(s) to overcome the additional pressure drop of said mixing equipment. The goal of this work is, therefore, to investigate whether or not additives can be blended to a satisfactory level using an existing in-service industrial-scale gear pump.

One may browse a mixing equipment manufacture's Web site and find common examples of static mixers for viscous liquid applications, the use of COV (local standard deviation divided by the local mean) for a mixedness measure, and how the COV at the outlet of such devices depends on the COV at the inlet. There appears to have been few studies of mixing within metering (positive displacement) gear pumps in the open literature and patent databases. U.S. Patent Nos. 6,313,200 and 6,601,987, for example, involve planetary gear arrangements. In fact, no computational metering gear pump mixing investigation could be found, nor could concrete data from an experimental study be located. Kramer [1] stated in his industrial gear pump performance study, "The mechanism is basically a straight-through device, though, and does no mixing" (underline included). In an agricultural engineering study by Bouse et al. [2], the improved performance of certain chemical sprays was noted as a result of multiple passes through a gear pump. The authors, however, did not make a quantifiable distinction between shear history effects and improved mixedness resulting from multiple gear pump passes.

Studies of mixing within axial (primarily) flow units, such as extruders, are more common. An interesting experimental study is that of Valsamis and Pereira [3] in which enhancements to the Farrel continuous mixer concept are explored. Localized circulatory cells, which promote backmixing and lateral motion of material, are shown to improve blending. In a metering gear pump, there is little to no flow in the direction normal to the primary flow axis; therefore, it would typically not have this sort of lateral mixing. Also, "inserts/dams," which convert axial flow to radial flow, were shown to reduce melt defects in these extruders. It must be noted, however, that the unit in the study of [3] is nonintermeshing. In other words, the swept areas/volumes of the rotating members do not interfere with one another. The difficulties associated with CFD modeling of intermeshing units (such as gear pumps) would not be present in the study of said device.

An example of the study of flow in an intermeshing corotating extruder is the computational work of Bruce et al. [4]. The authors discuss forward mixing, back mixing, and generally swirling compartments within various extruder sections. They employ a mixing efficiency parameter, also called an extensional efficiency, as in Heniche et al. [5]. The parameter is defined as the ratio of the symmetric rate of deformation tensor magnitude to the sum of this magnitude and the vorticity tensor magnitude. Although the tensors, themselves, are not frame invariant, their magnitudes (scalars) are indeed frame invariant [6]. As a result, fair comparisons can be made between various studies. An efficiency value of 0 would represent purely rotational flow, while a value of unity would correspond to purely elongational flow. In general, a higher value indicates better mixing as long as the areas of higher efficiency are not segregated or isolated. The volume-averaged value of the mixing parameter ranged from approximately 0.52 to 0.55 in the extruder studies of [4]. Typical values for a laminar static mixer from [5] ranged from 0.4 to 0.8 axially, but averaged 0.6.

A common technique employed in CFD investigations of intermeshing systems, as in the study by Bruce et al. [4], is the process of superposition. Volumes of stationary and rotational components are constructed and gridded separately. The grid nodes need not

Contributed by the Fluids Engineering Division of ASME for publication in the JOURNAL OF FLUIDS ENGINEERING. Manuscript received December 16, 2005; final manuscript received October 27, 2006. Assoc. Editor: Dennis Siginer.

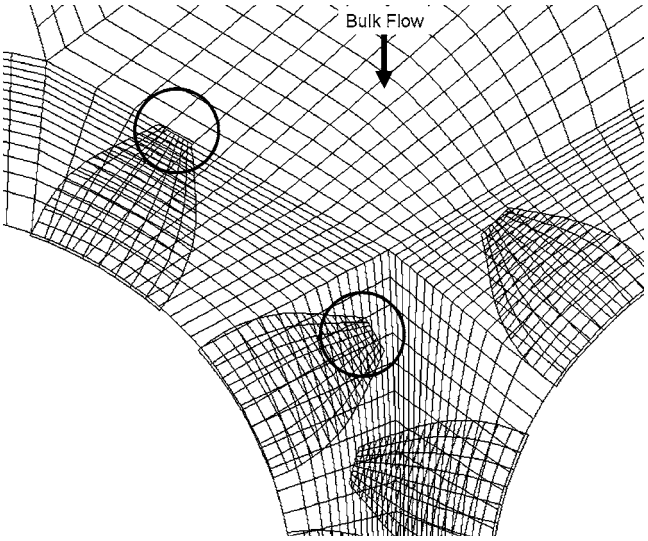

Fig. 1 Computational grid from a Polyflow® study (not related to present work)

conform to one another at any instant in model time over the course of the simulation. Grid cells are allowed to overlap freely, and information is interpolated accordingly. Figure 1, from a Web site example by FLUENT, Inc., shows the instantaneous computational grid of a gear pump study using Polyflow® (finite element formulation). Note the dramatic shifts in grid cell size/centroid that occur throughout the domain during the gear rotational sequence. As shown in the circle, grid cells are approximately 1/20 the area of a neighboring grid cell at some locations in the computational domain. Sharp grid cell size or centroid shifts are known to produce substantial numerical diffusion, making the calculated mixing rate appear to be better than in reality. Even if the grid were more uniform, this method may work for pressure profiles and mass flow rate, but not be ideally suited for mixing studies. Although the author is not aware of any studies of numerical diffusion of superposition nodal interpolations, one would expect the diffusive nature of this approach to be similar to that of nonconformal interfacial interpolations.

An alternative to superposition is a moving-deforming grid. This concept is relatively new and appears to be somewhat unexplored. At each computational time step, the model geometry is advanced a predetermined amount. The computational grid is then altered/recreated to accommodate new shapes before the flow or thermal solution is sought through iterative means. One would expect this to be more computationally expensive than superposition. Not only are the grid cell counts likely to be larger, but the grid reconstruction time is added to each time step. Improved accuracy and reduced numerical diffusion are the rewards. FLUENT, Inc. offered this method commercially beginning in February of 2003 in their finite volume code. The mesh within FLUENT® will not only automatically deform to accommodate changes in the shape of the base geometry, but will also automatically ***create/agglomerate*** cells to maintain grid quality. One can imagine that cell aspect ratio or skewness can become a significant problem for dramatic changes in geometry shape with only a deformable grid. For this reason, FLUENT® was seen as advantageous for this work.

Model

The present study involves unsteady, laminar, multiphase flow of a mixture of viscous materials through an intermeshing industrial-scale metering gear pump. The two materials involved are different "phases" only in the sense that they have significantly differing properties. The process fluid has a viscosity which is one to two orders of magnitude larger than that of the additive. The additive is fed at relatively low mass concentrations ($<10\%$) in the pump intake as individual stream(s) of essentially pure additive. The FLUENT 6.2.16 commercial finite volume solver is used to evaluate the mixing of these streams inside the pump. The problem involves all three spatial dimensions because there is a helical nature to the gears in the pump. The axial flow components are expected to be comparatively small, and the axial mixing should be minimal. As a result, the problem was condensed to two dimensions. This makes the study more conservative in that any three-dimensional (3D) flow would only increase phase blending.

Physics. The Eulerian mixture model is a simplification of the full Eulerian-Eulerian multiphase approach. Each liquid is treated as a separate interpenetrating phase. Mass transfer between phases is ignored, as well as momentum exchange through processes such as drag, lift, surface tension, etc. Properties are volume fraction weighted (except for heat capacity, which is mass fraction weighted), as shown in the Nomenclature, and consistent with the "mixture" model concept. There is a single pressure and a single velocity field shared by both phases. In other words, it is assumed that, on a subgrid scale, the phases have reached local equilibrium. In the mixture approach, the effects of two-way phase coupling are included in order to be able to address systems in which the fluids have very different viscosity ratios. In general, it is expected that this volume-weighted approach would be more diffusive than the full Eulerian-Eulerian approach, but this effect will be quantified in the Numerical Diffusion Tests section. Linear momentum of the mixture is conserved via the following (shown in Cartesian coordinates):

$$\rho_m\left(\frac{\partial u_i}{\partial t}+\frac{\partial u_i u_j}{\partial x_j}\right)=\frac{\partial \tau_{ij}}{\partial x_j}+S \tag{1}$$

The materials have similar densities so the effects of natural convection could be ignored. The mixture stress tensor is calculated

$$\tau_{ij}=-p+\eta_m\left(\frac{\partial u_i}{\partial x_j}+\frac{\partial u_j}{\partial x_i}\right) \tag{2}$$

For the computational cases in which the primary fluid is non-Newtonian, the deviation from Newtonian behavior is incorporated into η_P (subset of η_m). The author is aware that viscous fluids, such as polymers, often exhibit normal stress differences upon shearing [7]. That is, a viscous tension is developed along a streamline. In addition, there is sometimes "memory" associated with these stresses. A thorough discussion of interesting secondary flows that accompany these types of fluids is given by Siginer and Letelier [8]. For this particular process fluid, however, it is known through testing within Eastman Chemical Company that Carreau-Yasuda relations can predict the correlation between apparent viscosity and shear rate throughout the conditions modeled (Eqs. (3)–(5)). The concept of having η_P be a scalar function of deformation is discussed in Bird et al. [9] and is not new,

$$\eta_{P0}=B_1\exp\left\{B_2\left[\frac{1}{T}-\frac{1}{B_3}\right]\right\} \tag{3}$$

$$\theta=B_4\exp\left\{B_5\left[\frac{1}{T}-\frac{1}{B_3}\right]\right\} \tag{4}$$

$$\eta_P=\eta_{P0}[1+(\theta\gamma)^{B_6}]B_7 \tag{5}$$

The additive phase volume fraction is conserved using phase continuity,

$$\frac{\partial(\alpha_A\rho_A)}{\partial t}+\frac{\partial(\alpha_A\rho_A u_i)}{\partial x_i}=0 \tag{6}$$

Energy of the mixture is conserved via

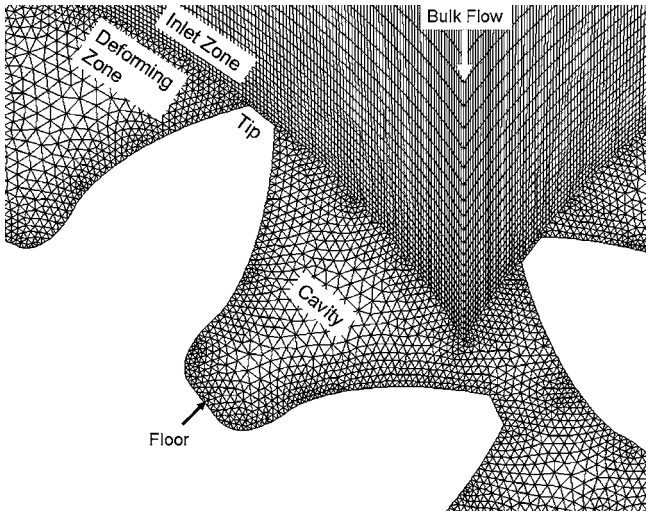

Fig. 2 Typical computational grid used in present study

$$\rho_m C_m \left(\frac{\partial T}{\partial t} + \frac{\partial u_i T}{\partial x_i} \right) = k_m \left(\frac{\partial^2 T}{\partial x_i^2} \right) - \tau_{ij} \frac{\partial u_i}{\partial x_j} \tag{7}$$

Of course, the kinetic and potential energy terms have been neglected because they have little to no impact in the present simulation. Viscous heating effects are included for some of the cases using the definition of the irreversible dissipation of energy through viscous losses as shown in the last term of Eq. (7). The pressure-work term $T(\partial p/\partial T)(\partial u_i/\partial x_i)$ has been neglected from the right-hand side of Eq. (7) because all models were run at the same low operating pressure differential (<1 bar), and the fluid is effectively incompressible. The walls and gear surfaces were treated as adiabatic; thus, there was no net thermal exchange within the pump or externally. The rotational speed of the gear set matched the typical for the process fluid at plant throughput.

Computational Grid. Numerical diffusion is an important consideration in any mixing study. Artificial smearing of gradients would produce a computational mixing level higher than reality. (This will be discussed in further detail in a later section). Solution boundedness is an equally important consideration in order to prevent the opposite problem from occurring. The computational grid was built using lessons learned from transonic gas turbine passage gridding discussed in Strasser et al. [10] to minimize the numerical error associated with these two issues.

Figure 2 displays a typical computational grid (nominally 65,000 grid cells in a pump cross section) in the present study. Quadrilateral cells make up the inlet (top of Fig. 2) as well as the outlet (not shown). The "deforming" zone filling the spaces around the gears is made up of triangular cells. As shown in Fig. 2, grid cell area/centroid shifts are handled gradually, especially the quadrilateral-triangular cell transition that is often overlooked in computational studies. Exceptional resolution is provided across the inlet zone (nearly 400 grid points) and outlet zone to minimize cross-diffusion. Grid cell aspect ratios (in the directions normal to the flow) were minimized. As the gears rotate, triangular cells in the deforming zone are agglomerated and/or created (using spring-based smoothing) to maintain grid quality. Cells are created on the trailing tooth edge, while cells are destroyed on the leading tooth edge. In the gear intermeshing zone, where the teeth pass very near each other, the cell creation/destruction process must proceed aggressively but smoothly. In a real-world gear pump, the teeth actually touch, but computationally they are kept apart by a small cushion about the size of the smallest cell in the domain. Area-averaged grid cell equivolume skewness values for the deforming zone are typically 0.15 (0 being an equilateral triangle and 1 being a sliver cell) over the course of the run and never exceed 0.16. Minimizing grid cell skewness is another factor that is important for minimizing numerical diffusion. In addition to being diffusive, highly skewed cells (skewness $>\sim 0.8$) have been found to cause the local computation of artificially high strain rates in other internal Eastman Chemical Company CFD models. Gridding parameters in the code are utilized such that the computational cell sizes in the deforming zone are maintained to be nearly the same size as the boundary cells (smallest in the figure), i.e., cell size growth is minimized in the boundary-normal direction in order to improve accuracy. Other methods and measures of controlling deforming grid quality are available, such as that in [11] in which smaller cells are adjusted relatively less than larger cells from time step to time step, but cell skewness was the primary concern in this study. During cell agglomeration and creation, mass and momentum are conserved and gradients are interpolated based on the numerical grid at the previous time step.

Discretization. Care was taken to utilize discretization schemes within FLUENT 6.2.16 that were a blend of diffusion and boundedness considerations. For example, switching from first-order upwinding to second-order upwinding has been found to have dramatic effects on multiphase calculations [12]. For the momentum balance, a bounded central differencing scheme was used for spatial interpolation in both quadrilateral and triangular cells. This is the most accurate stencil that is offered in this particular code release for grids that are not always aligned with the flow. A third-order MUSCL scheme is available, but does not contain flux limitations and could cause overshoot for nonaligned flows [13]. Since grid cell peclet numbers were everywhere less than unity, it was concluded that central differencing would not experience dispersion problems. All other variables (except pressure) were spatially interpolated using a second-order upwind/central differencing blended scheme. For quadrilateral cells, the blending constant was solution dependent and varied locally to stay as close to central as possible without the introduction of new maxima in the flow field. For triangular cells, the blending constant was zero, meaning that second-order upwinding was used. Pressure interpolation was handled using a purely second-order upwinding scheme for all grid cells. In all cases, first-order interpolation was used for the transient terms because this was the only option available for multiphase models in FLUENT 6.2.16. Derivatives were discretized using the nodal method (weighted by nodal values on surrounding faces instead of simple arithmetical grid cell center averages), which is more accurate especially for triangular cells. The settings discussed here are consistent with the best practices proposed by FLUENT, Inc.

Convergence. The SIMPLE algorithm was used for pressure-velocity coupling via the segregated implicit solver. Although it is known that, for some problems, coupling can be more efficiently handled by SIMPLEC or other methods, numerical tests confirmed that the flux corrections within SIMPLEC were not worth the additional CPU time in residual reduction. An advanced multidimensional slope-limiting scheme (total variation diminishing) was utilized to keep cell gradients under control. Pressure checkerboarding was prevented using a second-order Rhie-Chow method. The single precision solver version was used in that it was found that the use of double precision did not change the results to three significant figures. An algebraic multigrid was used to reduce large wave error propagation, and the multigrid termination criteria were lowered an order of magnitude from the default settings for pressure and volume fraction to ensure deep mass convergence. Time stepping was fixed at ~ 0.0003 revolutions per time step. Time-step increments above this caused the grid deformation algorithm to fail. Twenty-five subiterations were required per time step for the "flattening" of residuals. Certain underrelaxation factors were increased to values higher than the default in order to promote residual reduction. Residual rms values fell typically three orders of magnitude each time step, with the maximum rms value at the end of a time step being of order

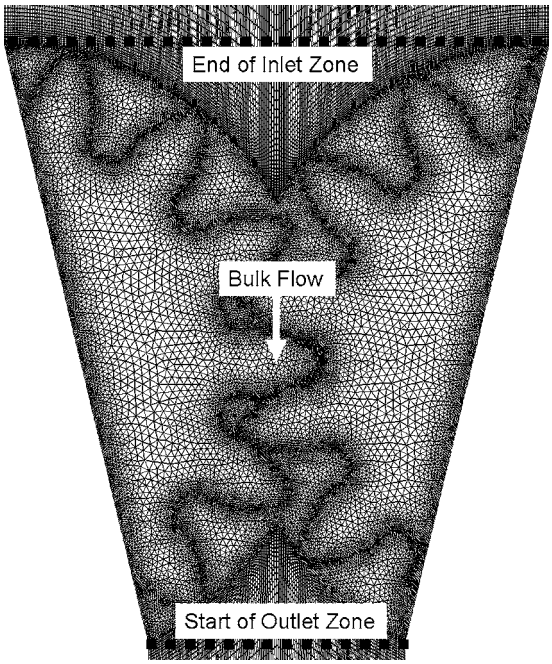

Fig. 3 Computational domain for the straight-through numerical diffusion test case

10^{-5}. Additive mass imbalance, in a time-averaged sense, was maintained to near zero. It did not typically exceed ±0.5% on an instantaneous basis. The model ran at a rate of nominally 0.6 computational revolutions per day of CPU time on a Dell Precision® 450 Workstation. Three to four weeks (>15 revolutions) of run time was normally required to reach a quasi-steady state. Quasi-steady was defined as the point at which the outlet additive statistics became stationary in time. Once this occurred, time-averaging data collection began.

Results

Numerical Diffusion Tests. As would be expected with any CFD "experiment," a sanity check should be performed to test the method. Numerical diffusion cannot be completely avoided although every reasonable attempt was made to do so. A steady-state CFD test case was built that somewhat mimicked the grid for the real gear pump CFD case. It contained a single additive feed stream (concentrated strand) at the pump intake centerline and a Newtonian process fluid. The inlet and outlet grid topology, shape, and size matched the real pump CFD cases exactly. In the triangular zone, the grid was expanded and contracted (similar to Fig. 2) in and around the outline of fictitious gear teeth so that opportunities for numerical diffusion could be brought to the forefront. Of course, there were no moving parts in the test case, and the flow proceeds straight through each cell zone. Based on discussions in the classic Patankar text [14] and shockwave-capturing findings of [15], the triangular zone is expected to provide the most numerical mixing. Besides the fact that the test case was run in steady-state mode, all other solver settings were exactly the same as those discussed in the previous sections. The computational domain for this straight-through test case is shown in Fig. 3.

Figure 4 shows additive concentration profiles normalized by the mass flow-weighted area-averaged (MFWAA) additive concentration of the feed. Note the additive concentration profile changes from a square wave to a Gaussian-type distribution simply as a result of numerical mixing. Again, there are no moving gears or other blending stimuli in this case. Specifically, all of the diffusion occurred in the triangular zone. The end of the quadrilateral-celled inlet zone is marked with triangular symbols,

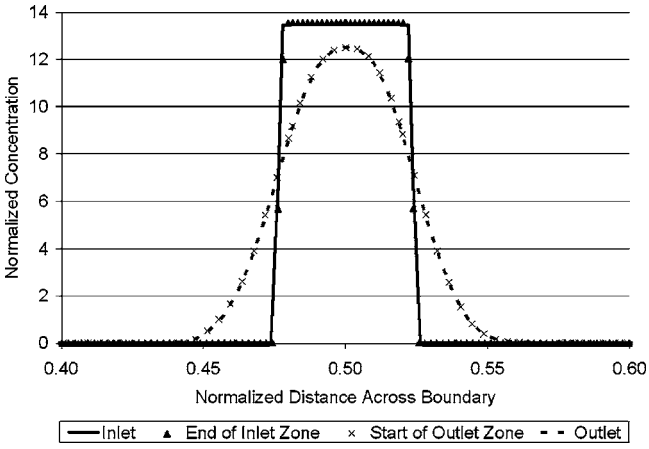

Fig. 4 Normalized additive mass concentration profiles for the straight-through numerical diffusion test case

whereas the beginning of the quadrilateral-celled outlet zone is marked with x-shaped symbols. The concentration distribution is not changed as the fluid moves through these zones. The overall COV was reduced through the triangular zone from 350 (equal to the inlet) to 290.

The author was not satisfied with this result, specifically the distance traveled by the fluid mixture through the diffusive triangular zone; thus, another test case was built. In the new test case, the Newtonian mixture of materials (with a single additive feed stream) had to flow around a perimeter of similar distance magnitude experienced in the gear pump simulations. The triangular zone was made up of larger triangles than in the first test case in order to attempt to maximize the effects of numerical blending. Figure 5 shows the second test case (perimeter-flow) computational grid.

The outlet spatial concentration profile was similar in shape to that in Fig. 4 and has not been repeated here. The profile, however, was more spread out, indicating a higher level of numerical blending (outlet COV=240). Another mixedness measure could be the width about the outlet centerline of a given percent accumulated area under the spatial concentration curve. The resulting width measure depends on the particular percent threshold chosen; therefore, a number of thresholds were tested. In general, the distribution width was approximately doubled across the triangular

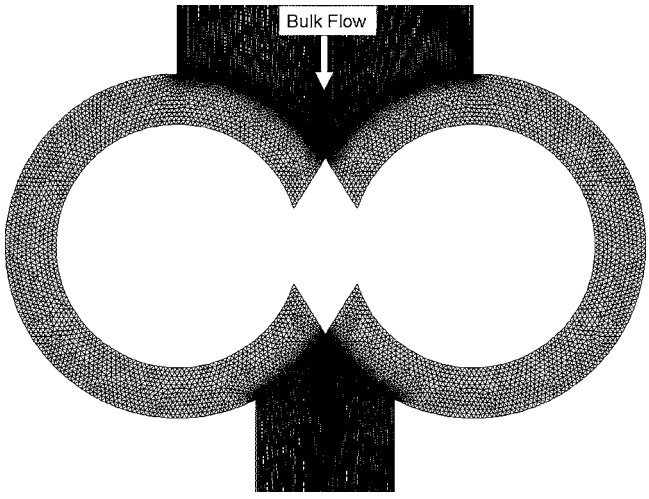

Fig. 5 Computational domain for the perimeter-flow numerical diffusion test case

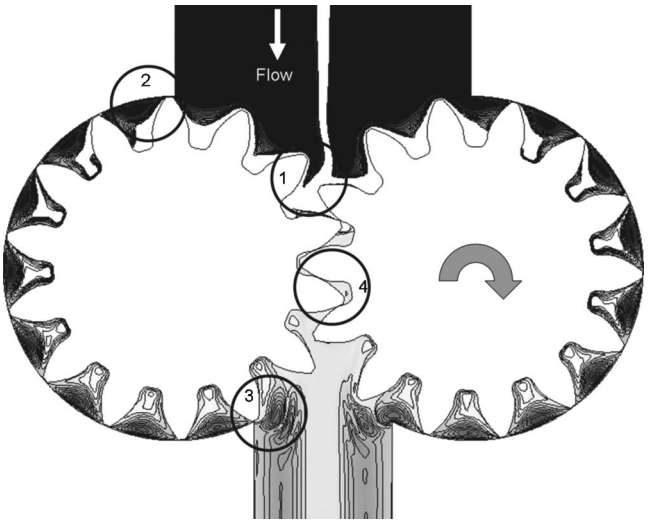

Fig. 6 Typical instantaneous normalized additive mass concentration contours for a single additive injection stream and a Newtonian process fluid; white represents material having a mass concentration ⩾60% higher than the outlet instantaneous MFWAA concentration

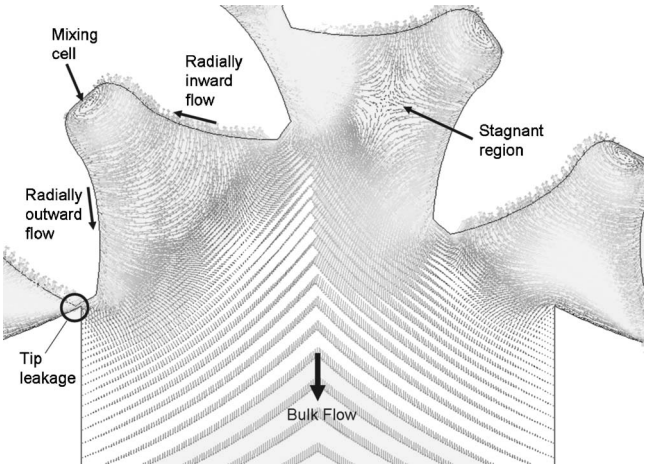

Fig. 7 Typical instantaneous fluid vectors downstream of gear meshing zone; white represents a velocity ⩾10% higher than the gear blade tip velocity magnitude

zone in the first numerical test case and nearly tripled in the second numerical test case.

Still not satisfied with these results, in that they did not take into account gradient smearing through cell creation/agglomeration and first-order upwinding in time, a third test case was constructed. The grid was similar to that in Fig. 5, except that it involved the Newtonian mixture (with a single additive feed stream) flowing around a single center cylinder anchored in the triangular cell zone. The cylinder's angular velocity and the solution time step were typical of gear pump simulations discussed in the upcoming sections. The rotation of the cylinder forced the triangular mesh to deform (squeeze, create, and agglomerate) just as it would in a gear pump simulation. The wall of the cylinder was set as a slip boundary condition so that no vorticity would be created and no flow disturbance would occur. The time-averaged (TA) outlet COV was reduced to 180 through the triangular zone in this test. Because this third test took into account all foreseeable numerical mixing caused by the mixture approach, deforming mesh, and spatial/temporal discretization, all upcoming COV results will be scaled by a similar ratio ($\sim$0.5) in order to isolate real gear pump mixing effects. Incidentally, the area-averaged value of the mixing parameter for the three numerical test cases were 0.5, indicating simple shear flow.

Single Additive Injection Stream (Case 1). Figure 6 shows a typical cross-sectional instantaneous concentration contour plot for the first gear pump case in which a single additive inlet feed was utilized. Viscous heating and thermal/shear-thinning (VHTST) were ignored for this case. The white shade represents anything ⩾60% higher than the outlet MFWAA mass concentration. Black, of course, represents zero additive concentration. The contour lines are scaled in-between these two values. The single "strand" of additive coming down from the inlet is 100% additive, and the white area enclosed by the gear outline is simply unoccupied space. The inlet additive COV is >300%. The examples of flow phenomena discussed (and the associated numbered regions) in the next two figures will arbitrarily be associated mainly with the left-hand side gear.

Note how the additive-rich strand is pulled into encircled region 1 just above the gear meshing zone (encircled region 4). For the most part, it remains bound near the cavity floor throughout the gear movement cycle from the intake to the discharge. Encircled region 2 marks the near-wall additive-depleted region that is created by the inlet-fed process fluid being cut off from the inlet by the sweeping gear teeth. As consecutive cavity-bound fluid zones merge above the pump outlet at encircled region 3, additive-rich material gets split into two main regions. Some of the cavity-bound rich material gets pushed toward the outlet walls, while the majority of the rich material moves toward the outflow core. Gear-induced fluid motion appears to create interfacial surface area for phasic mixing. The mechanisms proposed to be responsible for this are discussed in the upcoming text. The TA outlet additive COV (already adjusted for expected numerical diffusion) is 45% for this case.

Figure 7, showing normalized velocity vectors for a typical instantaneous flow field, helps to explain further what is causing the mass concentration trends. Here, the white shade represents any velocity ⩾10% higher than the tip rotational velocity magnitude, and black corresponds to zero velocity. Any vector passing across a surface boundary is simply an artifact of increasing the length scale of the postprocessed vectors to make them visually insightful. During the rotational cycle, the peak local velocity magnitude exceeds 15 times the gear angular velocity in the gear meshing zone (encircled region 4 in Fig. 6). Also in region 4, peak local strain rate magnitude exceeds 40 times the gear angular velocity divided by the diametrical gear-housing clearance. The area-averaged value of the mixing parameter (used in [4,5]) in the present case is 0.71, indicating that the flow is more elongational than simple shear flow.

Small mixing cells are created by fluid moving radially inward on backward-facing teeth faces and fluid moving radially outward on forward-facing teeth faces. The mixing cells remain near the cavity floor and mostly unchanged in each tooth cavity throughout the revolution process, except where the teeth mesh. In the meshing zone, the mixing cells are mashed and distorted, but never fully extinguished since there is always sufficient radial spacing. Tooth-housing diametrical clearance allows a small amount of each cavity's fluid to leak ("tip leakage") into each subsequent gear swept area. It is difficult to tell in any of the instantaneous contours shown in this paper, but the coupling of the mixing cell and the tip leakage creates a counterrotating motion in each cavity, providing increased interfacial area between the phases. The additive-depleted regions near the walls and the rich regions near the floor tend to mix through this motion, but the exchange is weak. A wider radius of vortex rotation in the floor would probably help exchange these two materials more efficiently. A design change in the contour of the gear teeth may allow the vortex entrainment to be increased.

Stagnant regions are created at the outlet side of the gear mesh-

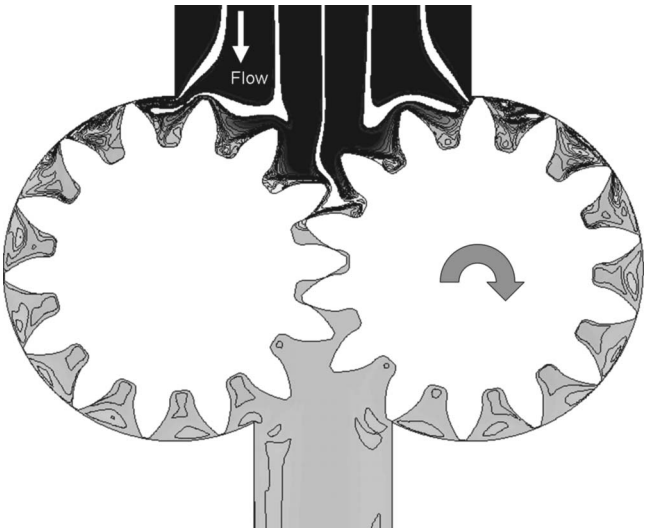

Fig. 8 Typical instantaneous normalized additive mass concentration contours for five injection streams and a Newtonian process fluid; white represents material having a mass concentration ⩾60% higher than the instantaneous outlet MFWAA concentration

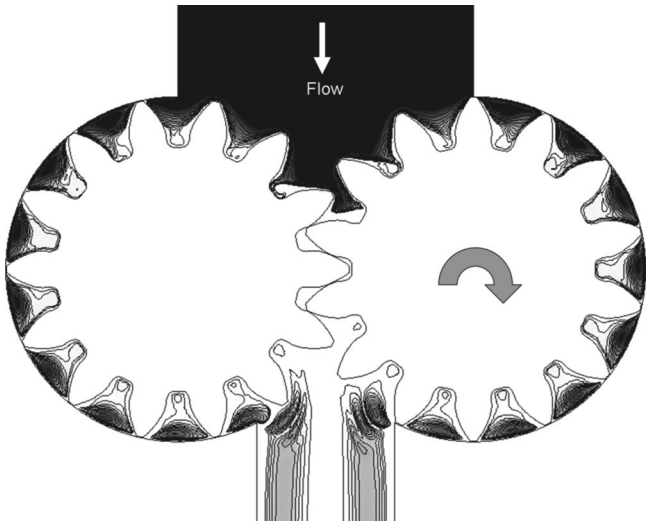

Fig. 9 Typical instantaneous normalized temperature contours for five injection streams in which VHTST effects are taken into account; white represents material having a temperature ⩾10°C higher than the inlet temperature

ing zone in an alternating fashion as the fluids moving radially outward from alternating gear teeth meet and come to rest. Similar stagnant regions occur on the inlet side (not shown) of the meshing zone. It must be noted that where the fluids meet head-on in the stagnant zones, there will likely be a three-dimensional component to the flow. That has been ignored in the present two-dimensional (2D) study.

Multiple Additive Injection Streams (Case 2). The TA outlet COV is dramatically lowered from 45% to 5.5% by the introduction of four other inlet streams of pure additive across the inlet, resulting in five equally spaced concentrated feed strands. This is near the 5% COV typically sought in static mixer applications. Here, again, VHTST effects are ignored. The total additive feed rate is held constant, and the inlet COV again is >300%. Figure 8, same gray scale as Fig. 6, provides instantaneous normalized mass concentration contours on a pump cross section for this case. The weaving and breaking up of the strands at the intake side prevent the building up of relatively high mass concentration additive regions in the cavity floors as was the tendency of the single-injection case. Since these strands seem to get pushed radially outward near the housing wall, the higher mass concentration regions for this model stayed nearer the walls. The area-averaged value of the mixing parameter is 0.71 also for case 2.

Viscous Heating, Thermal/Shear-Thinning (Case 3). Further reduction in outlet COV, down to 3.2%, was found by the incorporation of VHTST considerations into the five-stream injection case. The cross-sectional mass concentration contours look extremely similar to those in Fig. 8; therefore, they are not included here. The area-averaged value of the mixing parameter is, again, 0.71 for case 3. Figure 9, however, shows new information regarding normalized static temperature. The white shade represents anything ⩾10°C higher than the inlet temperature, while black corresponds to the inlet temperature.

There are obvious similarities between the temperature contours here and the mass concentration contours in Fig. 6. The temperature is relatively higher in the near-floor cavity-bound material. At the outlet there is a split between core high-temperature flow and near-wall high-temperature flow as in Fig. 6. The difference, of course, in the two figures is that the additive source comes from the intake, while the thermal source lies in the near-tooth regions (especially in the meshing zone). Moving from the top of the figure to the bottom around the gear circumferential direction, note the fact that the high-temperature material in the cavity floor somewhat disperses into the fresh feed material captured by the gears. Then, as the material is exposed to strain, it heats up moving toward the outlet.

The viscosity of the process fluid varies across the outlet instantaneously (time-averaged results not available), as can be seen in Fig. 10. The local process fluid viscosity is scaled by the MFWAA process fluid viscosity across the outlet. Mixture strain rate magnitude, shaped like the typical laminar strain rate profile, and mixture static temperature are scaled in a similar fashion. The x-axis is the normalized distance across the outlet from left to right. Velocity magnitude (not shown here) is laminar parabolic, as one might assume.

As expected, the viscosity profile is a mirror image of the temperature profile. The interesting feature, however, is how low the viscosity drops near the walls. The temperature does not rise any more here than it does in the core, yet the viscosity is much lower than in the core. This lower viscosity occurs because of the increased strain rate at the wall.

Bulk fluid viscosity reduction is believed to be the source of the mixing improvement achieved by the VHTST case. This is expected to improve stirring action within the cavities throughout the gear rotational cycle. Although there is variation in the localized viscosity across the outlet, the average process fluid viscosity at the outlet is 22% less than that of the inlet. This is a result of the overall increase in bulk temperature and the instantaneous shear values at the outlet. Again, shear-history effects have been excluded from this study.

Figure 11 gives insight into the outlet additive mass spatial concentration profiles for all three full-scale cases. The TA local concentration is normalized by the TA MFWAA concentration. Time did not permit running the cases long enough to develop perfectly symmetrical TA profiles. There was a dramatic reduction in variability when the additive injection stream count was increased from 1 to 5. There was further reduction in variability when VHTST was incorporated. Both of these effects are consistent with the previously mentioned COV values. Another notable feature of this plot is the inversion of the outlet profile when the additive injection stream count is increased from 1 to 5. Instead of the highest concentration being at the outlet centerline (single injection), a below-average value is seen at the centerline for multiple injection streams. VHTST effects keep the profile similar, but

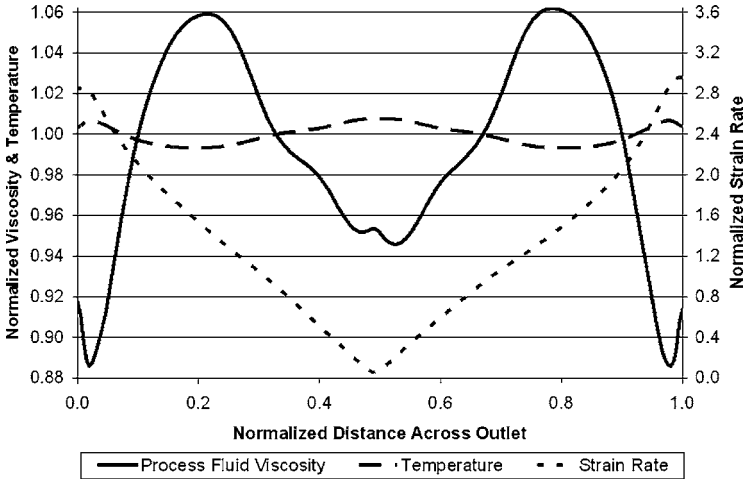

Fig. 10 Typical instantaneous normalized outlet process fluid viscosity, mixture temperature, and mixture strain rate magnitude for five injection streams and VHTST effects

the peaks are moved slightly closer to the centerline. The two multiple additive inlet concentration profiles are similar in shape to the process fluid viscosity profile in Fig. 10.

Scale and Speed Effects (Cases 4 and 5). Two more runs were carried out to attempt to isolate the effects of pump scale and pump speed, respectively, in the presence of multiple additive inlet streams and VHTST effects. Each of these two new runs was initialized with the resulting flow field from the most recently discussed case (case 3) and then run in tandem. For case 4, case 3 was scaled down by a factor of 0.48. This scaling applies linearly to everything geometrically in the setup. The relative inlet additive concentration and pump rotational speed were kept nearly the same. Since the fluid properties remained the same, the system Reynolds number fell by the scale factor. The outlet profiles (like those in Figs. 10 and 11) look extremely similar to those of case 3 and have not been included here. The difference, however, is that the TA outlet additive COV is even lower than the full-size pump to a value of 2.0%. It seems counterintuitive that a lower Reynolds number system would mix more efficiently. To help relate case numbers, Table 1 tabulates all CFD cases in this paper.

Case 5 involved the scaled-down pump (case 4) being slowed to 55% of the typical speed (Reynolds number lowered accordingly). Again the outlet profile plots have been omitted due to their similarity with those already shown in Figs. 10 and 11. The TA outlet additive COV fell to 1.5%. Once again, a system with an even lower Reynolds number (about 1/4 of that in case 3) shows a better mixedness at the outlet. The bulk viscosity reduction from inlet to outlet for the scaled-down pump (case 4) was 19%, while that of the scaled-down/slowed pump (case 5) was 14%. Both of these values are less than that of the full-scale case (case 3 at 22%), due mainly to less viscous heating for the scaled-down cases. This further magnifies the inverse Reynolds number—mixing rate trend. One does not expect, however, that Reynolds number would play an important part in laminar flow.

It is not clear why the smaller cases are more mixed. There must be some subtle differences in the counter-rotating mixing cells inside the cavities and/or the tip leakage rate between cavities that allow the level of additive blending to be higher in scaled-down cases 4 and 5. These differences could not be detected from reviewing transient contour plots and moving videos from the runs. The area-averaged mixing parameter remained 0.71 in both scaled-down cases, so it appears that scale and/or speed do

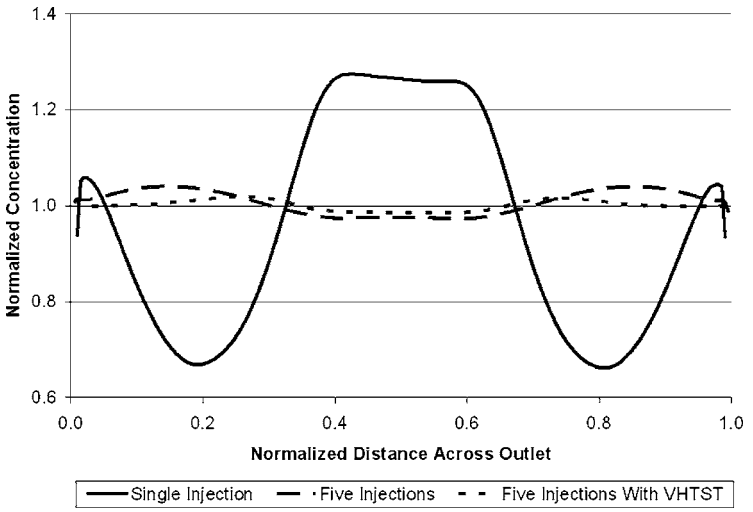

Fig. 11 Time-averaged outlet additive mass concentration profiles for the three full-scale cases normalized by the time-averaged MFWAA outlet concentration

Table 1 CFD results summary: The shaded cells show the modeling aspect that was changed from the previous run

Case #	# Additive Feed Streams	Process Fluid Physics	Geometric Scale	Speed Scale	TA Outlet Additive COV
1	1	Newtonian	Full	Full	45%
2	5	Newtonian	Full	Full	5.5%
3	5	VHTST	Full	Full	3.2%
4	5	VHTST	Half	Full	2.0%
5	5	VHTST	Half	Half	1.5%

not have a major impact on the mixing efficiency. The fact that the COV was nearly halved, while the mixing parameter did not change supports what is discussed in [5] that a single mixing measure should not be used to judge improved mixing in all cases. The mixing parameter value seems to be unique to this particular pump design.

Experimental Validation. A short experimental test of the gear pump additive mixing concept has been carried out for a single additive feed stream configuration. Although the experimental pump was a half-scale unit operated at full speed with VHTST effects like case 4, it is the closest to case 1 for COV comparative purposes. Factors other than the number of feed streams affected the computational COV results, but feed stream count was the single largest COV determining factor. After adjusting the computational case 1 COV results for scale and VHTST effects (assuming the effects in Table 1 are independent), one would expect the adjusted COV result to be 16%. The experimental pump outlet COV varied in the range of 15–30%, which was viewed as an acceptable match. The computational bulk throughput for the full-scale cases at full speed was lower than the vendor-claimed value at the modeled conditions by $<9\%$. This discrepancy is partially caused by the fact that the gears do not actually touch (forming the intended seal) in the computational gear meshing zone.

Conclusions

A high-resolution computational study was undergone to investigate additive mixing (mass concentrations $<10\%$) within a viscous process fluid inside an industrial-scale intermeshing metering gear pump. Additive feed arrangement, fluid properties, pump scale, and pump speed effects on mixing were evaluated. A relatively new moving/deforming grid approach within a commercial CFD solver was used to resolve transient additive concentrations within the pump. Careful consideration was given to numerical discretization, computational grid, and convergence (building blocks for any CFD study) to ensure sound results. Typically, >15 full computational gear pump revolutions were required to reach quasi-steady state. Numerical diffusion is known to play a role in any CFD simulation, even when the computational grid and numerical recipes seek to minimize said effects. The COV results are adjusted for such effects based on three numerical diffusion tests employed in the present study.

For the case in which a single additive injection stream is utilized at the intake of the pump, the model predicted an outlet additive TA COV of 45%. Mixing cells in the gear teeth cavities and tip leakage work to increase phasic interfacial area and improve mixing but is relatively small in extent. A modification to the gear tooth profile may allow the local cavity-bound circulation to increase. The TA COV is lowered to 5.5% by the inclusion of five injection streams at the pump intake. The waving and breaking of these high-concentration streams helps to prevent the buildup of high-concentration zones in the teeth cavity floors. This is near the 5% COV value typically sought in static mixer applications. The inclusion of viscous heating and thermal/shear-thinning effects in the multiple inlet stream CFD model shows an even further reduction in the outlet COV to 3.2%. It is proposed that most of this improvement came from bulk process fluid viscosity reduction.

Intriguing results were found by first scaling the geometry of the pump to nearly half size and then slowing it down to nearly half speed. Both cases involved multiple inlet additive streams and VHTST physics. The half-scale pump at full speed had a TA outlet COV of 2.0%, but the same pump slowed down had a TA outlet COV of 1.5%. There does not appear to be an obvious answer for why lower Reynolds number systems would produce less additive variability at the pump outlet. The value of the mixing efficiency parameter remained 0.71, in an area-averaged sense, for all cases studied here.

The computational COV result was in the range of that found in an experimental study for a scaled-down pump with a single additive feed stream. Since it was always possible, computationally, to get a COV near or less than 5% with at least five additive feed streams, the blending was considered satisfactory. Future work could include an investigation of the effects of operating pressure differential and/or tip leakage on mixing efficiency. Also, coupling effects of the variables that have been independently evaluated in this work could be considered.

Nomenclature

B = generic constant
C_m = mixture heat capacity $=\Sigma\alpha_k\rho_k C_k/\Sigma\rho_k\alpha_k$
k_m = mixture thermal conductivity $=\Sigma\alpha_k k_k$
p = static pressure
S = source associated with pump movement
T = mixture static temperature
u_i = velocity component of the mixture
τ_{ij} = stress tensor of the mixture
ρ_m = mixture density $=\Sigma\alpha_k\rho_k$
α_k = volume fraction of phase k
η_m = mixture apparent viscosity $=\Sigma\alpha_k\eta_k$
η_{P0} = zero-shear viscosity of process fluid
θ = relaxation time of process fluid
γ = mixture strain rate magnitude

Subscripts

A = additive phase, or fluid
k = generic phase, or fluid
m = mixture property
P = process phase, or fluid

References

[1] Kramer, W., 1988, "Gear Pump Characteristics and Application," *Plastics South—Conference Proceedings of SPE*, SPE, Atlanta, pp. 91–110.
[2] Bouse, L. F., Carlton, J. B., and Jank, P. C., 1988, "Effect of Water Soluble Polymers on Spray Droplet Size," Trans. ASAE, **31** (6), pp. 1633–1648.
[3] Valsamis, L. N., and Pereira, J. M., 1999, "Rotor Developments in the Farrel Continuous Mixers Post Reactor Processing of Bimodal HDPE Resins," *Proc. of 1999 International Conference on POLYOLEFINS XI*, SPE, Houston, pp. 233–248.
[4] Bruce, D., Wilson, M., and Generalis, S., 1997, "Flow Field Analysis of Both the Trilobal Element and Mixing Disc Zones Within a Closely Intermeshing, Co-Rotating Twin-Screw Extruder," *Intern. Polymer Processing XII*, Hanser Publishers, Munich, Vol. 4, pp. 323–330.
[5] Heniche, M., Tanguy, P., Reeder, M., and Fasano, J., 2005, "Numerical Investigation of Blade Shape in Static Mixing," AIChE J., **51**, pp. 44–58.
[6] Aris, R., 1962, *Vectors, Tensors, and the Basic Equations of Fluid Mechanis*, Dover, New York.
[7] Panton, R. L., 1996, *Incompressible Flow*, 2nd ed., Wiley, New York.
[8] Siginer, D. A., and Letelier, M. F., 2002, "Pulsating Flow Flow of Viscoelastic Fluids in Straight Tubes of Arbitrary Cross-Section, Part II: Secondary Flows," Int. J. Non-Linear Mech., **37**, pp. 395–407.
[9] Bird, R. B., Steward, W. E., and Lightfoot, E. N., 1960, *Transport Phenomena*, Wiley, New York.
[10] Strasser, W. S., Feldman, G. M., Wilkins, F. C., and Leylek, J. H., 2004, "Transonic Passage Turbine Blade Tip Clearance With Scalloped Shroud: Part

II—Losses With and Without Scrubbing Effects in Engine Configuration," ASME Paper No. IMECE2004-59116.
[11] Musad, A., and Khurram, R., 2005, "A Multiscale Finite Element Method for Fluid-Structure Interaction," ASME Paper No. IMECE2005-79767.
[12] Hulme, I., Clavelle, E., van der Lee, L., and Kantzas, A., 2005, "CFD Modeling and Validation of Bubble Properties for a Bubbling Fluidized Bed," Ind. Eng. Chem. Res., **44**, pp. 4254–4266.
[13] FLUENT, 2005, *FLUENT 6.2 User's Guide*, FLUENT, Inc., Lebanon, NH.
[14] Patankar, S. V., 1980, *Numerical Heat Transfer and Fluid Flow*, Taylor & Francis, New York.
[15] Tezduyar, T. E., and Senga, M., 2005, "Comparison of Some New and Old Stabilization and Shock-Capturing Parameters in SUPG Fine Element Computation of Inviscid Compressible Flows With Quadrilateral and Triangular Elements," ASME Paper No. IMECE2005-80969.

Waterjet Peening and Surface Preparation at 600 MPa: A Preliminary Experimental Study

A. Chillman[1]

M. Ramulu

Department of Mechanical Engineering,
University of Washington,
Seattle, WA

M. Hashish
Flow International Corporation,
Kent, WA

An experimental study was conducted to explore the surface preparation as well as the effects of high-pressure waterjet peening at 600 MPa *on the surface integrity and finish of metals. The concept of larger droplet size and multiple droplet impacts resulting from an ultra-high-pressure waterjet was used to explore and develop the peening process. A combination of microstructure analysis, microhardness measurements, and profilometry were used in determining the depth of plastic deformation and surface finish that result from the surface treatment process. It was found that waterjet peening at* 600 MPa *induces plastic deformation to greater depths in the subsurface layer of metals than laser shock peening. The degree of plastic deformation and the state of the material surface were found to be strongly dependent on the peening conditions and desired surface roughness. Based on these first investigation results, water peening at* 600 MPa *may serve as a new method for introducing compressive residual stresses in engineering components.* [DOI: 10.1115/1.2436580]

Introduction

Waterjet (WJ) peening has been developed to overcome the limitations of shot peening. In waterjet peening, instead of using the solid media, a high-pressure waterjet, which has been disintegrated in the droplet zone to impact the material surface, is applied. The main benefit of the induced plastic deformation is that it can enhance the fatigue life of the component or structure [1–3]. However, ultra-high-pressure waterjets can cause surface erosion or surface damage. Erosion and microfracture can be induced on the material surface by the jets if the applied peening conditions are beyond a certain threshold value of the target material [4–6]. If erosion-caused damages are induced, it will decrease the fatigue life of the component, which is an undesirable effect. This erosion is due to the transfer of kinetic energy to the work piece, and it has been shown [7] that the energy transfer is related to the waterjet process parameters. For this reason, it is important to determine the optimum conditions to promote a controlled surface preparation without inducing detrimental material erosion.

Most surface processing methods not only affect the surface layers, but also alter the surface microstructure irregularities. The local irregularities, or the areas of surface roughness, are responsible for causing stress concentrations that reduce the fatigue limit of the material. The reliability of manufactured components is often critically dependent on the quality of surface produced, and the surface layer may drastically affect the strength and chemical resistance of the material. Prior studies [8–13] have reported that the high-pressure flow of water at supply pressure below 150 MPa have the same deformation effects as conventional shot peening, but with negligible changes in surface roughness and topology. However, the common problem of using peening is the introduction of surface and subsurface damage and erosion on the target [14,15]. Process conditions of concern include pressure, traverse rate, standoff distance, jet exposure time, and jet type (round or fan or fuzzy). Currently, there has been no systematic investigation conducted to study the surface finishes generated by waterjet peening processes that includes the fuzzy jets. Fuzzy jets are formed when a fluid is either injected or entrained into the jet stream to cause the jet to break down in contrast to the highly coherent (not fuzzy) jet typically used in waterjet cutting.

The objective of this preliminary study is to evaluate the performance of high-pressure waterjets or, more so, to define the appropriate peening conditions for waterjet peening (with those conditions being nozzle-to-surface distance, nozzle type, and nozzle transverse rate) on Titanium 6Al-4V through the examination of surface characteristics. The surface characteristics induced by different jet conditions were examined, evaluated, and discussed. Surface characteristics of the component, in general, are discussed, in terms of surface finish and surface integrity. Surface finish is a term used to describe the exterior features of the surface, such as surface roughness, texture, lay, pits, etc. Surface integrity is defined as the inherent condition of a surface layer, which pertains to properties such as microstructural transformations, hardness alteration, residual stress distribution, etc. The analysis of the surface characteristics can yield the information that is vital to effectively controlling the manufacturing processes on material surfaces.

Experimental Setup and Procedure

The peening tests were performed on Titanium (Ti-6AL-4V) sheets approximately 300 mm wide by 450 mm long. The peening jet was traversed along the width of the sample at rates of 84.7 mm/s and 169.3 mm/s and at standoff distances varying from 12.7 mm to 63.5 mm. Enough spacing was provided between the exposed tracks of the jets to eliminate any interference. Additional tests were performed on a superplastic formed titanium alloy surface preparation sample. These were performed at varying traverse speeds and a standoff distance of 25.4 mm. The pressure used was 600 MPa, and the lateral displacement between the traverses was 0.2 mm.

This study applied the high-pressure waterjets to surface preparation and peening of a Titanium alloy using different jets. The various types of jets were formed using different kinds of nozzles (Fig. 1). Three types of jets were used:

1. Plain waterjet (WJ): In this case, a regular round waterjet was used. The diameter of the jet was 0.127 mm. At 600 MPa pressure, the water flow rate was 0.0375 l/min. For this setup the air entrainment tube was plugged.
2. Water-Air Jet (WAJ): In this case, air was injected into the

[1]Corresponding author.

Contributed by the Fluids Engineering Division of ASME for publication in the JOURNAL OF FLUIDS ENGINEERING. Manuscript received April 3, 2006; final manuscript received December 11, 2006. Review conducted by Joseph Katz.

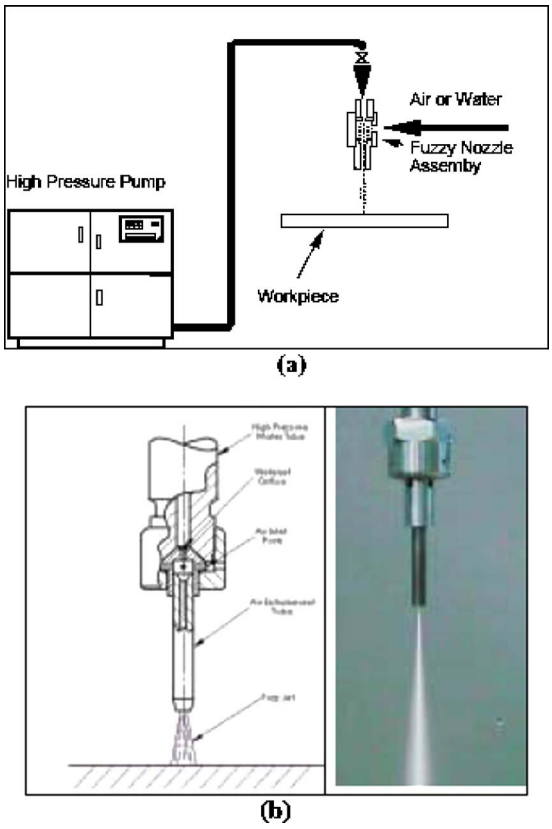

Fig. 1 (*a*) Schematic diagram of a peening system and (*b*) peening nozzle assembly

600 MPa pressure waterjet. Air water mixing occurred in a mixing tube of 0.75 mm dia and 75 mm long.

3. Water-Water Jet (WWJ): In this case, water was entrained, instead of air, in the above nozzle. The water flow rate was ~0.01 *l*/min.

The variations that existed in the peening conditions were standoff distances, traverse rate, nozzle type, and nozzle pressure. A detailed list of the variable conditions can be seen in Tables 1–3. It is important to note that the pressure remained constant at 600 MPa and the orifice diameter remained constant at 0.127 mm for all of the peening runs. For the experimental set 1 peening trials, the surface peening was performed with the plain waterjet (WJ) and with a fuzzy jet (WAJ) formed by the introduction of atmospheric pressure into a waterjet (Table 1). The term fuzzy jet is used to define the jet stream that forms when injected/entrained fluid causes an accelerated breakdown of the stream.

The peening conditions for experimental set 2 (Table 2) were varied to compare the effects of a 0.103 MPa applied pressure and a 0.207 MPa applied pressure. Screening tests (experimental sets 1 and 2) were first performed to select one of the above jets for further tests. Experimental conditions and test matrices for experimental sets 1 and 2 are given in Tables 1 and 2, respectively. Visual inspection showed that the WAJ-type jet does not cause noticeable erosion and can easily be controlled. The WWJ, although not included in experimental set 1 or 2, was observed to be violently vibrating and produced a pattern that was not uniform. However, this concept promises highly effective peening when the process is further developed for uniform and consistent exposure. Another experimental test matrix (experimental set 3) is shown in Table 3. The narrow profile of the jet suggested that multiple parallel passes be performed to create a peened area for analysis. Accordingly, 50 parallel passes were run side by side, with a spacing of 0.254 mm.

Table 1 Peening conditions for experimental set 1

Run #	*Traverse Rate*	*Stand off Dist.*	*Jet Type*	*Air Pressure Applied*
	(mm/s)	*(mm)*		*(MPa)*
1	84.7	63.5	WJ	-
2	84.7	50.8	WJ	-
3	84.7	38.1	WJ	-
4	84.7	25.4	WJ	-
5	84.7	12.7	WJ	-
6	169.3	63.5	WJ	-
7	169.3	50.8	WJ	-
8	169.3	38.1	WJ	-
9	169.3	25.4	WJ	-
10	169.3	12.7	WJ	-
11	84.7	63.5	WAJ	Atm
12	84.7	50.8	WAJ	Atm
13	84.7	38.1	WAJ	Atm
14	84.7	25.4	WAJ	Atm
15	84.7	12.7	WAJ	Atm
16	169.3	63.5	WAJ	Atm
17	169.3	50.8	WAJ	Atm
18	169.3	38.1	WAJ	Atm
19	169.3	25.4	WAJ	Atm
20	169.3	12.7	WAJ	Atm

The surface roughness of machined and peened samples was measured using contact profilometry with a SurfAnalyzerTM 4000 profilometer and a 5 μm dia probe. Profiles of the machined surface were obtained in a direction that is perpendicular to the direction the nozzle traverses during the peening process. All measurements were obtained according to ANSI B46.1-1986 using a 0.8 mm cutoff length and 3.5 mm traverse length. Standard roughness parameters, including the arithmetic average roughness (R_a) and peak-to-valley height (R_y) were calculated from each profile. The distribution in subsurface plastic deformation was determined from Knoop hardness measurements along the peening depth. Hardness measurements were obtained from a polished surface according to ASTM E92-82. All measurements were performed with a 500 g indentation load over a 15 s period. Optical microscopy and scanning electron microscopy were used in examining the surface erosion mechanics and subsurface features.

Table 2 Peening conditions for experimental set 2

Run #	*Traverse Speed*	*Stand off Dist.*	*Jet Type*	*Pressure Applied*
	(mm/s)	*(mm)*		*(MPa)*
21	84.7	63.5	WAJ	0.103
22	84.7	50.8	WAJ	0.103
23	84.7	38.1	WAJ	0.103
24	84.7	25.4	WAJ	0.103
25	84.7	12.7	WAJ	0.103
26	169.3	63.5	WAJ	0.103
27	169.3	50.8	WAJ	0.103
28	169.3	38.1	WAJ	0.103
29	169.3	25.4	WAJ	0.103
30	169.3	12.7	WAJ	0.103
31	84.7	63.5	WAJ	0.207
32	84.7	50.8	WAJ	0.207
33	84.7	38.1	WAJ	0.207
34	84.7	25.4	WAJ	0.207
35	84.7	12.7	WAJ	0.207
36	169.3	63.5	WAJ	0.207
37	169.3	50.8	WAJ	0.207
38	169.3	38.1	WAJ	0.207
39	169.3	25.4	WAJ	0.207
40	169.3	12.7	WAJ	0.207

Table 3 Peening conditions for experimental set 3

Run #	Traverse Speed (mm/s)	Stand off Dist. (mm)	Jet Type	Water Flow Pressure (MPa)
1	84.7	12.7	WAJ	0.103
2	84.7	25.4	WAJ	0.103
3	84.7	38.1	WAJ	0.103
4	84.7	50.8	WAJ	0.103
5	84.7	63.5	WAJ	0.103
6	169.3	12.7	WAJ	0.103
7	169.3	25.4	WAJ	0.103
8	169.3	38.1	WAJ	0.103
9	169.3	50.8	WAJ	0.103
10	169.3	63.5	WAJ	0.103
11	84.7	12.7	WAJ	0.207
12	84.7	25.4	WAJ	0.207
13	84.7	38.1	WAJ	0.207
14	84.7	50.8	WAJ	0.207
15	84.7	63.5	WAJ	0.207
16	169.3	12.7	WAJ	0.207
17	169.3	25.4	WAJ	0.207
18	169.3	38.1	WAJ	0.207
19	169.3	50.8	WAJ	0.207
20	169.3	63.5	WAJ	0.207

Results and Discussion

Figure 2 shows the optical micrographs of the peened surfaces on experimental sets 1 and 2. The micrograph of the peening track for run 1 of experimental set 1 presents evidence that a significant amount of erosion occurred with the plain waterjet (WJ). In contrast to that, the peening track for run 22 of experimental set 2 appears to exhibit a "cutlike" appearance; it does not appear that the material was eroded away in the same fashion as run 1 of experimental set 1.

The peening track was also characterized by analyzing the end view of the track. A comparison of two peening runs can be conducted, one with a standoff distance of 63.5 mm and one with a standoff distance of 12.7 mm (the smallest standoff distance). The images in Fig. 3 depict the observed valleys of the cuts for these two standoff distances. The left image depicts the observed track for a standoff distance of 12.7 mm, where the volume diplaced is greater. This is as expected because the nozzle is located closer to the sample, and thus, the waterjet has less distance to travel over where energy is dissipated.

In order to quantify and evaluate the jet performance, analysis was made by viewing the end cross section of the peening track to determine the erosion volume rate for each run on experimental set 1. A plot can be created to determine if the erosion volume rate behaves as a function of standoff distance or the distance from the nozzle to the surface that is being peened. From the kerf geometries (Fig. 3), erosion volumes were calculated and plotted in Fig. 4 for experimental set 1. By analyzing, it is evident that the erosion volume rate behaves as a function of both the standoff distance and the jet traverse rate. Also, the two plots can be compared to show that the erosion rate is greater for the WAJ conditions.

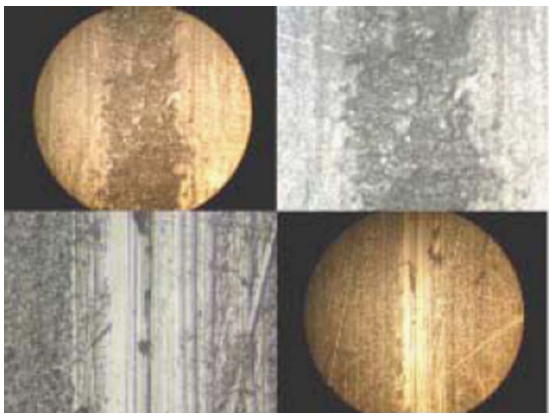

Fig. 2 Top left: 10× magnification of run 1 of experimental set 1. Top right: Close up of peening track on run 1. Bottom right: 10× magnification of run 22 of experimental set 2. Bottom left: Close up of peening track on run 22.

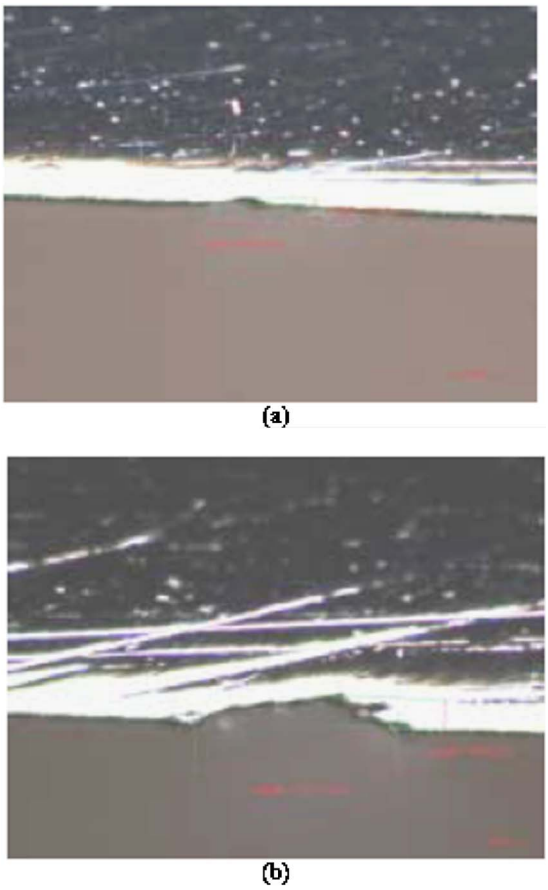

Fig. 3 Sectional Kerf profiles: (*a*) end view of peening run 11 of experimental set 1, peened at a 63.5 mm standoff distance and (*b*) end view of peening run 15 of experimental set 1, 12.7 mm standoff distance

No visible tracks were observed with the fuzzy nozzle width of 0.762 mm under the conditions of experimental set 2. Optical examination merely showed the cleaned surface at 63.5 mm standoff distance, regardless of the applied pressure. This observation led us to explore further to systematically study the surface processing and peening with the design of experiment (DOE) approach for experimental set 3.

The fuzzy nozzle (WAJ) in experimental set 3 had a width of 0.762 mm; thus, the parallel passes overlapped slightly. In this series of experiments, 50 parallel passes were run side by side, with a spacing of 0.254 mm between each pass. Figure 5 shows a typical aerial image of the surface peening tracks on experimental set 3. The lighter-colored tracks are the areas exposed to the WAJ for peening. The treated regions seen in Fig. 5 show evidence that the affected width from each individual pass does not completely overlap, and a series of ridges and valleys becomes evident. To further understand the effects that each of the above peening conditions had, surface roughness and subsurface hardening were investigated.

Typical surface profiles taken on the tracks are plotted in Fig. 6.

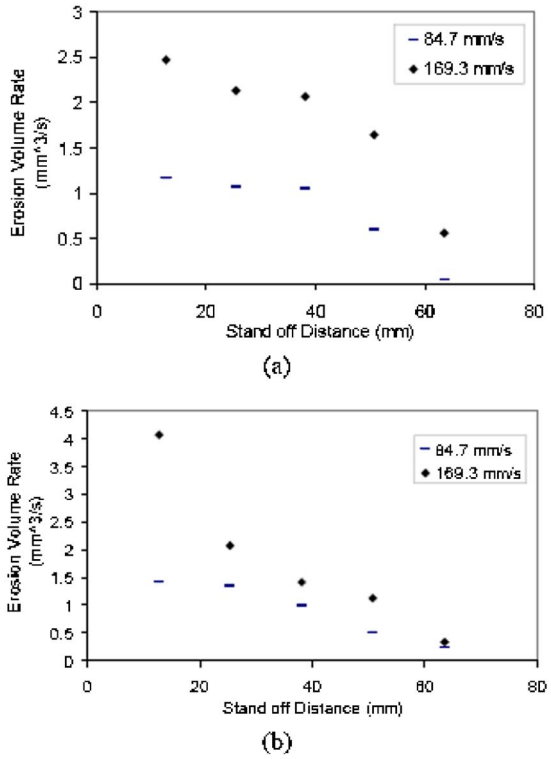

Fig. 4 Erosion volume rate versus standoff distance for cases of (*a*) plain waterjet (WJ) and (*b*) fuzzy nozzle (WAJ) with atmospheric pressure as described for experimental set 1 in Table 1

The first corresponds to the surface profile of run 1, which had a feed rate of 84.7 mm/s, standoff distance of 12.7 mm, and 0.103 MPa airflow pressure used to form a fuzzy nozzle (Fig. 6(*a*)). The profile seen in Fig. 6(*b*) corresponds to run 20, which had a feed rate of 169.3 mm/s, a standoff distance of 63.5 mm, and 0.207 MPa airflow pressure, and used a fuzzy nozzle. These profiles show what can be considered the best (Fig. 6(*b*), run 20: R_a=0.2 μm) as the profile height variations were between ±1.5 μm, and worst cases for R_a (Fig. 6(*a*), run 1: R_a=5.6 μm), where the profile height varied between ±20 μm. This relationship shows that a higher airflow pressure, accompanied by a greater standoff distance, resulted in a smaller centerline average roughness.

Further analysis of surface profiles taken on the wide peened areas of experimental set 3 can be used to calculate surface characterizing parameters; the arithmetic average roughness (R_a) and peak-to-valley height (R_y). Figure 7 shows the effect of standoff distance on R_a, for a given fuzzy jet traverse rate at airflow pressures of 0.103 MPa (Fig. 7(*a*) and 0.207 MPa (Fig. 7(*b*)), respectively. It is clear from the plots that the average surface roughness R_a shows a decreasing trend as the standoff distance increases, as expected. In addition, the results show that R_a is higher for the feed rate of 84.7 mm/s (lowest in this series of experiments). Finally, the larger airflow pressure of 0.207 MPa produces a smooth surface with a smaller R_a.

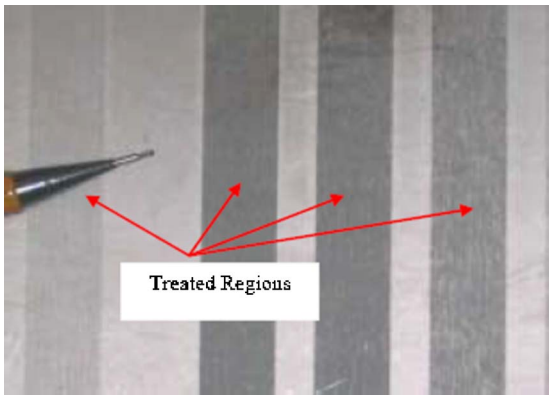

Fig. 5 Experimental set 3: Exposed surface of peening sample with 50 passes taken at a 0.254 mm index using a fuzzy nozzle (WAJ) of width 0.762 mm

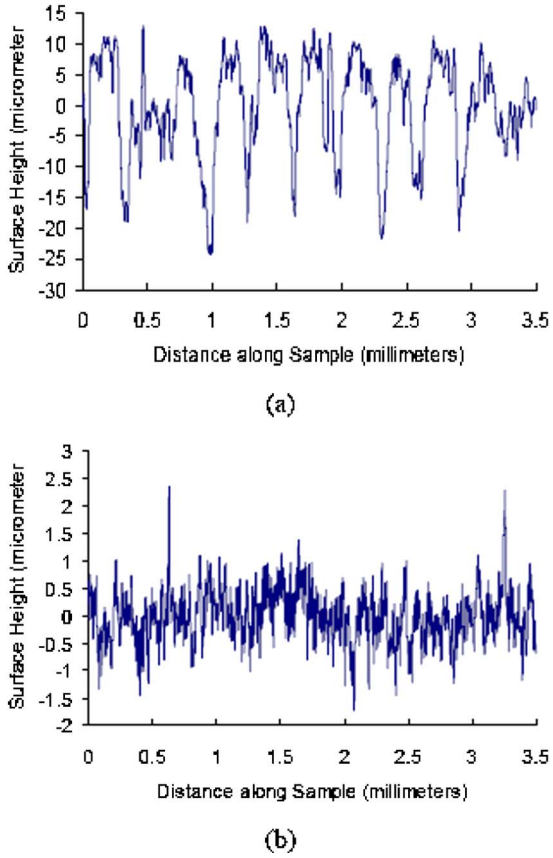

Fig. 6 Surface profiles for (*a*) experimental set 3, run 1 and (*b*) experimental set 3, run 20

Surface roughness calculations gave similar values of the arithmetic surface roughness (R_a) and the root-mean-square (rms) roughness (R_q), while the ten-point roughness values (R_z) were within the scatter of $<5\%$; this data is not presented here. It was observed that the values of average surface roughness parameters obtained between peened and unpeened surface were found to have little difference in magnitude. However, maximum peak-to-valley height (R_y), plotted and shown in Fig. 8, and the ten-point roughness (R_z) varied; both of these parameters had a minimum roughness value at higher standoff distance. The R_y value of each peened area varied as a function of the feed rate, standoff distance, and pressure. Surface roughness parameters were clearly dependent on the jet exposure time (or jet traverse rate) and standoff distance as shown in Figs. 8(*a*) and 8(*b*).

Further surface preparation experiments were performed on a superplastically formed titanium alloy using the plain WJ. In these processes, the goal was to erode the oxidation layer of the titanium due to the superplastic forming. The parameters used were a 600 MPa pressure, a lateral displacement of 0.2 mm between each traverse, and a standoff distance of 25.4 mm. For the experiment, eight lateral passes were made. Also, a plain WJ was used for the surface preparations. A typical sample with erosion marks can be

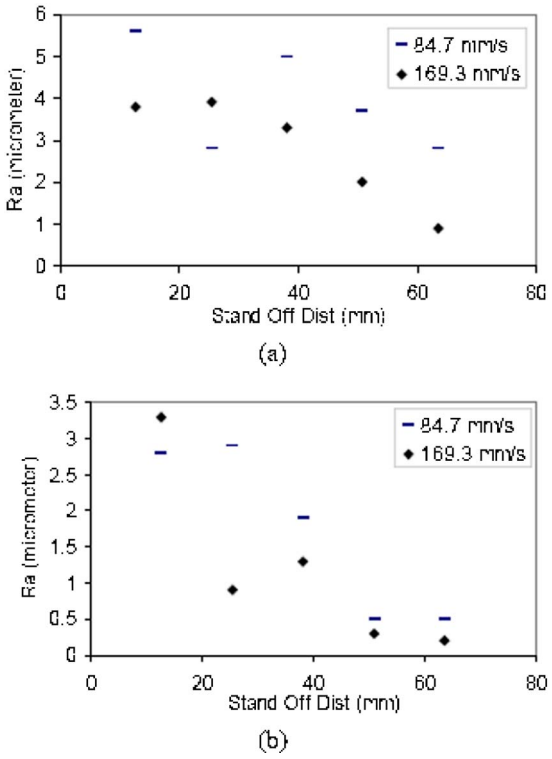

Fig. 7 R_a **values as a function of standoff distance for experimental set 3: (*a*) 0.103 MPa applied air pressure and (*b*) 0.207 MPa applied air pressure**

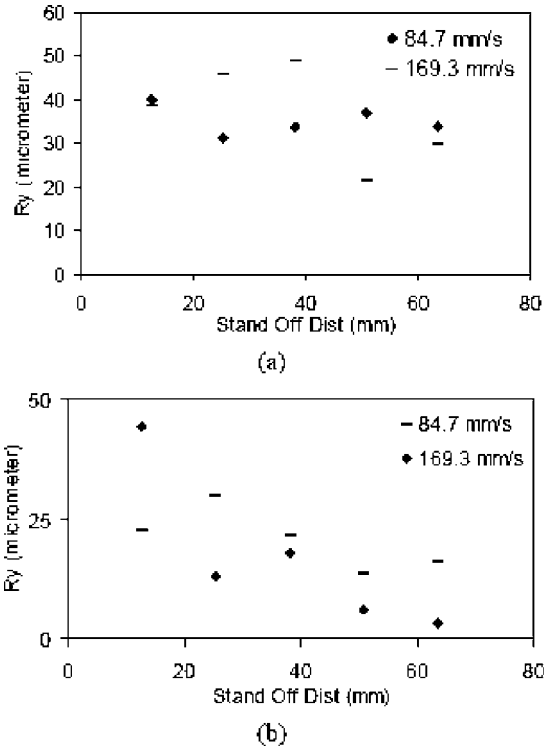

Fig. 8 R_y **values as a function of standoff distance for experimental set 3: (*a*) 0.103 MPa applied air pressure and (*b*) 0.207 MPa applied air pressure**

seen in Fig. 9, specifying the traverse speed for each case. It is important to note the severity of the erosion mechanism when the traverse rate is 21.2 mm/s; the base material is completely exposed. As the traverse rate increased, the depth of cut was found to reduce. However, an interesting trend with the surface roughness was found. The values of R_a and R_y held reasonably constant for traverse rates higher than 31.7 mm/s. This implies that a threshold traverse rate may exist above which the surface roughness does not change considerably.

Surface structure of waterjet-treated, superplastically formed Ti alloy was examined using a scanning electron microscope (SEM). These SEM micrographs were taken at 2000x magnification and are shown in Fig. 10. Note that as the traverse speed increases, the erosion becomes less severe. This can be seen by comparing the images in Figs 10(*a*) and 10(*c*). It is clear that the erosion mechanism is dependent on the jet exposure time, which, in turn, depends on the traverse speed. Based on the preliminary tests, there exists an ideal traverse speed to induce the creation of a desired surface finish. It can be seen that the image in Fig. 10(*a*) has a vast amount of surface erosion and the original surface is no longer present.

However, in Fig. 10(*b*), the original surface remains in contact. The amount of surface erosion that occurred in this case is substantial, yet not totally detrimental to the original surface.

In order to evaluate the peening effect, or the degree of plastic deformation, in the Ti-6Al-4V material with experimental set 3 conditions, the Knoop hardness test was performed on runs 1–10. The hardness was calculated using the Knoop hardness equation

$$H_{\text{Knoop}} = 14.229 \frac{M_{\text{impact}}}{d^2}$$

where d is the longest diagonal of the Knoop impact (in millimeters) and M_{impact} is the applied indentation load in kilograms. Subsurface hardness values were analyzed to determine if hardness variations exist in the peened regions.

Microhardness measurements were normalizing by the hardness of the unpeened region and plotted in Fig. 11 as normalized hardness as a function of depth beneath the jet impinged surface. This plot shows the highest normalized hardness value at the surface, and the hardness reaches the unpeened value at a depth of ~300 μm. Another interesting trait is that the highest value reached is ~1.17 times the normal hardness of the titanium sample at 50 μm depth. These results showed that a maximum increase in microhardness of specimen peened using the fuzzy nozzle was ~20% greater than that of the base material and was strongly dependent on the surface peening conditions.

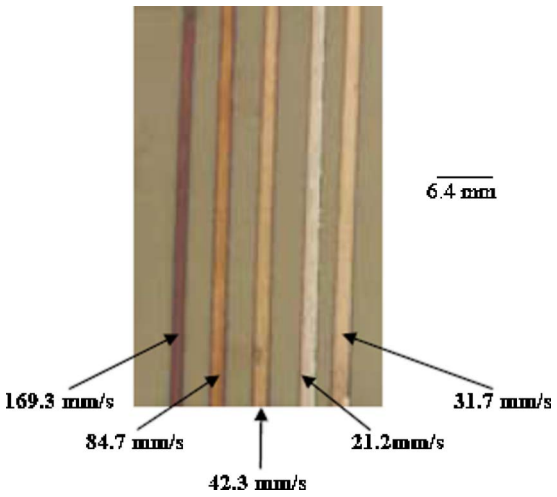

Fig. 9 Superplastic formed specimen with erosion marks for varying traverse rates

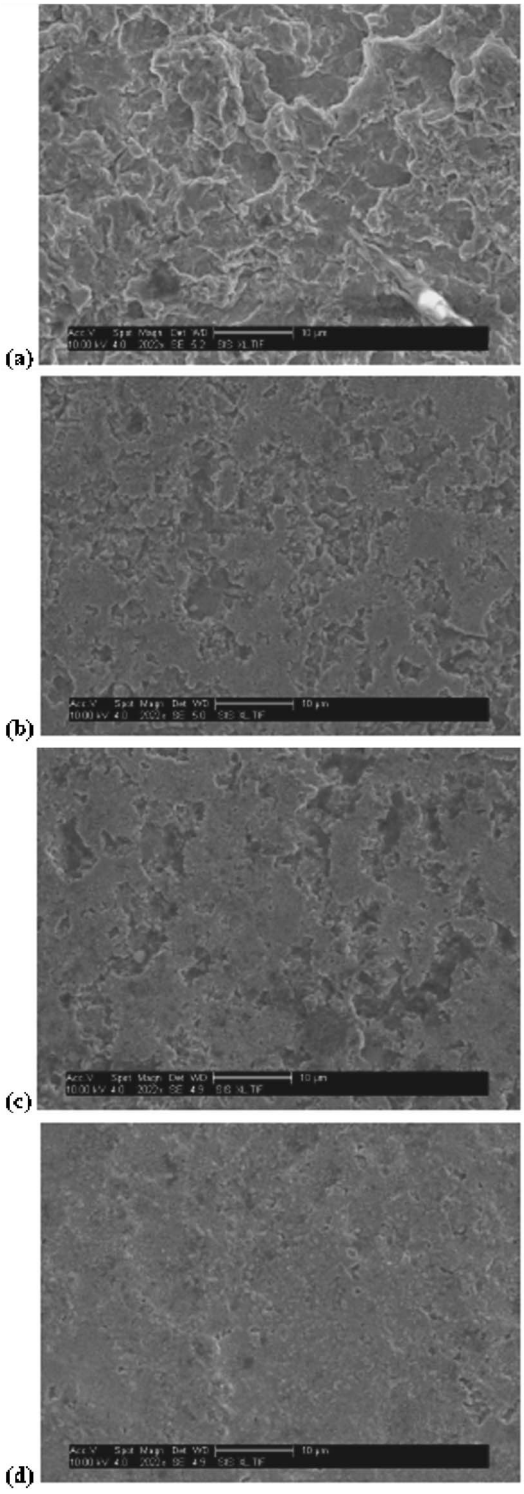

Fig. 10 SEM Surface erosion images of SPF Titanium Alloy. The traverse speeds are (*a*) 21.2 mm/s, (*b*) 31.7 mm/s, (*c*) 42.3 mm/s, and (*d*) 169.3 mm/s.

Summary and Conclusions

An exploratory research on surface preparation and treating of titanium alloy Ti-6AL-4V and superplastic formed titanium alloys was conducted using high-pressure waterjets with a fuzzy nozzle at a constant pressure of 600 MPa. Based on the preliminary results of the investigation, surface characteristics produced by high-pressure waterjets were strongly dependent on peening parameters. It was found that waterjets with the fuzzy nozzle did induce plastic deformation on the material surface. An increase in compressive residual stress was expected at longer peening exposure times and shorter standoff distances when material removal occurred. Results also showed that the changes in surface roughness are directly influenced by the kinetic energy that has been transferred to the target material. Therefore, the same surface characteristics on the target material are obtained by using an equal amount of energy supplied by the jet. These results present useful information in waterjet peening and surface preparation applications. Further study is in progress to apply statistical analysis to distinguish and define appropriate standoff distance, airflow pressure, and traverse rate for water peening with the fuzzy nozzle (WAJ).

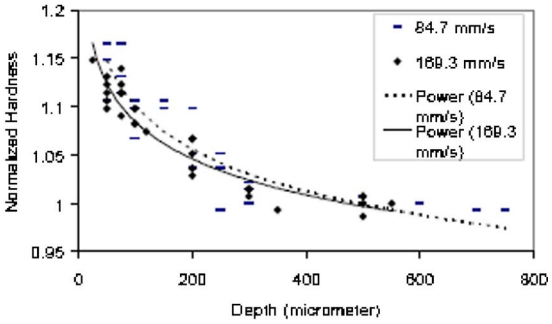

Fig. 11 Normalized Knoop hardness values for runs 1–20 of experimental set 3

References

[1] Tonshoff, H. K., Kroos, F., and Hartmann, M., 1995, "Water Peening—An Advanced Application of Water Jet Technology," 8th American Water Jet Conference, Aug. 26–29, Paper No. 33, pp. 473–486.
[2] Ramulu, M., Kunaporn, S., Jenkins, M. G., Hashish, M., and Hopkins, J., 1999, "Peening With High Pressure Waterjets," SAE Technical Paper No. 1999–01–2285.
[3] Daniewicz, S. R., and Cummings, S. D., 1999, "Characterization of Water Peening Process," ASME J. Eng. Mater. Technol., **121**, pp. 336–340.
[4] Ramulu, M., Kunaporn, S., Arola, D., Hashish, M., and Jordon, H., 2000, "Waterjet Machining and Peening of Metals," ASME J. Pressure Vessel Technol., **122**(1), pp. 90–95.
[5] Blickwedel, H., Haferkamp, H., Louis, H., and Tai, P. T., 1987, "Modification of Material Structure by Cavitation and Liquid Impact and Their Influence on Mechanical Properties," *Erosion by Liquid and Solid Impact, Proc. 7th International Conference on Erosion by Liquid and Solid Impact*, 7–10 Sept. pp. 31.1–31.6.
[6] Yamaushi, Y., Soyama, H., Adashi, Y., Sato, K., Shindo, T., Oba, R., Oshima, R., and Yamabe, M., 1995, "Suitable Region of High-Speed Submerged Water Jets for Cutting and Peening," JSME Int. J., Ser. B, **8**(1), pp. 31–38.
[7] Hashish, M., 2004, "Waterjet Cutting at 600 MPa," BHR Group Symposium of Water Jetting, pp. 47—60.
[8] Mathias, M., Gocke, A., and Pohl, M., 1991, "The Residual Stress, Texture and Surface Changes in Steel Induced by Cavitation," Wear, **150**, pp. 11–20.
[9] Colossi, B. M., Monno, M., Semeraro, Q., 2000, "Process Parameters Control in Water Jet Peening," Int. J. Mater. Prod. Technol., **15**(1–2), pp. 10–19.
[10] Arola, D., and McCain, M. L., 2000, "Abrasive Waterjet Peening: A New Method of Surface Preparation for Metal Orthopedic Implants," J. Biomed. Mater. Res., **53**(5), pp. 536–546.
[11] Arola, D., and Ramulu, M., 1997, "Material Removal in Abrasive Waterjet Machining of Metals. Part I: Surface Integrity and Texture," Wear, **210**(6), pp. 50–58.
[12] Arola, D., and Ramulu, M., 1997, "Material Removal in Abrasive Waterjet Machining of Metals: A Residual Stress Analysis," Wear, **211**(2), pp. 302–310.
[13] Ramulu, M., Kunaporn, S., Jenkins, M. G., Hashish, M., Hopkins, J., 2000, "Fatigue Performance of High Pressure Waterjet Peened Aluminum Alloy," *High Pressure Technology-2000, Proc. of ASME* Pressure Vessel Conference, ASME, New York, PVP-Vol.406, pp. 250–257.
[14] Kunaporn, S., Ramulu, M., Hashish, M., and Jenkins, M. G., 2004, "Residual Stress Induced by Waterjet Peening: A Finite Element Analysis," ASME J. Pressure Vessel Technol., **126**(3), pp. 333–340.
[15] Kunaporn, S., Ramulu, M., and Hashish, M., 2005, "Mathematical Modeling of Ultrahigh Pressure Waterjet Peening," ASME J. Eng. Mater. Technol., **127**(2), pp. 186–191.

A Study of the Effect of Polymer Solution in Promoting Friction Reduction in Turbulent Channel Flow

F. R. Cunha
Department of Mechanical Engineering,
University of Brasília,
Campus Universitário,
70910-900, Brasília-DF,
Brazil

M. Andreotti
Laboratoire des Ecoulements Géophysiques et Industriels,
Institut National Polytechnique de Grenoble,
Ecole Nationale Supérieure d'Hydraulique et de Mécanique de Grenoble,
1025, rue de la Piscine,
Domaine Universitaire,
BP 95, 38402 Saint-Martin-d'Hères Cedex,
France.

In this work, turbulent drag reduction in a pipe is investigated by using laser Doppler velocimetry. The effect of decreasing the friction factor of the flow is obtained by addition of high molecular weight polymers. The mechanism of drag reduction is explained in terms of a stress anisotropy that inhibits the transversal transport of momentum by turbulent fluctuations. Semi-theoretical models based on a nonlinear constitutive equation, which takes into account an extra extensional rate of strain in the flow produced by the local additive orientation, are presented. The semi-theoretical models used to predict the friction factor of the flow in the presence of the polymer have successfully described the experimental measurements. The results have revealed a reduction in the friction factor of 65% for a concentration of 350 ppm *in volume of polyacrylamide (PAMA) in an aqueous solution. In addition, the flow statistics, such as the axial and radial velocity fluctuations, the normalized autocorrelation functions as well as the power spectra for both velocity fluctuation components, are examined for the Newtonian flow of pure water and the flow of a* 120 ppm *solution of PAMA at the same friction velocity. Next, the results are compared in order to characterize the effect of the additive on the turbulent flow.* [DOI: 10.1115/1.2436579]

Keywords: macromolecules, drag reduction, anisotropy, extensional viscosity, turbulent flow

1 Introduction

The drag reduction phenomenon in the turbulent flows by the presence of anisotropic particles, especially, high molecular weigh polymers, has been the subject of research during the last years [1–4]. The understanding of the drag reduction mechanism is important in several engineering applications; a decreasing friction of flows in pipelines up to 50% may be obtained either by the addition of a few parts per million (ppm) of polymers or by the addition of fibers at low volume fraction. Reduction of turbulent drag has been also observed with other agents, such as flexible walls [5] and gradient of magnetic fields [6,7]. The field of action of this study is extensive, including its use to reduce the costs of flows in pipelines, cavitation prevention in turbo machines, reduction of noise, increase of speed of boats and ships with a polymer layer covering the skulls, and in the stability of jets for fire combat.

The physical mechanisms responsible for the phenomenon of drag reduction are not completely understood and remain a subject of debate. The role of stress anisotropy due to polymer extension versus elasticity in the mechanism of drag reduction is still an ongoing subject of controversy. Several theories have been presented to explain the mechanisms responsible for the drag reduction. Lumley [8] was the first to suggest that a molecular extension of polymer is responsible for drag reduction. Lumley argued that this extension will take place outside the viscous sublayer, causing an increase in effective viscosity there. Ryskin [9] developed a theory of drag reduction using the yo-yo model to predict this effective viscosity increase in turbulence and related this viscosity increase to a drag reduction parameter. L'vov et al. [10] have proposed a mechanism of drag reduction by polymers in turbulent wall-bounded flows based on a y-dependent effective viscosity. In particular, we have noted that although both works have been based on the notation of polymer extension, they do not contain any anisotropic stress effect caused by specific stress orientation. We suspect that this may be the reason why Ryskin's quantitative model does not predict a significant drag reduction.

De Gennes [11], Joseph [12], and Min et al. [13], among other authors, suggest that polymer elasticity is the main mechanism behind drag reduction by polymer additives. In particular, the latter authors suggest a mechanism of drag reduction, arguing that polymer relaxation time is essentially associated with the transport of elastic energy in the boundary layer. Massah and Hanratty [14] showed that the polymer chains are stretched in the very near-wall region and released in the buffer and log layers. In contrast, other authors maintain that the main mechanism is associated with the anisotropy arising from the particular orientation of the polymer chains once they are fully stretched by the flow [15–20]. Experiments by Sasaki [21], who measured the effectiveness for drag reduction of various polymers in combination with several kinds of solvents, also suggests the existence of rodlike entities in the solution, which introduce anisotropic effects, is essential. Moreover, these experiments found that the drag-reducing ability of polymer solutions tends to decrease when the polymer becomes more flexible. It seems still premature to clearly identify which of the two mechanisms is dominant for drag reduction, which was the main motivation to develop the present work. A linear stability analysis of a mixing layer in the presence of fiber additives has been performed by Azaiez [22]. The application of direct numerical simulations of turbulent flows in order to demonstrate the drag reduction phenomenon was first addressed by Handler and Levich [23]. Direct numerical simulations (DNS) of a fully turbulent channel flow of a dilute polymer solution by Dimitropoulos et al. [24] have shown that the polymer induces several changes in the

Contributed by the Fluids Engineering Division of ASME for publication in the JOURNAL OF FLUIDS ENGINEERING. Manuscript received February 14, 2006; final manuscript received November 8, 2006. Assoc. Editor: Dennis Siginer.

turbulent flow characteristics. Depending on the details of the phenomenological model used, the numerical simulations are able to qualitatively capture several effects observed experimentally, such as the upward shift in the logarithmic region of the mean flow profile, enhanced axial velocity fluctuations, decreased radial wall-normal velocity fluctuations, and relaxing or fading memory effects [25]. Recent numerical simulation by Benzi et al. [26] of the finite-extensibility nonlinear elastic dumbbell with the Peterlin approximation of the non-Newtonian approximation revealed that the phenomenon of drag reduction by polymer additives exists also in homogeneous turbulence, but it is not a universal phenomenon.

The aim of the present work is to characterize the mechanism of drag reduction when low-volume fractions of anisotropic additives are present in a channel turbulent flow. To this end, we have developed an extension of the classical Prandtl logarithmic law modeling the effect on the flow of polymers of high molecular weight at low-volume fractions in terms of an extensional viscosity. The semi-theoretical models have revealed that a stress anisotropy created in the flow by the presence of additives drastically affects the transversal mechanism of momentum transport by turbulent velocity fluctuations, and consequently, the friction factor of the flow is decreased. The results suggest that if the polymer relaxation time is greater than a typical scale of the flow, the macromolecule behaves closely to anisotropic fibers. This analogy may be taken far if the flexibility that polymer chains usually have does not make significant hydrodynamic effects and if the polymer chain can retain its conformation without degradation, therefore behaving approximately like a long rigid fiber. Under this condition, an extensional viscosity would depend on the macromolecule aspect ratio and volume particle volume fraction, being independent of any elastic parameter, such as Deborah number, i.e., the dimensionless relaxation time of the polymer [16,17,27]. Certainly our model does not perfectly represent a polymer solution, but on the other hand, some aspects of the model may be applied to capture the essence of how particle anisotropy reduces the drag of very robust flows, such as turbulent ones. The purpose of the present paper is actually to shed more light on the role of anisotropy connected to fully stretched macromolecules in polymeric drag reduction or fiber suspension drag reduction.

2 Mathematical Description

In the present work, we consider a Newtonian incompressible fluid of viscosity μ and density ρ, containing N_f long fibers (or macromolecules of high molecular weight polymers) per unit of volume, confined between two infinite parallel plates separated by a distance h. The additives are characterized by a length ℓ and a diameter b. The aspect ratio is defined as ℓ/b and, in most of the cases, is much larger than unity. It is assumed that the time for a typical additive to fall significantly is much larger than a characteristic time scale of the flow; thus, the particles are neutrally buoyant [28].

2.1 Macromolecule Relaxation Time. Dilute polymer solution behavior can be idealized as being a polymer chain composed of two beads representing drag forces, linked to an elastic spring representing a restoring force. This configuration, called dumbbell, was introduced by Kuhn and Kuhn [29]. A vector $\mathbf{r}$ between the centers of the spheres represents the distance between the ends of the macromolecule. In solution, the configuration of a particular macromolecule is constantly changing as the result of collisions with the solvent molecules. In quiescent fluid, this Brownian motion will randomize the configuration distribution so that each configuration is equally probable. In this randomly coiled state, the mean end-to-end distance is much smaller than the overall length of the polymer chain. As a simplified model, we can consider the polymer to be a chain of N rigid segments (each corresponding to an individual monomer) of length δ, with each segment randomly orientated with respect to the adjoining segments. The number of monomers N is equal to the molecular weight of the polymer divided by the molecular weight of a single monomer and, thus, is proportional to the molecular weight of the polymer. Typically, N is in the range 10^4-10^5, with δ of the order of 0.5 nm. The equilibrium configuration distribution is then given by a random walk of N steps each of length δ, and the mean end-to-end distance of the polymer r is proportional to $\sqrt{N}\delta$.

In a flow, the distribution of polymer configurations will be affected by the local velocity gradient. The local velocity gradient acting in the polymer will cause the molecule to extend. This extension is opposed by Brownian motion, which will tend to restore the equilibrium distribution. In dynamic equilibrium, the elastic Brownian force, $F_b \sim |\mathbf{r}|KT/(N\delta^2)$, where K is the Boltzmann constant and T is the absolute temperature, is of the same order of magnitude of the frictional force (Stokes law), $F_v \sim |\mathbf{r}|^2(6\pi\mu/\tau)$. Thus, a typical time scale is order of the time that the macromolecule stretched by the flow restores its equilibrium configuration. Therefore, the relaxation time τ of an extended polymer to the randomly coiled state is estimated as being [11]

$$\tau \sim \frac{6\pi\mu\delta^3}{KT}\left(\frac{M}{M_i}\right)^{3/2} \tag{1}$$

where M is the molecular weight of the polymer and M_i is the molecular weight of a monomer. It should be important to note from the scaling in Eq. (1) that polymers of high molecular weight have a large relaxation time and, consequently, a large aspect ratio when stretched by the flow.

2.2 Balance Equations. The continuum equations that governing the motion of an incompressible fluid are

(i) Continuity equation:

$$\nabla \cdot \mathbf{u} = 0 \tag{2}$$

(ii) Cauchy equation:

$$\rho\left(\frac{\partial \mathbf{u}}{\partial t} + \mathbf{u} \cdot \nabla \cdot \mathbf{u}\right) = \nabla \cdot \boldsymbol{\Sigma} \tag{3}$$

where $\mathbf{u}$ is the velocity field of the flow and $\boldsymbol{\Sigma}$ is the hydrodynamic stress tensor.

2.3 Constitutive Model. A polymer solution is often described by non-Newtonian models. Since the polymers are stretched by the flow, it produces stress anisotropy in the flow, which causes a nonlinear effect. The following expression for the stress tensor is proposed [28]:

$$\boldsymbol{\Sigma} = -p\mathbf{I} + 2\tilde{\mu}\mathbf{D} + \boldsymbol{\Sigma}_f \tag{4}$$

where p is the static fluid pressure, $\mathbf{I}$ the identity tensor, and $\tilde{\mu}(\dot{\gamma}, \phi)$ is the shear viscosity of the polymeric solution that, for very low particle volume fraction, is reasonable to assume $\tilde{\mu}(\dot{\gamma}, \phi) \approx \tilde{\mu}(\phi)$. Actually, for very dilute suspensions the shear viscosity can be evaluated by Einstein [30], who proposed $\tilde{\mu}(\phi) = \mu(1 + A\phi)$, where A is a constant that assumes the value of 5/2 for rigid spheres. $\mathbf{D} = (\nabla\mathbf{u} + (\nabla\mathbf{u})^T)/2$ is the rate of strain and $\boldsymbol{\Sigma}_f$ denotes the extra stress tensor due to the presence of the additive in the flow. We shall consider a suspension of rigid fibers where the axial deformation of the fibers is much smaller than their thickness. The fibers are long enough so that they are not affected by Brownian diffusion.

The present work will explore the case of long fiber suspension or polymers of high molecular weights. That means, the additives have a high relaxation time compared to a typical time scale of the flow. Several constitutive models have been developed to determine the expression for anisotropic particles to the bulk stress tensor $\boldsymbol{\Sigma}_f$. All these models, whether derived from slender-body theory [31,32] or by invoking continuum mechanics theory [33], led to a general expression of the form

$$\boldsymbol{\Sigma}_f = \mu_e \mathbf{D}:\langle \mathbf{ssss} \rangle + \alpha_e (\mathbf{D} \cdot \langle \mathbf{ss} \rangle + \langle \mathbf{ss} \rangle \cdot \mathbf{D}) + \gamma_e \langle \mathbf{ss} \rangle \tag{5}$$

where the material constants μ_e, α_e, and γ_e may depend on the particle properties and volume fraction ϕ. In general, for suspensions that have weak or no Brownian motion, the third term on the right-hand side can be neglected. Furthermore, for the large-aspect-ratio particle explored in this work, $\alpha_e \ll \mu_e$, and the anisotropic particle stress reduces simply to $\boldsymbol{\Sigma}_f = \mu_e \mathbf{D}:\langle \mathbf{ssss} \rangle$. Here, $\boldsymbol{\Sigma}_f$ the non-Newtonian term of the stress tensor represents the macroscopic average contribution of the additive to the fluid stress with μ_e being an extensional viscosity associated with the extensibility of the additives. By definition, $\boldsymbol{\Sigma}_f$ is symmetric and positive definite and does not depend on the translation, rotation or acceleration of the frame of reference. Considering a change of frame of reference given by $\mathbf{y} = \mathbf{Q}(t) \cdot \mathbf{x} + \mathbf{b}(t)$, with $\mathbf{Q}(t)$ being a rotation tensor and $\mathbf{b}$ a translation vector, the stress $\boldsymbol{\Sigma}_f^y$ in the new frame of reference ($\mathbf{y}$) is given by

$$\boldsymbol{\Sigma}_f^y = \mathbf{Q}(\mathbf{t}) \cdot \mu_e (\mathbf{D}:\langle \mathbf{ssss} \rangle) \cdot \mathbf{Q}^T(\mathbf{t}) = \mu_e \mathbf{D}^y:\langle \mathbf{s}^y \mathbf{s}^y \mathbf{s}^y \mathbf{s}^y \rangle \tag{6}$$

The above result states that the stress constitutive equation (6), which describes the behavior of the complex fluid considered, is material frame indifferent, preserving its form for all observers.

Note that $\boldsymbol{\Sigma}_f$ is an extra stress in the direction $\mathbf{ss}$ and proportional to the rate of strain in the direction of the additive orientation ($\mathbf{s} \cdot \mathbf{D} \cdot \mathbf{s}$). It is clear that the additive contribution to the fluid stress in a dilute solution will be small unless the additivelike polymers become highly extended by a strong flow. This description is still coupled to a kinematics equation that describes the evolution of the local orientation of the additives with the flow. Additives with long aspect ratio rotate approximately as fluid line elements so that [34]

$$\frac{D\mathbf{s}}{Dt} = \mathbf{s} \cdot \nabla \mathbf{u} - (\mathbf{s} \cdot \nabla \mathbf{u} \cdot \mathbf{s})\mathbf{s} \tag{7}$$

The complexity and the usually prohibitively high computational cost associated with the use of Eq. (7) to describe particle orientation have lead to many alternative approaches. The most reasonable one is to employ the so-called aligned particle approximation, which is based on the observation that large-aspect ratio fibers align quickly with the flow direction. In this approach, one solves only for the velocity field, which plays the dual role of predicting the fluid motion and the particle orientation. As the simplest approach for describing the additive action on a turbulent flow, one assumes then that the particles align with the local velocity vector. This approach is convenient to describe the flow of additives as being slender fibers in the absence of Brownian motion and additive-additive interactions, as the particles tend, indeed, to align with the streamlines. In addition, we also neglect that (i) the flow direction can fluctuate rapidly because of the turbulence and (ii) changes in the flow kinematics are assumed to be slow enough so that the anisotropic additive orientation can keep up. Under these conditions,

$$\mathbf{s} = \frac{\mathbf{u}}{|\mathbf{u}|} \tag{8}$$

The solution given by the kinematics model described by (8) is an approximate approach for additives of large aspect ratio, ($\ell/b \gg 1$). The experiments show that, under these conditions, the stretched particles tend locally to the direction of the flow, i.e., along the streamlines at all positions. This approach is also supported by observations of Stover et al. [35] and numerical simulations of Keiller and Hinch [36], who have shown that the orientation of the additive parallel to the velocity is always a steady solution of Eq. (7).

The constitutive model described here is used to predict the contribution of high molecular weight polymers to the flow. In this case, the relaxation time τ of the macromolecules is larger than the characteristic time of the flow. The monomers of those molecules remain extended, and supposing they do not degrade, they behave, approximately, in a similar way to fibers of large aspect ratio. In this context, the material constant μ_e/μ, may be assumed to be close to the extensional viscosity predicted by slender body theory for a dilute rigid-rod suspension [31,37]. Therefore,

$$\frac{\mu_e}{\mu} = \frac{4\pi n \ell^3}{3 \ln(\ell/b)} \tag{9}$$

where n is the additive number density (the number of additivies by unit volume).

It should be important to note that the analogy of polymer chains with a suspension of long rigid fibers seems to be a reasonable model for polymers of very high molecular weigh (long relaxation times). This analogy should be taken for very dilute polymer solution so that the flexibility of the macromolecule may have not been important to the hydrodynamic effect due to particle interaction and for the absence of polymer degradation so that we can assume that an extended macromolecule can retain its conformation and therefore behave approximately like long rigid fibers.

The expression for the extensional viscosity given by Eq. (9) shows that in a suspension of long fibers or stretched macromolecules there exists an important contribution, proportional to $n\ell^3$. We could think of the rigid fibers in a very dilute suspension as being equivalent to Einstein-like [30] effective shear viscosity $\tilde{\mu}$, for a suspension of rigid spheres with diameter equal to the length of the fibers, giving $\tilde{\mu} \sim n\ell^3$. The effect $n\ell^3$ is more intense than any other proportional to the volume concentration of the additives, $\phi = 2n\ell b^2$, when $b/\ell \ll 1$. A more accurate expression for the extensional viscosity derived by Shaqfeh and Frederickson [38] takes into account the effect of two-particle hydrodynamic interaction for semi-dilute regimes ($\phi \ll 1 \ll n\ell^3$). The dimensionless extensional viscosity based on this second-order analysis is given by

$$\frac{\mu_e}{\mu} = \frac{4}{3}\left(\frac{\ell}{b}\right)^2 \frac{\phi}{\ln(1/\phi)}\left(1 - \frac{\ln[\ln(1/\phi)]}{\ln(1/\phi)} + \frac{E(\phi)}{\ln(1/\phi)}\right) \tag{10}$$

It is important to note that $\mu_e/\mu = (4/3)(\ell/b)^2(\phi/\ln(1/\phi))$ is closely to the result of Batchelor's theory in the limit $\phi \mapsto 0$. For aligned cylindrical particles, Shaqfeh and Frederickson [38] found that $E(\phi)$ is equal to 0.1585. Since we are dealing with large-aspect-ratio molecules that will be aligned in the direction of the flow, we will adopt this value of E throughout this analysis. In a flow, anisotropic particles tend to resist the stretching along their own axis. In the present context, the extensional viscosity, $\mu_e \sim \mu n \ell^3$, represents the importance of this resistance.

2.4 Turbulent Flow of Polymer Solution. A physical model to explain drag reduction is still premature because the behavior of turbulence in the presence of a polymer is still largely unknown. Next, we discuss a possible formulation of a theory for drag reduction in a turbulent flow with dilute polymer. The stress tensor is expressed in the following way:

$$\boldsymbol{\Sigma} = -p\mathbf{I} + 2\tilde{\mu}(\phi)\mathbf{D} + \boldsymbol{\Sigma}_f \tag{11}$$

where

$$\boldsymbol{\Sigma}_f = \mu_e G(\mathbf{u})\mathbf{uu} \tag{12}$$

is the nonlinear term due to additive. Here, $G(\mathbf{u})$ is the rate of strain in the direction of polymer orientation defined by

$$G(\mathbf{u}) = \frac{\mathbf{u} \cdot \mathbf{D} \cdot \mathbf{u}}{|\mathbf{u}|^4} \tag{13}$$

Using Reynolds decomposition in the polymer stress tensor, the turbulent flow is then decomposed in an average component and a fluctuation component, namely, $\mathbf{u} = \bar{\mathbf{u}} + \mathbf{u}'$. Therefore, the Eq. (12) can be rewritten in the following form:

$$\mu_e G(\mathbf{u})\mathbf{uu} = \mu_e[G(\bar{\mathbf{u}}+\mathbf{u}')](\bar{\mathbf{u}}+\mathbf{u}')(\bar{\mathbf{u}}+\mathbf{u}') \tag{14}$$

and, now using the Eq. (13), one obtains the following approximation:

$$\mu_e G(\mathbf{u})\mathbf{uu} = \frac{\mu_e \mathbf{D}(\bar{\mathbf{u}}+\mathbf{u}'):(\bar{\mathbf{u}}+\mathbf{u}')(\bar{\mathbf{u}}+\mathbf{u}')}{|\bar{\mathbf{u}}|^4\left(1+\frac{\mathbf{u}'}{\bar{\mathbf{u}}}\right)^4}(\bar{\mathbf{u}}+\mathbf{u}')(\bar{\mathbf{u}}+\mathbf{u}') \tag{15}$$

After making slight algebraic manipulation and retaining the leading-order terms related to the fluctuations, we obtain a first approximation of the constitutive Eq. (12) in terms of the mean and the perturbed flow (i.e., turbulent fluctuations), namely,

$$\begin{aligned}\mu_e G(\mathbf{u})\mathbf{uu} = &\left(\frac{\mu_e \mathbf{D}(\bar{\mathbf{u}})}{|\bar{\mathbf{u}}|^4}:\bar{\mathbf{u}}\bar{\mathbf{u}}\right)(\bar{\mathbf{u}}\bar{\mathbf{u}}+\bar{\mathbf{u}}\mathbf{u}'+\mathbf{u}'\bar{\mathbf{u}}+\mathbf{u}'\mathbf{u}')\\ &+\left(\frac{\mu_e \mathbf{D}(\bar{\mathbf{u}})}{|\bar{\mathbf{u}}|^4}:\bar{\mathbf{u}}\mathbf{u}'\right)(\bar{\mathbf{u}}\bar{\mathbf{u}}+\bar{\mathbf{u}}\mathbf{u}'+\mathbf{u}'\bar{\mathbf{u}}+\mathbf{u}'\mathbf{u}')\\ &\times\left(\frac{\mu_e \mathbf{D}(\bar{\mathbf{u}})}{|\bar{\mathbf{u}}|^4}:\mathbf{u}'\bar{\mathbf{u}}\right)(\bar{\mathbf{u}}\bar{\mathbf{u}}+\bar{\mathbf{u}}\mathbf{u}'+\mathbf{u}'\bar{\mathbf{u}}+\mathbf{u}'\mathbf{u}')\\ &+\left(\frac{\mu_e \mathbf{D}(\bar{\mathbf{u}})}{|\bar{\mathbf{u}}|^4}:\mathbf{u}'\mathbf{u}'\right)(\bar{\mathbf{u}}\bar{\mathbf{u}}+\bar{\mathbf{u}}\mathbf{u}'+\mathbf{u}'\bar{\mathbf{u}}+\mathbf{u}'\mathbf{u}')\end{aligned} \tag{16}$$

Now, consider stationary and ergodic turbulence so that the temporal average is representative of the ensemble average for a time scale T much longer than the velocity fluctuation correlation time. Taking the time average of Eq. (16), and ignoring fluctuation terms of high order, we propose the following form for the average stress tensor of the flow due to the presen of additives

$$\begin{aligned}\overline{\mu_e G(\mathbf{u})\mathbf{uu}} = &\left(\overline{\frac{\mu_e \mathbf{D}(\bar{\mathbf{u}})}{|\bar{\mathbf{u}}|^4}}\right):(\overline{\bar{\mathbf{u}}\bar{\mathbf{u}}\bar{\mathbf{u}}\bar{\mathbf{u}}}+\overline{\bar{\mathbf{u}}\bar{\mathbf{u}}\mathbf{u}'\mathbf{u}'}+\overline{\bar{\mathbf{u}}\mathbf{u}'\bar{\mathbf{u}}\mathbf{u}'}+\overline{\bar{\mathbf{u}}\mathbf{u}'\mathbf{u}'\bar{\mathbf{u}}}\\ &+\overline{\mathbf{u}'\bar{\mathbf{u}}\bar{\mathbf{u}}\mathbf{u}'}+\overline{\mathbf{u}'\bar{\mathbf{u}}\mathbf{u}'\bar{\mathbf{u}}}+\overline{\mathbf{u}'\mathbf{u}'\bar{\mathbf{u}}\bar{\mathbf{u}}})\end{aligned} \tag{17}$$

As a first approximation in order to examine the interaction between the additives and the turbulent flow, we model such a mechanism by keeping the average component term and one of the typical fluctuation contribution terms given in Eq. (17). Therefore,

$$\bar{\boldsymbol{\Sigma}}_f = \overline{\frac{\mu_e \mathbf{D}(\bar{\mathbf{u}}):(\bar{\mathbf{u}}\bar{\mathbf{u}})}{|\bar{\mathbf{u}}|^4}}(\bar{\mathbf{u}}\bar{\mathbf{u}})+\overline{\frac{\mu_e \mathbf{D}(\bar{\mathbf{u}}):(\mathbf{u}'\bar{\mathbf{u}})}{|\bar{\mathbf{u}}|^4}}(\mathbf{u}'\bar{\mathbf{u}}) \tag{18}$$

Then, a possible constitutive equation for modeling the average stress tensor in a turbulent flow with additives is supposed to be

$$\bar{\boldsymbol{\Sigma}} = -\bar{p}\mathbf{I}+2\mu(\phi)\bar{\mathbf{D}}-\rho\overline{\mathbf{u}'\mathbf{u}'}+\overline{\frac{\mu_e \mathbf{D}(\bar{\mathbf{u}})}{|\bar{\mathbf{u}}|^4}}:(\overline{\bar{\mathbf{u}}\bar{\mathbf{u}}\bar{\mathbf{u}}\bar{\mathbf{u}}}+\overline{\mathbf{u}'\bar{\mathbf{u}}\mathbf{u}'\bar{\mathbf{u}}}) \tag{19}$$

The constitutive equation (19) certainly does not perfectly represent the behavior of a polymeric solution in turbulent flow, but we shall show that even though it is simple, it actually captures the most essential features of a dilute polymer solution in turbulent flows.

2.5 Turbulent Unidirectional Flow. Now we apply the constitutive equation (19) for a steady two-dimensional turbulent flow parallel to a plane surface with $\bar{u}=\bar{u}(y)$, $\bar{v}=\bar{w}=0$, and the eddy stresses varying with respect to y only. The corresponding Reynolds equation for the flow in the presence of the additive takes the form

$$\frac{\partial \bar{p}}{\partial x} = \frac{\partial}{\partial y}\left[\mu(\phi)\frac{d\bar{\mu}}{dy}-\rho\overline{u'v'}+\mu_e\frac{1}{\bar{u}^2}\bar{D}_{xy}(\overline{u'v'}+\overline{v'^2})\right] \tag{20}$$

It is instructive to note that under the above condition the contribution of the polymer stress reduces to

$$\bar{\Sigma}^f_{xy} = \frac{\mu_e \bar{D}_{xy}}{\bar{u}^2}(\overline{u'v'}+\overline{v'^2}) \tag{21}$$

When there is a drag reduction in the buffer boundary layer and part of the logarithmic layer, the axial velocity fluctuation u' increases whereas the transversal velocity fluctuation v' may drastically decrease. Under this condition, it is reasonable to assume in Eq. (21) that $\overline{v'^2} \ll \overline{u'v'}$. Now, introducing the rate of strain for the bidimensional flow $\bar{D}_{xy}=(d\bar{u}/dy)$ into (21), one obtains

$$\bar{\Sigma}^f_{xy} = \frac{\mu_e}{\bar{u}^2}\frac{d\bar{u}}{dy}\overline{u'v'} \tag{22}$$

Applying the boundary condition for the shear stress, $\tau_{xy}=\tau_w$ on the wall ($y=0$) and performing the integration of the Eq. (21) with respect to y, yields

$$\mu(\phi)\frac{d\bar{u}}{dy}+\left(\mu_e\frac{1}{\bar{u}^2}\frac{d\bar{u}}{dy}-\rho\right)\overline{u'v'} = y\frac{\partial \bar{p}}{\partial x}+\tau_w \tag{23}$$

Using the well-known Prandtl mixing length theory for parallel turbulent flows,

$$\overline{u'v'} = -\kappa^2 y^2\left(\frac{d\bar{u}}{dy}\right)^2 \tag{24}$$

where κ is the so-called universal constant of the Prandtl theory. Then, Eq. (23) is rewritten as

$$\mu(\phi)\frac{d\bar{u}}{dy}+\left(\rho-\mu_e\frac{1}{\bar{u}^2}\frac{d\bar{u}}{dy}\right)\kappa^2 y^2\left(\frac{d\bar{u}}{dy}\right)^2 = y\frac{\partial \bar{p}}{\partial x}+\tau_w \tag{25}$$

For the turbulent boundary layer region, i.e., $(\tau_w/\rho)^{1/2}y/\nu > 30$, we neglect the viscous stress, i.e., the molecular transport of momentum $\mu(\phi)d\bar{u}/dy$ from the average flow. If we further assume that the depth of the turbulent boundary layer is small, the term $y\partial\bar{p}/\partial x \ll \tau_w$. Under these conditions, the turbulent transport of momentum velocity fluctuations becomes

$$\left(\rho-\mu_e\frac{1}{\bar{u}^2}\frac{d\bar{u}}{dy}\right)\kappa^2 y^2\left(\frac{d\bar{u}}{dy}\right)^2 = \tau_w \tag{26}$$

For convenience, let us define the additive rate of strain function $G(y)$ as follows:

$$G(y) = \frac{1}{\bar{u}^2}\frac{d\bar{u}}{dy} \tag{27}$$

thus, Eq. (26) takes the form

$$[\rho-\mu_e G(y)]\kappa^2 y^2\left(\frac{d\bar{u}}{dy}\right)^2 = \tau_w \tag{28}$$

The model proposed here may be interpreted as a modified version of the mixing-length model proposed by Prandtl (see [39]) due to the change of momentum transport produced by the presence of anisotropic additives in the boundary layer. A modified mixing length can be defined then as being

$$\ell^* = \left[1-\frac{\mu_e}{\rho}G(y)\right]^{1/2}\kappa y \tag{29}$$

The radius of the tube and the friction velocity, $u_f=(\tau_w/\rho)^{1/2}$ of the turbulent flow are defined as being the typical length and velocity scale, respectively. In addition, the friction velocity of the flow is evaluated from the pressure gradient measurements according to $u_f=[(d\Delta P)/(4\rho\Delta Z)]^{1/2}$, where d is the diameter of the pipe, ΔP the pressure difference, and ΔZ the distance over which

ΔP is measured. The governing equation (26) is now written in terms of dimensionless variables in the following form:

$$\left(1-\frac{\mu_e}{\mu}\frac{1}{\mathrm{Re}_w}\frac{d\tilde{u}}{d\tilde{y}}\frac{1}{\tilde{u}^2}\right)\kappa^2\tilde{y}^2\left(\frac{d\tilde{u}}{d\tilde{y}}\right)^2=1 \tag{30}$$

where $\mathrm{Re}_w=u_f r_0/\nu$ is the Reynolds number based on the friction velocity and the radius of the tube, $r_0=d/2$.

2.6 Methods of Solutions to Governing Equation. The governing equation (30) is nonlinear. In this section, we develop analytical and numerical solutions for this equation, which form the main results of the present theory and the basis for subsequent discussions. For convenience, we redefine the additive shear rate function in the following manner:

$$F(\tilde{y})=\frac{1}{\mathrm{Re}_w}\frac{\mu_e}{\mu}\tilde{G}(\tilde{y}) \tag{31}$$

Finally, the differential equation governing the turbulent flow in the core of the boundary layer takes the following dimensionless form:

$$[1-F(\tilde{y})]\kappa^2\tilde{y}^2\left(\frac{d\tilde{u}}{d\tilde{y}}\right)^2=1 \tag{32}$$

Next, we examine four different conditions that lead to different levels of approximated solutions for the differential equation (32).

2.7 In the Absence of Additives, $F(\tilde{y})=0$. In this case, the additive volume fraction is null, the extensional viscosity vanishes, and, consequently, $F(\tilde{y})=0$. Therefore, (32) reduces simply to

$$\kappa^2\tilde{y}^2\left(\frac{d\tilde{u}}{d\tilde{y}}\right)^2=1 \tag{33}$$

with boundary conditions $\tilde{y}=1$, $\tilde{u}=\tilde{u}_{\max}$. The solution of (33) is the well-known Prandtl's logarithmic law [39], given in terms of the wall coordinate $y^+=yu_f/\nu$ by

$$\tilde{u}=\tilde{u}_{\max}+\frac{1}{\kappa}\ln(y^+/r_0^+) \tag{34}$$

where $\tilde{u}_{\max}$ is the maximum dimensionless velocity and $r_0^+=r_0u_f/\nu$.

2.8 Constant Additive Shear Rate Function. Considering $\tilde{G}(\tilde{y})$ as being constant, the differential equation (32) can be still solved analytically. The present theory is proposed to describe the polymer-induced drag reduction as a consequence of the stress anisotropy caused by the stretching and the orientation and reorientation of the additive in a turbulent boundary layer.

Now, the velocity profile of the flow is obtained by applying the boundary conditions: $\tilde{y}=1$ (in the center of the tube), $\tilde{u}=\tilde{u}_{\max}$. Therefore, the following equation holds:

$$\tilde{u}=\tilde{u}_{\max}+\frac{1}{\kappa(1-F)^{1/2}}\ln(\tilde{y}) \tag{35}$$

where $\tilde{u}_{\max}$ is the maximum dimensionless velocity of the average velocity profile and $\kappa=2/5$ is the universal constant for fully turbulent flow in smooth pipes. From Eq. (31), we argue that, in general, F is a small parameter for turbulent flows. Therefore, using a binomial expansion at $\mathcal{O}(F)$, the Eq. (35) could be rewritten after some algebraic manipulation in the following form:

$$\tilde{u}=\tilde{u}_{\max}-\frac{1}{\kappa}\ln(r_0^+)-\frac{1}{2\kappa}F\ln(r_0^+)+\frac{1}{\kappa}\left(1+\frac{1}{2}F\right)\ln(y^+) \tag{36}$$

where $r_0^+=r_0u_f/\nu$ it is the dimensionless radius of the tube, $y^+=yu_f/\nu$ is the dimensionless radial distance of tube wall and ν is kinematics viscosity of the fluid. Also, it is well known from experimental data (e.g., Pao [39]) that

$$\tilde{u}_{\max}-\frac{1}{\kappa}\ln(r_0^+)=5.5 \tag{37}$$

for all turbulent flows in smooth pipes.

In the sequence, an expression for the friction factor of the flow is determined. By definition, the average velocity U in a pipe of circular section is calculated as follows:

$$U=\frac{1}{\pi r_0^2}\int_0^{r_0}\bar{u}2\pi(r_0-y)dy \tag{38}$$

where the change of variables: $r=r_0-y$ and $dr=-dy$ becomes more appropriated. Substituting Eq. (36) into (38) and integrating, one obtains

$$\frac{U}{(\tau_w/\rho)^{1/2}}=\frac{11}{2}-\frac{3}{2\kappa}+\frac{1}{\kappa}\ln r_0^+ +\frac{3}{4\kappa}F \tag{39}$$

From the definition of the friction factor, $f=\tau_w/\frac{1}{2}\rho U^2$, for fully developed turbulent flow in pipes, we find

$$\frac{1}{f^{1/2}}=\frac{1}{2\sqrt{2}}\frac{U}{(\tau_w/\rho)^{1/2}} \tag{40}$$

It should be important to note that Re_w may be written in terms of the most common Reynolds number based on the average velocity U, $\mathrm{Re}=\rho U r_0/\mu$. Using the Eq. (40), we immediately find that $\mathrm{Re}_w\sim\mathrm{Re}\sqrt{f}$.

Now, substituting Eq. (39) into (40), an expression for friction factor in terms of the additive parameters (volume fraction and aspect ratio) is obtained

$$\frac{1}{f^{1/2}}=\frac{35\sqrt{2}}{80}+\frac{\sqrt{2}}{4\kappa}\ln(r_0^+)+\frac{\sqrt{2}}{4\kappa}\left[C\frac{1}{\mathrm{Re}_w}\left(\frac{\ell}{b}\right)^2\frac{\phi}{\ln(1/\phi)}\times\left(1-\frac{\ln[\ln(1/\phi)]}{\ln(1/\phi)}+\frac{E(\phi)}{\ln(1/\phi)}\right)\right] \tag{41}$$

Here, C is a calibration constant. We have verified that $C=2\times10^{-4}$ in Eq. (41) is the best fit of the experimental data.

2.9 Logarithmic Approximation for the Additive Shear Rate Function. By nothing more sophisticated than scaling analysis, assuming $\tilde{u}\sim\ln(\tilde{y})$, we immediately show that $\tilde{G}(\tilde{y})\sim\tilde{y}^{-1}[\ln(\tilde{y})]^{-2}$. Based on this scaling, the differential equation (32) can be expressed in the following form:

$$\left(1-\frac{\mu_e}{\mu}\frac{1}{\mathrm{Re}_w}\frac{C}{\tilde{y}[\ln(\tilde{y})]^2}\right)\kappa^2\tilde{y}^2\left(\frac{d\tilde{u}}{d\tilde{y}}\right)^2=1 \tag{42}$$

where C is the same experimental constant given above. Defining the new parameter $C_1=C\mu_e\kappa^2/(\mathrm{Re}\,\mu)$, Eq. (42) may be rewritten in a more convenient form as

$$\frac{d\tilde{u}}{d\tilde{y}}=\frac{1}{\kappa\tilde{y}\sqrt{C_1}}\left(1+\frac{\tilde{y}(\ln\tilde{y})^2}{C_1}\right)^{-1/2} \tag{43}$$

For the case in which $|\tilde{y}(\ln\tilde{y})^2/C_1|<1$, it is valid to represent the right-hand side of Eq. (43) in terms of a binomial series, and after integrating the resulting differential equation, we found

$$\tilde{u}=\frac{1}{\kappa\sqrt{C_1}}\left[\tilde{y}\left(\frac{9}{32C_1^2}\tilde{y}-\frac{1}{C_1}\right)+\ln\tilde{y}\left(1+\frac{\tilde{y}}{C_1}-\frac{9}{16C_1^2}\tilde{y}^2-\frac{\tilde{y}}{2C_1}\ln\tilde{y}+\frac{9}{16C_1^2}\tilde{y}^2\ln\tilde{y}-\frac{3}{8C_1^2}\tilde{y}^2(\ln\tilde{y})^2+\frac{3}{16C_1^2}\tilde{y}^2(\ln\tilde{y})^3\right)\right]+C_2 \tag{44}$$

where C_2 is integration constant. Now, applying the boundary condition at the center of the pipe, i.e., $\tilde{y}=1$, $\tilde{u}=\tilde{u}_{\max}$, we obtain

$$C_2 = \tilde{u}_{\max} - \left(\frac{-1/C_1 + 9/32C_1^2}{\kappa\sqrt{C_1}} \right) \tag{45}$$

Using Eqs. (38) and (40), the velocity profile given in (44) leads to the following new expression for the friction factor:

$$\frac{1}{\sqrt{f}} = \frac{1}{2\sqrt{2}} \left(\frac{-1805 + 5888C_1 - 41472C_1^2 + 27648\tilde{u}_{\max}C_1^2\kappa\sqrt{C_1}}{27648C_1^2\kappa\sqrt{C_1}} \right) \tag{46}$$

2.10 Numerical Solution. We have also solved Eq. (32) by using an iterative numerical integration. The updating scheme is started when a first estimative of $\tilde{G}(\tilde{y})$ is given in the interval of integration. At the end of each iteration, the function $\tilde{G}(\tilde{y})$ is computed by using the solution for the intermediate velocity $\tilde{u}$ obtained in the previous step. The inputs of the numerical scheme are the volume fraction ϕ of the additive and the aspect ratio ℓ/b so that the dimensionless μ_e/μ can be calculated. In addition, the maximum velocity $\tilde{u}_{\max}$, its position $\tilde{y}_{\max}$, and the low boundary $\tilde{y}_{\min} > 0$ are specified. The problem is converted into an initial value problem after the appropriate change of variable $y^* = \tilde{y}_{\max} - \tilde{y}$, so that $\tilde{u} = \tilde{u}_{\max}$ at $y^* = 0$. Here, $\mathbf{u} = (u_1, u_2, \ldots, u_{N^*})$ denotes the solution vector of the axial velocity for the N^* discrete nodes along the transversal direction. The numerical algorithm is presented next.

First, the additive shear rate function is made null, i.e., $\tilde{G}(\tilde{y}) = 0$ at all points of the one-dimensional domain of integration. For this case, Eq. (32) reduces to the classical Prandtl mixing theory. The velocity profile is well known and may be calculated analytically. Let this solution be $\mathbf{u}_0$.

At the second step, $\mathbf{u}_0$ is used to advance the function $\tilde{G}(\tilde{y})$ to an intermediate step, and the numerical integration of (32) is performed to give the new solution vector $\mathbf{u}_1$ at this step of the updating scheme. The numerical integration was performed using a fourth-order Runge-Kutta scheme. The length step Δh for the numerical integration was $(1/2)\delta y$, with δy being the grid length $(\tilde{y}_{\max} - \tilde{y}_{\min})/N_I$, and $N_I = 10^3$ is the number of intervals of the one-dimensional domain. It gives a typical $\Delta h = 10^{-3}$. The errors in the numerical integration were $< 10^{-3}$.

At the end of an updating step, the relative vector of residue $\mathbf{r}^e$ with components $r_i^e = (u_i^{n+1} - u_i^n)/u^n$, where u_i^{n+1} denotes the value of velocity at the current step, is evaluated. The converge criterion of the iterative scheme is based on the maximum absolute value of the $\mathbf{r}^e$ components, i.e., the updating process is interrupted if $\max_{1 \le i \le N^*} |r_i^e| < \epsilon$, where ϵ is a small parameter that controls the convergence, typically, 10^{-3}. If the convergence conditions are not satisfied at the current iteration, then $\tilde{G}(\tilde{y})$ is corrected by considering the current solution u^{n+1} and Eq. (32) is numerically integrated for giving the new intermediate solution vector for the explicit updating scheme. The procedure is repeated until the convergence condition is satisfied.

3 Description of Experiments

Experiments for investigating polymer-induced drag reduction were conducted as well. A schematic of the experimental setup used is depicted in Fig. 1. Flow visualization was carried out in an acrylic pipe of 2000 mm length and 50 mm dia (test section 1). The top section 2 was a horizontal pipe of 2250 mm length and 32 mm dia. In operation, this section was used to measure the friction factor of the turbulent flow. A centrifugal pump with 2300 W potency of open rotor with diameter of 145 mm was used to circulate the mixture of water and polymer solution in a closed loop from a 1000ℓ tank through the test section. The temperature of the circulating solution was measured inside the holding tank. Flow-rate measurements were carried out by a digital balance

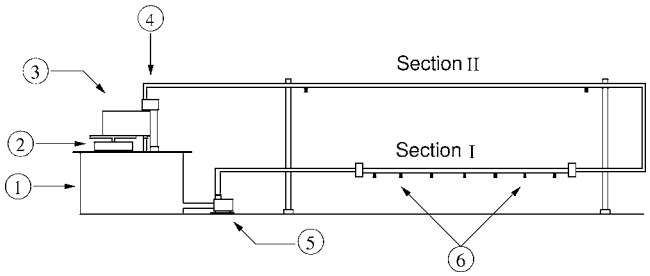

Fig. 1 Schematic experimental setup: (1) main reservoir, (2) digital balance, (3) secondary reservoir, (4) switch flow, (5) centrifuge pump, and (6) pressure gages

with uncertainty ±50 g and a digital chronometer with uncertainty ±1/100 s. The flow rate in the system was controlled by a frequency invertor with frequency varying from 0 Hz up 60 Hz. The maximum flow rate produced by the pump was 15 m^3/hr. The pressure measurements in the test sections were carried out with a water column (WC) multimanometer with ±2.5 mm-WC uncertainly.

The polymer used in our experiments was Art Floc/SCP 1530 (Art-Aratrop Industries), which is an aqueous polymer solution with a volumetric concentration of 0.34 of an anionic polyacrylamide (PAMA) of a high molecular weight (i.e., $\approx 10^6$ g/mol). Figure 2 illustrates a sketch of the macromolecule structure. In fact, the solution at this high concentration was the stock solution that was diluted down to desire the concentrations used in the drag reduction experiments. The tested polymer solutions (PAMA-water) were achieved by preparation of a primary solution with the volume fraction varying from 0.1% to 0.3%. Before operation, the solution was mixed gently for ~1 hr. At the end of this procedure, the solution obtained was visibly clear and did not contain any detectable inhomogeneities. Strong agitations were always avoided so that the polymeric chains did not degrade and the polymer was added completely dissolved in the base water. To proceed with the experimental runs, the primary solution was first mixed in the tank shown in the schematic of the experimental setup (see Fig. 3) in an amount requested to reach the desired parts per million of concentration for the test PAMA-water solution (ranging from 0 ppm to 450 ppm).

The experimental runs were initially carried out with pure water, in order to calibrate the experimental setup relative to the friction factor of this flow. The calibration of the system was verified by comparing our data to other available experimental results in the literature for smooth pipes. The system achieved the steady state in ~10 min. For each experimental run, the differential pressure drops and flow rates were measured as describe be-

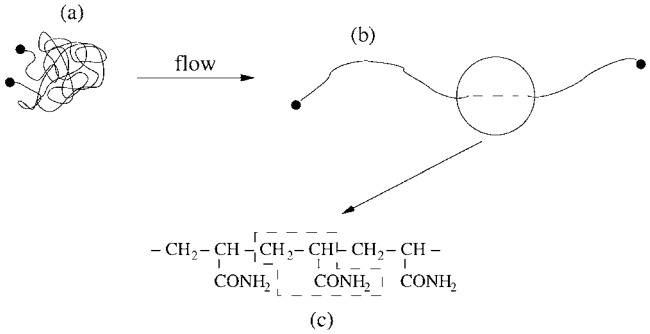

Fig. 2 Schematic representation of a polyacrylamide macromolecule: (*a*) macromolecule in dynamic equilibrium, (*b*) macromolecule stretch by the flow, and (*c*) structural unity of polyacrylamide

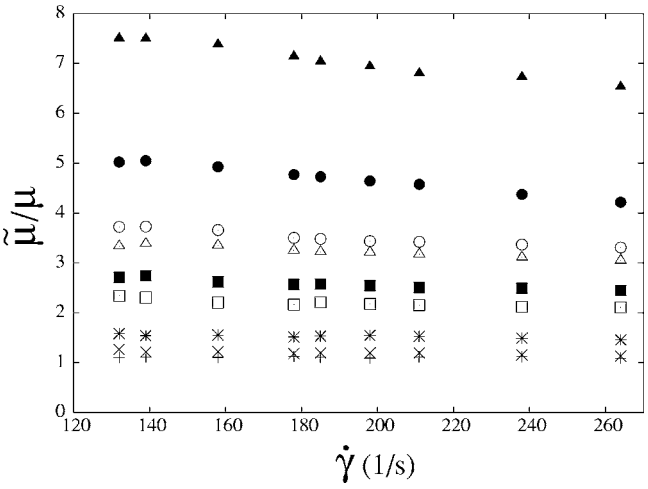

Fig. 3 Dimensionless effective shear viscosity of the solution as a function of shear rate for several values of particle volume fraction ϕ. The points represent +, $\phi=0$; ×, $\phi=2\times10^{-5}$; ∗, $\phi=4\times10^{-5}$; □, $\phi=8\times10^{-5}$; ■, $\phi=1.2\times10^{-4}$; △, $\phi=2\times10^{-4}$; ○, $\phi=3\times10^{-4}$; ●, $\phi=3.5\times10^{-4}$; and ▲, $\phi=4.5\times10^{-4}$

fore. Once the data are collected, Darcy-Weisback's equation is used in order to quantify the friction factor of the flow, namely,

$$f=\frac{2\Delta Pd}{\rho U^2 L} \tag{47}$$

where L and d are, respectively, the length and the diameter of the test section, ΔP is the pressure difference among two pressure gages, ρ is the specific mass of the water, and U is the average velocity of the turbulent flow. The same experimental procedure was used to evaluate the friction factor corresponding to different polymer concentrations. The experiments were carried out for eight concentrations: 20 ppm, 40 ppm, 80 ppm, 120 ppm, 200 ppm, 300 ppm, 350 ppm, and 450 ppm, and the drag reduction quantified by the following formula:

$$\mathrm{DRF}(\%)=\left(1-\frac{f}{f_a}\right)100 \tag{48}$$

where DRF is the drag reduction factor, f is the friction factor of the solution (PAMA and water), and f_a is the friction factor of the pure water flow.

3.1 Velocity Profile Measurements. The mean velocity profile measurements were carried out by a laser Doppler velocimetry (LDV) system. The system uses a pair of laser beams with a wavelength of 683 nm to measure the fluid velocity in one direction. This pair forms a so-called measure volume at the position where the two beams intersect. The light that is scattered by a particle traveling through the measurement volume is collected in the backscattered direction. The optics to focus the laser beams into the pipe and also to receive the scattered light is built into one measuring probe with a focusing front lens with focal length of 250 mm. That probe also contained a diode laser that produces laser beams with 50 mW of potency. The dimension of the measurement volume was estimated to be 2 mm, 190 μm, and 85 μm in the spanwise, streamwise, and normal directions, respectively. The data acquisition by the probe is sending for a processor that is connected to a microcomputer through a data acquisition board.

The curvature of the pipe wall leads to problems in measuring close to the wall with LDV due to the refraction of the laser beams by the curved pipe wall and the lens effect that causes a scattering of the incident laser beams. This difficulty arises because of the differences in refractive index of the test fluid (i.e., water) and the material of the pipe (i.e., acrylic). This problem was softened with the construction of a rectangular box filled with water that involves the cylindrical section. Hence, the laser beams from the probe attain in a plane section, reducing the reflection and refraction phenomena in surface curves, sensibly improving the quality of the measurements. In all experiments, the fluid was seeded with iriodin particles. This product contains particles with diameters in the range of 0.1–1.0 μm, which has produced a good light scattering, consequently a high data rates. The mean velocity profile measurements were performed for pure water and for a PAMA-water solution of 120 ppm. The LDV experiments were carried out for equal friction velocity u_f. Time series of 3000 samples were acquired every 0.5 mm on the region between $y^+=50$ and the center of the tube.

3.2 Rheology of Polymer Solution. Measurements of the effective shear viscosity $\tilde{\mu}$ as a function of the concentration ϕ and the shear rate $\dot{\gamma}$ of the PAMA-water solutions were carried out in a typical Couette device of major radius $R=19$ mm and gap width $W=0.75$ mm. The experiment consisted of a laminar flow between two concentric cylinders in a rotating relative motion. The internal cylinder rotates while the external cylinder stays static. The stability of the flow during the measurements was guaranteed because $W\ll R$. The shear stress in the gap of polymer solution between the cylinders was measured following the standard Couette rheometry described by Barnes et al. [40]. We consider viscous polymeric solutions with effective shear viscosity $\tilde{\mu}$ as a function of the concentration ϕ of the polymer macromolecule and shear rate, $\dot{\gamma}$. The stress tensor is given by $\boldsymbol{\tau}=2\tilde{\mu}(\phi,\dot{\gamma})\mathbf{D}$, where $\mathbf{D}$ is the rate-of-strain tensor and $\dot{\gamma}=\sqrt{2tr(\mathbf{D}:\mathbf{D})}$.

The effective viscosity measurements were carried out with a model programmable DV-II+viscometer. The viscometer allows the angular velocity of the internal cylinder to vary producing the desired indirect measures, such as the viscosity, the shear rate, and the shear stress. The data acquisition of the rheology experiment was made through a microcomputer, with the viscometer connected to its serial port. The experimental procedure consisted of a rheological characterization of the shear viscosity for all sample solutions tested in the present drag reduction experiments. A sample of 8 ml at each experimental run was analyzed. The viscosity was determined for nine different values of angular velocity of the internal cylinder. Ten measurements were carried for each quantity. During the experiments, temperature was kept $\sim25\,^{\circ}\mathrm{C}$ in order to have viscosity measurements little affected by temperature variations.

Results of the polymer solution (PAMA-water) rheology are presented next. The shear viscosity dependence of the polymer solution on the shear rate is shown in Fig. 3. It is seen that shear viscosity is approximately constant for shear rates, $\dot{\gamma}$, beyond $180\ \mathrm{s}^{-1}$ for all concentration investigated. The viscosity of PAMA-water solution is observed to be about three times larger than solvent viscosity for concentrations of 200 ppm and 300 ppm of PAMA. This, of course, contributes to an increase of the friction factor of the flow in contrast with the drag reduction promoting by enhanced of the extensional viscosity due to the macromolecule stretching. In addition, Fig. 3 shows that one of the consequences of the addition of polyacrylamide (PAMA) in water is the well-known result of a shear rate dependence viscosity in simple shear flow. For larger concentrations (i.e., 350 ppm and 450 ppm), a shear thinning behavior is observed, i.e., the shear viscosity of the PAMA solution decreases as a function of the shear rate. We argue that this effect may be important in order to obtain proper wall scales and capture the contribution of the polymer stress at the laminar sublayer.

In (4), we show that for a concentration up to 120 ppm of PAMA the hydrodynamic interactions between the macromolecules can be neglected, resulting in a linear behavior of the viscosity with the additive volume fraction. In these regimes, the contribution associated with the shear viscosity of the polymer solution is treated as a Newtonian equivalent fluid of viscosity $\tilde{\mu}$,

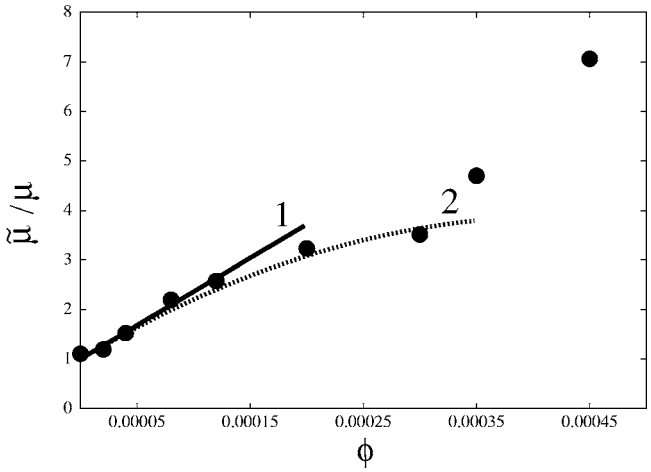

Fig. 4 Dimensionless effective shear viscosity as a function of the additive volume fraction. The solid line (1) fits the experimental data with the Einstein theory [30], where $\tilde{\mu}=\mu(1+1.4\times10^4\phi)$; The dashed line (2) refers to Batchelor and Green's theory [41], $\tilde{\mu}=\mu(1+1.4\times10^4\phi-1.6\times10^7\phi^2)$.

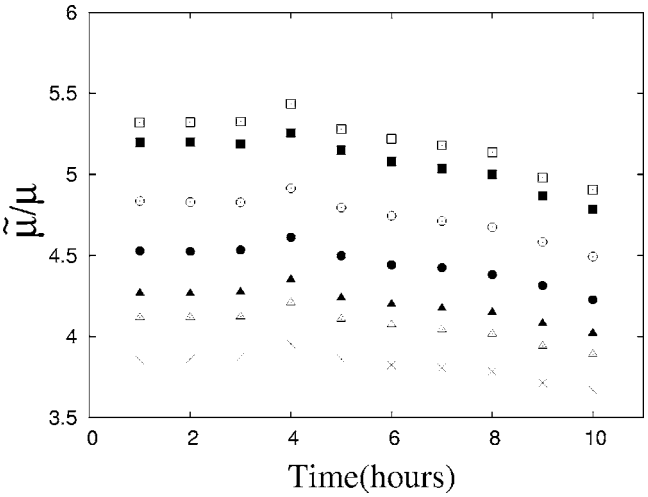

Fig. 5 Dimensionless effective shear viscosity as a function of the experimentation time: □, $\dot{\gamma}=132\ s^{-1}$; ■, $\dot{\gamma}=139\ s^{-1}$; ○, $\dot{\gamma}=158\ s^{-1}$; ●, $\dot{\gamma}=178\ s^{-1}$; ▲: $\dot{\gamma}=198\ s^{-1}$; △: $\dot{\gamma}=211\ s^{-1}$; ×: $\dot{\gamma}=264\ s^{-1}$

with energy dissipation larger than the solvent. At low concentrations each macromolecule behaves as a single particle, with no hydrodynamic disturbance that influences the motion of its neighborhood. This behavior can be predicted by the formula of the effective shear viscosity proposed by Einstein [30], i.e., $\tilde{\mu}=\mu(1+A\phi)$, being $A=1.4\times10^4$ for our experiments. If the PAMA volume fraction increases, a linear regime is no longer observed. For volume fractions of PAMA varying from 120 ppm to 300 ppm, the effective shear viscosity is described by a second order theory given by [41], namely, $\tilde{\mu}=\mu(1+A\phi+B\phi^2)$, being $A=1.4\times10^4$ and $B=-1.6\times10^8$. The values of the constants A and B were determined from the experimental data of the present work for denoting the additive volume fractions as considered in the plots of the Figs. 3 and 4. As a physical interpretation, the nonlinear behavior $O(\phi^2)$ can be attributed to the hydrodynamic interactions among the additives that cause a significant change in the rheology of the polymer solution. These interactions lead to particle reorientation, modifying the configuration of flow anisotropy. This effect reaches in the limit ($\phi\simeq350$ ppm) when the friction factor begins to increase in contrast with the decrease promoted by the mechanism of drag reduction. In this regime, the shear viscosity should no longer be treated as a simple equivalent Newtonian fluid with effective viscosity, $\tilde{\mu}=\mu(\phi)$, because the shear thinning effect and the reorientation of the macromolecule induced by the hydrodynamic interaction between them becomes important. Our observations suggest that for a concentration of $\sim$400 ppm, $\tilde{\mu}/\mu\sim5$ (at low shear rates) the viscous dissipation may be not a negligible contribution. Actually, it begins to dominate the effect of the extensionality of the macromolecules, producing an increase of the friction factor. In addition, at this volume fraction it is symptomatic that particle reorientation induced by the flow disturbance due to hydrodynamic interaction between the particles attenuates the contribution of the extensional viscosity since the particles tend to deviate from the fully aligned anisotropic orientation.

3.3 Macromolecule Degradation. One of the problems involved in the use of polymers is their degradation in strong turbulent flows. This rupture in the polymer chain might be due to chemical reactions, radiation, heat, bacteria, or mechanical forces on the thread [42]. In this work, the breakup of the polymer chains due to the flow was evaluated by the analysis of a 350 ppm solution submitted to 10 hr of a recirculatory pipe flow. When the steady state was achieved, ten samples of the solution were collected with 1 hr interval between each other. In order to quantify the effect of the polymeric chain degradation, shear viscosity measurements of the polymeric solution were carried out for all the samples. The behavior of the effective shear viscosity as a function of time for different shear rates is presented in Fig. 5. It is seen that the shear viscosity is reduced up to 7% after 10 hr of flow (a period of time 10^6 longer than the average relaxation time of the macromolecules), indicating that in this time scale a degradation of the polymer chains was not significant for producing appreciable changes on the rheology of the solution. This points out that the stretched polymer chain in our experiments can retain its conformation without an appreciable degradation and therefore may be assumed to behave closely to long rigid fibers, such as assumed in our constitutive model presented in Sec. 2.3. This part of the experiments has also pointed out that the polyacrylamide is very resistant to degradation in turbulent flows.

4 Results and Discussions

In Sec. 3, we developed a modified Prandtl equation for turbulent channel flow that predict drag reduction of a turbulent boundary layer in the presence of anisotropic additives. In what follows, we will present a comparison between the predictions and the experimental results of drag reduction supplied and a statistical analysis of the flow in the presence of the additives.

Figure 6 shows some experimental results of $f^{-1/2}$ as a function of $\mathrm{Re}\,f^{1/2}\sim\mathrm{Re}_w$ (in a logarithmic scale) for several volume fractions of polyacrylamide (PAMA). The error bars are also shown according to the uncertainties analysis described in [44]. It is seen from this figure that the variations of $f^{-1/2}$ with $\log(\mathrm{Re}\,f^{1/2})$ are straight lines (within the error bars) for all examined volume fraction. The experimental data obtained from a preliminary test with pure water are fitted with good accuracy by the classical logarithmic law of Prandtl-Kárman for smooth pipes. This is an indicative that the experimental setup was calibrated properly. The plots also show a slope increment of the friction factor curves with the concentration below 350 ppm. A drag reduction of 22% can be observed even for the low concentration of 80 ppm. The maximum value of drag reduction seen in our experiments was 65% for a concentration of 350 ppm. For smaller values of Reynolds numbers, weaker drag reductions are observed because the macromolecule stretching was not sufficient to produce appreciable values of the extensional viscosity and flow anisotropy. In other words, we can say that, in the regime of weaker flows examined, the relaxation time of the macromolecules was comparable to the

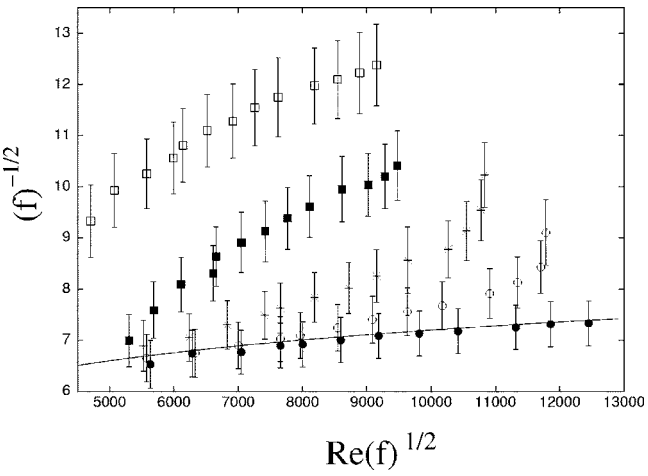

Fig. 6 Friction factor for dilute aqueous solutions of PAMA in the turbulent regime. Note that $\mathrm{Re}f^{1/2} \sim \mathrm{Re}_w$. The solid line represents the Kárman-Prandtl logarithmic law for smooth pipes, and the symbols represent: ●, $\phi=0$; ○, $\phi=8\times10^{-5}$; ∗, $\phi=2\times10^{-4}$; □, $\phi=3.5\times10^{-4}$; ■, $\phi=4.5\times10^{-4}$.

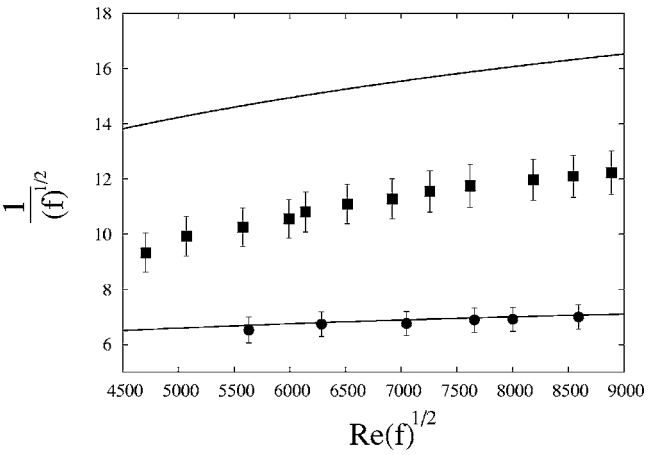

Fig. 7 The curve of maximum drag reduction for 350 ppm. The solid line represents the Kárman-Prandtl logarithmic law for smooth pipes; the symbols ● denotes the friction factor measurements for pure water, $\phi=0$ ppm; the symbols ■ denote the maximum friction factor measured by the present work and the upper dotted line corresponds to the asymptotic Virks [43] maximum drag reduction given by $f^{1/2}=19\log_{10}(\mathrm{Re}f^{1/2})-32.4$

typical time scale of the flow and the extensional contribution of the macromolecules is a small contribution for very dilute polymer solution. The results have also indicated an increase in the friction factor of the flow for concentration of PAMA beyond 350 ppm as a consequence of the rheological changes of the polymer solution. Since the solution is no longer too dilute, the hydrodynamic interactions between the additives become important. We speculate that there is a critical volume fraction depending on the nature of each polymer for which the friction factor reverses its behavior. This occurs as a consequence of the viscous dissipation and the reorientation of the particles produced by particle interactions, both mechanics increasing with the volume fraction of the additives.

As mentioned before, when the hydrodynamic interaction between the particles becomes important, the mechanism of drag reductions cannot be solely attributed to the anisotropy introduced by the long particles. Actually, the tendency of the particles deviate from the fully aligned anisotropic orientation could be interpreted as a factor of attenuation of drag reduction, and it acts as a kind of dissipative effect. In the present work, the concentration at which the chains touch one another is typically 400 ppm. Under this condition, the drag reduction is substantially attenuated. As a complementary result of the plots depicted in Fig. 6, we show in Fig. 7 a comparison of the experimental plot of $f^{-1/2}$ as a function of $\mathrm{Re}\,f^{1/2}(=2\sqrt{2}\,\mathrm{Re}_w)$, corresponding to the maximum observed drag reduction curve for 350 ppm, with the lower and upper bounding drag reduction curves given by the Prandtl-von Kárman curve for Newtonian fluids in a smooth pipe and Virk's [43] maximum drag reduction asymptote $f^{-1/2}=19\log(\mathrm{Re}\,f^{1/2})-32.4$, respectively. As expected, our experimental results of the friction factor for 350 ppm of PAMA have values between these two well-known limits.

In addition, Table 1 presents the values of the experimental friction factor and the related drag reduction $drf(\%)$ for additive concentrations of 0 ppm, 20 ppm, 40 ppm, 80 ppm, 120 ppm, 200 ppm, 300 ppm, and 350 ppm. The Reynolds number based on the average velocity U was $\mathrm{Re}=10^5$. The results show conclusively that the maximum reduction in the friction factor was 65% for the concentration 350 ppm. We see that even the small amount of 40 ppm of PAMA produces a significant drag reduction of 15%. This indicates that just few parts per million of additives are able to promote drag reduction when the macromolecule is sufficiently stretched by the flow.

In Fig. 8, we present a comparison between the experimental data and the semi-theoretical fits for the friction factor as a function of the macromolecules concentration. It is seen that for the calibration constant $C=2\times10^{-4}$ and an aspect ratio equal to 10^7, the calculations performed by using the two semi-theoretical fits given, respectively, by (41) and (46) and the numerical scheme are in excellent agreement with the experiments of drag reduction (within the error bars of the experimental data) for all values of polymer volume fraction investigated.

Table 2 presents more details of the comparison between $f^{-1/2}$ given by the experiments and the semitheoretical predictions adopted here. The calculations based on an additive shear rate function $\tilde{G}$ constant gives a relative error of 2%, showing that even when using this lower-order approximation accurate results might be obtained from the semi-empirical fit given in (41). However, the calculations of the friction factor using the logarithm dependence of $\tilde{G}$, Eq. (46), gives an error of $<1\%$, whereas the iterative scheme gives a still smaller error of 0.4%, since in this procedure the function $\tilde{G}$ is always updated for its correct values. Very good agreement is observed, especially for the calculations predicted by the numerical scheme. It is interesting to note, however, that for the dilute range of concentrations studied our semi-empirical formulas does fit with good accuracy the amounts of drag reduction observed from the experiments.

Figure 9 depicts the nondimensional mean velocity profile as a function of wall distance for a $\mathrm{Re}_w=3300$. The error bars are not omitted in these plots. The LDV measurements for pure water

Table 1 Experimental results of the friction factor and the corresponding drag reduction for different concentration of PAMA and a Reynolds number, $\mathrm{Re}=10^5$.

Concentration (ppm)	Friction factor $\times10^{-2}$	DRF (%)
0	1.83	—
20	1.69	7.5
40	1.56	14.5
80	1.42	22.5
120	1.16	37.0
200	0.96	47.5
300	0.66	64.0
350	0.65	65.0

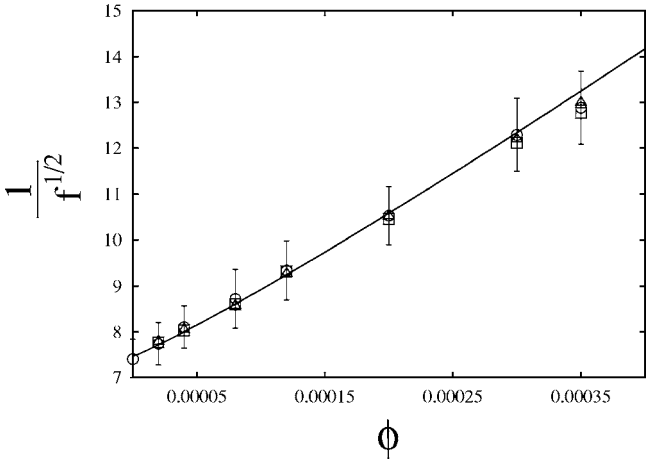

Fig. 8 The inverse of the square root of the friction factor as a function of the polymer volume fraction. Comparison between experimental data and the semi-theoretical models proposed in the present work for Re=10^5 and $\ell/b=10^7$: ○, experimental data; solid line: constant shear rate additive function; □: logarithm additive function; △, iterative model of the additive function (numerical integration). The best-fit constant of the semi-empirical models was $C=2\times10^{-4}$.

(i.e., $\phi=0$) are fitted by Pradtl's universal logarithmic law, whereas the experimental mean velocity profile for the PAMA solution with volumetric concentration of 120 ppm are fitted by

Table 2 Comparison between the adopted models in this work with the experimental data of $1/\sqrt{f}$.

ϕ (ppm)	Experimental	Constant G model	Logarithmic G model	Numerical scheme
20	7.74	7.97	7.77	7.79
40	8.10	8.25	8.03	8.05
80	8.72	8.89	8.65	8.69
120	9.34	9.53	9.27	9.32
200	10.53	10.73	10.46	10.52
300	12.28	12.52	12.12	12.20
350	12.88	13.14	12.77	12.94

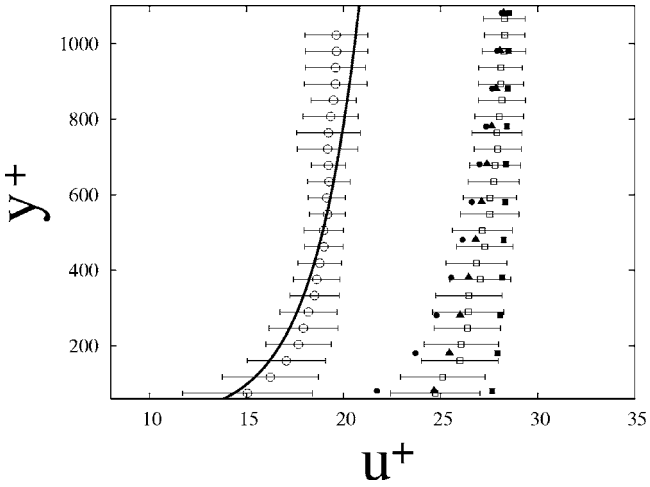

Fig. 9 The mean flow velocity profile as a function of wall distance: ○, experimental data for pure water ($\phi=0$); solid line denotes the Prandtl's universal logarithmic law; ■, constant shear rate additive function; ●, logarithmic shear rate additive function; ▲, iterative shear rate additive function (numerical solution); □, experimental data for $\phi=120$ ppm

the semi-theoretical approaches developed in this work. Within the error bars of experimental data, and using the same constant of calibration again (i.e., $C=2\times10^{-4}$), both expressions for the friction factor given by Eqs. (41) and (46) and the calculation of the friction factor performed by the numerical scheme are in good agreement with experiments.

Figures 10 and 11 show the plots of nondimensional velocity fluctuations obtained from the LDV measurements for pure water and for a polymer solution of 120 ppm, respectively, for a $\mathrm{Re}_w=2700$ based on the friction velocity of the flow. The error bars are shown for each point, and the time average is represented by the full line. In both cases, the signals were acquired at the same turbulent boundary layer position; $y^+\approx50$. From these plots, we have the relative axial and radial fluctuations equal to $\overline{(u'^2)}_p^{1/2}/\overline{(u'^2)}_w^{1/2}\cong1.4$, and $\overline{(v'^2)}_p^{1/2}/\overline{(v'^2)}_w^{1/2}\cong0.5$, respectively, where subscripts w and p indicate the flow with pure water and polymer solution, respectively. It is seen that when the polymer macromolecules are added to the flow, a small increment of the velocity fluctuation in the axial direction is observed, whereas the velocity fluctuation in the radial direction is attenuated of a factor 2. This is equivalent to saying that there exists an inhibition of the transport of momentum by the cross-stream velocity fluctuations relative to their Newtonian values due to the stress anisotropy in the flow induced by the stretching of the macromolecules, while along the stream, the fluctuations are actually enhanced. For a polymer of high molecular weight such as the polyacrylamide tested here, the relaxation time is long enough because inhibition of stretching reduces the gathering together slow-speed wall fluid into a jet away from the wall, which is transported by turbulence and, thus, is drag. The action of the polymers is then primarily to modify turbulent behavior near the walls. There, wall eddies are formed that transport momentum in the fluid interior, which exerts drag on the flow [45]. The macromolecule's high resistance to extension makes these eddies wider and less frequent and, consequently, less efficient in transporting moment away from the walls.

It is seen in Fig. 12 that the introduction of a few parts per million of a PAMA solution in the flow not only reduces the intensity of fluctuations but also reduces the intensity of the wall eddies and increases their average size. The thickness of the buffer layer is defined as the value of y^* at which the extrapolated viscous and the inertial sublayer profiles intersect. For pure water, the thickness of the buffer layer is found to be $y_1^*\cong11$, whereas a PAMA solution of 120 ppm gives $y_2^*\cong24$ (i.e., two times larger than y_1^*). It suggests that, in the presence of the macromolecule, the average size of the turbulent eddies near the wall increases as a consequence of the interaction of them with the polymer in the buffer and log layers. This results in an increase of the buffer layer thickness. We believe that the polymers become stretched by the turbulence when there is drag reduction; to find out where the near-wall stretched polymer interacts with the turbulent eddies should be an important future research subject. To truly measure polymer extension, one needs to use light scattering, which takes too long in the rapidly changing flow. Birefringence only measures chain alignment, which may be sufficient. But both optical techniques require large quantities of very clean polymer solution, which is expensive for a sample with a narrow molecular-weight distribution. Moreover, the good drag reduction polymers have a low optical contrast because, of course, they are like water, chemically.

Figures 13 and 14 give the experimental plots of the normalized autocorrelation function for the axial $(R_{\parallel}(\tau)=\langle u'(t)u'(t+\tau)\rangle/\langle u'(t)^2\rangle)$ and radial $(R_{\perp}(\tau)=\langle v'(t)v'(t+\tau)\rangle/\langle v'(t)^2\rangle)$ velocity fluctuations components, respectively, at $y^+=50$ for pure water. Figures 15 and 16 present the corresponding plots for the solution of 120 ppm of PAMA. The error bars are also shown in these plots. The inserts in log-log scale show the details of the exponential decay of these functions for both directions. The longitudinal

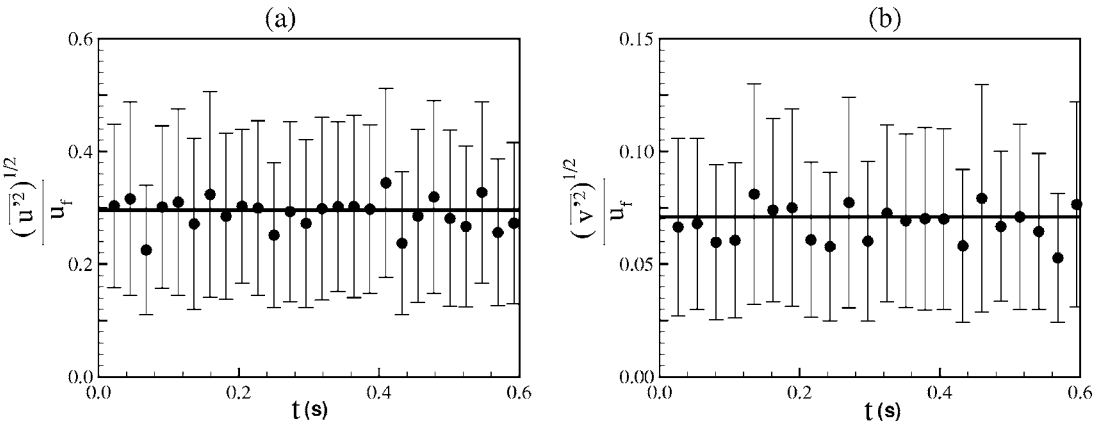

Fig. 10 Nondimensional velocity fluctuations for pure water: (*a*) axial fluctuations and (*b*) radial fluctuations

correlation times for pure water and for the solution of 120 ppm of PAMA are $4\times10^{-3}d/u_f$ and $6\times10^{-3}d/u_f$, respectively. The result changes completely for the radial direction when the corresponding correlations times are $5\times10^{-3}d/u_f$ for pure water and $1.2\times10^{-2}d/u_f$ for the polymer solution. In accordance with the experimental data, Figs. 17 and 18 show that while adding 120 ppm of PAMA to the flow produces an increase of 35% of the axial correlation time; this increase is even more pronounced (140%) for the radial direction. This result indicates changes in the structure of the turbulence scales with a frequency of the same order as the relaxation rate of the macromolecules. We suspect that the increase of the turbulent memory in the presence of additives is a direct consequence of the macromolecule-turbulent scale interactions. These interactions certainly involve transference of elastic energy from the macromolecules to the intermediate scales of the turbulence in the buffer and log layers. It is important to note that the presence of 120 ppm of PAMA in the flow introduces an increase of 80% of the correlation time anisotropy, while the anisotropy for the flow of pure water was 1.2, this anisotropy changes to 2.3 in the flow with 120 ppm of polymer. In addition, Fig. 17 depicts a comparison between the transversal diffusivity as a function of time made nondimensionalized by the friction velocity u_f and the pipe diameter d. This quantity is associated with the transport of momentum by the transversal turbulent velocity fluctuations for the flow of pure water and the flow with 120 ppm of PAMA. The diffusivity is evaluated by $\Psi_\perp(\tau)=\langle v'^2\rangle\int_0^T R_\perp d\tau$. A decrease of ~140% of the diffusion coefficient is seen in the presence of the polymer. Accounting for the effect of the additive in the flow, this leads to less diffusive velocity fluctuations giving a drag reduction of ~40% in the flow of 120 ppm of PAMA.

Finally, the dimensionless power spectra of the axial and radial velocity fluctuations have been computed at $y^+=50$ for the LDV measurements. The spectra are plotted as the logarithm of the dimensionless power as a function of the logarithm of the dimensionless frequency. The spectra were calculated by using a typical algorithm of rapid Fourier transform of the velocity fluctuation autocorrelation function [46]. For each frequency examined, the average values of the power were evaluated over 100 temporal series.

Power spectra of the axial velocity fluctuations at $y^+=50$ are given in Fig. 18 for the Newtonian case (pure water) and for 120 ppm of PAMA-water solution. A shift of the energy is seen in the presence of macromolecules in comparison to the pure water case. This means that the total energy associated with the axial fluctuations is increased when macromolecules are added to the flow. For both cases, the spectra decay toward intermediate dimensionless frequencies following the well-known Kolmogorov's power-law prediction, $\omega^{-5/3}$ (see [47]). In contract, Fig. 19 shows that the behavior of the spectra is completely reversed when examining the radial components of the fluctuations. In the presence of the polymer, the full energy associated with the radial velocity fluctuations presents a negative shift in comparison to the Newtonian case. This means an attenuation of the radial fluctuations decreasing the efficiency of transporting momentum by the radial velocity fluctuations and, consequently, reducing drag. The measured radial power spectrum in Fig. 19 also has indicated that the

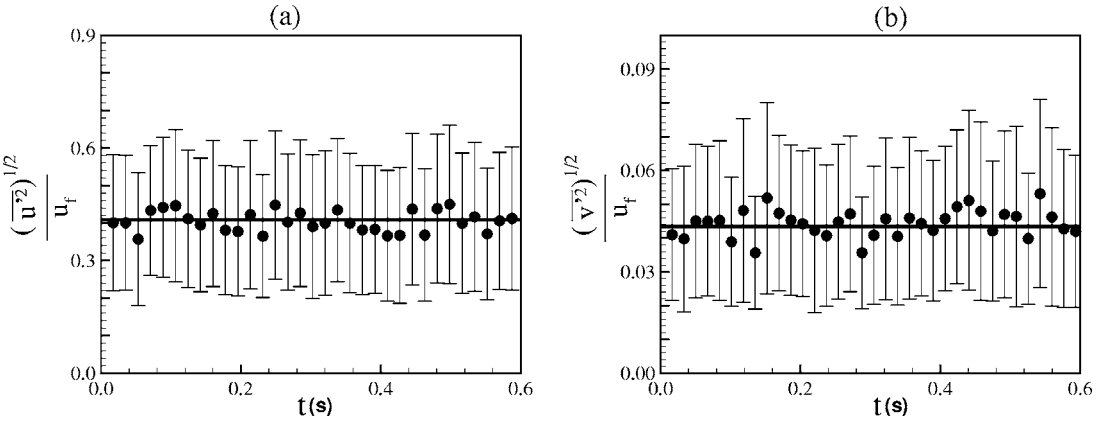

Fig. 11 The nondimensional velocity fluctuations for a volume fraction $\phi=1.2\times10^{-4}$ of the polymer solution: (*a*) axial fluctuations and (*b*) radial fluctuations

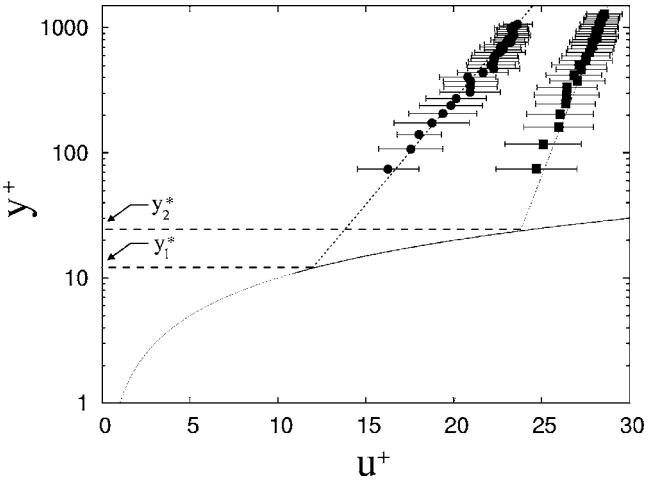

Fig. 12 The mean flow velocity profile as a function of wall distance. ●, pure water (ϕ=0); dashed line denotes Prandtl universal logarithmic law; □, experimental data for (ϕ =120 ppm); and the solid line denotes the numerical solution for our semi-empirical model. The solid curve of intersection represents the velocity profile of the viscous boundary layer.

smaller scale of the turbulence (i.e., high-frequency scales or dissipative scales) does not seem to be affected by the macromolecules. This conclusion is consistent with computer simulations of homogeneous viscoelastic flows by Benzi et al. [26]. These authors have shown that the mechanism of drag reduction operates mainly on a larger scale. The change in the power-law decay from (−5/3) to (−6/5), observed in the plot of Fig. 19, may be an indication that the polymer action in the inertial sublayer (buffer layer) becomes less dissipative, and a redistribution of turbulence energy between the fluctuation scales is evident in this region of the flow. In addition, the spectrum in Fig. 19 presumes that the same amount of energy in the buffer layer in the presence of polymer is associated with a smaller frequency in comparison to the Newtonian case. We argue that the macromolecules do not interact with those scales of turbulence corresponding to low frequency (large scale, only productive) or high frequency (small scale, only dissipative). The mechanism, responsible for producing drag reduction, seems to be a consequence of the interaction between the intermediate scales of turbulence and the macromolecule, having these intermediate scales characteristic frequencies of the same order of the macromolecule relaxation rate.

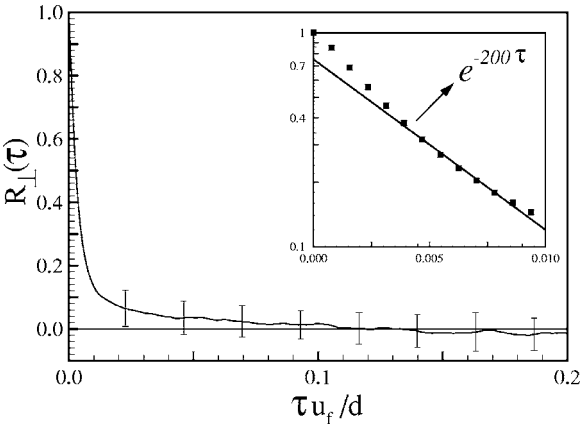

Fig. 14 Normalized velocity fluctuation autocorrelation function in the radial direction. The plots correspond to the flow of pure water at position y^+=50. In the inset, the autocorrelation function has been plotted in a log-log scale in order to show the exponential decay of this function with a correlation time about 1/200.

5 Conclusion

In this work, a theoretical analysis and experiments have successfully been performed to explore the effect of the macromolecules stretching of high molecular weight polymers on the drag reduction phenomenon in turbulent flows. We have used a constitutive model based on a theory of suspensions of elongated particles. Although, in particular, our approximation of the particles locally aligned with the flow is strictly not correct in a turbulent flow, it seems to be reasonable as a first approximation, and thus, in our opinion the model captures the essence of extensional viscous effects presumably introduced by elongated polymers.

The present studies show that, for small concentrations of anisotropic additives, the efficiency of the transport of momentum by turbulent fluctuations can be drastically reduced, providing a friction-factor reduction of up to 65%. The semi-theoretical models for the friction factor developed in the present work have very satisfactorily described the experimental data. Polyacrylamide macromolecules submitted to turbulent flow remain stretched for a

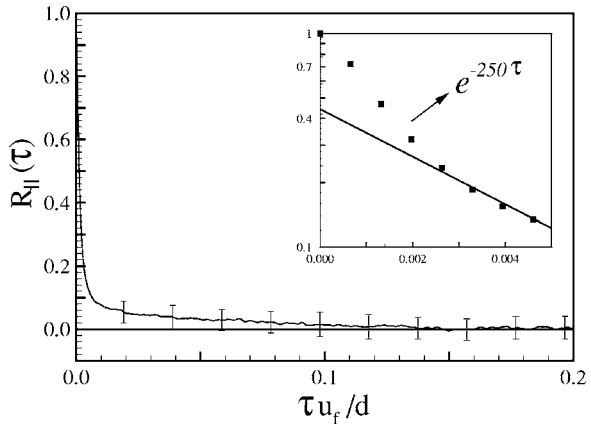

Fig. 13 Normalized velocity fluctuation autocorrelation function in the axial direction. The plots correspond to the flow of pure water at position y^+=50. In the inset, the autocorrelation function has been plotted in a log-log scale in order to show the exponential decay of this function with a correlation time about 1/250.

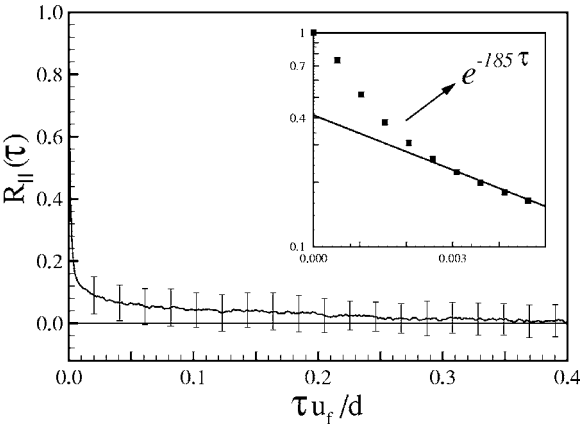

Fig. 15 Normalized velocity fluctuation autocorrelation function in the axial direction. The plots correspond to the flow of a 120 ppm solution of PAMA at position y^+=50. In the inset, the autocorrelation function has been plotted in a log-log scale in order to show the exponential decay of this function with a correlation time about 1/185.

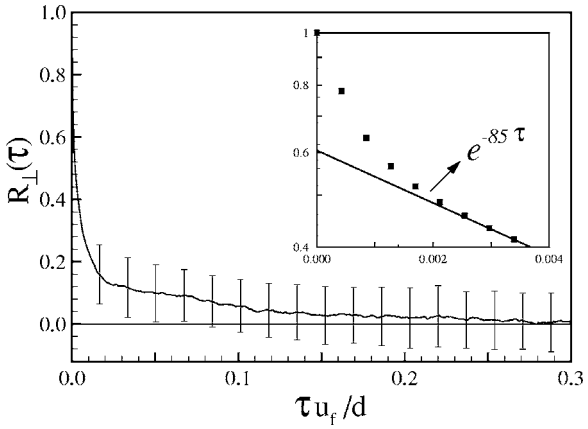

Fig. 16 Normalized velocity fluctuation autocorrelation function in the radial direction. The plots correspond to the flow of a 120 ppm solution of PAMA at position $y^+=50$. In the inset, the autocorrelation function has been plotted in a log-log scale in order to show the exponential decay of this function with a correlation time about 1/85.

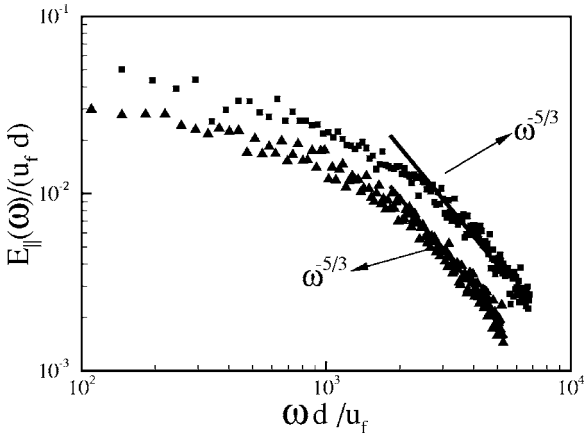

Fig. 18 Dimensionless power spectra at $y^+=50$ as a function of the frequency for the axial component of the velocity fluctuations for pure water (▲) and the solution of 120 ppm of PAMA (■), measured with LDV

time longer than the characteristic time of the flow. Significant evidence has been provided by this work on the role of an enhanced extensional viscosity of a polymer solution in promoting drag reduction. In the absence of macromolecule degradation of a high molecular weight polymer, the mechanism produced by macromolecule stretching is similar to the effect produced by long fibers oriented in the direction of the flow. This anisotropy of the fluid with a high extensional viscosity produces anisotropy in the flow, and the anisotropic wall eddies transported momentum less efficiently. In the presence of 120 ppm of PAMA, the velocity profiles measured with the LDV have shown a decrease of the radial velocity fluctuations over almost the entire pipe cross section.

On the basis of our results, we propose that the mechanism responsible to produce drag reduction results from the interaction between the intermediate scales of turbulence and the macromolecule, having these intermediate scales characteristic frequencies of the same order of the macromolecule relaxation rate. We attribute the effect of a few parts per million of polymer in strong flows, such as the turbulent flow examined here, to an anisotropic viscous mechanism characterized with an extensional viscosity as suggested by [17]. The results have suggested that for a regime of fully extended macromolecules in rapid flows, the elastic effect may be dominated by the anisotropic viscous effects. The drag reduction is then a direct consequence of the anisotropy produced in the flow by the polymer, depending on the relaxation time of the macromolecules in relation to the time scale of the turbulence in the buffer and log regions of the boundary layer. The measured radial power spectrum has indicated that the macromolecules do not change the turbulence structure at dissipative high frequencies of the flow.

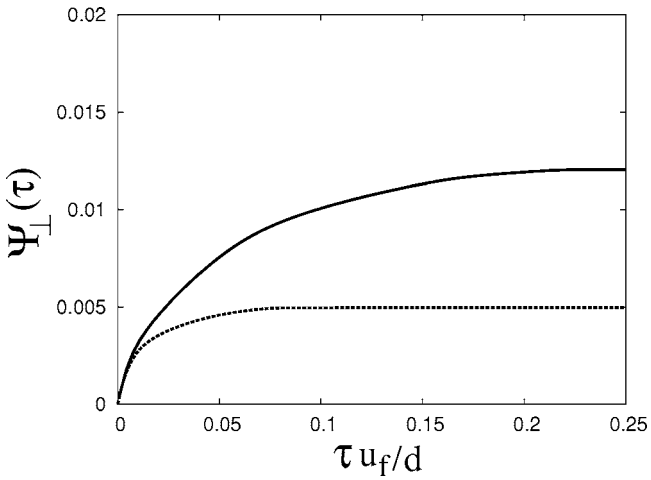

Fig. 17 Dimensionless diffusion coefficient associated with the radial component of the velocity fluctuations at the position $y^+=50$. The solid line denotes the 120 ppm solution of PAMA and dashed line, pure water.

Acknowledgment

The authors would like to thank Prof. John Hinch of the DAMTP-University of Cambridge who provided some relevant notes on drag reduction during the preparation of this work. We are grateful to Hugo L. G. Couto of the VORTEX-University of Brasilia for stimulating discussions. These authors gratefully acknowledge the support of this work by CNPq-Brasil, CAPES-Brazil, and FINATEC-DF.

Nomenclature

C, C_1 = calibration constants
C_2 = integration constant
$\mathbf{D}$ = rate of strain tensor

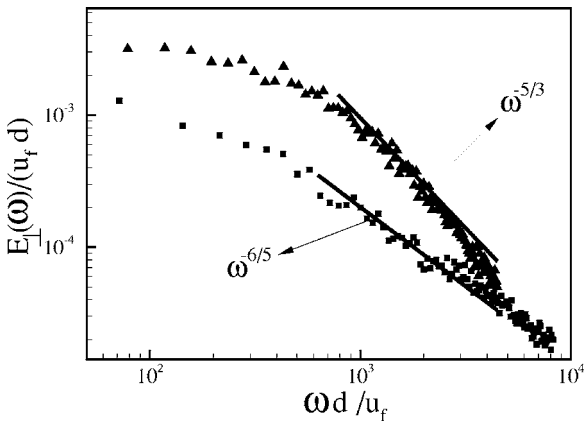

Fig. 19 Dimensionless power spectra at $y^+=50$ as a function of the frequency for the axial component of the velocity fluctuations for pure water (▲) and the solution of 120 ppm of PAMA (■), measured with LDV

$E(\omega)$ = spectral density
F_b = Brownian force
F_v = viscous force
G = additive shear rate function
$\tilde{G}$ = additive dimensionless shear rate function
K = Boltzmann constant
$\mathbf{I}$ = identity tensor
L = length of the test section
M = molecular weight
M_i = molecular weight of a monomer
N = number of the rigid segments
N_f = number of fibers
N^* = number of discrete nodes
N^I = number of intervals
$\mathbf{Q}$ = rotation tensor
$R(\tau)$ = normalized autocorrelation function
Re = Reynolds number based on the average velocity
Re_w = Reynolds number based on the friction velocity
T = absolute temperature
U = mean velocity of the turbulent velocity profile
$\mathbf{b}$ = translation vector
b = diameter of the additive
d = tube diameter
DRF = drag reduction factor
f = friction factor
f_a = friction factor of the water
h = distance between infinite parallel plates
ℓ = length of the additive
n = number density of additives
p = pressure
$\bar{p}$ = average pressure
$\mathbf{r}$ = distance between macromolecules ends
$\mathbf{r}^e$ = relative vector of residue
r_0 = radius of the tube
r_0^+ = dimensionless radius
$\mathbf{s}$ = unit vector in the direction of additive orientation
t = time
$\mathbf{u}$ = Eulerian fluid velocity
$\mathbf{u}'$ = velocity fluctuation vector
$\bar{\mathbf{u}}$ = average velocity vector
$\bar{u},\bar{v},\bar{w}$ = x,y,z components of the average velocity
u',v' = axial and transversal components of the velocity fluctuations
$\tilde{u}$ = dimensionless velocity
$\tilde{u}_{\max}$ = dimensionless maximum velocity
u_f = friction velocity
x = axial coordinate
y = transversal coordinate
$\tilde{y}$ = dimensionless transversal coordinate
y^+ = dimensionless wall coordinate
y^* = thickness of the buffer layer

Greek Symbols

ΔP = pressure drop
δ = length of the rigid segments
δ_h = length step
δy = grid length
ε = convergence parameter
ϕ = volume fraction of the additives
γ = shear rate
κ = Prandtl's universal constant
ω = frequency
μ = fluid viscosity
$\tilde{\mu}$ = apparent viscosity
μ_e = extensional viscosity
∇ = nabla operator
ν = fluid kinematic viscosity
ψ = diffusivity
ρ = fluid density
$\boldsymbol{\Sigma}$ = hydrodynamic stress tensor
$\boldsymbol{\Sigma}_f$ = particle stress tensor
$\boldsymbol{\tau}$ = shear stress tensor
τ = relaxation time
τ_w = wall shear stress

Subscripts

$\parallel$ = axial direction
$\perp$ = transversal direction
max = maximum
p = polymer
w = water

Superscripts

$n+1$ = denotes the velocity of the current time
T = transpose of a tensor
y = change of a reference frame

References

[1] Toms, B. A., 1948, "Some Observations on the Flow of Linear Polymer Solutions Through Strait Tubes at Large Reynolds Numbers," *Proc. of 1st Intern. Congress on Rheology*, North Holland, Amsterdam, Vol. 2 pp. 135–141.

[2] Bark, F. H., Hinch, E. J., and Landahl, M. T., 1975, "Drag Reduction in Turbulent Flow Due to Additives: A Report on Euromech 52," J. Fluid Mech., **68**, pp. 129–138.

[3] Pinho, F. T., and Whitelaw, J. H., 1990, "Flow of Non-Newtonian Fluids in a Pipe," J. Non-Newtonian Fluid Mech., **34**, pp. 129–144.

[4] Gyr, A., and Bewersdorff, H. W., 1995, *Drag Reduction of Turbulent Flow by Additives*, Kluwer Academic Publishers, Dordrecht.

[5] Blick, E. F., Walters, R. R., Smith, R., and Chu, H., 1969, "Compliant Coating Skin Friction Experiments," AIAA J., **69**, p. 165.

[6] Fraim, F. W., and Heiser, W. H., 1967, "The Effect of a Strong Longitudinal Magnetic Field on the Flow of Mercury in a Circular Pipe," J. Fluid Mech., **33**, pp. 397–413.

[7] Cunha, F. R., and Sobral, Y. D., 2005, "Asymptotic Solution for Pressure Driven Flow of Magnetic Fluids in Pipes," J. Magn. Magn. Mater., **289**, pp. 314–317.

[8] Lumley, J. L., 1969, "Drag Reduction in Turbulent Flow by Polymer Additives," J. Polym. Sci., Part A-1, **7**, pp. 263–290.

[9] Ryskin, G., 1991, "Turbulent Drag Reduction by Polymers: A Quantitative Theory," Phys. Rev. Lett., **59**, pp. 2059–2062 (see also Erratum: 1991, Phys. Rev. Lett., **66**, p. 968).

[10] L'vov, V. S., Pomyalov, A., Procaccia, I., and Toberkevich, V., 2004, "Drag Reduction by Polymers in Wall Bounded Turbulence," Phys. Rev. Lett., **92**(24), pp. 244503.

[11] De Gennes, P. G., 1990, *Introduction to Polymer Dynamics*, Cambridge University Press, Cambridge, England.

[12] Joseph, D. D., 1990, *Fluid Dynamics of Viscoelastic Liquids*, Springer-Verlag, Berlin.

[13] Min, T., Yoo, Y. J., Choi, H., and Joseph, D. D., 2003, "Drag Reduction by Polymer Additives in a Turbulent Channel Flow," J. Fluid Mech., **486**, pp. 213–238.

[14] Massah, H., and Hanratty, T. J., 1997, "Added Stress Because of the Presence of FENE-P Bead-Spring Chains in a Random Velocity Field," J. Fluid Mech., **337**, pp. 67–101.

[15] Landhal, M. T., 1973, "Drag Reduction by Polymer Addition," *Theoretical and Applied Mechanics, Proc. 13th Intl. Congr. Theor. and Appl. Mech.*, E. Becher, and G. K. Mikhailov, eds., Springer, New York, Vol. 1, pp. 177–199.

[16] Hinch, E. J., 1977, "Mechanical Models of Dilute Polymer Solutions in Strong Flows," Phys. Fluids, **20**, pp. 22–30.

[17] Hinch, E. J., 1994, "Uncoiling a Polymer Molecule in a Strong Extensional Flow," J. Non-Newtonian Fluid Mech., **54**, pp. 209–230.

[18] Draaad, A. A., and Hulsen, M. A., 1995, "Transition From Laminar to Turbulent Flow for Non-Newtonian Fluids," *Advances in Turbulence V, Proc. of European Turbulence Conference V*, R. Benzi, ed., Siena, Italy, Vol. 1, pp. 105–110.

[19] Den Toonder, J. M. J., Hulsen, M. A., Kuiken, G. D. C., and Nieuwstadt, F. T. M., 1997, "Drag Reduction by Polymer Additives in a Turbulent Pipe Flow: Numerical and Laboratory Experiments," J. Fluid Mech., **337**, pp. 193–231.

[20] Andreotti, M., Cunha, F. R., and Sousa, A. J., 2003, "Investigation of Friction Affected by Additives in Turbulent Flows in Pipelines," Bol. Tec. Petrobras, **46**, pp. 55–77.

[21] Sasaki, S., 1992, "Drag Reduction Effect of Rod-Like Polymer Solution, 3. Molecular Weight Dependence," J. Phys. Soc. Jpn., **61**(6), pp. 1960–1963.

[22] Azaiez, J., 2000, "Linear Stability of Free Shear Flows of Fiber Suspensions," J. Fluid Mech., **404**, pp. 179–209.

[23] Handler, R. A., and Levich, E., 1993, "Drag Reduction in Turbulent Channel

Flow by Phase Randomization," Phys. Fluids A, **5**(3), pp. 686–694.
[24] Dimitropoulos, C. D., Sureshkumar, R., and Beris, A. N., 1998, "Direct Numerical Simulation of Viscoelastic Turbulent Channel Flow Exhibiting Drag Reduction: Effect of the Variation of Rheological Parameters," J. Non-Newtonian Fluid Mech., **79**, pp. 433–468.
[25] Orlandi, P., 1995, "A Tentative Approach to the Direct Simulation of Drag Reduction by Polymers," J. Non-Newtonian Fluid Mech., **60**, pp. 277–301.
[26] Benzi, R., De Angelis, E., Govindarajan, R., and Procaccia, I., 2003, "Shell Model for Drag Reduction With Polymer Additives in Homogeneous Turbulence," Phys. Rev. E, **68**, pp. 016308.
[27] Salas, F. A., Oliveira, T. F., and Cunha, F. R., 2006, "A Note on the Extensional Viscosity of Elastic Liquids Under Strong Flows," Mech. Res. Commun., **33**(3), pp. 401–414.
[28] Cunha, F. R., 1995, "Hydrodynamic Dispersion in Suspensions," Ph.D thesis, DAMTP-University of Cambridge, Cambridge.
[29] Kuhn, W., and Kuhn, H., 1945, "Bedeutung Beschrnkt Freier Drehbarkeit fr die Viskositt und Strmungsdoppelbrechung von Fadenmolekellsungen," Helv. Chim. Acta, **28**, pp. 1533–1579.
[30] Einstein, A., 1956, *Investigations on the Theory of the Brownian Movement*, Dover Publications, New York.
[31] Batchelor, G. K., 1970, "Slender-Body Theory for Particle of Arbitrary Cross Section in Stokes Flow," J. Fluid Mech., **44**, pp. 419–440.
[32] Hinch, E. J., and Leal, L. G., 1976, "Constitutive Equations in Suspension Mechanics, Part 2. Approximate Forms for a Suspension of Rigid Particles Affected by Brownian Rotations," J. Fluid Mech., **76**(1), pp. 187–208.
[33] Ericksen, J. L., 1960, "Trasversaly Isotropic Fluids," Kolloidn. Zh., **173**, pp. 117–122.
[34] Aris, R., 1962, *Vectors, Tensors, and the Basic Equations of Fluid Mechanics*, Dover, New York.
[35] Stover, C. A., Koch, D. L., and Cohen, C., 1992, "Observations of Fibre Orientation in Simple Shear Flow of Semi-Dilute Suspensions," J. Fluid Mech., **238**, pp. 277–296.
[36] Keiller, R. A., and Hinch, E. J., 1991, "Corner Flow of a Suspension of Rigid Rods," J. Non-Newtonian Fluid Mech., **40**, pp. 323–335.
[37] Batchelor, G. K., 1971, "The Stress Generated in a Non-Dilute Suspension of Elongated Particles by Pure Straining Motion," J. Fluid Mech., **46**(4), pp. 813–829.
[38] Shaqfeh, E. S. G., and Frederickson, G. H., 1990, "The Hydrodynamic Stress in a Suspension of Rods," Phys. Fluids A, **2**, pp. 7–24.
[39] Pao, R. H. F., 1967, *Fluid Dynamics*, Charles E. Merrill Books, Columbus.
[40] Barnes, H. A., Huton, J. F., and Walters, K., 1991, *An Introduction to Rheology*, Elsevier, Amsterdan.
[41] Batchelor, G. K., and Green, J. T., 1972, "The Hydrodynamic Interaction of Two Small Freely-Moving Spheres in a Linear Flow Field," J. Fluid Mech., **56**, pp. 375–400.
[42] Lim, S. T., Choi, H. J., Lee, S. Y., So, S. J., and Chan, C. K., 2003, "λ-DNA Induced Turbuelnt Drag Reduction and Its Characteristics," Macromolecules, **36**, pp. 5348–5354.
[43] Virk, P. S., 1975, "Drag Reduction Fundamentals," AIChE J., **21**, pp. 625–656.
[44] Kline, S. J., and McClintock, F. A., 1991, "Describing Uncertainties in Single-Sample Experiments," Mech. Eng. (Am. Soc. Mech. Eng.), **75**, pp. 3–8.
[45] Hinch, E. J., 2004, Private communication.
[46] Press, W. H., Teukolsky, S. A., Vetterling, W. T., and Flannery, B. P., 1992, *Numerical Recipes in Fortran*, Cambridge University Press, Cambridge, England.
[47] Landau, L. D., and Lifshitz, E. M., 1987, *Course in Theoretical Physics: Fluid Mechanics*, Pergamon, Oxford.

Mixed Convection From a Heated Square Cylinder to Newtonian and Power-Law Fluids

A. K. Dhiman

N. Anjaiah

R. P. Chhabra[1]
e-mail: chhabra@iitk.ac.in

Department of Chemical Engineering,
Indian Institute of Technology,
Kanpur 208016, India

V. Eswaran
Department of Mechanical Engineering,
Indian Institute of Technology,
Kanpur 208016, India

Steady laminar mixed convection flow and heat transfer to Newtonian and power-law fluids from a heated square cylinder has been analyzed numerically. The full momentum and energy equations along with the Boussinesq approximation to simulate the buoyancy effects have been solved. A semi-explicit finite volume method with nonuniform grid has been used for the range of conditions as: Reynolds number 1–30, power-law index: 0.8–1.5, Prandtl number 0.7–100 ($\mathrm{Pe} \leqslant 3000$) *for Richardson number 0–0.5 in an unbounded configuration. The drag coefficient and the Nusselt number have been reported for a range of values of the Reynolds number, Prandtl number, and Richardson number for Newtonian, shear-thickening* ($n > 1$) *and shear-thinning* ($n < 1$) *fluids. In addition, detailed streamline and isotherm contours are also presented to show the complex flow field, especially in the rear of the cylinder. The effects of Prandtl number and of power-law index on the Nusselt number are found to be more pronounced than that of buoyancy parameter* ($\mathrm{Ri} \leqslant 0.5$) *for a fixed Reynolds number in the steady cross-flow regime* ($\mathrm{Re} \leqslant 30$). [DOI: 10.1115/1.2436586]

1 Introduction

Flow past a heated cylinder of a square cross section with its longitudinal axis aligned normal to the direction of the approaching flow has attracted a great deal of attention over the years. Such studies have been motivated both due to its fundamental significance as well as its relevance in many engineering applications such as in cooling of electronic components, compact heat exchangers, combustion chambers in chemical process, and flow dividers in polymer processing. Most of the heat transfer work reported in the literature pertains to the unsteady laminar flow region and forced convective heat transfer with a built-in square cylinder, where the main thrust is to find the effect of von Karman vortex street on the forced convective heat transfer and to find time averaged Nusselt number as a function of the pertinent variables. Furthermore, many fluids of industrial interest are adequately characterized rheologically by the purely viscous power-law behavior, and owing to their highly viscous nature, the processing conditions are often within the steady flow regime. In spite of their wide occurrence, only limited numerical results are available on the forced convective heat transfer from a square cylinder in the steady flow regime to Newtonian and power-law fluids [1–5]. None of these studies included the influence of buoyancy and suggest a slight enhancement in heat transfer in shear-thinning fluids and a very small reduction in heat transfer in shear-thickening fluids over moderate range of conditions of the Reynolds and Prandtl numbers. It is well known that the buoyancy effects superimposed on forced flow conditions can strongly influence the flow patterns thereby influencing convective heat transfer. The effects are known to be particularly significant both at low velocity and/or when the temperature difference between the body and the ambient fluid is large. Strictly speaking, natural convection effects are always, how so ever small, present in all heat transfer applications. The commonly used parameter to characterize the extent of mixed convection is the Richardson number, defined as $\mathrm{Ri} = \mathrm{Gr}/\mathrm{Re}^2$. Obviously, the larger the value of the Richardson number (>0), the more significant the free convection, with values beyond unity being generally accepted to be indicative of the mixed convection regime.

Extensive literature focusing on various aspects of mixed convection is available for a circular cylinder, including aiding flow or opposing flow conditions depending upon the direction of the flow relative to the cylinder [6–18], as will be seen in the next section. In contrast, limited work has been reported for the mixed convection even from a circular cylinder for the cross-flow configuration, when the mean flow is oriented normal to the direction of gravity (cross-stream buoyancy). Such cross-buoyancy flow is highly complex because the velocity induced by the (thermal) buoyancy is normal to the flow direction and thus distorts the flow field near the body, thereby altering the values of the drag coefficient and the heat transfer, irrespective of the value of the Reynolds number. One may encounter such flows in a plate-fin heat exchanger with horizontally mounted tubes or heating elements. This study endeavors to investigate mixed convection from a horizontal two-dimensional square rod oriented normal to the direction of flow with superimposed buoyancy currents transverse to the imposed flow.

2 Previous Work

Badr [6] has investigated the problem of cross buoyancy ($0 \leqslant \mathrm{Ri} \leqslant 5$) from an isothermally heated circular cylinder to air in the steady flow regime ($1 \leqslant \mathrm{Re} \leqslant 40$). Subsequently, Badr [7] extended this work for the aiding and opposing flow regimes. Notwithstanding significant changes in the detailed flow and temperature fields, Badr reported an increase of up to 41% in the average Nusselt number with Grashof number. Noto et al. [8] experimentally found the presence of steady twin vortices instead of a vortex street beyond a critical value of the Richardson number. Chang and Sa [9] have numerically studied the effects of aiding and opposing buoyancy ($-1 \leqslant \mathrm{Ri} \leqslant 1$) for an upward flow of air past a hot/cold circular cylinder for a fixed value of the Reynolds number of 100. They found a critical Richardson number of 0.15 at which the purely unsteady periodic flow degenerated into a steady twin vortex pattern and these findings are consistent with the experimental results [8] and the other numerical studies [10]. Patnaik et al. [11] have also studied this problem for $\mathrm{Re} = 20, 40, 100, 200$ for $-1 < \mathrm{Ri} < 1$ and obtained the value of Rich-

[1]Corresponding author.

Contributed by the Fluids Engineering Division of ASME for publication in the JOURNAL OF FLUIDS ENGINEERING. Manuscript received May 10, 2006; final manuscript received September 28, 2006. Assoc. Editor: Dennis Siginer.

ardson number of 0.12 at which the vortex shedding ceased. Furthermore, the phenomenon of vortex shedding could be triggered at low Reynolds number ($Re < 40$) depending upon the value of Richardson number. Ahmad and Qureshi [12] have extensively examined the mixed convection from a horizontal circular cylinder for air for $1 \leq Re \leq 60$ and $0 \leq Ri \leq 25$. They found both the Nusselt number and the drag coefficient to increase with the Richardson number. Maas et al. [13] have experimentally shown that three-dimensional (3D) transition in the wake flow behind the horizontal heated circular cylinder occurs at a lower Reynolds number than for the unheated case; for instance, they reported the wake to become 3D for $Ri > 0.3$ at $Re = 117$. Ren et al. [14] have performed both numerical and experimental investigations over the range of conditions as $80 < Re < 130$ and $0 < Ri < 1.5$ for water and documented the 3D transition to occur at $Re = 85$ for $Ri = 1.0$. In view of all these findings, it is probably fair to assume that the flow remains 2D for the range of conditions ($Re \leq 30$, $Ri \leq 0.5$) embraced by the present study. Apart from the aforementioned numerical studies, Abu-Hijleh [15] has proposed Nusselt number correlations for forced and mixed convection from a circular cylinder for air flow at different angles from the horizontal for $1 \leq Re \leq 200$ and $0 \leq Ri \leq 35$. Subsequently, Wang et al. [16] have obtained a universal relationship between the effective Reynolds and Strouhal numbers applicable for a wide range of cylinder temperatures. Most of the literature relating to the flow past and heat transfer from circular cylinders has been reviewed by Zdravkovich [17,18].

In contrast, as far as is known to us, there have been only two numerical studies on the mixed convection heat transfer from a square cylinder in an unbounded configuration. Sharma and Eswaran [19] studied the effect of aiding and opposing buoyancy ($-1 \leq Ri \leq 1$) on the flow and heat transfer from an isothermal square cylinder to air for a fixed Reynolds number of 100. The average Nusselt number for the cylinder increases monotonically with the Richardson number, albeit only slightly. They also found that the degeneration of Karman vortex street to occur at a Richardson number of 0.15 for a square cylinder, as seen above for a circular cylinder. Recently, Bhattacharyya and Mahapatra [20] have studied the effect of buoyancy on vortex shedding and heat transfer from a horizontal square cylinder to air for Reynolds number ≤ 1400 for $0 \leq Ri \leq 1$. As expected, the heat transfer from the cylinder increases with an increase in the Reynolds number and/or Grashof number. Although the present work is concerned with the unconfined flow, for the sake of completeness, it is appropriate to add that not only much less is known about the flow for a confined square cylinder, but there is very little agreement among the various results [21–23].

In summary, hence very limited information is available on mixed convection from a square cylinder and most of it relates to the flow of air. No prior results are available for viscous Newtonian and power-law fluids which are generally processed at low flow rates (Reynolds numbers) except for a preliminary study by Anjaiah et al. [24] which employed a relatively coarse uniform grid. More accurate and detailed computations have highlighted the deficiencies of these preliminary results. It is thus necessary to understand the buoyancy effects thoroughly within the steady flow regime. This work sets out not only to fill this gap in the literature, but also to investigate the influence of Prandtl number on heat transfer to Newtonian fluids from an unconfined square cylinder in the mixed convection regime.

3 Problem Statement and Mathematical Formulation

The geometry and the relevant dimensions considered in the present study are shown schematically in Fig. 1. A fixed two-dimensional square cylinder with side b (which is also the nondimensionalizing length scale) maintained at a constant temperature T_w is exposed to a constant free-stream velocity U_∞ and temperature T_∞. In order to make the problem computationally tractable, artificial confining boundaries are imposed in the form of plane

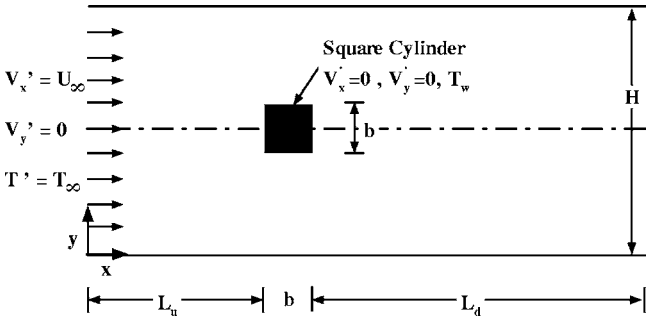

Fig. 1 Schematics of the flow across a square cylinder

parallel walls. The free-slip boundary conditions are implemented so that there is no extra energy dissipation due to these artificial walls. Furthermore, the boundaries are sufficiently far away from the body so that their presence has negligible effect on the flow characteristics near the obstacle. Owing to the 2D nature of the flow, there is no flow in the z direction and $\partial(\,)/\partial z = 0$ (z being along the length of the square rod). The relevant governing equations are the continuity, Cauchy's, and the thermal energy equations (used in their dimensionless forms) and are written as follows:

continuity

$$\frac{\partial V_x}{\partial x} + \frac{\partial V_y}{\partial y} = 0 \tag{1}$$

x momentum

$$\frac{\partial V_x}{\partial t} + \frac{\partial (V_x V_x)}{\partial x} + \frac{\partial (V_y V_x)}{\partial y} = -\frac{\partial p}{\partial x} + \frac{\eta}{\mathrm{Re}}\left(\frac{\partial^2 V_x}{\partial x^2} + \frac{\partial^2 V_x}{\partial y^2}\right) + \frac{2}{\mathrm{Re}}\left(\varepsilon_{xx}\frac{\partial \eta}{\partial x} + \varepsilon_{yx}\frac{\partial \eta}{\partial y}\right) \tag{2}$$

y momentum

$$\frac{\partial V_y}{\partial t} + \frac{\partial (V_x V_y)}{\partial x} + \frac{\partial (V_y V_y)}{\partial y} = -\frac{\partial p}{\partial y} + \frac{\eta}{\mathrm{Re}}\left(\frac{\partial^2 V_y}{\partial x^2} + \frac{\partial^2 V_y}{\partial y^2}\right) + \frac{2}{\mathrm{Re}}\left(\varepsilon_{yy}\frac{\partial \eta}{\partial y} + \varepsilon_{xy}\frac{\partial \eta}{\partial x}\right) + \mathrm{Ri}\, T \tag{3}$$

energy equation

$$\frac{\partial T}{\partial t} + \frac{\partial (V_x T)}{\partial x} + \frac{\partial (V_y T)}{\partial y} = \frac{1}{\mathrm{Pe}}\left(\frac{\partial^2 T}{\partial x^2} + \frac{\partial^2 T}{\partial y^2}\right) \tag{4}$$

In Eqs. (1)–(4), implicit are the assumptions, negligible dissipation, and the constant thermo-physical properties (heat capacity, thermal conductivity, power-law constants) except for the body force term in the momentum equation (Boussinesq approximation). Evidently, these form a set of coupled equations.

For a power-law fluid, the viscosity is given by

$$\eta = (I_2/2)^{(n-1)/2}$$

and

$$I_2 = \left(\frac{\partial u}{\partial x}\right)^2 + \left(\frac{\partial v}{\partial y}\right)^2 + \frac{1}{2}\left(\frac{\partial u}{\partial y} + \frac{\partial v}{\partial x}\right)^2$$

The physically admissible (dimensionless) boundary conditions for velocity and temperature may be written as follows:

- At the inlet boundary, $V_x = 1$, $V_y = 0$, and $T = 0$;
- On the upper and lower boundaries, $\partial V_x/\partial y = 0$, $V_y = 0$, and $\partial T/\partial y = 0$;
- On the surface of the square cylinder, $V_x = 0$, $V_y = 0$ (no-slip), and $T = 1$; and
- At the exit boundary, $\partial \phi/\partial x = 0$, where $\phi = V_x, V_y, T$.

Equations (1)–(4) together with the above-noted boundary conditions are solved to map the flow domain $0 \leq x \leq 26$ or 28 and $0 \leq y \leq 20$ or 30 in terms of the primitive variables, i.e., $V_x(x,y)$, $V_y(x,y)$, $p(x,y)$, and $T(x,y)$. These, in turn, can be post-processed to obtain the values of the gross parameters like drag, Nusselt number, and of the derived variables like stream function, isotherms, and so on as described elsewhere [1–4].

4 Numerical Methodology

In the present work, the finite volume method [25] for complex 3D geometries on a nonstaggered grid has been used here in its simplified form for 2D flows as detailed elsewhere [1–4]. In brief, the semi-explicit finite volume method has been used on a nonuniform grid to solve the unsteady momentum equations in which the momentum equations are discretized in an explicit manner, with the exception of pressure gradient terms which are treated implicitly [26]. The explicit scheme has been used for the solution of energy equation to obtain the temperature field from the velocity field at each time level and is used for the solution of velocity field at the next time level. The convective terms are discretized using the QUICK scheme while the diffusive and non-Newtonian terms are discretized using the central difference scheme [2].

Since the computational grid used here is described in detail by Dhiman et al. [2], only the salient features are recapitulated here. In brief, the grid structure comprised five separate zones with both uniform and nonuniform grid spacings, having a close clustering of grid points close to the cylinder and relatively coarser grids farther away. Overall, the grid distribution is uniform with a constant cell size of 0.25 in an outer region that extends beyond 4 units from the cylinder. An extremely fine grid size of 0.01 is clustered in an inner region around the cylinder over a distance of 1.5 units to adequately capture the wake dynamics. The expression suggested by Thompson et al. [27] has been used for stretching the cell sizes between 0.01 and 0.25.

4.1 Choice of Numerical Parameters. In order to obtain reliable and accurate results, it is imperative to choose carefully the following parameters defining the flow domain, i.e., height of the computational domain H, upstream length L_u, downstream length L_d, and the grid size, $M \times N$. Naturally, each of these parameters exerts varying levels of influence on the accuracy of the flow and temperature fields which, in turn, determine the values of the gross engineering parameters, as discussed in detail for the case of forced convection [1–5]. However, a terse discussion of the role of each of these parameters within the context of mixed convection is presented here.

In this work, three nonuniform grids ($M \times N$, 222×254, 264×316, and 304×376 with 52, 80, and 100 cells on each side of the cylinder, respectively) have been used to demonstrate the grid independence of the present results for Re=30, Ri=0.5, and Pr=100. The relative percentage changes in the value of the drag coefficient, C_D, are 0.58%, 0.20% and of lift coefficient, C_L are 0.76%, 0.18% for the grid sizes of 222×254, 264×316 as compared to the values for the grid size of 304×376, respectively. The corresponding differences in the values of the mean Nusselt number, Nu, are found to be 0.2% and 0.04%. Therefore, the grid size of 304×376 for Re=10, 20, and 30 with $L_u=8.5$, $L_d=16.5$, and $H=30$ has been used here. However, for Re=1 and 5, the grid size of 331×304 (with 100 cells on the side of the cylinder) with $L_u=10.5$, $L_d=16.5$, and $H=30$ has been used in this work to account adequately for the entrance effects.

The effect of upstream distance, L_u, has been studied for $L_u=8.5$ (304×376), 10.5 (331×304), and 12.5 (339×304) for Re=1 (expected to be most severe) at Ri=0.5 for Pr=1 with $L_d=16.5$ and $H=30$. The resulting changes in the value of C_D are about 5.34% for $L_u=8.5$ and of 1.84% for $L_u=10.5$ with respect to the value of C_D for $L_u=12.5$. However, the corresponding changes in the value of C_L are found to be about 20.6% for $L_u=8.5$ and of 7.6% for $L_u=10.5$. The changes in the values of the mean Nusselt number, Nu, are 1.06% for $L_u=8.5$ and of 0.38% for $L_u=10.5$ with respect to the value of Nu for $L_u=12.5$. Similarly, the percentage differences between the values of C_D for $L_u=8.5$ and 10.5 are about 2.67% for Re=5 and about 2.26% for Re=10 for Ri=0.5 and Pr=1, respectively. The differences between the values of C_L for $L_u=8.5$ and 10.5 are about 5% for Re=5 and about 1.6% for Re=10 for Ri=0.5 and Pr=1, respectively. The corresponding changes in the values of mean Nusselt number, Nu, are 0.65% and 0.61% for Re=5 and 10, respectively. Therefore, bearing in mind the tradeoff between the small change in the results vis-a-vis the enormous increase (>100%) in CPU time, the upstream distance of 10.5 is used for Re=1,5, whereas $L_u=8.5$ is used for Re=10,20,30 in this work, as the entry effects decrease with the increasing Reynolds number.

The influence of the downstream distance L_d on the flow parameters has been checked for $L_d=16.5$ (304×376) and 18.5 (331×304) for Re=30, Ri=0.5, and Pr=100 with $L_u=8.5$, $H=30$. The relative changes in the values of C_D, C_L, and Nu are found to be 0.05%, 0.2%, and 0.02%, respectively. Therefore, the downstream distance of 16.5 has been used here for all combinations of the values of Re, Ri, Pr, and n.

The effect of domain height H on C_D, C_L, and Nu was also studied for Re=10, 20, and 30 and Ri=0.5 at Pr=1 for $H=20$ (323×264) and for $H=30$ (304×376) with $L_u=8.5$, $L_d=16.5$, and $L=26$. The relative changes between the values of C_D are 0.33% for Re=10,0.12% for Re=20, and of 0.07% for Re=30 for $H=20$ and 30. The corresponding changes between the values of C_L are about 1.4% for Re=10 and 1.03% for Re=20, whereas for Re=30, C_L is found to be zero. The corresponding changes in the values of Nu are less than 0.11% for Re=10, 20, and 30. Since $\mathrm{Pr} \approx 1$ denotes the minimum value of the Prandtl number used in this work, when the thermal boundary layer thickness would be maximum, the computational domain height of 30 is regarded to be adequate for other values of the Prandtl number used in this work. However, for shear-thinning behavior ($n<1$), the computational domain height of 20 is used for Re=10, 20, and 30, as suggested by a previous study [2].

Thus, in summary, the results reported here are based on $L_d=16.5$, $H=30$, $L_u=8.5$ for Re=10,20,30 and $L_u=10.5$ for Re=1,5. The stopping or the steady-state criterion used in this work is 10^{-4}, i.e., the root mean square of the change in velocities and temperature variables in one time step is less than or equal to $10^{-4}\Delta t$. Furthermore, it was also observed that the results changed by an amount less than 0.5%, when the convergence criterion was relaxed to 5×10^{-4}.

It is appropriate to add here that special attention was paid in handling the singularities at the corners of the square cylinder [1,3,4]. This has been achieved by assigning different values to the real cells at corner points by a dual prescription of values at the fictitious corner cells, a practice also used by others [19,23,26]. As mentioned previously, the grid consisting of 100 cells on each side of the cylinder used here is considered to be sufficiently fine to obtain global results that are essentially grid independent.

5 Results and Discussion

The effect of power-law index ($0.8 \leq n \leq 1.5$) on the 2D steady flow and heat transfer has been studied for Reynolds numbers of 5 and 30, Prandtl number of 1, and Richardson numbers from 0 to 0.5 in an unbounded flow configuration. The effect of Prandtl number ($0.7 \leq \mathrm{Pr} \leq 100$) has been explored for the range of conditions as: $1 \leq \mathrm{Re} \leq 30$ and $0 \leq \mathrm{Ri} \leq 0.5$ for Newtonian fluids ($n=1$). It is, however, useful to first establish the reliability and accuracy of the new results obtained herein.

5.1 Validation of Results. As mentioned previously, no prior numerical/experimental results are available on the effect of buoyancy on the flow and the heat transfer characteristics for a square

Table 1 Comparison of C_D, Nu, and St at Ri=0 and 0.5 for Re =100 and n=1

Source	C_D	Nu (Pr=0.7)	St
		Ri=0	
Present	1.487	4.022	0.148
Sharma and Eswaran [19]	1.493	4.044	0.149
		Ri=0.5	
Present	1.558	4.130	0.153
Sharma and Eswaran [19]	1.553	4.146	0.153

cylinder placed normally to an approaching steady flow except for the limited results of Sharma and Eswaran [19] for Re=100, Pr =0.7, and Ri=0.25–1. In order to make a comparison with these results, time-dependent simulations were carried out for these conditions for Ri=0.5. A comparison is shown in Table 1 and the two values are seen to be within ±0.5% of each other. In addition, extensive benchmarking of the present results at Ri=0 (forced convection case) in the steady flow regime has also been reported elsewhere [1–4] and is thus not repeated here. The present results are therefore believed to be quite reliable and accurate.

5.2 Flow and Temperature Fields. Figures 2 and 3 show the streamline and isotherm profiles close to the cylinder for Re =5,30 and Ri=0.5 at Pr=1 for three values of power-law index corresponding to a shear thinning (n=0.8), a Newtonian, and a shear-thickening fluid (n=1.5). Unlike in the case of the forced convection case (Ri=0) in the steady cross-flow regime, as the value of the buoyancy parameter is increased, streamlines ahead of the cylinder have a downward slope toward the forward stagnation point (Fig. 2). Likewise, the streamlines behind the cylinder have a positive slope and the rise in the downstream streamlines is greater than that in the upstream streamlines, similar to the case of a circular cylinder [12]. Furthermore, for the forced convection case [2], the flow separates from the trailing edge of the cylinder and forms two symmetric vortices behind the obstacle. The wake size of these vortices is larger in the shear-thickening fluid ($n>1$) than that in the shear-thinning fluid ($n<1$). In contrast, for mixed convection, these twin vortices break down and

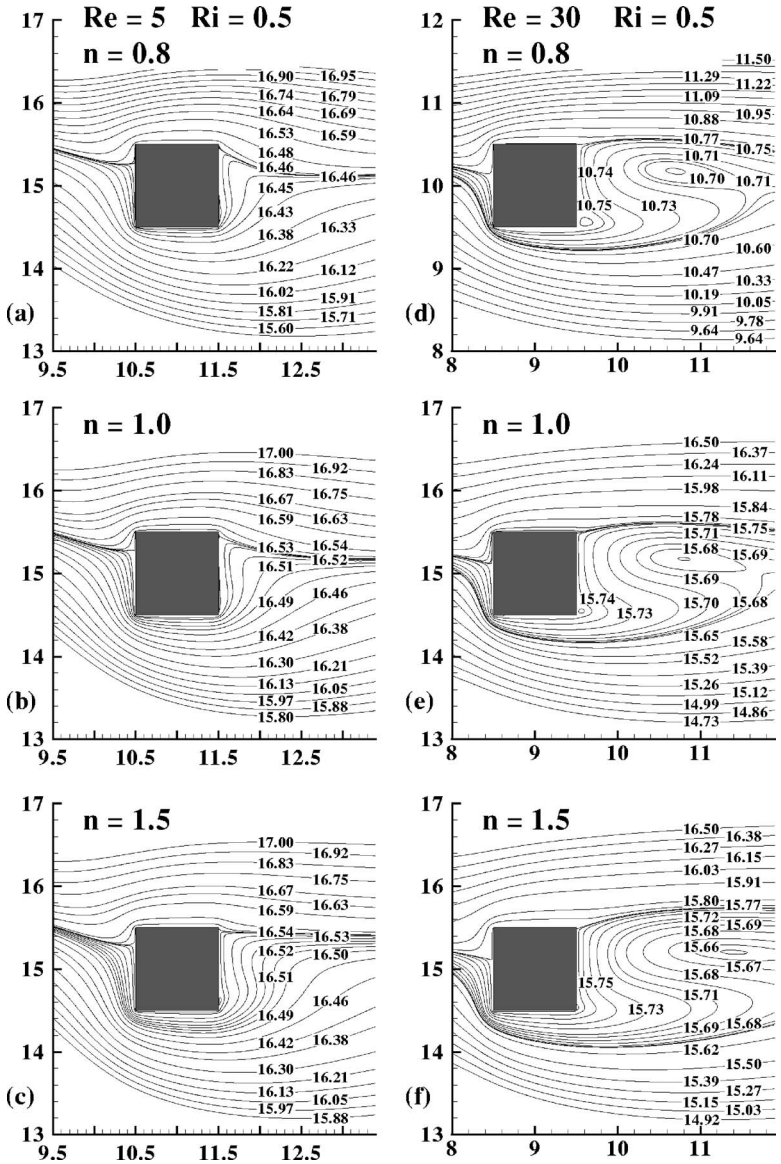

Fig. 2 Streamline profiles for Re=5 and 30, Ri=0.5, and Pr=1 at different values of n

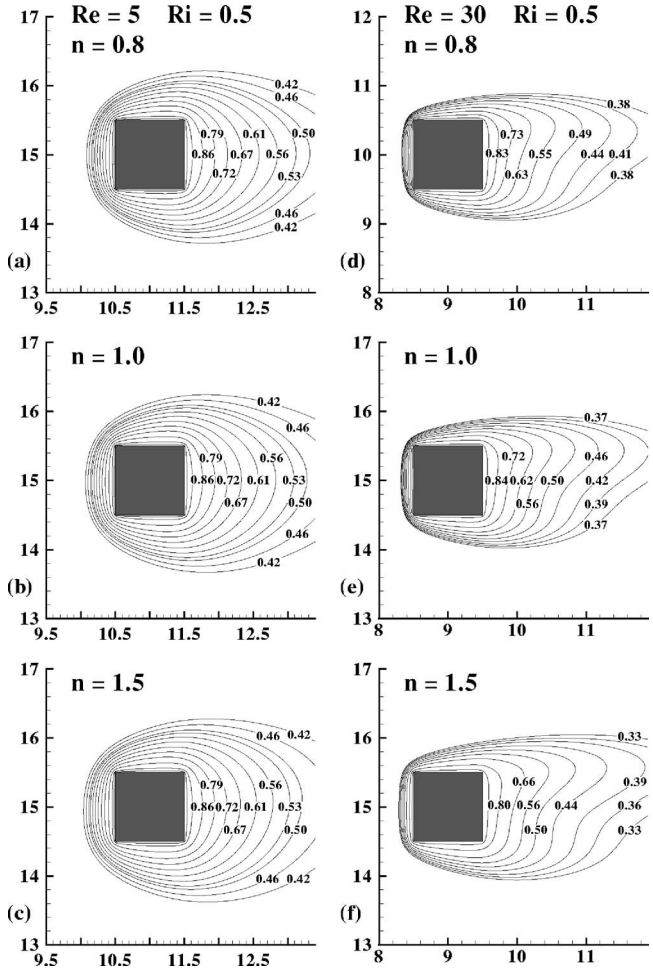

Fig. 3 Isotherm profiles for Re=5 and 30, Ri=0.5, and Pr=1 at different values of *n*

the flow field becomes asymmetric, as also noted by others [19,20]. Irrespective of the value of n, the circulation of the fluid behind the cylinder for Re=5 is seen to be almost absent due to the cross-buoyancy effect (Figs. 2(*a*)–2(*c*)). On the other hand, at Re=30, a vortex appears which is detached from the rear of the cylinder. Evidently, the flow is asymmetrical with a larger flow rate going below the cylinder than that above the cylinder (Figs. 2(*d*)–2(*f*)).

The effects of the Richardson number and of the power-law index on the thermal boundary layer is shown by plotting isotherms for Re=5 and 30 in Fig. 3. It is useful to recall that the temperature field is symmetrical about the center line for a range of conditions $\mathrm{Re} \leqslant 45$ and $\mathrm{Pe} \leqslant 4000$ for Ri=0 [1], while for mixed convection, no such symmetry exists, but the asymmetry in the temperature field also increases with the increasing Richardson number and/or Reynolds number (Fig. 3). It is also seen that isotherms turn sharply at the lower rear corner for Re=30 (Figs. 3(*d*)–3(*f*)). This clearly suggests that the cross-buoyancy influences the flow on the rear surface much more than that on the other surfaces of the cylinder. The effect of the power-law index on the isotherms is seen to be rather small. Slight thinning of the thermal boundary layer is evident for non-Newtonian fluids.

5.3 Drag and Lift Coefficients. Intuitively, one would expect the dramatic changes in the detailed kinematics to influence the values of the gross parameters too, namely, drag coefficient (C_D), and lift coefficient (C_L). Both the drag ($2F_D/\rho U_\infty^2 b$) and lift ($2F_L/\rho U_\infty^2 b$) coefficients are made up of pressure and friction forces, respectively. Table 2 shows the effects of Ri and n on the values of the drag coefficient for Re=5,30 and Pr=1 for three values of power-law index. The effect of the power-law fluid index on the drag is seen to be qualitatively similar both in the forced and mixed convection conditions, i.e., it is reduced below the Newtonian value for $n>1$ and enhanced for $n<1$ at Re=5. On the other hand, this dependence flips over at Re=30. It is also observed that the value of the drag coefficient decreases with the increasing value of the Richardson number for fixed values of n and the Reynolds number.

The appearance of a nonzero value of lift, even in the steady cross-flow regime, is clearly due to the asymmetry in the flow field close to the square cylinder for $\mathrm{Ri} \neq 0$ which gives rise to unbalanced shearing and pressure forces, whereas owing to the complete symmetry about the midplane yields zero lift for Ri=0. Owing to the weak advection, the lift coefficient is negative at Re=5 for Ri=0.5; however for Re=30, the lift is absent for the range of conditions considered here. This is presumably due to the nature of the incoming velocity profile on the front of the cylinder. As a result, the downward directed force (or negative lift) for Re=5 is higher than that for Re=30 at a low value of Prandtl number (Pr=1).

5.4 Nusselt Number. The average Nusselt number for each surface of the square cylinder is obtained by averaging the local Nusselt number over each face of the obstacle. Finally, the overall mean value of the cylinder Nusselt number (Nu) is obtained by

Table 2 C_D, C_L, and Nu results for Re=5 and 30 at different values of n (0.8, 1, 1.5) and Ri

	Re=5								
	C_D			C_L			Nu (Pr=1)		
Ri	**0.8**	**1**	**1.5**	**0.8**	**1**	**1.5**	**0.8**	**1**	**1.5**
0	5.305[a]	4.833[a]	4.096[a]	0	0	0	1.398	1.344[b]	1.282
0.5	4.965	4.508	3.789	−1.911	−1.852	−1.644	1.384	1.332	1.272
	Re=30								
	C_D			C_L			Nu (Pr=1)		
0	1.930[a]	1.978[a]	2.066[a]	0	0	0	2.860	2.704[b]	2.476
0.5	1.856	1.918	2.012	0	0	0	2.848	2.703	2.490

[a]Dhiman et al. [2].
[b]Dhiman et al. [1].

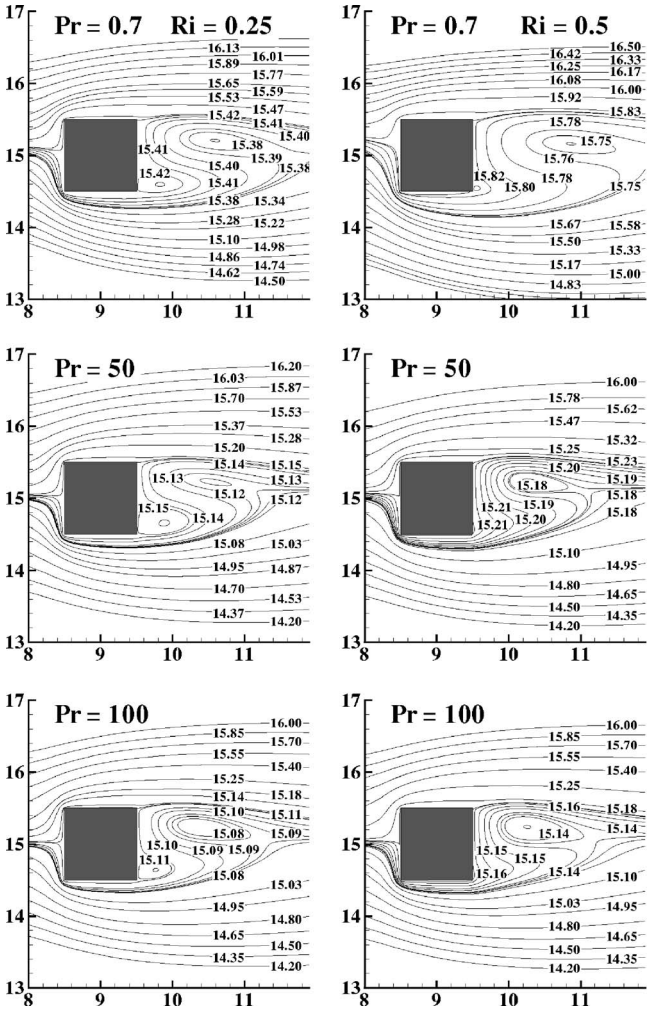

Fig. 4 Streamline profiles for Re=30, for Ri=0.25, and 0.5 at different Prandtl numbers

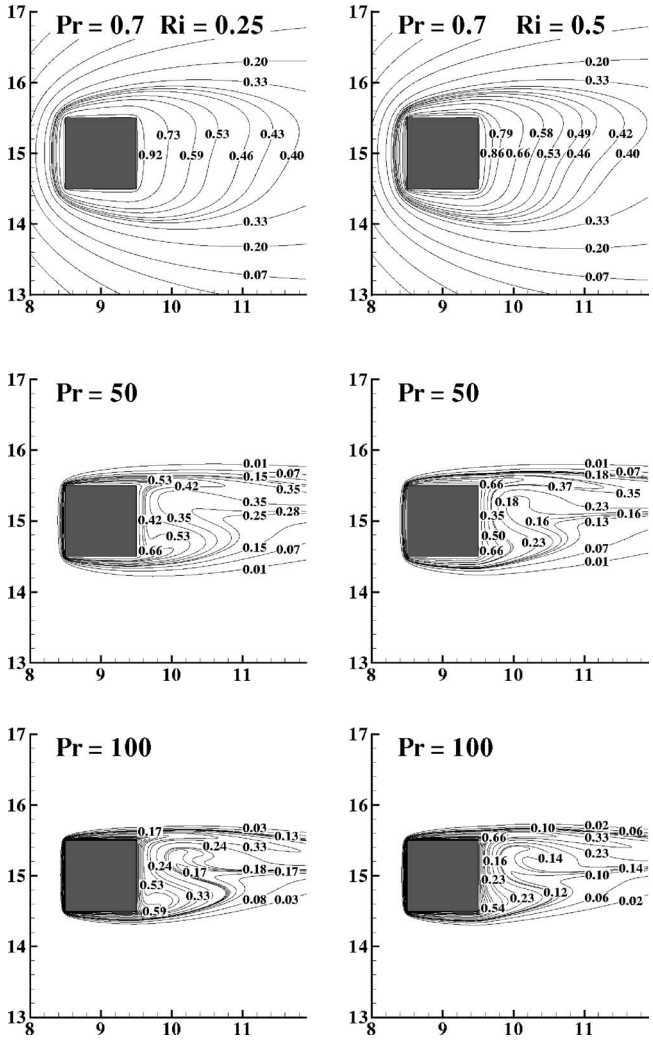

Fig. 5 Isotherm profiles for Re=30, for Ri=0.25, and 0.5 at different Prandtl numbers

averaging the individual average Nusselt number for each surface of the cylinder. Table 2 also shows the overall average value of the Nusselt number for Re=5,30 and Pr=1 at different values of power-law index and of the Richardson number. Similar to the drag results, the influence of the power-law index on the average Nusselt number, though weak, is seen to be similar in the forced and mixed convection conditions. The average Nusselt number is seen to decrease for Re=5 and 30 as the power-law index increases for both forced (Ri=0) and mixed (Ri=0.5) convection. However, the Nusselt number shows a weak dependence on the Richardson number regardless of the value of n, thereby suggesting that the modified definition of the Reynolds number adequately accounts for the effect of power-law rheology. This is partly due to the fact that the isotherm patterns seen in Fig. 3 are nowhere near as asymmetric as the streamline patterns seen in Fig. 2.

5.5 Effect of Prandtl Number on Newtonian Flow and Temperature Fields. The effect of the Prandtl number (Pr=0.7, 1, 5, 10, 50 and 100) on the flow and temperature fields is shown here by way of streamline (Fig. 4) and isotherm (Fig. 5) profiles, respectively, for the Newtonian flow ($n=1$) for an unconfined square cylinder. Here also, with the introduction of buoyancy superimposed on the forced flow (i.e., $\mathrm{Ri}\neq 0$), the flow pattern becomes increasingly asymmetric as the value of the Richardson number is gradually increased. It can also be seen from the streamline plots (Fig. 4) that the vortex behind the cylinder at the rear corner of the obstacle gradually diminishes as the Richardson number increases up to Ri=0.5 for $10\leqslant \mathrm{Re}\leqslant 30$ for all values of Prandtl number. This is partly due to the strong upward flow near the lower end of the cylinder.

Likewise, the symmetry of isotherm profiles about the midplane for Ri=0 (see Fig. 5), is lost with the introduction of buoyancy effects (i.e., $\mathrm{Ri}>0$). Figure 5 also shows the profound effect of Prandtl number on the gradual thinning of the thermal boundary layer.

5.6 Effect of Prandtl Number on Gross Parameters. In order to elucidate the influence of Prandtl number and of Richardson number on the flow and thermal parameters, the variations of drag and lift coefficients with Re and Pr are presented in Figs. 6(*a*)–6(*c*). Clearly, within the somewhat limited range of conditions covered here, the drag value is seen to be quite insensitive to the value of the Richardson number (Figs. 6(*a*)–6(*c*)), the maximum change being about 3% for Ri=0.25 and 0.5 at Re=5 and Pr=0.7.

On the other hand, the influence of the cross-buoyancy on the lift coefficient is seen to be significant (Figs. 6(*a*)–6(*c*)). At a low value of the Prandtl number (Pr=1) for a fixed value of the Richardson number, the lift coefficient increases with the increasing Reynolds number in the range $1\leqslant \mathrm{Re}\leqslant 30$ (Fig. 6(*a*)). The nature of the C_L–Re relationship is also strongly influenced by the value of the Prandtl number. For instance, at Pr=10, the lift is almost

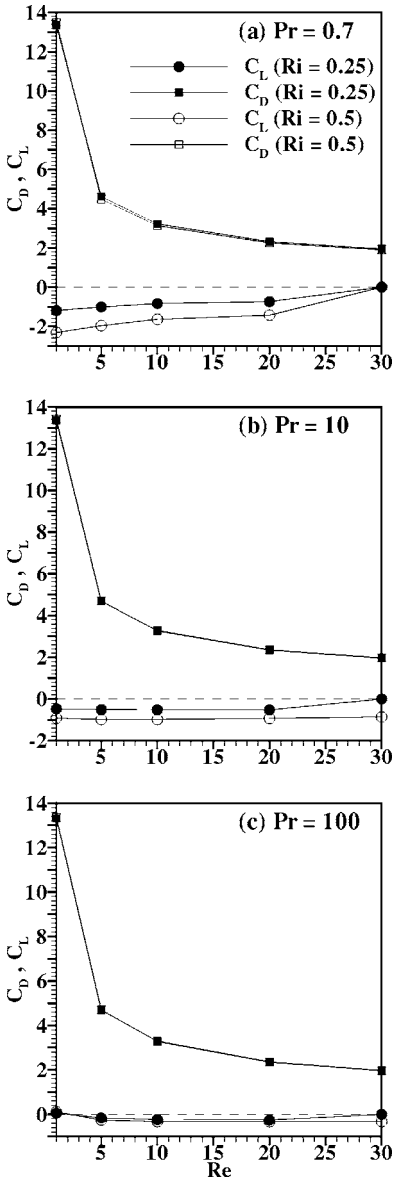

Fig. 6 Variation of C_D and C_L with Re at different Ri and Pr. The dashed line presents the results for Ri=0 case.

independent of the Reynolds number for $\mathrm{Re} \leqslant 20$ and it increases slightly at Re=30 (Fig. 6(*b*)). Yet at a high Prandtl number of 100 (Fig. 6(*c*)), the lift coefficient is seen to decrease with the Reynolds number in the range $1 \leqslant \mathrm{Re} \leqslant 20$, whereas it rises a little for Re=30 for a fixed Richardson number.

In spite of the fact that the buoyancy alters the flow and temperature fields appreciably, the value of the Nusselt number is even less sensitive to the value of Ri than the drag coefficient. For instance, the maximum change in the value of the average Nusselt number is 1.5% for Ri=0.25 and 0.5. However, the average Nusselt number increases monotonically with the Reynolds number and/or Prandtl number for a fixed value of the Richardson number.

6 CONCLUSIONS

In this study, the general characteristics of the combined effects of forced and natural convection (mixed convection) on the flow and the heat transfer during the steady, incompressible flow of viscous Newtonian and power-law fluids over a heated square cylinder placed normally to the approaching fluid have been explored numerically. The results presented herein embrace the range of conditions as follows: Reynolds number 5 and 30, power-law index 0.8–1.5, Prandtl number of 1, and Richardson number 0–0.5. These results are supplemented by further exploring the effect of Prandtl number for Newtonian fluids in the range of conditions as $1 \leqslant \mathrm{Re} \leqslant 30$, $0.7 \leqslant \mathrm{Pr} \leqslant 100$, and $0 \leqslant \mathrm{Ri} \leqslant 0.5$.

As expected, the mixed convection conditions can initiate asymmetry in the flow and temperature fields even within the steady flow regime, i.e., at $\mathrm{Re} \leqslant 45$. The effects of Prandtl number and of power-law index on the average Nusselt number in the mixed convection regime are qualitatively similar to that in the forced convection case for the range of physical parameters considered here. The total drag coefficient and the average Nusselt number show rather weak dependence on the Richardson number in the steady cross-flow regime.

NOMENCLATURE

b = side of the square cylinder (m)
C_D = total drag coefficient $=2F_D/\rho U_\infty^2 b$
C_L = total lift coefficient $=2F_L/\rho U_\infty^2 b$
c_p = specific heat of the fluid (J/kg K)
f = shedding frequency (L/s^{-1})
F_D = drag force on the cylinder (N/m)
F_L = lift force on the cylinder (N/m)
Gr = Grashof number $g\beta_V(T'_w - T_\infty)\rho^2 U_\infty^{2(1-n)} b^{(2n+1)}/\mathrm{m}^2$
h = heat transfer coefficient ($\mathrm{W/m^2\,K}$)
H = height of the computational domain in the lateral direction (m)
k = thermal conductivity of the fluid (W/m K)
L = length of the computational domain in the axial direction (m)
L_u = upstream face distance of the cylinder from the inlet (m)
L_d = downstream face distance of the cylinder from the outlet (m)
M = number of grid points in the x direction
m = power-law consistency index ($\mathrm{Pa\,s}^n$)
N = number of grid points in the y direction
n = power-law index
Nu = average Nusselt number of the cylinder $=hb/k$
p = pressure $=p'/(\rho U_\infty^2)$
Pe = Péclet number $=\mathrm{RePr}$
Pr = Prandtl number $=(mc_p/k)(U_\infty/b)^{n-1}$
Re = Reynolds number $=\rho U_\infty^{2-n} b^n/\mathrm{m}$
Ri = Richardsson number $=\mathrm{Gr/Re}^2$
St = Strouhal number $=fb/U_\infty$
t = time $=t'/(b/U_\infty)$
T = temperature $=(T'-T_\infty)/(T'_w - T_\infty)$
T_∞ = temperature of the fluid at the channel inlet (K)
T'_w = Constant wall temperature at the surface of the cylinder (K)
U_∞ = velocity of the fluid at the inlet (m/s)
V_x = component of the velocity in x direction $=u'/U_\infty$
V_y = component of the velocity in y direction $=v'/U_\infty$
x = stream-wise coordinate $=x'/b$
y = transverse coordinate $=y'/b$

Greek Symbols

β_V = coefficient of volumetric expansion (1/K)
ε = component of the rate of deformation tensor $=\varepsilon'/(U_\infty/b)$
η = power-law viscosity $=\eta'/\eta_0$
η_0 = reference viscosity (Pa s) $=m(U_\infty/b)^{n-1}$

I_2 = second invariant of the rate of deformation tensor$=I_2'/(U_\infty/b)^2$

ρ = density of the fluid (kg/m^3)

Subscripts

∞ = inlet condition

w = surface of the square cylinder

Superscript

$'$ = dimensional variable

References

[1] Dhiman, A. K, Chhabra, R. P., Sharma, A., and Eswaran, V., 2006, "Effects of Reynolds and Prandtl Numbers on the Heat Transfer Across a Square Cylinder in the Steady Flow Regime," Numer. Heat Transfer, Part A, **49**, pp. 717–731.

[2] Dhiman, A. K, Chhabra, R. P., and Eswaran, V., 2006, "Steady Flow of Power-Law Fluids Across a Square Cylinder," Chem. Eng. Res. Des., **84**(A4), pp. 300–310.

[3] Dhiman, A. K, Chhabra, R. P., and Eswaran, V., 2005, "Flow and Heat Transfer Across a Confined Square Cylinder in the Steady Flow Regime: Effect of Peclet Number," Int. J. Heat Mass Transfer, **48**, pp. 4598–4614.

[4] Dhiman, A. K., Chhabra, R. P., and Eswaran, V., 2006, "Effect of Peclet Number on the Heat Transfer Across a Square Cylinder in the Steady Confined Channel Flow Regime," Proc. 18th National and 7th ISHMT-ASME Heat and Mass Transfer Conf., Indian Institute of Technology, Guwahati, India, January 4–6.

[5] Paliwal, B., Sharma, A., Chhabra, R. P., and Eswaran, V., 2003, "Power-Law Fluid Flow Past a Square Cylinder: Momentum and Heat Transfer Characteristics," Chem. Eng. Sci., **58**, pp. 5315–5329.

[6] Badr, H. M., 1983, "A Theoretical Study of Laminar Mixed Convection From a Horizontal Cylinder in a Cross Stream," Int. J. Heat Mass Transfer, **26**, pp. 639–653.

[7] Badr, H. M., 1984, "Laminar Combined Convection From a Horizontal Cylinder—Parallel and Contra Flow Regimes," Int. J. Heat Mass Transfer, **27**, pp. 15–27.

[8] Noto, K., Ishida, H., and Matsumoto, R., 1985, "A Breakdown of the Karman Vortex Street due to the Natural Convection," *Flow Visualization* III, Springer, New York, pp. 348–352.

[9] Chang, K.-S., and Sa, J.-Y., 1990, "The Effect of Buoyancy on Vortex Shedding in the Near Wake of a Circular Cylinder," J. Fluid Mech., **220**, pp. 253–266.

[10] Hatanaka, K., and Kawahara, M., 1995, "A Numerical Study of Vortex Shedding Around a Heated/Cooled Circular Cylinder by the Three-Step Taylor-Gaylerkin Method," Int. J. Numer. Methods Fluids, **21**, pp. 857–867.

[11] Patnaik, B. S. V., Narayana, P. S. A., and Seetharamu, K. N., 1999, "Numerical Simulation of Vortex Shedding Past a Circular Cylinder Under the Influence of Buoyancy," Int. J. Heat Mass Transfer, **42**, pp. 3495–3507.

[12] Ahmad, R. A., and Qureshi, Z. H., 1992, "Laminar Mixed Convection From a Uniform Heat Flux Horizontal Cylinder in a Cross-Flow," J. Thermophys. Heat Transfer, **6**, pp. 277–287.

[13] Maas, W. J. P. M., Rindt, C. C. M., and van Steenhoven, A. A., 2004, "The influence of heat on the 3-D transition of the von Karman vortex street," Int. J. Heat Mass Transfer, **46**, pp. 3069–3081.

[14] Ren, M., Rindt, C. C. M., and van Steenhoven, A. A., 2004, "3-D vortices in the wake flow behind a heated cylinder," Int. J. Transp. Phenom., **6**, pp. 177–187.

[15] Abu-Hijleh, B. A. K, 1999, "Laminar Mixed Convection Correlations for an Isothermal Cylinder in Cross Flow at Different Angles of Attack," Int. J. Heat Mass Transfer, **42**, pp. 1383–1388.

[16] Wang, A. B., Travnicek, Z., and Chia, K. C., 2000, "On the Relationship of Effective Reynolds Number and Strouhal Number for the Laminar Vortex Shedding of a Heated Circular Cylinder," Phys. Fluids, **12**, pp. 1401–1410.

[17] Zdravkovich, M. M., 1997, *Flow Around Circular Cylinders: Fundamentals*, 1, Oxford University Press, New York.

[18] Zdravkovich, M. M., 2003, *Flow Around Circular Cylinders: Applications*, 2, Oxford University Press, New York.

[19] Sharma, A., and Eswaran, V., 2004, "Effect of Aiding and Opposing Buoyancy on the Heat and Fluid Flow Across a Square Cylinder at Re=100," Numer. Heat Transfer, Part A, **45**, pp. 601–624.

[20] Bhattacharyya, S., and Mahapatra, S., 2005, "Vortex Shedding Around a Heated Square Cylinder Under the Influence of Buoyancy," Heat Mass Transfer, **41**, pp. 824–833.

[21] Biswas, G., Laschefski, H., Mitra, N. K., and Fiebig, M., 1990, "Numerical Investigation of Mixed Convection Heat Transfer in a Channel With a Built-In Square Cylinder," Numer. Heat Transfer, Part A, **18**, pp. 173–188.

[22] Turki, S., Abbassi, H., and Nasrallah, S. B., 2003, "Two-Dimensional Laminar Fluid Flow and Heat Transfer in a Channel With a Built-In Heated Square Cylinder," Int. J. Therm. Sci., **42**, pp. 1105–1113.

[23] Sharma, A., and Eswaran, V., 2005, "Effect of Channel-Confinement and Aiding/Opposing Buoyancy on the Two-Dimensional Laminar Flow and Heat Transfer Across a Square Cylinder," Int. J. Heat Mass Transfer, **48**, pp. 5310–5322.

[24] Anjaiah, N., Dhiman, A. K., and Chhabra, R. P., 2006, "Mixed Convection Heat Transfer From a Square Cylinder to Power-Law Fluids in Cross-Flow," Proceeding's Symposium on Flows in Manufacturing Processes, ASME Joint U.S.–European Fluids Engineering Summer Meeting, Miami, FL, July 17–20.

[25] Eswaran, V., and Prakash, S., 1998, "A Finite Volume Method for Navier-Strokes Equations," Proc. 3rd Asian CFD Conference, Bangalore, India, Dec. 7–11, Vol. 1, pp. 127–136.

[26] Sharma, A., and Eswaran, V., 2003, "A Finite Volume Method" *Computational Fluid Flow and Heat Transfer*, K. Muralidhar and T. Sundararajan, eds., Narosa Publishing House, New Delhi, India, pp. 445–482.

[27] Thompson, J. F., Warsi, Z. U. A., and Mastin, C. W., 1985, *Numerical Grid Generation: Foundation and Applications*, Elsevier Science, New York, pp. 305–310.